NASA/CR—2006-214326

NASA Hydrogen Research at Florida Universities

Program Year 2003

David L. Block and Ali Raissi
Florida Solar Energy Center, Cocoa, Florida

August 2006

NASA STI Program . . . in Profile

Since its founding, NASA has been dedicated to the advancement of aeronautics and space science. The NASA Scientific and Technical Information (STI) program plays a key part in helping NASA maintain this important role.

The NASA STI Program operates under the auspices of the Agency Chief Information Officer. It collects, organizes, provides for archiving, and disseminates NASA's STI. The NASA STI program provides access to the NASA Aeronautics and Space Database and its public interface, the NASA Technical Reports Server, thus providing one of the largest collections of aeronautical and space science STI in the world. Results are published in both non-NASA channels and by NASA in the NASA STI Report Series, which includes the following report types:

- TECHNICAL PUBLICATION. Reports of completed research or a major significant phase of research that present the results of NASA programs and include extensive data or theoretical analysis. Includes compilations of significant scientific and technical data and information deemed to be of continuing reference value. NASA counterpart of peer-reviewed formal professional papers but has less stringent limitations on manuscript length and extent of graphic presentations.

- TECHNICAL MEMORANDUM. Scientific and technical findings that are preliminary or of specialized interest, e.g., quick release reports, working papers, and bibliographies that contain minimal annotation. Does not contain extensive analysis.

- CONTRACTOR REPORT. Scientific and technical findings by NASA-sponsored contractors and grantees.

- CONFERENCE PUBLICATION. Collected papers from scientific and technical conferences, symposia, seminars, or other meetings sponsored or cosponsored by NASA.

- SPECIAL PUBLICATION. Scientific, technical, or historical information from NASA programs, projects, and missions, often concerned with subjects having substantial public interest.

- TECHNICAL TRANSLATION. English-language translations of foreign scientific and technical material pertinent to NASA's mission.

Specialized services also include creating custom thesauri, building customized databases, organizing and publishing research results.

For more information about the NASA STI program, see the following:

- Access the NASA STI program home page at *http://www.sti.nasa.gov*

- E-mail your question via the Internet to *help@sti.nasa.gov*

- Fax your question to the NASA STI Help Desk at 301–621–0134

- Telephone the NASA STI Help Desk at 301–621–0390

- Write to:
  NASA STI Help Desk
  NASA Center for AeroSpace Information
  7121 Standard Drive
  Hanover, MD 21076–1320

NASA/CR—2006-214326

NASA Hydrogen Research at Florida Universities

Program Year 2003

David L. Block and Ali Raissi
Florida Solar Energy Center, Cocoa, Florida

Prepared under Grant NAG3–2751

National Aeronautics and
Space Administration

Glenn Research Center
Cleveland, Ohio 44135

August 2006

This report contains preliminary findings, subject to revision as analysis proceeds.

Level of Review: This material has been technically reviewed by NASA expert reviewer(s).

Available from

NASA Center for Aerospace Information
7121 Standard Drive
Hanover, MD 21076–1320

National Technical Information Service
5285 Port Royal Road
Springfield, VA 22161

Available electronically at http://gltrs.grc.nasa.gov

Contents

NASA Hydrogen Research at Florida Universities Program Year 2003

PI: D. Block, Florida Solar Energy Center
A. T-Raissi, Florida Solar Energy Center

Abstract

This document presents the final report for the NASA Hydrogen Research at Florida Universities project for program year 2003. This multiyear hydrogen research program has positioned Florida to become a major player in future NASA space and space launch projects. The program is funded by grants from NASA Glenn Research Center with the objective of supporting NASA's hydrogen-related space, space launch and aeronautical research activities. The program conducts over 40 individual projects covering the areas of cryogenics, storage, production, sensors, fuel cells, power and education.

At the agency side, this program is managed by NASA's Glenn Research Center and at the university side, co-managed by FSEC and the University of Florida with research being conducted by FSEC and seven Florida universities: Florida International University, Florida State University, Florida A&M University, University of Central Florida, University of South Florida, University of West Florida and University of Florida. For detailed information, see the documents section of www.hydrogenresearch.org. This program has teamed these universities with the nation's premier space research center, NASA GRC, and the nation's premier space launch facility, NASA Kennedy Space Center.

It should be noted that the NASA Hydrogen Research at Florida Universities program has provided a shining example and a conduit for seven Florida universities within the SUS to work collaboratively to address a major problem of national interest, hydrogen energy and the future of energy supply in the U.S.

NASA Benefits

Lowering Payload-to-Orbit Costs.—Densified propellants can lower payload-to-orbit costs because they enable more cryogenic propellant to be packed into a given volume. Assuming a launch cost of about $4,000 to $10,000 per pound, this weight savings translates into an increased payload value of $20 to $50 million for each launch.

Hydrogen Production Storage and Handling.—Using data from the past 21 years, the Space Shuttle has been launched, successfully, an average of five times per year (109 launches, in all), at a cost of more than $5 million annually for its hydrogen fuel. The research will provide savings in four major areas:

- The annual cost for trucking the needed hydrogen from Louisiana to the Kennedy Space Center is $2 million. Producing hydrogen locally will eliminate these transportation costs.
- For each launch, more than 50 semi-tractor-trailers must drive 640 miles from New Orleans to KSC to deliver the hydrogen. Local production will eliminate the infrastructure costs related to increased highway usage and the potential for accidents on our busy interstate highway system.
- At the launch site, 400,000 gallons of liquid hydrogen is lost because of storage boil-off and transfer. Capturing boil-off and improving hydrogen transport technologies can save an additional $250,000 per year.
- From past history, KSC has been able to launch the Shuttle, successfully, three out of every 5 attempts - or 60 percent of the time (109 times out of 191 possible launches). The scrubbing of 82 shuttle launches has resulted in an average annual loss of $2 million in hydrogen costs alone, which could have been saved if NASA had produced hydrogen locally. These savings grow significantly when considering future Cape flight schedules, which call for greatly expanded launch schedules of more than 50 per year – schedules that can only be met if liquid hydrogen is produced and densified locally near the Cape.
- Another very important aspect of having local hydrogen production at KSC is that it provides valuable data for operating future automotive fueling stations. Our analysis has shown that the KSC launch operation mimics future vehicular hydrogen fueling stations in both fuel volume dispensed and its

energy content. Thus, the local hydrogen production at KSC will present a model that will be replicated throughout the U. S. for the nation's future hydrogen economy.

Projects at Each of the Universities

The cooperative efforts of the state's universities are evident in the work supported by the NASA grant. The premise of the SUS effort is that fundamental and applied research is required to create the "disruptive" technologies that will push hydrogen from being a "potential" solution to the nation's transportation energy dilemma to that of dominating energy vector. New corporations and investment capital follows those that successfully engineer the disruptive technologies of the future. Each of our partner universities has identified areas of expertise and interest while contributing to the overall success of the program. A brief discussion of program year 2003 accomplishments by university follows:

Florida Solar Energy Center

- Densified Hydrogen – Researchers have designed and constructed the first ever small-scale cryocooler capable of maintaining hydrogen at 16.5 K with zero boil-off.
- Photoelectrochemical Water Splitting Using a Multiple Bandgap Thin-Film Photovoltaic-Cell – Laboratory scale cells and a photoanode container have been developed that show a solar to hydrogen conversion efficiency of greater than 5 percent at one sun insolation.
- High Temperature Separation Membranes – Researchers have developed novel gas separation membranes with mixed ionic-electronic conductivity based on perovskite and pyrochlore material structures.
- Liquid Hydrogen Storage – This task has validated a 3-D CFD simulation model against measured data from NASA KSC Pad A and B tanks. Researchers have estimated the size of the Pad B void area and the amount of perlite insulation remaining and showed that external insulation will not be an effective solution.
- Hydrogen Sulfide Methane Reforming – Researchers have developed a high-temperature thermochemical process to reform hydrogen sulfide and methane from ultra sour natural gas resources of Florida. The process converts a toxic compound, hydrogen sulfide, into useful products – hydrogen and sulfuric acid.
- Photoelectrochemical Hydrogen Production – This process is based on the use of organic pigments deposited on wide band gap semiconductors to perform oxidative and reductive water-splitting to generate hydrogen from water. Its unique advantage is lower capital cost.
- Hydrogen Purification and Storage Using Lithium Borohydrides – This project has developed a complete hydrogen capture and purification system using lithium borohydride. The novel aspects of the system are its large storage capacity, low cost and the ability to regenerate of the borohydride material.
- Smart Paint Hydrogen Detection – Researchers have developed and demonstrated a smart paint material that will change color to reveal the presence of hydrogen. Recent innovations have demonstrated the ability of the material to reverse to the original color when the hydrogen flow stops.
- Local Hydrogen Production via Catalytic Reformation of Fossil and Renewable Feedstocks – This project developed and demonstrated a novel catalytic hydrogen production process with 80 percent efficiency and 99.9 vol % purity at a significantly reduced greenhouse gas emissions. The value of the carbon byproduct lowers the net hydrogen cost below present NASA costs.
- Hydrogen Storage in Amine Boranes – Researchers have demonstrated hydrogen storage of up to 20 percent by weight (as compared to DOE storage goal of 6 percent by weight) by hydrogenation of various amine borane complexes.
- Waste Oil to Hydrogen – This project developed a new process to produce hydrogen from used lubricating oils at a cost of one-tenth of the current NASA price ($0.40/kg versus $4.50/kg). The quantity of waste oil generated in Florida can supply hydrogen for more than 100 Shuttle launches per year.

Florida International University

- Citrus Peel Gasification – This project designed and constructed a biomass gasification unit for hydrogen production using Florida citrus peel waste. The unit has successfully generated hydrogen with yields as high as 51 percent.
- Florida Biomass Resource – This project produced map on the availability of the major biomass resources in Florida using GPS technology.

Florida State University

- Optical Mass Gauging – A proof of concept optical mass gauging device has been constructed and used to measure mass of solid hydrogen in liquid helium. The device detects hydrogen mass by measuring the absorption of laser light at the resonant frequency of solid hydrogen. The system will work in a micro-gravity environment.
- Experimental and Numerical Investigations of Cryogenic Multiphase Flow – This project has developed fundamental understanding of cryogenic multiphase flows in order to predict the solidification of hydrogen particles in liquid helium and the transport of these particles in a horizontal channel. These are original experiments generating unique data and the knowledge will increase understanding of solid hydrogen particle fuel systems for future spacecraft.
- Fundamental Properties of Densified Liquid Hydrogen and Oxygen at Sub-Cooled Temperatures – Experimental measurements have been completed giving liquefied hydrogen and oxygen transport property data at below 20 K that is one order of magnitude improvement over past NIST data.

University of Central Florida

- Reverse Turbo Brayton Cycle Cryocooler for Liquid Hydrogen Systems – Researchers have designed and built a miniature and fully integrated helium compressor and motor which is capable of removing 20-30 W of heat at 18K with a projected mass of 22 kg (10 times less than existing technology). The cryocooler will be required for future manned and robotic Mars missions and will find wide applications in distributed power generation fuel cells and microturbines.
- Hydrogen and Helium Separation, Recovery, and Purification – This project discovered that the addition of an inexpensive dopant increases hydrogen storage capacity and kinetics yielding a significantly cheaper and more efficient storage system. The project has also resulted in the development of a novel gas-phase reaction and a patent application. (Project is cooperative effort with D. Slattery of FSEC.)
- Highly Sensitive Room Temperature Sensor – Existing hydrogen sensors operate at high temperatures and pose a potential risk for explosion. This new sensor integrates nanostructures into a MEMS device to detect hydrogen at room temperatures.
- Shape Memory Actuator Materials – Researchers have developed and fabricated a thermo mechanical processing methodology for cryogenic shape memory actuator materials. These new materials are applicable to thermal conduction switching at cryogenic temperatures.

University of South Florida

- Rectenna – This project developed innovative full rectification structures and a method to capture orthogonal polarizations with a single rod antenna and electromagnetic coupling to be used for capturing solar energy by a rectenna (patent submitted).
- Magnetic Liquefaction – This project developed new technology based on magneto-caloric materials with potential to double efficiency of microcoolers for liquefaction of hydrogen.
- Hydrogen Sensors – This project produced hydrogen sensors based on nano-material sensing layers and shear mode acoustic wave. Results have demonstrated sensitivity improvements of 50-100 fold for organic vapors, faster response times and capability to operate in a wide temperature range.
- Hydrogen Storage Simulation – This project developed the only available numerical simulation model to predict fluid circulation and heat transfer in a liquid hydrogen storage vessel used by NASA.

University of West Florida

- Launch, Fueling and Processing Software Agents – Researchers at the Institute for Human and Machine Cognition have advanced the state-of-the-art for space shuttle fueling and launch processing by applying automated real-time monitoring of complex process conditions and imposing dynamic user-defined limits and alarm conditions.

Reports and Presentations

Numerous formal written reports and conference papers have been developed which have presented the results of the funded work. The program year 2003 accomplishments by numbers are as follows:

- Individual university projects: 42
- Faculty/staff involved: 85
- Students involved: close to 100
- Publications: more than 100
- Presentations: more than 100
- Patent applications filed: 12

In addition, the NASA project has been leveraged by the University faculty to produce more than $10 million in additional hydrogen related funding that was secured from other federal agencies – DOE, DOD and NSF. The NASA work has also produced several tens of millions of dollars of additional hydrogen-related R&D proposals that are still pending before various funding agencies.

Final Reports for Each Individual Project by University

The next sections of this final report present each of the individual final reports for the projects funded by this program. The final reports are organized as individual reports from each of the universities and are presented in the following order:

Florida Solar Energy Center

Baik, J. -- Experimental Design and Evaluation of ZBO of Cryogenic Systems
Baik, J. -- R & D Processes for Increasing the Fluid Density of Cryogenic Liquids
Dhere, N. -- Development of Tribological Coatings for Cryocoolers
Dhere, N. -- Photoelectrochemical Water Splitting for Hydrogen Production Using Multiple Bandgap Combination of Photovoltaic-Cell using Multiple Bandgap Combination of Photovoltaic-Cell and Photocatalyst
Elbaccouch, M. -- Characterization of Spin-Coated Terbium-Doped Strontium Cerate Thin Film Membranes
Gu, L. -- Liquid Hydrogen Storage at Kennedy Space Center
Henzmann, A. -- Education and Outreach
Huang, C. -- Analysis of Alternative Hydrogen Production Processes Liquid Hydrogen Production via Sub-Quality Natural Gases
Linkous, C. -- Hydrogen Production via Photocatalysis
Linkous, C. -- Hydrogen Purification and Storage Using Lithium Borohydride
Mohajeri, N. -- Smart Paints and Pigments for Hydrogen Sensing
Muradov, N. -- Local Hydrogen Production via Catalytic Reformation of Fossil and Renewable Feedstocks
Raissi, A. -- Hydrogen Storage and Recovery in Ammonia Borane Complex
Raissi, A. -- Hydrogen Production from Used Lube Oil via Supercitical Water Reformation
Raissi, A. -- System Analysis of Hydrogen Production and Utilization at KSC

Florida International University

Srivastava, R. -- Development and Demonstration of a Pilot-Scale Biomass Gasification Unit for Hydrogen Production

Florida State University

Van Sciver, S. -- Development of Optical Systems for Mass and Two Phase Flow Gauging
Van Sciver, S. -- Experimental and Numerical Investigations of Cryogenic Multiphase Flow
Van Sciver, S. -- Measurement of Transport Properties of Densified LH_2 and LO_2

University of Central Florida

Chow, L. -- Reverse Turbo Brayton Cycle Cryocooler Development for Liquid Hydrogen Systems
Hampton, M. -- Metal Hydrides for Hydrogen for Hydrogen Separation, Recovery and Purification (Cooperative effort with D. Slattery of FSEC)
Seal, S. -- High Selective Nano-MEMS Low Temperature Sensor
Sellar, G. -- Novel Technique for the Detection and Location of Hydrogen Leaks
Vaidyanathan, R. -- Development of Cryogenic Shape-Memory Actuator Materials for Switches, Seals and Valves

University of South Florida

Bhansali, S. -- Prototype and Simulation Model for a MEMS Magneto-Caloric Refrigerator
Bhethanbotla, V. -- Hydrogen Gas Sensors by Surface Acoustic Waves
Buckle, K. -- Development of Rectenna Solar Energy Conversion for Local Hydrogen Production
Rahman, M. -- Development of a Numerical Simulation Model for Thermo-Fluid Analysis and Design Optimization of Cryogenic Storage Systems with Zero Boiloff
Stefanakos, E. -- By-Product Hydrogen Production
Wolan, J. -- Hydrogen Production via Methane Nonoxidative Aromation

University of West Florida

Bunch, L. -- Software Agents and Knowledge Discovery and Data Mining for Enhanced Safety and Control of Hydrogen Operations

The complete name, title and affiliation of each project investigator is presented in appendix A.

Development and Demonstration of a Pilot-Scale Biomass Gasification Unit for Hydrogen Production

PI: R. Srivastava (Florida International University)
A. Mazumdar (Florida International University)
W. Conklin (Florida International University)
Z. Chen (Florida International University)
G. Philippidis (Florida International University)

Executive Summary

Concerns about the depletion of fossil fuel reserves, energy security, and pollution caused by continuously increasing energy demands make biomass and hydrogen attractive alternative energy sources. Recently, there has been an increasing interest in taking the necessary steps to move towards a hydrogen-based economy. Furthermore, the NASA Kennedy Space Center (KSC) and the Cape Canaveral Air Force Station (CCAFS) will eventually be required to manufacture the hydrogen they use locally. Local production of hydrogen is necessitated by economic, transportation safety, and energy security considerations. It is therefore desirable to investigate what improvements can be made to hydrogen operations at the spaceport facilities considering new hydrogen production and storage technologies under research and development at universities, federal facilities and industrial research laboratories through the auspices of the NASA Hydrogen Research Program. Hydrogen is currently derived from nonrenewable resources by steam reforming in which fossil fuels, primarily natural gas, react with steam at high pressures and temperatures in the presence of a nickel-based catalyst. In principle, hydrogen can also be generated from renewable resources such as biomass by gasification. Gasification yields clean fuel gas that makes a wide array of power options possible, including traditional internal combustion engines and fuel cells. Earlier, citrus peels had been identified as a promising local fuel source due to its overabundance and depressed market value. The farmland acreage dedicated to citrus almost exceeds 800,000. The citrus industry generates more than 1 million tons/yr of citrus waste residue (dry basis). The research focuses on utilizing waste residue from juice production to co-produce hydrogen and heat. Hydrogen can then be used to generate electricity and additional heat. The pilot-scale gasification system has been designed using mostly off-the-shelf components. Bench-scale batch citrus peel gasifier experiments have shown that high hydrogen yields are possible.

Background

Concerns about the depletion of fossil fuel reserves, energy security, and pollution caused by continuously increasing energy demands make biomass and hydrogen attractive alternative energy sources that require further development towards commercialization. The nation's reliance on imported oil and the continued volatility in the Middle-East necessitate the development of alternative energy sources. NASA's KSC is one of the primary users of hydrogen in the state of Florida. Hydrogen is used as rocket fuel and in the fuel cells for spacecrafts. The KSC spaceport hydrogen requirements vary due to fluctuations in launch activities, program changes and other technical and weather related factors. This historically has had an adverse effect on the hydrogen procurement costs from commercial off-site locations. In addition, quiescent storage tank boil-off and losses due to transfer operations add to the operational expenses. Coupled with this is manpower costs associated with tanker offloading and concerns with transportation safety and production disruptions. Local production of hydrogen will alleviate some of the concerns related to transportation safety and energy security.

Hydrogen is currently derived from nonrenewable resources using steam reforming in which fossil fuels, primarily natural gas, react with steam at high pressures and temperatures in the presence of a nickel-based catalyst. Another possible pathway for hydrogen generation is through gasification of renewable resources. Among the available renewable resources, biomass holds special promise as future fuel and feedstock. Biomass is eco-friendly, locally available in abundance and hence an excellent distributed energy source. Sustainable exploitation of biomass for generating energy has a potential to act as a catalyst for overall sustainable development. In order to increase the share of biomass (obtained

preferably from bio-residues) in the country's energy resource portfolio, new power generation systems need to be developed to provide high-energy efficiency and clean environmental performance.

In Florida, almost 800,000 acres are planted with citrus trees. The Florida citrus industry processes more than 80 percent of the citrus crop into juice products. Fortunately, citrus processing plants are concentrated in a relatively small area within a radius of approximately 100 miles and sufficiently close to KSC. Figure 1 shows a map of the citrus processing facilities in Florida. During citrus juice processing, approximately one half of the fruit weight is left behind as waste. The Florida industry generates more than 1 million tons/yr of citrus waste residue on a dry basis. This residue cannot be disposed of in landfills due to its large volume. To dispose the citrus waste stream, the peel waste is dried into citrus peel pellets and sold as cattle feed to Europe. The value of citrus peel pellets has been declining over the last five years and is currently at approximately $40 to $45/ton, while the production costs range from $65 to $80/ton, depending on fuel cost for drying. The reasons for the decline in value are the abundance of other commodities available for use in cattle feed formulations, the low protein content of citrus peel compared to other feedstock, and temporarily, the lingering effect of the "mad cow" disease on European cattle operations. As a result, the disposition of the citrus peel as cattle feed is a losing venture and the Florida Citrus Processors Association is very keen on finding alternate uses for the citrus peel. Citrus peel and similar co-products represent a large reservoir of inexpensive raw material for the production of energy (combined electricity and heat). As a bio-based product, it has the potential to provide a distributed energy generation source particularly in the rural areas. We envision that the proposed citrus peel-based power plant in central Florida will serve as a prototype for other biomass based power plants elsewhere in the country.

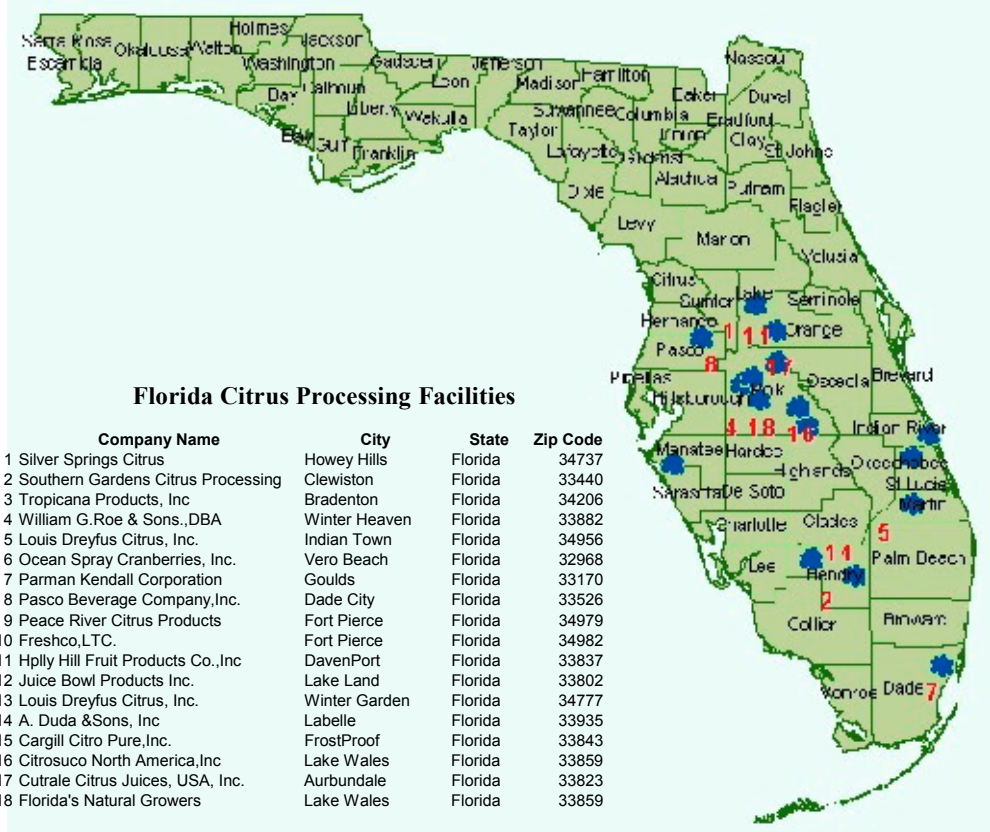

Figure 1.—Map showing Florida citrus processing facilities.

Objectives

The objective of the project is to design, fabricate, and operate a pilot-scale biomass gasification unit for the production of a hydrogen-rich gas from local Florida biomass resources, such as citrus peel, and to validate its performance, efficiency, economics, and reliability as a sustainable hydrogen source.

Vision

Successful demonstration of biomass gasification for hydrogen generation using local resources will bring a new generation of small-scale biomass residue power plants much closer to technical and economic reality. Data from the project will be used to ascertain the viability of a biomass gasification plant to address the long-term hydrogen needs of KSC (and CCAFS). Furthermore, the development of the new technology will help the local economy by developing a market for the citrus peel, a waste byproduct of citrus processing, and by generating jobs associated with power production.

Benefits to NASA

Data from the project will be used to ascertain the viability of biomass gasification plant to provide for the long- term NASA KSC hydrogen needs. Local production of hydrogen will secure a renewable and environmentally friendly fuel for the spaceport operations, Furthermore, the development of the new technology will help the local economy by generating jobs associated with power production. As a renewable energy source, biomass-derived hydrogen offers an alternative to conventional energy sources and provides environmental, rural economic growth, and national energy security benefits.

Results

The research focuses on the biomass gasification testing in a pilot-scale gasifier. Effort is directed towards maximizing the hydrogen yield in the synthesis gas, which is the main product of chemical conversion of biomass involving partial oxidation of the feedstock.

Ultimate and Proximate Analysis of the Citrus Pellets

The citrus peels pellets were obtained from Citrus World Inc. in Lake Wales, Florida. Citrus World, Inc. is one of the largest producers for Citrus products in the U.S.. The citrus pellets are used for the cattle feed. The citrus pellets have approximately 14 wt % moisture content. The ultimate composition is shown in table 1. The peels show an equivalent amount of Hydrogen that is present in wood chips. The ultimate analysis does show trace amounts of Sulfur that may have to be dealt with the downstream side of the gasifier.

TABLE 1.—ULTIMATE ANALYSIS OF THE CITRUS PEELS PELLETS

Elements	wt %	Method used
Carbon	38.80	ASTM D 5291
Hydrogen	6.71	ASTM D 5291
Nitrogen	0.91	ASTM D 5291
Oxygen	43.86	ASTM D 5291
Sulfur	0.052	ASTM D 1552
Ash	9.67	----

The elemental analysis (table 2) on ash revealed the following metals. Sodium, potassium, calcium, magnesium, and silicon are the major elements found in ash. Solid wastes generated will be subject to the state of Florida leaching tests and will need to be certified as non-hazardous. We plan to carry out the leaching tests once the pilot-scale gasifier is operational so that the ash can be certified and can be disposed of using conventional methods.

TABLE 2.—ELEMENTAL ANALYSIS OF ASH

Element	(mg/kg)	Element	(mg/kg)
Sodium	126.1	Barium	4.610
Manganese	5.211	Boron	7.227
Nickel	2.544	Chromium	1.570
Copper	2.830	Magnesium	1926
Potassium	7025	Silicon	44.11
Calcium	17090	Rubidium	2.168
Iron	62.80	Vanadium	8.224
Aluminum	58.32	Zinc	7.526

Preliminary Simulation Results

Using the elemental analysis and a gasifier model developed by researchers from Biomass Gasification Group (BGG) of the Department of Mechanical Engineering at the Technical University of Denmark was used to carry out preliminary simulations. The gasifier model assumes a downdraft type gasifier with air and steam as gasification agents. The schematic of the gasifier is shown in figure 1.

The model is based on mass and energy balances and chemical equilibrium and does not take into account the reaction kinetics and/or mass transport. As such, its use is limited to first approximations only. Some of the results are summarized in appendix A. We also tried to use ASPEN Plus (Aspen Technology, Inc.) for the simulation. However, since FIU does not have a chemical engineering program the procurement of the software was cost prohibitive given the budgetary constraints. We plan to use the expertise of UCF researchers led by Dr. Ali Raissi for ASPEN simulations once we have data from the pilot-scale gasifier.

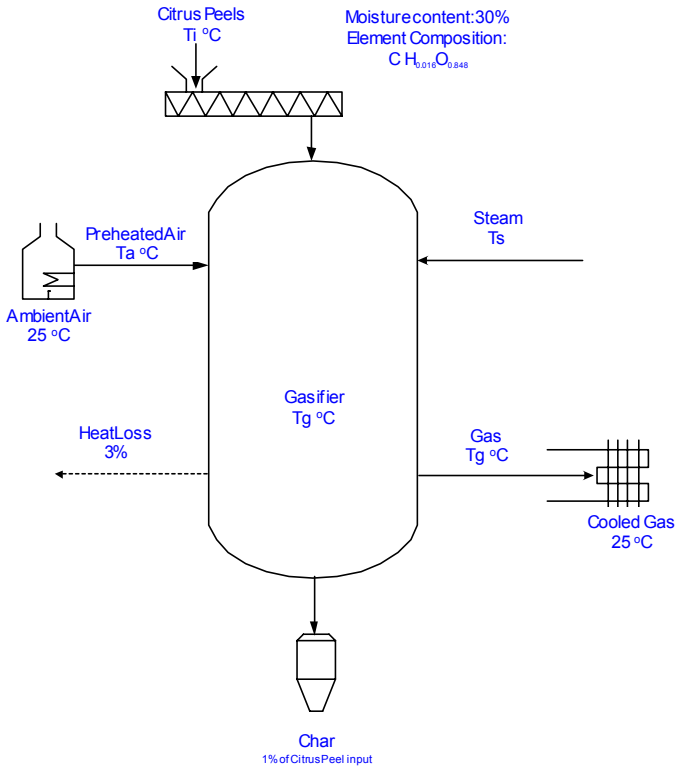

Figure 2.—Schematic of a simplified gasifier with process streams and variables.

Pilot-scale Gasifier

The pilot-scale gasifier will generate dry producer gas from palletized orange-skins. The system is designed for 30 nm^3/hr of producer gas using a positive displacement blower for motive force on the gasifier. The system is skid mounted including the pellet feeder, gasifier, heat exchangers, gas cleanup, and the control module. The system also includes a flare system and the control system uses off-the-shelf PLC platform.

Gasifier

The gasifier is a two stage fixed bed downdraft gasifier. Citrus peels will be fed through the top of the gasifier and is converted to char and then char ash within the central core of the gasifier. Char and char ash is supported by a grate that is vibrated periodically to clear the buildup. Some of the ash also gets entrained in the exiting gas that is cleaned downstream of the gasifier. Air is also fed at the top of the gasifier and helps in breaking down the biomass. Air is also fed at the bottom of the gasifier to help combust the char to form hydrogen and carbon monoxide. The gasifier has five strategically placed thermocouples and a differential pressure gauge to measure the pressure drop across the char bed. Detail gasifier specifications are shown in appendix B.

Heat Exchanger System

The gasifier temperature is at approximately 650 to 800 ◦C. The gas loses heat when it goes through the char bed to drop to 500 ◦C. A shell and tube exchanger is used to cool the gas further less than 100 ◦C for use of baghouse filter to clean the gas of its particulates. The gas entrains all the char. Large char particles are removed before entering the heat exchanger. Fines are carried through the heat exchanger, and in the process most of the residual tars are condensed and absorbed into the fines that are removed later using the fines filter. Inefficient heat exchanger may result in condensation of tars and fines that will cause fouling and require frequent maintenance. The heat exchanger is accessible form the top and the bottom for periodic cleaning operations. Details of the heat exchanger are shown in appendix C.

Tar and Particulate Removal

The cleanup system consists of a char separator and a fines separator. The char separator removes the large char particles that are entrained with the gas as it exits the gasifier. The char separator assembly is a modified cyclone. As the gas exits the heat exchanger assembly, it enters a bag-house (large surface area pleated fiber material). The bag is manually shaken from time to time to remove deposited cake.

Bench-scale Gasification

While the pilot-scale gasifier is being fabricated and assembled, we focus our efforts on operating a bench-scale gasifier. A bench-scale gasification unit was setup to test the concept of heat pipes as heat exchange media for indirect gasification of citrus peels. Heat pipes are known to be efficient heat exchangers, compared to conventional surface or space heat conduction, due to the involvement of the latent heat of the heat-sinking material (HSM) within the pipes. The HSM changes phase when it comes into contact with both the cold and hot end of the heat pipes and thus it releases or takes up the latent heat. Overall, the heat transfer capacity is enhanced for a given set of hot and cold end temperatures resulting in a more uniform distribution of temperatures throughout the gasification chamber. As a result, the application of heat pipes to the indirect gasification system could significantly improve the composition of the product gases at a competitive operating cost. The bench scale experiments are providing guidance and valuable insight for the subsequent pilot scale experiments. The bench scale unit consists of an isothermal well, 6 in. outer diameter and 18 in. height (fig. 3). The annulus of the two cylindrical tubes contains an efficient heat transfer medium, which through phase change provides the energy for biomass gasification in the inner core. The heat pipes provide uniform radial temperature distribution inside the inner core of the furnace.

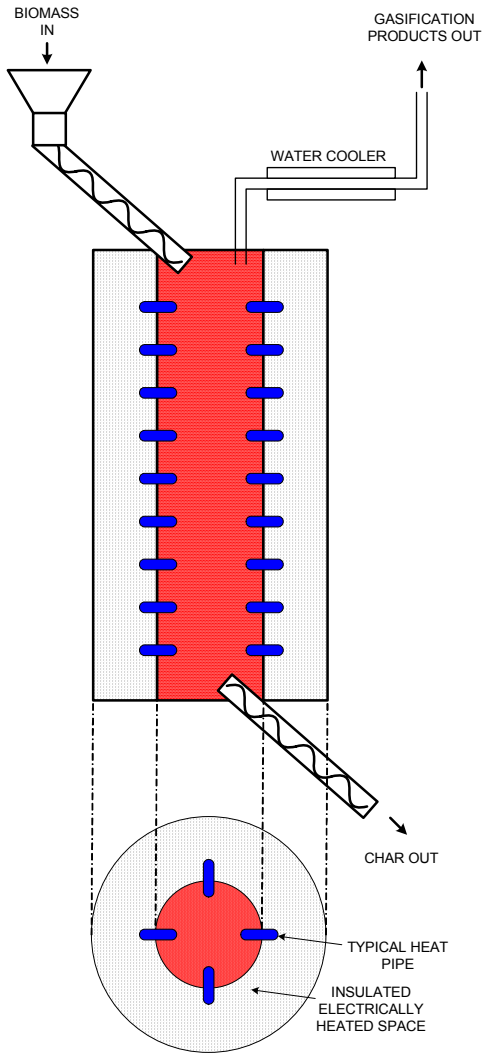

Figure 3.—Bench-scale gasifier.

The bench-scale system has the capability to operate in both batch and continuous mode. The product gases are collected, cooled and analyzed. In the continuous mode, citrus pellets are fed with a screw-drive feeder from the top and char is carried away with a screw-drive belt. The batch mode does not involve the screw-drives, and thus is useful in evaluating material balances and reaction yields. Typical experiment results are shown in appendix C.

Publications

1. Use of GIS in the Assessment of Florida's Biomass Resources for Hydrogen Production at Kennedy Space Center, ESRI International User Conference, San Diego, CA, July 2003.
2. Citrus Peel Gasification using Molten Sodium Heat Pipes, AIChE Annual Meeting, Austin, TX, Nov 2004 .
3. Citrus Peel Gasification for Hydrogen Production using Molten Sodium Heat Pipes, *manuscript under preparation*.

Invention Disclosure/Patent Applications List

Intent to file patent for gasification using molten sodium heat pipes.

Appendix A

A simple gasifier model developed by researchers from Denmark was used to provide preliminary estimates of hydrogen that can be generated (without using steam). The results from the model are shown in tables A2-A3.

TABLE A1.—EXIT GAS COMPOSITION (vol %) From SINGLE STAGE GASIFIER FOR CITRUS PEEL WITH STOICHIOMETRIC AMOUNTS OF AIR (450 °C)

Gasifier Temp (°C)	CO (vol %)	CO_2 (vol %)	CH_4 (vol %)	H_2 (vol %)	H_20 (vol %)
500	27.0	27.1	1.0	17.9	0.6
550	27.6	256	1.0	15.6	2.5
600	27.7	24.6	1.0	15.6	2.5
650	27.6	23.9	0.9	12.5	5.1
700	27.3	23.3	0.9	11.2	6.0
750	26.9	22.9	0.9	10.2	6.8
800	27.7	21.1	0.9	7.5	9.1
850	25.9	22.3	0.9	8.2	8.2
900	25.3	22.3	0.9	7.4	8.7

TABLE A2.—EXIT GAS COMPOSITION (vol %) FROM SINGLE STAGE GASIFIER FOR CITRUS PEELS WITH STOICHIOMETRIC AMOUNTS OF AIR (450 °C) AND 20% (wt) STEAM

Gasifier Temp (°C)	CO (vol %)	CO_2 (vol %)	CH_4 (vol %)	H_2 (vol %)	H_20 (vol %)
500	4.0	37.8	1.8	27.9	8.6
550	7.8	32.9	1.7	22.0	13.6
600	10.0	29.7	1.7	17.9	16.9
650	10.9	28.0	1.6	15.5	18.7
700	11.4	26.8	1.6	13.5	20.0
750	11.6	25.9	1.6	11.9	21.0
800	11.9	24.9	1.6	10.1	22.1
850	11.5	24.7	1.5	9.2	22.5
900	11.3	24.3	1.5	8.0	23.1

Appendix B

Gasifier Details	
Type	Fixed bed downdraft
Material construction	304 Stainless steel
Diameter	6 in.
Height	40 in.
Footprint	24 in. x 24 in.
Gross weight	250 lb
Fuel moisture specifications	0–15% MC
Fuel size specifications	Pelletized orange peels
Feed gate	Solenoid butterfly valve
Fuel level control	Infrared level sensor
Char air injection design	Multiple layers of fixed injectors on a central tree
Char air control	Single char air blower
Bed temperature monitoring	High temperature K rated thermocouples
Bed pressure monitoring	Pressure transducer
Bed uniformity control	Vibrator mounted to char air tree
Grate design	Reciprocating positive displacement
Gas flow measurement	Venturi flow meter
Gas production rate	>30 Nm^3/hr
Power consumption	< 100 W average

Appendix C

Heat Exchanger	
Type	Gas to air
Construction	Tube and shell, dual pass
Material construction	304 Stainless steel
Length	4 ft
Height	20 in.
Width	20 in.
Gross weight	300 lb
Blower size	1/3 hp
Power consumption	< 500 W

Filter	
Type	Insulated baghouse
Bag construction	Teflon coated woven polyester
Bag configuration	Pleated construction
Cake removal	Manual shaker
Safety filters	None
Char and ash collection	Manual cleanout port
Char and ash storage	30 gallon drum
Diameter	25 in.
Height	40 in.
Gross weight	150 lb
Filter dP control	dP display and alarm only; non-automated
Power consumption	None
Particulate removal performance	< 25 ppm clean glass
Maintenance requirements	Periodic bag replacement
Bag life	> 500 hr

Appendix D

Gasification experiments were conducted at 550, 650, 750, and 850 ◦C, respectively. At the start of the batch experiment, approximately 3 kg of dried citrus peels is loaded into the gasification chamber. The furnace temperature is then increased to the desired setting. Outgases from the gasifier were monitored continuously using a Residual Gas Analyzer.

The initial gas composition at the outgas port of the gasifier is similar to that of the air (fig. D1). As the temperature rises, major air components, such as O_2 and Ar, disappear and are replaced with gasification products primarily H_2, CO, CO_2, higher hydrocarbons, and water (fig. D2). We typically observed high gas outflow at around 550 to 600 ◦C. The outflow rate remained high for about 30 to 40 min and gradually decreased as the mass spectrum of outgases became less complex (fig. D3).

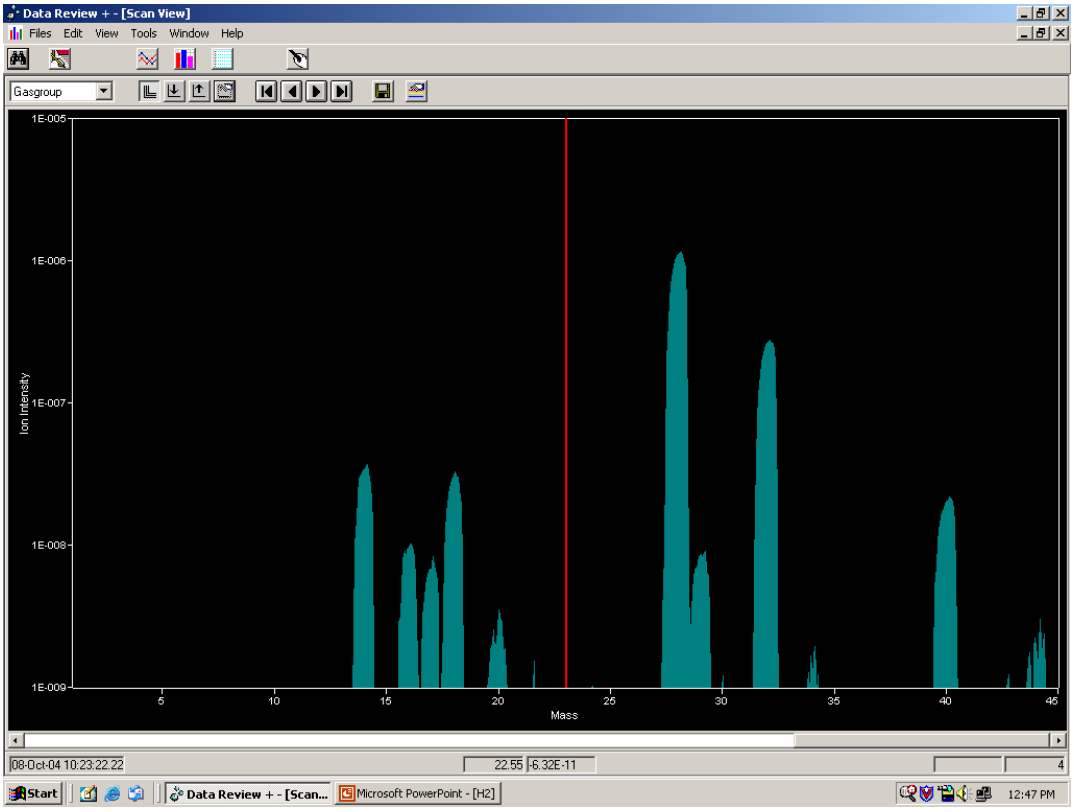

Figure D1.—Mass spectrum at the start of experiments (no H_2 peak).

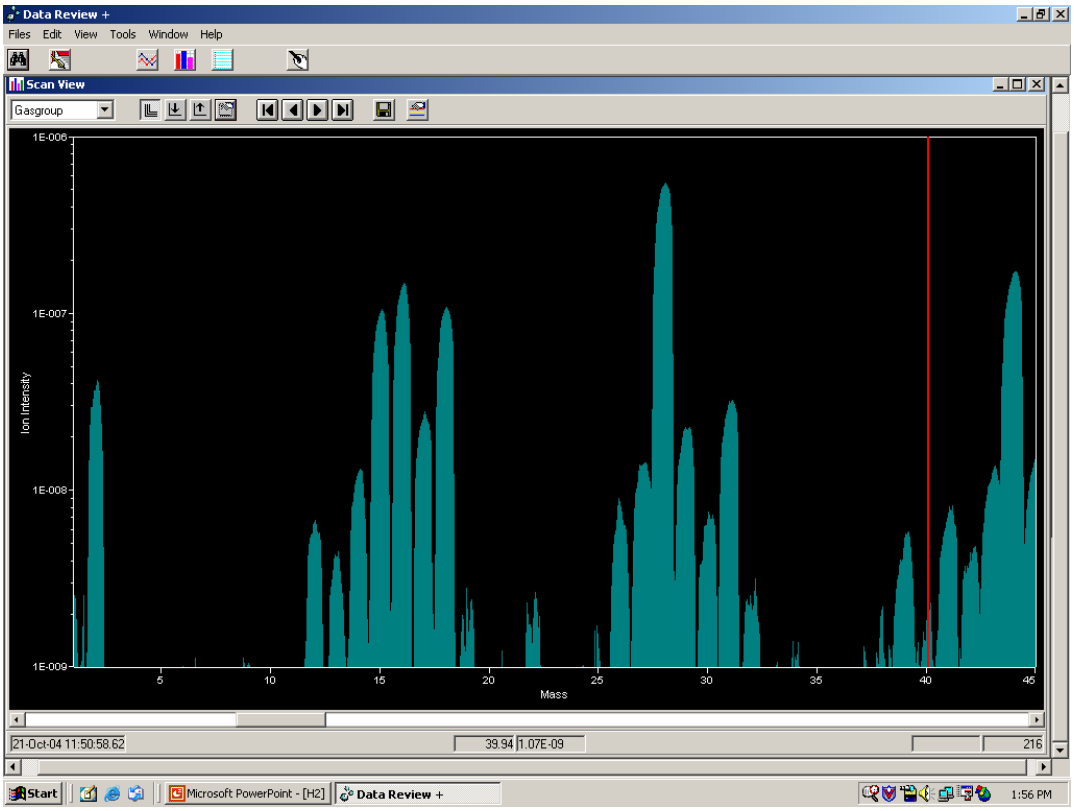

Figure D2.—Mass spectrum at peak gasification reaction.

For the bench scale experiments, no hydrogen was observed for temperature below 550 °C. Higher hydrogen yields were obtained at higher temperatures (fig. D4).

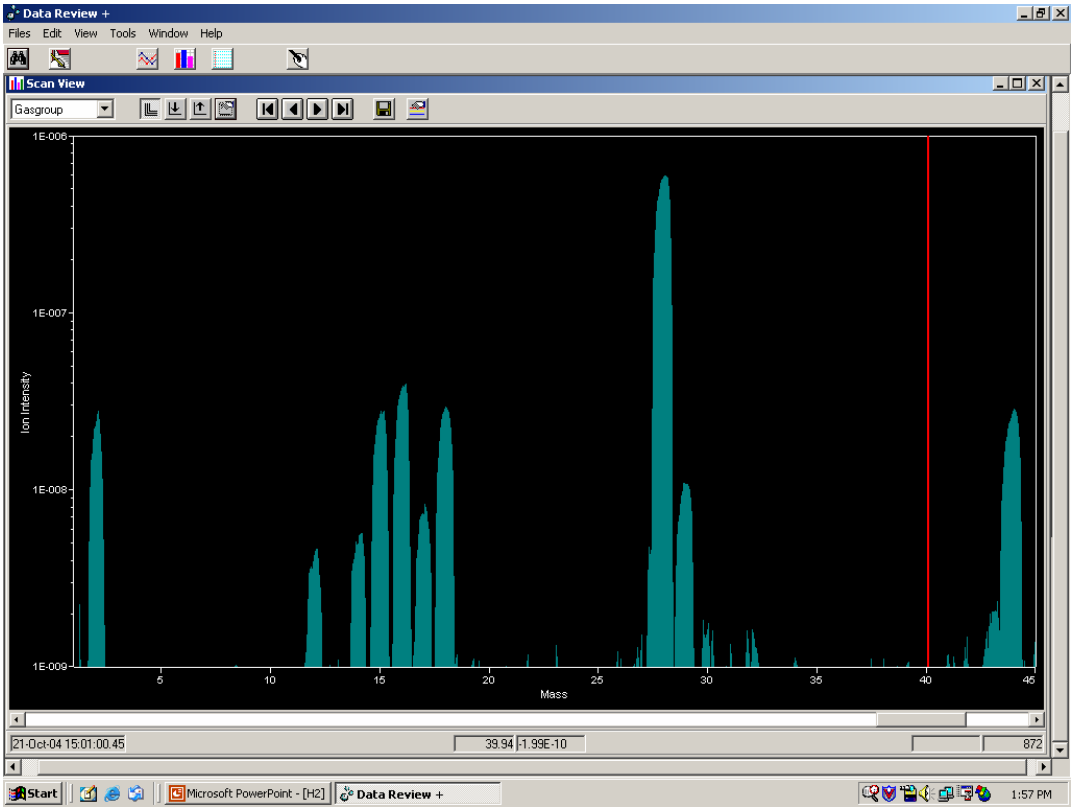

Figure D3.—Mass spectrum at the end of the experiment.

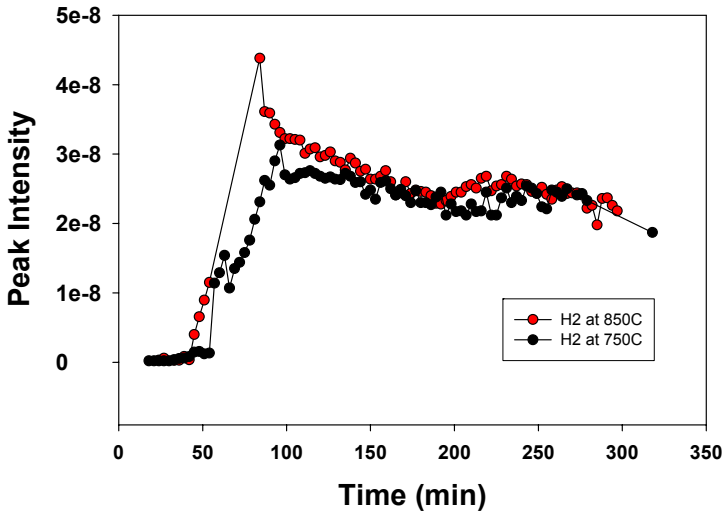

Figure D4.—Hydrogen yields for batch gasification experiments at 750 and 850 °C.

Experimental Design and Evaluation of ZBO Cryogenic Systems

PI: J. Baik (Florida Solar Energy Center)
This project partnered with William Notardonato of NASA Kennedy Space Center

Description

One performance enhancement under consideration for the next generation of space launch vehicles is densification of the cryogenic propellants. Propellant densification refers to subcooling the cryogens below their normal boiling point (NBP). Propellant densification has many beneficial properties when space launch systems are considered. Among these are reduced tank volumes, decreased vapor pressures, and increased enthalpy gain before boil off.

A 150-liter capacity test bed has been designed and built to gain operational experience in various handling techniques of densified hydrogen. This test bed has the capability to refrigerate and store liquid hydrogen to temperatures near 15 K using a commercial G-M cryocooler integrated into the storage tank. Integration of a refrigeration source into the dewar allows advanced handling techniques such as zero-boil-off (ZBO) storage, densification, liquefaction, pressure control, and recovery of chill down losses. The design and fabrication of the test bed has been completed. Preliminary experiment using liquid nitrogen will be conducted followed by using hydrogen gas and liquid hydrogen.

Objectives

To design and build a experimental test bed in order to perform hydrogen densification, ZBO storage, pressurization and boil-off loss recovery in chill-down and filling process, and in result, to obtain various handling techniques of densified hydrogen in densification, transfer and storage processes.

Benefit to NASA

Previous NASA investigations have focused on advanced methods of producing densified propellants, but not much work has been accomplished in the area of storing and handling densified propellants. NASA KSC has 50+ years experience in handling cryogenic propellants, but all that experience is with NBP saturated liquids. This experimental effort will provide operational techniques of continuous densification unit, ZBO storage techniques for liquid and densified liquid hydrogen, densification enhancement using cryocooler and heat pipe, pressurization techniques for transportation, handling of thermal stratification layers in storage tank, liquefaction enhancement using cryocooler and heat exchanger, and recovery techniques of boil-off losses at initial chill down procedures.

Notes

The followings are detailed descriptions of hydrogen liquefaction, densification and ZBO storage test performed at FSEC. In this report, to describe actual technical activities in detail, several main activities were selectively chosen among multiple experiments in time order.

Liquid Nitrogen Chilldown

The cryocooler was not operating and the system was at ambient temperature. It was decided that a stored cryogen supply would be used for the system chilldown to save time, as opposed to using the cryocooler refrigeration power. No readily available supply of liquid hydrogen was found in small quantities for this purpose. Liquid helium was determined to be too expensive. The solution was to use liquid nitrogen to chill down to 77 K, then drain and purge the liquid nitrogen using gaseous helium, evacuate then turn on the cryocooler and supply gaseous hydrogen to complete the chilldown process. Figure 1 shows the data from the initial phase of this chilldown.

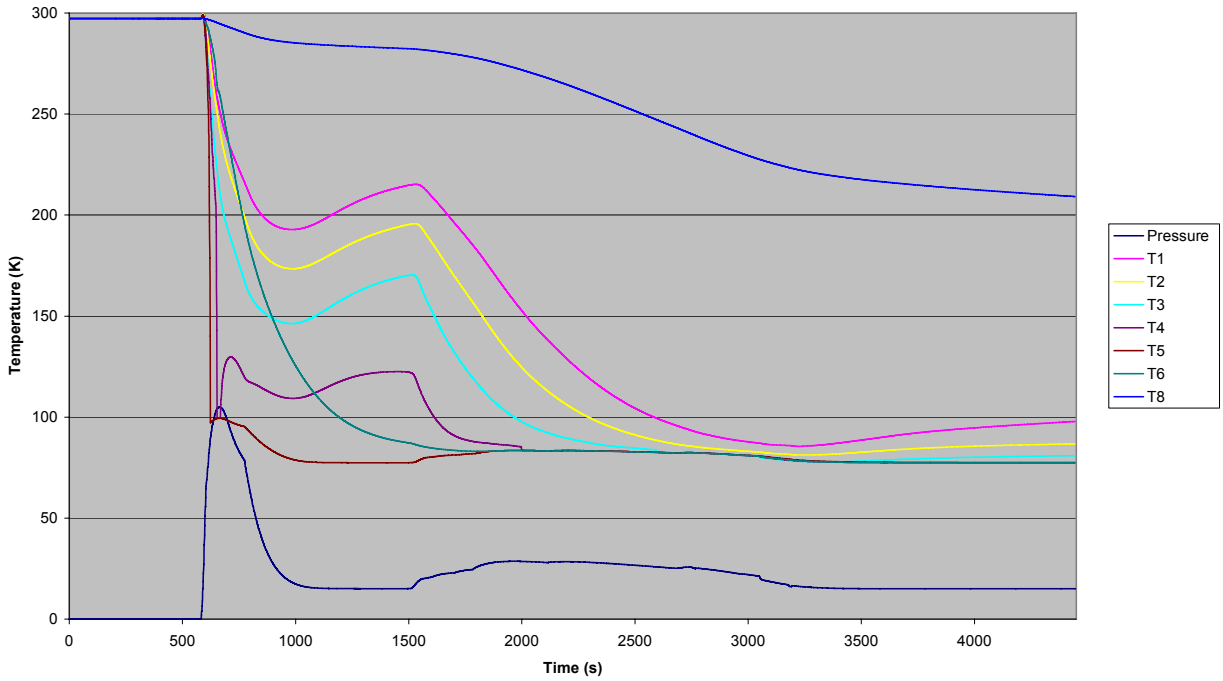

Figure 1.—LN_2 chilldown.

At the start of the test, all valves on the system were closed and the system was evacuated to a pressure of 0.02 psia. The vacuum annulus was evacuated to a vacuum in the range of $1x10^{-4}$ Torr. All temperatures were reading in the range of 297 K. A portable, 160 liter dewar of liquid nitrogen was connected to the liquid fill and drain line, and the dewar supply valve and the liquid hydrogen drain valve were opened. The system vent valve was then opened. Unfortunately, the supply dewar pressure was not vented prior to the transfer, and the valve was not opened slowly enough. As liquid nitrogen entered the warm hydrogen storage tank, it vaporized and expanded beyond the flow capability of the ½ inch vent line. Frost was observed at the outlet of both the relief valve and the burst disk, indicating cold vapor flow out of these devices. The liquid nitrogen supply valve was closed and the system pressure began to decrease. The nitrogen storage pressure was vented and supply valve was very slowly opened to reestablish the chilldown process.

Figure 2 shows more detail of the over pressurization of the system. Note the pressure increasing in surges, as is expected in a chilldown process as liquid flashes off, creating a localized pressure spike that reduces further liquid flow. In spite of these spikes, the overall pressure increases in a fairly linear profile until the burst disk relieves at 64.5 psia (49.8 psig), slightly higher than the 45 psig specification. It is worth noting there was no corresponding decrease in pressurization rate when the relief valve opens, indicating the flow capacity was not sufficient to relieve that quantity of gas. Pressure continued to increase until the delta pressure between tanks reached a point where the liquid mass flow rate into the system equaled the gaseous mass flow rate out of the system. Once the frost was observed on the relief line, the liquid nitrogen supply valve was closed, and pressure decreased to match the atmospheric pressure. Later, after the chilldown was complete and while the system was open to ambient, a new burst disk was installed to provide a redundant method of overpressure protection.

Looking at the temperature profiles during the chilldown in more detail (fig. 3), notice the lowest diode (T5) quickly reaches the liquid state (97.8 K, 96.5 psia) and remains liquid during the flow interruption. The liquid temperature decreases after the flow stops since the vapor pressure is decreasing. T5 eventually reaches 77 K (NBP) as the pressure in the tank vents to ambient. Similarly, T4

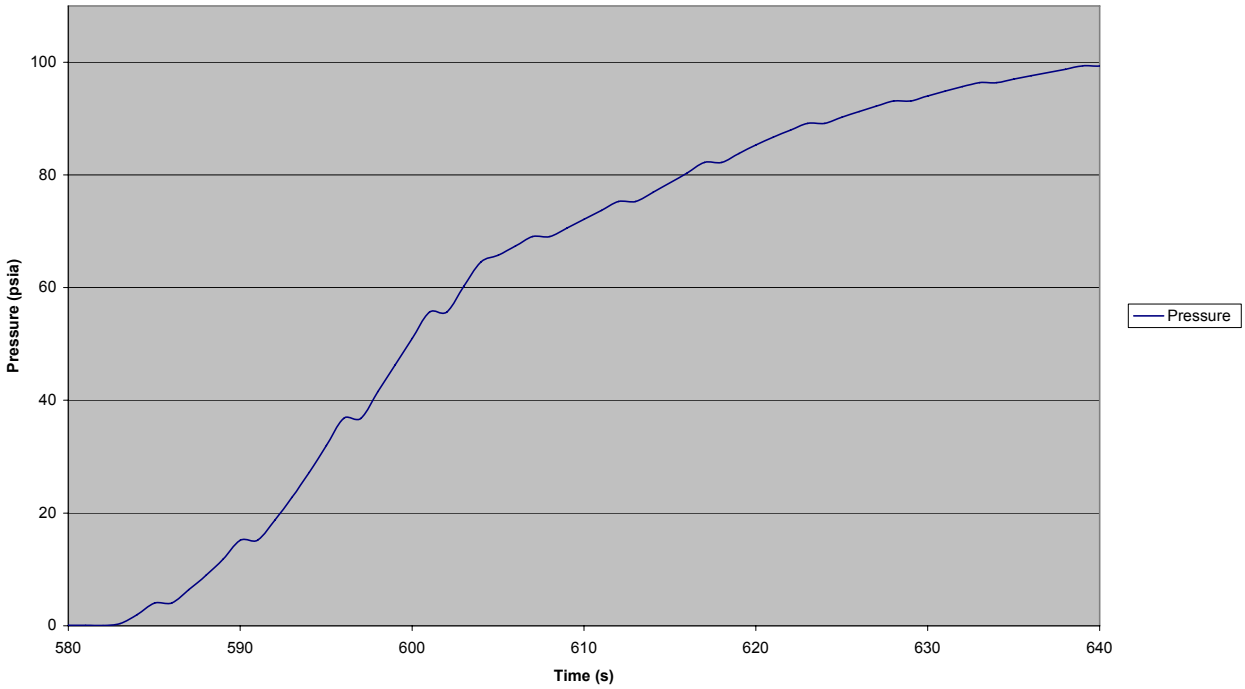

Figure 2.—Hydrogen dewar over pressurization.

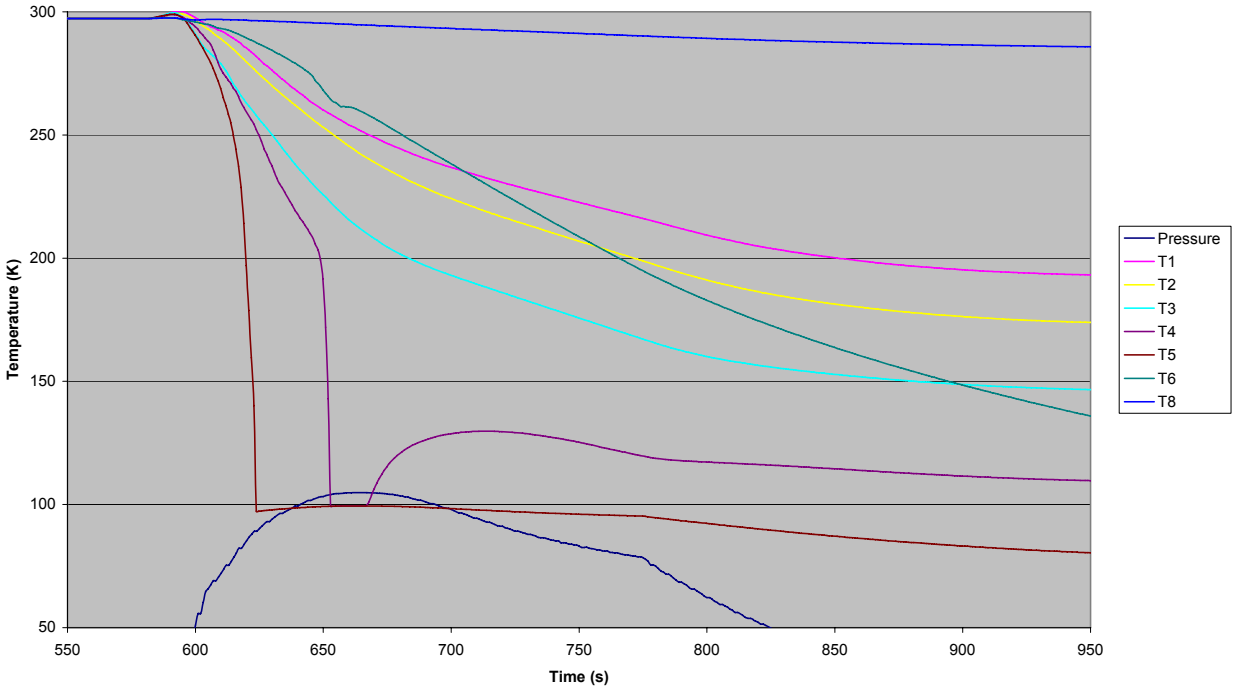

Figure 3.—Initial chilldown details.

initially reaches the liquid point, but turns to vapor shortly after the flow is terminated. The other three diodes in the temperature rake are gradually decreasing in temperature, even when the flow is stopped initially. This is due to the fact that liquid nitrogen is boiling off in the bottom of the tank, removing heat from the saturated liquid as the vapor pressure drops. Once the depressurization rate decreased enough, the tank heat leak and heat capacity of the semi-warm metal overcomes this cold vapor supply and the ullage temperatures seek to stabilize at a higher temperature. Another interesting point is the temperatures on the cryocooler and heat pipe themselves, which gradually decrease in temperature compared to the diodes on the rake. This is due to the much larger thermal mass associated with these locations taking longer to chill.

After the burst disk rupture had been diagnosed and determine not to be a constraint on further testing, the liquid nitrogen supply valve was reopened. Figure 4 below shows details on this process. The nitrogen dewar had been vented to a much lower pressure and the lack of a burst disk gave a larger path to vent, so the system pressurized in a much more controlled manner. Extra care was also used to open the supply valve more slowly. The maximum system pressure was only 28 psia during this chilldown sequence. Data shows that T5 increased slightly as the pressure increases, following the liquid saturation line. T6 and T4 quickly reached liquid temperature, followed by T3 about 18 min after the start of flow. Flow was terminated at T+3054 sec, when liquid level was approaching T2. Pressure in the system vented to ambient, accompanied by a drop in saturated liquid temperature. Shortly after the pressure reached ambient, the T3 measurement increased past the saturation temperature, indicating enough liquid boiled off to leave the diode in the vapor region. Another interesting phenomenon was observed in the temperature profiles in the liquid. During flow, all liquid temperatures were equal, indicating mixing of the liquid. Shortly after the flow was stopped the temperature of the upper liquid layers decreased (T3, T4) compared to the lowest liquid layer (T5). Evaporation at the surface caused liquid temperatures to decrease, but there was a time delay before the natural convection currents created a normal temperature gradient in the liquid. The tank, half full of liquid nitrogen was left open to atmosphere overnight to ensure a complete chill down. A stable temperature profile was recorded with T4 and T5 reading 77 K, T3 reading 95 K, T2 reading 117 K, and T1 reading 138 K. At this point, the tank drain and purge was performed.

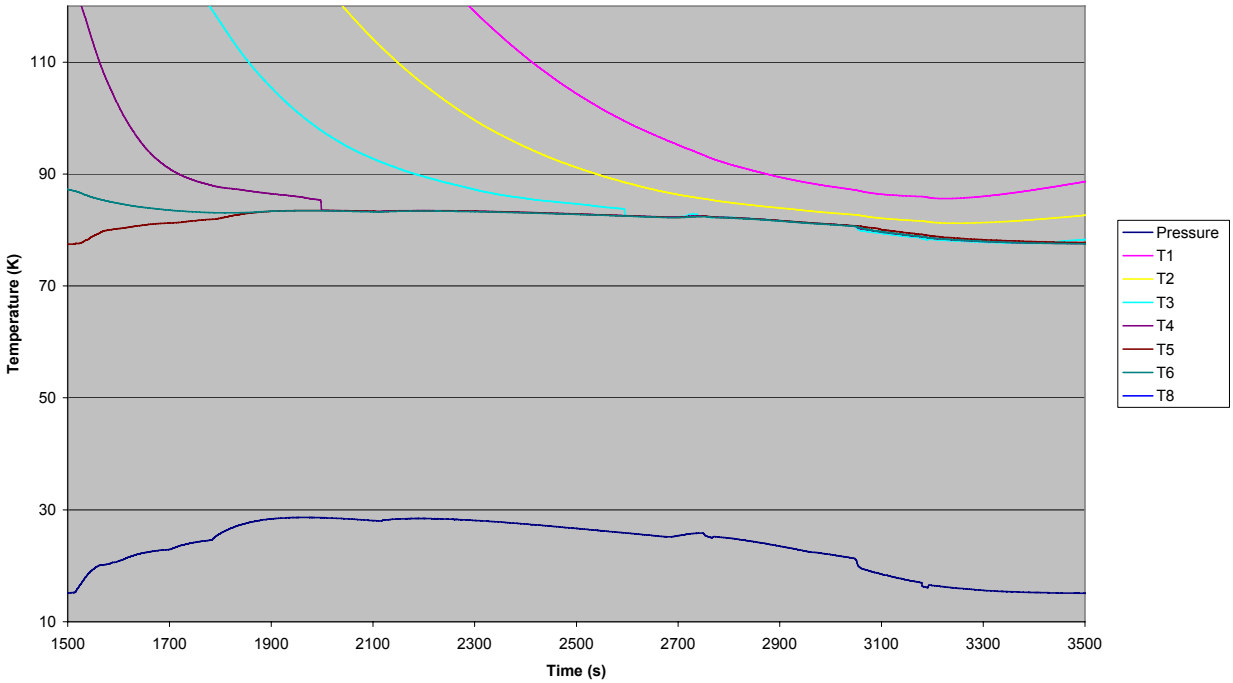

Figure 4.—Second chilldown details.

Liquid Nitrogen Drain and Purge

Drain and purge of the liquid nitrogen was started. A data overview of the next 4 hr is shown in figure 5. First the system vent valve was closed. The system immediately began self pressurizing. A gaseous helium K-Bottle was connected to the system and the line was evacuated to eliminate any contaminants. The system was then pressurized to 18.2 psia. A series of 5 positive pressure purge and vent cycles was completed. Once the remaining liquid was expelled, two helium purge and vacuum cycles were completed to remove all the gaseous nitrogen which would solidify at liquid hydrogen temperatures. Finally, after all the nitrogen was removed and the system was still under vacuum, the cryocooler was turned on.

More insight on the system behavior can be found by examining the data in greater detail. Figure 6 shows the tank pressure profile during the purges, drains, and evacuation. Starting at 18.2 psia, the gaseous helium inlet valve was opened to pressurize to 20.7 psia. The system vent valve was then opened starting the first purge cycle. When the pressure decreased to 17.5 psia, the vent was closed to repressurize. This was repeated five times, to get the nitrogen ullage replaced with helium. While this is occurring, enthalpy from the warm helium is causing liquid nitrogen to boil. Notice the pressurization and depressurization rate decreases as the boil off leaves a greater ullage volume. At the end of the fifth cycle, the gas supply valve is closed and the vent valve is closed. The system is repressurized to 18.5 psia and the liquid withdraw valve is opened.

There is a noticeable slope change in the depressurization curve when comparing a gas vent to a liquid withdraw. As most of the liquid is drained, the system reaches near ambient pressure and valve is closed. Next, two evacuations are performed using the vacuum pump, with a backfill of gaseous helium in between. The system remained evacuated until the following day when the gaseous hydrogen was introduced into the system.

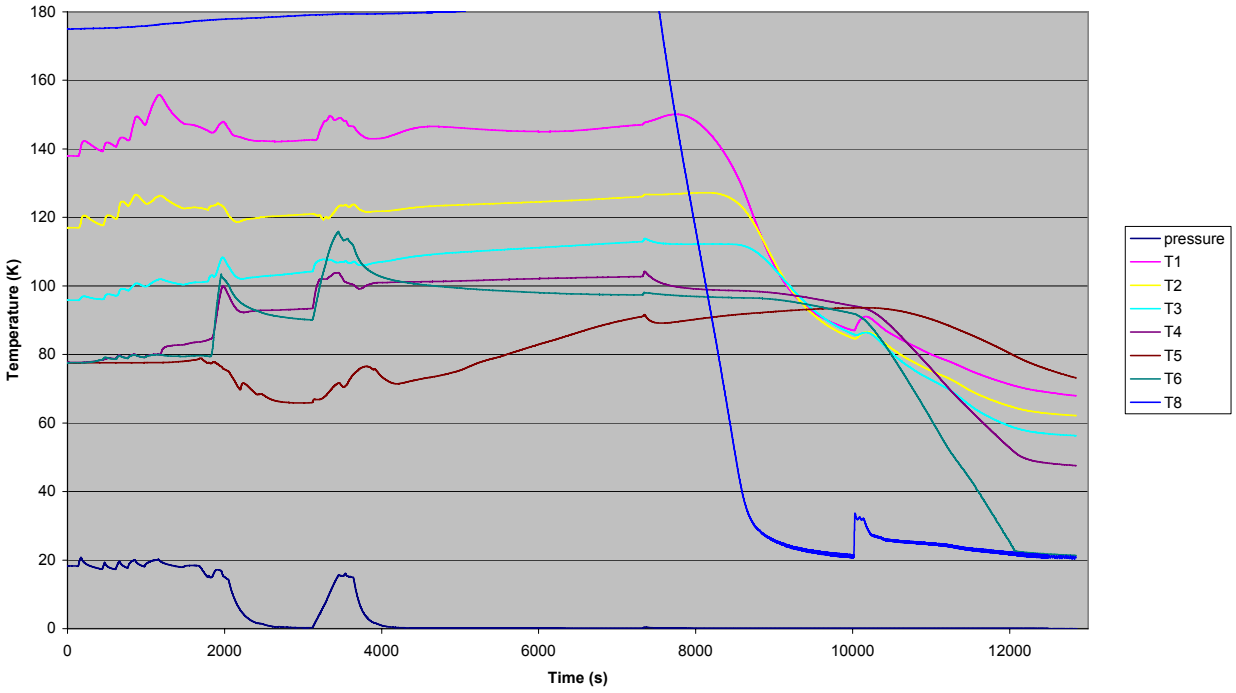

Figure 5.—Liquid nitrogen drain and purge.

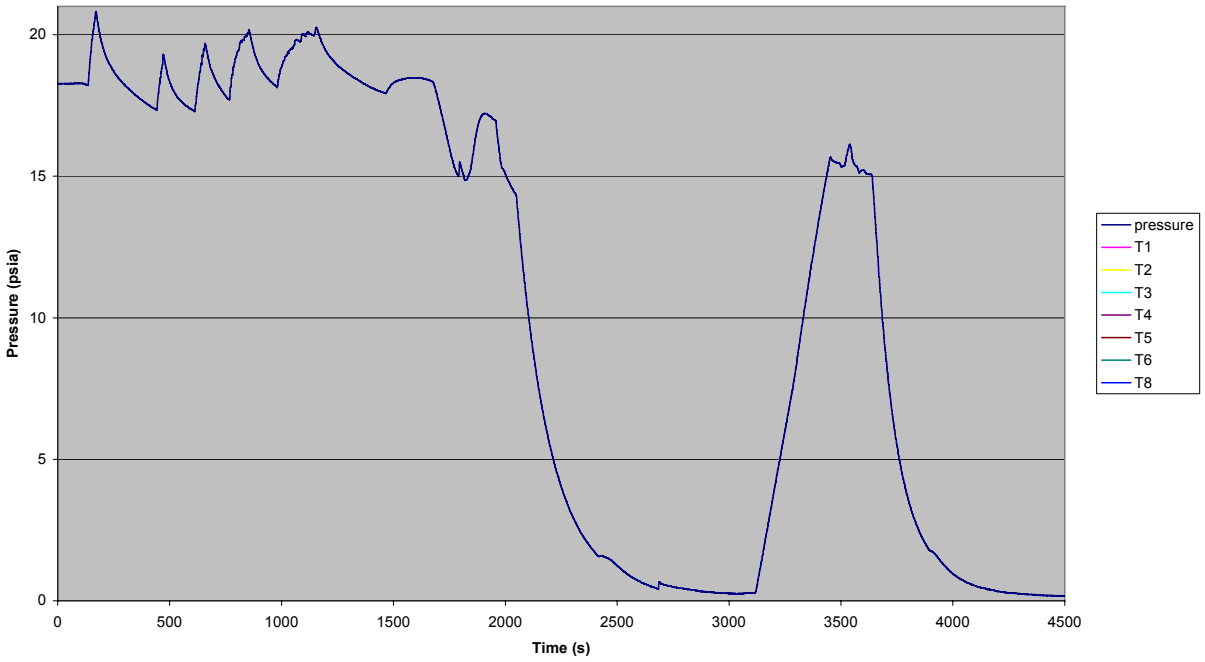

Figure 6.—System pressure during purge and drain.

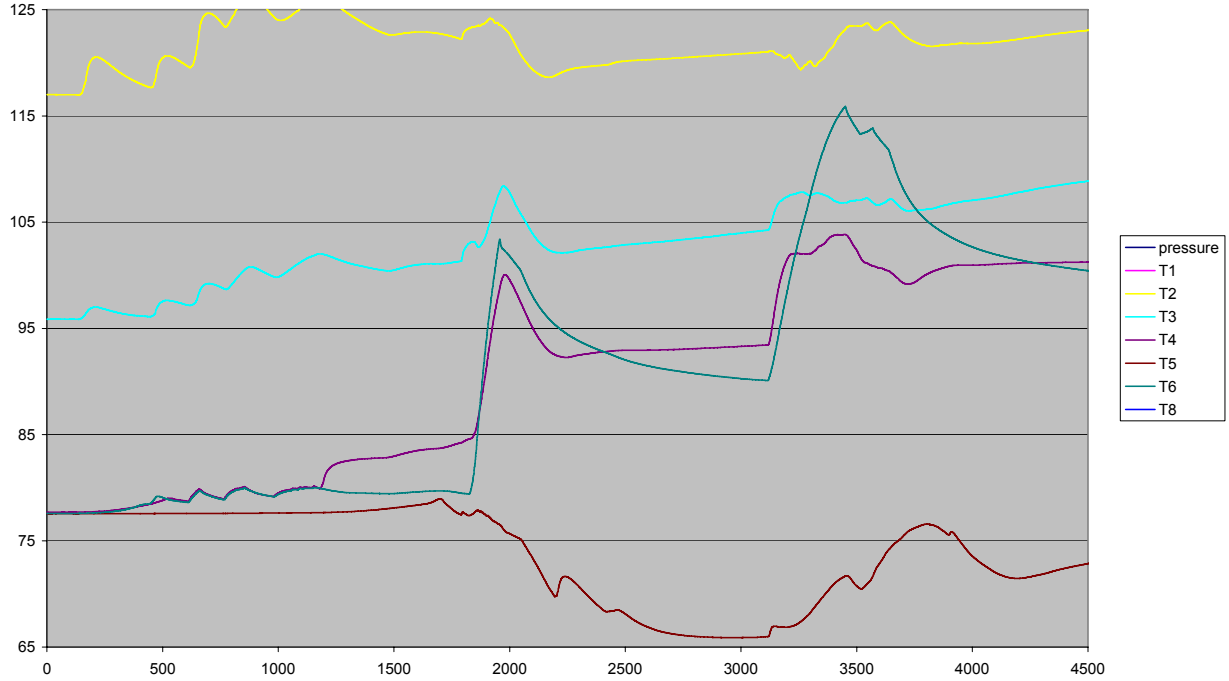

Figure 7.—Temperature profile during purge, drain, and evacuation.

Temperature profiles during this operation are shown in detail in figure 7. All five purge and vent cycles are clearly evident in the ullage temperature measurements. By the second purge cycle, enough warm gas had entered the system that the liquid level had reached the T4 level.

After this point, T4 behaves in a similar manner to the other ullage temperatures, except the final pressurization cycles during the liquid withdraw procedure created much higher temperature spikes in T4 that T3, T2, and T1. Liquid stayed in the bottom of the tank through all five purge cycles, as is evident by the lowest tank temperature continuing to track the saturation line. After the five purge cycles, the liquid

withdraw valve was opened. Most, but not all of the tank was drained. Note the differences in behavior between the diodes in gas versus diode in liquid. The ullage temperature drops initially as the pressure decreases, and during this phase it is measuring the gas temperature directly thru convection. Eventually the temperature decrease stops, although the pressure continues to decrease. The liquid diode decreases in temperature as the pressure drops, roughly following the saturation line. At this point it was decided to do a second drain operation, and the system was repressurized to 16 psia. The drain valve was reopened and the system vented to ambient. The vacuum pump was reconnected and turned on and this time it appeared the remaining liquid was removed from the tank. The T5 reading began increasing, along with all the other temperatures, and the decision was made to turn on the cryocooler.

When the cryocooler was started, the cold head temperature was reading 182 K. Within 30 min, the temperature had decreased to 22 K, and many of the other temperatures near the top of the tank were decreasing. However, the lower tank temperatures and the bottom heat pipe temperature did not start decreasing until the heat pipe was charged with gaseous hydrogen. The charge operation caused an immediate spike in cold head temperature due to the enthalpy of the warm gas entering the pipe, and this spike is also evident in the upper tank temperatures. Once the heat pipe was fully charged, the lower heat pipe temperature immediately began decreasing as the refrigeration power was pumped down the length of the pipe by the internal hydrogen gas. Within 30 min, the lower heat pipe temperature had completed its chilldown. The delta temperature between the cooler and the heat pipe end was approximately 0.7 K, which is very efficient considering there was thermal contact resistance between the top of the pipe and the cold head, and thermal resistance down the length of the pipe. One puzzling piece of data is that the expected temperature profile was established with the exception of the lowest diode T5. This temperature did not decrease as quickly as the others, and remained the warmest of all the temperatures during this phase of operation. This is potentially explained by the internal configuration of the tank, with the internal G10 support tube partially blocking the radiation path between T5 and the heat pipe cold mass. With little pressure in the tank, the primary heat transfer mechanism would be radiation. The cryocooler was left on overnight to achieve maximum chill down and the next morning the hydrogen liquefaction process began.

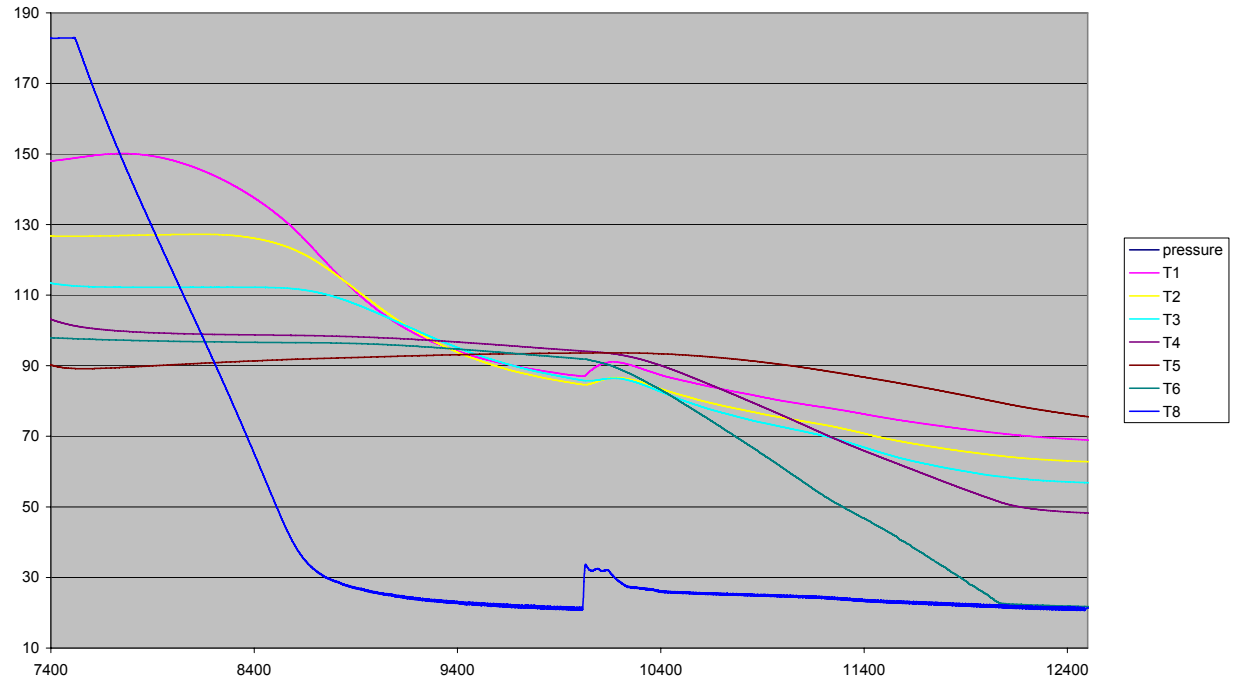

Figure 8.—Cryocooler chilldown with vacuum.

Hydrogen Liquefaction

After the cryocooler operated overnight, the cold head temperature and heat pipe temperature were reading approximately 15.5 K. The cold head temperature was actually experiencing temperature oscillations of a magnitude near 1.5 K, which were damped out by the thermal mass of the heat pipe. Ullage temperatures varied between 28 and 37 K, and were still decreasing slightly. Hydrogen gas at room temperature was introduced into the vessel. Figure 9 below shows this operation, from start of gas flow until termination of gas flow 4.5 hr later. The temperature and pressure profiles are driven by the mass flow rate into the vessel, as is expected since the enthalpy from the warm gas introduces the energy in the system while the cryocooler tries to remove this thermal energy. If the mass flow rate exceeds what the cryocooler can liquefy, the pressure increases. Accurate control of the mass flow rate of gaseous hydrogen was somewhat difficult since the only means of control were globe valves that had imprecise adjustments, with fluctuating pressures upstream and downstream of the valve, and in some cases, vibration from the cryocooler displacer that caused changes in valve positions. Future modifications to the experimental set up will include the addition of a mass flow controller.

As soon as the gas flow was initiated into the vessel, the temperatures started to rise on all temperature sensors, with the exception of T5. Recall that during the overnight chilldown T5, the lowest sensor on the rake, was expected to read a lower temperature than T1 thru T4, but in fact it did not. This was attributed to the fact that the dominant heat transfer mechanism in the tank ullage at that time was radiation, not convection, and T5 was shielded from a direct view of the lower end of the heat pipe. However, as soon as gas was introduced into the system, convection became the primary means of heat transfer, and T5 initially cooled off as stratification of the gas occurred. When the gas pressure was

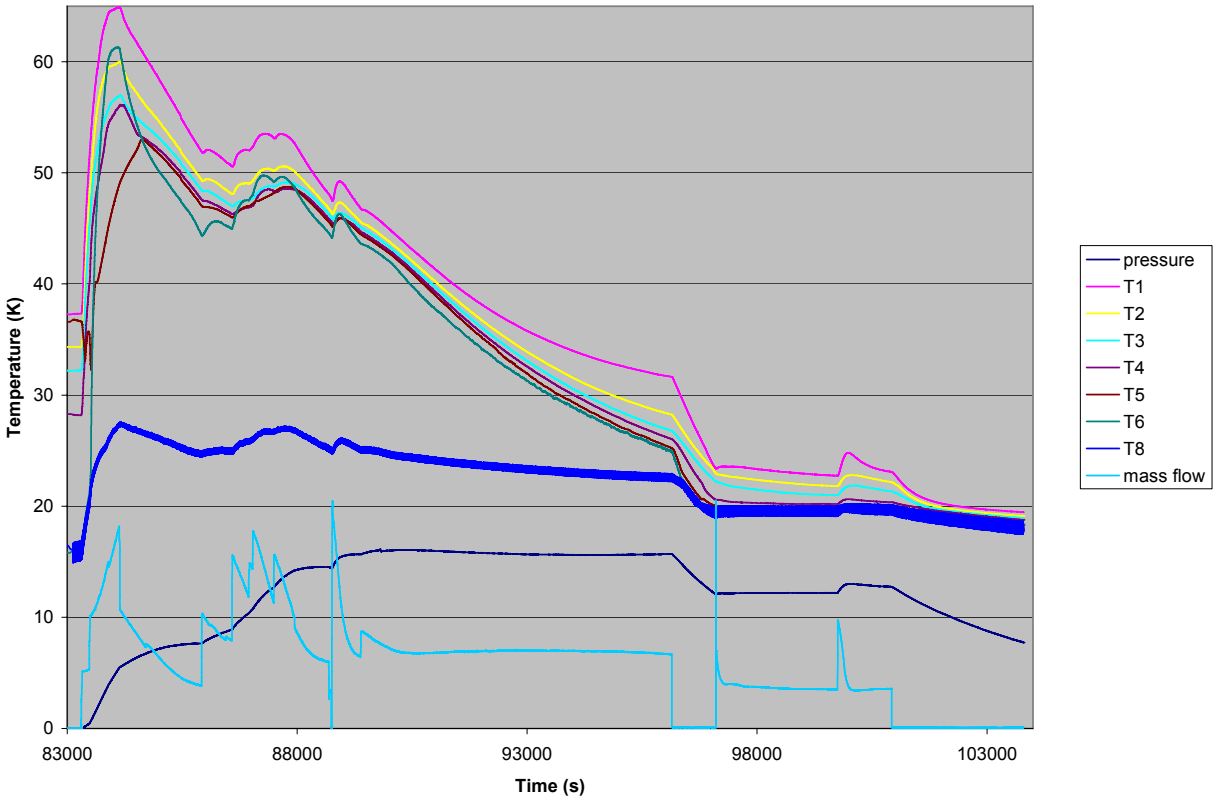

Figure 9.—Hydrogen liquefaction.

sufficient so as to allow T5 to read the temperature accurately (around 0.5 psia), the measurement began to rise. At this point, the expected temperature profile was recorded in T1 thru T5. As the pressure continued to increase, greater convective heat transfer began to occur between the heat pipe end (T6) and the measurement on the rake, and T5 began to decrease again. This continued until the heat pipe and cold head warmed up beyond the boiling point of the hydrogen in the heat pipe. At this point, heat transfer down the heat pipe was limited to convection instead of a phase change, and the heat transfer down the pipe was restricted. T6 began to increase as a result, and this caused T5 to start increasing as well. This initial warm up phenomenon is shown in greater detail in figure 10.

At this point the decision was made to increase gas flow in the tank to get to the point where the internal pressure was above atmospheric, so as to minimize the possibility of air leaking into the system. The valve was opened numerous times to increase flow, but the flow rate decayed immediately afterward. Eventually the k-bottle regulator pressure was decreased to minimize delta pressure, and flow rates became somewhat more controllable. Pressure changes in the tank were directly related to the value of the mass flow rate by the relation $\frac{\partial P}{\partial t} \propto \dot{m}$. This is shown graphically in more detail in figure 11, with the slope of the pressure curve related to the magnitude of the mass flow rate. Some effort was made to determine the mass flow rate that gave a constant pressure in the tank, such a flow rate would roughly approximate the liquefaction rate of the cryocooler (neglecting ortho-para conversion losses). There were two periods of time when the tank pressure was roughly constant, corresponding to flow rates of 7 standard liters per minute and 3.5 slm. However, there were still too many transient effects at this time to come to any conclusions.

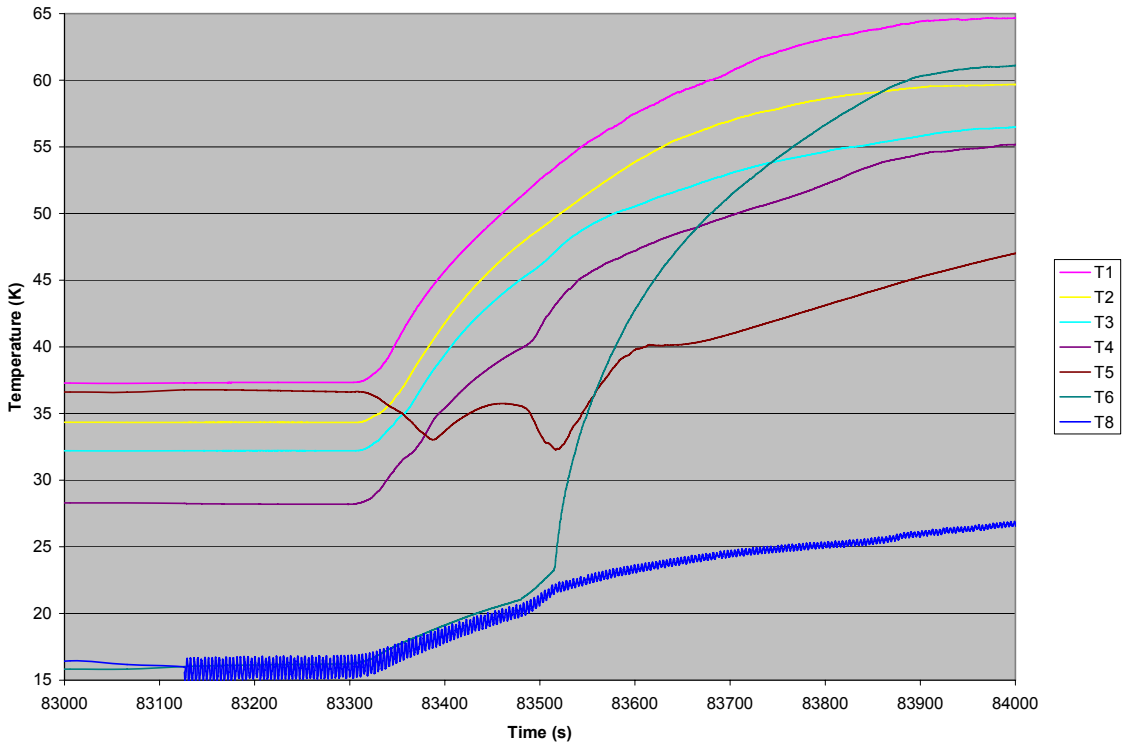

Figure 10.—Temperature transients during initial gas flow.

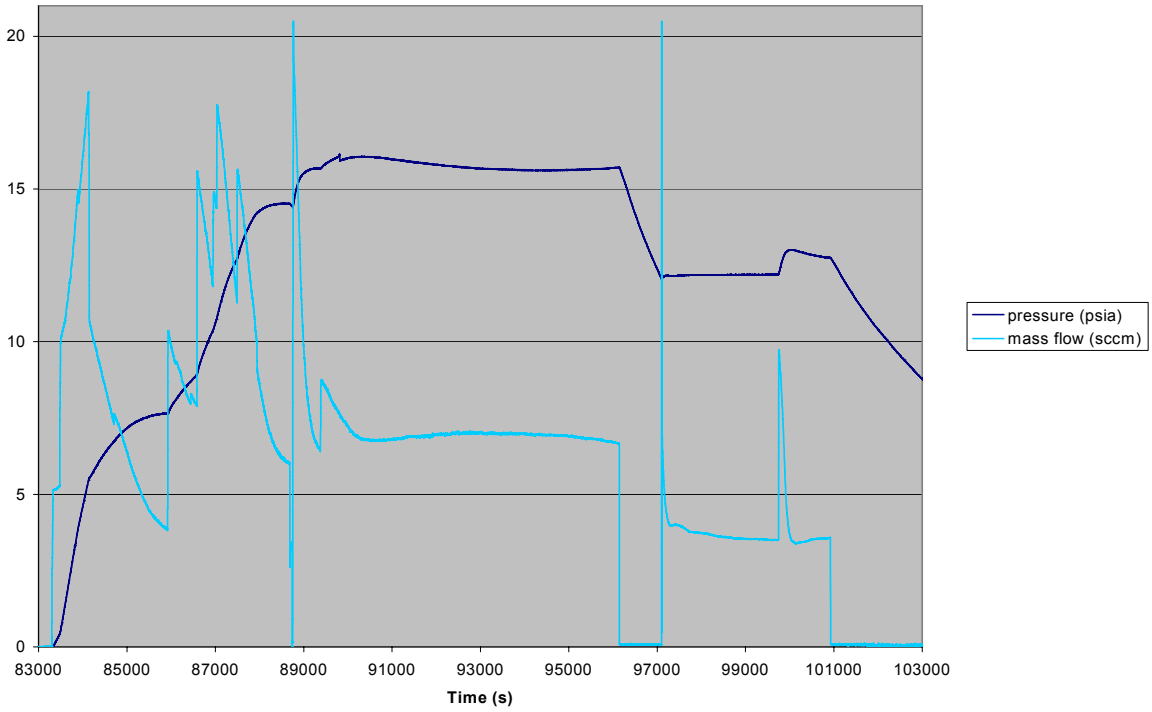

Figure 11.—Mass flow and pressure relation during liquefaction.

From this data it is easy to numerically integrate the mass flow rate with respect to time to obtain the total quantity of hydrogen in the system. This result is shown in figure 12. During the course of the day, a total of 2000 standard liters of gaseous hydrogen was introduced into the tank. Knowing the standard volume of hydrogen gas in the tank, combined with the total volume of the tank, the specific volume of the hydrogen can be computed. The hydrogen mass is found to be $m = \rho V = 0.0824\,kg/m^3 * 2m^3 = 0.165kg$, and the specific volume is $\upsilon = V/m = 0.15m^3/0.165\,kg = 0.91\,m^3/kg$. When this is combined with the tank pressure, the thermodynamic state of the hydrogen can be found. At the time the mass flow is shut off, the pressure is 12.6 psia, so a quick check of hydrogen properties shows the state point to be in the vapor region. At this point, no hydrogen liquid has been produced, just cold vapor, however as the cryocooler continued to operate the vapor pressure continued to decrease and when the pressure reached the saturation point (11.89 psia) liquid droplets started to form. By the next morning the pressure had dropped to 3.78 psia, well inside the two phase region. Another interesting point is where the hydrogen inside the heat pipe becomes saturated again, which is evident by the sharp decrease in heat pipe temperature and change in the slope of the ullage temperature curves. Figure 13 shows this event in more detail.

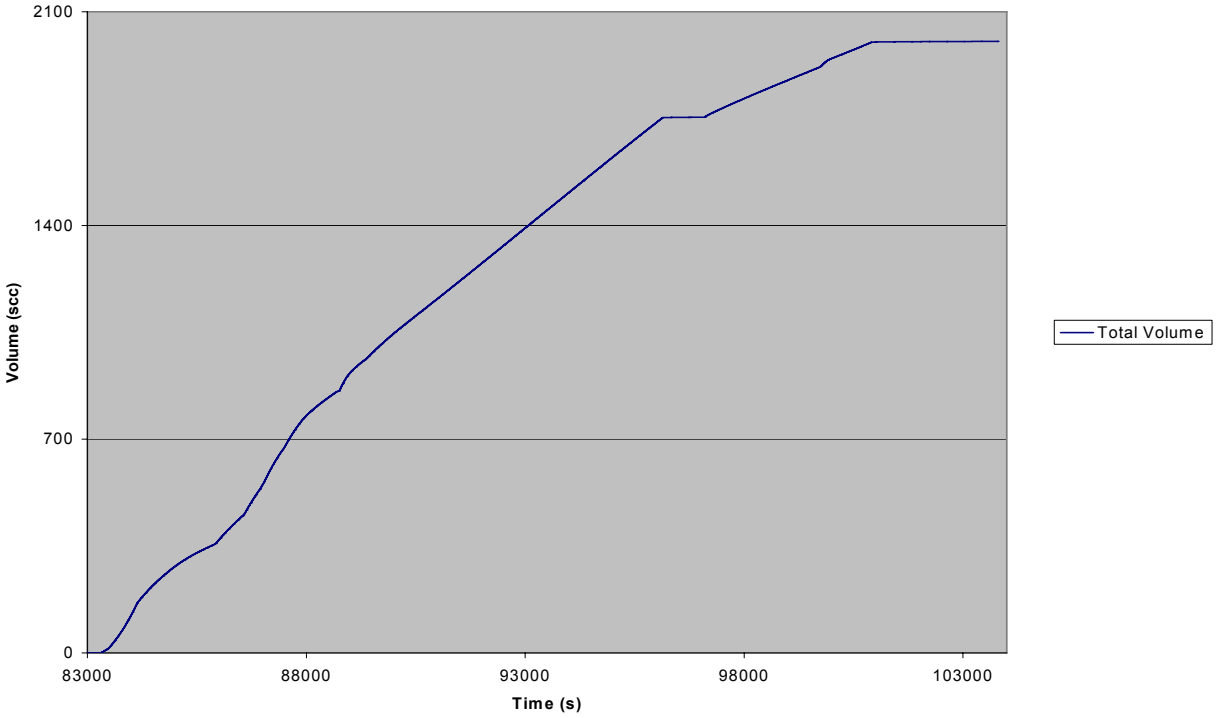

Figure 12.—Total volume of hydrogen in tank.

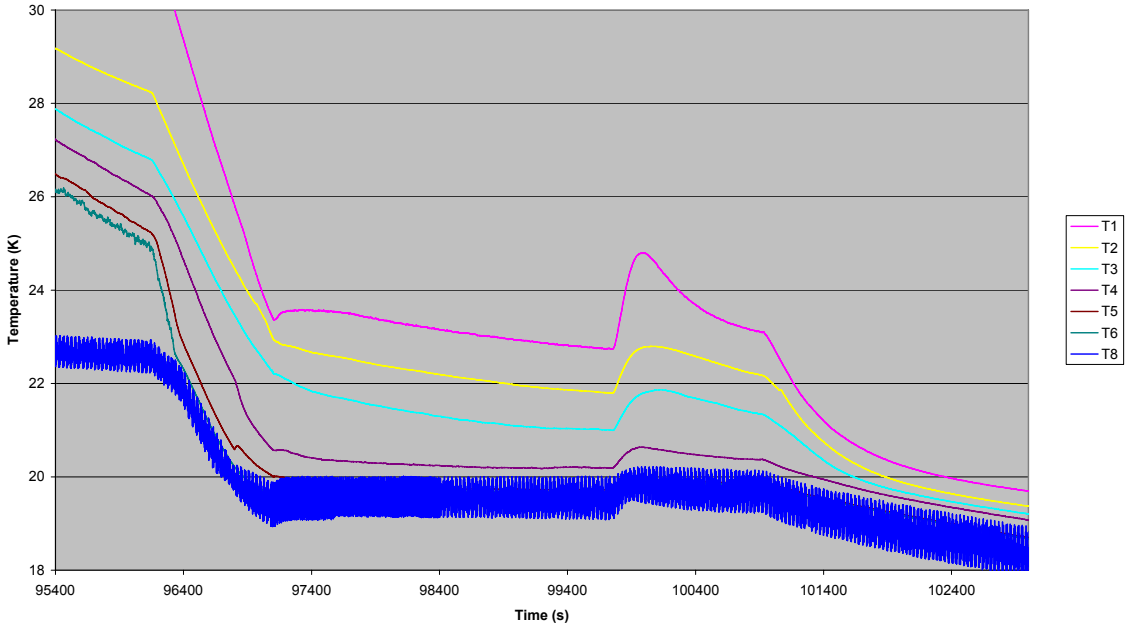

Figure 13.—Heat pipe saturation.

Densification

The hydrogen flow was terminated and the cryocooler remained on overnight to continue to refrigerate the hydrogen remaining in the tank. As was discussed above, the hydrogen was not yet saturated when the flow was terminated, but shortly thereafter it reached the saturated state. The following morning the tank pressure and temperature had stabilized to an expected condition. The pressure was 3.88 psia and the temperatures varied between 16.5 and 18.7 K. There were several unexplained jumps in temperature and pressure measurements, but at this time it is undetermined whether this represents some physical process or an error in the way the data files were manipulated. In either case, the state of the fluid is known at this time. The specific volume is still 0.91 m^3/kg, since no changes occurred either to the system volume or the mass overnight. The saturated vapor specific volume is 2.49 m^3/kg, and the saturated liquid specific volume is 0.0134 m^3/kg. The quality of the fluid is then found to be $x = \frac{\upsilon_x - \nu_f}{\nu_g - \nu_f} = 36.2\%$, or a total liquid mass of 0.06 kg. The density of the saturated liquid is 74.7 kg/m^3, an increase of 5.5 percent over the normal boiling point of the liquid. Figure 14 shows temperature and pressure profiles during this densification period.

The system was allowed to continue to pump down over the weekend, with the exception being a quick period when the cryocooler was turned off for a relocation of the system within the lab for safety purposes. The system warmed up slightly during this time, with the largest increase in temperature being in the cold head. This is expected since the temperature measurement that is most succeptable to increases is the cold head due to conduction down the length of the regenerator portion of the cryocooler. The warm up data is shown in figure 15. From this figure it is obvious the heat pipe never reached the unsaturated state.

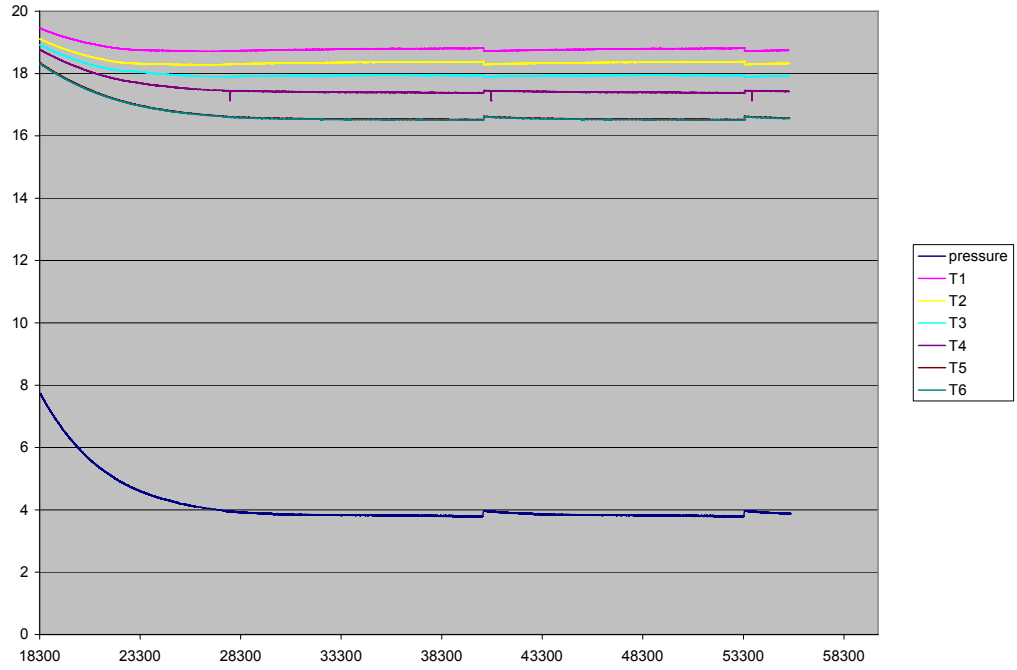

Figure 14.—Overnight densification.

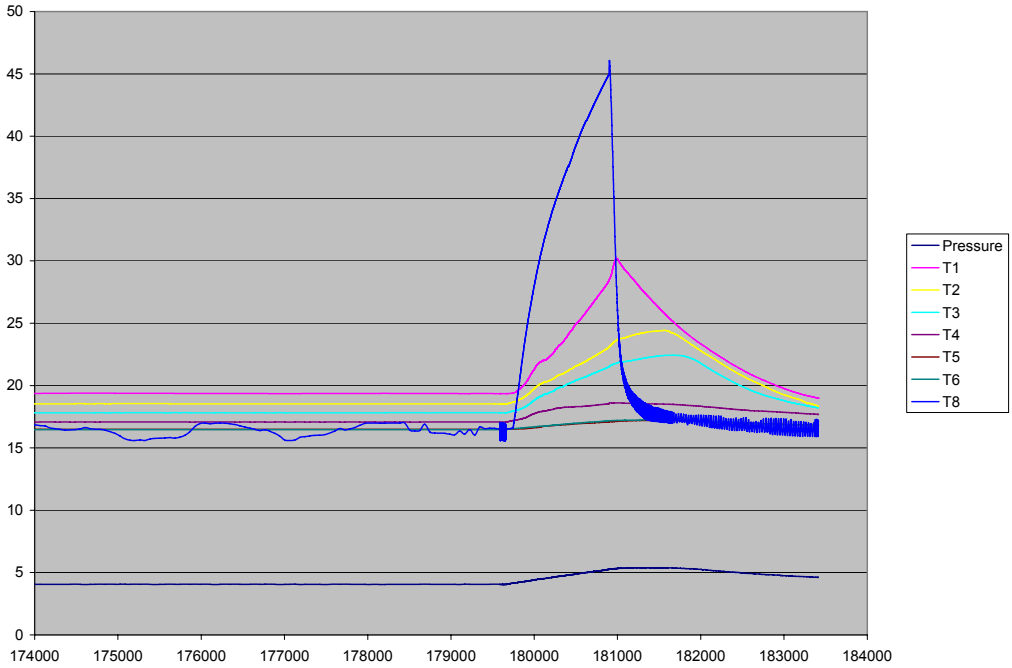

Figure 15.—System relocation warm up.

Continuing Liquefaction

Liquefaction operations was restarted (fig. 16). This operation was slightly different from before since there was a small amount of liquid already in the tank and the system was completely chilled down, as opposed to the hard vacuum on the system prior to the start of the first operation. As such, there were slightly different temperature profiles. Note that the lowest temperature measurements did not increase at nearly the same rate as the upper measurements. This is probably due to the thermal mass of refrigeration stored in the system from cooling overnight. The heat pipe temperature and T4 and T5 on the rake did not increase above 21 K, in fact T5 seemed to stay within the temperature saturation line indicating it remained in liquid (fig. 17). The heat pipe remained partially filled with liquid, allowing for maximum heat transfer to the bottom of the tank. Again, there was some trouble maintaining a constant hydrogen flow rate. At the end of the day, integration showed the total volume of hydrogen inside the tank had risen to 3153 standard liters.

There was some behavior in the tank that was not expected. Once the hydrogen gas flow was terminated, the pressure began to decrease as expected, since the cryocooler was condensing the ullage gas. However, the ullage temperatures fairly quickly collapsed to the saturated state, equaling the liquid temperature. The ullage remained saturated for approximately 30 min, and then the expected temperature gradients began to reappear in the ullage. This behavior was not observed on the first day, due to the fact that there was still no liquid in the tank at the time the gas flow was terminated. Similar behavior was observed to some extent on all subsequent days the hydrogen flow was terminated. Figure 18 shows this ullage collapse graphically.

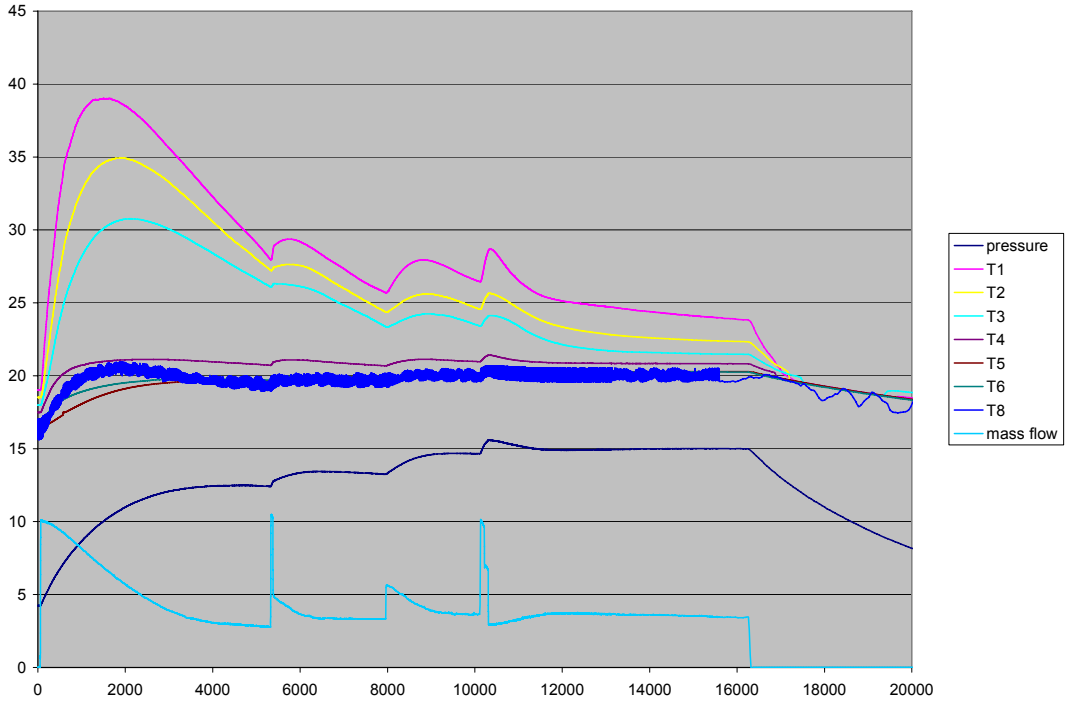

Figure 16.—Day 2 liquefaction.

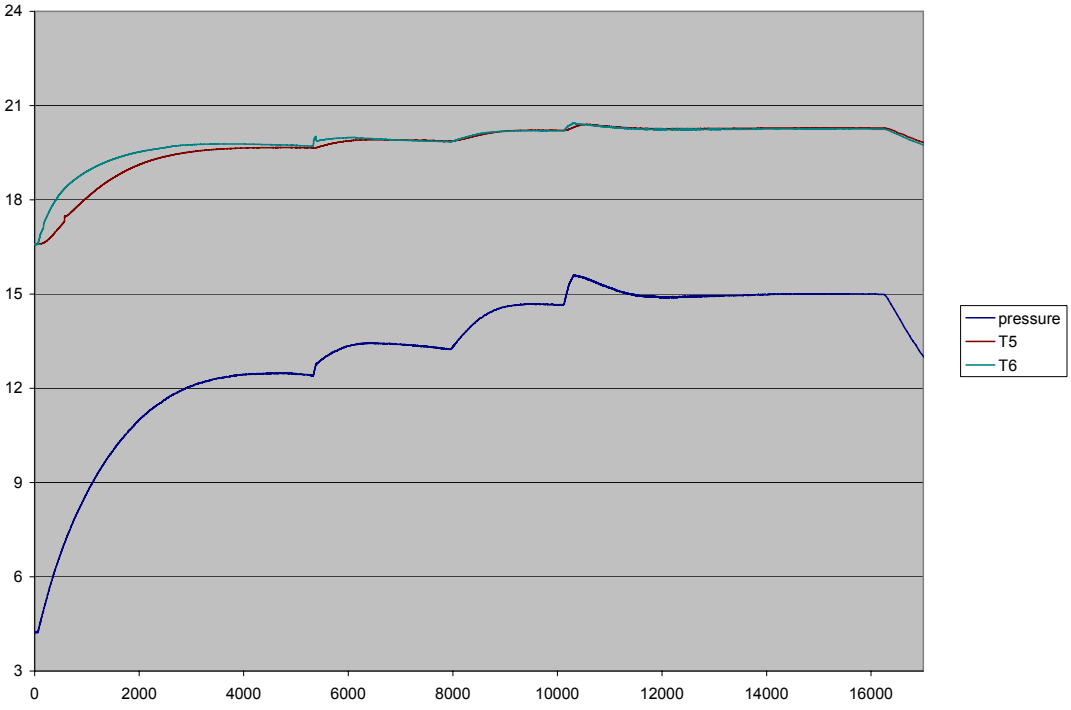

Figure 17.—T5 and pressure saturation curve.

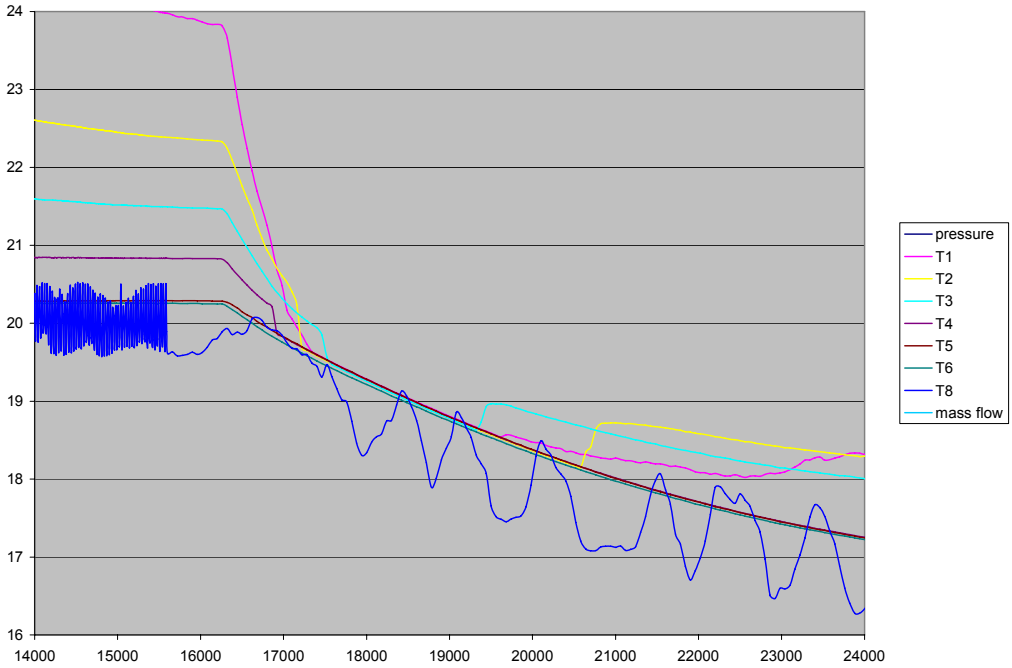

Figure 18.—Ullage temperature collapse.

Hydrogen flow and liquefaction operations continued for the next several days on first shift only, with only slight changes in data. Plots are shown in figures 19 and 20 for the next two days. At the end of these two days, a total of 7565 standard liters of hydrogen had been liquefied. At this point, hydrogen flow was terminated for the next week, and densification operations continued around the clock. After one week of densification, the stabilized temperature at the bottom of the system remained 16.7 K, roughly equal to the temperature achieved at the end of an overnight chill down. A second bottle of gaseous hydrogen was purchased and connected to the system, and liquefaction operations recommenced.

Following another week of densification, the liquefaction operations began again. A second K-bottle of gaseous hydrogen was connected. Liquefaction occurred on first shift all five days that week, with very similar temperature and pressure profiles as was recorded previously. At the end of the week, a total of 15,214 standard liters of gaseous hydrogen had been liquefied, or 1.25 kg. This is equal to 17.65 liters of liquid in the tank. At this time it was decided no further liquefaction would be allowed in the small laboratory that was being used, due to safety constraints. Further liquefaction would occur once the outdoor hydrogen test facility was completed.

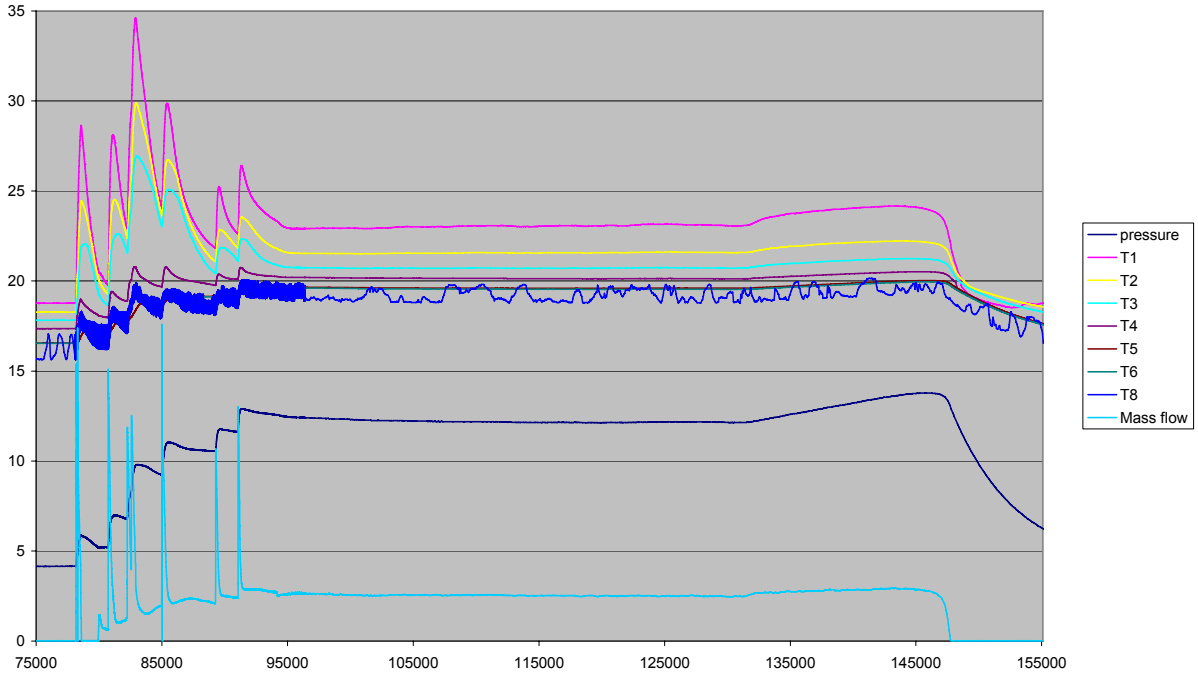

Figure 19.—Liquefaction.

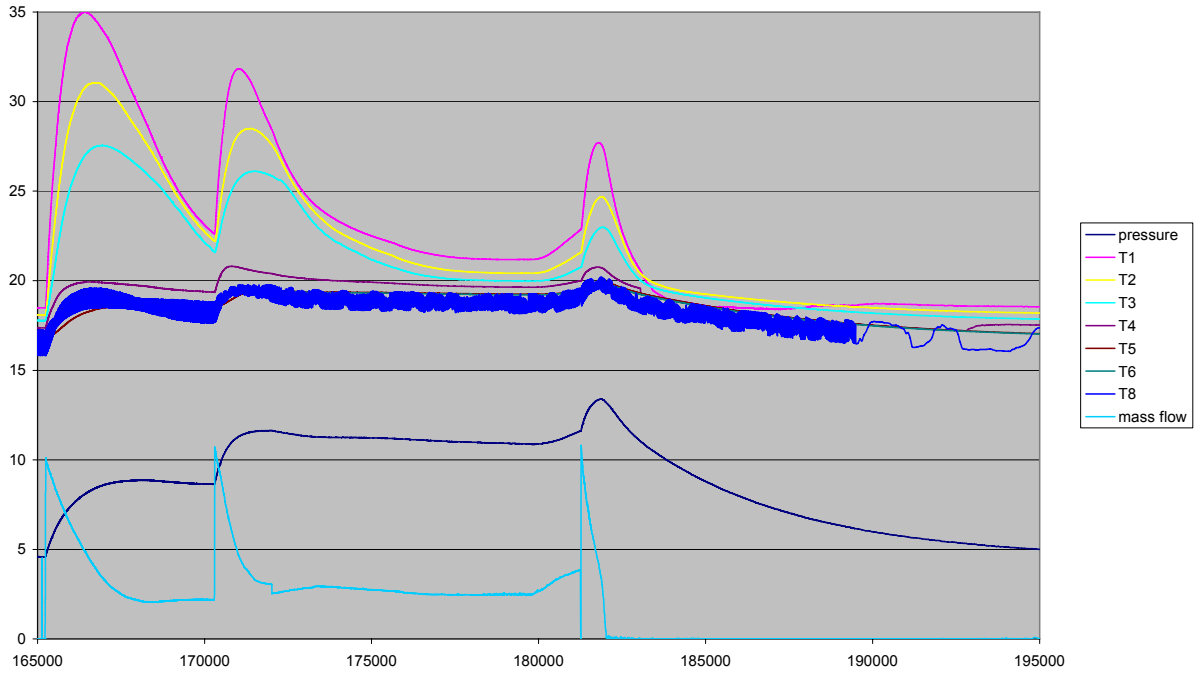

Figure 20.—Liquefaction.

Zero Boil-Off Storage

Although no further liquefaction was allowed, the system remained partially full of liquid hydrogen. Testing was performed to determine the minimum cryocooler run time necessary to maintain the hydrogen in the tank without boil off losses. This was done for two reasons; first, to minimize the energy expended, and second, to minimize the excessive noise in the lab that the G-M refrigerator caused. Figure 21 shows the typical temperature and pressure profiles of the ZBO testing for two days. The cryocooler was turned off for 8 to 9 hr on first shift, then turned back on at the start of second shift and allowed to cool overnight. Pressure rise in the tank reached 33 psia, below the relief valve set point, so no venting occurred. The cryocooler generally took about 7 hr to recondense the boil-off and achieve the densified condition again. Since there was no way to turn on and off the cryocooler automatically, the cooler continued to operated over third shift and was then turned off at the start of the next first shift. Future performance upgrades to the system will include a control system to automatically start the cryocooler when the pressure reaches a set point (33 psia), and turn off the cooler when the low point pressure is reached. The ZBO operations continued until securing for Hurricane Charley dictated the system be drained and purged of H_2.

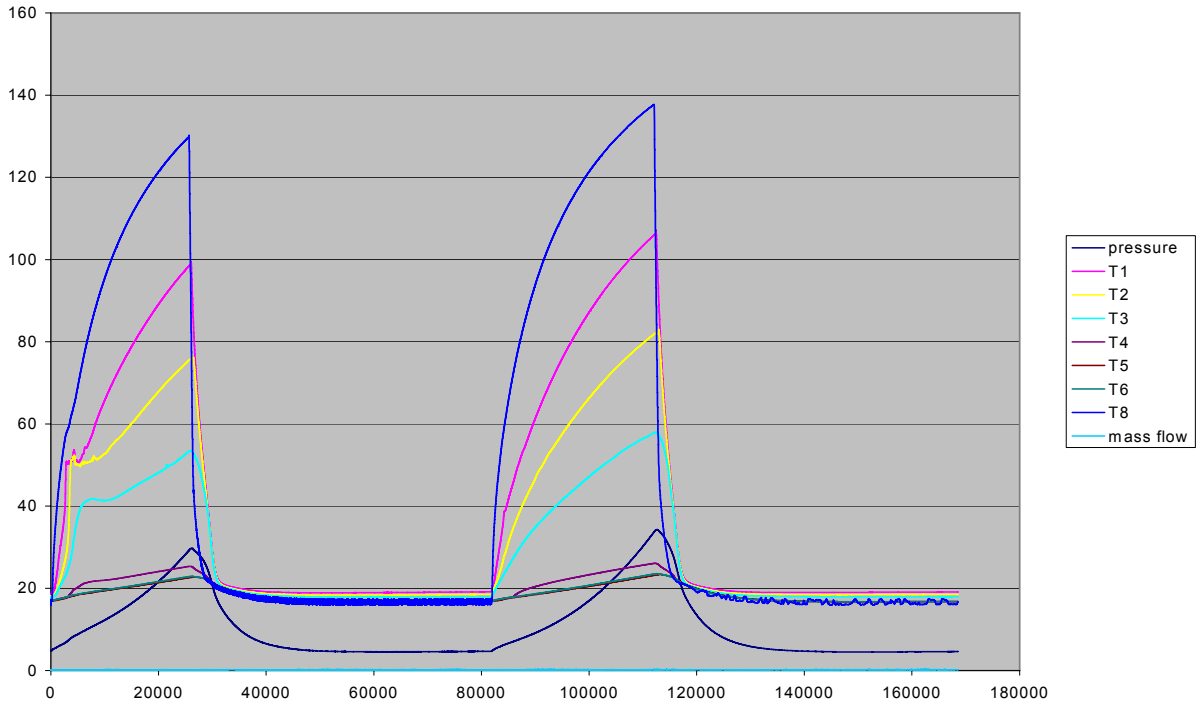

Figure 21.—Zero boil-off testing.

R&D Processes for Increasing the Fluid Density of Cryogenic Liquids

PI: J. Baik (Florida Solar Energy Center)

Description

Technologies that provide for the densification (sub-cooling) of cryogenic propellants, conditioning, transfer, storage and mass gauging are of prime interest for spaceports of the future and space launch environments. Density improvements of 8 percent for densified LH_2 (DLH_2) and 10 percent for densified LO_2 (DLO_2) can provide benefits including reduced gross lift-off weight of a launch vehicle system by up to 20 percent or increased payload capability. Densification technology may even be applied to liquid air separation plants. This effort involves the engineering study and development of second-generation densification production systems that could be used to increase the fluid density of the product cryogenic liquids. Metrics to be used for evaluating advanced densification processes are: higher efficiency, lower capital and operating costs, and improved safety and reliability. Benefits of high density propellants include: (a) reduced boil-off loss of cryogens in storage resulting from the lower vapor pressure, and (b) increased delivery loads of cryogenic fluids to a customer's site given a fixed capacity tanker-trailer to transport the liquids. This task will include an assessment of land-based zero boil off systems using advanced and innovative process design concepts. It is of interest to define and quantify the potential economic benefits and cost impacts associated with handling densified propellants in storage and transportation systems.

Objectives

To determine the optimum combination of densification system components including liquefier, cryocooler and heat exchangers for ground support system and launch vehicles.

To demonstrate various operation conditions and metrics to be used for optimization of densification processes that include higher efficiency, improved reliability and functionality with the state-of-the-art technology.

Benefit to NASA

The results from this task will determine an optimized combination of 2^{nd} generation densification system which is efficient, reliable and safe. The optimized densification system will be suggested based on various densification cycle analysis and operability simulations. Parametric study of densification system will provide optimum operating condition including operating pressure, required mass flow rate, effectiveness and efficiencies of system components. Capital cost, life-cycle cost and operational cost analysis will be investigated and provided to determine the feasibility of actual installation of the densification system at NASA Kennedy Space Center (KSC).

Summary

At Florida Solar Energy Center (FSEC) of the University of Central Florida (UCF), we are probing processes for increasing density of cryogenic propellants for launch vehicle applications. Technologies that provide for the densification of cryogenic propellants, conditioning, transfer, storage and mass gauging are of prime interest to the spaceport of the future and space launch activities. Density increases of 8 percent for LH_2 and 10 percent for LO_2 have been shown to have the advantages of reduced gross lift-off weight of a launch vehicle by up to 20 percent or increased payload capability.

First, thermodynamic system analysis was performed for various liquefaction, densification and recirculation systems. The objectives are to determine the optimum combination of system components including liquefier, cryocooler and heat exchangers for ground support system and launch vehicles. The base analysis results demonstrate various operation conditions and metrics to be used for optimization of

densification processes that include higher efficiency, improved reliability and functionality with the state-of-the-art technology.

Second, thermodynamic design on two-stage refrigeration cycles is performed as one of feasibility studies for the densified propellant technologies. The refrigeration is required to increase the density of liquid oxygen and liquid hydrogen by subcooling to 65 and 15 K, respectively. The objective of this study is to seek the most efficient and economic two-stage refrigeration cycle, which satisfies the specific cooling requirements at the two temperature levels so that both densified propellants can be supplied simultaneously on a scheduled launch countdown. Recuperative cycles such as Claude and reverse Brayton refrigeration can be modified for subcooling liquid oxygen and liquid hydrogen, as is commonly used for large capacity at lower temperatures. It is proposed to use a hybrid or cascade cycle, combining recuperative heat exchangers, expander and Joule-Thomson (J-T) valve at 65 and 15 K. A variety of two-stage cycles derived from J-T, reverse Brayton and Claude cycles are examined. The essential features and characteristics of selected hybrid two-stage cycles are reported through a rigorous thermodynamic analysis. Among the examined cycles, two-stage reverse Brayton helium refrigeration system shows a very suitable possibility for the cryogenic propellant densification technology.

Introduction

The densification of cryogenic propellants for launch vehicle applications is one of the most promising technologies to realize the single-stage-to-orbit (SSTO) and the reusable launch vehicles (RLV) by reducing the vehicle's mass. Propellants densification is a technique for reducing propellants' saturation temperatures below their normal boiling point (NBP) and render them denser. By densifying the propellants that must be carried on-board launch vehicles, a significant decrease in the propellant tank volume and mass is realized. This in turn reduces the gross lift-off weight (GLOW) of a launch vehicle. For example, density increases of 8 percent for DLH_2 (densified liquid hydrogen) and 10 percent for DLO_2 (densified liquid oxygen) have the advantage of reduced GLOW of a launch vehicle by up to 20 percent or increased payload capability.

In 1994, NASA Marshall Space Flight Center (MSFC) performed a feasibility study of densification system (ref. 1) to identify candidate concepts and determined their performance, operational, and cost issues. In MSFC study, a system using helium gas injection, sub-atmosphere boiling bath heat exchanger, refrigeration, LHe cooler for LH_2 and LN_2 cooler for LO_2 etc. were considered and assessed in terms of performance, impacts to existing Space Transport System (STS), operational considerations and costs. According to MSFC study, the subatmospheric boiling bath heat exchanger (or, thermodynamic venting system), refrigeration and LHe/LN_2 coolers were shown to be more appropriate devices to be used for densification of LH_2 and LO_2 propellants.

More recently, NASA and Lockheed Martin Space Systems Company (MLSSC) have developed and tested subscale LH_2 and LO_2 densification units based on the subatmospheric boiling bath heat exchanger method (refs. 2 to 6). The NASA/MLSSC subscale LH_2 densification unit with open-loop no-recirculation demonstrated its ability to produce 0.9 kg/s of LH_2 at 14 K in the initial tests. In addition, a series of closed-loop LO_2 densification and recirculation tests was successfully carried out in a 20,000 gal (76 m^3) propellant tank with subatmospheric boiling bath heat exchanger unit installed. The NASA/MLSSC unit processed a maximum flow rate of 13.6 kg/s of LO_2 at 67 K (ref. 5). However, the safety and operational concerns in using subatmospheric boiling bath heat exchanger and cold compressor were raised after the tests began since the boiled-off propellant needed to be vented to atmosphere in case of open-loop and limitations on the performance of cold compressor used.

Other refrigeration cycle technologies have also been considered. One utilizes an orifice pulse tube refrigerator driven by thermoacoustic engine and another employs a packed column cooling tower design based on evaporation of liquid into a non-condensable gas. These technologies present other alternatives and especially for their promise of operational simplicity and reliability. Even though the orifice pulse tube refrigerator can be expected to have a higher efficiency than other conventional cryocoolers such as Gifford-McMahon refrigerator, nonetheless it has remained at the developmental stage, thus rendering it a high-risk technology. The operation of a packed column cooling tower technology is expected to be expensive because of its high helium consumption as a non-condensable gas. The use of commercially available cryocoolers presents another option because of their stable operation and proven technology, but their cooling efficiency is comparatively lower. Thus, each prospective densification technology has pros and cons for use at the launch site.

The densification system for next generation RLV should be able to produce required amount of densified propellants at each required temperature within scheduled time. It also should be designed to minimize boil-off rate of propellants or re-condense them. It should minimize the use of supplemental cryogens such as He, H_2, O_2 and N_2 during operation at the launch site and it should be technically viable in a near future. To reach the goal of the development of an efficient, reliable and safe densification system and to operate such a system for various launch schedule of space vehicles, a question arises as to which option would be the best? The answer is that a combination of prospective candidates so that the combined approach would mitigate the disadvantages of each prior technique and at the same time satisfies the requirements and optimization of the various launch scenarios. In fact, the subatmospheric boiling bath heat exchanger technology is very efficient way of densifying propellant. However, cryogens used in subatmospheric boiling bath could be recovered by a cryocooler or a heat sink.

In order to optimize the densification system for cryogenic propellants, thermodynamic analysis of various liquefaction, densification and recirculation systems will have to be performed. In this task, Claude, reverse-Brayton cycle, subatmospheric boiling bath were used as refrigeration and densification heat sinks. Performance data for various commercial cryocoolers were collected to determine the densification process feasibility. Thermodynamic analysis including various cycle simulations was carried out to determine the performance of densification/recirculation system. Actual specifications of system components such as compressor, liquid cryogen pump, type and size of heat exchangers etc. were used to provide realistic results. The optimization analysis determines the most efficient and achievable combination for ground densification / storage / transportation and recirculation system at launch pad by reviewing available technologies that may be applicable. Figure 1 shows a summary of the system optimization parameters for densified propellants.

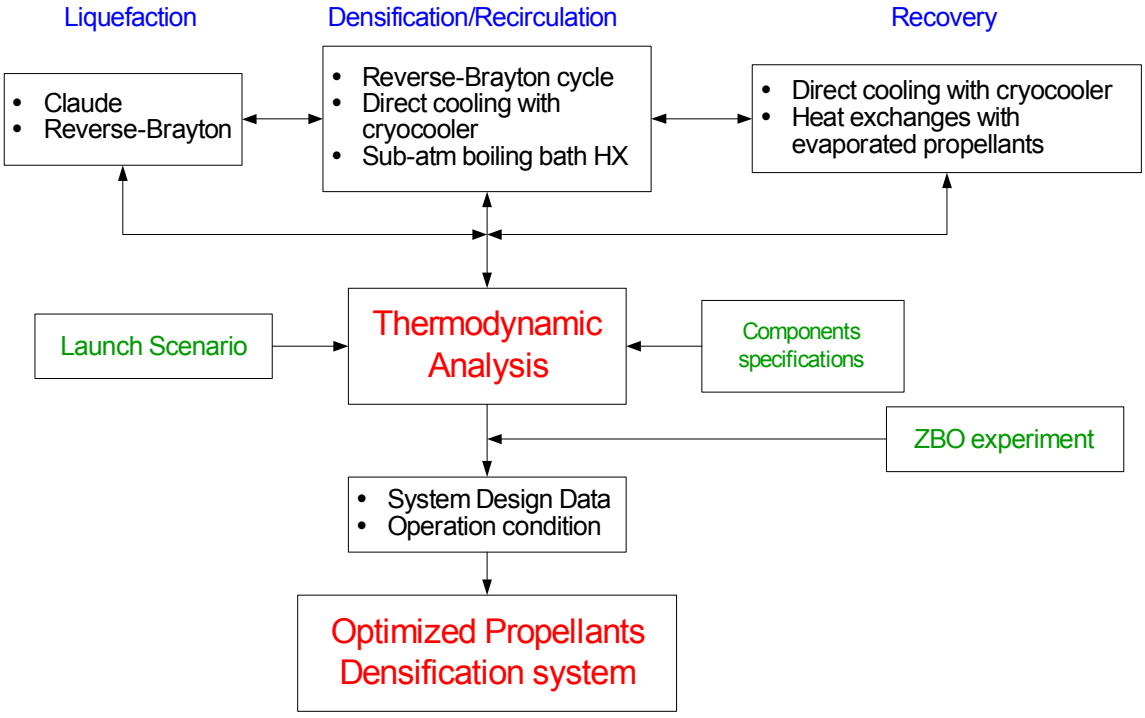

Figure 1.—A summary of the system optimization process for propellants densification.

Launch Scenarios and Cooling Power

Launch scenarios.—All thermodynamic calculations should be based on a specific ground operation scenario at the launch site that incorporates propellant storage, densification and loading to the flight tanks. There are many options for ground operations when designing a launch pad operation with densified propellants. These options are based on how the propellant is stored, when it is densified, and how it is loaded into the vehicle. Figure 2 shows several possible launch scenarios that were selected because they required least amount of change from the present launch system operation.

The *load-and-go* is the scenario that takes near boiling point (NBP) propellants stored at the pad storage tank, densifies and loads them back into the launch vehicle external tank during the nominal 3 hr launch countdown timeline. It requires the maximum cooling power of the densification system within the shortest operation time possible. Since there's no recirculation of boiled-off gas at the flight tank, the state of the densified propellant in the flight tank degrades over time after it is loaded but before it is launched. It has an advantage that it doesn't need other modifications at the present launch pad except adding a new densification system between the storage tanks and the flight tanks.

The *load-and-recirculation* option is for conditioning the densified propellant in the flight tank by recirculating the warm fluid off the top of the tank and recooling it in the densification unit. This adds some complexity and cost to the ground operation and flight systems such as a recirculation pump, but ensures maximum benefit to densified propellants. Since this option may be appropriate for 3 to 12 hr period prior to the launch countdown timeline, the cooling capacity requirement in the densification unit can be reduced.

The *pre-launch densification-and-storage* option reduces the required refrigeration capacity by increasing the timeline allowed for densification. This option densifies NBP propellant stored in a 1st storage tank at 12 to 24 hr prior to launch and then shifted to a 2nd pad storage tank. This densified storage tank is used to load the launch vehicle at the proper time during countdown. The advantage of this option is that it provides an order of magnitude or more reduction in the densification unit size compared to load-and-go, but the disadvantage is its increased ground system complexity and costs due to the addition of a second storage tank.

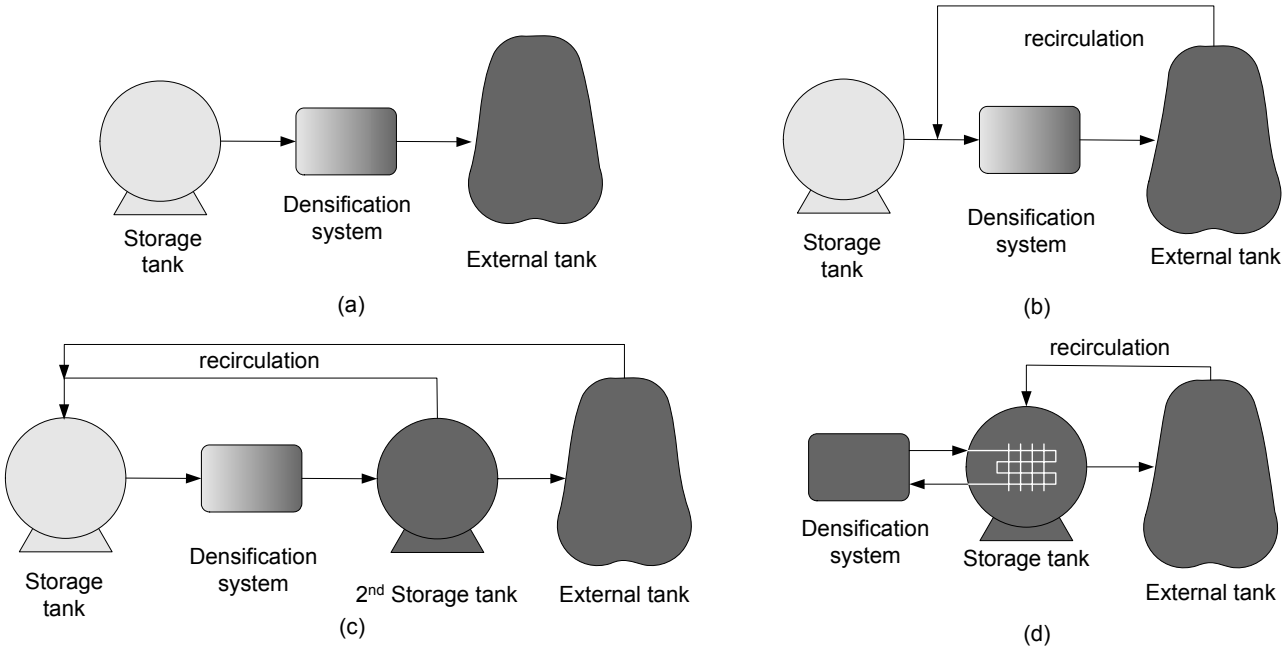

Figure 2.—Launch scenarios of space launch vehicle: (a) load-and-go, (b) load-and-recirculation, (c) predensification-and-storage, (d) continuous densification

Depending on the launch frequency, the *continuous densification* scenario may be advantageous to continuously densify the propellant and keep it stored in the densified or subcooled state. This option can minimize the required cooling power by starting the densification unit for 10 days, for example, prior to the launch schedule. There is no longer propellant boil-off problem at the launch site, and thus it has great potential for substantial cost savings. This approach also enhances launch operation flexibility and eliminates potential hazards of venting when the launch is scrubbed.

Cooling power analysis.—Four different launch scenarios described above will have dominant effects on the required cooling capacity of densification system. Table 1 shows base assumptions for the densification system analysis including target densification temperatures and cooling power required. For heat leaks to the storage tank and vehicle external tank, the present performances of STS launch vehicle and propellant storage tanks at the NASA KSC were used. Figure 3 depicts the required cooling power of densification system as a function of densifier operation time prior to launch based on table 1 assumptions. For load-and-go option, since it has only 3 hr operation time to densify the propellants, the required cooling power should be maximum, which exceeds 6MW for LO_2 and 1MW for LH_2. On the other hand, the continuous densification option minimizes the required cooling power of the densification unit down to only those of heat leak into the vehicle external tank. These results show that selection of densification system is affected by the launch rate, launch scenarios, techno-economic analysis of the system including capital, operating and life-cycle costs.

TABLE 1.—BASE ASSUMPTIONS FOR DENSIFICATION SYSTEM ANALYSIS

	LO_2	LH_2
Densification temperature (K)	65	15
Propellant mass in external tank (ET) (kg)	1,554,800	259,200
Heat leak to ET (kW)	90	180
Heat leak to storage tank (kW)	11	0.8
Required cooling power (kW)	90~6100[a]	180~1100[a]
COP_{carnot}	0.277	0.053
Required ideal electrical power (MW)	0.4~22	3.4~20

[a]Based on 'load-and-go' scenario (prior to 3 hr launch countdown)

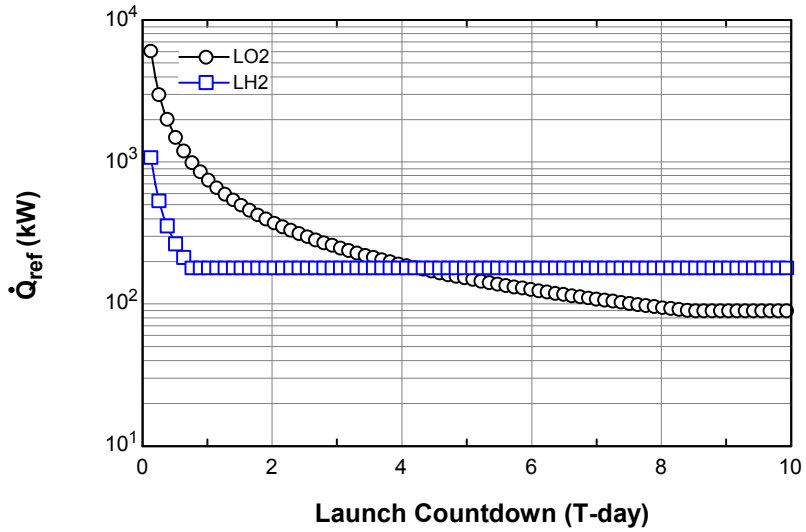

Figure 3.—The required cooling power of densification system as a function of densifier operation time prior to launch for LO_2 and LH_2.

Single-Stage Densification Systems

Introduction.—The number of system combination for conducting propellant densification is virtually unlimited. Claude cycle, Collins cycle, cascade refrigeration and mixed refrigerants refrigeration and so on. Also, depending on the system configuration, the choice of system components including compressor, pump, expander, expansion valve, heat exchangers etc. is very large. However, the densification temperature of cryogenic propellants narrows the choice of prospective refrigeration cycle or system that can be employed as a heat sink in the densification system. In particular, densifying liquid hydrogen limits the selection of cryogenic refrigeration cycles available. In this work, several well-known cryogenic liquefaction and/or refrigeration cycles were selected for this densification feasibility study.

The Claude cycle is used in large scale nitrogen, hydrogen and helium liquefaction processes. It consists of multi-stage compressor, heat exchangers, expanders and expansion valve. Precooling with LN_2 can be used to decrease cooling loads at cold temperature. Figure 4 shows a schematic diagram of the Claude cycle for hydrogen densification. In this illustration, Claude cycle directly generates densified hydrogen at 15 K and exchanges its cold heat with NBP hydrogen stored at storage tanks. In addition, a helium Claude cycle operating at 15 K is another available option. For oxygen densification, almost the same Claude cycle can be used with nitrogen instead of helium or hydrogen gas. The Claude cycle analysis for both oxygen and hydrogen densification will be discussed in a later section. Likewise, reverse-Brayton cycle shown in figure 5 that has cold expander instead of expansion valve may be considered as an alternative densification system.

Thermodynamic venting system (TVS) is another option for generating densified propellants. TVS is a proven technology (refs. 5 to 6). Figure 6 depicts the concept of combining the Claude cycle and TVS using subatmospheric boiling bath for hydrogen densification. For hydrogen densification, the same Claude cycle at 20 K operation, produces liquid hydrogen near NBP, and then it is densified via the use of a centrifugal multi-stage cold compressor. In TVS system for oxygen densification, the Claude cycle operates with nitrogen instead of hydrogen and generates NBP liquid nitrogen. Cold compressor changes NBP liquid nitrogen bath to 65 K densified nitrogen bath, and then NBP liquid oxygen stored at storage tank can be densified by exchanging heat with the 65 K nitrogen bath. Both analysis results will be discussed in this report.

It is possible to run any number of cryocoolers at required densification propellant temperature even if the cooling powers of cryocoolers are much smaller than the other liquefaction cycle. For 65 K operation, the-state-of-the-art cryocoolers such as GM cryocooler and pulse tube refrigerator produce 80~850 W of cooling power with 6~20 kW of electric input power, and for 15 K operation, their COP and Figure of Merit (FOM) are less than 0.005 and 0.07, respectively. The more detailed discussion regarding densification system efficiency and cooling power are given below.

Cycle optimization.—To optimize propellant densification, the author performed several cycle simulations for selected densification models described before to determine system feasibility and derive system efficiencies. For component specifications, commonly acceptable values were used. For example, 80~85 percent was assumed for adiabatic efficiencies of compressors and expanders, and 85~95 percent for heat exchangers effectiveness. In all of the cycle simulations, real thermodynamic properties were used to determine thermodynamic states.

Figure 7 shows a sample of cycle simulation for combination of Claude cycle and TVS for hydrogen densification. Claude liquefaction cycle with continuous LN_2 precooling generates NBP of hydrogen after expansion valve. TVS using multistage centrifugal cold compressor densifies NBP hydrogen to 15 K densified hydrogen. The TVS exhausts hydrogen back to Claude liquefaction cycle and completes closed-loop system. The adiabatic efficiency of compressor was assumed to be 85 percent, and expander 80 percent. All the heat exchangers were assumed at 90 percent effectiveness. For a fixed cooling power required (1100 kW in fig. 7), our results indicate that a mass flow rate of 6 and 11 kg/s for hydrogen and LN_2 will be required in the combination Claude cycle and TVS, respectively. With 40 percent of Carnot COP assumed in LN_2 liquefier, 20 K Claude liquefier and 15 K TVS show 60 percent of Carnot COP. Once every node in the cycle satisfies thermodynamic equilibrium for given operating condition, all the parameters in the simulation can be easily modified for different performance levels of the system components. For example, we can change operating pressure of the compressor in the Claude cycle, fraction of mass flow rate flowing through expander, effectiveness of heat exchanger, the number of stage of centrifugal gas compressor in the TVS and so on.

The similar cycle simulations have been carried out for various densification systems with reasonable operating conditions and these results are demonstrated in table 2. Even though the performance of each densification system has not been optimized, we still see the range of their performance. Noting that all the densification systems except cryocooler has been assumed as ideal without taking account of any practical inefficiency. If system inefficiencies are included in the detailed simulation, actual performance will be much lower. The performance of cryocoolers includes all the possible inefficiencies in actual operation since they are collected data. Regarding the performance of cryogenic refrigeration system, the "Strobridge plot" has been used since 1974 to display the relationship between system efficiency and size of refrigeration system (ref. 7). Very wide ranges of performance of cryogenic refrigerators are condensed in this plot. According to the contemporary version of the Strobridge plot, it is clear that the efficiency of system increases as the system size or cooling power increases. However, there has been a 'practical' upper limit of about 40 percent of Carnot efficiency that can be found only in huge liquefaction plants. The larger size of densification system, the higher efficiency, and it moves the launch scenario towards 'load-and-go' option. However, large densification system at launch site requires large expenditures for its huge size and must be justified by the launch frequency. On the other hand, small size of densification system significantly reduces the required cooling power of densification unit at launch site despite the loss of economy-of-scale.

TABLE 2.—A SUMMARY OF CYCLE SIMULATIONS
FOR VARIOUS DENSIFICATION SYSTEMS

$\dot{Q}_c$ (kW)		System	COP	FOM	$\dot{W}_{ideal}$ [b] (MW)
LO_2 (65 K)	90~6,100	Claude	0.11	0.41	0.8~54
		Modified Claude[a]	0.13	0.49	0.7~45
		TVS+Claude	0.16	0.57	0.6~39
		Cryocooler	0.04	0.14	2.3~153
LH_2 (15 K)	180~1,100	Claude	0.026	0.49	7~42
		Reverse Brayton	0.019	0.36	10~58
		TVS+Claude	0.032	0.61	6~35
		Cryocooler	0.004	0.07	50~306

[a]One heat exchanger at warm temperature is removed from Claude cycle.
[b]Ideal electric input power based on calculated FOM.

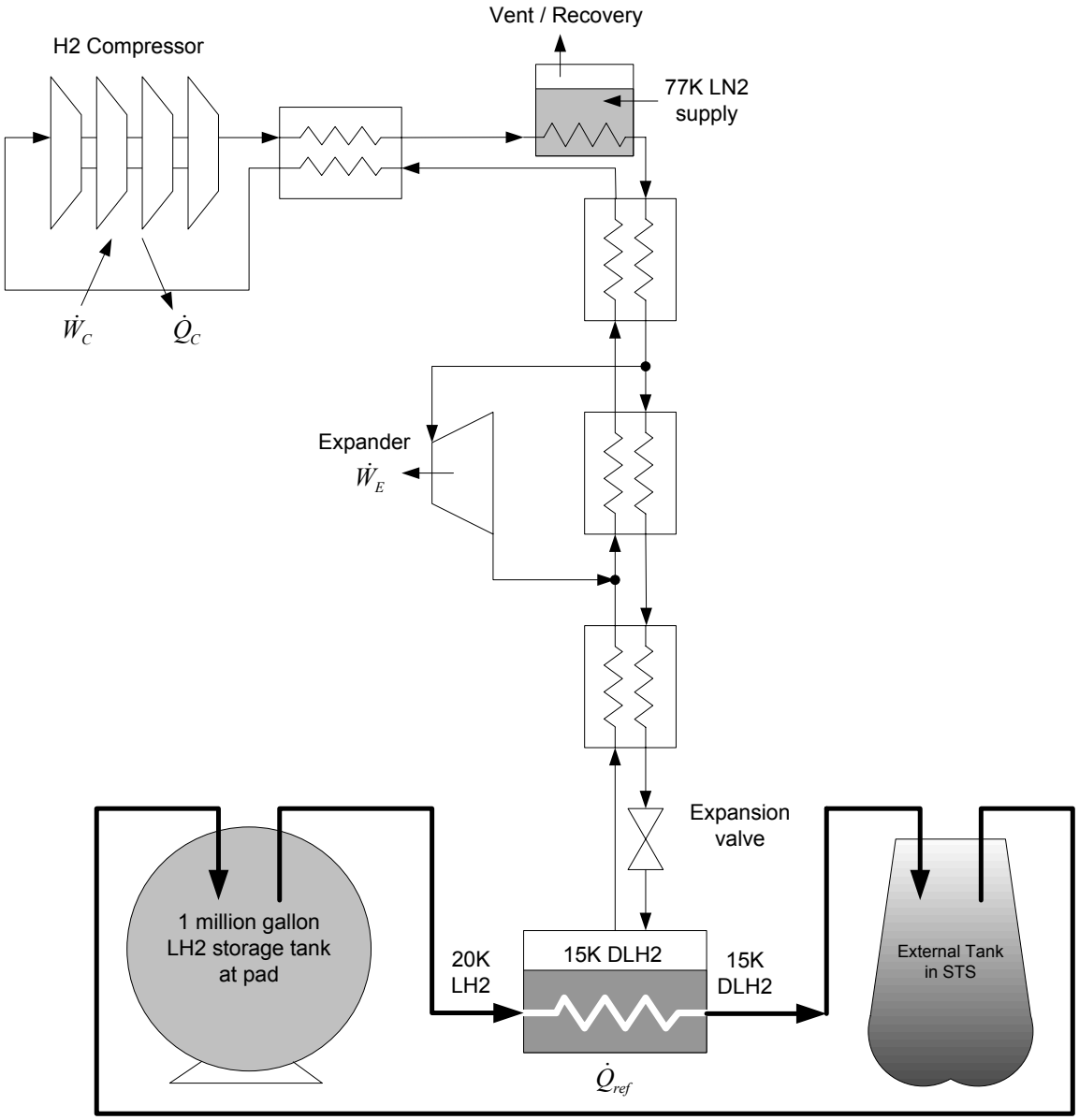

Figure 4.—Schematic diagram of Claude cycle for hydrogen densification.

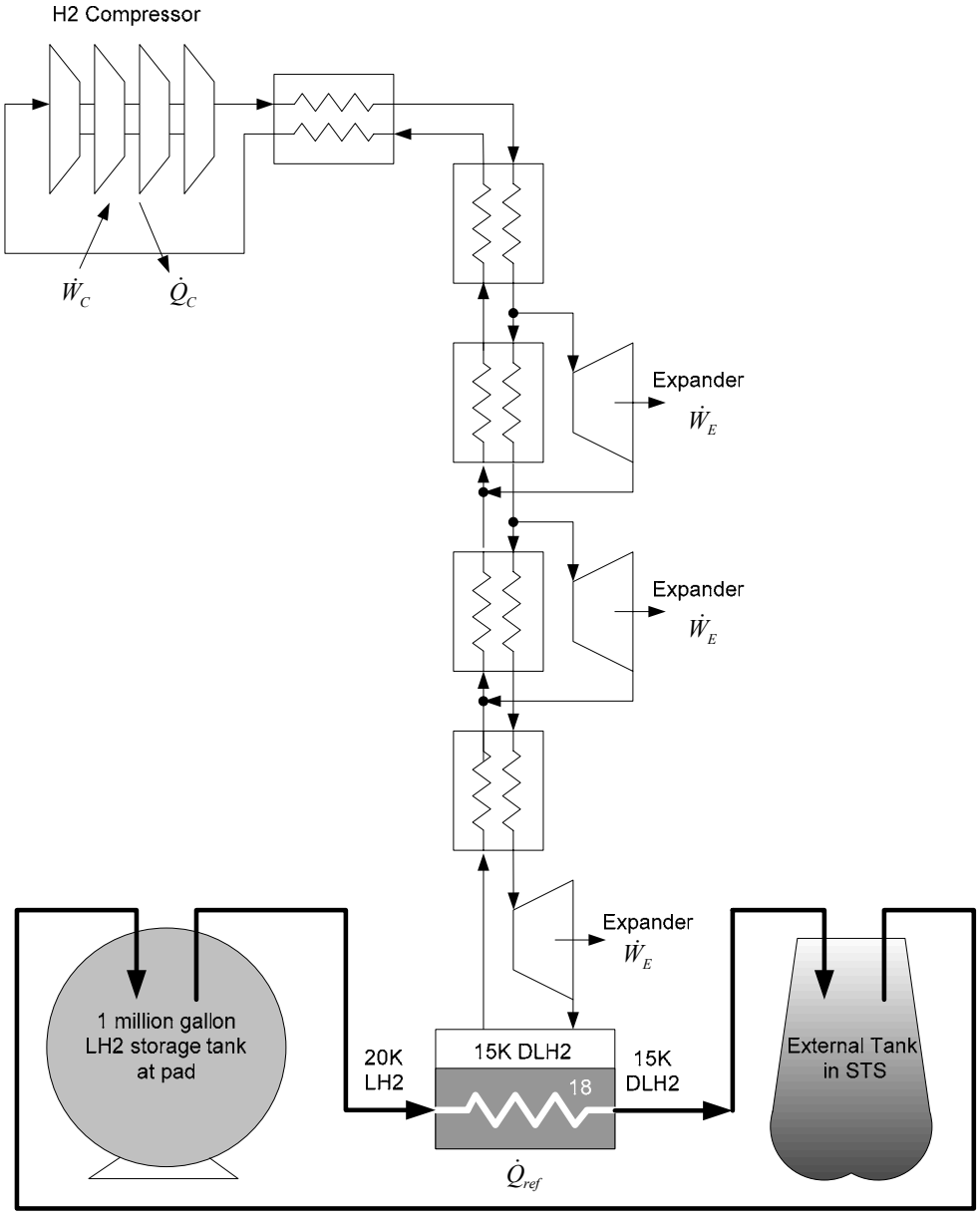

Figure 5.—Schematic diagram of reverse-Brayton Cycle for hydrogen densification.

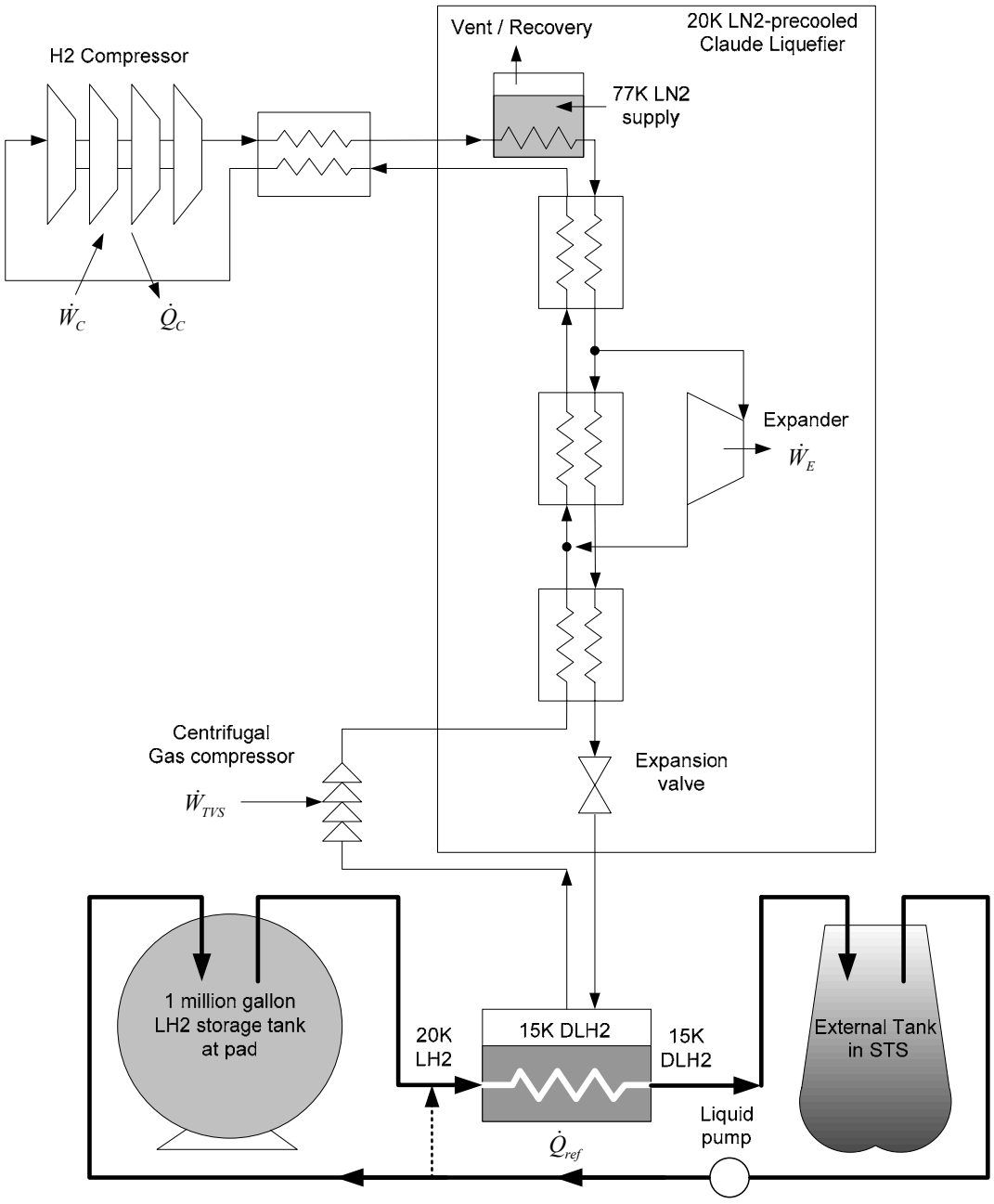

Figure 6.—Schematic of diagram of combination of Claude Cycle and TVS for hydrogen densification.

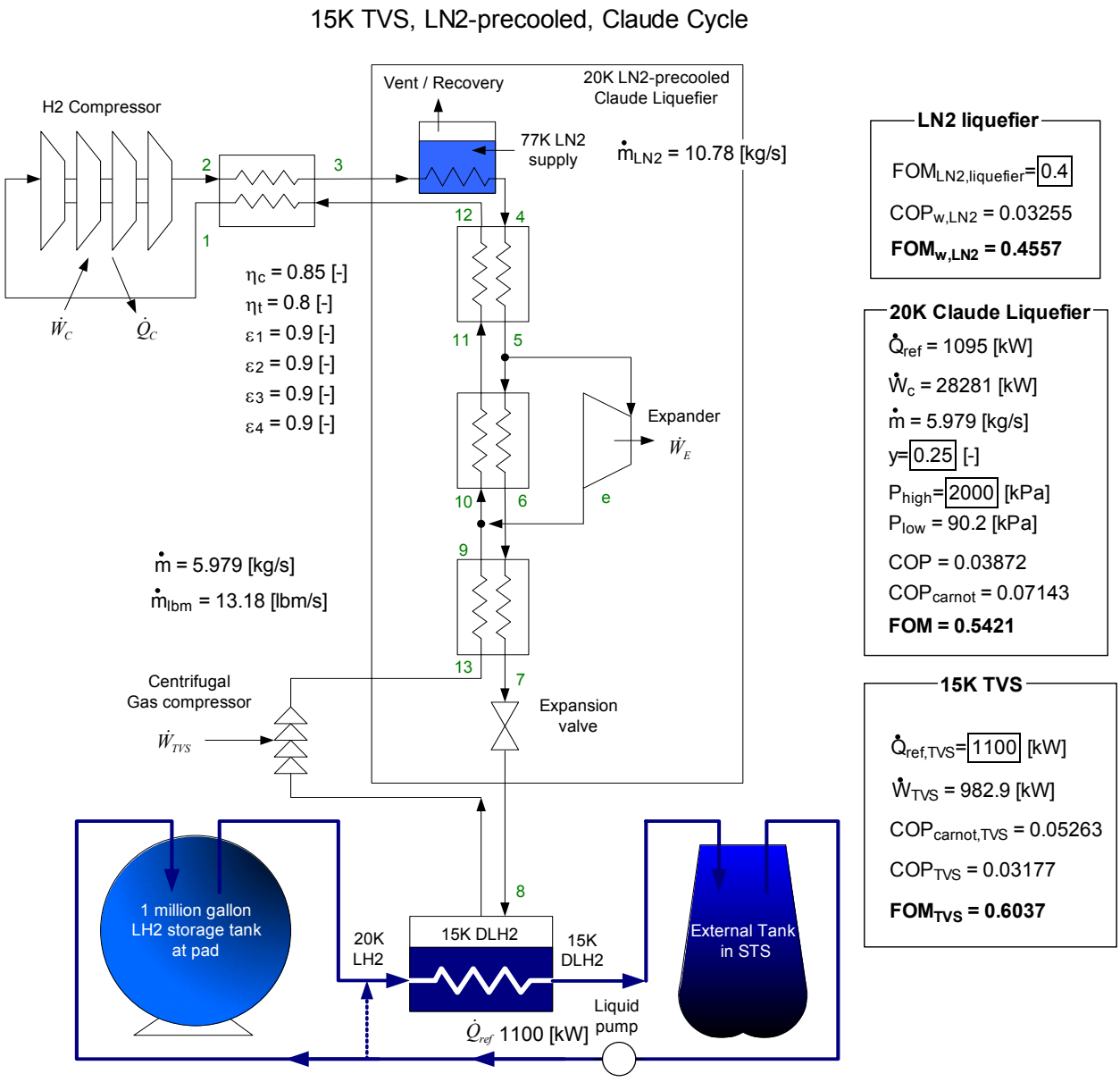

Figure 7.—A sample cycle simulation for combination of Claude Cycle and TVS for hydrogen densification.

Two-Stage Densification Systems

Introduction.—In the previous chapter, as an initial investigation, several promising densification systems were investigated based on various launch scenarios, and a rigorous thermodynamic analysis using real propellant properties was performed to suggest the most feasible and reliable system for the launch vehicle applications. It turned out from the investigation that a combination of thermodynamic venting system (TVS) and Claude refrigerator for each propellant showed a good possibility of highly efficient system from thermodynamic point of view but the system becomes rather complicated. The TVS system or subatmospheric boiling bath heat exchanger technology requires an additional gas compressor to densify NBP cryogenic propellants by lowering its vapor pressure. Furthermore, this technology requires two independent densification systems for liquid oxygen and liquid hydrogen, even if it may be suitable for large cooling power requirements.

In this chapter, it is suggested for thermodynamic efficiency and economic practice that a two-stage refrigeration cycle be used to satisfy the specific cooling requirements at the two densification temperatures. The two-stage refrigeration cycle provides the two specific cooling powers at the two temperatures so that both densified propellants can be supplied simultaneously on a scheduled launch countdown. This technology is achievable by employing recuperative cycles such as reverse Brayton and Claude refrigeration cycle, which are commonly used for large capacity application at lower temperatures. By designing a hybrid or cascade cycle with recuperative heat exchangers, expander and Joule-Thomson valve, it is possible for us to provide the specific cooling requirements at specific densification temperatures at the same time. To verify the feasibility and characteristics of this new concept, a rigorous thermodynamic analysis is performed for a variety of two-stage cycles combined from J-T, reverse Brayton and Claude cycles.

Ideal (Reversible) Cycles.—For a case that two cooling temperatures and their cooling capacities are given, we can classify possible refrigeration systems into three main categories as shown in figure 8. Figure 8(a) shows ‘Two single-stage coolers’ system. Two separate cooling systems with two input powers provide the required cooling capacities at each cooling temperature. As the densification temperatures, 65 and 15 K are selected for oxygen and hydrogen, respectively. Figure 8(b) shows ‘One two-stage cooler’ system which provides two independent cooling powers at two cooling temperatures and requires one work input power. Also, ‘cascade cooler system’ in figure 8(c) can be considered as one of candidates for two cooling temperatures and two cooling powers application. For ideal reversible refrigeration cycles, however, the minimum required work input power should be the same for the three cases. By combining the energy and entropy balances, the minimum required work inputs for three cases in figure 8 can be expressed as eq. (1).

This implies that when we construct ideal cycles, any variation of system configuration does not affect the thermodynamic performances unless operating temperatures and cooling requirements are changed. In reality, however, there must be differences among them since their performances depend on thermodynamic and mechanical efficiencies of system components. For instance, system (a) and (c) in figure 8 have at least two work input components which is, in general, compressors. The requirement of two compressors to run the system may result in more complicated, more expensive, less reliable and less efficient system. On the other hand, system (b) in figure 8 can be operated by only one compressor so that it has an inherent simplicity in system constitution. Furthermore, it can be a versatile system to provide various cooling powers at each cooling stage by controlling system design parameters such as work input, cooling power distribution ratios. Therefore, the choice of appropriate refrigeration system and optimal operating condition based on both thermodynamic and practical consideration should be made at the design stage.

Two-Stage Coolers.—Figure 9 schematically shows a few simplified variations of two-stage refrigeration cycle. Figure 9(a) depicts two-stage reverse Brayton helium cycle. Two expanders are located at each densification stage to densify cryogenic propellants. The gas temperatures at the exits of the 1st and the 2nd expander are required to be low enough to densify saturated cryogenic propellants.

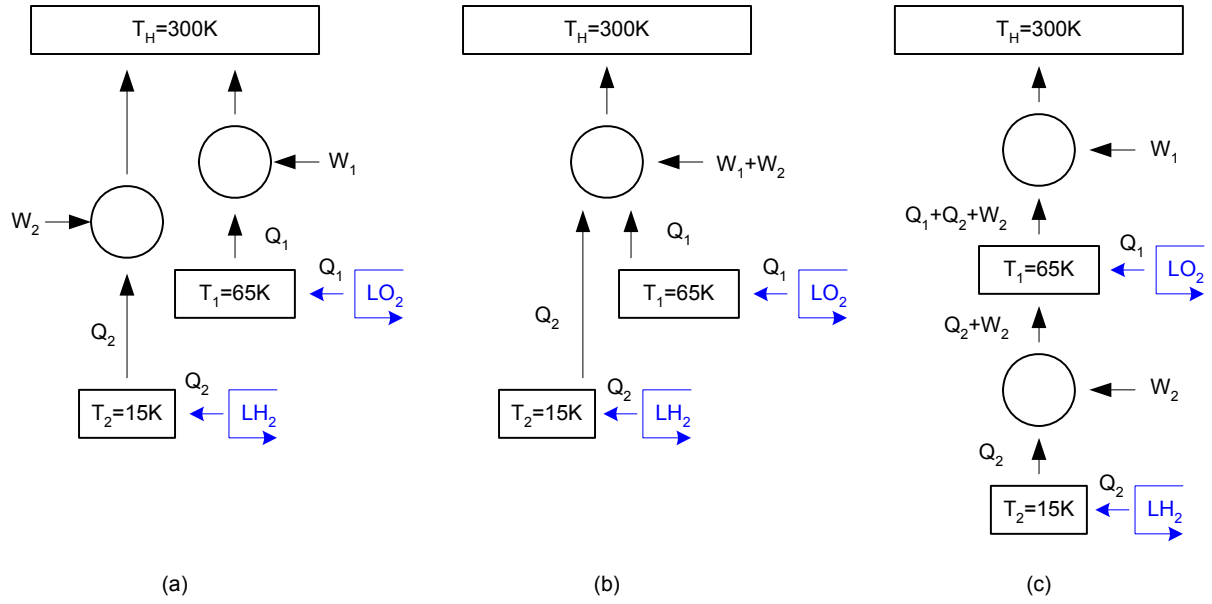

Figure 8.—Ideal reversible cycles operating at two cooling temperatures: (a) two single-stage coolers system, (b) one two-stage cooler system, (c) cascade cooler system

$$
\begin{aligned}
W_{\text{A or B}} &= W_1 + W_2 = Q_1\left(\frac{T_H}{T_1} - 1\right) + Q_2\left(\frac{T_H}{T_2} - 1\right) \\
W_C &= W_1 + W_2 = (Q_1 + Q_2 + W_2)\left(\frac{T_H}{T_1} - 1\right) + Q_2\left(\frac{T_1}{T_2} - 1\right) \\
&= Q_1\left(\frac{T_H}{T_1} - 1\right) + Q_2\left(\frac{T_H}{T_1} - 1\right) + Q_2\left(\frac{T_1}{T_2} - 1\right)\left[\left(\frac{T_H}{T_1} - 1\right) + 1\right] \\
&= Q_1\left(\frac{T_H}{T_1} - 1\right) + Q_2\left(\frac{T_H}{T_2} - 1\right)
\end{aligned}
\tag{1}
$$

Since helium is maintained at gaseous state at the exit of the 2nd (lower temperature) expander, a dry expander can be used. The helium gas temperatures at expander exits and the required cooling powers at each stage can be controlled by varying the mass flow fraction at the inlet of the first expander, the total mass flow rate in compressor and the compressor discharge pressure. Figure 9(b) shows another two-stage cooling cycle, combined from the reverse Brayton and Claude cycles with J-T expansion valve. Even if a Claude cycle is self explanatory that it uses a expander in the 1st stage and a J-T expansion valve in the 2nd stage, this configuration is named as a two-stage reverse Brayton-Claude cycle in this paper because of additional densification heat exchanger at the exit of the 1st stage expander. Since the isenthalpic process in J-T expansion valve is a major source of irreversibility, a lower system efficiency is expected and a higher operating pressure is required. For hydrogen as a working fluid, we expect a benefit of obtaining subcooled liquid hydrogen at the exit of J-T valve to enhance heat transfer in densifying saturated liquid hydrogen. Figure 9(c) and (d) depict more complicated combinations of reverse Brayton, J-T and Claude system as references. These hybrid systems consist of both expander at liquid oxygen stage and J-T expansion valve at liquid hydrogen stage in two independent helium or hydrogen cycles to take advantage of each system component. However, the system configurations tend to be complicated and maintenance issue can be evolved. Therefore, two configurations in figure 9(a) and (b) are chosen in this paper to explore the possibility of using two-stage coolers providing required cooling powers at required densification temperatures.

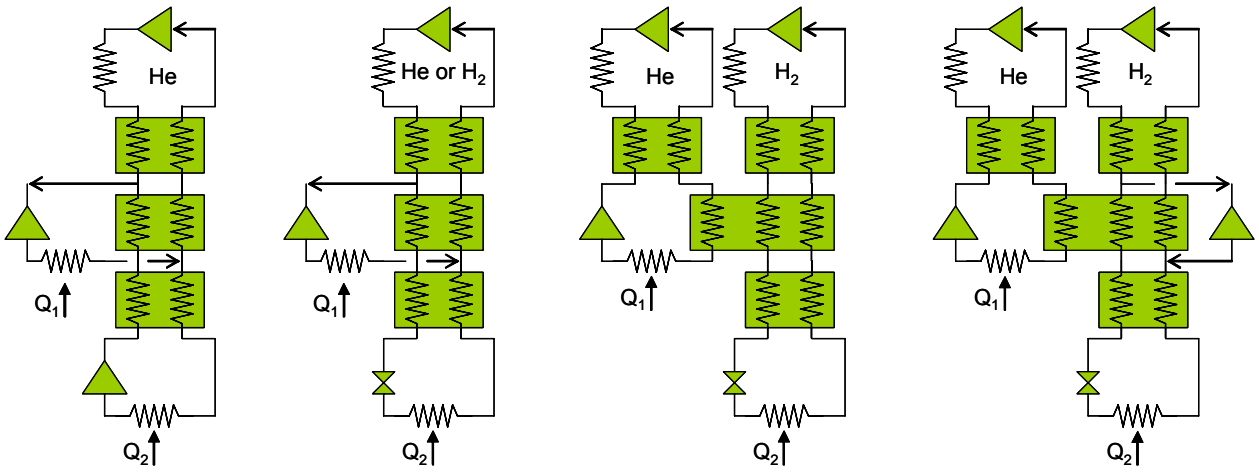

Figure 9.—Two-stage cooler variations: (a) two-stage reverse Brayton helium cycle, (b) reverse Brayton-Claude helium/hydrogen cycle, (c) combination of reverse Brayton helium and J-T hydrogen cycle, (d) combination of reverse Brayton helium and Claude hydrogen cycle.

(1) Two-Stage Reverse Brayton Helium Cycle: Based on the preliminary investigation (ref. 8) on required cooling power for various launch scenarios, the cooling powers that are required to densify 1 kg/s of liquid hydrogen and 6 kg/s of liquid oxygen are fixed in the rest of thermodynamic analysis. These flow rates depend on cooling the propellants before the start of the loading process. If the densification occurs during vehicle load, the rates become much higher. The corresponding cooling powers are 48 kW at 15 K and 268 kW at 65 K, respectively. In this analysis, discharge and suction pressures of compressor are set to 2020 and 101 kPa, respectively. The mass flow fraction at the inlet of the 1st expander, *y*, is defined as the following.

$$y \equiv \frac{\dot{m}_{1\text{st expander}}}{\dot{m}_{compressor}} \tag{2}$$

Figure 10 shows results of thermodynamic cycle analysis for two-stage reverse Brayton helium cycle. In this analysis, computerized real properties of helium are used (ref. 9). Figure 3(a) and (b) show required total mass flow rates of system and mass flow fractions at the inlet of the 1st expander as functions of densification stage temperatures. To obtain 65 and 15 K of cold helium gas after the expanders at densification stages, the system requires about 1.2 kg/s of total mass flow rate in the compressor and the mass flow fraction should be slightly over 50 percent of total mass flow rate from figure 10(a) and (b). Figure 10(c) and (d) shows the same results from different angle of view. By changing total mass flow rate of system and mass flow fraction, it is possible to get various densification temperatures at each stage for a fixed compressor discharge pressure. For a given total mass flow rate, liquid oxygen densification temperature decreases as mass flow fraction increases, since mass flow rate expanded in the 1st expander increases for a fixed cooling power. However, liquid hydrogen densification temperature has a minimum value because the liquid hydrogen densification temperature is affected by the liquid oxygen densification temperature and mass flow rate at the 2nd stage at a fixed cooling power. In this analysis, Figure of Merit (FOM: percent Carnot) is calculated at 0.54.

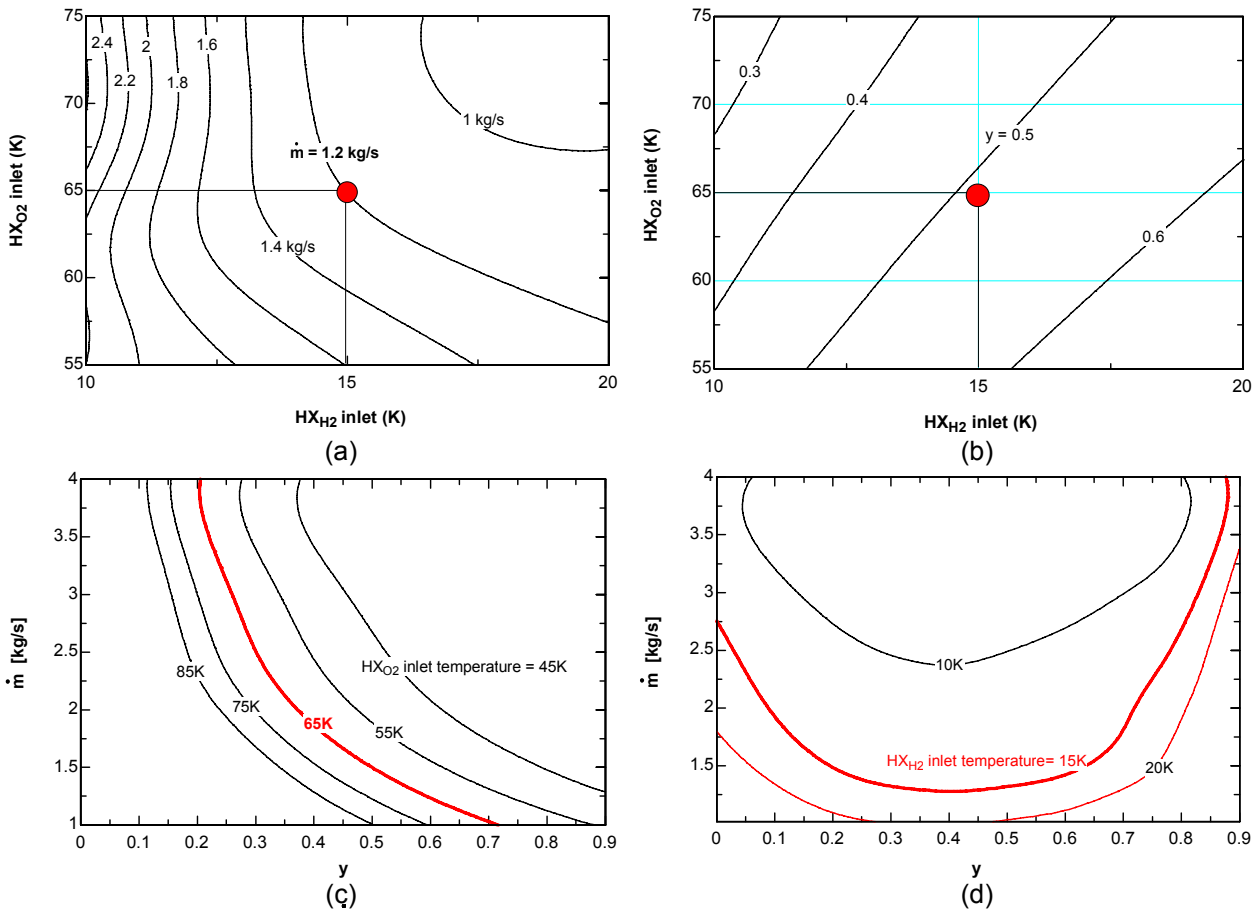

Figure 10.—selected analysis results of two-stage reverse Brayton helium cycle ($P_{discharge}$=2020 kPa, $P_{suction}$=101 kPa, heat exchanger effectiveness=0.95, expander efficiency=0.8).

(2) Two-stage reverse Brayton-Claude helium cycle: *The* same analysis was performed for the two-stage reverse Brayton-Claude helium cycle, and its results are shown in figure 11. Since this cycle includes a J-T expansion valve, calculated total mass flow rates of the system to satisfy required cooling power at given densification temperature are much higher than those of two-stage reverse Brayton helium cycle for the same discharge pressure. In addition, available densification temperature ranges, in particular, for liquid oxygen are too low so that oxygen may be frozen or frosted in heat exchanger. The same analyses were performed for higher/lower compressor discharge pressures, total mass flow rates and mass flow fractions. In spite of intensive efforts to obtain better densification temperature ranges and operating conditions, this configuration seemed to be inappropriate for this specific propellant densifier application.

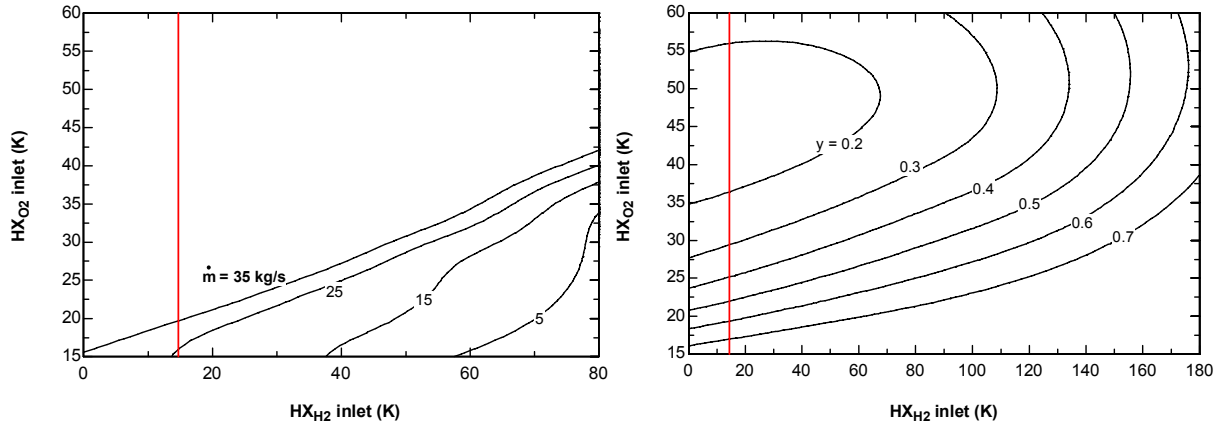

Figure 11. —Selected analysis results of two-stage reverse Brayton-Claude helium cycle. ($P_{discharge}$=2020 kPa, $P_{suction}$=101 kPa, heat exchanger effectiveness=0.95, expander efficiency=0.8).

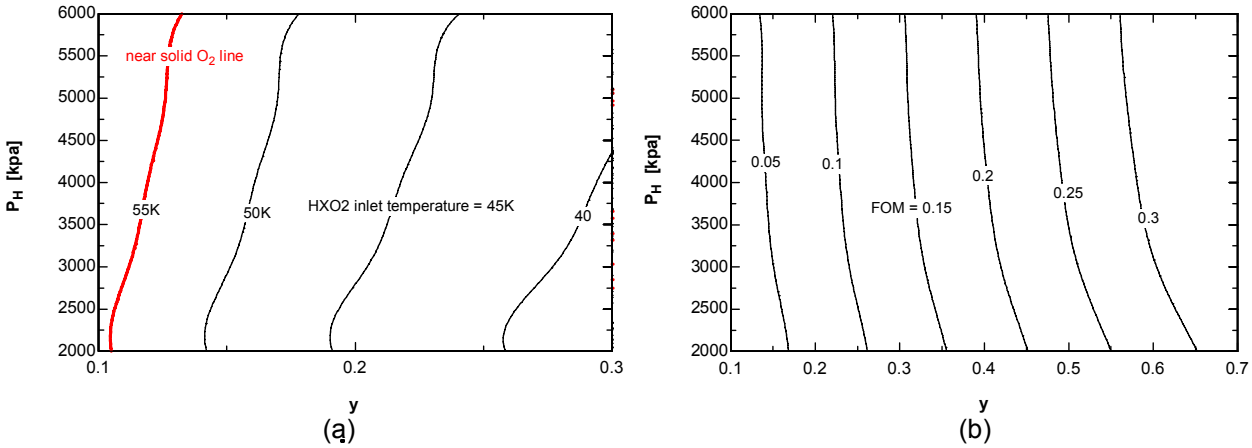

Figure 12.—Selected analysis results of two-stage reverse Brayton-Claude hydrogen cycle. (P_H : compressor discharge pressure, heat exchanger effectiveness=0.95, expander efficiency=0.8).

(3) Two-Stage Reverse Brayton-Claude Hydrogen Cycle: As in the previous analysis, real properties of hydrogen (ref. 10) are incorporated into the reverse Brayton-Claude hydrogen cycle analysis. First, various ranges of compressor discharge pressures were explored to obtain appropriate operating conditions that satisfy specific cooling requirements. Figure 12 that it is difficult for this hydrogen cycle to find the densification temperatures within a reasonable range. Again, the main reason for these imbalances is associated with the assumption that the ratio of cooling requirements associated with the ratio of mass flow rates of densified propellants (hydrogen:oxygen = 1:6) at each densification temperature are fixed. Also, the system efficiency becomes very lower than that of two-stage reverse Brayton helium cycle because of the higher pressure ratio for J-T expansion. In addition, using hydrogen to cool oxygen in a heat exchanger has safety issues and may not be allowed at a launch site.

From the thermodynamic analysis for the three two-stage refrigeration configurations, one of the best candidates for the cryogenic propellants densifier application seems to be the two-stage reverse Brayton helium cycle. This configuration has many attractive advantages. For instance, it uses helium as working fluid which is one of the most common fluids in cryogenic engineering industry. It consists of heat exchangers, a helium compressor and expanders, thus all these system components are commercially available. This configuration can be dedicated to both propellants or one of them independently. The cooling temperature and cooling power can be controlled by the operating pressure, the total mass flow rate and the mass flow fraction through the 1st expander. In addition, this cycle has proven to be scalable from the range of a few watts, for example, for the Hubble's Near Infrared Camera and Multi-Object Spectrometer (NICMOS) cooler to a few kilowatts for particle accelerators to many megawatts for large

hydrogen liquefiers. In general, efficiency increases with increased capacity of refrigerator, due to increases in cycle complexity and greater efficiency in physically larger compressors and turbines. A useful rule of thumb to estimate the power required for hydrogen liquefiers is a simplified assumption of 2 kWh/100 scf for midsized units (ref. 11), so 834 kW of cooling power would be required for liquefaction of 1 million scf/day of hydrogen. This rate of hydrogen production is available via methane reformers in skid mounted systems, and an efficient liquefier to handle this capacity may have a market demand as hydrogen power becomes widely accepted. For this reason, this configuration might be a very promising design concept for other liquid hydrogen applications such as liquid hydrogen stationary storage facility for hydrogen fuel infra structure development. This cycle is also a candidate for a combined hydrogen and oxygen liquefier for use on the surface of the moon or Mars if a water source is found. One of main concerns in realizing this concept would be obtaining appropriate expanders that provide specific cooling requirements.

Comparison with Single-Stage Coolers.—In the previous section, three two-stage systems were explored to suggest an appropriate cooling system for cryogenic densified propellants. In the previous chapter, similar thermodynamic analyses were performed for various single-stage coolers for the same application. Now, it becomes interesting for us to compare their performances with those of two single-stage coolers at given cooling requirements and densification temperatures. The detailed system configurations for various single-stage coolers can be found in the chapter 3, and the final analysis results are discussed in this section. Table 3 shows comparison of thermodynamic performances between two single-stage cycles and one two-stage reverse Brayton helium cycle. In the analysis of single-stage cycle, the same required cooling power and densification temperature are used. For both hydrogen and oxygen densification, a combination of thermodynamic venting system (TVS) and Claude cycle produces the best performance among selected single-stage systems. Total power required to operate independent hydrogen and oxygen system becomes about 3 MW to densify 1 kg/s of liquid hydrogen and 6 kg/s of liquid oxygen. This value is comparable with the power required to operate two-stage reverse Brayton cycle. For the same cooling requirements, two-stage reverse Brayton helium cycle needs about 4 MW of work input and overall system efficiency is about 54 percent of Carnot COP. Even if the two-stage cycle shows a slightly lower thermodynamic performance, it has considerable advantages over combination of TVS and Claude cycle in reality regarding system reliability and potential safety concerns as listed in table 4.

TABLE 3.—COMPARISON OF THERMODYNAMIC PERFORMANCES
BETWEEN SELECTED TWO SINGLE-STAGE CYCLES AND ONE TWO-STAGE CYCLE

Propellant	System	Power required	FOM
Hydrogen (1kg/s, 48 kW@ 15 K)	TVS+Claude cycle	1408 kW	0.648 (COP_{ideal} = 0.053)
Oxygen (6kg/s, 268 kW@ 65 K)	TVS+Claude cycle	1698 kW	0.571 (COP_{ideal} = 0.277)
Total	Two single-stage cycles	3106 kW	
Hydrogen(1kg/s)+Oxygen(6kg/s)	One two-stage reverse Brayton helium cycle	**3990 kW**	**~0.54**

TABLE 4.—SYSTEM CHARACTERISTICS COMPARISON

Two single-stage TVS + Claude systems	One two-stage reverse Brayton helium system
• Two H_2 and N_2 compressors for main cycles	• One He compressor for main cycle
• Additional gas compressors for TVS are required	• No gas compressor for TVS is needed
• J-T expansion valve : potential clogging	• Gas expanders
• H_2 is used in main cycle	• H_2 is used in densification heat exchanger
• Liquid-to-liquid heat transfer in densification	• Gas-to-liquid heat transfer in densification

Conclusions

In order to identify the most cost effective cryogenic propellants densification system for launch vehicle applications, several liquefaction/refrigeration combinations were considered for densifying hydrogen and oxygen propellants. Required cooling powers corresponding to several launch scenarios affected the prospective densification system used. Claude cycle, reverse-Brayton cycle, thermodynamic venting system and cryocooler were selected for demonstration of thermodynamic cycle simulation. Cycle simulation results demonstrated the range of system efficiency, required system components and the extent of performance enhancement achievable.

A two-stage hybrid refrigeration system is suggested to provide the most efficient, reliable and economic densification system for launch vehicle applications. A variety of hybrid systems, combining recuperative heat exchangers, expander and J-T expansion valve were examined by a rigorous thermodynamic analysis. In the analysis, three hybrid systems were selected based on their essential features and practical considerations to demonstrate system feasibilities. Thermodynamic cycle simulations using real fluid properties were performed for two-stage reverse Brayton helium system, two-stage reverse Brayton-Claude helium system and two-stage reverse Brayton-Claude hydrogen system. As a result, it is concluded that the two-stage reverse Brayton helium refrigeration system shows a very suitable possibility for the cryogenic propellant densification technology, and its feasibility in practical should be proved by a physical demonstration.

A subscale hydrogen densification, pressure control, zero-boil-off chilling, filling and storage experiments are being conducted at FSEC. A detailed analysis and experimental results will provide the optimized operational condition and procedures corresponding to launch scenarios. Further analysis including system component specifications, actual inefficiencies in the real system, capital and life-cycle costs estimations for various system designs are suggested in accordance with the comments provided by the NASA KSC launch operation engineers.

References

1. Fazah, M.M., “STS Propellant Densification Feasibility Study Data Book,” NASA TM 108467, 1994.
2. Tomsik, T.M., “Performance Tests of a Liquid Hydrogen Propellant Densification Ground System for the X33/RLV,” NASA TM 107469, AIAA-97-2976, 1997.
3. Green, W.D. and Vaughan D.A., “Simulation and Testing of In-Tank Propellant Densification For Launch Vehicles,” AIAA-98-3688, 1998.
4. Anthony, M. and Green, W.D., “Analytical Model of an Existing Propellant Densification Unit Heat Exchanger,” AIAA-98-3689, 1998.
5. Green, W.D., Knowles, T.E. and Tomsik, T.M., “Propellant Densification for Launch Vehicles : Simulation Testing 1999,” AIAA-99-2335, 1999.
6. Nguyen, K. et al., “Propellant Densification for Launch Vehicles: Simulation and Testing,” AIAA 2002-4293, 2002.
7. Strobridge, T.R., “Cryogenic Refrigerators,” NBS Tech. Note 655, 1974.
8. Baik, J.H. and Raissi, A-T., “R&D process for increasing density of cryogenic propellants at FSEC,” *Cryogenics*, accepted on Feb.2004.
9. McCarty, R.D. and Arp, V.D., "A New Wide Range Equation of State for Helium,” *Advances in Cryogenic Engineering*, Vol. 35 (1990), pp. 1465-1475.
10. McCarty, R.D., Hydrogen, Technological Survey-Thermophysical Properties, NASA SP-3089 (1975).
11. Evans, J., “The Economics of Small to Medium Liquid Hydrogen Facilities,” *Cryogas International*, May 2003 (2003).

Development of Tribological Coatings for Cryocoolers

PI: N. Dhere (FSEC)
L. Chow (UCF)
J. Kapat (UCF)
Pai (FSEC)
V. Hagadali (FSEC)

Project Summary

The efficiency of the compressor and motor of the Two Stage Reverse Turbo Brayton Cycle (RTBC) CryoCooler to be used for storage and transport of hydrogen in spaceport and space vehicle application depends mainly on the friction and wear between the mating parts. The tribological coatings will reduce the friction and wear considerably resulting in improved efficiency. Titanium nitride (TiN) and molybdenum disulphide (MoS_2) coatings deposited by DC magnetron sputtering and RF magnetron sputtering were developed. Morphological and tribological properties of TiN and MoS_2 layers and TiN/MoS_2 bilayer on glass and aluminum substrates were analyzed. Dense well adherent coatings of TiN/MoS_2 were obtained. Both TiN and MoS_2 coatings showed that the grains are nanocrystalline in nature. Microwave assisted chemical vapor deposition (MWCVD) setup was designed and built. Deposition of DLC films have been carried out.

Project Description

Objective

The objective of this project is to develop tribological coatings having extremely high hardness, ultra-low coefficient of friction, and high durability at temperatures lower than 60 K.

Accomplishments

Diamond like carbon (DLC) depositions has been carried out to optimize the process parameters. Initially depositions were carried out for 60 min. The microwave power was at a 150 or 250 W. Argon partial pressure was maintained at 51 mtorr and methane partial pressure was maintained at 27 mtorr by adjusting the flow rate at 100 and 15 sccm respectively. The position of the sample was optimized. The thickness measured using Dektak Profilometer was 0.4 and 0.2 μm at microwave power of 150 and 250 W respectively. Films were also deposited by biasing the substrate to –150 V. The deposition time varied from 9 to 60 min. The optical spectroscopy measurement was carried out to verify the presence of DLC film (figs. 1 and 2). The straight line in is an indication of higher thickness of DLC film deposited at 150 W (fig. 2).

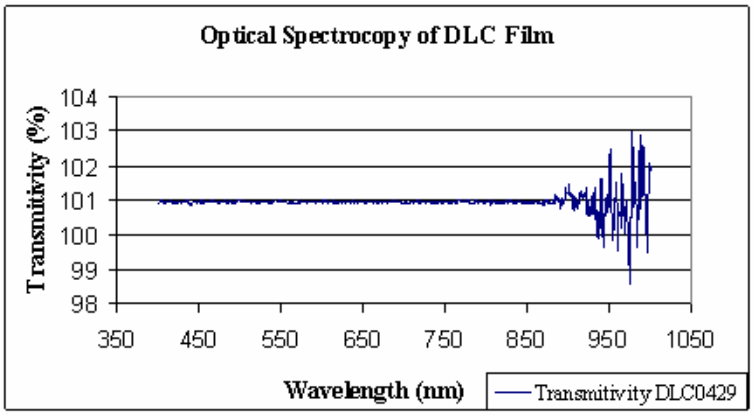

Figure 1.—Optical spectroscopy of DLC film at 250 W.

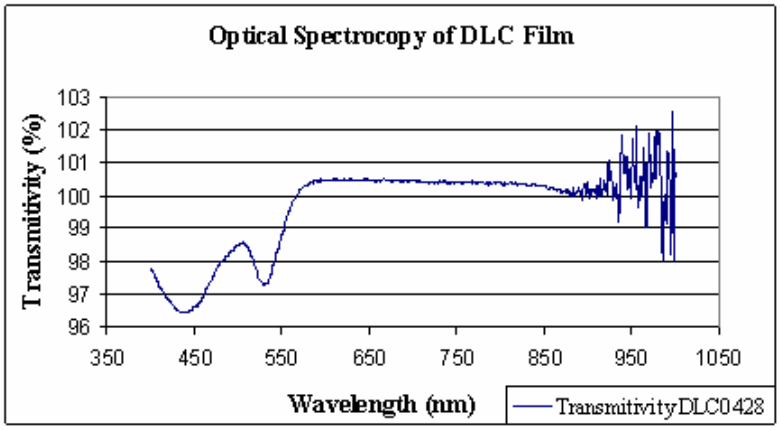

Figure 2.—Optical spectroscopy of DLC film at 150 W.

Future Work

Future work will address the endurance issues of this coating at the cryogenic temperatures and development of Quantum Dot Solar Cells.

- Preparation and characterization of TiN/MoS_2, DLC and DLC/MoS_2 coatings.
- Improving tribological properties of bilayer coating of TiN/MoS_2 and DLC/MoS_2.
- Preparation and characterization of Ultra-low (COF < 0.01 at RT) MoS_2 coating.

Along with the preparation of DLC using MWCVD, major efforts will be directed towards the preparation of CuIn1-xGaxSe2-ySy (CIGSS) thin film with intermediate band of quantum dots (QDs). Detailed literature search on the preparation techniques and also suitable materials to be used as QDs will be carried out.

Presentations and Publications

1. “Single and Bilayer Tribological Coatings for Cryocoolers,” Vinay V. Hadagali and Neelkanth G. Dhere, Poster Presentation, FLAVS-2005, Orlando, Florida, Mar 13-17, 2005

Photoelectrochemical Water Splitting for Hydrogen Production
Using Multiple Bandgap Combination of Photovoltaic-Cell and Photocatalyst

PI: N. Dhere (FSEC)
U. Avachat (FSEC)
A. Jahagidar (FSEC)

Project Summary

The operating voltage of present photovoltaic (PV) cells cannot supply the overvoltage required for water splitting. The objective of this project is to develop photoelectrochemical (PEC) cells with multiple bandgap tandem of PV cell and thin-film photocatalyst that can be activated by infrared (IR) photons transmitted through PV cell for efficient and economic production of hydrogen and oxygen by water splitting. The concept of multiple band gap combination is being used widely in solid-state PV technology in the form of tandem cells and also the concept of PEC is also being used widely. However, in the proposed project the bandgap regions are different; the photocatalyst need not be grown directly over the PV cell as is usually the case with solid-state tandem PV cells and also the PV cells are not in direct contact with the electrolyte medium thus eliminating the problem of corrosion. With the setup developed at FSEC PV Materials Lab a PEC efficiency of 5.25 percent has been achieved.

During this Phase extensive research has been carried out on the development of p-type transparent conducting back layer for the PV cells. P-type ZnTe:Cu transparent conducting layer was successfully developed at the back of superstrate CdS/CdTe thin film PV cell using hot wall vacuum evaporation (HWVE) setup. Preparation and optimization of better photoanode for efficient oxygen evolution was carried out with the preparation of RuS_2, $Ru_{0.99}Fe_{0.01}S_2$ and analyzing both RuS_2, $Ru_{0.99}Fe_{0.01}S_2$ with X-ray diffraction (XRD) for the structure and secondary ion mass spectroscopy (SIMS) for the depth composition.

Further, research will be carried out on development of p-type transparent conducting back layer for substrate type $CuIn_{1-x}Ga_xS_2$ (CIGS2)/CdS thin film PV cells. With this regard, a very thin layer of MoS_2 will be deposited on indium tin oxide (ITO) layer, to provide a tunneling between highly doped ITO and thin MoS_2. Moreover, it will be transparent. This will be a very good base for the growth of CIGS2/CdS thin PV cells. With the experience gained through the ongoing NASA Hydrogen project and based on the excellent facilities developed at FSEC PV Materials Lab for the fabrication of CIGS2 and CdTe PEC cells, better photoanode for efficient oxygen evolution and p-type transparent conducting back layer for the PV cells to transmit the IR photons onto photoanode, it is expected to achieve a PEC efficiency of >6 percent during the Phase 3.

Project Description

Objective

The objective of this project is to develop photoelectrochemical (PEC) cells based on substrate type $CuIn_{1-x}Ga_xS_2$ (CIGS2)/CdS with p-type transparent MoS_2/ITO conducting back layer and efficient p-type ZnTe:Cu transparent conducting layer for superstrate type CdS/CdTe photovoltaic (PV) cells that will transmit the unabsorbed infrared (IR) photons onto photoanode for efficient oxygen evolution. It is expected that with further improvement, the PEC cells along with the better photoanodes will be used in PEC setup for efficient and economic production of hydrogen and oxygen by water splitting.

PV Cell Preparation and Characterization

CIGS2/CdS thin film PV cells are being developed and characterized routinely. The CIGS2 thin films are grown in the copper rich format and the excess copper which segregates on top as $Cu_{2-x}S$ layer is etched away in KCN. These thin films are then analyzed using electron probe microanalysis (EPMA) for atomic concentrations, XRD for structure, scanning electron microscopy (SEM) for morphology. Typical atomic concentration is Cu:In:Ga:S = 24.34:21.97:4.89:48.80. Figure 1 shows the SEM micrograph of etched CIGS2 thin film, showing highly compact grains with very little porosity. Figure 2 shows the XRD

pattern of etched CIGS2 thin film. XRD pattern for a sample sulfurized at 475 ◦C for 20 min showed (101), (112), (103), (200), (220), (312), and (424) reflections from $CuIn_{0.9}Ga_{0.1}S_2$ phase with a = 5.50659 Å and c = 11.01318 Å as well as reflections from molybdenum. CIGS2 thin films were characterized with SIMS for composition-depth profiling. Figure 3 shows the SIMS profile of etched CIGS2 thin film. Copper and sulfur signals are constant in the CIGS2 thickness. Gallium is increasing towards the back contact while indium is decreasing. SEM, XRD and SIMS were carried out at AMPAC's MCF.

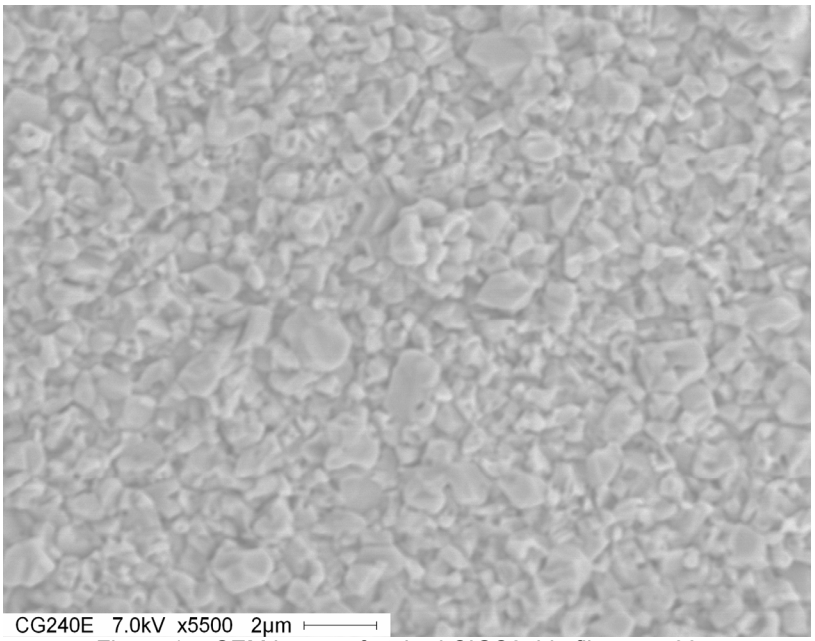

Figure 1.—SEM image of etched CIGS2 thin film at 5500x.

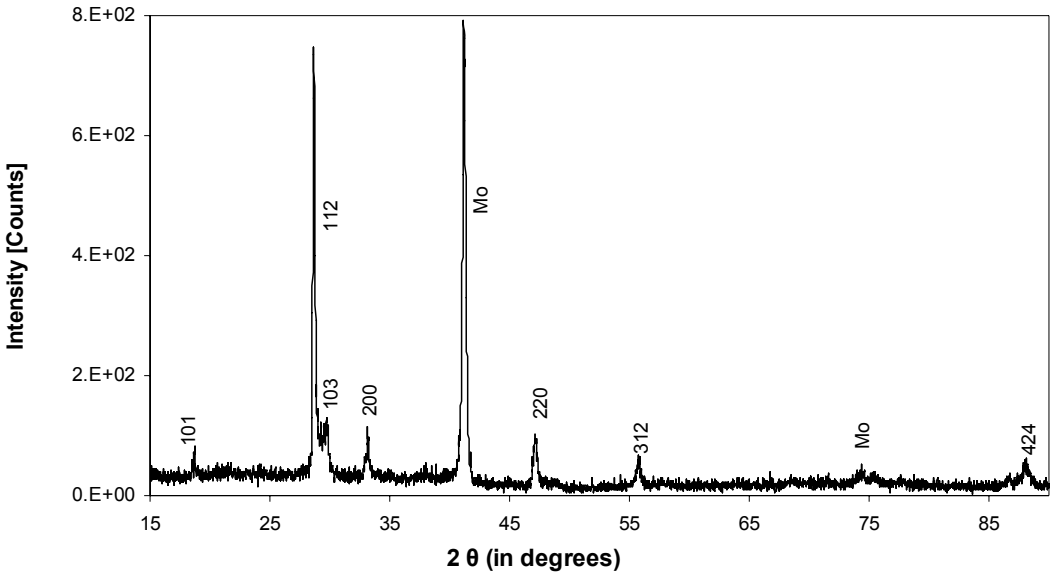

Figure 2.—XRD pattern of etched CIGS2 thin film.

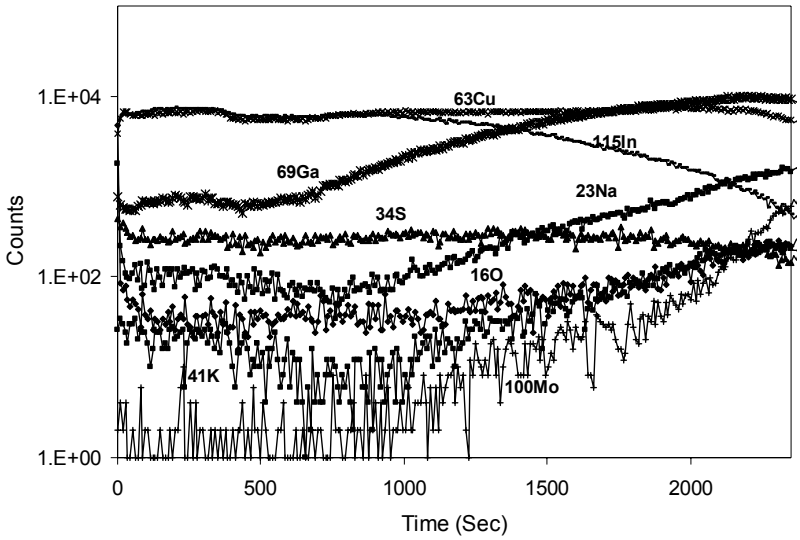

Figure 3.—SIMS depth profile of etched CIGS2 thin film.

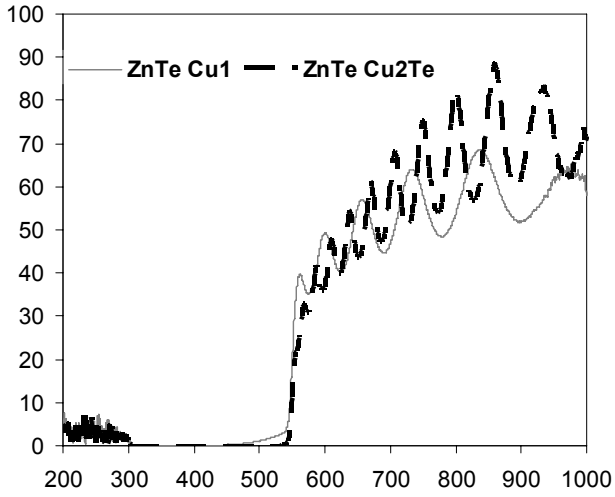

Figure 4.—Optical transmittance spectroscopy plot for ZnTe doped with copper.

Transparent Conducting Back Layer Preparation and Characterization

Materials chosen for this research are ZnTe:Cu for superstrate type CdS/CdTe and ITO/MoS2 layer for substrate type CIGS2/CdS thin film PV cells.

Transparent and conducting ZnTe:Cu films were grown using HWVE on 10 cm x 10 cm glass substrate. Deposition parameters were optimized for obtaining highly stoichiometric 5000 Å thick ZnTe film. Various experiments were carried out by doping ZnTe film with Cu and Cu2Te for comparison of their optical properties near IR region. ZnTe:Cu thin films were obtained by doping ZnTe with 2 to 3 at.% copper and annealing at 3000 ◦C for 30 min. Substrate temperature was 300 °C, hot wall temperature: 350 ◦C, and deposition time was 10 min.

These films were characterized with transmittance spectroscopy and X-ray diffraction (XRD) for the structure. Figure 4 shows the optical spectroscopy measurements. ZnTe film doped with Cu_2Te showed better transparency (~80 to 90 percent near IR region) as compared to films doped with Cu (~60 to 65 percent near IR region) and hence was used for final deposition for obtaining CdS/CdTe cell. Figure 5

shows the XRD pattern showing (111), (222) planes Pattern shows highly textured growth in 111 direction.

ZnTe:Cu thin films with optimized parameters were deposited on SnO_2:F/CdS/CdTe samples procured from First Solar and cell was completed with following configuration, SnO_2:F/CdS/CdTe/ZnTe:Cu/ZnO:Al/Ni-Al. The transparent conducting back layer of ITO/MoS2 for the substrate type CIGS2/CdS thin film PV cells are being prepared and characterized.

Photoanode Preparation and Characterization

The photoanodes for better oxygen evolution are being prepared and characterized. One percent Fe was incorporated into RuS_2 which improve the bandgap to 1.1 from 1.3 eV, which will enable further reduction of the overpotential required for oxygen evolution. These photoanodes were characterized with XRD for their structure and SIMS for the depth composition. Figures 6a and 6b show the XRD pattern of RuS_2 and $Ru_{0.99}Fe_{0.01}S_2$ respectively.

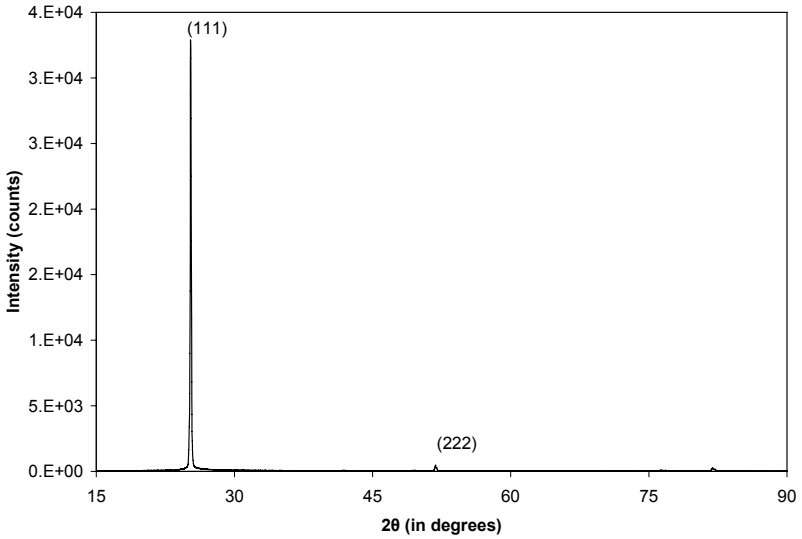

Figure 5.—XRD pattern of ZnTe:Cu film deposited on glass using HWVE technique.

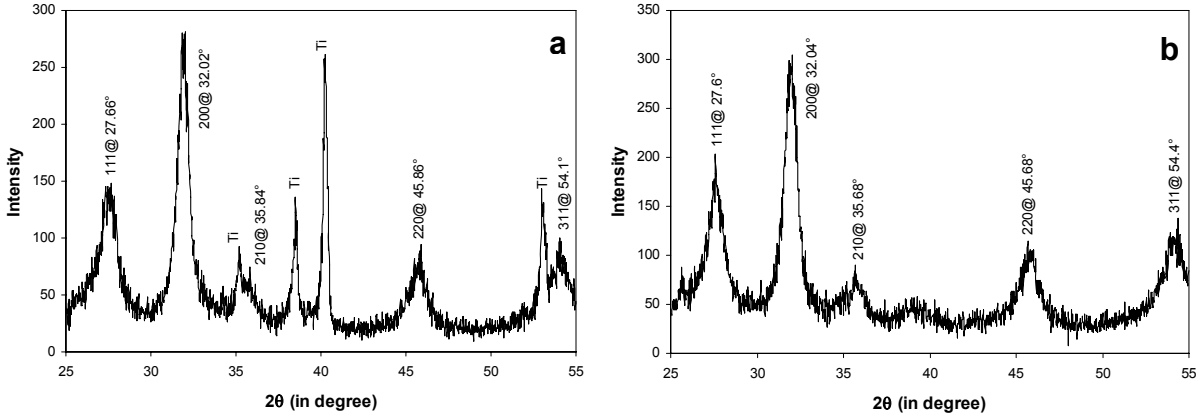

Figure 6.—(a) XRD pattern of RuS_2, (b) XRD pattern of $Ru_{0.99}Fe_{0.01}S_2$.

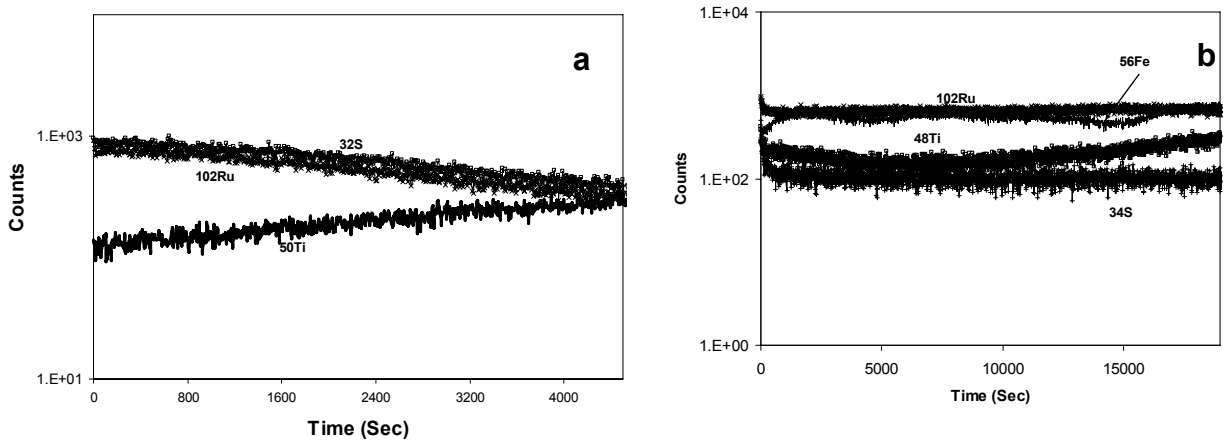

Figure 7.—(a) SIMS depth profile of RuS_2, (b) SIMS depth profile of $Ru_{0.99}Fe_{0.01}S_2$.

Related Publications

N.G. Dhere and A.H. Jahagirdar, Photoelectrochemical water splitting for hydrogen production using combination of CIGS2 solar cell and RuO_2 photocatalyst, Thin Solid Films, In Press, Corrected Proof, 2004.

N.G. Dhere, A.H. Jahagirdar, U.S. Avachat and A.A. Kadam, Photoelectrochemical Water Splitting For Hydrogen Production Using Combination Of CIGS2 Solar Cell And RuO_2 Photocatalyst, Proceedings of 2004 Solar Conference, 2004.

A.H. Jahagirdar, U.S. Avachat, and N.G. Dhere, Photoelectrochemical Water Splitting for Hydrogen Production Using Photovoltaic-cell and Photocatalyst, Poster Presentation FLAVS, 2005.

A.H. Jahagirdar, U.S. Avachat and N.G. Dhere, Direct Water Splitting Using Multiple Bandgap Tandem of Thin Film Photovoltaic Cell and a Photocatalyst, To be presented, MRS Spring Meeting, San Francisco, March 2005.

A.H. Jahagirdar and N.G. Dhere, Preparation and characterization of RuS_2 and $Ru_{1-x}Fe_xS_2$ photoanodes for photoelectrochemical water splitting, to be presented at 207th ECS Meeting, Quebec City Canada, May 2005.

A.H. Jahagirdar and N.G. Dhere, Photoelectrochemical Water Splitting Using Multiple Bandgap Combination of Thin Film Photovoltaic Cell and Photocatalyst: Clean and Renewable Hydrogen Source, to be presented, ISES Solar World Conference 2005, Orlando, August 2005.

Future Work

Further improvements in the PEC efficiency will be carried out using the $Ru_{0.99}Fe_{0.01}S_2$ photoanodes and characterizing these photoanodes with the current-voltage (I-V) parameters. Substrate type CIGS2/CdS thin film PV cells will be developed on transparent conducting back layers of ITO/MoS_2 and PEC efficiency of 6 percent is expected.

Characterization of Spin-Coated Terbium-Doped Strontium Cerate Thin Film Membranes

PI: M. Elbaccouch (Florida Solar Energy Center)
S. Shukla (University of Central Florida)
N. Mohajeri (Florida Solar Energy Center)
S. Seal (University of Central Florida)
A. Raissi (Florida Solar Energy Center)

Abstract

In this report we present the synthesis and characterization of thin film membranes based on a ceramic oxide system with a perovskite structure, which is of interest in the development of solid oxide fuel cells (SOFCs) and hydrogen (H_2) separation membranes. Continuous and homogenous dense thin film membranes of terbium-doped strontium cerate ($SrCe_{0.95}Tb_{0.05}O_{3-\delta}$) have been prepared from ethylene glycol-based polymeric precursors using spin-coating technique. The Polymeric precursors have been deposited on silicone-based substrates and converted to dense polycrystalline metal oxide films after a sequence of annealing treatment at relatively low temperatures (400 ◦C). Fourier transform infrared spectroscopy (FTIR) and x-ray diffraction (XRD) techniques are used to characterize the polymeric precursor chemistry and to confirm the perovskite structure of the calcined thin films respectively. The effect of sintering temperature and number of spin-coating cycles on the surface morphology and film thickness of the calcined thin films have been studied systematically using scanning electron microscopy (SEM) and focused ion-beam (FIB) milling techniques respectively. The surface chemistry of the thin membranes has been revealed using the x-ray photoelectron spectroscopy (XPS) analysis. FIB cross-section images indicate that thin membrane films having varying thicknesses within the range of 200 nm to 2 μm can be effectively produced by controlling the number of spin-coating cycle combined with the proper drying and annealing cycles after each individual coating-step.

Introduction

Hydrogen (H_2) separation ceramic-based membranes must exhibit both ionic and electronic conductivity in order to achieve H_2 permeation flux suitable for practical applications (refs. 1 to 3). Also, they must be dense in order to achieve infinite H_2 selectivity (ref. 4). At high temperatures (>500 ◦C), ceramic oxide materials with perovskite structures ($A^{2+}B^{4+}O_3$) have the required ionic-electronic conductivity when the B-sites are doped with trivalent cations (M) (refs. 5 and 6) This doping process creates oxygen-ion vacancies ($V_o^{\cdot\cdot}$) within the lattice as means of charge compensation (refs. 5 to 10). The general formula of a doped perovskite material is given as $AB_xM_{1-x}O_{3-\delta}$, where x and δ represent cations molar ratio and oxygen-ion vacancy respectively (ref. 11).

The mixed conductivity of doped perovskite ceramic oxides have been receiving considerable attention in the development of solid oxide fuel cells (SOFCs), gas sensors, and H_2 permeation membranes (refs. 11 and 12). The doped perovskite structure for the H_2 separation membranes have several characteristics including, infinite H_2 selectivity, low H_2 chemical potential gradient, lower operating temperature range of 500 to 1000 ◦C, inexpensive compared to Pd membranes, simple and flexible compared to pressure swing adsorption process, and does not require external power (refs. 13 and 14).

A typical H_2 permeation process, through the doped perovskite ceramic oxides, involves three consecutive steps: (i) a gas-solid interfacial reaction for the adsorption of H_2 at the membrane surface, where it dissociates into protons and electrons, (ii) a pressure gradient across the membrane transports the protons through the solid-state membrane-lattice, where the protons associate with oxygen sites ($OH_o^{\cdot}$) and hops between adjacent sites, and (iii) a solid-gas interfacial reaction for the protons to re-combine and form H_2 (refs. 6 to 8, and 11).

The current membrane geometries (i.e., disks and tubes) are considerably thick (~2 mm) and have low H_2 permeation rates (refs. 5 and 11). In order to enhance the H_2 permeation rate, it is essential to control the membrane thickness. Since the permeation rate is inversely proportional to the membrane

thickness, dense and thin (sub-micron thick) membrane films supported on the porous substrates should lead to much higher H_2 permeation rates (refs. 11 and 15). The H_2 preparation of dense and thin membrane films have been reported earlier using polymeric precursors and utilizing both the spin and the sol-gel dip-coating techniques on silicone and sapphire substrates (refs. 4, 15 to 17). Work is still needed to enhance and produce high quality thin membrane films that are smooth, homogeneous, and free of pin holes and cracks.

Hence, from this perspective, the goal of the present study is aimed to prepare and characterize strontium cerate ($SrCe_{0.95}Tb_{0.05}O_{3-\delta}$) (SCT) thin membrane films by spin-coating using a polymeric precursor containing ceramic cations. Continuous homogenous $SrCe_{0.95}Tb_{0.05}O_{3-\delta}$ membrane films having thickness within the range of 200 nm to 2 μm, with neither pin-holes nor cracks, are reported here. The polymeric precursor and the micro structure of the $SrCe_{0.95}Tb_{0.05}O_{3-\delta}$ membranes are characterized using several techniques including Fourier transform infrared spectroscopy (FTIR), X-ray diffraction (XRD), X-ray photoelectron spectroscopy (XPS), Scanning electron microscopy (SEM), and focused ion-beam (FIB) microscopy.

Experimental

Chemicals

$SrCe_{0.95}Tb_{0.05}O_{3-\delta}$ perovskite-type material was prepared from metal nitrate precursors. Strontium nitrate ($SrNO_3$) (99.995 percent) was obtained from Aldrich Chemical Co. 1.5 N cerium nitrate ($Ce(NO_3)_4.31H_2O$) solution and terbium nitrate ($Tb(NO_3.6H_2O$) (99.9 percent) were obtained from Alfa Aesar. Ethylene glycol (EG) (99 percent) and nitric acid (HNO_3) were obtained from Fisher Scientific. Distilled water was supplied by the Florida Solar Energy Center (FSEC). All chemicals were used as-received without further purifications. Polished and etched 500 to 550 μm silicone substrates were purchased from International Wafer Service Inc.

Synthesis of Polymeric Precursor

$SrCe_{0.95}Tb_{0.05}O_{3-\delta}$ precursor solution was prepared by quantitatively weighing the nitrate chemicals in the defined molar ratio. Then, the chemicals were mixed with chelating agents composed of 40 ml ethylene glycol, 25 ml distilled water, and 10 ml nitric acid forming a red solution (refs. 4,18, and 19). After stirring and complete dissolution, the clear solution was set on a hot plate and heated at 85 to 90 ◦C for approximately 3 hr to expel water and other volatile materials until it turned to a gelatinous liquid. The heating process polymerized the system and formed a complex mixture between the polymeric precursor and the metal cations.

Spin-Coating

The silicone substrate was pre-heated at 600 ◦C for 12 hr in air to form a SiO_2 layer. Vacuum was applied to affix the 1 in. Si/SiO_2 substrate on the spin-coater (Cookson Electronics Equipment–Model P6204). A pipet was used to place drops of the synthesized polymeric precursor on the surface of the Si/SiO_2 substrate. The spin-coating was conducted at 3000 rpm for 20 sec. It is important to monitor the viscosity of the polymeric precursor in order to obtain high quality films (200 to 300 cP). A precursor with low viscosity will not wet the surface of the Si/SiO_2 substrate, while very viscous precursor results in the formation of cracks and deformed films. The spun-coated films were dried on a hot plate at 80 ◦C for 1 min before sintering in air at 400 ◦C for 4 hr. For multiple coatings, the films were dried at 80 ◦C for 1 min, and then set on another hot plate at 300 ◦C for 1 min to remove the organic content before going through a new coating cycle (ref. 4). All spun-coated membrane films were sintered once in air at 300 ◦C for 4 hr to form high quality polycrystalline metal oxide films.

Characterization

FTIR Analysis

The progress of the polymerization process of the precursor was monitored via FTIR spectroscopy (Perkin Elmer, Spectrum 2000). Figure 1 shows the FTIR spectra of EG (as a reference) and polymeric precursors as a function of reaction time (I-intermediate and II-final). The comparison between EG and the precursors spectra shows the formation of new C = O bonds at 1637 cm^{-1} for ionic metal chelated oxalate groups and 1730 cm^{-1} for covalently bonded metal chelated oxalate groups. The decreased intensity of the C-H_2 stretching at about 2900 cm^{-1} indicates the oxidation of EG.

Figure 2 shows the possible reaction mechanism for the EG process (ref. 19). First, nitric acid oxidizes EG to form oxalic acid. Then, the simultaneous formation of the polyester and the metal chelated oxalate leads to the final precursor to be used for the preparation of thin film membrane via spin-coating. The FTIR provides the required mechanism needed to ensure that the chelating cations remain in solution throughout the entire polymerization process. That ensures a uniform cation distribution, stability, and homogeneity throughout the film deposition process.

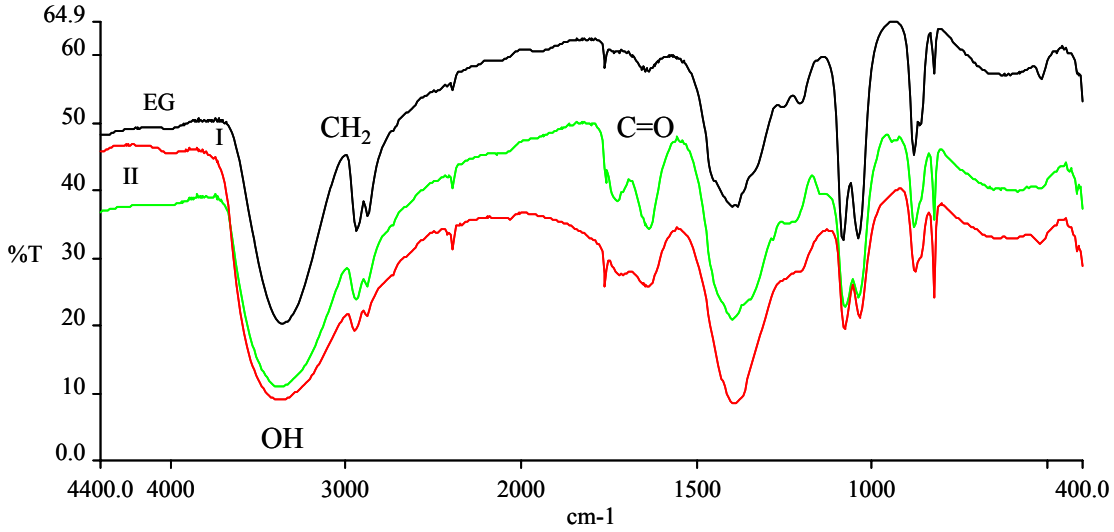

Figure 1.—FTIR spectra of the precursors for the ethylene glycol (EG) process.

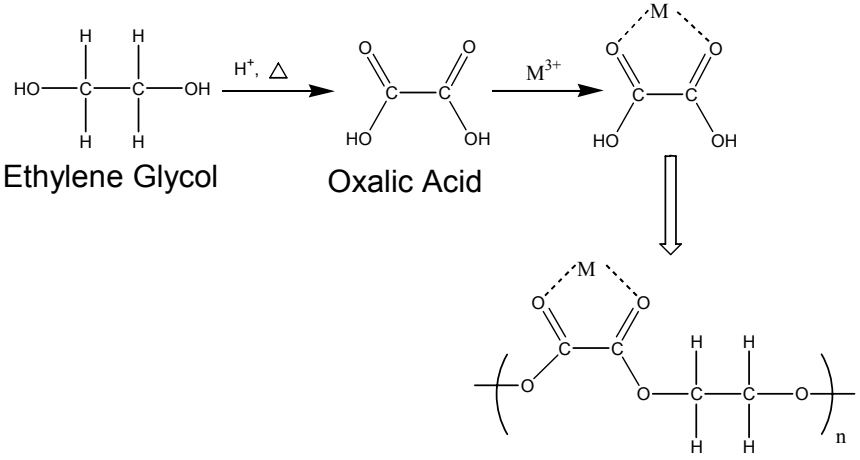

Figure 2.—Possible reaction mechanism of the EG process (ref. 19).

SEM and FIB Analysis

SEM (JSM-6400F, JEOL Ltd., Tokyo, Japan) was used to analyze the surface morphology of the membrane thin films. To avoid any surface charging during the SEM analysis, the membrane thin films were coated with approximately 20 to 30 nm thick film of Au-Pd layer using a sputter coater (K350, Emitech, Ashford, Kent, England).

Figure 3(a) and (b) show the SEM surface morphology at low and high magnifications respectively of $SrCe_{0.95}Tb_{0.05}O_{3-\delta}$ membrane films deposited on the Si/SiO_2 substrates after one spin-coating cycle at 3000 rpm for 20 sec and subsequent sintering at 400 °C for 4 hr. On the other hand, figure 4(a) and (b) show the SEM surface morphology at low and high magnifications respectively of $SrCe_{0.95}Tb_{0.05}O_{3-\delta}$ membrane films deposited on the Si/SiO_2 substrates after twenty-five spin-coating cycles at 3000 rpm for 20 sec and subsequent sintering at 400 °C for 4 hr. The SEM images show that the membrane film surfaces are homogeneous, continuous, and crack free. It should be noted that the homogeneity and continuity of the films in figures 3 and 4 are intended to mean that films have the same morphology, shape, composition, and feature across the film surface. Also, crack free or pin holes free aspects of the film can be seen in figure 5(b), which is discussed next.

Comparison between figures 3 and 4 reveals different surface morphology as exhibited by the membrane films spin-coated for one and twenty-five cycles. For the $SrCe_{0.95}Tb_{0.05}O_{3-\delta}$ membrane, spin-coated for twenty five-cycles (fig. 4), the average grain size is noted to be 200 nm. However, the surface morphology for the single coated-surface has a pattern of crystal diffusion resulting in coarser grain size (500 nm) than the observed in figure 3. Moreover, the membrane spin-coated for a single-cycle (fig. 3(b)) qualitatively has a less pore volume fraction than that in figure 4(b) under similar processing conditions. Hence, it appears that the average grain size at the surface decreases, but the amount of surface porosity increases with increasing the number of spin-coating cycles.

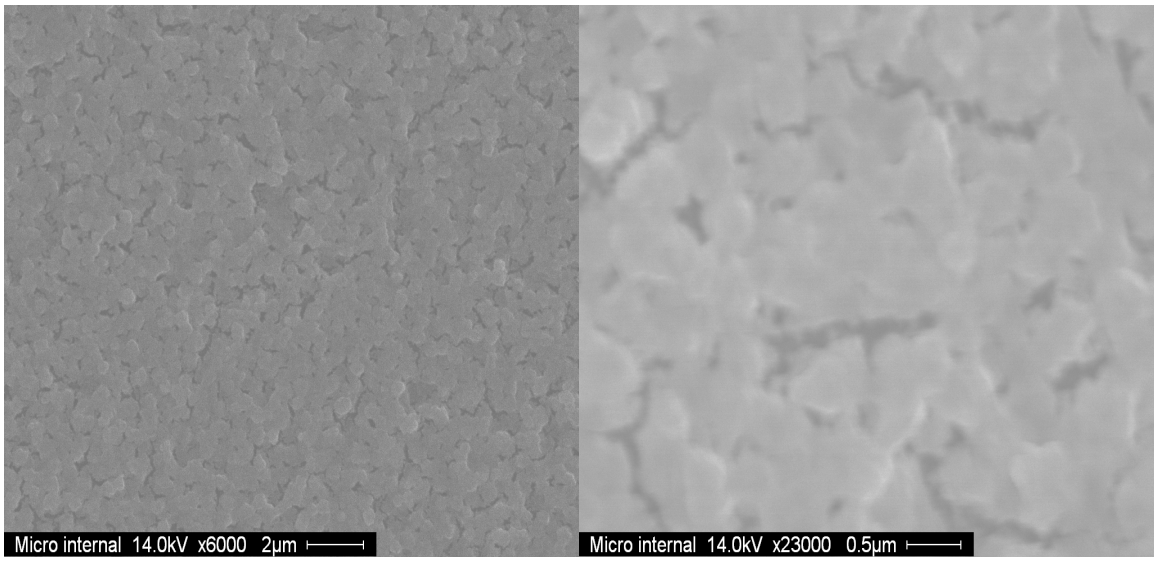

(a) (b)

Figure 3.—SEM surface morphology at low (a) and high (b) magnifications of $SrCe_{0.95}Tb_{0.05}O_{3-\delta}$ after one spin-coating cycle at 3000 rpm for 20 sec and sintering at 400 °C for 4 hr.

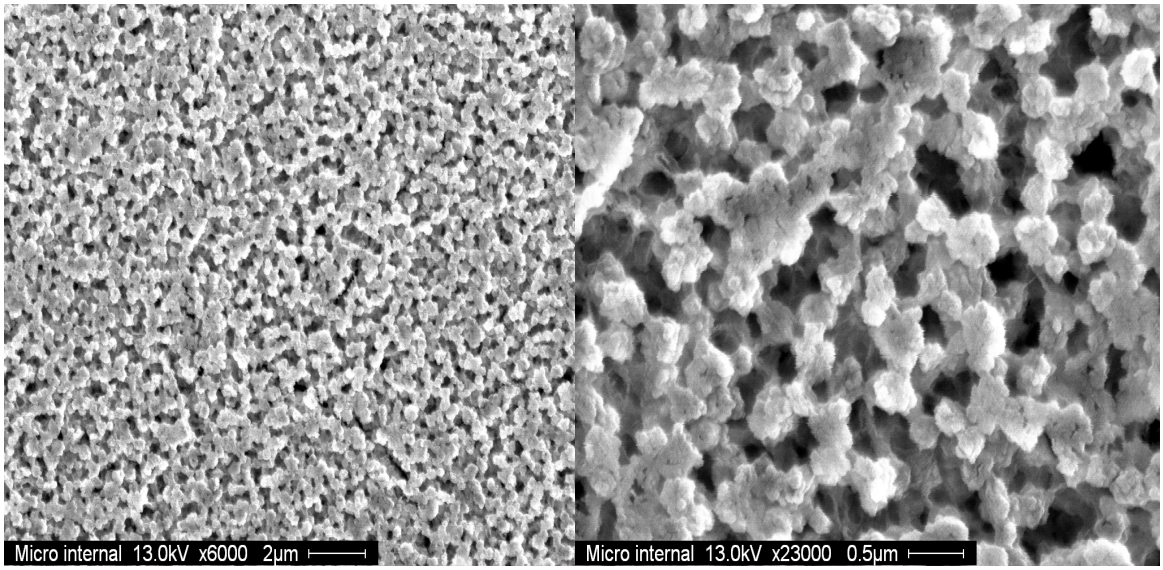

(a) (b)

Figure 4.—SEM surface morphology, at low (a) and high (b) magnifications of $SrCe_{0.95}Tb_{0.05}O_{3-\delta}$ after twenty-five spin-coating cycles at 3000 rpm for 20 sec and sintering at 400 °C for 4 hr.

FIB (FIB 200 TEM, FEI Company, Hillsboro, OR) milling technique was utilized to observe the cross-section of the membrane thin films. The procedure utilized for observing the thin film cross-section via FIB has been described in detail elsewhere (ref. 20). Our experience has showed that the precision of film thickness using FIB milling technique is much higher than the SEM technique. Typical FIB-milled images of $SrCe_{0.95}Tb_{0.05}O_{3-\delta}$ membrane films, showing the film thicknesses after spin-coating for one and twenty-five cycles at 3000 rpm for 20 sec with subsequent sintering at 400 °C for 4 h, are presented in figure 5(a) and (b) respectively. The FIB-milled images suggest that film thickness increases with the number of coating-cycles. The average film thicknesses of 200 nm and 2 μm are observed after spin-coating for one cycle and twenty-five cycles under similar processing conditions. Hence, via the present synthesis approach, sub-micron as well as micron-sized thick membrane films can be obtained using the multiple-coating steps. It is to be noted that a single coating-cycle results in a film thickness of 200 nm. As a result, twenty-five coating-cycles should ideally produce a film with a thickness of 5 μm. However, in the present analysis, much lower film thickness (2 μm) has been observed after twenty-five coating cycles (fig. 5(b)).

It appears that, in the present film forming process, the coating develops by filling the porosity of the previously deposited films, which is clearly observed in figure 5(b). After twenty-five coating-cycles, the obtained membrane film consists of two distinct layers. First is the bottom layer, which is 1 μm thick and is highly dense (i.e., crack free and pin holes free). The second one is a top layer, which is 100 to 200 nm thick, and is highly porous. Hence, it appears that the subsequent coating-steps fill the porosity in the films obtained in the previous coating-steps. In agreement with this, the surface morphology observed via SEM analysis (fig. 4(b)) also indicates the presence of large amount of surface porosity for the membrane film obtained after twenty-five coating-cycles. Interestingly, the FIB image (fig. 5(a)) of the membrane film obtained after a single coating-cycle indicates that this film is less porous, which is in confirmatory with the SEM analysis in figure 3. Moreover, the average grain size of 500 nm can be observed in figure 5(b), which is also in consonance with the SEM analysis in figure 3(b).

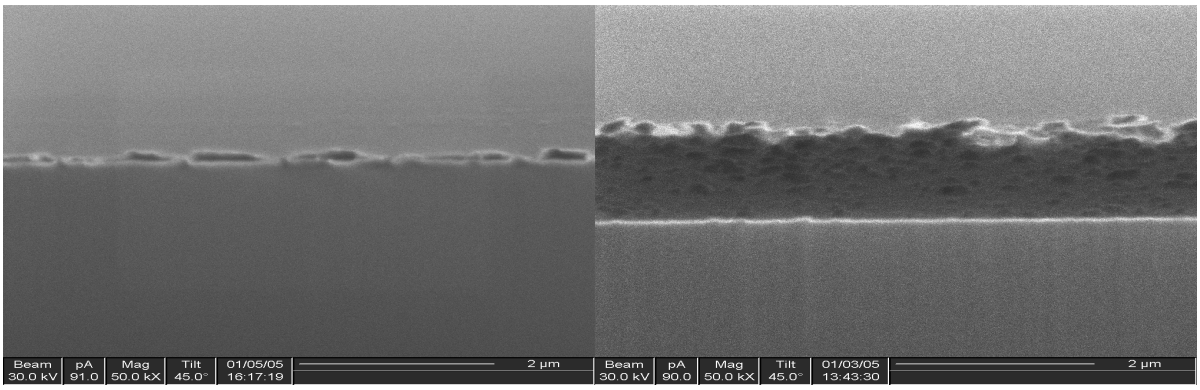

(a) (b)

Figure 5.—FIB film thickness of $SrCe_{0.95}Tb_{0.05}O_{3-\delta}$ with One (a) and twenty-five (b) coating cycles at 3000 rpm for 20 sec and sintering at 400 °C for 4 h.

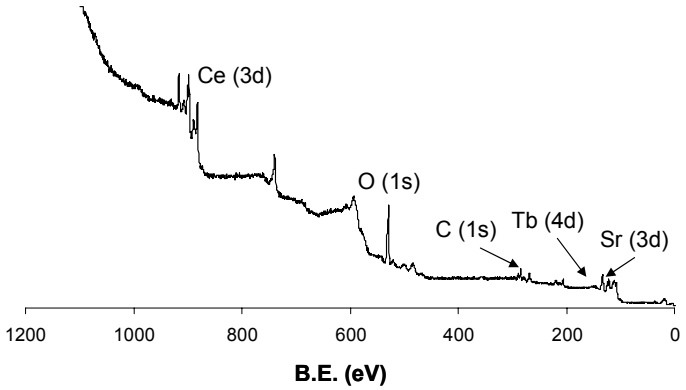

Figure 6.—XPS analysis for the twenty-five coating cycles $SrCe_{0.95}Tb_{0.05}O_{3-\delta}$ film.

XPS Analysis

The surface chemistry of the membrane thin films was studied using an XPS technique utilizing PHI ESCA spectrometer (Perkin Elmer, 5400). Details of calibrations and operations are published elsewhere (ref. 21). Typical XPS broad-scan spectrum within the range of 0 to 1100 eV binding energy (B.E.), obtained from the twenty-five coating-cycles membrane thin films and calcined at 600 ◦C for 4 h, is presented in figure 6. Via XPS analysis, the major elements such as Sr, Ce, O, and Tb are detected on the membrane thin film surface. The Ce $3d_{5/2}$ and Sr $3d_{5/2}$ B.E. levels of 882.0 eV and 133.0 eV are observed, which indicate the presence of Ce^{4+} and Sr^{2+} oxidation states within the coating. The broad Ce (3d) peak also suggests the possible presence of Ce^{3+} ions within the membrane thin film. Ce^{4+} reflects the existence of large number of oxygen-ion vacancies within the membrane thin film. The large oxygen-ion vacancy concentration is very essential for enhancing the H_2 permeation rate through the membrane and also to reduce its operating temperature.

XRD Analysis

The crystalline phases present in the membrane thin films were determined using a standard Rigaku X-ray diffractometer (XRD). Line traces were obtained over 2-θ values ranging from 10° to 60°. Typical XRD patterns obtained from the $SrCe_{0.95}Tb_{0.05}O_{3-\delta}$ membrane films, obtained after twenty-five coating-cycles and calcination at 400 and 1000 °C for 4 h, are presented in figure 7(a) and (b) respectively. The presence of the x-ray diffraction patterns itself suggests the crystalline nature of the membrane films after

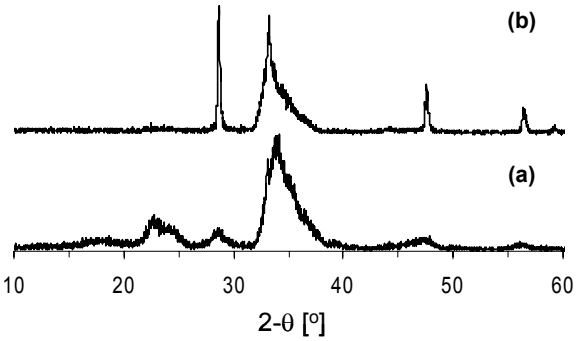

Figure 7.—XRD Analysis of $SrCe_{0.95}Tb_{0.05}O_{3-\delta}$ Film with Twenty five Coating Cycles at (a) 400 °C and (b) 1000 °C.

calcination at higher temperatures. The x-ray peaks appear to be very broad (fig. 7(a)) after calcination at lower temperature indicating the nanocrystalline nature of the membrane films. However, the peaks become narrower (fig. 7(b)) at higher calcination temperature indicating an increase in the crystallite size due to higher calcination temperature. The comparison of the obtained XRD patterns with those reported earlier in literature indicates the perovskite-structure of the $SrCe_{0.95}Tb_{0.05}O_{3-\delta}$ membrane films (ref. 22).

Conclusions

The overall analysis suggests that $SrCe_{0.95}Tb_{0.05}O_{3-\delta}$ membrane films have been successfully synthesized by using the polymeric precursor spin-coating technique. The membrane films are characterized using various analytical techniques, such as FTIR, SEM, FIB, XPS, and XRD to study the film formation, surface morphology, thickness, surface chemistry, and crystal structure. Homogeneous, continuous, crack-free membrane films having thickness of 200 nm to 2 μm have been successfully synthesized by controlling the number of coating-cycles within the range of one to twenty-five. The surface morphology of the membrane films and its thickness are shown to depend on the number of coating-cycles. The crystal structure of the spin-coated and calcined membrane films resembles that of the perovskite-structure within the calcinations temperature range of 400 to 1000 °C.

Acknowledgements

The authors acknowledge the support provided by the National Aeronautics and Space Administration through Glenn Research Center under contract No. NAG3–2751, and the National Science Foundation (NSF CTS 0350572). The authors also thank the Materials Characterization Facility (MCF) at the University of Central Florida for offering various analytical instruments for conducting the present research.

References

2. J. Guan, E. Dorris, U. Balachandran, and M. Liu. Transport properties of $BaCe_{0.95}Y_{0.05}O_{3-\delta}$ mixed conductors for hydrogen separation. Solid State Ionics 100 (1997) 45-52.
3. C. Zuo, T. H. Lee, S. E. Dorris, U. Balachandran, and M. Liu. Composite membranes for hydrogen separation. Electrochemical Society, Abs. 1053, 204th Meeting, 2003.
4. K. D. Kreuer. On the development of proton conducting materials for technological applications. Solid State Ionics 97 (1997) 1-15.
5. C. C. Chen, M. M. Nasrallah, and H. U. Anderson. Synthesis and characterization of YSZ thin film electrolytes. Solid State Ionics 70/71 (1994) 101-108.
6. D. Dionysiou, X. Qi, Y. S. Lin, G. Meng, and D. Peng. Preparation and characterization of proton conducting terbium doped strontium cerate membranes. J. membrane Sci. 154 (1999) 143-153.

7. S. M. Haile, G. Stanefe, and K. H. Ryu. Non-stoichiometry, grain boundary transport and chemical stability of proton conducting perovskites. J. Membr. Sci. 36 (2001) 1149-1160.
8. E. D. Wachsman, and M. C. Williams. Hydrogen production from fossil fuels with high temperature ion conducting ceramics. The electrochemical Society Interface, Fall 2004.
9. S. M. Haile, D. L. West, and J. Campbell. The role of microstructure and processing on the proton conducting properties of gadolinium-doped barium cerate. J. Mater. Res. 13-6 (June 1988) 1576-1595.
10. S. D. Flint, and R. C. T. Slade. Variations in ionic conductivity of calcium-doped barium cerate ceramic electrolytes in different atmospheres. Solid State Ionics 97 (1997) 457-464.
11. T. Shimada, C. Wen, N. Taniguchi, J. Otomo, and H. Takahashi. The high temperature proton conductor $BaZr_{0.4}Ce_{0.4}In_{0.2}O_{3-\delta}$. J. Power Sci. 131 (2004) 289-292.
12. S. J. Song, and E. D. Wachsman, J. Rhodes, S. E. Dorris, and U. Balachandran. Hydrogen permeability of $SrCe_{1-x}M_xO_{3-\delta}$ (x = 0.05, M = Eu, Sm). Solid State Ionics 167 (2004) 99-105.
13. X. Qi, and Y. S. Lin. Electrical Conducting properties of proton-conducting terbium-doped strontium cerate membrane. Solid State Ionics 120 (1999) 85-93.
14. T. R. Armstrong, R. D. Carneim, and M. K. Ferber. Stability of perovskite hydrogen separation membranes. Presented at AR Materials Conference, Baltimore, MD, 2003.
15. F. Lau, and S. Doong. Coal to hydrogen: A novel membrane reactor for direct extraction. Presented at GCEP Energy Workshops at Stanford University. April 26-27, 2004.
16. S. Hamakawa, L. Li, and E. Iglesia. Synthesis and hydrogen properties of membranes based on dense $SrCe_{0.95}Yb_{0.05}O_{3-\delta}$ thin films. Solid State Ionics 48 (2002) 71-81.
17. T. Suzuki, I. Kosacki, and H. U. Anderson. Microstructure-electrical conductivity relationships in nanocrystalline ceria thin films. Solid State Ionics 151 (2002) 111-121.
18. J. Eschenbaum, J. Rosenberger, R. Hempelman, D. Nagengast, and A. Weidinger. Thin films of proton conducting $SrZrO_3$-ceramics prepared by the sol-gel method. Solid State Ionics 77 (1995) 222-225.
19. Nicholas G. Eror, and H. U. Anderson. Polymeric precursor synthesis of ceramic materials. Mat. Res. Soc. Symp. Proc. Vol. 73, 571-577.
20. C. C. Chen, M. M. Nasrallah, and H. U. Anderson. Synthesis and Characterization of$(CeO_2)_{0.8}$ $(SmO_{1.5})_{0.2}$ thin films from polymeric precursors. J. Electrochem. Soc. Vol. (140) No. (12) (12, December, 1993) 3555-3560.
21. S. Shukla, S. Seal, J. Akesson, R. Oder, R. Carter, and Z. Rahman. Study of mechanism of electroless copper coating of fly-ash cenosphere particles. Appl. Surf. Sci. 181 (2001) 35.
22. T. L. Barr, and S. Seal. Nature of the use of adventitious carbon as a binding energy standard. J. Vac. Sci. Tech. A 13(3, Pt.2) (1995) 1239-1246.
23. I. Kosacki, and H. U. Anderson. The structure and electrical properties of $SrCe_{0.95}Yb_{0.05}O_3$ thin film protonic conductors. Solid State Ionics 97 (1997) 429-436.

Liquid Hydrogen Storage at Kennedy Space Center

PI: L. Gu (Florida Solar Energy Center)
G. Bokerman (Florida Solar Energy Center)
A. Raissi (Florida Solar Energy Center)
D. Block (Florida Solar Energy Center)

Project Summary

The objective of this project is to develop a computer model to examine the thermal performance of the Pad B LH_2 tank at the NASA Kennedy Space Center (KSC) and measure the experimental parameters that are needed for modeling of the granular effects of using glass bubbles as tank insulation. A detailed 3-D model was developed to simulate thermal performance of the tank with a void, a vacuum space without perlite between inner and outer shells. The model was validated against measured data, including boiloff rates, IR images, point temperature and heat flux measurements. A parametric study was performed after validation to investigate which solutions are feasible for future tank renovation. Preliminary recommendations from thermal simulations were provided to KSC. Experimental data from 3M Corp were also sent to KSC to support KSC's model efforts.

Background

The liquid hydrogen and oxygen storage tanks at KSC have served the space launch operations for more than 40 years. Although KSC has two identical liquid hydrogen storage tanks, the current boiloff rate is 750 gal/day for the Pad B tank and 300 gal/day for the Pad A tank. The main cause for the Pad B tank boiloff is a void inside the vacuum space between inner and outer shells generated near the top of the tank, because some perlite used as tank insulation was missing. The void was discovered by IR images taken last summer by a KSC engineer. It is estimated that KSC losses $1 million per year due to liquid hydrogen and oxygen boiloff.

KSC plans to renovate the Pad B tank in 2005. Although there are many possible tank renovation options, it is the main objective of the present project to find out which options may be more realistic and economic. For example, one of these options is to add external insulation over the void area. The questions raised are how large the coverage area and what the thermal resistance level should be. Thermal simulation can be used to answer these questions. The simulation is a cost-effective way to provide recommendations for KSC to determine which renovation plan is the most feasible. Since the tank geometry is complicated and the void area is required to be simulated, detailed 3-D simulations have to be performed.

In order to use a thermal model with a high confidence level, the model has to be validated against measured data before the evaluation of possible renovation options is undertaken. Although KSC provided measured data of tank boiloff rates and IR images, the data may not be sufficient to validate models. A site visit to obtain more measurements is essential.

Replacement of perlite insulation, currently filled in the vacuum space between the inner and outer spheres of the LH_2 tanks, is one of options for tank renovation. Hollow glass microspheres are the leading candidate for replacing perlite. The microspheres provide improved thermal performance and are significantly stronger particles. While perlite is known to compact with age, the microspheres are expected to remain as free flowing particles. However, their limited use in cryogenic applications has raised questions about particle behaviors.

Granular particles act similar to the familiar solids, liquids and gasses, but have unique behaviors due to the large size of the particle (60 μm for microspheres). The differences result from the elimination of thermodynamics, and interactions between grains are dissipative. Of particular relevance to the insulation application are low reproducibility of behavior, no height dependent pressure head in a cylindrical container, the development of force chains, and jamming. The latter two are illustrated in the following diagrams:

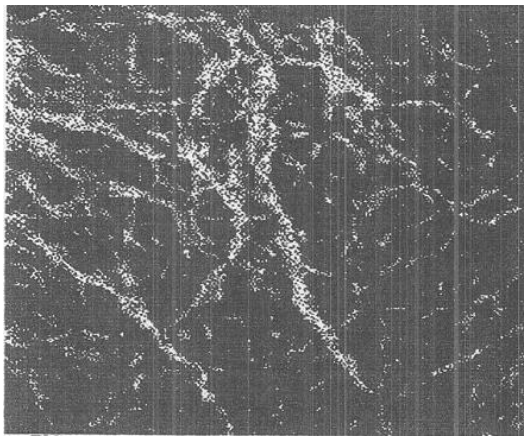

Figure 1.—Force chains highlighted for Pyrex glass spheres.

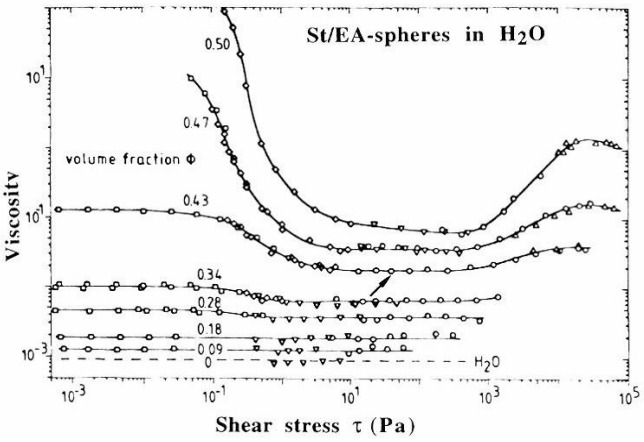

Figure 2.—Viscosity versus shear stress for polystyrene ethylacrylate latex.

The force chains reveal that a small number of particles carry a large portion of the load when stressed, in contrast to an expected averaging process. The second illustration shows the development of a jammed state as the concentration of an emulsion is increased beyond 43 percent. To achieve flow in these systems a yield stress (to flow) must be exceeded. Since the glass microspheres will have no dilution mechanism, a yield stress is expected.

The latter behavior is presumed to be relevant during LH_2 tank thermal cycles. The inner sphere expands and contracts enough during a thermal cycle to change the volume between the inner and outer sphere by 2 percent. Upon initial cool down a void is created with expected settling of the filler by gravity. When the tank is warmed the particles must return to the void space at the top. The concern is whether the force (yield stress) necessary to break the jammed particles exceeds the crush strength of the microspheres, leading to significant collapse of particles and loss of thermal insulation behavior.

An additional unknown behavior is the impact of the observed expansion of the glass microsphere volume when subjected to cryogenic conditions (Allen et al., Cryogenic Engineering Conference, 2003, C2-C-01). The reported expansion is approximately 5 percent while the additional space created by contraction of the inner sphere of the tank is only 2 percent. Large variations in packing factors (ration of bulk density to true particle density) of microspheres have been reported by 3M (55 to 68 percent), and may allow for the observed change. If not, the microspheres would be under additional stress.

Tasks

Based on the needs of KSC, the following tasks were performed in the current project:

- Development of a thermal model of the Pad B LH_2 tank based on Mark Berg's data with input from Bob Youngquist at KSC.
- Delivery of a thermal model of KSC tanks and documentation and training for its use. Bob Youngquist will be the KSC contact.
- Work with Mark Berg (KSC) and taking high quality IR images of both LH_2 tanks.
- Work with Phil Metzger (KSC) to measure the experimental parameters that are needed for modeling of the granular effects of using glass bubbles as insulation

Site Visit and Data Analysis

IR images taken by Mark Berg revealed a cold spot near the top of the tank close to the external vent line. Without perlite insulation in the void area, heat flux increases dramatically, such that cold surface temperatures over the void are expected. The purpose of the site visit was to take high quality images to examine the void area. Point temperatures and surface heat fluxes were also measured. The IR images

were able to provide information on surface temperature distribution. The point temperature measurements can be used to calibrate IR images in order to provide exact temperature values. The surface heat flux measurement is able to calculate how thick the insulation level is in the void area.

Thermal Images of Pad A and B

Thermal images of Pad A and B tanks are shown in figure 3 and 4, respectively. Since there is no void in the Pad A tank, the color is almost homogenous on the surface, except for edges with green color due to night sky temperature. However, there is an area near the top with green color for the Pad B tank, as shown in figure 4. That area is where the void is.

Figure 5 shows an IR image of the Pad B tank and horizontal line surface temperature distribution. Since accuracy of temperature measurement with an IR camera is based on estimation of surface emissivity, the thermocouple measurement was used to calibrate the thermal images. The calibrated surface emissivity is 0.65 based on the thermal couple point measurements. There are five horizontal lines at the top, which indicate surface temperature distribution. Line 1 near the top edge shows a temperature drop near the right edge at –16 ◦C, where the void area is.

Figure 6 shows an IR thermal image of the Pad B tank and its vertical line surface temperature distribution. The IR thermal image is the same as in figure 5. However, instead of plotting surface temperature horizontally, the surface temperature is plotted vertically using the image processing software.

Heat flux measurements were also performed. The heat flux transducer (HFT) is made by Hy Cal Engineering, Inc. The measurement range is from 0 to 500 Btu/ft^2.h. Any measured values less than 1 or 2 Btu/ft^2.h are considered noise. Since the heat flux with perfect perlite insulation is about 0.07 Btu/ft^2.h, it is beyond the resolution of the HFT. However, the HFT can measure heat flux over the void area and

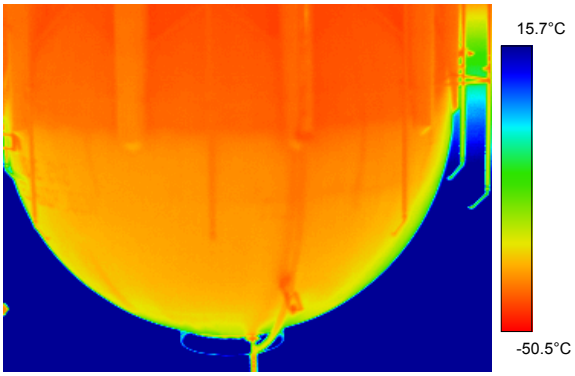

Figure 3.—Thermal image of pad A tank.

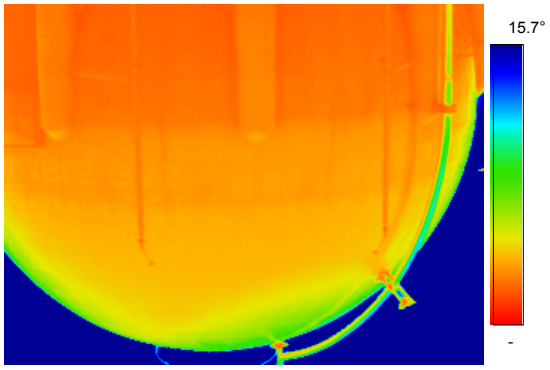

Figure 4.—Thermal image of pad B tank.

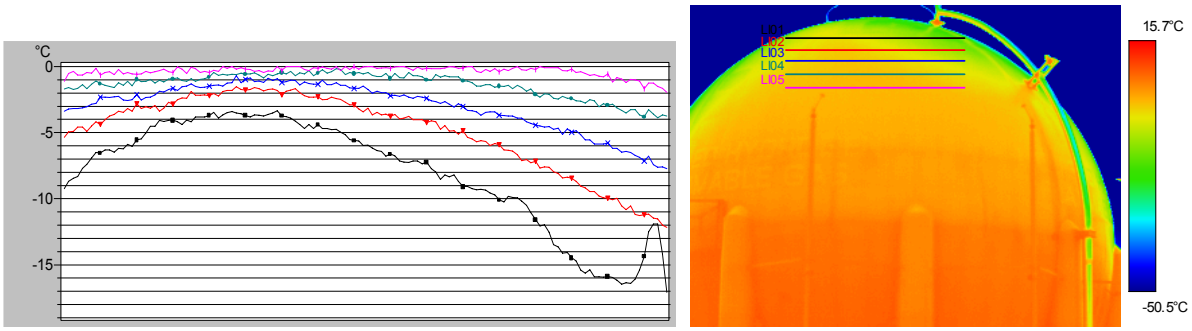

Figure 5.—Pad B tank thermal image and associated horizontal surface temperature distribution.

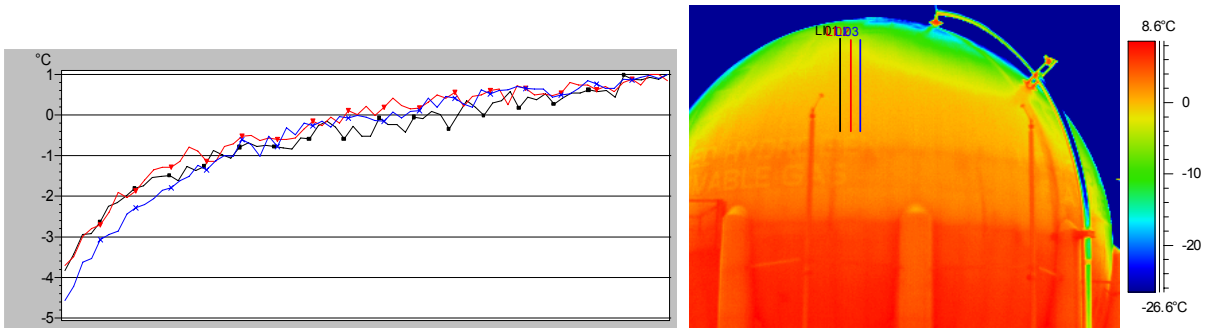

Figure 6.—Pad B tank thermal image and associated verticalsurface temperature distribution.

other direct contact areas, such as the manhole, mechanical supports, etc. The following tables list heat flux values in Pad A and B tanks, respectively. The negative sign of heat fluxes indicates the heat flows from outside to inside in the tank.

TABLE 1.—MEASURED SURFACE HEAT FLUXES IN PAD A TANK

Location	q (W/m^2)	q ($Btu/ft^2.h$)
Outside the manhole	–10.50	–3.33
Inside the manhole	–8.08	–2.56
Mechanical supports	–27.56	–8.74

TABLE 2.—MEASURED SURFACE HEAT FLUXES IN PAD B TANK

Location	q (W/m^2)	q ($Btu/ft^2.h$)
Top surface	–27.62	–8.76
Outside the manhole	–14.60	–4.63
Inside the manhole	–11.10	–3.52
Center of the cold spot	–21.17	–6.71
Cold spot	–48.12	–15.26
Outside the cold spot	–64.11	–20.33
Mechanical supports	–5.75	–1.82

Comparing measured surface heat fluxes between the two tanks, the measured values from outside and inside the manhole in the Pad B tank are higher than the ones in the Pad A tank, while the value from mechanical supports are lower than the one in Pad A tank. The main reason is that when the measurement took place in the early morning, the point heat measurement might measure different locations. Since the heat fluxes are heavily dependent on locations, different measured locations would provide different values.

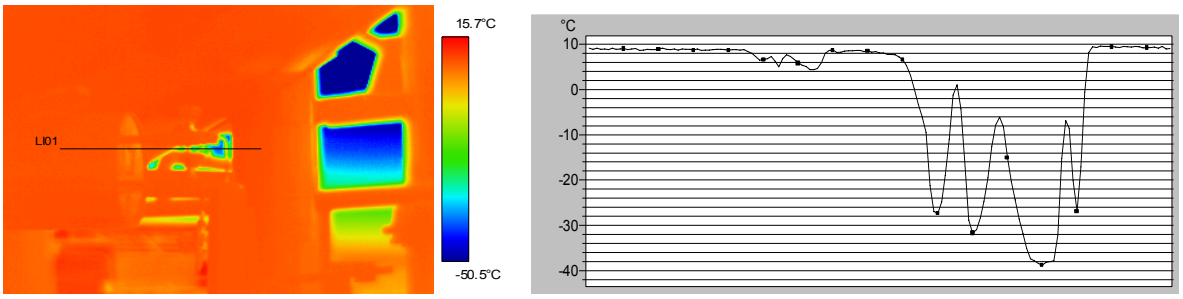

Figure 7.—Leaking Valve in pad b tank and associated horizontal surface temperature distribution.

Leaking Valve

During the site visit, a leaking valve was found near the bottom of the Pad B tank. Ice had formed around the valve and connecting pipes. Figure 7 shows a thermal image with the lowest temperature at –39 ◦C. Although the leaking valve study is beyond the scope in the present study, this topic how to reduce heat leaks will be studied.

1-D Calculation

As mentioned earlier, the HTF can detect any values over the void and other metal connection areas, but cannot detect any heat fluxes over the perfect perlite insulation area, due to HTF resolution and sensitivity. The main purpose of HTF measurement is to determine how much insulation left in the void area. The effective thermal conductivity in the void area can be calculated after given heat flux and temperature difference. In order to ensure the measured heat fluxes were valid, 1-D thermal calculation was performed to calculate insulation levels in the void area.

The assumptions used in the 1-D calculation are:

- Heat flux is a function of perlite thickness
- Conduction only inside perlite
- Radiation only between perlite and interior surface of the outer shell

Figure 8 presents comparison of heat flux between measurement and 1-D calculation results at different perlite thickness. The solid lines represent 1-D calculation results based on different internal surface emissivity and thickness of perlite. It should be pointed out that since the interior surface emissivities are unknown, various emissivities were used to cover the possible variation. The green symbol represents the measured heat flux values. The measured values show that the maximum thickness in the void area is less than 0.02 ft, compared to the ideal thickness at more than 4 ft. In other words, there is little perlite left in the void area. Although we did not use non-destructive technology to detect internal perlite levels in the void area, the heat flux measurement did provide equivalent information. The disadvantage is that the heat flux measurement provides point information. In order to determine how large the void area is and how much perlite is left, more point measurements in conjunction with IR images are needed. Because of high conductivity of the carbon steel outer shell, 3-D thermal simulation should be performed to determine the void area based on the boiloff rate.

From the comparison, the heat flux measurement was successful and measurement goal was reached.

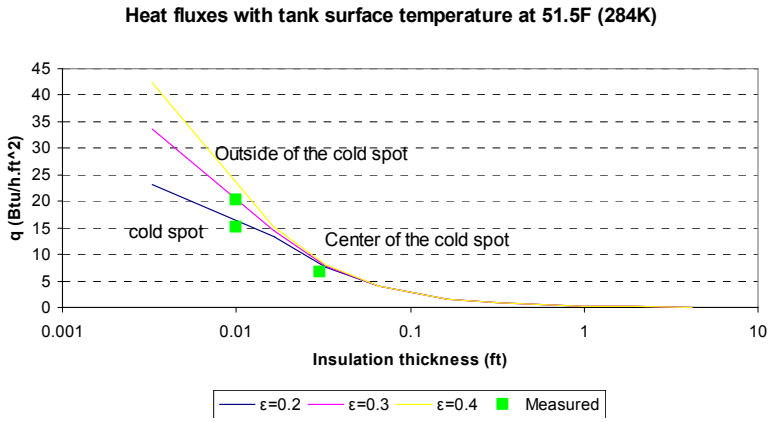

Figure 8.—Heat flux comparison between measurement and prediction.

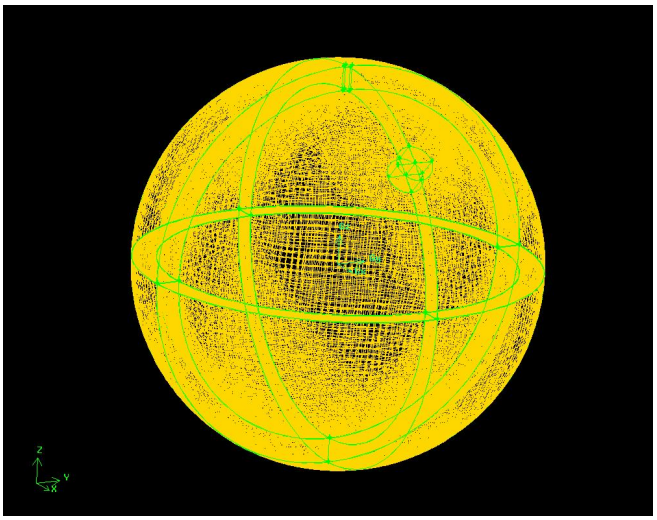

Figure 9.—3-D mesh used in simulations.

Thermal Model Development

A thermal model was developed with exact geometry (3-D) of the Pad B tank. FLUENT (Fluent, Inc.), a powerful computational fluid dynamics software, was used to perform thermal simulations. Figure 9 illustrates 3-D mesh used in FLUENT thermal simulations. The model was validated against measured data to ensure that the model provide realistic results before performing a parametric study. The measured data consisted of boiloff rate, IR images, point measurements of surface temperatures and heat fluxes. As mentioned earlier, the point surface temperature measurement was primarily used to calibrate surface emissivity for IR image post-processing. The point surface heat flux measurement was used mainly to estimate how much insulation was left in the void area. Unfortunately, due to the limitation of IR images obtained from the site visit, the exact void area was unable to be determined. The one more site visit will be proposed as a task in FY05 project. For the time being, the estimation of void area will be a parameter in detailed thermal simulations.

The first model validation was compared to a 300 gal/day boiloff rate of the Pad A tank with perfect insulation. Simulation result indicated a boiloff rate at 270 gal/day. The largest heat loss is from the perlite component. The second and third largest losses are from the access manhole and mechanical supports. Since there are many unknowns in the tank structure and 3-D mesh only covered main components, the simulation result was good enough as a starting point for examination of the thermal performance of the Pad B tank with a known void.

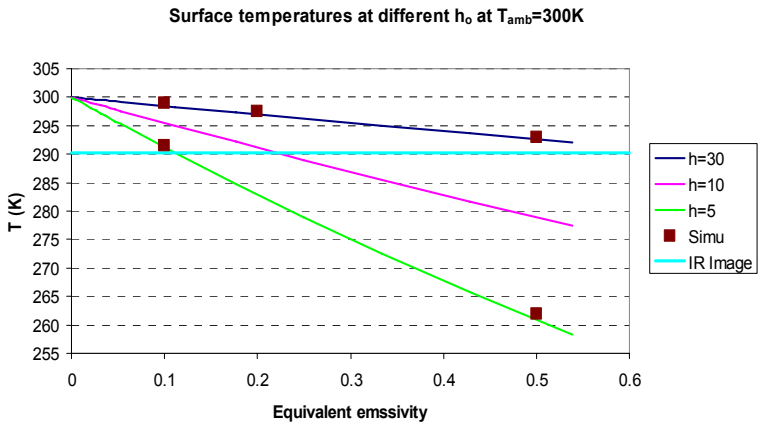

Figure 10.—Tank IR image with a cold spot.

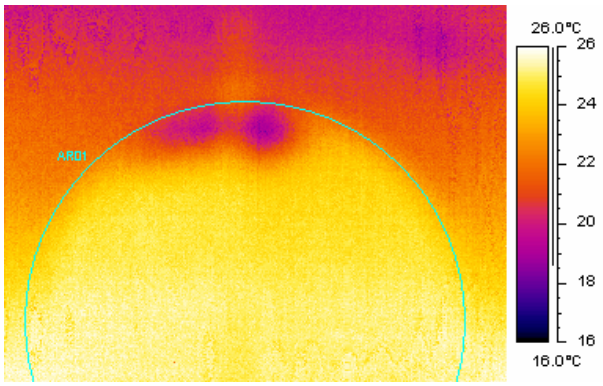

Figure 11.—Surface temperature comparison between measurement and prediction.

By assuming that there was no perlite remaining in the void derived from the heat flux measurement, simulations were performed to calculate surface temperature and boiloff rate caused by the void. Figure 10 is an IR image taken by Mark Berg. The dark area is a cold spot near the vent line close to the top of the tank. Figure 11 reveals temperature prediction obtained from the 1-D calculation and the 3-D simulations with different equivalent emissivities of the void surfaces. The solid lines, except for the blue line, represent the surface temperature with various exterior convection conditions. The symbols represent results from the 3-D simulations. The 1-D calculation results compare well with the 3-D simulation results. As long as the void area is large enough, the 1-D calculation can be used to predict surface temperatures, once lateral thermal conduction in the outer shell can be eliminated. The blue line represents measured surface temperature at the cold spot. The simulation agrees well with the actual physical measurement with the exterior convective heat transfer coefficient of 5 $W/m^2.K$ and equivalent interior surface emissivity of 0.1.

Since the measurement took place at night, a still air heat transfer at the exterior surface was assumed with h = 5 $W/m^2.K$. Figure 11 also presents a boil off rate at different heat transfer coefficients. The value of 30 $W/m^2.K$ represents day time convective heat transfer caused by heavy winds. The value of 10 $W/m^2.K$ represents convective heat transfer under mild wind condition. It is clear that convective heat transfer is an important factor in boiloff with a void. However, if there is no void in a tank, the impact of convection may be insignificant.

Parametric Study

After model validation, the sensitivity study consists of the following parameters:

- Convective boundary condition at the exterior surface of the outer shell (5 to 30 W/m^2.K)
- Equivalent solar air temperature varies from 35 to 125 °F.
- A void with diameter from 2 to 4 m near the top of the tank
- Equivalent surface emissivity from 0.05 to 0.5 inside the void
- Add an external insulation to cover the void area with double and triple coverage over the possible void area
- A localized area near a single mechanical support was simulated to examine the thermal impact of the single support on boiloff rate.

Void Size Impact

As mentioned earlier, we were unable to determine the exact void size from the March visit. However, from the image taken by Mark Berg, the estimated void diameter is about D = 2.5 to 4 m. That is why we selected a 2 and 4.5 m void size in order to cover possible void size variations. Figure 12 shows boiloff rates at different interior equivalent emissivities with void size at D = 2 and 4.5 m. The red line represents the Pad B tank boiloff rate. It is observed that it is most likely that the void area is about 4.5 m with effective emissivity of 0.1, which is consistent with the estimation derived from the heat flux measurement.

Exterior Surface Convection

Figure 13 shows impact of boiloff rate on exterior surface convection. The dark blue and green line represent perlite insulation without a void. The boiloff rate remains almost constant with different exterior surface convective rates. The other three lines represent boiloff rates with a void at different interior effective emissivities. The impact of exterior surface convection from still air to heavy wind is 10 percent at ε = 0.1. Therefore, the exterior surface convection is an important factor in tank boiloff rate with a void.

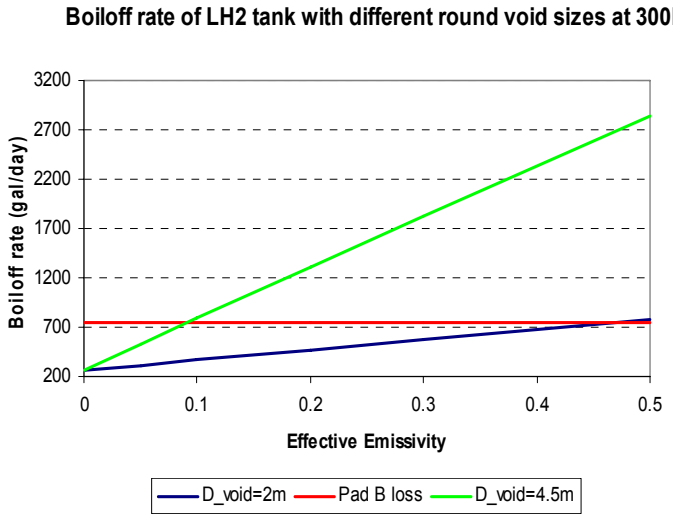

Figure 12.—Boiloff rate with two void sizes.

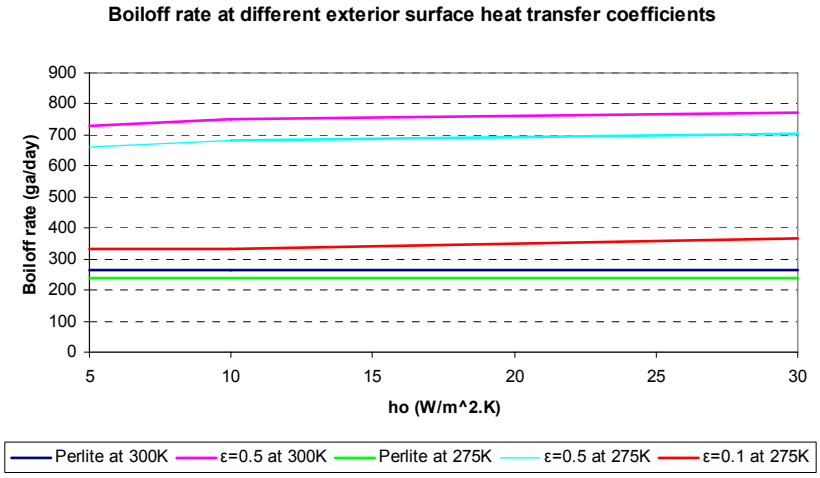

Figure 13.—Boiloff rate versus exterior surface convection.

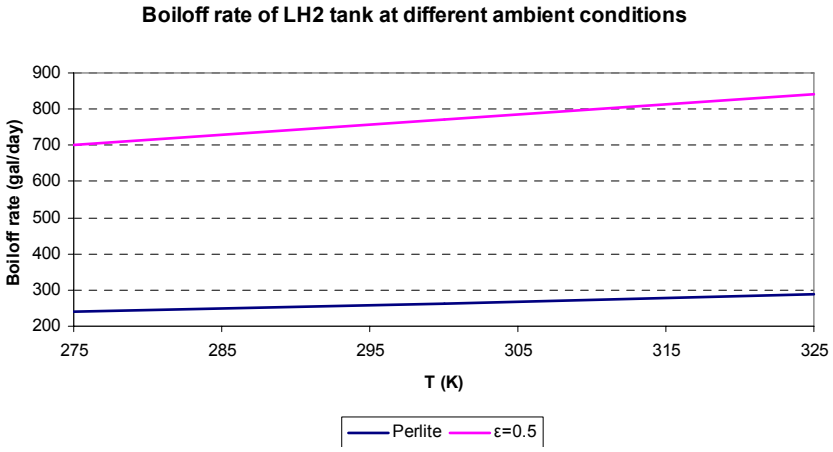

Figure 14.—Boiloff rate versus ambient temperature.

Ambient Temperature

Figure 14 reveals impact of ambient temperature on boiloff rates with and without a void. The boiloff is proportional to the outdoor temperatures. The slope of the change is based on how large the void is.

External Insulation

One of possible solutions proposed by Bob Youngquist at KSC was to add insulation over the void area to reduce heat transfer. The present study examines how large the coverage over the void area is and how effective the external insulation is through detailed 3-D simulations.

By assuming the void size to be D = 2 m and the external insulation size to be D = 4 m (double coverage) and 6 m (triple coverage), simulations were performed at different external insulation thickness, equivalent to different insulation levels. For convenience, we assumed that perlite was used as the external insulation material. Figure 15 illustrates boiloff rates at two interior emissivities varying with external insulation thickness. When the external thickness is less than 0.01 m, the boiloff rate drops dramatically. However, the boiloff rate remains almost constant when the external thickness is above 0.01 m. Therefore, the option by increasing external insulation can not reduce the boiloff rate to the level where the tank has no void.

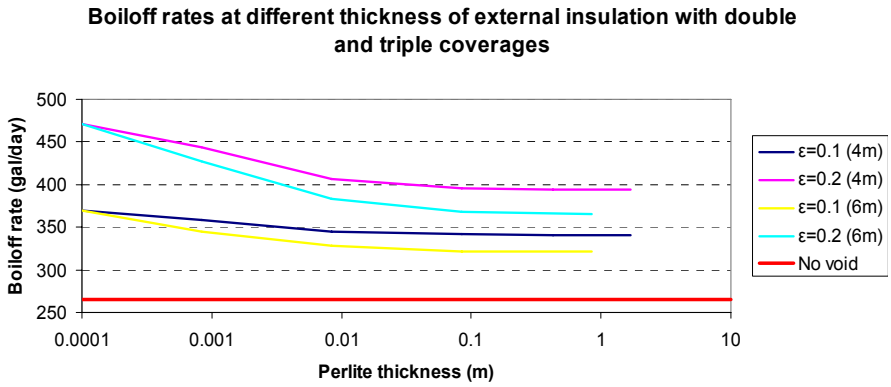

Figure 15.—Boiloff rate versus external insulation.

By assuming an interior effective emissivity of ε = 0.1 and 9 times external insulation coverage with infinity insulation level over the void area, a 13 percent boiloff reduction can be reached, compared to the case with the void and without external insulation. Compared to the case without the void with the same base, the reduction of boiloff rate is 28 percent. By assuming an interior effective emissivity of ε = 0.2 and keeping 9 times external insulation coverage with infinity insulation level over the void area, a 22 percent boiloff reduction can be reached, compared to the case with the void and without external insulation. Compared to the case without the void with the same base, the reduction of boiloff rate is 46 percent. Therefore, external coverage never reaches the boiloff level without the void. This may not be the solution from simulation results.

Insulation Experimental Program

Evaluation of Microsphere Crush Strength

Values for the crush strength of glass microspheres have been extensively published by the manufacturer, 3M Corp. These values have been determined by methods to duplicate the typical usage, as a filler in plastic formulations. In this application isostatic conditions apply with equal stress exerted across the surface area of the particle. The insulation application, however, is a bulk usage where point-to-point contact occurs producing much higher localized stress.

A recent publication (Koopman et al., Scripta Materialia, 50, (5), Mar. 2004, pp. 593-596) served as a guide to expected behavior. A nanoindenter was used in this study in uniaxial compression to measure the crush strength of individual glass microspheres. By extrapolation to a bulk application, the crush strength would be expected to be almost a factor of 10 smaller than the isostatic value.

3M Corp. graciously explored a modification of their quality assurance test to change the particle test from isostatic conditions to point-to-point contact. The test is closely described by ASTM D3102-78 in which the glass microspheres are placed in a rubber balloon along with an agent to prevent direct contact between spheres. This system is then pressurized by liquid or gas and the amount of crushing determined.

Several variations were explored with the elimination of the agent to prevent direct contact between spheres. Gas pressurization of the balloon resulted in measurable crush values. The initial feasibility results were significantly below the published isostatic crush strength (>50 percent versus <10 percent crushed), but further experimental refinements are necessary for reproducible results.

Evaluation of Flow Yield Stress

Thermal Analysis Instruments graciously conducted two feasibility studies to find methods to determine the yield stress (to flow) for glass microspheres. The first method explored used a Dynamic Mechanical Analyzer in compressive mode to simulate the expanding internal sphere of the LH_2 tanks. Evidence of flow or resistance to flow could not be distinguished by this method.

The second evaluation utilized their AR 2000 Advanced Rheometer equipped with a vane rotor (four paddles at 90◦) immersed in a container of glass microspheres. Increasing shear stresses were applied until rotation of the vane occurred. Torque values were determined with the glass microspheres in a loose state and a more compact state achieved by vibrating the container. The resulting yield stress increased by 5X to 10X with two different types of glass microspheres. Unfortunately, sample limitations prevented the determination of traditional rheological parameters or comparison to crush strengths. Any additional studies will be designed to complement the modeling effort or other project needs.

Conclusions and Recommendations

Following conclusions and recommendations may be drawn from the above investigations:

- Simulation results using the 3-D mesh are comparable with measured data on temperature distribution and boiloff rates.
- Heat transfer coefficient at exterior surface plays an important role in determining surface temperature distribution. The cold spot above the void area can be detected by IR images at night only due to still air convection, while not detected during day time due to high convection.
- Boiloff rate is proportional to effective void interior surface equivalent emissivity and ambient conditions.
  - 20 percent due to ambient (from 275 to 325 K)
  - 40 percent with 34 ft^2 void at $\varepsilon = 0.5$, 200 percent with 170 ft^2 void at $\varepsilon = 0.5$
  - 10 percent from heat convection with a void (5 to 30 $W/m^2.K$)
- The most important impact on boiloff rate is void size
- External insulation coverage may not be an effective method to reduce boiloff rate
  - 13 percent boiloff reduction at $\varepsilon = 0.1$ with 9 times external area coverage, compared at 28 percent without void
  - 22 percent boiloff reduction at $\varepsilon = 0.2$ with 9 times external area coverage, compared at 46 percent without void

The puzzling differences in thermal performance of the Pad A and B liquid hydrogen tanks is best explained by the development of an exposed area of the inner sphere which is not covered by perlite in Pad B. This thermal performance difference was noted immediately upon first usage of the tanks, and is most likely due to less efficient filling of the Pad B tank around the complex hydrogen vent line that is routed between the spheres. As a free flowing particulate, small voids may have formed near the pipe supports, then filled with subsequent launch vibrations, leaving more space at the top of the tank. In addition, the thermal contraction of the inner sphere generates a void at the top comprising 2 percent of the space between the spheres. With Pad B, this combination was significant enough to expose a small portion of the inner sphere. This is very consistent with the observed location of the thermal cost spot. This interpretation of the thermal performance leads to the conclusion that the filling efficiency of the tank is a key aspect that must be controlled when the refurbishment of the tanks occurs.

Education and Outreach

PI: A. Henzmann (Florida Solar Energy Center)
S. Schleith (Florida Solar Energy Center)
D. Block (Florida Solar Energy Center)

Description

Education and outreach are important components of the hydrogen research program. These activities have supported three main areas: education for K-12 students and teacher professional development; participation in seminars and workshops; and pubic outreach. Much of the work has been accomplished through publications, presentations and web site information, as well as personal interaction with the public.

Objectives

Primary objectives of the Education and Outreach Task are to educate and support graduate and undergraduate students, develop and offer public outreach, and develop and conduct K-12 educational programs.

Benefit to NASA

Knowledge and understanding of hydrogen technologies and uses by NASA on the part of the public assist the public in their support of NASA. The objectives of this task support education as a major goal of the NASA administration. These activities supply educational programs for students from kindergarten through graduate level for the long-term goal of stimulating student interest in and public understanding of the relationship of hydrogen to the space program.

Approach

FSEC staff members have and will continue to develop, coordinate and participate in a variety of education and outreach activities.

Results

The objectives of K-12 education programs are:

1. Create an awareness of hydrogen as a fuel carrier through school events and other public events, which include exhibits, displays, and presentations.
2. Provide opportunities for students to explore the potential of hydrogen through programs such as the Hydrogen Vehicle Sprint and the High School Hydrogen Summit.
3. Coordinate professional development opportunities for teachers to learn how to integrate hydrogen content into their existing curriculum.
4. Develop user-friendly resources for students and teachers.
5. Create interactive web-based activities for the Energy Whiz website.
6. Collaborate with industry professionals to provide a wide range of opportunities in Hydrogen Education.

Seminars, Workshops and Public Outreach

- Participation in numerous conferences, workshops and seminars, presenting papers, posters, leading seminars.

- Participation in the third annual Florida Space Day in Tallahassee. Space businesses from across Florida met at the Capitol to emphasize the importance of space business to Florida. The event included a meeting with Lt. Governor Toni Jennings and opportunities to meet with Legislators.
- Planning and initial development of Hydrogen Technology Learning Center.
- Initial planning of Hydrogen Youth Program, designed to be a two-phase program, Phase One includes professional development for teachers, to guide them through the process of developing the plan for the Hydrogen Youth Education Summit (H_2 YES), a conference planned by students to showcase their understanding of the use of hydrogen as a fuel carrier and their concept of a hydrogen economy.

Analysis of Alternative Hydrogen Production Processes Liquid Hydrogen Production via Sub-quality Natural Gases

PI: C. Huang (Florida Solar Energy Center)
A. Raissi (Florida Solar Energy Center)

Abstract

Sub-quality natural gases (SQNGs) are defined as those natural gases, which exceed pipeline specifications in nitrogen, carbon dioxide and/or hydrogen sulfide content. Because of the high cost of treatment with current processing technologies, SQNG cannot be extracted and must remain in the ground. It has been reported (ref. 1) that approximately one-third of the U.S. natural gas resource is low or SQNG that does not meet the specifications for pipeline shipment. However, SQNGs are very important hydrogen sources. Compared to hydrogen production via water splitting, coal and biomass gasification, hydrogen production through SQNGs has many advantages. First, hydrogen production from natural gas is currently the most efficient and low cost process and is considered to be a near-to-medium term hydrogen source. Second, there are a number of mature technologies available for hydrogen production via natural gas, such as steam methane reforming, the autothermal process, partial oxidation and thermal dissociation. In addition, there are several methods available for hydrogen production via hydrogen sulfide. However, the current technologies are designed to deal with high quality natural gas while hydrogen production via SQNG remains a major challenge because of the coexistence of hydrocarbons and hydrogen sulfide in most SQNG. We are proposing for the first time a process combining methane pyrolysis and hydrogen sulfide methane reformation to efficiently produce hydrogen, carbon and carbon disulfide products using SQNG without requiring separation. In the first part of this research we present thermodynamic analyses for the direct pyrolysis of SQNG. The results reveal that hydrogen sulfide coexisting in SQNG is stable and can be considered an inert gas within the temperature range of the thermal pyrolysis of hydrocarbons. The hydrogen sulfide can reform with the remaining methane to further produce hydrogen carbon disulfide. During the autothermal process, thermodynamic analysis indicates that no sulfur dioxide and/or sulfur trioxide are formed from the introduction of oxygen to SQNG. The significance of this finding is that the pyrolysis of SQNG will not produce environmentally harmful acid gas. In addition to the new approach, some possible approaches for the purification of SQNG are reviewed and discussed.

Key words: hydrogen, natural gas, sub-quality natural gas, thermodynamic analysis, hydrogen sulfide, sulfur dioxide and sulfur trioxide.

Background

One important objective of the National Aeronautics and Space Administration (NASA) hydrogen project is to investigate the feasibility of local production of hydrogen for NASA at the Kennedy Space Center (KSC). We have reviewed and analyzed the sub-quality natural gas (SQNG) sources in the panhandle area of Florida and have pointed out that hydrogen production from hydrogen sulfide available in Florida's SQNG could be sufficient to support space launch applications for more than a century. Because of the ready availability of SQNGs in Florida as a feedstock for the production of hydrogen, it is our belief that the continuation of this research would have a significant impact on future space applications.

Hydrogen sulfide concentration in NG varies from traces to 90 percent by volume. For example, the Smackover zone and a deeper, contiguous zone called the Cotton Valley pinnacle reef in East T exas contain deposits wherein the subterranean gas composition at one location contains as much as 87 percent by volume H_2S gas. Closer to NASA KSC, in Santa Rosa County, in Florida panhandle, the Blackjack Creek and Jay fields in Smackover reservoir of mid-Gulf Coast Basin contain gas deposits with as much as 10 mol % H_2S. The cumulative production capacity of these two ultra-sour gas fields has been estimated to be close to 0.52 Tcf. Typical gas composition and volumetric data for these fields are given in table 2.

Based on the data of table 2, we estimate that, in Florida, just from hydrogen sulfide portion of the available SQNG resource alone, sufficient quantities of LH_2 cam be produced (via processes described in this report) to provide fuel more than 775 Shuttle launches (assuming each Shuttle launch requires 260 tons of LH_2). At an average of seven Shuttle launches per year, Florida can generate hydrogen from its own indigenous resource (i.e., H_2S), generally viewed as a pollutant and removed by treatment and burning to SO_2, to supply NASA's Shuttle fleet with LH_2 to last more than hundred years.

Introduction

A representative range of U.S. gas compositions and typical pipeline specifications are listed in table 1.

TABLE 1-1.—NATURAL GAS PIPELINE COMPOSITIONS AND TYPICAL COMPOSITION RANGES

Component	Typical pipeline specification	Typical composition range	Percentage
Hydrogen sulfide, H_2S	<4 ppm	<4 ppm 4-1,000 ppm 1,000-10,000 ppm	76 11 4
Carbon dioxide, CO	80-140 ppm	>10,000 ppm <1% 3-10%	8 72 3
Water, H_2O	80-1400 ppm	800-1,200 ppm	
Nitrogen (ref. 3), N_2	1.10%	0-30%	

To meet the specifications of pipeline natural gas three basic issues need to be considered. The first issue is the removal of impurities. The greatest concern for the quality of natural gas is the concentration level of any of the following impurities: hydrogen sulfide, carbon dioxide, water and nitrogen. Since the latter three components only affect the heating value of the natural gas, they do not have a significant impact if the natural gas is used as a hydrogen production resource. Water is required for steam-methane reformation while carbon dioxide and nitrogen can be removed through a pressure swing adsorption process. However, hydrogen sulfide in natural gas not only causes severe corrosion to pipelines, but it also deactivates catalysts during steam methane reformation. In addition to the corrosive and catalyst deactivation effects, it is well known that hydrogen sulfide is an extremely toxic air pollutant. The second issue is the loss of methane during the impurity removal processes. It is acceptable if the loss is less than 3 percent, while losses over 10 percent are unacceptable. With the offset of other advantages, the losses between 3 to 10 percent can be acceptable. The third issue is the final disposition of the impurities removed from the original natural gas. It is well known that carbon dioxide is a green house gas and needs to be sequestered. However, the hydrogen sulfide removed can be a useful resource for hydrogen and sulfur.

The compositions of two SQNGs found in the Florida panhandle area are shown in table 2. Because of high hydrogen sulfide concentrations, the sources cannot be treated using current technologies to meet pipeline natural gas requirements. However, compared to some other hydrogen sources, such as landfill gas, gob gas and biomass, SQNGs are highly concentrated hydrogen resources. Abundant SQNGs can be important alternatives to replace increasingly exhausted reserves of high quality natural gas. Therefore, the development and utilization of SQNG sources for hydrogen production can be both economically and environmentally beneficial. Table 2 shows that the production of liquid hydrogen alone from these two resources is worth an estimated 135.95 billion dollars. As a rough estimation, the values of the carbon and sulfur produced could pay for the interest on capital as well as operational costs (128.86 and 0.256 billion dollars respectively) so $135.95 billion is a huge potential future source of hydrogen.

TABLE 1-2.—GAS COMPOSITIONS AND ECONOMIC ESTIMATIONS FOR TWO FLORIDA SQNG RESOURCES

	Field Name							
	Jay				Blackjack Creek			
Composition	mol %	H_2 mol %	C mol %	S mol %	mol %	H_2 mol %	C mol %	S mol %
Methane	61.60	123.20	61.60		62.10	124.20	62.10	
Ethane	12.0	36.00	24.00		11.70	35.10	23.4	
Propane	6.20	24.80	18.60		3.40	13.60	10.20	
Butanes	3.60	18.00	14.40		2.30	11.50	9.20	
Pentanes	1.50	9.00	7.50		0.80	4.80	4.00	
Hexanes	0.60	4.20	3.60		0.20	1.40	1.20	
Hydrogen	9.00	9.00		9.00	10.00	10.00		10.00
Sulfide	3.30				2.40			
Nitrogen	2.30				6.90			
Helium	0.02				0.040			
Other	0.20				0.10			
Heating value (Btu/scf)	1268				1113 51989			
Total volume (mmcf)	466858							
Total mole fraction (mol %)		224.20	129.70	9.00		200.60	110.10	10.00
Total H_2 volume (mmcf)		1046696				104290		
Total Mass (lb)		6.2E+11	1.6E+10	3.0E+9		6.2E+10	1.5E+9	3.7E+08
$ (Billion)		123.64	0.57	0.025		12.32	0.054	0.003

[a] Liquid hydrogen price: $2/lb (ref. 16); carbon black: $0.78/lb (ref. 17); sulfur: $0.085/lb (refs. 12 and 18).

Currently, the commercial plant process for hydrogen sulfide treatment is the Claus process in which a portion of hydrogen sulfide is burned to make sulfur dioxide, and the latter is then recombined with the main hydrogen sulfide to produce elemental sulfur and water vapor according to:

$$2H_2S + 3O_2 = 2SO_2 + 2H_2O \quad (1)$$

$$2H_2S + SO_2 = 3S + 2H_2O \quad (2)$$

Thus the overall reaction can be written as:

$$2H_2S + O_2 = 2S + 2H_2O \quad (3)$$

In this process the hydrogen in hydrogen sulfide is wasted as water vapor. Furthermore, since Claus units do not convert all the hydrogen sulfide into sulfur, tail gas cleanup units are needed to remove small amount of sulfur dioxide.

In addition to the Claus process, some innovative processes for utilizing hydrogen sulfide both as hydrogen and sulfur sources have been widely explored for decades. The typical approaches include thermal decomposition, thermochemical methods, electrochemical methods, photochemical methods and plasma methods. A detailed review and comparison of these methods are given by Zaman and Chakma (ref. 4).

From the preceding discussion it is clear that hydrogen production via SQNG depends upon the efficient removal of hydrogen sulfide from SQNG, and dealing with its final disposition. Currently, the commonly accepted technology for the removal of hydrogen sulfide from natural gas is amine absorption. Membrane-based treatment of natural gas can be used to remove carbon dioxide, but this is far more expensive than the traditional amine absorption process if it is used to remove high concentrations of hydrogen sulfide. One of important advantage of using amines to treat natural gas is that the process can remove hydrogen sulfide and carbon dioxide simultaneously without significant methane loss (ref. 2).

The amine absorption process can be separated into several steps (ref. 5). First a water-saturated natural gas is absorbed with an amine solution in an amine contactor, and the rich amine stream is then

flashed from 1000 psia to 90 psia to remove most of the absorbed hydrocarbon gases. Next the rich amine stream is distilled to remove hydrogen sulfide, and finally the regenerated amine is fed back into the amine contactor tower to start a new cycle. The amines used for this purpose include MEA, DEA, PIPA, DGA and MDEA. In addition to the capital and operational costs of this process, the loading of amine is an important factor to be considered. Concentrations of acid gas components in an amine stream are typically expressed in terms of loading of the amine, defined as moles of a particular dissolved acid gas divided by the moles of the circulating amine (ref. 5). The parameter describes the amount of amines used for the circulation. The maximum acid gas loadings are listed in table 3 (ref. 5).

TABLE 1-3.—MAXIMUM ACID GAS LOADINGS
(MOLES ACID/MOLE OF AMINE)

	CO_2	H_2S
MEA, DGA	0.5	0.35
DEA	0.45	0.30
TEA, MDEA	0.30	0.20

Since loadings of amine are limited, the high concentrations of carbon dioxide and hydrogen sulfide in SQNG will require more circulating amines, resulting in higher capital and operational costs. In addition to the cost considerations, amine solutions cannot be used for an infinite number of regenerations. They can be contaminated by hydrogen sulfide and other impurities in the SQNG and finally must be removed. The treatment of hydrogen sulfide-containing amine solutions will cause the same pollution problems as the pure hydrogen sulfide treatment and can be even more complicated because of the involvement of multi-components.

Now the remaining question is whether there is an alternative technology to economically and efficiently remove highly concentrated hydrogen sulfide from SQNG. As Lokhandwla et al (ref. 2) pointed out, the best treatment for natural gas right now is no treatment, which means that millions upon millions of tons of SQNG must remain underground and require occasional monitoring for hydrogen sulfide release. In case of earthquakes or other destabilizing events, those gases can have disastrous consequences for humanity. On the other hand, with today's increasing demand for energy, thoughtful deliberation and evaluation must be given these potentially valuable hydrogen resources. The impact of their successful utilization would be immeasurable not only in the untapping of new energy sources, but also in the securing of safer conditions for all people.

With the exception of amine absorption, hydrogen sulfide can be most readily absorbed by an alkaline solution through the following reactions:

$$H_2S + 2NaOH = Na_2S + 2H_2O \quad (3)$$

$$CO_2 + 2NaOH = Na_2CO_3 + H_2O \quad (4)$$

while at the same time methane and other hydrocarbons will not be absorbed. Equations (3) and (4) are also kinetically favorable reactions. This absorption process is far less complicated than hydrogen sulfide amine absorption and there is no amine final treatment needed. One remaining problem is the conversion of sodium sulfide into hydrogen and sulfur and the reuse of the alkaline solution (NaOH) to absorb hydrogen sulfide. Another question is whether the presence of sodium carbonate affects the production of hydrogen and sulfur from a sodium sulfide solution.

Typically, there are two technologies that can be applied for the production of hydrogen from hydrogen sulfide: Electrochemical methods and photochemical methods.

Sulfide ions are formed when hydrogen sulfide is dissolved in an alkaline solution according to:

$$H_2S + OH^- = H_2O + HS^- \quad (5)$$

During the electrolytic process, sulfur is generated at the anode and hydrogen is evolved at the cathode in the following electrochemical reactions (ref. 4):

$$\text{Anode: } HS^- + OH^- = S + H_2O + 2e^- \quad (6)$$

$$\text{Cathode: } 2H_2O + 2e^- = H_2 + 2OH^- \quad (7)$$

The overall reaction for Reactions (5) to (7) is:

$$H_2S(g) + (\text{electrolysis}) = S(s) + H_2(g) \quad (8)$$

No alkaline is consumed during this process, enabling the solution to be recycled to absorb hydrogen sulfide in a closed-loop process. A similar reaction can be applied to the photolytic decomposition of hydrogen sulfide for the production of hydrogen and sulfur (ref. 6). It has been found that a sodium sulfide aqueous solution can be photolytically dissociated into hydrogen and sodium disulfide (Na_2S_2) according to the following (ref. 6):

$$HS^- + h_2 \longrightarrow HS^{-*} \text{ (photo-activation)} \quad (9)$$

$$HS^{-*} \longrightarrow HS^- + e^- \text{ (photo-oxidation)} \quad (10)$$

$$HS^{\cdot} + HS^- \longrightarrow S_2 = \quad (11)$$

$$2H_2O + 2e \longrightarrow H_2\uparrow + 2OH^- \text{ (water reduction)} \quad (12)$$

The overall reaction of Reactions (9) to (12) is:

$$2HS^- + 2h\nu \longrightarrow H_2\uparrow + S_2^{2-} \quad (13)$$

Disulfide ions can further react with hydrogen sulfide to produce bisulfide ions and solid sulfur, forming the following closed cycle:

$$S_2^{2-} + H_2S \longrightarrow HS^- + S(s) \quad (14)$$

No photocatalysts are needed in this process. Another important characteristic of the photolytic process is that (refs. 6 and 7) the concentration of sodium carbonate does not affect the hydrogen release rate. Clearly, this approach can be applied to remove hydrogen sulfide from SQNG and utilize it to produce hydrogen and sulfur. However, it is noted that an obstacle to this approach is the low efficiency of the process of extracting hydrogen and sulfur from the bisulfide solution. It is well known that the major disadvantage of the electrochemical method applied for this purpose is the passivation of the electrodes due to the deposition of sulfur. As for the photolytic technology, because it requires a multi-step conversion from electrical energy to UV light and then to the chemical reaction, the efficiency of the process is a major concern.

Mizuta et al (refs. 4 and 8) developed a hybrid process based on iron chloride for the production of hydrogen and sulfur from hydrogen sulfide gas. The process consists of a hydrogen sulfide absorption step and an electrolysis step according to the following reactions:

$$H_2S(g) + 2FeCl_3(aq) \longrightarrow 2FeCl_2(aq) + 2HCl(aq) + S(c) \quad (15)$$

$$2FeCl_2(aq) + 2HCl(aq)\text{-}(\text{electrolysis}) \longrightarrow H_2(g) + 2FeCl_3(aq) \quad (16)$$

$$\text{Overall reaction: } H_2S(g) \longrightarrow H_2(g) + S(c) \quad (17)$$

It is reported that the process can approximate 100 percent hydrogen sulfide absorption at 343 K. The electrolysis requires a voltage of 0.7 V and 100 mA/cm2 current density. The feed gas used was a mixture of 30 percent hydrogen sulfide and 70 percent argon. Common features of the three processes reviewed above are that SQNG can be directly fed into the system, hydrogen sulfide is absorbed and used to produce hydrogen and sulfur in one plant while hydrocarbons are not absorbed and are therefore separated from the hydrogen sulfide.

The other process which also does not need a waste gas treatment plant to separate hydrogen sulfide from natural gas is known as a high temperature electrolytic process. The process directly converts hydrogen sulfide to hydrogen and sulfur at an elevated temperature. Hydrogen goes with the process stream while sulfur is condensed and collected s a product (refs. 4, 9 to 11). The electrochemical reaction takes place as:

$$H_2S + 2e^- \longrightarrow S^{2-} + H_2 \quad (15)$$

$$S^{2-} \longrightarrow 0.5S_2 + 2e^- \quad (16)$$

Up to 80.7 percent of the hydrogen sulfide can be removed from an input concentration of 2000 ppm. The process can also remove carbon dioxide from natural gas.

In addition to hydrogen sulfide absorption processes, Raissi (ref. 12) proposed an innovative approach using hydrogen sulfide to reform methane to produce hydrogen and, instead of elemental sulfur, carbon disulfide. The latter is a high heat value chemical with a multiple usages. This approach is a pure thermal process that is fundamentally different from the other hybrid approaches: thermal processing of methane and electrolytic or photolytic processing of hydrogen sulfide.

Similar with the steam methane reformation the process can be written as follows:

$$2H_2O(g) + CH_4 \longrightarrow 4H_2(g) + CO_2(g) \quad \Delta H_{298K} = 165.2 \text{ kJ/mol} \quad (17)$$

In the new process, water is replaced with hydrogen sulfide. The hydrogen sulfide methane reformation consists of two steps:

$$H_2S = H_2 + 0.5S_2 \qquad \Delta H_{298K} = 79.9 \text{ kJ/mol} \quad (18)$$

$$CH_4 + 2S_2 = CS_2 + 2H_2S \qquad \Delta H_{298K} = -107 \text{ kJ/mol} \quad (19)$$

The overall reaction for the hydrogen sulfide methane reforming process can be written as:

$$2H_2S(g) + CH_4 \longrightarrow 4H_2(g) + CS_2(l) \qquad \Delta H_{298K} = 232.4 \text{ kJ/mol} \quad (20)$$

The advantages of this process are obvious. Firstly, it eliminates the step of separating hydrogen sulfide from natural gas. Secondly, unlike elemental sulfur, the carbon disulfide produced from the reformation has broad applications, including sulfuric acid production and the manufacture of xanthate. Thirdly the process does not produce carbon dioxide as does steam methane reformation, thus greatly reducing the greenhouse gas effect. Fourthly, since the process is highly endothermic, it is can be used to efficiently absorb heat from a high temperature heat source such as concentrated solar energy. Therefore the process has potential application in the efficient use of solar energy.

It is noteworthy that during hydrogen sulfide methane reformation, the following two additional pyrolytic reactions take place at the same time:

$$CH_4 = C + 2H_2 \quad (21)$$

$$H_2S = 0.5S_2 + H_2 \quad (22)$$

Since carbon deposits cause the deactivation of catalysts, reaction conditions chosen for Reaction (20) must guarantee that no carbon lay-down occurs during the process. The thermodynamic analysis of Reaction (20) has revealed that (refs. 12 and 13) there exist pinch points at which no methane decomposition occurs when the ratio of hydrogen sulfide to methane (H_2S:CH_4) is greater than 4. The pinch point temperature decreases as the ratio increases. Based on these results, we find that SQNGs can be separated into two groups based on their H_2S:CH_4 ratios. For highly soured SQNG with a hydrogen sulfide concentration greater than 80 percent, the hydrogen sulfide methane reformation process can be directly applied to produce hydrogen and carbon disulfide. When the concentration is less than 80 percent, the reforming process cannot be directly applied. Therefore this type of SQNG requires a

pre-treatment step to establish the necessary hydrogen sulfide to methane ratio. This step either adds pure hydrogen sulfide or removes part of the methane to increase the hydrogen sulfide proportion in the gas mixture. Because highly soured SQNGs are just a small portion of available SQNGs, the application of the reformation process for hydrogen production from SQNGs is greatly limited. Table 1-4 summarizes and compares the above approaches.

TABLE 1-4.—COMPARISON OF POSSIBLE TECHNOLOGIES FOR HYDROGEN SULFIDE SEPARATION AND TREATMENT IN NATURAL GASES

Technology	Advantage	Disadvantage	Reference
Amine absorption + Claus plant	Commercialized	No H_2 produced. Amine regeneration needed. Limited H_2S absorption. Tail gas treatment.	5
Alkaline absorption + electrolysis	Fast and selective absorption. High H_2S conc. absorption. High efficiency H_2 and S production.	Anode Passivation	4 and 6
Alkaline absorption + photolysis	Fast and selective absorption. High H_2S conc. absorption. High efficiency H_2 and S production.	Low quantum efficiency	6 and 7
Fe-Cl Hybrid Process $FeCl_3$ absorption + electrolysis	Fast and selective absorption. High H_2S conc. absorption. High efficiency H_2 and S production.	Highly acidic process	8 to 11
H_2S CH_4 reforming $2H_2S+CH_4 = 4H_2+CS_2$	No H_2S separation needed. Co-producing CS_2. Pure thermal process.	High temperature required. High H_2S to CH_4 ratio required. Only applied H_2S >80% natural gas.	12 and 13

In addition to the above technologies for the removal of hydrogen sulfide from SQNG, another potential use for SQNG is the direct production of hydrogen through SQNG purification. One very obvious approach is to separate its individual components. There are existing technologies for the purification of SQNG: membrane separation, pressure swing adsorption (PAS) and cryogenic processing. Membrane technology can only be applied to low hydrogen concentrations. PSA technology is not suitable for hydrogen sulfide separation from SQNG because high concentrations of hydrogen sulfide can cause adsorption column deactivation. A cryogenics process can be one of the alternatives. It is has been reported that gob gases can be purified to meet typical pipeline specifications (ref. 14) through a cryogenic process.

The objective of this research was to explore possibilities for efficiently producing hydrogen, sulfur and/or carbon disulfide from SQNG. A typical SQNG composition with 10 percent hydrogen sulfide was selected for the calculation, based on the Blackjack Creek SQNG field in the Florida panhandle area. The AspenPlus chemical process simulator was used to conduct thermodynamic analyses based on minimized Gibbs free energies. SQNG pyrolysis was performed as isothermal processes at varying temperatures and oxygen inlet flow rates.

Thermal Decomposition of SQNG

Hydrogen production through natural gas pyrolysis or autothermal process has been extensively reported. However, hydrogen production via SQNG pyrolysis in the presence of hydrogen sulfide is rare in literature citations. One major reason for this is that hydrogen sulfide is considered a harmful component to the methane pyrolysis catalysts. Sulfur produced from hydrogen sulfide decomposition can deposit on the surfaces of catalysts, causing their deactivation. Another important consideration is that hydrogen sulfide can be oxidized into sulfur dioxide that is an environmentally toxic gas which must be controlled. The final reason is that hydrogen sulfide eventually must be removed from products. The commonly accepted approach is to remove it prior to the pyrolytic process, which is costly and requires a follow up treatment. An unanswered question is whether or not hydrocarbons can be thermal chemically decomposed to produce hydrogen in the presence of hydrogen sulfide. If, in the methane pyrolysis temperature range, hydrogen sulfide is stable, the hydrogen produced can be easily separated from the main stream with many readily available technologies, while the remaining hydrogen sulfide and un-

decomposed methane can reform to further produce hydrogen and carbon disulfide. This approach greatly reduces the hydrogen sulfide separation costs. Furthermore, hydrogen sulfide methane reforming (HSMR) is a less costly process than either electrolysis or photolysis. In addition to the hydrogen production, the HSMR process can produce a higher value product, carbon disulfide.

Here we take the Blackjack Creek SQNG source (listed in table 1) as a case study. The thermodynamic analysis is conducted based on an assumed isothermal process. In this calculation we also assume that the inlet component mole flow rates are equal to their mole fractions listed in table 1.

1. Equilibrium flow rates of methane, hydrogen and carbon. Figure 1 demonstrates the changes of flow rates of methane, hydrogen and carbon with the pyrolytic temperature. It indicates that when the temperature is lower than 500 ◦C, hydrocarbons (C2 to C6) are quickly decomposed to methane and hydrogen, with methane the flow rate increasing to about 90 kmol/hr. With increasing temperature the methane flow rate decreases. When the temperature exceeds 500 ◦C methane is decomposed into carbon and hydrogen. When temperature is higher than 850 ◦C equilibrium flow rates of methane and carbon just slightly depend upon temperature increase.

Using ethane as an example, hydrocarbon decomposition takes several paths, illustrated in the following reaction:

$$H_3C - CH_3 \xrightarrow{600\ ^\circ C} \begin{cases} C_2H_4 + H_2 \\ CH_4 + C + H_2 \end{cases} \tag{23}$$

Since the bond energies of C-C and C-H are 347 and 414 kJ/mol, respectively, the C-C bond is easier broken than C-H bond. The equilibrium flow rates of hydrocarbons in this system are extremely low in compared to methane and hydrogen. Holman et al (ref. 18) agree with this result.

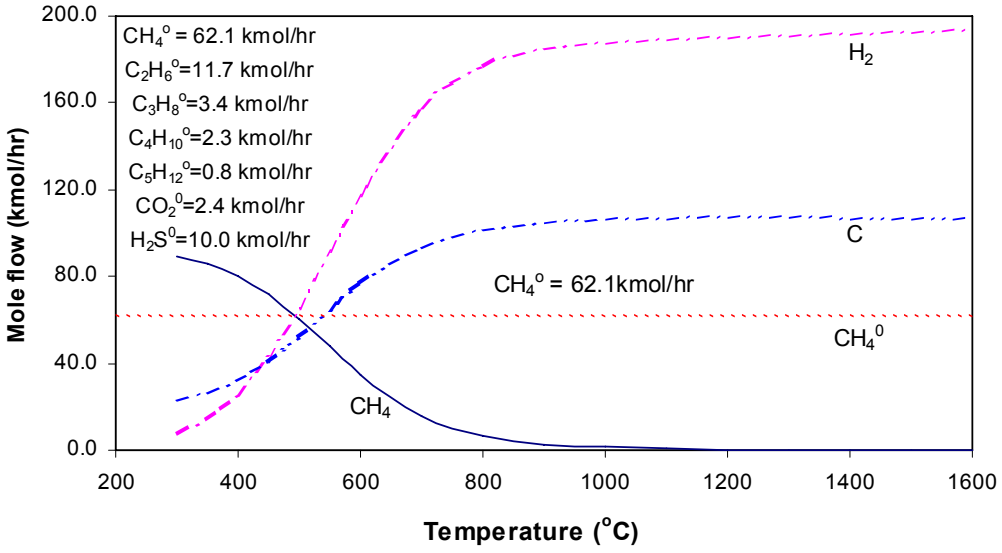

Figure 1.—Temperature dependence of equilibrium methane, hydrogen and carbon mole flow rates (O_2 = 0 kmol/hr).

2. Equilibrium flow rates of carbon dioxide, carbon monoxide and water. The removal of carbon dioxide from natural gas is one of the important steps in improving natural gas quality. The initial carbon dioxide level in this case is 2.4 percent, corresponding to the 2.4 kmol/hr inlet flow rate. Water flow rate is assumed to be 0.1 kmol/hr while carbon monoxide is zero in the inlet stream. Figure 2 shows the carbon dioxide flow rate to be lower than 0.1 kmol/hr in the given temperature range. At a low temperature range (300 to 500 ºC), the flow rate of carbon monoxide is at a very low level, while the water flow rate doubles compared to the initial carbon dioxide flow rate. This result indicates that carbon dioxide is converted to water according to the Reaction (24) while a water gas shift reaction is unlikely to occur. Reaction (25):

$$CO_2 + 4H_4 = CH_4 + 2H_2O \qquad \Delta H_{298K} = -165.2 \text{ kJ/mol} \qquad (24)$$

$$CO_2 + H_2 = CO + H_2O \qquad \Delta H_{298K} = 41.2 \text{ kJ/mol} \qquad (25)$$

As a result, the abrupt increase in the methane flow rate shown in Figure 1 is partially due to the Reaction (24). As the temperature increases, steam methane reforming occurs, to produce carbon monoxide and hydrogen according to the following:

$$CH_4 + H_2O = CO + 3H_2 \qquad \Delta H_{298K} = 206 \text{ kJ/mol} \qquad (26)$$

The overall reaction of Reactions (24) and (26) can be written as:

$$CO_2 + CH_4 = 2CO + 2H_2 \qquad \Delta H_{298K} = 247 \text{ kJ/mol} \qquad (27)$$

Reaction (27) may indicate that the carbon dioxide concentration in natural gas may not be too critically important for the pipeline gas specifications since it can be reformed to produce carbon monoxide and hydrogen. The higher heat requirement for Reaction (27) can be compensated by the oxidation of carbon monoxide and hydrogen.

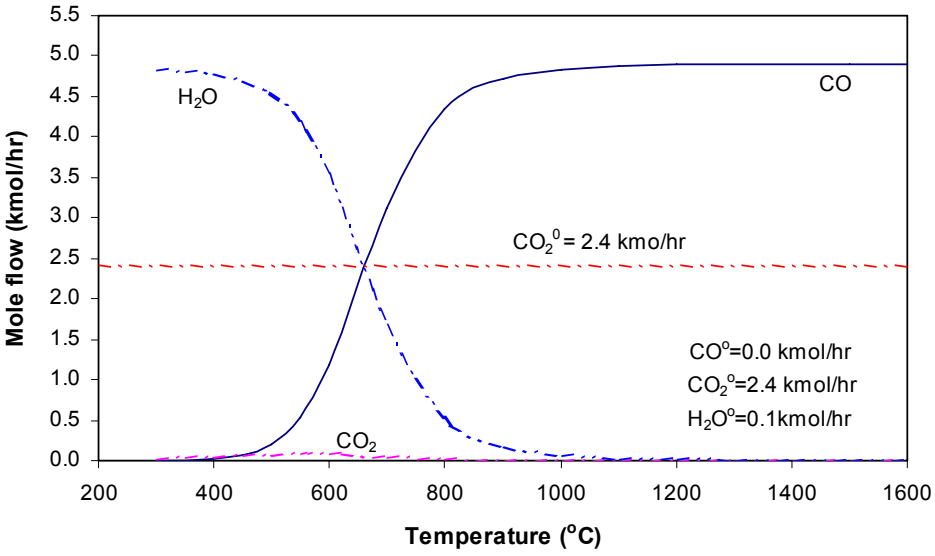

Figure 2.—Temperature dependence of equilibrium water, carbon dioxide and carbon monoxide mole flow rates (O_2 = 0 kmol/hr).

3. Equilibrium flow rates of hydrogen sulfide, carbon disulfide and sulfur dimer. It is understandable that the behavior of hydrogen sulfide during pyrolysis of hydrocarbons in SQNG is a major concern above all other issues. If hydrogen sulfide is decomposed into hydrogen and elemental sulfur, the pyrolysis is considered practically useless since sulfur deposition will deactivate the catalysts of methane decomposition. To evaluate hydrogen sulfide decomposition, the best way is to examine its stability during the pyrolytic process. The equilibrium flow rates of hydrogen sulfide, carbon disulfide and sulfur dimer are shown in Figure 3. The initial mole fraction of hydrogen sulfide is 10.0 percent corresponding to 10.0 kmol/hr inlet to a Gibbs reactor.

Two primary reactions for hydrogen sulfide involved in the SQNG pyrolysis are hydrogen sulfide decomposition (Reaction (18)) and methane hydrogen sulfide reforming (Reaction (20)). The products of these two reactions are hydrogen sulfide, sulfur dimer and carbon disulfide. Figure 3 demonstrates equilibrium flow rates of hydrogen sulfide, carbon disulfide and sulfur dimer. The results indicate that hydrogen sulfide is very stable below a temperature of 1000 ºC. Since the normal methane pyrolysis temperature is in 700 to 900 ◦C range, the stability of hydrogen sulfide in this temperature range suggests that it can be treated as an inert gas which does not affect the course of methane pyrolysis. At a temperature greater than 1000 ◦C methane reacts slightly with hydrogen to produce low flow rates of carbon disulfide. However, hydrogen sulfide decomposition occurs at a higher temperature because the equilibrium flow rate of sulfur dimer is much less than that of carbon disulfide. In fact, during the course of SQNG pyrolysis, the sulfur dimer flow rate is at a very low level. For example, the sulfur dimer flow rate is 0.00324 kmol/hr (lower than 0.3 ppm mole fraction in the outlet stream) below a temperature of 1000 ◦C.

To illustrate the stability of pure hydrogen sulfide, equilibrium calculations were conducted for hydrogen sulfide at various pressures. The results are shown in figures 4 and 5. It is clearly indicated that pure hydrogen sulfide is much easier to decompose than that in SQNG. The conversions of pure hydrogen sulfide at temperature 1000 ◦C are 20 percent for pressure of 1 atm and 35 percent for 0.1 atm, respectively. The hydrogen sulfide partial pressure in SQNG is 0.1 atm but the conversion is close to zero at the same temperature (fig. (3)). The result suggests that the stability of hydrogen sulfide in SQNG is greatly enhanced by the presence of hydrogen produced from hydrocarbon pyrolysis. This result is critically important to the utilization of SQNG to produce hydrogen since hydrogen sulfide can be treated as an inert gas during the pyrolytic process. Therefore no hydrogen sulfide separation process is required for the SQNG because stabilized hydrogen sulfide can be used to reform methane to further produce hydrogen and carbon disulfide.

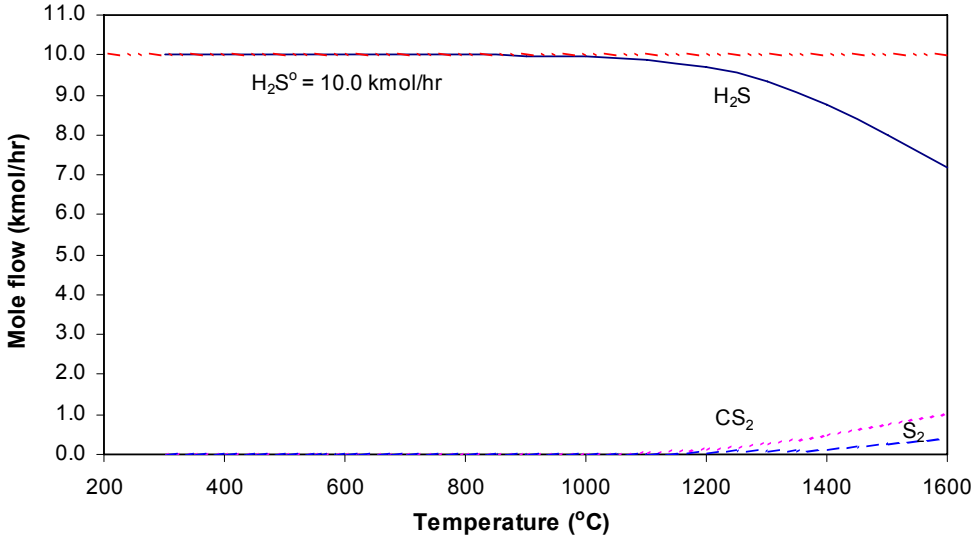

Figure 3.—Temperature dependence of equilibrium hydrogen sulfide, carbon disulfide, and sulfur dimer mole flow rates (O_2 = 0 kmol/hr).

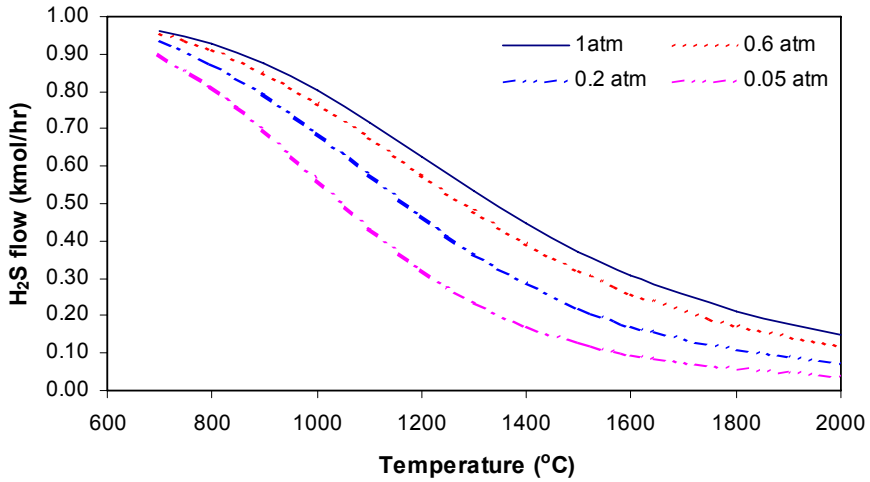

Figure 4.—Temperature dependence of equilibrium hydrogen sulfide mole flow rates (1 kmol/hr of initial inlet hydrogen sulfide).

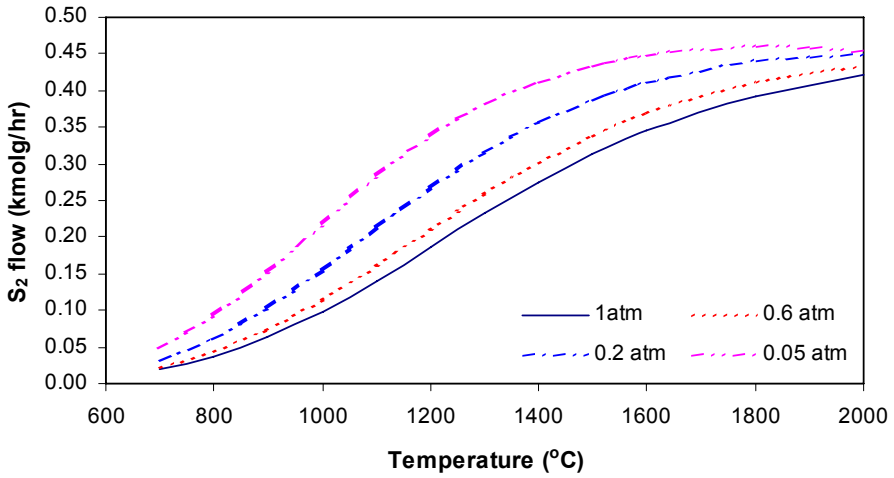

Figure 5.—Temperature dependence of equilibrium sulfur dimer mole flow rates (1 kmol/hr of initial inlet hydrogen sulfide).

Autothermal Decomposition of SQNG

Pyrolysis is a highly endothermic process requiring a large amount of heat input. The autothermal process uses partial methane oxidation to provide heat energy for the decomposition of the rest of the methane. In the presence of hydrogen sulfide, oxygen may react with it to produce environmentally harmful gases such as sulfur dioxide. Therefore the key issue of the thermodynamic analyses for SQNG autothermal processes is to determine if sulfur dioxide is produced in the methane pyrolysis temperature range. In addition to this objective, the other aims of the analyses are to determine the equilibrium flow rates of output hydrogen, carbon and carbon dioxide. The oxygen source can be either pure oxygen or air. In this paper we use air as the oxygen source mixed with SQNG inlet into the Gibbs reactor and we calculate equilibrium flow rates in the outlet stream. Inlet airflow rates to the Gibbs reactor are 0, 10, 20, 30, 40 and 80 kmol/hr, respectively, corresponding to oxygen flow rates of 0, 2.1, 4.2, 6.3, 8.4 and 16.8 kmol/hr.

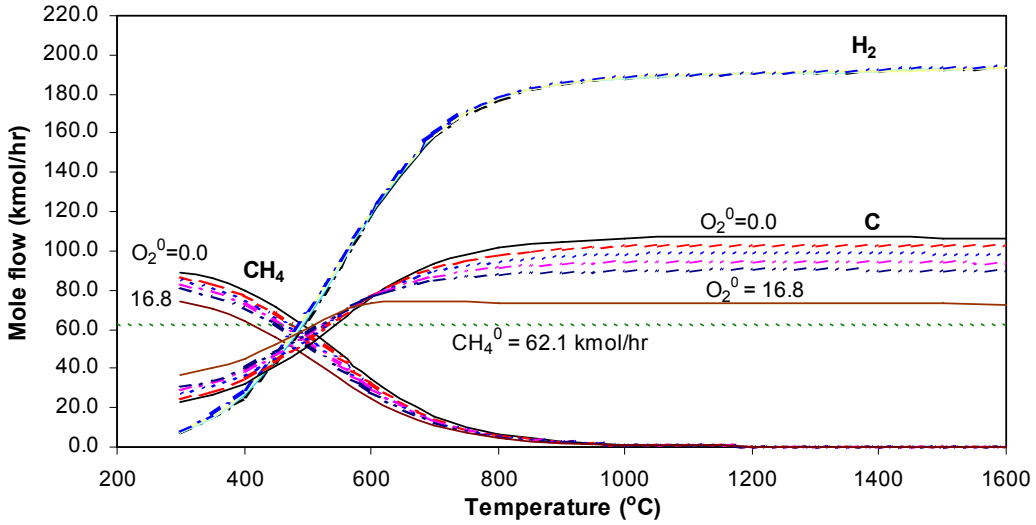

Figure 6.—Temperature dependence of equilibrium mole flow rates of methane, hydrogen sulfide and carbon in an autothermal process (O_2 = 0.0, 2.1, 4.2, 6.3, 8.4, and 16.8 kmol/hr).

1. Equilibrium flow rates of methane, carbon and hydrogen during autothermal process. Figure 6 depicts equilibrium flow rates of hydrogen, carbon and methane at various inlet oxygen levels. Firstly, similar to the pyrolysis of SQNG, all other hydrocarbons are decomposed into hydrogen, methane and carbon within a temperature range of 300 to 500 ◦C. The methane flow rates decreases with increases of either temperature or oxygen flow rate. Interestingly, equilibrium hydrogen output flow rates are independent of oxygen input within the range of 0 to 16.8 kmol/hr. In fact, three factors play an important role in hydrogen production: methane decomposition, steam methane reforming and water gas shift reaction. It is true that the portion of hydrogen production via methane decomposition is reduced coincident with the inlet of oxygen. However, once the methane has been oxidized, any water produced can react with carbon to produce hydrogen. Therefore, the total hydrogen produced does not decrease as the inlet oxygen flow rate increases. In comparison, carbon output can be separated into two temperature ranges: (1), 300 to 600 ◦C and 600 to 1600 ◦C. Within the first range, equilibrium carbon output increases with the increase of the oxygen flow rate, suggesting that oxygen promotes the hydrocarbon decomposition process. At the second temperature range, carbon can be partially oxidized into carbon oxides resulting in the decrease of carbon output. The total mass balance consideration has to include both carbon and oxygen. The latter is depicted in figure 6.

2. Equilibrium flow rates of carbon dioxide, carbon monoxide and water distribution during autothermal process. Figure 6 demonstrates the equilibrium flow rates of carbon dioxide, carbon monoxide water during SQNG autothermal processes. At the low temperature range (300 to 600 ◦C) the water output flow rate increases with the increase of the inlet oxygen flow rate, however, at the higher temperature range (600 to 1600 ◦C), the direct result of increasing the oxygen inlet flow rate is an increase in the carbon monoxide output flow rate. Carbon monoxide produced has to be shifted to produce hydrogen and an equal molar amount of carbon dioxide. Therefore, an increase of the oxygen inlet flow rate means an increase of carbon dioxide output. So the cost of the autothermal process is the increased greenhouse effect. Figure 7 also suggests that carbon dioxide in this process forms an intermediate link with water and carbon monoxide through Reactions 24 and 25.

3. Equilibrium mole flow rates of hydrogen sulfide, sulfur disulfide and sulfur dimer during autothermal process. Equilibrium outputs of hydrogen sulfide, carbon disulfide and sulfur dimer at various oxygen inlet flow rates are depicted in figure 8. As in pure thermal decomposition of SQNG, oxygen inlet does not have significant effect on the stability of hydrogen sulfide. Because a temperature range of 700 to 1000 ◦C is most suitable for methane thermal decomposition, the hydrogen sulfide stability data are of critical concern within this temperature range. Equilibrium data for sulfur species, such

as hydrogen sulfide, carbon disulfide, carbonyl sulfide and sulfur dimer are listed in table 5. The total gaseous flow rates are calculated as total outlet gas flow rates, including nitrogen from the air when air is input as an oxygen source.

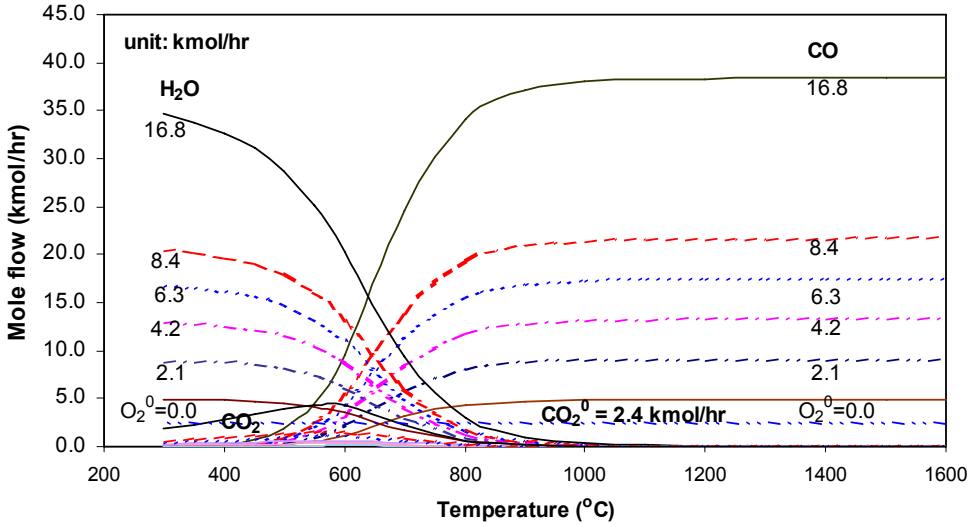

Figure 7.—Temperature dependence of equilibrium mole flow rates of carbon dioxide, carbon monoxide and water in autothermal process (O_2 = 0.0, 2.1, 4.2, 6.3, 8.4, 6.8 kmol/hr).

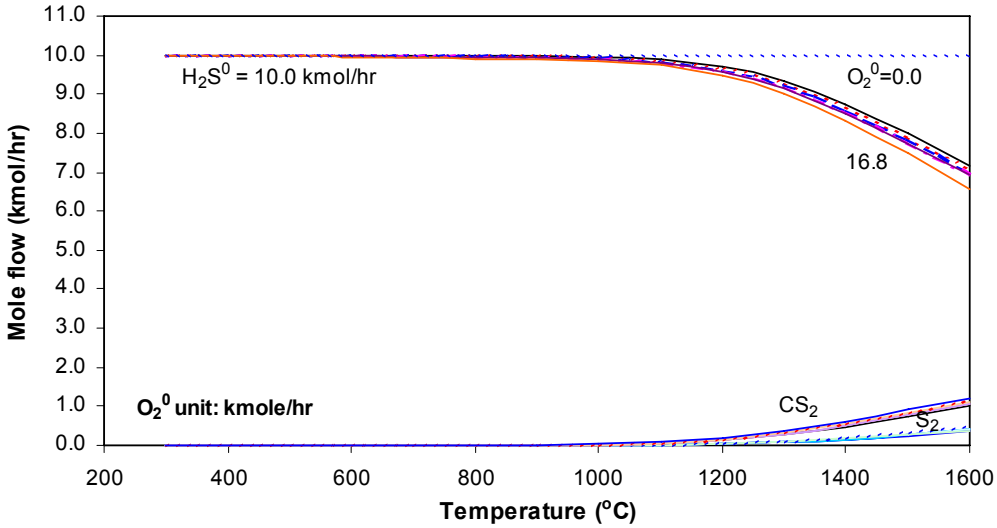

Figure 8.—Gibbs reactor calculation for hydrogen sulfide, carbon disulfide and sulfur dimer distribution in autothermal process (O_2 = 0.0, 2.1, 4.2, 6.3, 8.4, and 16.8 kmol/hr).

TABLE 5.—SULFUR SPECIES CONCENTRATIONS IN TEMPERATURES FROM 700 TO 1000 °C

O_2 inlet (kmol/hr)	0	2.1	4.2	6.3	8.4	16.8
Temp. (°C)	**Hydrogen sulfide conversion (%)**					
700	0.00	0.18	0.27	0.35	0.43	0.76
800	0.02	0.24	0.34	0.44	0.53	0.93
900	0.11	0.33	0.43	0.54	0.64	1.06
1000	0.40	0.64	0.76	0.87	0.99	1.45
	Total gas phase mole flow rate (kmol/hr)					
700	195.16	206.67	218.17	229.66	241.13	279.70
800	205.46	247.46	229.45	241.44	253.41	294.20
900	209.50	221.62	233.73	245.83	257.93	299.32
1000	211.11	223.24	235.36	247.48	259.59	301.10
	Carbon disulfide (CS_2) mole concentration (ppm)					
700	0.88	0.88	0.87	0.87	0.86	0.85
800	4.83	4.21	4.77	4.74	4.72	4.66
900	21.81	21.66	21.58	21.50	21.42	21.17
1000	79.70	79.23	78.95	78.69	78.43	77.52
	Sulfur dimer (S_2) mole concentration (ppm)					
700	0.11	0.11	0.11	0.11	0.11	0.11
800	0.72	0.63	0.71	0.71	0.71	0.70
900	3.72	3.69	3.68	3.67	3.65	3.61
1000	15.36	15.27	15.21	15.16	15.11	14.94
	Sulfur dioxide (SO_2) mole concentration (ppm)					
700	1.13E-07	6.73E-07	1.29E-06	2.02E-06	2.81E-06	6.51E-06
800	2.09E-07	5.62E-07	8.80E-07	8.37E-07	2.68E-06	6.25E-06
900	1.67E-07	4.83E-07	9.28E-07	8.83E-07	2.03E-06	4.71E-06
1000	1.21E-07	3.72E-07	7.14E-07	6.79E-07	1.38E-06	1.27E-06
	Carbonyl sulfide (COS) mole concentration (ppm)					
700	49.68	87.03	120.35	150.26	177.25	268.88
800	56.01	86.27	135.84	169.67	200.23	304.38
900	55.74	97.73	135.27	169.02	199.52	303.57
1000	54.56	95.69	135.01	165.54	195.42	297.37

As a result of an autothermal process in the 700 to 1000 °C range, hydrogen sulfide conversion is very low, yielding a maximum of 1.45 percent at a temperature of 1000 °C and 16.8 kmol/hr of oxygen. The conversion increases slightly with an increased oxygen inlet flow rate. The converted hydrogen sulfide has four outlets: (1) decomposes into hydrogen and sulfur dimer; (2) reacts with methane to form carbon disulfide; (3) combines with carbon monoxide to produce carbonyl sulfide and (4) oxidizes into sulfur dioxide. Figure 7 indicates that hydrogen sulfide decomposition is a weak function of the inlet oxygen flow rate, indicating that oxygen inlet flow rate does not significantly affect both carbon disulfide and sulfur dimer output flow rates. More detailed data are shown in table 5. Since flow rates of sulfur dioxide are close to zero during the autothermal processes, the effect of oxygen inlet flow rates on the production of sulfur is negligible. Of the four components, carbon disulfide, sulfur dimer, sulfur dioxide and carbonyl sulfide, carbonyl sulfide has the highest concentrations (50 to 300 ppm range). The concentration increases with the increase of the oxygen inlet flow rate. However, it is a weak function of temperature. Carbonyl sulfide is formed according to the following reaction:

$$H_2S + CO = COS + H_2 \quad (28)$$

The boiling temperature of carbonyl sulfide is –58 °C. As a gaseous phase existing in the system, carbonyl sulfide does not affect the activity of the methane pyrolysis catalysts. At the same time, carbonyl sulfide is a useful chemical in organic synthesis to produce fuels.

4. Enthalpy calculation for autothermal process. Heat requirements for the SQNG autothermal process are depicted in figure 9. With increases in the oxygen inlet flow rate the total heat energy requirement decreases significantly. The zero energy requirement points are those whose enthalpy curve intersects with the temperature axis. Figure 10 reveals a linear relationship between the zero heat input temperature and the oxygen flow rates:

$$T_{\Delta H = 0} = 12.05 * O_2 \text{ flow rate} + 440\ (^{\circ}C) \quad (29)$$

As discussed above, autothermal processes require reduced or zero energy input for the pyrolysis of SQNG. However, the input of oxygen produces a higher concentration of carbon dioxide. This is a major disadvantage of the process. In order that the process can be operated in an optimal condition, the oxygen inlet flow rate should be established based on several parameters: minimum energy input, minimum carbon dioxide output and maximum hydrogen output. To determine the proper oxygen inlet flow rate a systemic analysis is required based on an entire flow sheet development. This will be discussed in Part II of this paper.

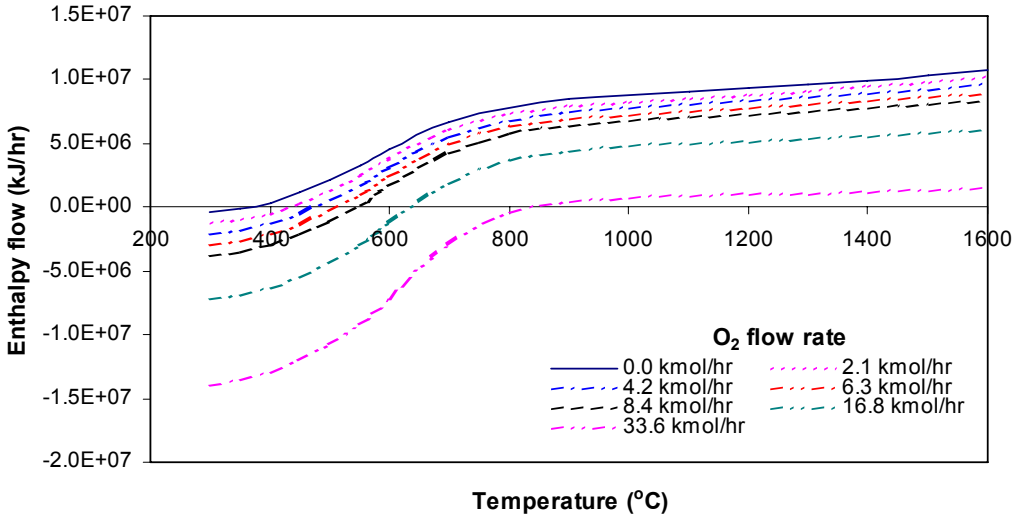

Figure 9.—Heat requirements of SQNG autothermal process at different oxygen levels (O_2 = 0.0, 2.1, 4.2, 6.3, 8.4, 16.8 and 33.6 kmol/hr).

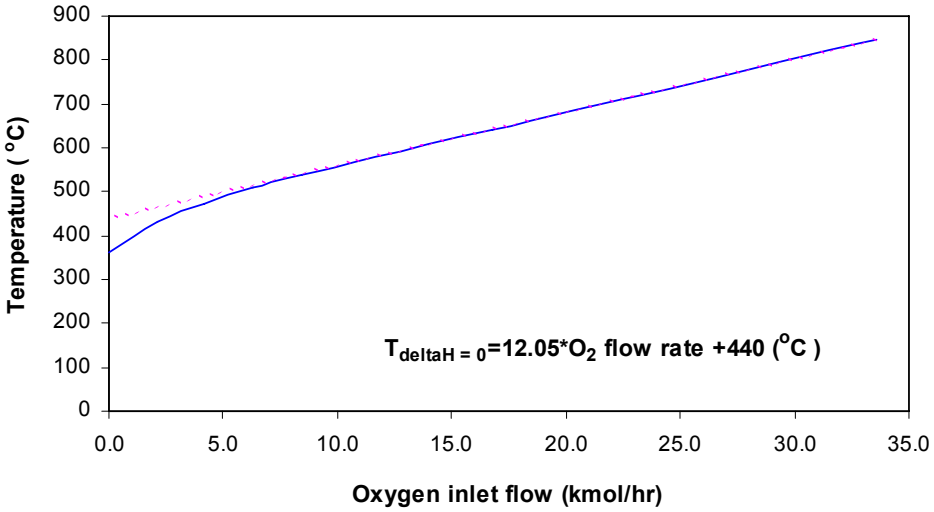

Figure 10.—Zero Heating input temperature versus oxygen input flow rate.

Conclusions

SQNG is an important hydrogen source. Due to the interference between the decomposition of hydrogen sulfide and methane, current technologies cannot be applied economically either for the production of hydrogen or for pipeline natural gas production from SQNG. The thermodynamic analyses reported in this paper reveal for the first time that, within the methane pyrolysis temperature range of 700 to 1000 ◦C, hydrogen sulfide in SQNG is highly stabilized due to the presence of hydrogen. Therefore, hydrogen sulfide can be treated as an inert gas during the pyrolysis of methane at temperatures lower than 1000 ◦C. The only detectable product resulting from the hydrogen sulfide conversion is carbonyl sulfide, which is in ppm range. The thermodynamic analyses reveal a possibility of treating SQNG in two steps: hydrocarbon pyrolysis and hydrogen sulfide methane reformation with prior hydrogen sulfide separation needed. An autothermal process can also be used for hydrogen production through SQNG with a reduced heat energy requirement. The zero input energy requirements are a linear function of the input oxygen flow rate.

References

1. Hugman, R.H., Vidas, E.H., Springer, P.S., “chemical composition of Discovered and Undiscovered Natural Gas in the United States – 1993 Update.” GRI-93/0456.
2. Lokhandwala, K.A., Baker, R.W., Toy, L.G. and Amo, K.D., “Sour Gas Treatment Process including Dehydration of the Gas Stream” United States Patent 5,401,300, 1995.
3. Lane, J.M., Spath, P.L., “Technoeconomic Analysis of the Thermocatalytic Decomposition of Natural Gas” 2001, NREL/TP-510-31351.
4. Zaman, J. and Chakma, A., “Production of hydrogen and sulfur from hydrogen sulfide” *Fuel Processing Technology*, 41, 159-198, 1995.
5. HYSYS 3.0 Tutorials and Applications manual, pG1-3-G1-34, 2001.
6. Linkous, C.A., Huang, C. and Fowler, R.J., “Photochemical oxidation of sodium sulfide aqueous solution to produce hydrogen and sulfur,” (accepted), *Photochemistry and photobiochemistry* 2003.
7. Huang, C. and Linkous, C.A., “Photochemical oxidation of sulfur dioxide to produce hydrogen and sulfate” U.S. Patent (Pending, 2002).
8. Mizuta, S., Kondo, W., Fujii, K., Iida, H., Isahiki, S., Noguchi, A., Kikuchi, t., Sue, H. and Sakai, K., Ind. Eng. Chem. Res., 30: 1601 1991.
9. Lim, H.S. and Winnick, J., J. Electrochem. Soc. 131:562, 1984.
10. Weaver, D. and Winnick, J., J. Electrochem. Soc. 134:2451, 1987.
11. Winnick, J., Sci. Techno., 25:2057, 1990.
12. T-Raissi, A., ”Technoeconomic Analysis of Area II Hydrogen Production, Part I,” Proceedings of the U.S. DOE Hydrogen Program Annual Review, Baltimore, MD, April 18, 2001, URL: http://www.eere.energy.gov/hydrogenandfuelcells/pdfs/30535bq.pdf.
13. Huang, C. and Raissi, A.T., “Liquid Hydrogen Production via Hydrogen Sulfide Methane Reformation: Part I. One-Step Process” NASA Hydrogen Project Report (2003).
14. Kim, J. and Deo, M. D., “Technical economic assessment of Potential to Upgrade Gob Gas to Pipeline Quality” A report to EPA Coalbed Methane Outreach Program Atmospheric Pollution Prevention Division U.S. Environmental Protection Agency, 430-R-97-012, Dec. 1997.
15. NASA report. (Liquid hydrogen price).
16. Lane, J.M. and Spath, P.L., “Technoeconomic Analysis of Thermocatalytic Decomposition of Natural Gas” NREL/TP-510-31351, p12, December, 2001.
17. Chem, Market Reporter. 2000, “chemical Prices.” Schnell Publishing company, 258(25):22-41.
18. Holmen, A., Olsvik, O. and Rokstad, O.A., “Pyrolysis of natural gas: Chemistry and process concepts” *Fuel Processing Technology*, 42, 249-267, (1995).

Publications

1. Huang, C**.** and Raissi A., “Analysis of Sulfur-Iodine Thermochemical Cycle for Solar Hydrogen Production-Part I: Decomposition of Sulfuric Acid,” Journal of Solar Energy (in press) (2004).

2. Huang, C. and Raissi A., Analysis of Liquid Hydrogen Production from Methane and Landfill Gas, Proceedings of the 15th WHEC, Japan (2004).
3. Huang, C. and Raissi A., A New Solar Thermochemical Water-Splitting Cycle for Hydrogen Production, Proceedings of the 15th WHEC, Japan (2004).
4. Muradov, N., Huang, C., Raissi, A., and Smith, F., Hydrogen Production from Natural Gas with Reduced CO_2 Emissions, Proceedings of the 15th WHEC, Japan (2004).
5. Linkous, C.A., Huang, C. and Fowler, R., "UV photochemical Oxidation of Aqueous Sodium Sulfide to Produce Hydrogen and Sulfur". Journal of Photochemistry and PhotoBiology A: Chemistry (in press) (2004).
6. Huang, C. and Raissi, A., "Liquid Hydrogen Production via Hydrogen Sulfide methane Reformation" Preprint of the 228th ACS National Meeting, Philadelphia, PA, August 22-26,2004
7. Huang, C. and Ali T-Raissi, "Evaluation of Kinetic Models for the Solar Decomposition of Sulfur Trioxide," (Abstract accepted), International Solar Energy Conference and *Journal of Solar Engineering*, Orlando USA, (2005)
8. Ali T-Raissi, Nazim Muradov, Huang, C., "Solar Hydrogen via High-Temperature Water-Splitting Cycle with Quantum Boost," (Abstract accepted), International Solar Energy Conference and *Journal of Solar Engineering*, Orlando USA, (2005).

Patent and Award

1. Huang, C., and Ali T-Raissi, Nazim Muradov, "Zero emission liquid hydrogen production via methane and landfill gas" (pending, application no. 60/578212), (2004).
2. Huang, C., and Ali T-Raissi, "Innovative Technology Award," 15th International Hydrogen Energy Conference, Yokohama Japan (June 27 to July 2, 2004).

Hydrogen Production via Photocatalysis

PI: C. Linkous (Florida Solar Energy Center)
C. Bateman (Brevard Community College)
Q. Chen (University of Central Florida)
S. Seal (University of Central Florida)

Executive Summary

Hydrogen for rocket launches is derived mainly from natural gas. Dwindling natural gas supplies and unstable markets make for great uncertainty in its price and availability long-term. Consequently, it would behoove NASA to look at other means of producing fuel hydrogen than the current approach of converting natural gas. Establishing a nearby locale for H_2 production would also minimize transport and safety issues. In particular, they should consider the use of solar energy and water, both of which are renewable, locally available resources.

Another advantage of deriving H_2 from water is that O_2 is produced as the anodic by-product of the reaction. While O_2 production does not always provide economic value to industrial electrolytic processes, it would certainly have value to the space launch business that utilizes high purity liquid O_2 as on-board oxidant.

Photoelectrochemistry involves incorporating the semiconductor materials used in photovoltaic cells into an aqueous environment, where the same electrical charge carriers generated via light absorption perform reductive and oxidative reactions on water to generate H_2. This research investigated a dye-sensitization scheme for photoanode fabrication, where organic pigments specifically designed for oxidative or reductive water-splitting are deposited on wide band gap semiconductors, such as TiO_2. Photocatalytic systems, where the semiconductor electrodes chosen for H_2 or O_2 evolution are deposited as immobilized powders in separate planar modules, or beds, were also examined. This was a collaborative effort, where Dr. Sudipta Seal of AMPAC/UCF worked on the TiO_2 substrate, Dr. Linkous of FSEC/H_2 R&D modified the surface with dye sensitizers, Dr. Bateman of Brevard Community College Lab School Cocoa Beach, working at the FSEC laboratory, studied host-guest complexes as redox mediators, and Dr. Chen of MMAE/UCF used a nanotechnological approach for depositing discrete co-catalyst structures.

Objective and Rationale

Most merchant H_2 produced today is derived from steam reforming of natural gas. As one of the "fossil fuels," natural gas is a nonrenewable resource. What little resources of natural gas that were once possessed by Florida were for the most part depleted in the 1980's. As reserves nationwide and worldwide are depleted, the cost of natural gas is certain to rise. As a long-term H_2-consuming facility, it would behoove NASA to look beyond natural gas and identify other sources of H_2 that could be derived using renewable energy.

Optimally, the hydrogen should be produced locally. Establishing a nearby locale for H_2 production would minimize transport and safety issues. In particular, one may consider the use of solar energy and water, both of which are renewable, locally available resources.

Another advantage of deriving H_2 from water is that O_2 is produced as the anodic by-product of the reaction. While O_2 production does not always provide economic value to industrial electrolytic processes, it would certainly have value to the space launch business that utilizes high purity liquid O_2 as on-board oxidant.

The objective of this project is to develop a solar photocatalytic method for generating H_2 from water. This would constitute an on-site approach to H_2 fuel supply involving renewable energy resources that integrates photolytic advances in semiconductor physics, biochemistry, and electrochemistry.

Background/State-of-the-Art

For applications involving high purity and small gas volumes, the electrolysis of water is already the technology of choice for the production of H_2. While the energy cost per unit of H_2 is significantly higher than fossil fuels, it is possible to derive that energy from renewable sources and become independent of the fossil fuel economy.

The most obvious approach is to couple an electrical generator that is powered by renewable energy to a conventional electrolyzer. The renewable energy could come from any number of sources: hydroelectric, windpower, ocean thermal, geothermal, tidal motion, and finally, solar photovoltaics. A more direct approach than photovoltaic electrolysis would be photoelectrochemistry, where the semiconductor materials used in photovoltaic cells are incorporated as electrodes into an aqueous electrolytic environment. In this technology, the same electrical charge carriers generated via light absorption perform electrochemical oxidative and reductive reactions on water to generate O_2 and H_2, respectively. Solar-to-hydrogen conversion efficiencies have exceeded 10 percent.

Yet another refinement is to reduce the electrode size to the microscopic particle dimension. In this configuration, surface area is maximized and charge carrier path length is minimized. This approach, known as photocatalysis, has been demonstrated and studied at great length at the Florida Solar Energy Center. While module production costs are quite modest, on order of $\$50/m^2$, efficiencies need to be greatly improved to make a practical system.

A major problem in photoelectrochemistry has been the mismatch between the solar spectrum and the absorption spectrum of the photoelectrode, which mainly has been TiO_2. One approach to deal with that problem is the use of organic dyes and pigments to “sensitize” the electrode to sunlight. Through a combination of molecular orbital calculations, ionization potentials, and voltammetry, we have identified a number of organic pigments that demonstrate activity toward O_2 and H_2 evolution, such as indanthrone and perylene diimides for O_2 evolution, and quinacridone and phthalocyanines for H_2.

Several materials aspects of the photoelectrochemical dye sensitization process can be identified. The key research issues are how to: 1) match the absorption spectrum of the pigments to that of the solar spectrum; 2) maximize the quantum efficiency for charge transfer from chromophore to semiconductor support; 3) dovetail the excited state energy levels to provide a continuum within which charge carriers would have high mobility; 4) design a large scale reactor that would have minimal losses due to solution resistance, optical transmission, and parasitic electricity usage (pumps, compressors, etc.); and 5) incorporate materials that can withstand the corrosive forces inherent in solar illumination and electrolytic environments.

To deal with the first of the research issues above, FSEC has investigated a dual bed approach, where semiconductors designed specifically for H_2 or O_2 evolution are immobilized in separate planar modules, or beds, where sunlight can penetrate and effect water-splitting reactions. By segregating the gas evolution reactions from each other, the energetic requirement for water decomposition is shared between the two modules, and therefore lower energy, more abundant solar photons may be utilized. Finally, safety issues involving co-evolution of H_2 and O_2 are obviated. A schematic showing how the dual bed system would work is shown in figure 1.

A redox mediator, M, must be added to the working fluid in order to transfer charge equivalents from one chamber to the other. After testing numerous redox couples, we determined that the I^-/IO_3^- couple exhibited an optimum of solubility, optical transparency, redox energy, and charge transfer reversibility. However, one reason that efficiencies remain low is the propensity for back reaction by such electrochemically reversible redox couples. In other words, the IO_3^- produced by the light-driven oxidation of I^- frequently traps free electrons that were meant for H_2 evolution. A way of protecting against back reaction across the semiconductor/electrolyte interface must be devised.

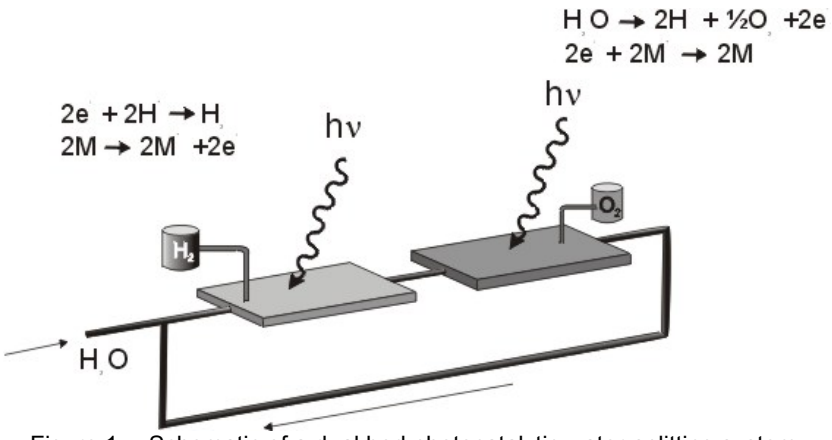

Figure 1.—Schematic of a dual bed photocatalytic water-splitting system.

Technical Approach

The microscopic arrangement of photocatalyst, co-catalyst, and dye sensitizer is critical in optimizing the efficiency of the system. This aspect of dual bed design was emphasized in Year II.

The following tasks were proposed.

3. Dye sensitization of H_2 and O_2 evolution reactions: Some materials are effective in transporting injected charge; others are good absorbers of visible wavelength light. Through dye sensitization, materials proficient in one attribute can be brought together with those of another to achieve effective light-to-charge carrier transduction. Representative dyes under consideration are shown below in figure 2.
4. Photocatalyst immobilization technology: In order to keep the respective H_2- and O_2-producing photocatalysts separate from each other, they must be affixed or otherwise immobilized in their respective containers. This must be done economically without substantially reducing the photoactivity of the photocatalyst. Various techniques involving polymer binding including solvent casting and hot pressing will be investigated.
5. Optimization of charge transfer kinetics: One negative aspect of photocatalysis is that the intrinsic segregation of reaction products in macroscopic electrochemical systems is lost. For a thermodynamically uphill reaction such as photocatalytic H_2 production, there exists the possibility of product consumption inside the reactor due to back reaction, i.e., the reaction between H_2 and the oxidized form of the redox mediator, either catalyzed on the photoparticle surface or homogeneously in the working fluid. To deal with this issue, we will investigate redox state-dependent conformers, whose forward and reverse rate constants for charge transfer vary considerably because of differences in the steady state molecular conformation. Cyclodextrins, iron porphyrin complexes, and other host-guest materials will be investigated.
6. Large module scale-up design analysis: In the simplest conceptualization, the modules would consist of large, thin, planar modules, arrayed in series to its complementary reactor, each with a single gas outlet, and single ports for fluid circulation. By modeling the photocatalytic reaction and working fluid dynamics, the effect of varying module size and associated plumbing will be investigated.

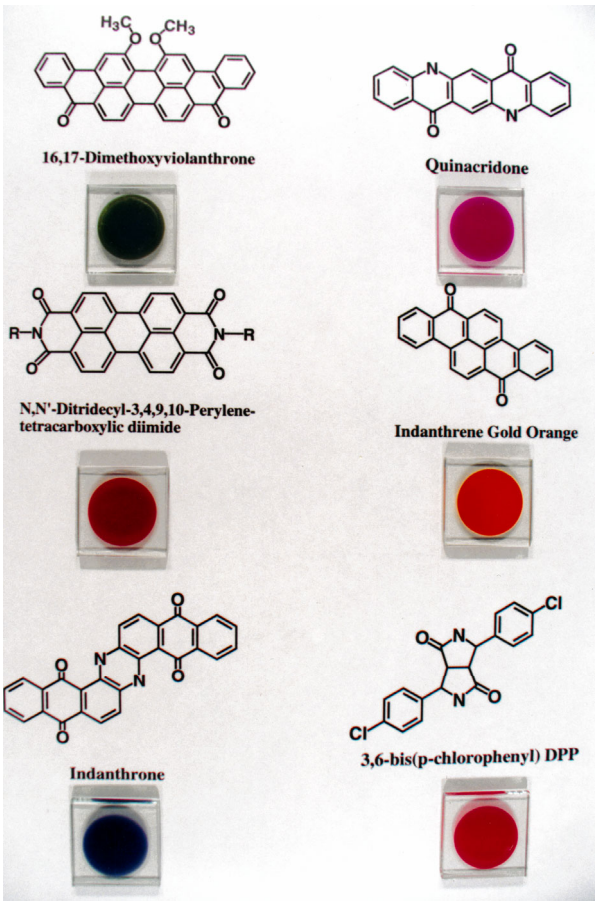

Figure 2.—Representative dye-sensitizing substances.

Results/Status

In Year I, we were mainly engaged in the first two tasks: 1) Dye sensitization of H_2 and O_2 evolution reactions; and 2) Photocatalyst immobilization technology. In this project period we also concentrated on 3) Charge transfer efficiency. Specific tasks included:

1. MEMS-derived microcatalyst arrays.
2. Thin film TiO_2 electrodes fabricated for dye sensitization experiments
3. Photoactive organic pigment films deposited via solution deposition and vacuum evaporation.
4. Protected charge transfer onto redox mediators.
5. Surface-bound host-guest complexes as charge transfer agents

The task distribution among the collaborators was as follows:

6. Quangfang Chen (UCF-MMAE): microarray distribution of co-catalyst deposits.
7. Sudipta Seal (UCF-AMPAC): sol-gel deposition of TiO_2 semiconductor films.
8. Colin Bateman (BCC-Cocoa): host-guest complex formation and characterization.
9. Clovis Linkous (UCF-FSEC): dye-sensitized photocatalytic cell assembly and testing.

The dye sensitizers are all highly stable, fused heteroaromatic compounds, possessing high extinction coefficients in some portion of the visible spectrum. They were adsorbed on the surface of TiO_2 powder and tested for either H_2 or O_2 evolution. For some samples, a Pt co-catalyst was first attached to the titania to make a 3-component system.

We also looked at photocatalyst immobilization technology. While certain characterization experiments can be performed with a powder suspension, ultimately the photocatalysts must be immobilized in separate containers for their respective gas evolution reactions. Our best results have been obtained by preparing a coatings formulation based on poly(methylmethacrylate). The photocatalyst is blended into a 10 wt % solution of the polymer in a chlorinated hydrocarbon, usually 1,2-dichloroethane. The suspension can then be painted on any of a number of substrates.

The important issue with immobilization technology is the trade-off between photocatalytic activity and mechanical stability of the coating. This is controlled by the binder: photocatalyst ratio. Results showed that a 30 percent binder content represents the best compromise for these two properties.

Quantum Dot/Nano Wire Promoted Dye-sensitized Photoelectrochemical Reaction for Hydrogen Production: While effective charge transfer between sensitizer and electrode is an important issue, it is also important to have good kinetics between the pigment and the respective gas evolution reactions. Development of co-catalysts that can facilitate the water-splitting reaction is necessary. Noble metals are needed for acidic media, while a number of transition metals (Ni, Fe) can be used in alkaline media. In the case of photocatalytic cells, the redox mediator must be able to act as a facile electron donor in the H_2-evolving module, while function as an electron acceptor in the O_2-evolving module. Quantum dots and nanowires are ideal for greatly increasing the hydrogen production rate due to: 1) a greater number of reaction cells formed per unit area; 2) quicker charge transfer since the connection between reaction cells is much shorter; and 3) quantum effects will enhance the reaction and charge transfer.

Deposition of Catalyst Microstructures on Organic Sensitizer Layers: The fabrication of metallic quantum dots and nano wires was to be accomplished by a nanofabrication process depicted in figure 3. There are basically two routes in terms of nanofabrication: 1) an etching route and 2) a molding route. In an etching route, a metallic film is deposited by physical vapor deposition on a pigment layer pre-made on a substrate (fig. 3(a)). An etching mask layer will be deposited subsequently and patterned by nano patterning technique such as electron beam writer. A chemical etchant which selectively etches only the metallic layer will be introduced to etch the exposed portion of the metallic layer. Metallic quantum dots or nano wires will be received after stripping off the etching mask.

On the other hand, in a nano molding process, a predefined nano patterned mold is required (fig. 3(b)). A layer of molding material is coated on the pigment layer first and patterned subsequently by an electron beam writer or a chemical reaction process. Metallic quantum dots and nano wires are fabricated by filling the nano molds with the desired metallic materials such as Ni and Pt. The metallic deposition of filling will be accomplished by two approaches 1) electroless deposition 2) physical vapor deposition (PVD). The electroless deposition of metallic material will start with pretreatment using an appropriate sensitizer, such as $SnCl_2$/ethanol solution. Then an activation process will be conducted. The activated nano molds will then be immersed into electroless plating solution consisting of metallic ions (Ni, Pt, Co, etc) and a reducing agent, such as NaH_2PO_2, and used to obtain the metallic deposition on pigments through the nano molds. After the metallic deposition, the nano molds will be removed with appropriate solutions. The typical physical vapor deposition will start from the above-mentioned nano molds. The pigment covered with nano molds will be placed into a physical vapor deposition chamber such as a thermal evaporation and/or sputtering chamber. The metallic material will be deposited on the pigment through the nano molds. At the end step of the fabrication, nano molds will be removed to achieve the desired pattern and arrangement of quantum dots and nano wires. The pigments of interest are inert to most chemicals, thus both the etching route and the molding route are practical.

Figure 4 shows preliminary results of fabricated nano molds. Periodically arranged nano molds with uniform size of 50 nm in diameter have been fabricated.

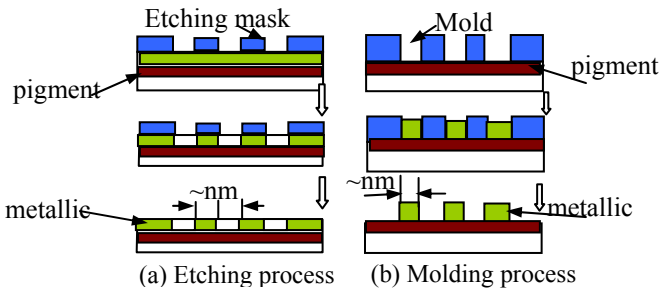

Figure 3.—Sketches of quantum dot/nanowire fabrication processes. (a) etching route; (b) molding route.

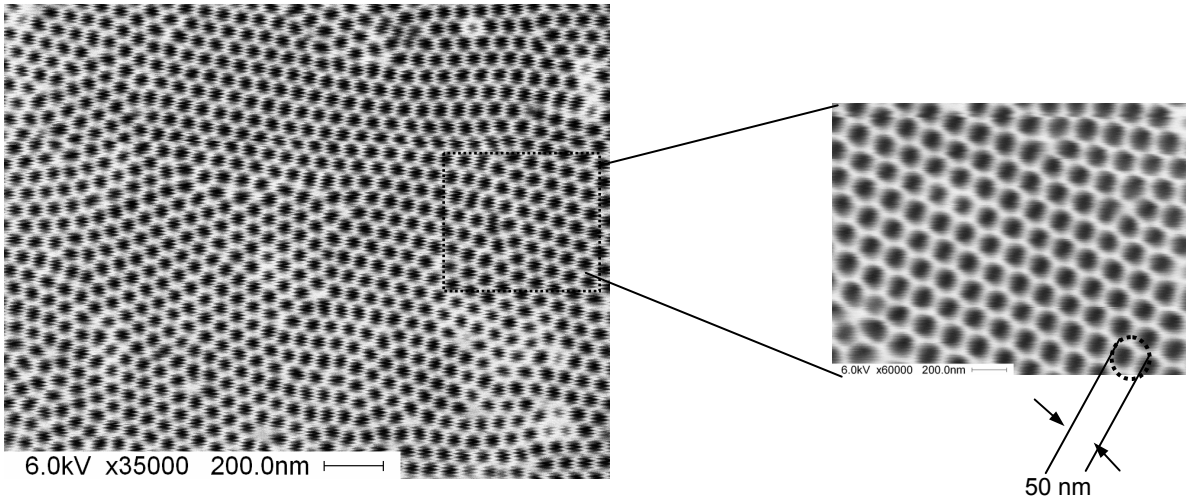

Figure 4.—SEM pictures of fabricated nanomolds of quantum dots (QDs) with predefined size and arrangement. The size of QDs fabricated is about 50 nm in diameter.

Preparation of Large-Scale, Highly Efficient TiO_2 Support Layers

A polymeric sol gel route was used to prepare TiO_2 sol. Titanium isopropoxide was chosen as a precursor. Isopropanol was used as solvent. The concentration of titanium isopropoxide was 0.2 mol/L in this study. To slow the hydrolyzation of the alkoxide, a complexing agent, acetylacetone, was added as stabilizer in a 1:1 molar ratio to titanium isopropoxide. The mixture was stirred for 2 to 3 hr; then a small amount of water (H_2O: alkoxide molar ratio 8) was added to hydrolyze the titanium isopropoxide. This resulted in a clear yellow sol. Aging was done at room temperature for 12 hr. This sol was used for dip coating. Aging time was adjusted as needed and the viscosity of the sol was adjusted to produce a crack-free film.

Host-Guest Complexes as Redox Mediators

Based on literature studies, various pairings of host and guest molecules were made with the idea of limiting the rate of charge transfer according to whether the guest molecule was complexed by the host or not. Cyclodextrins and calixarenes were chosen as hosts and phthalocyanines and quinines were chosen as guests. The cyclodextrin is selective for the phthalocyanine, while the calixarene is selective for the quinone. The molecular structures for the hosts are guests are shown in figures 5 and 6, respectively.

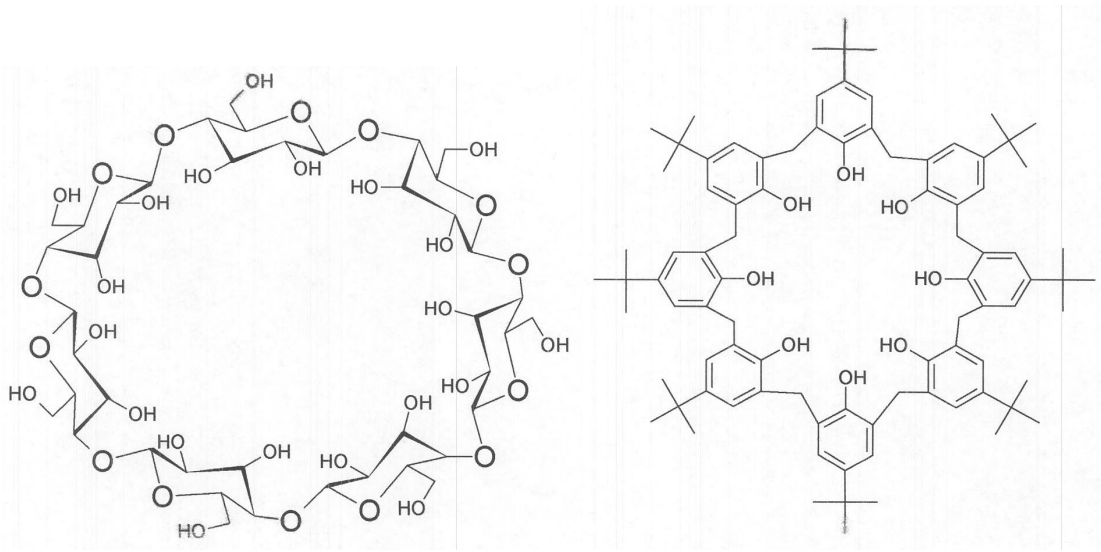

Figure 5.—Structures of host molecules cyclodextrin(l) and beta-calixarene(r).

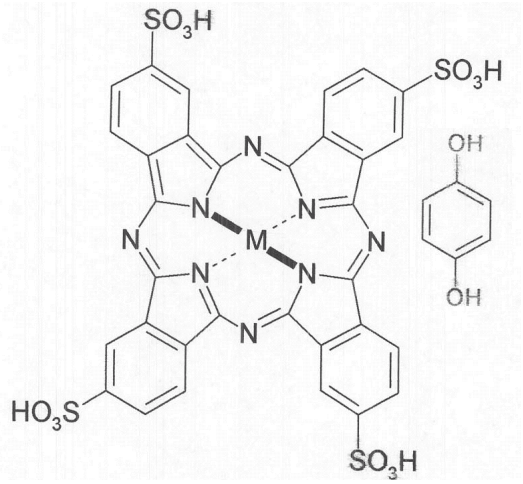

Figure 6.—Structures of guest molecules metal
(M = copper) phthalocyanine and benzhydroquinone.

Voltammetric methods were employed to determine the effect of host-guest complexes on semiconductor electrochemistry. In figure 7, the cyclic voltammogram for a TiO_2 film on fluorine-doped SnO_2 in the absence of complex is shown. A typical response exhibiting H_2 evolution in the negative potential regime and onset of O_2 evolution in the positive regime was obtained.

It is seen that the copper phthalocyanine is photoactive, in that larger currents are seen under illumination. On the other hand, the voltammograms are tilted more to the diagonal that the plain electrode, indicating some internal resistance. In figure 8, the calixarene/benzhydroquinone voltammetry is shown. Traces for host alone, guest alone, and both together are shown. It is seen that the host by itself (trace a) appears to have a resistive effect by itself, while the benzhydroquinone is reasonably active. In the presence of the host molecule, however, the guest is much enhanced, implying that the host has successfully increased the concentration of electroactive guest at the surface. X-ray photoelectron spectra taken of the C1S signal on F-SnO_2 showed an enhancement in signal for samples that had been exposed to the host molecule, implying preadsorption.

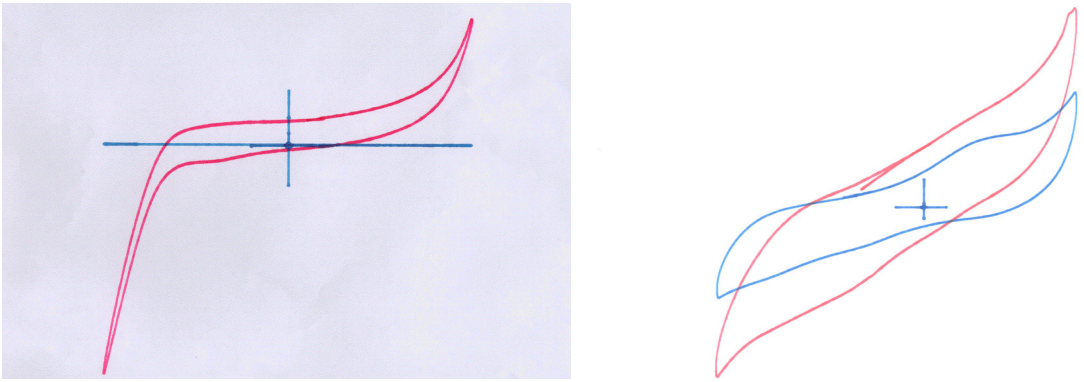

Figure 7.—Current-voltage curve for TiO_2 film on F-SnO_2 a) without sensitizing layer; b) with copper phthalocyanine sensitizing layer. Red trace: light; Blue trace: dark.

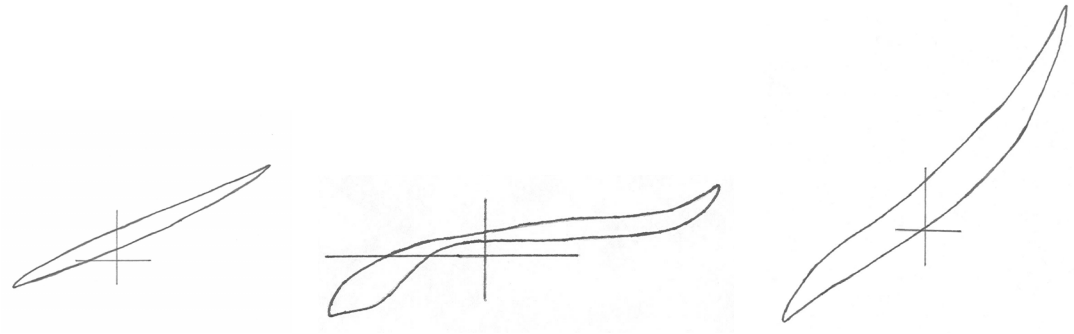

Figure 8.—Voltammetry of calixarene/benzhydroquine host/guest complex on F-SnO_2. a) host calixarene alone; b) guest benzhydroquinone alone; c) cost/guest together.

Conclusion

Numerous kinetic and mechanistic experiments were performed with the intent of identifying the rate-limiting steps in the overall water-splitting, H_2-evolving process. Of great concern is one must shift the concentration of redox mediator from oxidized to reduced form or vice versa, so that its companion module receive or acquire the electron equivalents to complete the reaction. Protection against the back reaction is necessary. Host-guest complexes were examined in this regard. Voltammetric and X-ray photoelectron data showed that the host molecule was adsorbing to the semiconductor electrode surface, but not in such a manner as to prevent a reaction from occurring at the semiconductor surface. Nevertheless, enhancement of the electrolysis of the guest molecule was observed. It is still uncertain whether the host was inside or otherwise associated with the guest species, since it also likely that the compound simply blocked the electrode surface, making it more difficult for any process to occur.

Hydrogen Purification and Storage Using Lithium Borohydride

PI: C. Linkous (Florida Solar Energy Center)
S. Bhuller (Florida Solar Energy Center)
D. Nangle (Florida Solar Energy Center)

Abstract

The objective of this project is to develop a system for H_2 storage and delivery based on lithium borohydride, $LiBH_4$. The theoretical H_2 content is 18.5% by weight, exceptional among organic and inorganic materials alike. Release of the H_2 is accomplished simply by mixing with water. This process may be controlled by a combination of solution conditions, i.e., borohydride concentration, solution pH, and temperature, and also by the use of heterogeneous catalysts. A new family of catalysts, consisting of fused ring heteroaromatic pigments has been identified for this application. The best catalyst of the group was pyranthrenedione, attributable to its low-lying molecular orbital. The borate salts resulting from borohydride decomposition can act as a buffering agent, providing a means of controlling the pH of the system.

Introduction

Metal Hydrides as H_2 Storage Media

Current approaches to hydrogen storage include compression, liquefaction, and cryogenic adsorption (ref. 1). Yet another method of hydrogen storage involves storage in the solid state in the form of metal hydrides (ref. 2). Certain metals, such as titanium, nickel, palladium, and related alloys will uptake H_2 directly from the gas phase to form the hydride with release of heat:

$$M + x/2\ H_2 \rightarrow MH_x + \text{heat}$$

Subsequent input of heat and/or depressurization will release the H_2 as needed. The hydrides under consideration are simple binary hydrides such as magnesium hydride, MgH_2, and complex hydrides such as $NaAlH_4$, which are made reversible with suitable application of a catalyst. The basic problem involves obtaining a reasonable compromise between the reversibly obtainable H-content and the H_2-recovery temperature, typically in the 100 to 200 ◦C range and higher.

Borohydrides

One large class of hydride compounds is the tetrahydroborates, or borohydrides (refs. 3 to 5), with general formula $M(BH_4)_x$. The Lewis acidity of boron enables it to complex with a hydride ion, H^-, to form BH_4^-; the anion forms a salt with any of a number of electropositive metals. For example, sodium borohydride, $NaBH_4$, is a common reducing agent and catalyst in organic chemistry (refs. 6 and 7).

The highly energetic nature of borohydride compounds in general led to their study early on as rocket fuels (ref. 8). It was found that in addition to the boranes, there were two different types of metal borohydride compounds. Some are largely covalent in nature, such as the aluminum borohydride, $Al(BH_4)_3$. These compounds tend to be volatile and spontaneously flammable. Other borohydrides, such as the alkali metal borohydrides, are ionic in nature. Thus they tend to be white crystalline solids at room temperature. While they are ultimately unstable in the presence of water, they are stable enough that they can be dissolved to make aqueous solutions.

The borohydride of interest here is lithium borohydride, $LiBH_4$. With all of its constituent elements occurring early in the first and second rows of the Periodic Table, it possesses an intrinsic gravimetric hydrogen density of 18.5 percent. The discovery of $LiBH_4$ was made in 1940 by Schlesinger and Brown (ref. 9), as part of a war time research program on developing agents for rapid deployment of signal balloons in the field.

Borohydrides in general may have been overlooked in the past as a hydrogen storage medium because they were thought to be non-reversible. Indeed, that conclusion is correct if they are tested in the same manner as most other hydride candidates, namely, in terms of their thermal decomposition and direct re-hydriding under H_2 pressure. In terms of thermal decomposition, $LiBH_4$ does not begin to decompose until 275 °C. Even then, the decomposition proceeds to lithium hydride and diborane, which further condenses to make $B_{10}H_{14}$ and H_2 (ref. 5).

Water + Borohydride Approach to Hydrogen Generation

If one considers the aqueous chemistry of $LiBH_4$, however, one encounters a different set of compounds. One mole of lithium borohydride will react with 4 moles of water to generate lithium hydroxide and boric acid plus hydrogen gas:

$$LiBH_4 + 4\ H_2O \rightarrow LiOH + H_3BO_3 + 4\ H_2$$

By this mechanism, one gram of $LiBH_4$ liberates 4.11 liters of hydrogen gas at STP.

A number of groups have recognized the facility of H_2 release from hydridic materials via controlled admixture with water. For example, Kong, et al., looked at binary hydrides, as well as borohydrides and aluminohydrides (ref. 10). They concluded that CaH_2 and LiH were most promising, even though their hydrogen storage densities were comparatively less, because they could obtain controlled H_2 evolution using water vapor. Nevertheless, Aiello, et al, looked at steam hydrolysis of $NaBH_4$ using an isothermal semi-batch reactor and showed that one could indeed evolve hydrogen from borohydrides using water vapor (ref. 11).

$LiBH_4$ should also score well in terms of safety, at least in comparison to other hydrides. While many of the other hydrides are spontaneously flammable in air or water, $LiBH_4$ is indefinitely stable in dry air, and will form solutions of varying stability, depending on concentration, pH, and temperature. Nevertheless, $LiBH_4$ can be brought to flammability if it is mixed suddenly with water in the presence of O_2. The key is whether the exothermicity of reaction with water can be dissipated quickly enough to prevent spontaneous ignition of the H_2.

Experimental

Hydrogen evolution was performed by dissolving borohydride salts into water in a closed vessel (3-neck round bottom flask), which had been purged with Ar beforehand. Gas evolution was monitored by connecting the vessel to a water-filled inverted graduated cylinder via a PVC or other gas-impermeable tube.

The sodium and lithium borohydride salts were obtained from Aldrich. The sodium salt was often used instead of lithium for preliminary work, because it was less expensive, and also due to the initial qualitative observation that the lithium salt was more reactive, to the point where the H_2 evolution rate could not be accurately monitored. The pigment catalysts were obtained from various sources, including Aldrich, TCI, and Ciba-Geigy. Most were obtained as impure powders that were extracted or refluxed with benzene or ethanol and dried before use. In the case of dimethoxyviolanthrone and indanthrene Gold Orange, they were obtained as vat dyes, and needed to be salted out of suspension, dried, and washed with ethanol before use.

Results

Catalytic H_2 Evolution

As for demonstrating H_2 recovery in a safe, economical manner, the most desirable situation would be to use plain water for the regeneration, and not have to acquire additional reagents. Two problems were discovered using plain water, however. First, as solid $LiBH_4$ is initially mixed with water, the gas evolution is quite vigorous and difficult to control, more so than if an alkaline solution was gradually acidified. Second, as the reaction progresses, the solution becomes progressively more alkaline, and so the reaction winds down to nothing well before the stoichiometric amount of H_2 is collected. This is

demonstrated in figure 1, where H_2 evolution from unbuffered aqueous borohydride solutions is shown. H_2 volume would increase rapidly for the first few minutes, and then begin to level off.

As can also be observed in figure 1, there was only limited success in controlling the rate of gas evolution by using catalysts instead of pH. In this approach to H_2 generation, one would add the borohydride to an inert alkaline solution at sufficiently high pH that the background evolution rate would be negligible. One would then add catalysts in sufficient amount to effect the desired rate of gas evolution. Heretofore all catalysts developed for borohydride decomposition were inorganic in nature. Typically they were transition metal salts or elemental powders such as ruthenium or cobalt. We have discovered a new class of catalyst materials that also effectively mediates the rate of H_2 gas evolution. Functionally they are organic pigments, since they are brightly colored and consist only of carbon and other nonmetals. While studying them for their use as chromophores in photocatalytic applications, the serendipitous observation was made that vigorous H_2 evolution occurred when performing the borohydride reduction of a metal salt in the presence of these compounds (ref. 12).

Catalyst loading was held constant at 100 mg. A gas evolution curve for an equivalent weight of Co powder is also shown for comparison. Subsequent trials with additional pigments were run. These results are shown in tabular form in table I. It can be seen that the best catalyst enabled a 6.5-fold increase in the rate of H_2 evolution over that obtained in a Pyrex vessel without any catalyst added.

It can also be seen that several of the pigments were as good as or better catalysts than the conventional cobalt catalyst: pyranthrenedione, indanthrene Gold Orange, and perylene diimide. In general, the molecular structure of the various organic pigments studied consists of an extended fused aromatic system, with one or more heteroatoms (nitrogen, oxygen, sulfur, etc.) affiliated with the π-electron cloud. Semi-empirical molecular orbital calculations done on these compounds in this laboratory have shown that they possess exceptionally low-lying π^* orbitals that make them more accessible for reduction, an attribute that undoubtedly plays a factor in their catalytic function (ref. 13).

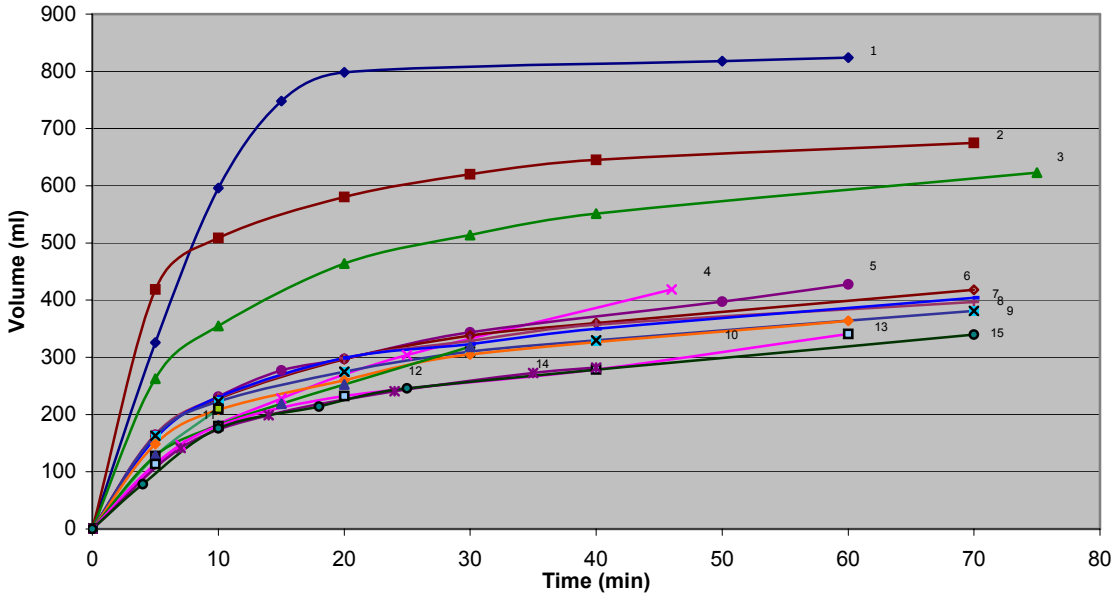

Figure 1.—Time dependence of H_2 evolution from $NaBH_4$ in pure water. 1) indanthrene Gold Orange; 2) perylene TCDA; 3) perylene diimide; 4) Co powder; 5) indanthrene Yellow; 6) Zn phthalocyanine; 7) indanthrene Black; 8) quinacridone; 9) pyranthrenedione; 10) isoviolanthrone; 11) indigo; 12) indanthrone; 13) Ni phthalocyanine; 14) no catalyst; 15) Cu phthalocyanine.

TABLE I.—RANKING OF PIGMENT CATALYSTS BASED ON SLOPE OF H_2 EVOLUTION CURVE. pH 11 PHOSPHATE BUFFER, 1.0 M IONIC STRENGTH.

Rank	Catalyst	Rate (ml/min)
1	pyranthrenedione	6.5
2	indanthrene Gold Orange	5.0
3	Cobalt powder	5.0
4	ditridecyl-3,4,9,10-perylenetetracarboxylic diimide	4.9
5	indanthrene Black	4.2
6	dimethoxyviolanthrone	4.0
7	poly(methylmethacrylate)	4.0
8	quinacridone	3.9
9	1,4-Di-keto-pyrrolo(3,4-C) pyrrole	3.8
10	indanthrene Yellow	3.5
11	copper phthalocyanine	3.4
12	3,4,9,10, perylenetetracarboxylic dianhydride	3.3
13	isoviolanthrone	3.3
14	perylenetetracarboxylic diimide	3.2
15	Indigo	2.8
16	phosphate buffer pH 11	1.0

pH Effect on H_2 Evolution

It is generally thought that H_2 evolution from a borohydride solution is driven by a bimolecular process involving borohydride ion, BH_4^-, and solvated hydrogen ions, H^+. The hydronium ion dependence in turn implies that the borohydride decomposition rate is pH-dependent. There are some literature references to a pH-independent process, but the rate constant is quite small. The corresponding overall rate expression would be

$$\text{Rate} = k\,[H^+][BH_4^-]$$

With both pH and background borohydride concentration changing during the course of the reaction, it was difficult to monitor the reactions so as to observe an unambiguous reaction rate. However, we were able to eliminate the pH variation by the use of buffered solutions. Instead of preparing KOH or NaOH solutions of an appropriate concentration so as to achieve the desired pH, we began preparing phosphate buffer solutions at ~1.0 M ionic strength. By utilizing borohydride solutions at nominal 0.1 M concentration, there would be a generous excess of acidic species to neutralize the OH^- ions as they were produced. As shown in figure 2, by using phosphate buffer solutions, the H_2 evolution curves straightened out, demonstrating simple first order kinetics. A pH of 11 using 0.1 M $NaBH_4$ allowed for a steady H_2 output that could be reasonably observed with volumetric collection apparatus.

Despite the ability of the pigments to accelerate the rate of H_2 evolution, the enhancement did not substantially change the effect of pH. In figure 3 below, H_2 evolution from borohydride solution versus time in the presence of pyranthrenedione catalyst for several pH values is shown.

It is seen that the decade dependence on hydronium ion concentration is once again observed, just as it was for the uncatalyzed case, except that the absolute rate for each pH is higher.

The results of figure 3 confirmed our general understanding of borohydride aqueous chemistry. At high pH (11-14), BH_4^- ion is essentially an inert material, forming a stable solution that could be stored for an indefinite period of time. At neutral pH (6-8), a mildly effervescent solution is obtained, i.e., there is a steady outgassing of H_2 from the system. Special precautions would have to be taken to store $LiBH_4$ solutions under these conditions. Finally, at acidic pH (1-4), the effervescence is quite vigorous. In addition, the H_2 production reaction is sufficiently exothermic that, unless the solution is protected from air, there is a risk of igniting the evolving gas.

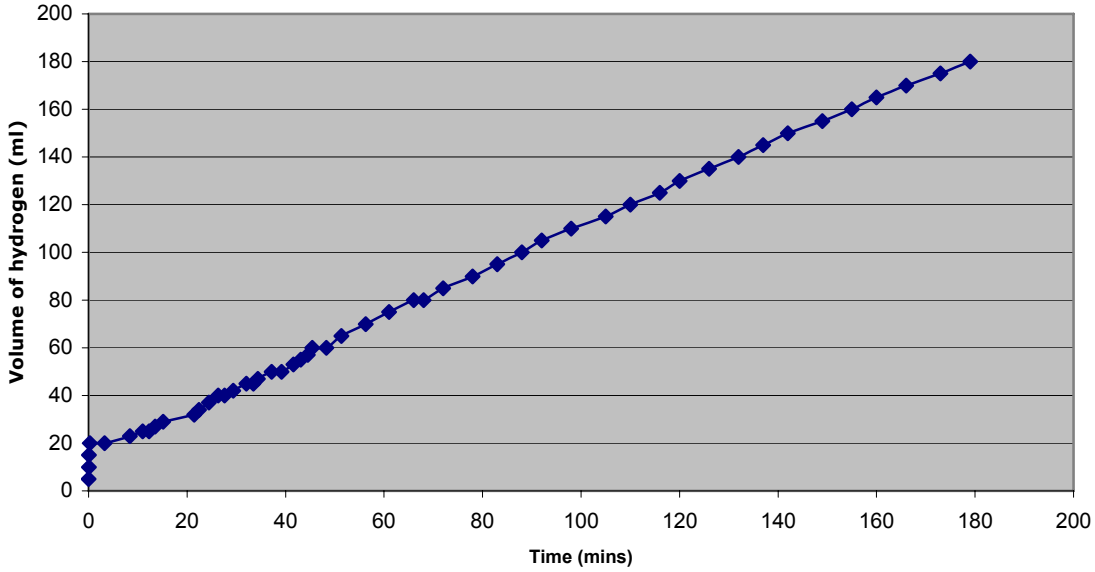

Figure 2.—H_2 evolution from phosphate-buffered borohydride solution at pH 11.

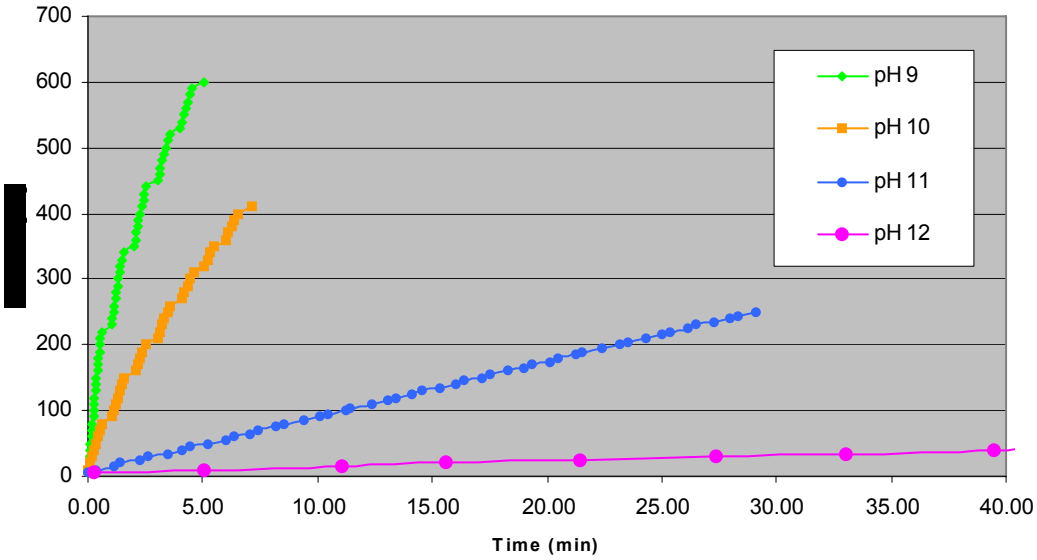

Figure 3.—pH dependence of H_2 evolution from borohydride solution using pyranthrenedione catalyst.

Borate Buffering Effect

The LiOH by-product from the decomposition reaction is the substance responsible for the pH-increasing effect. Boric acid is expected to react further with lithium hydroxide, however, to generate a hydrous metaborate salt:

$$LiOH + H_3BO_3 \rightarrow Li[B(OH)_4].$$

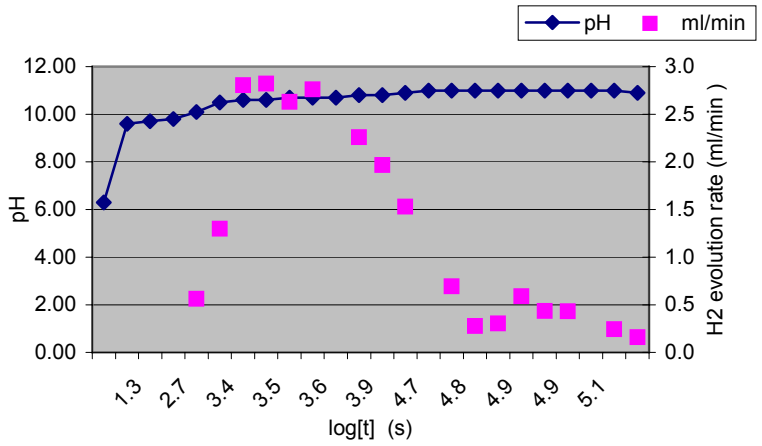

Figure 4.—Time dependence of pH and H_2 evolution rate from a 0.1 M $NaBH_4$ solution.

This reaction would tend to mask, or even eliminate, the production of free hydroxide ion, and thus the progressive attenuation of reaction rate. In an uncatalyzed BH_4^- decomposition experiment, pH was monitored versus time, along with the incremental H_2 evolution rate. These results are shown together in figure 4. It is seen that as the experiment continued over a 2-day period, the pH eventually reached 11.0. Therefore, a system already set to this pH would maintain that value, as the ratio of H_3BO_3 to $[B(OH)_4]^-$ would be preserved.

Conclusion

In conclusion, results have shown how rates of H_2 evolution from aqueous borohydride solution can be controlled by means of hydride concentration, pH, and the use of catalysts. In particular, we have discovered a new class of borohydride decomposition catalysts based on fused aromatic compounds containing sufficient heteroatoms to lower its first excited electronic state to where it can be accessed by the borohydride. Some of these catalysts, at least on a weight basis, are more active than the conventional inorganic metallic powder catalysts. Results also showed how holding the pH of the solution constant will enable a constant rate of borohydride ion decomposition. Borohydride decomposition in solution is a dynamic situation, where the LiOH produced may or may not interact with boric acid, depending on the pH. By operating the system near the maximum buffering pH, ~11, such fluctuation may be avoided.

References

1. D.L. Block, S. Dutta, and A. T-Raissi, "Storage of Hydrogen in Solid, Liquid, and Gaseous Forms," no. FSEC-CR-204-88, Florida Solar Energy Center, Cape Canaveral, Florida, June, 1988.
2. R. Wiswall, "Hydrogen Storage in Metals," ch. 5 in Hydrogen in Metals II. Application-Oriented Properties, G. Alefeld and J. Völkl, Topics in Applied Physics, vol. 29, Springer-Verlag, New York, 1978.
3. E.L. Muetterties, The Chemistry of Boron and its Compounds, Wiley, New York, 1967.
4. F.A. Cotton and G.W. Wilkinson, Advanced Inorganic Chemistry, 3rd Ed., Interscience, New York, p. 238.
5. P. Rittmeyer and U. Wietelmann, Hydrides, Chemetall. GmbH, Frankfurt, Germany, vol. A13, p. 199.
6. H.C. Brown, Boranes in Organic Chemistry, Cornell University Press, Ithaca, 1972.
7. H.C. Brown, Hydroboration, W.A. Benjamin, Inc., New York, 1962.
8. D.R. Martin, Chapter 1 in Borax to Boranes, T. Wartik, ed., Adv. in Chemistry Series, #62, American Chemical Society, 1961.
9. H.I. Schlesinger and H.C. Brown, J. Am. Chem. Soc., 62 (1940) 3429-3435.

10. V.C.Y. Kong, F.R. Foulkes, D.W. Kirk, and J.T. Hinatsu, Int. J. Hydrogen Energy, 24 (1999) 665-675.
11. R. Aiello, J.H. Sharp, and M.A. Matthews, Int. J. Hydrogen Energy, 24 (1999) 1123-1130.
12. Darlene Slattery, private communication, Florida Solar Energy Center, September 4, 1999.
13. D.K. Slattery, C.A. Linkous, N.E. Gruhn, and J.C. Baum, Dyes and Pigments, 49 (2001) 21-27.

Smart Paints and Pigments for Hydrogen Sensing

PI: N. Mohajeri (Florida Solar Energy Center)
G. Bokerman (Florida Solar Energy Center)
N. Muradov (Florida Solar Energy Center)
A. T-Raissi (Florida Solar Energy Center)

NASA Requirements for Hydrogen Gas Leak Detection Tape

The hydrogen detection tape used at the launch pad should not damage or change the launch pad materials in places that it is used. Ideally, the tape will be wrapped around suspected leaking areas. The longest the tape is expected to be in use at any one location is about two weeks. The tape should be easily removable. It is desirable that the chemochromic tape is in roll form that makes its application easy and resist shedding or causing any particulate to accumulate from its use. As depicted in the following photo taken at the NASA-KSC, the size of the valves the tape would be applied to varies dramatically from inches in diameter to almost 3 ft. The width varies as well.

False positives should not result from chemical exposure at the launch pad. The tape should still be able to detect hydrogen after exposure to nitrogen, ice, helium, Freon 113, sulfide, solid rocket booster residue, methyl ethyl ketone, and bubble soap. Other cleaning agents that are acceptable for use in the LH_2 lines can be found in SE-S-0073.

A reversible tape would ideally revert back to its original color at 1 percent H_2. Concentrations greater than 1 percent should cause the reversible tape to change color.

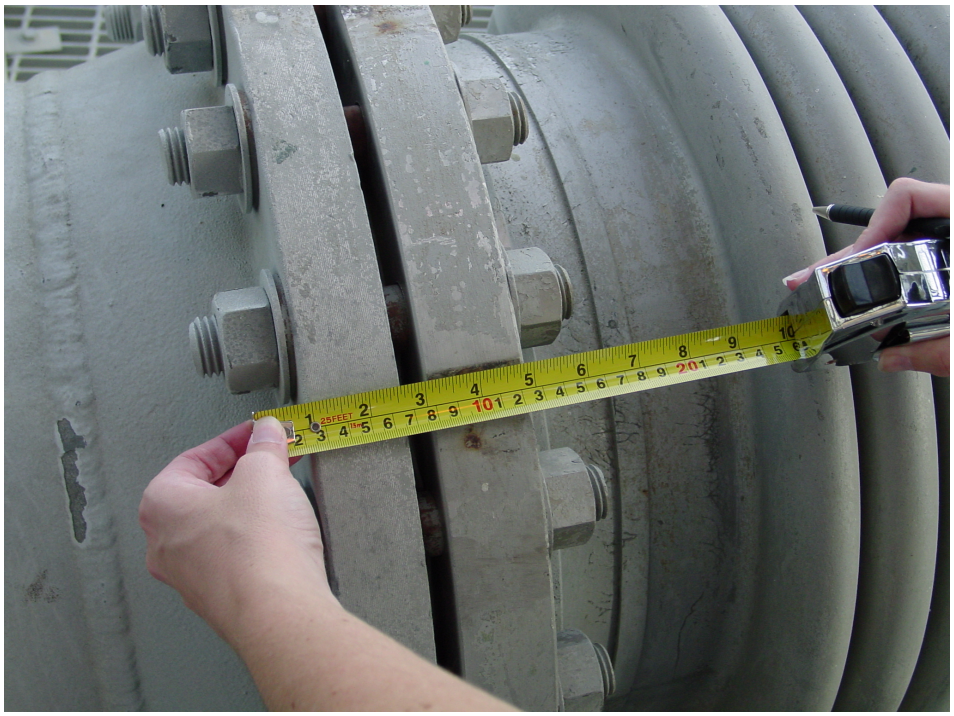

Background

Hydrogen is a colorless, odorless gas, and is also a flammable gas with a lower explosive limit of about 4 percent in air. Therefore reliable H_2 sensors are required to detect possible leaks wherever H_2 is produced, stored, or used.

To detect H_2, sensors that consist of a palladium alloy Schottky diode on a silicon substrate are known. These sensors are based on metal-oxide-semiconductor (MOS) technology that is used in the semiconductor industry. The gas sensing MOS structures are composed of a hydrogen-sensitive metal (palladium or its alloy) deposited on an oxide adherent to a semiconductor. This hydrogen sensor has been commercialized and exploited in detecting H_2 leaks during pre-launches of space vehicles. Other research groups have also used palladium or the like as a sensing element for detecting H_2.

A hydrogen sensor containing an array of micromachined cantilever beams coated with palladium/nickel has also been reported. Semiconductors (e.g., gallium nitride) with wide band-gap have also been used to make MOS diodes for H_2 detection. One of the concerns for all of these types of sensors using palladium or the like is the requirement of a high operating temperature (greater than 200 ◦C) and further elevated temperatures (greater than 500 ◦C) to reactivate the sensing element, bringing about lengthy analysis. Another issue is sensitivity of the sensing element to other compounds commonly found in the atmosphere, including water vapor, various hydrocarbons and various reducing gases such as carbon monoxide and hydrogen sulfide.

Although not conventionally used, chemochromic sensors for hydrogen sensing have been disclosed. For example, published U.S. Application No. 20040023595 to Liu et al. discloses a fast response, high sensitivity structure for optical detection of low concentrations of hydrogen gas, comprising a substrate, a water-doped WO_3 layer coated on the substrate; and a palladium layer coated on the water-doped WO_3 layer. In related work, published U.S. Application No. 20040037740 to Liu et al. discloses a sensor structure for chemochromic optical detection of hydrogen gas comprising; a glass substrate a vanadium oxide layer coated on the glass substrate; and a palladium layer coated on the vanadium oxide layer. The hydrogen sensors disclosed by Liu et al. lack field stability. Moreover, such sensors have a tendency to crack and peel, and can be washed off by precipitation and/or condensation.

U.S. Pat. No. 5,849,073 to Sakamoto discloses a pigment for sensing gas leakage which can be produced by adding at least one of salts of platinum group metals to a slurry of particulate substrate, neutralizing the resultant mixture to deposit at least one of oxides, hydroxides and hydrated oxides of platinum group metals on the surfaces of the particulate substrate, and if necessary, further adding to said slurry at least one of compounds of aluminum, silicon, titanium, zinc, zirconium, tin, antimony and cerium, neutralizing the resultant mixture to deposit at least one of compounds such as oxides, hydroxides and hydrated oxides of aluminum, silicon, titanium, zinc, zirconium, tin, antimony and cerium, on the particles.(something is missing here, there is no description of the organic resins revealed in the patent) The resinous composition disclosed is typically quite impervious to gas penetration. Sakamoto requires very thin coatings (typically 2 mils) with relatively high concentrations of active chemochromic compounds. In addition, compositions disclosed by Sakamoto do not show selectivity to hydrogen.

Description of the FSEC-Developed Hydrogen Sensing Formulations

FSEC-developed hydrogen (H_2) sensors comprise of a gas permeable matrix material intermixed and encapsulating at least one chemochromic pigment. The chemochromic pigment produces a detectable change in color of the overall sensor composition in the presence of H_2 gas. The matrix material provides high H_2 permeability, which permits fast permeation of H_2 gas but generally slow relative permeation of other gases that may be present in the surrounding environment, such as carbon monoxide, hydrogen sulfide, ammonia, water vapor, and hydrazine. Thus, diffusion of other gases present in the surrounding environment is generally very slow in the matrix to the extent that their presence does not measurably interfere with the function of the encapsulated chemochromic pigments disclosed herein. One exception noted below is relative to the sensor embodiment having a reversible pigment, where oxygen permeation is believed to be required to regenerate the original color. For the reversible formulation, the chemochromic pigment comprises PdO/TiO_2.

The high gas permeability matrix material allows the composition of FSEC-developed formulations to be used in thicker segments and with lower concentrations of the active pigment as compared to previous related sensors while retaining the rate and extent of color change similar to the free pigment. Most

pigments have high water solubility. The encapsulating matrix also provides enhanced protection to weather and environmental contaminants, including those being moisture comprising, and retains that behavior at temperature extremes. For example, H_2 detection color change using sensors based on the FSEC-developed formulations have been demonstrated at temperatures as low as –40 ◦C.

A wide variety of gas permeable encapsulating matrix materials can be used with the FSEC-developed formulations. Preferred gas permeable polymers generally provide a gas permeability that is at least equal to the gas permeability of low-density polyethylene. The encapsulating matrix materials are preferably cross linked polymers including silicone rubbers or silicone resins. Such polymers are water resistant which allows sensor composites based on the FSEC formulations to remain useful in wet environment applications despite the water solubility of most pigments. A polysiloxane available in cross linked form that provides higher permeability to gases than other polymers is poly(dimethylsiloxane) rubber or PDM Srubber. PDMS rubber can be prepared using a moisture cure typically referred to as a sealant, or as a high or low consistency preform of silicone rubber that is then cured to a rubbery consistency.

Silicone resins are usually primarily composed of trifunctional material, so are generally highly crosslinked. Other gas permeable polymers are expected to show similar behavior, such as natural rubber and ethyl cellulose. Cross linking can be important for certain polymers for use with the FSEC formulated compositions, particularly those with low glass transition temperatures (Tg) relative to the intended maximum temperature of sensor operation. PDMS has a reported Tg of –123 ◦C. Polymers that have no cross linking at all become viscous liquids above Tg. However, some cross linking renders the polymer above its Tg leathery or elastomeric and thus resistant to flow. Highly cross linked polymers are strongly resistant to flow for T>Tg and often provide modulii comparable to aluminum. Therefore, a polymer such as PDMS requires cross linking for use in a sensor composition according to the FSEC-developed formulations to prevent flow for operation at a temperature above its Tg, such as room temperature.

Opacity and/or transparency of the matrix material are generally preferred. Although the degree of transparency of the matrix material does not generally impact the color-changing function of pigments, transparency of the encapsulating compound can be important in facilitating observation of the color change by naked eye where even low levels of attenuation can be of significance.

In one formulation, PdO/TiO_2 or other chemochromic pigment is combined with a moisture curing silicone sealant in the specified ratio to give a composition that responds in a very controllable way to the presence of H_2. The active gas sensing pigment is generally 1 to 50 wt % of the overall composition, and is 5 to 20 wt % in a preferred embodiment.

Sensor compositions according to the FSEC-developed formulations are generally applied to a solid surface, and then cured on the solid surface. For example, mixed PdO/TiO_2 or other chemochromic pigment mixed with silicone paste is applied to a backing sheet such as a woven glass fiber tape. With this arrangement, only the side in contact with hydrogen will indicate the color change.

Alternatively, the paste can be cast as a film on a release surface such as polytetra-fluoroethylene or wax paper and then removed from the release surface after cure. After a 24 to 48 hr room temperature cure, the resulting film is generally rubbery and can be used directly as an indicator, which allows the color change to be viewed from either side of the sensor only when overcoated. In one form, the sensor composite is overcoated with additional virgin clear silicone or other gas permeable encapsulating matrix material as shown below.

Although not clearly shown below, the PdO/TiO_2 pigment is evenly distributed in the silicone throughout the full thickness of the top layer shown. In a preferred embodiment, the thickness of the virgin silicone overcoat is equal to or larger than the thickness of top portion containing the pigment. Using the overcoat, color change has been observed on both sides of indicator strips according to FSEC-developed indicators. The ability to employ thicker coatings also reduces the potential impact of environmental contaminants.

In one experiment, indicating matrix material was immersed in water for 24 hr. No color change to the indicator was observed. After immersion, the indicator composite material behaved normally when tested, demonstrating a strong color change in the presence of H_2.

In a preferred embodiment, the sensor composition is modified by adding a chemical additive to enhance the color change and increase the rate of color change. This behavior has been demonstrated on the permanent (or irreversible) color change system with hydrogen contact. For example, adding MoO_3 or $(NH_4)_6Mo_7O_{24}$ in levels varying from equivalent to about 10x the molecular content of PdO was found to

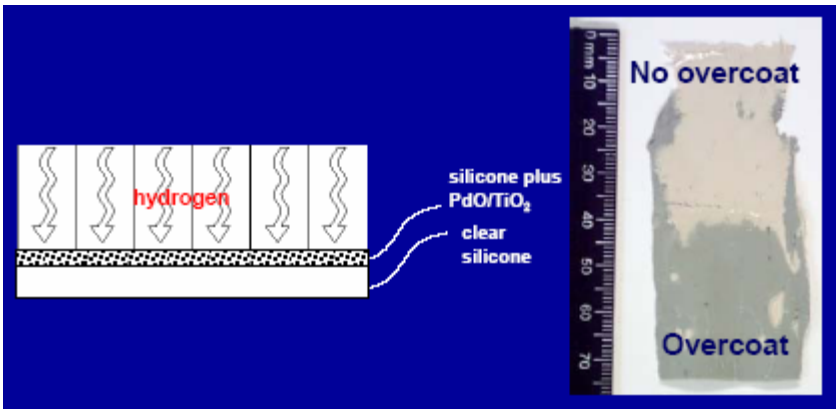

provide a chemochromic system that showed a visually darker color upon contact with hydrogen than without either of the above-described molybdenum compounds. In addition, the rate of color change also increased compared to the rate without the molybdenum complex and/or oxide. Other color contrast additives can be selected from the class of polyoxometalates that include V, Nb, Ta, Cr, Mo, and W, such as $H_3[P(W_3O_{10})_4]$ and $H_3[P(Mo_3O_{10})_4]$.

The color change can be made to be reversible, or made to be more reversible, by incorporating reversibility enhancing additives. However, for reversibility to proceed, it is believed that the sensor composition must allow a species other than H_2, such as oxygen, to also permeate to the pigment to regenerate the original color. Crosslinked Polymers including silicone rubber (e.g., PDMS) rubber, when used in conjunction with the reversibility enhancing additives, have demonstrated reversibility. In such compositions, the original color is reestablished/regenerated generally within about 1 to 30 sec after exposure of the material to hydrogen has ceased. This behavior was demonstrated with a PDMS rubber formulation comprising TiO_2-$H_4[SiW_{12}O_{40}]$ pigment doped with 0.001 to 1.0 wt % of platinum nanoparticles. The size of the particles was in a range from 10 to 100 nm.

Presence of Pt nanoparticles (Pt_{np}) significantly accelerates electron transfer from molecular hydrogen to pigments (e.g., $H_4[SiW_{12}O_{40}$) resulting in their color change. Without Pt_{np} color change would occur very slowly (hours), or may not occur at all. When subject to hydrogen, the original white (or grayish-white) color changed to blue in a matter of seconds. After exposure to hydrogen flow did cease, the original color reappeared within few seconds for the best candidate material tested. A variety of molybdenum and tungsten compounds are expected to function in the same fashion. Other reversibility enhancement additives include $H_3[P(W_3O_{10})_4]$). It is noted that the class of reversibility enhancement additives (reversible pigments) overlaps the class of contrast additives, which, advantageously, indicates their multi-functionality.

FSEC-developed formulations provide a high level of selectivity to H_2 compared to a variety of other species. Other sensors tend to lack selectivity. For example, U.S. Pat. No. 5,849,073 noted above discloses that other reducing compounds will activate color change, such as carbon monoxide. Under identical conditions and in the presence of carbon monoxide, a silicone encapsulated FSEC system did not undergo a color change, but when subjected to H_2 gave the usual dark color. Additional benefits are the enhanced selectivity described previously in which only the indicator side in contact with hydrogen changed color. As noted above, this effect can be reversed by overcoating to give a color change on both sides of the indicator system. This offers great potential to tailor the response to the application at hand to achieve the maximum safe hydrogen utilization environment.

FSEC-developed hydrogen sensing formulations can be used for a variety of hydrogen sensing applications. For example, they can be used for smart paints and tapes to warn of H_2 leaks, and for applications requiring one sided and two sided responses. FSEC-developed hydrogen sensing formulations can also be applied to fiber optic sensing heads provide remote detection. They can also be used for naked-eye human visual-sensing.

Following photo depicts the application of a chemochromic tape based on the FSEC-developed irreversible hydrogen detecting formulation before leak (at left) and with H_2 leak (at right) at the dark spot.

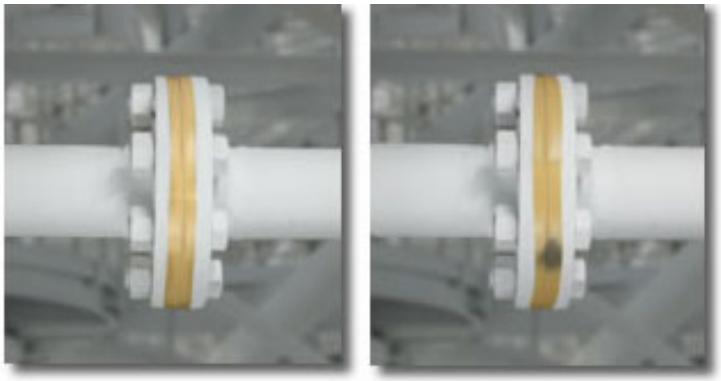

Preparation of the chemochromic pigments and formulations are illustrated via examples below:

Example 1.—A small quantity of HIT-46 pigment (ISK, TiO_2- 70 percent, Pd – 1.0 percent) was mixed with an equal amount of water and applied to a clean dry microscope slide. The slide was heated to eliminate the water in preparation for contact with hydrogen. The hydrogen contact chamber consisted of a glass vacuum trap housing the microscope slide. Hydrogen gas was allowed to flow for 5 min before inserting the slide. After approximately 1.5 min of hydrogen exposure, the original beige color of the pigment changed to gray. Upon removal from hydrogen chamber, the gray color remained.

Example 2.—1.01 g of HIT-46 pigment was manually admixed with 0.19 g of moisture curing silicone sealant (Dow Corning R 3145 RTV Adhesive/Sealant -Clear) to give 10.2 g of material. Some of this compound was applied to a clean microscope slide and allowed to cure for 24 to 48 hr. This slide was then contacted with hydrogen gas as in Example 1. After approximately 1.5 min exposure to hydrogen gas, the original beige color of the cured compound changed to gray. Upon removal from hydrogen chamber, the gray color remained.

Example 3.—A portion of the uncured pigment/sealant prepared by the method of Example 2 was applied to a piece of woven fiberglass tape. Using a draw down method with a blade, the surface of the woven fiberglass tape was covered with pigment/sealant mixture and allowed to cure. After a cure time of 24 to 48 hr, the flexible sheeting was ready for use as a hydrogen indicator.

Example 4.—Another portion of the uncured pigment/sealant prepared by the method of Example 2 was used to prepare a rubber sheet indicator. A flat Teflon (Dupont) board was lined with strips of vinyl tape to give the desired thickness to the sheet. The uncured pigment/sealant was spread on the Teflon plate and a draw down blade was used to prepare a uniform sheet of material for curing. After 24 to 48 hr, a thin rubbery sheet was pealed off of the TEFLON board and used as a hydrogen indicator.

Example 5.—18.0 mg of HIT-46 pigment was placed within the glass U-tube of AMI-200 (Altamira Instruments) temperature programmed desorption (TPD) instrument. A flow of 20 ml/min of 10 percent H_2 in Argon gas was maintained through TPD's U-tube. Sample temperature within the TPD's U-tube was ramped up at a rate of 10 ◦C/min from –100 to 50 ◦C. During the temperature ramping of the sample, TPD's thermal conductivity detector (TCD) showed a signal pickup and a color change was also detected when temperatures reached –98 ◦C as a result of pigment reacting with the hydrogen gas.

Example 6.—18.6 mg of HIT-46 pigment was placed within the glass U-tube of Altamira AMI-200 TPD instrument. A flow of 20 ml/min of 10 percent H_2 in Argon gas was maintained through TPD's U-tube. Sample temperature within the TPD's U-tube was kept isothermal at –90 ◦C. A TCD signal was detected as well as sample color change, which was attributed to the pigment reacting with H_2 gas. Reactions were complete after about 4 min.

Example 7.—26.1 mg of specimen prepared according to the method of Example 3 was placed within the glass U-tube of Altamira AMI-200 TPD instrument. A flow of 20 ml/min of 10 percent H_2 in Argon gas was maintained through TPD's U-tube. Sample temperature within the TPD's U-tube was kept isothermal at –30 ◦C. A TCD signal was detected and a sample color change as well which was attributed to the pigment reacting with the hydrogen gas. Reactions were complete after about 4 min.

Example 8.—39.6 mg of Example 3 specimen was placed within the glass U-tube of Altamira AMI-200 TPD instrument. A flow of 20 ml/min of 10 percent H_2 in Argon gas was maintained through TPD's U-tube. Sample temperature within the TPD's U-tube was kept isothermal at –30 ◦C. A TCD signal was detected and a sample color change as well which was attributed to the pigment reacting with the hydrogen gas. Reactions were complete after about 6 min.

Example 9.—18.2 mg of HIT-46 pigment was placed within the glass U-tube of Altamira AMI-200 TPD instrument and subjected to a 20 ml/min flow of 25 percent CO in Argon gas. Sample temperature was ramped up at a rate of 10 ◦C/min from –30 to 40 ◦C. A TCD signal was detected as well as sample color change within a range of temperatures from –10 to 35 ◦C, which is attributable to pigment reacting with CO gas and reactions were complete after about 4 min.

Example 10.—26.6 mg of the specimen prepared by the method of Example 3 was placed within the glass U-tube of Altamira AMI-200 TPD instrument and subjected to a 20 ml/min flow of 25 percent CO in Argon gas. Sample temperature was ramped up at a rate of 10 ◦C/min from –30 to 45 ◦C. No TCD signal and/or color change, as a result of hydrogen gas reacting with the pigment, was detected.

Example 11.—A sample from Example 10 was exposed to 10 percent H_2 in Argon gas using Altamira AMI-200 TPD instrument. The sample temperature was kept isothermal at –30 ◦C. A TCD signal was detected by the instrument, which was accompanied sample color change, similar to that of Example 7.

Example 12.—A sample of rubbery indicator sheet prepared according to the method of Example 4 was subjected to a set up simulating a leaking pipe. Two sections of stainless steel pipe with a threaded coupling were connected together loosely. One end of the line was attached to a hydrogen flow. The other end of the pipe was connected to a valve that if closed allowed hydrogen to leak out through the loose joint. A strip of the indicator sheet was wrapped around the joint and taped in place on the edge, and the hydrogen flow started. After closing the valve at the pipe's exit, hydrogen allowed to leak through the joint for 3 min. The color of the exterior of the indicator sheet was beige, while the inner face of the indicator sheet turned gray. This occurred regardless of the thickness of the rubbery indicator sheet used (minimum thickness used was 2.5 mils).

Example 13.—Example 12 was repeated by subjecting a sample of the rubbery indicator sheet of Example 4 to the hydrogen leak in the manner of Example 9 except that the indicator sheet was covered with Scotch (3M) tape. This resulted in the exterior face of the indicator sheet to change color from beige to gray within 1 to 2 min after exposure to hydrogen. The color of the interior face of the indicator sheet had also changed from beige to gray.

Example 14.—A sample of the rubbery indicator sheet of Example 4 was immersed in water for 24 hr before use in the leaking pipe test of Example 9. This sample was evaluated as in Example 10 (Scotch tape covering). Both faces of the indicator sheet changed color after 1 to 2 min of hydrogen exposure.

Example 15.—A sample of the rubbery indicator sheet of Example 4 was coated over with a layer of virgin clear silicone sealant of equal or greater thickness, and allowed to cure for 24 to 48 hr. The resulting cured double-layered sheet was subjected to the leaking pipe test of Example 9 by wrapping the indicator sheet with the clear overcoat around the loose pipe joint with the clear overcoat face on the exterior/outside. After 1 to 2 min of hydrogen exposure both sides of the over-coated indicator sheet had changed their color to gray.

Example 16.—Mixed PdO/TiO_2 chemochromic pigment together with silicone paste were applied to a backing sheet such as a woven glass fiber tape. After a 24 to 48 hr room temperature cure, the resulting rubbery film became ready for use as a two-sided indicator. In another experiment, MoO_3 or $(NH_4)_{6724}$ was added to the FSEC-developed compositions in levels varying from equivalent to 10X the molecular content of PdO, which gave a chemochromic system that showed a visually darker color upon contact with hydrogen than without the molybdenum complex, and/or oxide. In addition, the extent and rate of color change also was found to significantly increase compared to that without the molybdenum complex and/or oxide.

Example 17.—An exemplary FSEC-developed reversible H_2 sensor formulation is described as follows. 0.5 g of TiO_2 powder (average particle size 25 to 70 nm, surface area 20 to 25 nm) was mixed with 0.5 g of $H_3[P(W_3O_{10})_4]$ (Aldrich Chemicals). 5 ml of the colloidal platinum solution (0.025 wt% Pt) was added to this mixture. The colloidal Pt solution was obtained by mixing 2.5 ml of the aqueous solution of H_2PtCl_6 (0.1 wt%) with 2.5 ml of the aqueous solution (0.01 wt %) of the protective polymer (polyvinyl alcohol) followed by adding 0.1 g of sodium borohydride ($NaBH_4$) to the mixture under well-stirred conditions at room temperature until all hydrogen bubbles ceased to evolve. The TiO_2- $H_3[P(W_3O_{10})_4$-Pt slurry was carefully mixed and let dry overnight at ambient conditions. The resulting grayish powder was carefully mixed with 5 g of silicone paste, and the mixture was applied to the surface of a smooth sheet of perfluorinated polymer to form a thin film. After a 24 to 48 hr room temperature cure, the resulting rubbery film became ready for use as a reversible hydrogen sensor.

Local Hydrogen Production via Catalytic Reformation of Fossil and Renewable Feedstocks

PI: N. Muradov (Florida Solar Energy Center)
F. Smith (Florida Solar Energy Center)
C. Huang (Florida Solar Energy Center)

Objective

The objective of this project is to develop economically viable process for the production of high purity hydrogen at the NASA KSC site from locally available fossil and renewable feedstocks with minimal environmental impact.

Technical Approach

The innovative approach is based on the development of a feedstock-flexible catalytic process that allows converting both fossil (e.g., natural gas) and renewable feedstocks (landfill gas, LFG) into high-purity hydrogen gas suitable for liquefaction. The project explores two technological approaches to local hydrogen production: (i) direct reformation of landfill gas (LFG) from the nearby Cocoa facility, and (ii) catalytic pyrolysis of methane into hydrogen and value-added carbon products. In contrast to conventional processes, the significant part of the feedstock carbon will end up in the form of valuable carbon byproducts (activated carbon, pyrolytic graphite, carbon filaments) rather than CO_2. Marketing of carbon byproduct will reduce the net cost of hydrogen production. This approach will significantly expand the resources for local hydrogen production and allow a smooth transition from NG to local renewable feedstocks (as NG resources are dwindled and its selling prices increased).

Introduction

Economical, safety and other factors will potentially necessitate on-site manufacturing of liquid hydrogen at the NASA KSC site. Currently, steam methane reforming (SMR) is considered the lowest cost option for producing merchant liquid hydrogen. The shortcomings of SMR are the relatively high cost of natural gas (with its price volatility) and co-production of considerable amounts of CO_2 emissions, which may present a serious problem in a carbon-restricted environment. In view of the long-term uncertainties associated with natural gas (NG) supply, it is necessary to assess the non-fossil alternatives to NG and develop new hydrogen production technologies based on these feedstocks.

Two technological approaches to local hydrogen production have been selected for further evaluation: (i) catalytic pyrolysis of methane/NG into hydrogen and value-added carbon products, and (ii) direct reformation of landfill gas (which predominantly consists of CH_4 and CO_2) from the nearby landfill facility in Cocoa. The latter approach could be conveniently combined with the reformation of other renewable feedstocks, e.g., biogas, bio-ethanol, the producer gas from citrus waste pyrolysis/gasification unit. The advantages are as follows:

- feedstock flexibility and sustainability (practically any methane-containing feedstock could be utilized),
- possibility of a smooth transition from fossil (e.g., NG) to renewable feedstocks without drastic changes in the technological chain,
- production of valuable carbon byproducts such as pyrolytic graphite, carbon filaments, which may significantly reduce the net cost of hydrogen production, considerable reduction in overall CO_2 emissions

Description of the Proposed Concept

Figure 1 depicts a simplified schematic diagram of the proposed concept that utilizes NG, LFG and citrus waste. Based on the information provided by the Cocoa landfill facility management we estimated

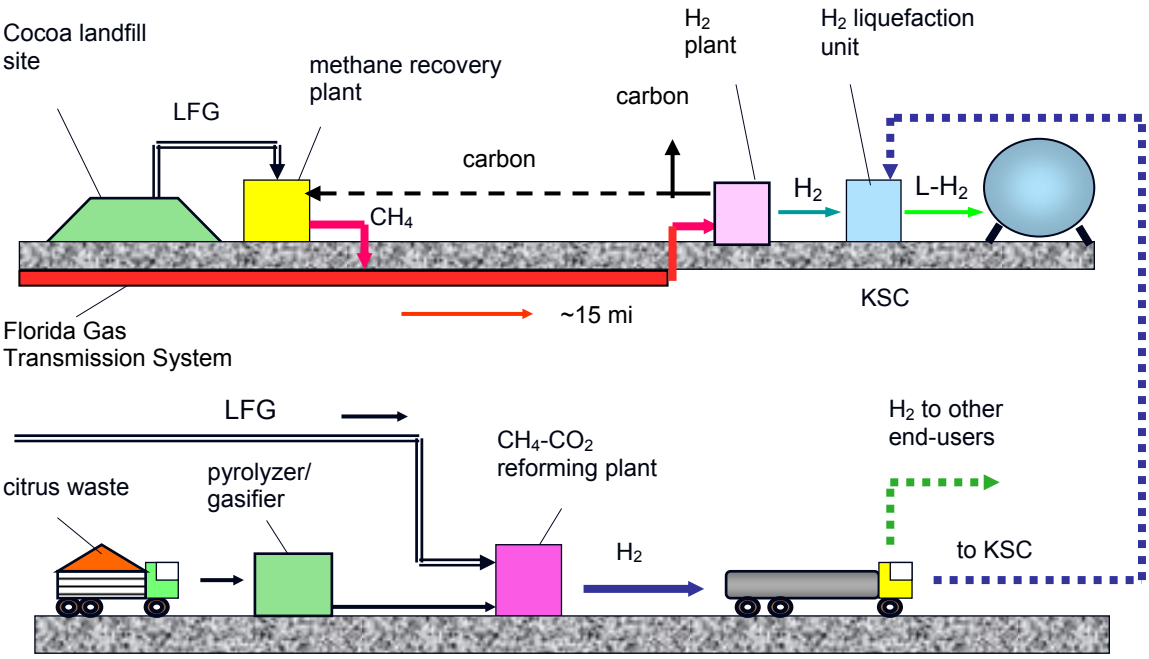

Figure 1.—Schematic diagram of the concept.

that the LFG resources from the facility would be adequate for the production of about 5 ton/day of hydrogen for the next 50 years. According to the proposed concept, the on-site production of liquid hydrogen could be realized via two technological options (or their combination).

In the Option 1, methane is separated from CO_2 at the LFG treatment plant and pumped into the Florida Gas Transmission System (which is in a short distance from the landfill site). Methane (in mixture with NG) is delivered to KSC site (the distance of approximately 15 miles), where it is pyrolyzed into hydrogen and carbon. Hydrogen is liquefied and stored for the use in the Space Shuttle program. Carbon could be marketed, thus reducing the net cost of hydrogen production.

According to the Option 2, LFG is purified of sulfurous and siloxane impurities and directly reformed into the synthesis gas (H_2-CO mixture of about equimolar composition). The synthesis gas is further conditioned and purified into hydrogen gas that is directed to a hydrogen liquefaction unit. The advantage of this approach is that it obviates the need for the expensive and energy intensive preliminary CO_2 separation stage. Another advantage relates to the possibility of co-processing of other renewable feedstocks such as biogas, bio-ethanol and the producer gas from biomass (e.g., citrus waste) pyrolysis or gasification unit.

Experimental

The premixed gaseous mixture with the composition of CH_4- 56.9, and CO_2- 43.1 vol % was obtained from Holox Inc. and used as a baseline feedstock in all experiments. Argon (99.999 vol %) and oxygen (99.5 vol %) (both from Air Products and Chemicals) were used in the experiments. Steam was produced from deionized water and introduced into the reactor using a precision syringe pump (Cole Palmer) and an evaporator. Several Ni- and Fe-based catalysts used in these experiments were obtained from Sud-Chemie and Alfa Aesar. Alumina-supported (0.5 and 1 wt %) Pt, Pd, Ru catalysts were obtained from Aldrich Chemical Co., Rh (5 wt %)/Al_2O_3 from Strem Chemicals and Ir (1 wt %)/Al_2O_3 from Alfa Aesar. The catalysts were used in the form of pellets 10-18 mesh. A catalyst (0.5 g) was placed inside a quartz micro-reactor (o.d. = 1 cm) and purged with Ar at 600 ◦C for 1 hr before the experiments. The reactor temperature was controlled using a type K thermocouple and Love Controls temperature controller. All the experiments were conducted at the atmospheric pressure. The flow rate of CH_4-CO_2 mixture into the reactor was 10 ml/min. The amount of carbon on the catalyst surface after the reforming experiments was determined by quantitatively combusting carbon in oxygen atmosphere and measuring the amount of CO

and CO_2 produced. The gaseous products were analyzed gas chromatographically using two SRI-8610A GC-TCD instruments: the first GC used Ar as carrier gas and silica gel as packed column, and the second one used He and Hayesep D_B column.

Results and Discussion

Direct Reformation of Landfill Gas

Landfill gas (LFG) and biogas (BG) present a very important source of renewable hydrogen. LFG and BG are complex gaseous mixtures containing methane and CO_2 as major components along with small amounts of H_2S and a variety of organic (e.g., alcohols, organic acids, esters) and element-organic (e.g., S-, N-, Si-containing) compounds. Methane concentrations in LFG and BG vary in the range of 40 to 70 vol % (the balance being mostly CO_2). According to a recent study, only small portion (330 out of 2100) landfill sites in the U.S. utilize LFG to generate heat or electricity, and over 500 landfills flare or burn the gas outright (ref. 1).

In principle, CO_2, H_2S and other contaminants could be removed from LFG and BG feedstocks using off-the-shelf technologies, thus leaving behind relatively pure methane that can be converted into hydrogen via steam methane reforming (SMR) process. However, in many cases this may not be economically and environmentally advantageous option, especially when the resources are not large enough or the sources are located in remote areas. From this point of view, it would be more advantageous to directly process (or reform) LFG or BG into synthesis gas (SG) and further to pure hydrogen that could be used by end users (e.g., in transportation or for on-site generation of heat and electrical energy using energy efficient fuel cells). Although the extensive resources of LFG and BG are available, no large-scale commercial hydrogen production process has been implemented yet. As an example, in Florida 59 landfill sites generate 1.6 mln m^3/day LFG (in methane equivalent, (ref. 2)), that can yield close to 100,000 tons of hydrogen per year.

CO_2 reforming (sometimes called, “dry” reforming) of methane occurs at elevated temperatures according to the following chemical equation:

$$CH_4 + CO_2 \rightarrow 2H_2 + 2CO \qquad \Delta H_{298} = 247 \text{ kJ/mol} \qquad (1)$$

This is an endothermic reaction that operates at the temperature range of 850 to 950 ◦C and produces SG with the H_2:CO ratio of approximately 1:1. Extensive studies on CO_2 reforming of methane using various catalysts have been reported in the literature (e.g., (refs. 3,4)). The technical difficulties associated with direct reformation of LFG or BG into SG stem mainly from two factors: (i) presence of potentially harmful impurities (S-, N-, Si- and halogen-containing compounds) that could easily deactivate catalysts, and (ii) source non-uniformity. In principle, the harmful contaminants could be efficiently removed from LFG or BG before the reforming stage using conventional (e.g., off-the-shelf scrubbers) or innovative (e.g., CO_2 Wash Process (ref. 5)) technologies.

Due to the fact that methane is the major component in LFG and BG (usually, $[CH_4] \geq 50$ vol %), an undesirable and potentially detrimental methane decomposition reaction may occur at the operating temperatures of the reforming process:

$$CH_4 \rightarrow C + 2H_2 \qquad \Delta H^\circ = 76 \text{ kJ/mol} \qquad (2)$$

The product carbon (or coke) blocks active sites of the catalyst leading to its rapid deactivation. It is noteworthy that the possibility of carbon deposition on the catalyst surface exists even when equimolar CH_4-CO_2 mixtures are used as a feed. It has been reported that Ni-, Fe- and Co-based catalysts are particularly efficient in catalyzing methane decomposition reaction (ref. 6). To prevent catalyst deactivation due to carbon deposition and to reform the excessive amount of methane in LFG or BG, additional CO_2 or steam should be added to the feedstock. To produce pure hydrogen, the SG has to be further processed by water gas shift (WGS) reaction (3) followed by a gas separation stage.

$$CO + (H_2O)_g \rightarrow H_2 + CO_2 \qquad \Delta H^\circ = -41.5 \text{ kJ/mol} \qquad (3)$$

The combination of high and low temperature WGS steps allows reducing CO concentration in SG down to less than 0.1 vol %. At the final gas separation stage of the process, a pressure swing adsorption (PSA) unit produces hydrogen with greater than 99.99 vol % purity.

Chemical Equilibrium Considerations

Aspen Technology's AspenPlus chemical process simulation (CPS) platform was used to determine equilibria of CO_2-methane mixtures. The reforming reactions were modeled using a Gibbs reactor minimizing the free energies in order to calculate the conversion rates at given operating conditions. The input parameters were: feed composition and flow rate, inlet temperature and pressure, and reactor temperature and pressure. Figure 2 depicts the equilibrium concentrations of reaction products produced from CH_4-CO_2 and CH_4-CO_2-H_2O mixtures at the temperature range of 600 to 1200 K and 1 atm pressure. The feedstock compositions corresponded to the reacting mixtures with the molar CH_4/CO_2 ratios of 1 and 1.3 (the rationale for this will be discussed in the next section).

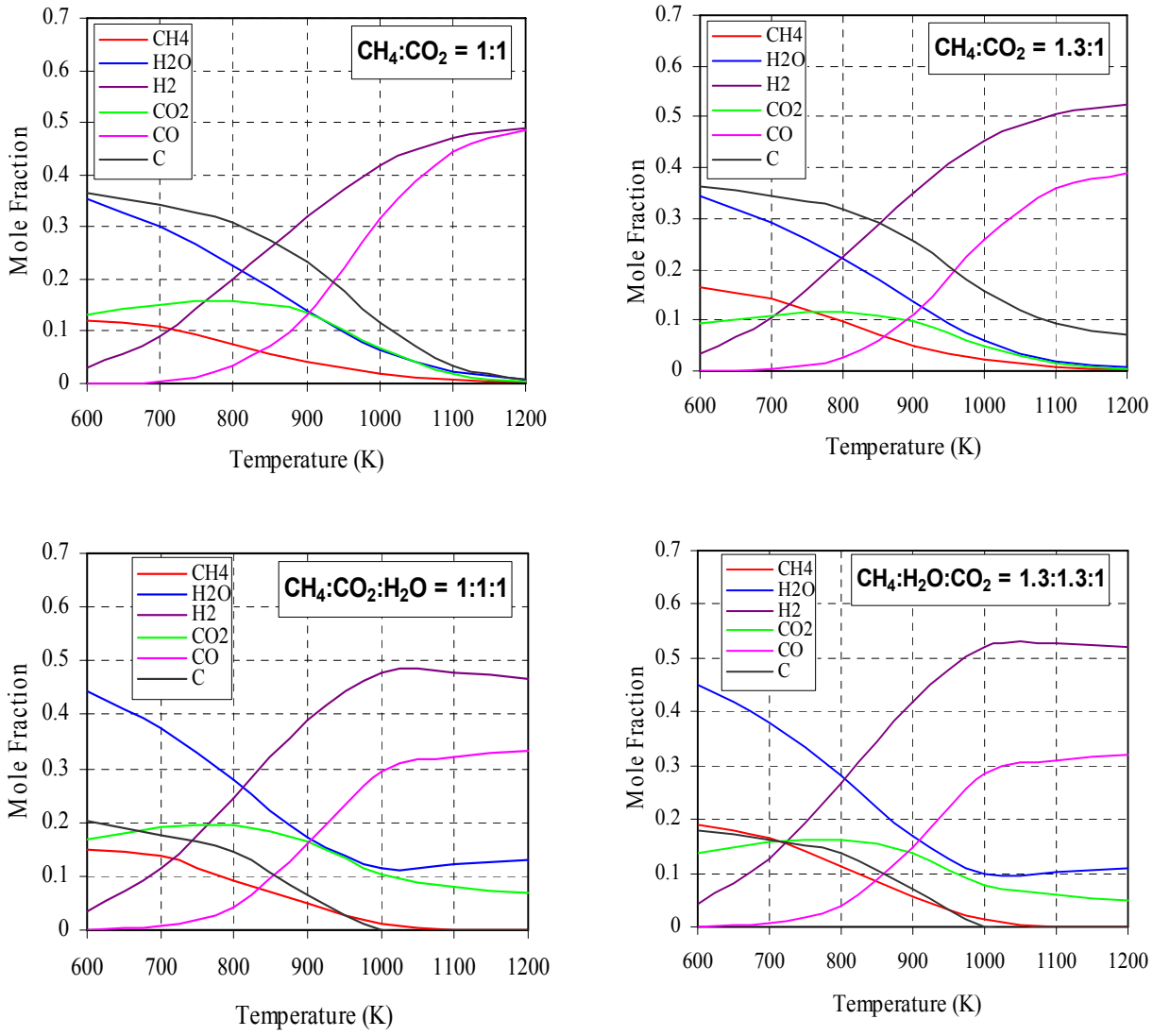

Figure 2.—Equilibrium compositions of CH_4:CO_2 and CH_4:CO_2:H_2O mixtures at P = 1 atm.

It is evident from the figure 2 that elemental carbon exists as one of the major products of CH_4-CO_2 reforming reaction in the entire range of temperatures examined. In the case of equimolar (i.e., CH_4/CO_2 = 1:1) reacting mixture, carbon practically disappears at $T \geq 1200$ K, whereas for the CH_4/CO_2 = 1.3:1 mixture a substantial amount of carbon remains in the products mix at T = 1200 K and higher. It is noteworthy that the latter mixture produces SG with the elevated H_2/CO ratio of ~1.4 (compared to SG produced from the equimolar mixture).

Apparently, the presence of both carbon and additional hydrogen in the products from CH_4/CO_2 = 1.3:1 mixture could be attributed to the contribution by the methane decomposition reaction (2). Two lower plots in figure 2 demonstrate the effect of steam on the distribution of the reaction products obtained from CH_4:CO_2:H_2O = 1:1:1 and CH_4:H_2O:CO_2: = 1.3:1.3:1 mixtures (note that in both cases molar ratio CH_4:H_2O = 1). For both systems, the addition of steam eliminates carbon lay down at $T \geq 1000$ K and complete conversion of methane at $T \geq 1050$ K. The presence of steam also results in a significant increase in H_2/CO ratio in SG (in both cases).

Experimental Studies of 3.2 Catalytic Reformation of CH_4-CO_2 and CH_4-CO_2-H_2O Mixtures

Figure 3 depicts the schematics of the laboratory scale unit used for catalytic reforming of CH_4-CO_2 gaseous mixtures mimicking LFG. The laboratory scale experimental unit for catalytic reforming of CH_4-CO_2 gaseous mixtures consists of three main sub-systems: (i) metering and delivery of gaseous feedstocks and steam, (ii) catalytic reformer, (iii) gas conditioning (including low and high temperature water gas shift reactors, (iv) hydrogen purification, and (v) analytical sub-system.

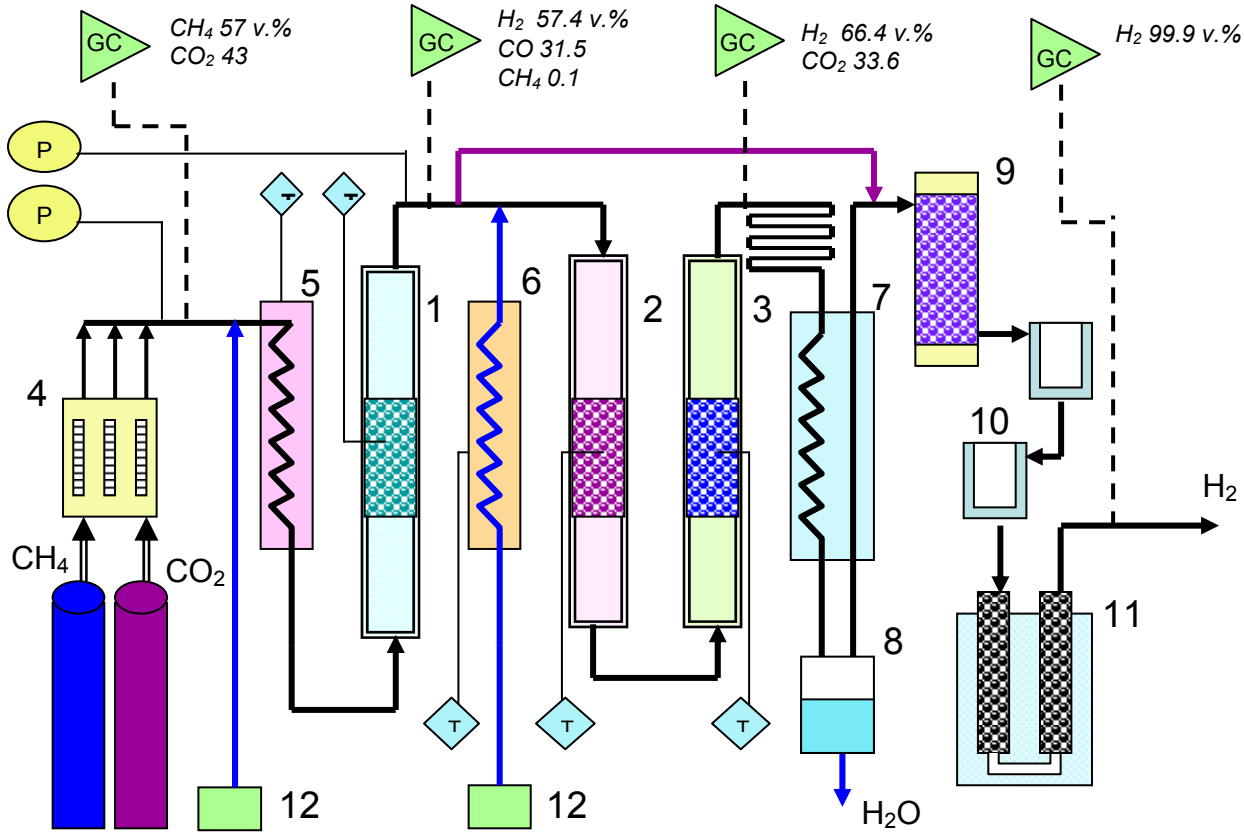

Figure 3.—Schematic diagram of experimental unit for catalytic reforming of CH_4-CO_2 gaseous mixtures. 1- reactor (reformer), 2- HT shift reactor, 3- LT shift reactor, 4- gas metering system, 5- pre-heater, 6- steam generator, 7- condenser, 8- water collector, 9- adsorbent, 10- cryo-trap, 11- cryogenic adsorption system, 12- water pump. G denotes GC analysis of the gaseous mixture and provides its composition; T- temperature controllers, P- pressure gauges.

We have conducted a series of experiments on catalytic reformation of CH_4-CO_2 and CH_4-CO_2-H_2O mixtures (in both cases, the molar ratio of CH_4/CO_2 = 1.3). This particular ratio mimics that of a LFG from the local landfill site in Cocoa, Florida. For the sake of simplicity, N_2, O_2 and minute amounts of H_2S and other impurities were not included in the tested feedstock. The objectives of this study were to: (i) determine the catalytic activity and selectivity of a number of catalysts for CO_2 reforming of CH_4, (ii) quantify the extent of catalyst deactivation due to carbon lay down, and (iii) determine the effect of steam on catalyst activity and stability.

Figure 4 depicts the experimental data for catalytic reformation of CH_4-CO_2 mixture (56.9-43.1 vol %) over alumina-supported Ru (left) and Ni (right) catalysts at 850 ◦C.

As illustrated in the figure 4, the catalysts behave differently. In the case of Ru-catalyst, CH_4-CO_2 mixture yielded SG with practically equimolar concentrations of H_2 and CO and an appreciable amount (~9 vol %) of unconverted methane. The composition of SG is consistent with the following chemical reaction:

$$1.3CH_4 + CO_2 \rightarrow 2H_2 + 2CO + 0.3CH_4 \qquad (4)$$

The amount of carbon detected on the surface of Ru-catalyst during 5 hr experiment corresponded to the carbon yield of 0.039 mol % (per total amount of converted methane). The data point to a negligible contribution of methane decomposition reaction to Ru-catalyzed reforming process. It should be mentioned that the observed behavior was typical of all the noble metal-based catalysts tested, including Pt, Pd, Rh, and Ir catalysts (with some insignificant variations in activity). Fe-based catalysts demonstrated relatively low catalytic activity for CH_4-CO_2 reforming reaction.

In striking contrast, NiO (1-15 wt %)/Al_2O_3 catalyst produced the SG with hydrogen as the major component (>50 vol %) and a small amount of unconverted methane (<4 vol %). Furthermore, the composition of the effluent gas was time-dependent with the hydrogen concentration dropping noticeably during the last 3 hr of the experiment. Amount of carbon accumulated on the catalyst surface after 5 hr corresponded to a methane-to-carbon conversion yield of 15.3 mol %. After the reaction, the catalyst completely disintegrated (from pellets into a fine powder). These experimental observations evidence a major role played by methane decomposition reaction in the overall reforming process (although, the contribution of Boudouard reaction: $2CO \rightarrow C + CO_2$ can not be excluded). Carbon produced by methane decomposition reaction blocks catalytic active sites causing gradual deactivation of the catalyst. Disintegration of Ni- catalyst can be explained by the growth of carbon particles inside the catalyst pores.

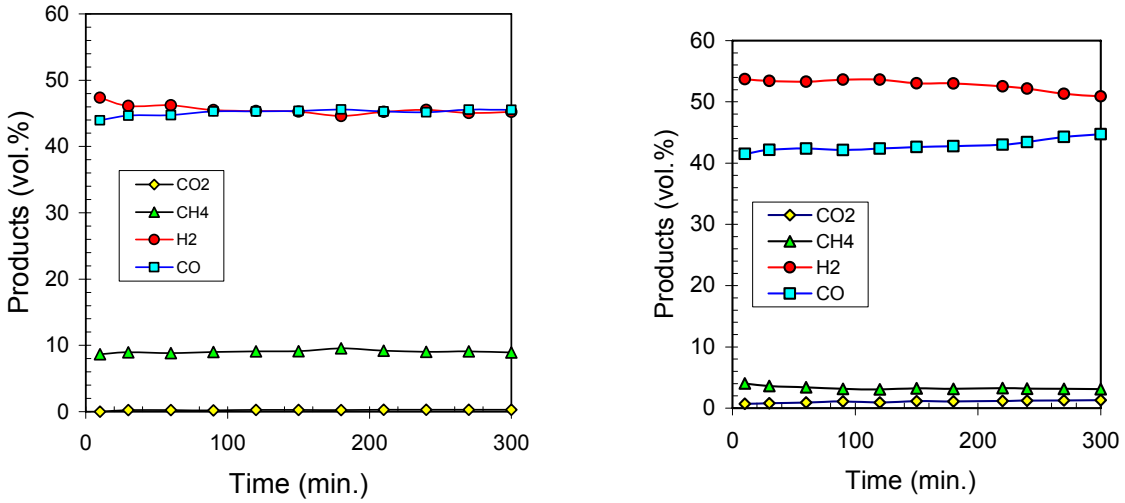

Figure 4.—Catalytic reforming of CH_4-CO_2 (56.9-43.1 vol %) mixture over Ru (0.5 wt %)/Al_2O_3 (left) and NiO(1-15 wt %)/Al_2O_3 Catalysts at 850 °C.

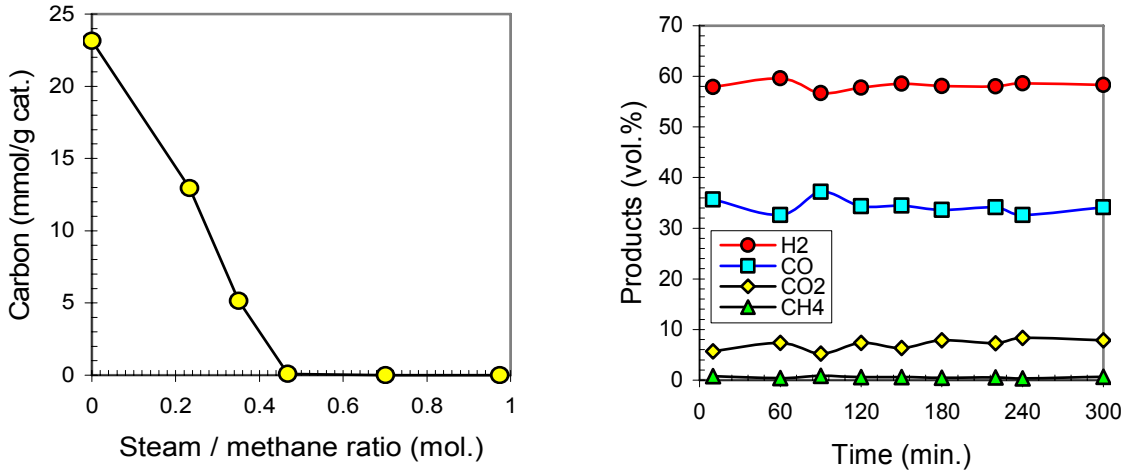

Figure 5.—Effect of steam on CO_2 reforming of methane over NiO (1 to 15 wt %)/Al_2O_3 Catalyst at 850 °C (using the feedstock with CH_4/CO_2 = 1.3 ratio).

It is interesting to compare the above data for Ru- and Ni-catalyzed reforming reactions with the results of the thermodynamic analysis for the CH_4/CO_2 = 1.3:1 mixture (see fig. 2, upper right). It is evident that the analytical data are more consistent with the results of Ni-catalyzed CH_4-CO_2 reforming (particularly, at the onset of the experiment), rather than the reaction catalyzed by the Ru-catalyst. This is an indication of high catalytic activity of Ni-catalyst for both CH_4-CO_2 reforming and methane decomposition reactions; but this also points to quite low selectivity of Ni-catalyst toward reforming reaction. In contrast, Ru-catalyst demonstrates both high activity and selectivity for CH_4-CO_2 reforming reaction (hence, a relatively low activity for the methane decomposition reaction).

In order to prevent carbon lay down on the NiO/Al_2O_3 catalyst surface, steam was added. We quantified the effect of steam on the reforming reaction by conducting several experiments with variable steam/methane (S/M) ratio. Figure 5 (left) depicts the extent of carbon lay down on the Ni-catalyst surface as a function of S/M ratio in the feed. It is apparent that the amount of carbon formed diminishes drastically with the increase in S/M ratio, and at S/M >0.5 practically all carbon disappears. Figure 5 (right) shows the composition of gaseous products obtained by processing the feedstock with the composition of CH_4:H_2O:CO_2: = 1.3:1.3:1 (note that S/M ratio is 1:1).

The average concentrations of hydrogen and CO in the effluent gas were 58 and 34.5 vol %, respectively. Note that the H_2/CO ratio in the presence of steam increased appreciably compared to the experiment where no steam was added (from H_2/CO$\approx$1.2 to $\approx$1.7). Carbon dioxide concentration in the SG also increased, most likely, due to competition between steam and CO_2 for methane molecules. No carbon deposits were detected on the catalyst surface after 5 hr (long-duration experiments are now in progress). There were no signs of Ni-catalyst disintegration after the reforming experiments involving steam.

The composition of SG obtained by Ni-catalyzed reforming reaction with the addition of steam is in a good agreement with the thermodynamic equilibrium calculations at the same temperature (for dry SG) (see fig. 2, lower right). This is an indication of high catalyst activity at given operating conditions of the process (temperature, pressure and steam/methane ratio). The experiments indicated that steam/methane ratios of 0.5:1 in the CH_4-CO_2-H_2O feedstock would be adequate to prevent catalyst deactivation and ensure high overall methane conversion yield. It should be noted that this amount of steam is significantly less than that normally used in the conventional SMR process, where S/M ratios are in the range of 3 to 4.

Based on the results of bench-scale experimental studies of CH_4-CO_2 reforming we have designed and fabricated a hydrogen production unit with the capacity of 1 SCFM (see fig. 6). The results of field testing of the 1 SCFM unit will be reported in next year's final report.

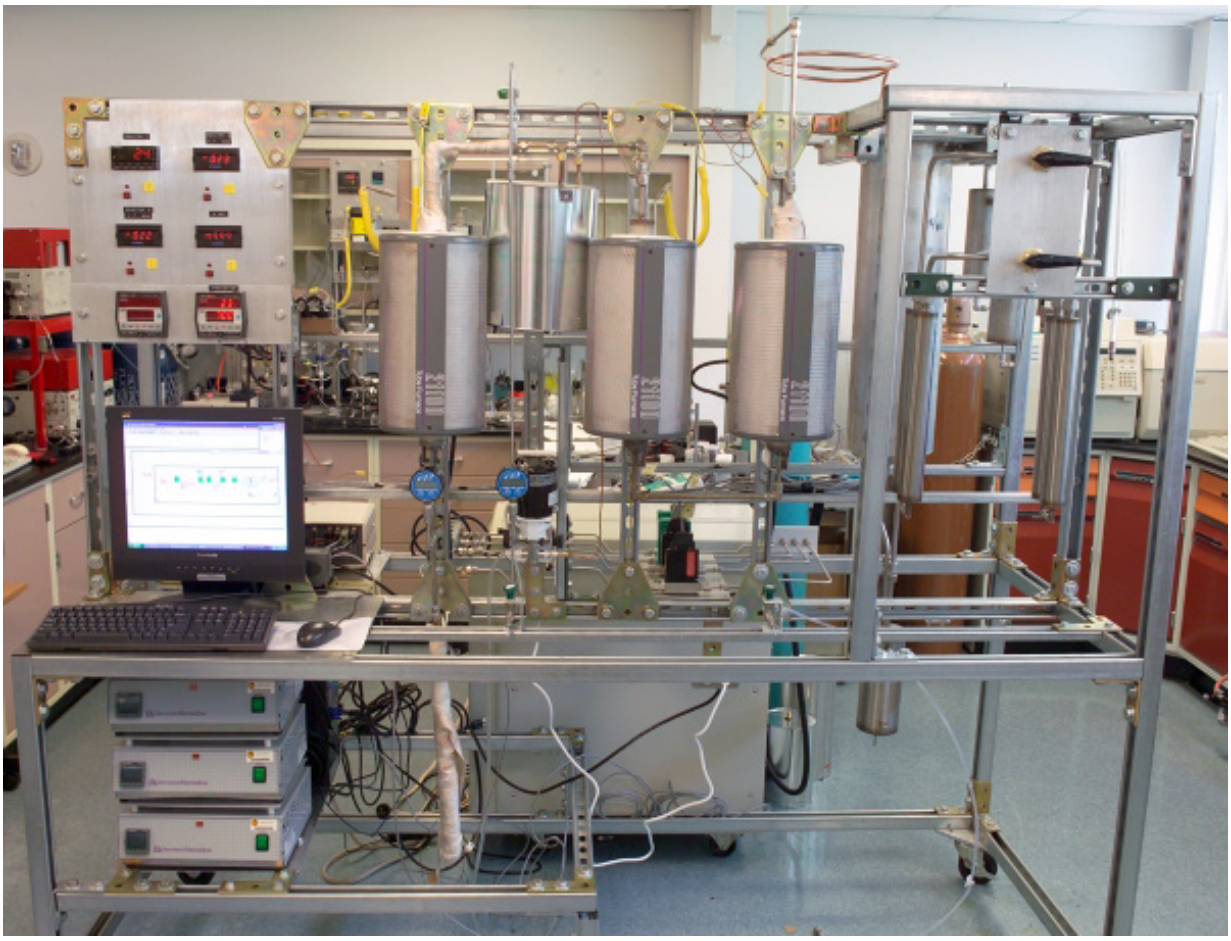

Figure 6.—Hydrogen production unit with the capacity of 1 SCFM.

Catalytic Pyrolysis of Natural Gas

Background

Currently, most of the industrial hydrogen production is based on steam methane reforming (SMR) process, which is a source of significant CO_2 emissions into the atmosphere. A typical hydrogen plant with the capacity of one million m^3 of hydrogen per day produces 0.3 to 0.4 million standard cubic meters of CO_2 per day, which is normally vented into the atmosphere. Different options to mitigate the CO_2 emission problem associated with fossil-based hydrogen production are being actively discussed in the literature (e.g., (ref. 7)). One approach that recently attracted the attention of researchers is CO_2-free production of hydrogen by thermal decomposition (or pyrolysis) of methane (refs. 8 to 10):

$$CH_4 \rightarrow C + 2H_2 \qquad \Delta H^\circ = 75.6 \text{ kJ/mole} \qquad (5)$$

Due to very strong C-H bonds methane decomposition occurs at elevated temperatures (>1000 °C). Different transition metal catalysts (e.g., Ni, Fe, Co, Pd) have been used to reduce the maximum temperature of methane thermal decomposition. The major problems associated with the use of metal catalysts relate to a catalyst deactivation (due to blocking of active sites by the carbon deposits) and technical difficulties with catalyst-carbon separation. The use of carbon-based catalysts offers some advantages over metal catalysts due to their availability, durability and low cost. In contrast to metal-based catalysts, carbon catalysts are sulfur resistant and can withstand much higher temperatures (in

excess of 1000 °C). Furthermore, there will be no need for the separation of a carbon product from the catalyst. The technical feasibility of using carbon materials as catalysts for methane decomposition reaction is discussed in several publications (e.g., (ref. 11)). The concept is based on thermocatalytic decomposition (TCD) of methane over catalytically active carbon particles with the production of hydrogen-rich gas and carbon deposited on the surface of original carbon particles. The data on catalytic activity of a variety of carbon materials of different origin and structure, including a wide range of activated carbons, carbon blacks, micro-crystalline graphites, nanostructured carbons, toward methane decomposition reaction is reported in (ref. 12).

Consideration of Heat Input Options for Methane Decomposition Process

Methane decomposition is a moderately endothermic reaction: the thermal energy requirement per mole of hydrogen produced is only 37.8 kJ/mole H_2 compared to 63 kJ/mole for SMR. Less than 10 percent of the methane heating value is needed to drive the endothermic process. Figure 7 (a), (b) and (c) illustrates three possible technological concepts of heat supply to the TCD process.

According to the option (a) the heat source is located inside the reaction zone. It could be a heat pipe, a heat exchanger or a catalytic burner that uses NG or a portion of hydrogen product as a fuel. In the first two cases the heat source could be located outside the reactor with heat carried to the reactor by a heat carrier, e.g., liquid metals. As an example of this approach, sodium-based heat pipes have been used as a mode of efficient heat transfer in methane steam reformers (ref. 13). In the concept (b), the process heat is introduced to the reactor by means of externally heated catalyst particles acting as a heat carrier (similar to fluid catalytic cracking process widely used in refineries). The process employs two fluid-solids vessels: a reactor and a heater with carbon particles circulating between the vessels in a fluidized state. Catalyst particles are heated (e.g., by burning part of carbon product or by hot combustion gases) and carry the necessary heat to the reactor to achieve NG decomposition. This technological concept has been described in our earlier publications (e.g., (ref. 7)).

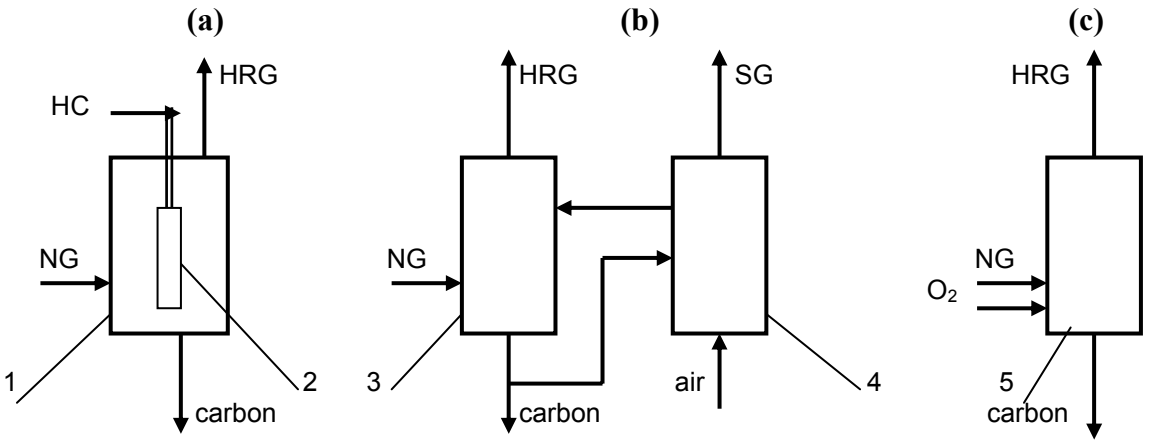

Figure 7.—Three process heat input options for thermocatalytic decomposition of methane. HRG- hydrogen-rich gas, SG- stack gases, HC- heat carrier. 1-methane decomposition reactor, 2-reactor heater, 3-fluidized bed reactor, 4-catalyst particles heater, 5-autothermal reactor.

According to the concept (c), a relatively small amount of oxygen is fed to the reactor along with the methane feedstock to generate necessary heat to carry out the endothermic methane decomposition reaction. One can notice that the concept looks similar to a well-known partial oxidation (POx) process. There is, however, a fundamental disparity between the two processes. In particular, POx process carries out the conversion of methane into synthesis gas and, therefore, it requires relatively large amount of oxygen (normally, $O_2/CH_4 \geq 0.5$). In contrast, the objective of oxygen-assisted methane decomposition is to maximize the yields of both hydrogen and carbon products by introducing oxygen in the quantity just enough to sustain the endothermic methane decomposition reaction. We call this process "autothermalpyrolysis" (ATP) since it involves the combination of an exothermic (methane oxidation) and endothermic (methane pyrolysis) reactions in one apparatus (similar to autothermal reforming, ATR, where methane oxidation is coupled with SMR). It is evident that this approach would use much less oxygen than ATR or POx, since methane decomposition is almost three times less endothermic (per mole of methane) than SMR, and the reaction does not advance to synthesis gas as a final product. As a result, CO_2 emissions from the process would also be significantly less than from ATR and POx. Advantageously, in ATP process most of the feedstock carbon ends up in the form of elemental carbon rather than CO_2. In this paper we explore some process development issues related to the production of hydrogen and carbon by ATP of methane. In particular, we conduct the thermodynamic analysis of ATP of methane in a wide range of temperatures and pressures with O_2/CH_4 ratio as a variable.

Thermodynamic Analysis of Autothermal Pyrolysis of Methane

AspenPlus chemical process simulator (CPS) was used to conduct thermodynamic analysis of CH_4-χO_2 system. The reactions involved were modeled using a Gibbs reactor to minimize the free energy in order to calculate thermodynamic parameters of the process at the given operating conditions. Input parameters are: a feed (CH_4-χO_2) composition, inlet pressure and temperature, and reactor temperature and pressure. Peng-Robinson property package was used for the reaction equilibrium calculations. Methane conversion, products yield, pyrolysis gas composition, process enthalpy, entropy and Gibbs energy flows as a function of temperature, pressure and O_2/CH_4 ratio (χ) have been determined. The temperature range of 300 to 1200 ◦C, the pressure range of 0.2 to 2.5 MPa and O_2/CH_4 ratio of χ = 0–1.5 (mol./mol.) were chosen for the thermodynamic analysis of the process. The following figures illustrate the results of the analysis.

Figure 8 depicts 3D plots of methane conversion as a function of temperature and O_2/CH_4 ratio at two baseline pressures: P = 200 kPa and 2.5 MPa. It is evident from figure 8 that in both cases methane conversion increases drastically with the increase in both T and χ. For example, at P = 200 kPa, T = 850 ◦C and relatively low O_2/CH_4 ratios ($\chi \leq 0.2$) methane conversion reaches up to 90 percent. At P = 2.5 MPa (with the rest of parameters being equal), methane conversion is below 60 percent, which indicates that the process is not favored by elevated pressures.

Figure 9 and 10 depict the temperature dependence of hydrogen and carbon yields at P = 200 kPa and different O_2/CH_4 ratios.

Figure 9 indicates that the hydrogen yield is not appreciably affected by the O_2/CH_4 ratio at $0<\chi<0.5$ in the entire range of temperatures. At $\chi>0.5$ hydrogen yield drops markedly, which is accompanied with the increase in water production yield. In contrast, carbon yield (fig. 10) is quite sensitive to even slight increase in χ value in a whole range of O_2/CH_4 ratios. At $\chi>0.6$ carbon is not present among the reaction products at $\geq$800 ◦C.

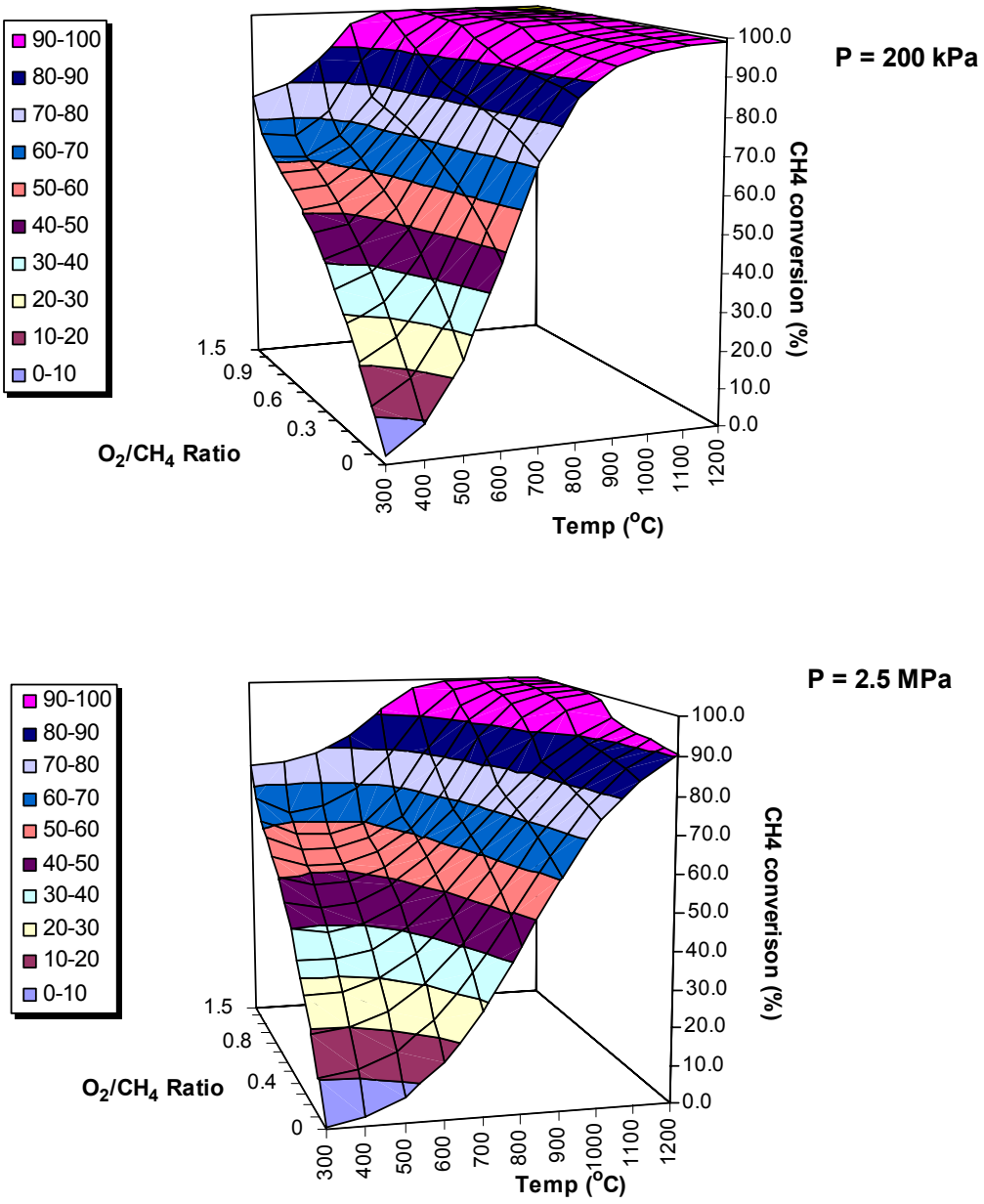

Figure 8.—Methane conversion as a function of temperature and O_2/CH_4 ratio at P = 200 kPa and 2.5 MPa.

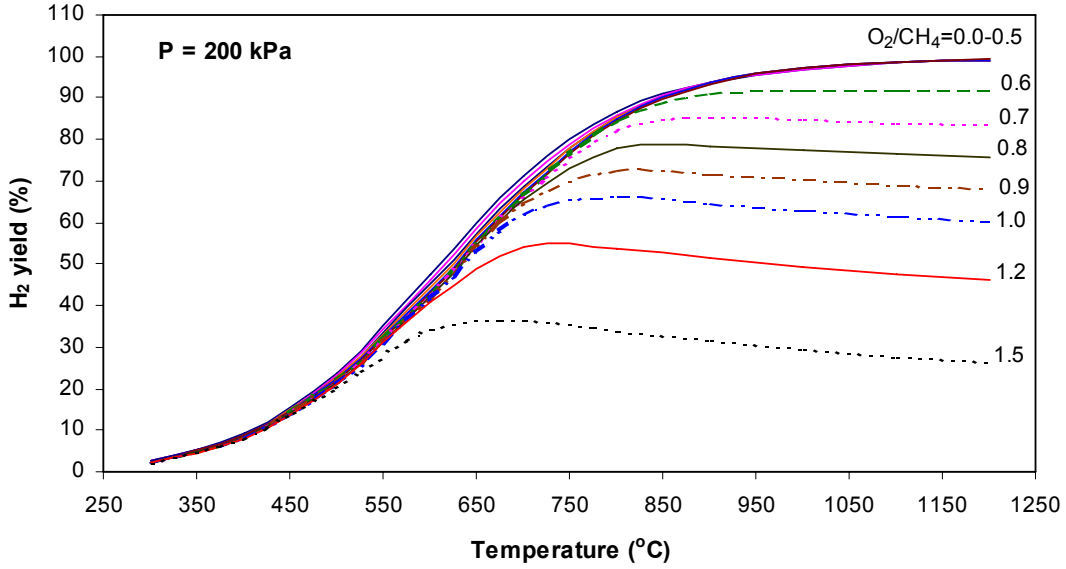

Figure 9.—Temperature dependence of hydrogen yield with O_2/CH_4 ratio as a variable at P = 200 kPa.

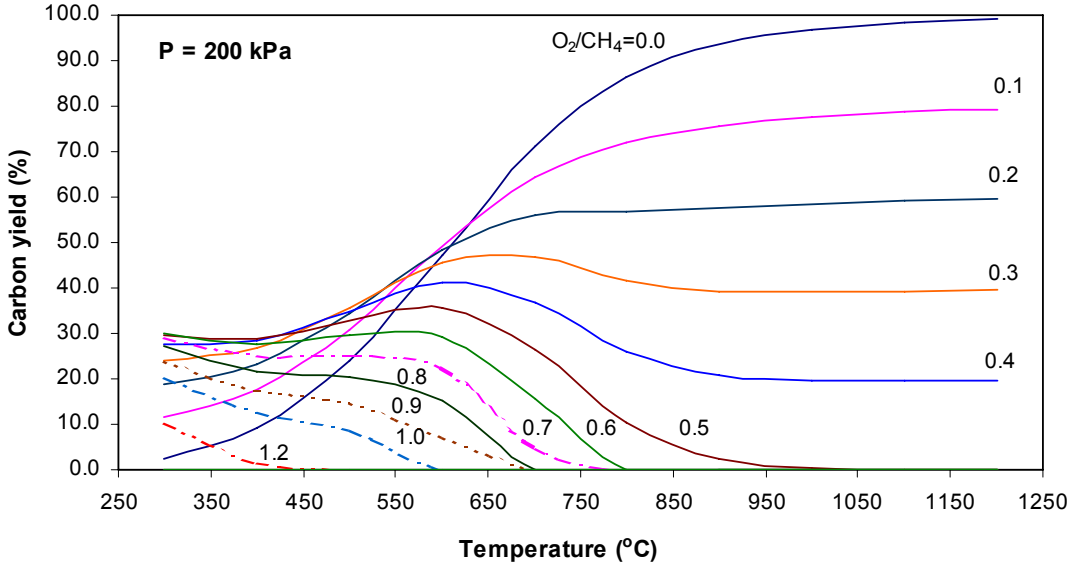

Figure 10.—Temperature dependence of carbon yield with O_2/CH_4 ratio as a variable at P = 200 kPa.

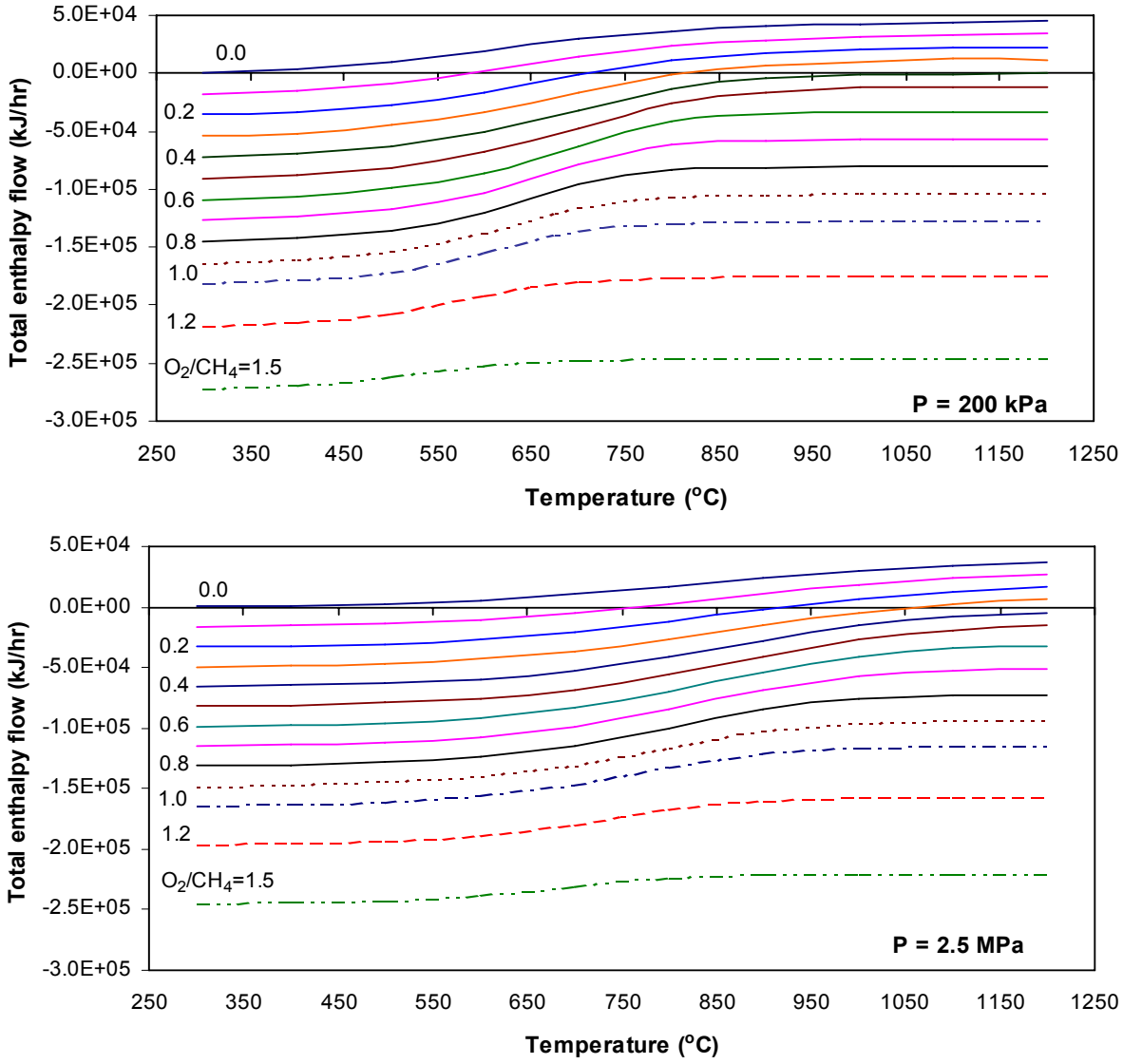

Figure 11.—Total enthalpy flow as a function of temperature at P = 200 kPa and 2.5 MPa. Enthalpy flow relates to 0.45 kmol/hr of CH_4-χO_2 mixture.

Figure 11 depicts the values of total enthalpy flow within the reactor at different temperatures and O_2/CH_4 ratios. The total enthalpy flow rate was calculated as a sum of outlet enthalpies of all products minus sum of inlet enthalpies of CH_4-χO_2 mixtures. A negative enthalpy flow indicates that at the given conditions (χ, T and P) the reactive system produces heat, which obviates the need for the heat input into the reactor. In contrary, positive enthalpy flow indicates that at given conditions a certain amount of thermal energy has to be supplied to the reactor in order to accomplish methane decomposition. It is evident from the figure 11 that for the practical range of temperatures (600 to 900 °C) and pressures of P = 0.2 to 2.5 MPa the enthalpy flow is close to zero at O_2/CH_4 ratio of $\chi \approx 0.2$ (which corresponds to an autothermal regime).

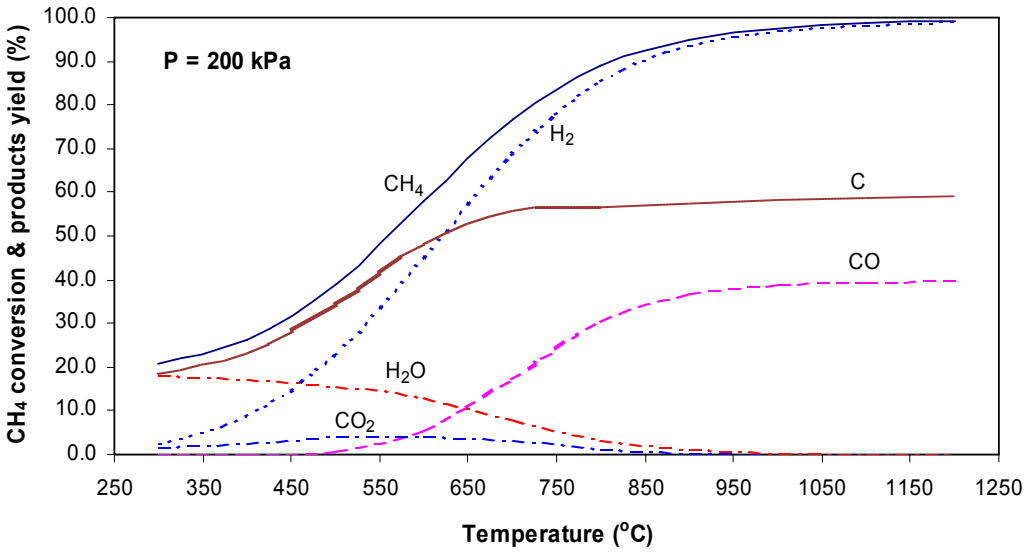

Figure 12.—Methane conversion and products yields as a function of temperature at P = 200 kPa and $\chi \approx 0.2$

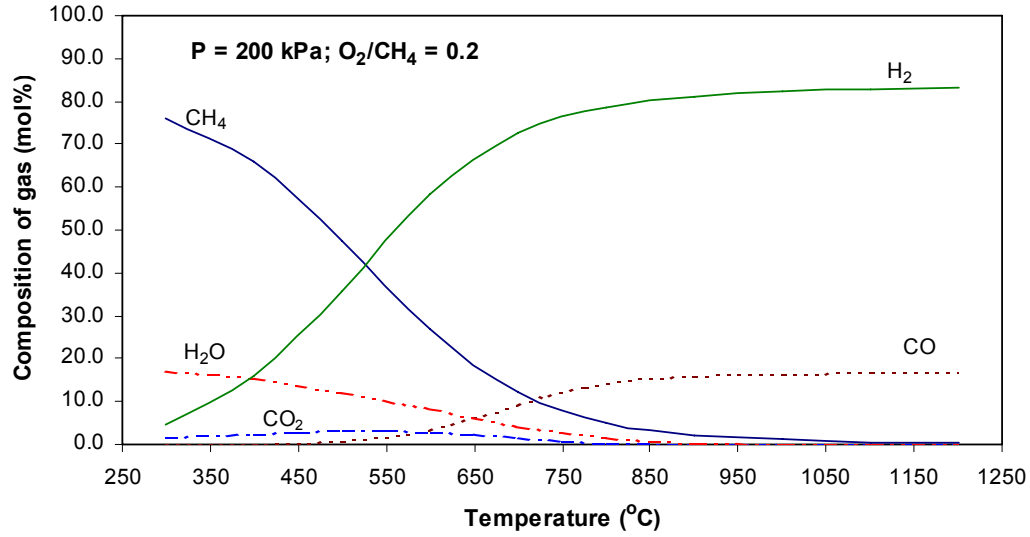

Figure 13.—Composition of gaseous product as a function of temperature at P = 200 kPa and $\chi \approx 0.2$

Figure 12 demonstrates methane conversion and the reaction products yields as a function of temperature at P = 200 kPa and $\chi \approx 0.2$. It can be seen that at T>850 °C hydrogen, carbon and CO are major reaction products and their yields are nearly independent of temperature.

The composition of the pyrolysis gas at P = 200 kPa and $\chi \approx 0.2$ is shown in figure 13. At T>850 °C hydrogen and CO are two main components of the gaseous mixture with the average concentrations of 83 and 17 vol %, respectively, that are nearly independent of the temperature.

At T>850 °C and $\chi \approx 0.2$ the composition of the gaseous product of the reaction is consistent with the following stoichiometric equation:

$$CH_4 + 0.2O_2 \rightarrow 0.4\ CO + 0.6C + 2H_2 \quad (6)$$

It is noteworthy that the concentration of hydrogen in the effluent gas is significantly higher than that of the reformate gas after steam reforming of methane (~52 vol % including water vapor and ~72 vol % on a dry gas basis (ref. 14)). The presence of CO in the gaseous product would require the addition of water-gas shift reactors to the technological chain of the process. At the final stage of the process, high-purity hydrogen (>99.99 vol %) will be recovered from H_2-CO_2 gaseous mixture using a standard pressure-swing adsorption system. Carbon is a valuable byproduct of the process and, if marketed, it could significantly reduce the cost of hydrogen production. The amount of CO_2 emissions from the process could potentially be as low as 0.17 m^3 CO_2/m^3 H_2, which is 2.5 times less than that from the SMR process (0.43 m^3 CO_2/m^3 H_2 (ref. 9)).

Experimental Studies of Catalytic Pyrolysis of Methane

The experimental studies on thermocatalytic pyrolysis of methane were conducted using pure (99.99 vol %) and industrial grade (i.e., pipeline NG) methane. The composition of natural gas used in the experiments is shown in table 1.

TABLE 1.—COMPOSITION OF PIPELINE NG

Composition of NG, ...vol %
N_2 ..... 0.9
CH_4.....93.1
C_2H_6.....4.1
C_3H_8.....0.3
CO_2.....0.9
CH_3SH .....4 ppm

In our previous work we reported the results of catalytic pyrolysis of methane using carbon-based catalysts, e.g., activated carbons (AC), carbon blacks (CB), etc. This year we studied inhouse-prepared proprietary metal-doped carbon (MDC) catalysts. It was found that doping with metal increases the catalytic activity and sustainability of the process. Figure 14 depicts the results of methane decomposition at 900 °C in the presence of MDC at the residence time of 1 and 2.2 s.

It is evident from the figure 14 that at higher residence time (2.2 s) initial hydrogen concentration in the effluent gas reaches up to 83 vol %. This however followed by a decrease in hydrogen yield to a quasi-steady level (hydrogen concentration about 60 vol %). During first hour there was a small amount CO present in the effluent gas, which could be attributed to some residual oxygen in the catalyst. At lower residence time (1 s) (or higher space velocity) the initial concentration of hydrogen in the effluent gas was somewhat lower and the process was not sustainable (i.e., H_2 concentration gradually dropped). This implies that the catalyst needs further improvement in its activity and stability. The work in this area is in progress.

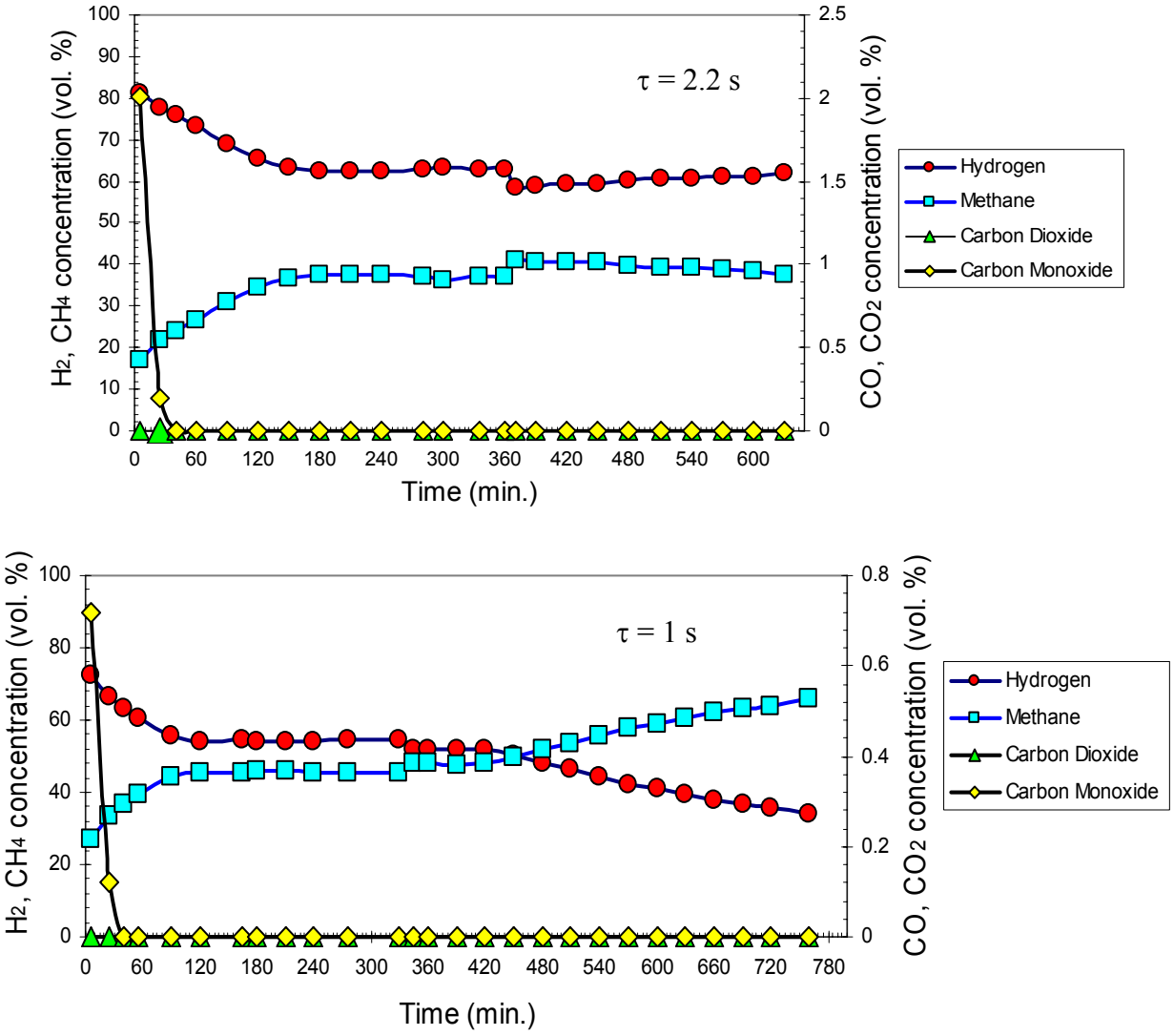

Figure 14.—Catalytic pyrolysis of methane over metal-doped catalyst at 900 °C and residence time of 1 and 2.2 s.

Analysis and Characterization of Carbon Products

Carbon byproduct of the process could play an important role in reducing the cost of hydrogen production. We have previously reported that depending on the operational parameters of the process (temperature, catalyst, feedstock), carbon could be produced in several modifications: amorphous (i.e., carbon black), turbostratic and filamentous carbon. X-ray diffraction (XRD) studies of carbon samples produced by methane decomposition over carbon catalyst revealed ordering in a “columnar” or stacking direction. The d-spacing (lattice spacing) or spacing between plates is practically uniform, so that the (003) columnar reflection is clearly present. Thus, the carbon produced by carbon-catalyzed decomposition of hydrocarbons revealed a graphite-like a-b-c-a type stacking of the carbon ring plates (as opposed to a-b-a-b for pure graphite). The actual d-spacing (d = 3.4948 Å) of this (003) peak is larger than that of the standard graphite structure (d = 3.3480 Å), which indicates that the plates are slightly further apart in the columnar stacking direction. This type of arrangement has been termed in the literature as a turbostratic structure.

Table 2 shows the data on the price and market for carbon products obtained in the process.

TABLE 2.—PRICE, APPLICATION AREA AND MARKET FOR CARBON PRODUCTS

	Turbostratic carbon	Pyrolytic graphite	Carbon filaments
Price, $/ kg	0.3	1-18	>1000
Application	electrodes, composites	aerospace, N-reactors	composites, electronics
Market	4-5 mln ton	N/A	N/A

Carbon samples were analyzed by scanning (SEM) and transmission (TEM) electron microscopy, XRD and focused ion beam (FIB) materials characterization techniques. Figure 15 (images A through E) depict SEM and TEM images of carbon products obtained by thermocatalytic decomposition of methane in the presence of proprietary metal-doped catalysts. It is evident that some of these catalysts produce filamentous forms of carbon. Dark spots on the TEM images are nano-size metal catalyst particles. These metal particles are seeds for the growth of carbon nanotubes. The TEM image (D) shows the fine structure of a multi-wall carbon nanotube. It is apparent that the metal catalyst particle (with the diameter of ~10 nm) is wrapped by about 80 carbon graphene layers. The TEM image (B) shows a bunch of carbon nanotubes with a hollow structure consisting of about 20 graphene layers.

It should be noted that carbon nanotubes and other carbon nano-structures were obtained from non-diluted methane and pipeline quality natural gas using inexpensive sulfur-resistant catalysts. This in contrast to previously reported works where carbon nanotubes were produced from methane-hydrogen mixtures using relatively expensive Ni-based catalysts. Thus, the hydrogen production method developed in this work could be a basis for the production of a value-added byproduct: filamentous carbon, which may significantly improve the commercial potential of the technology.

(a)

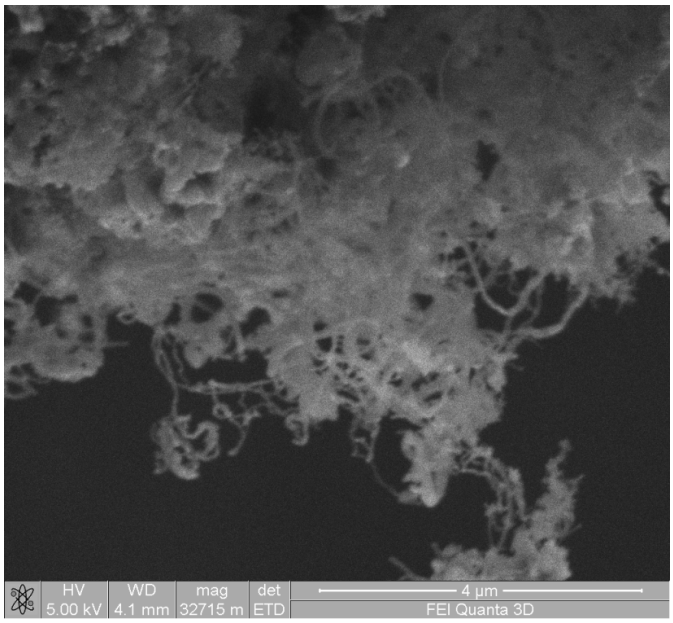

(b)

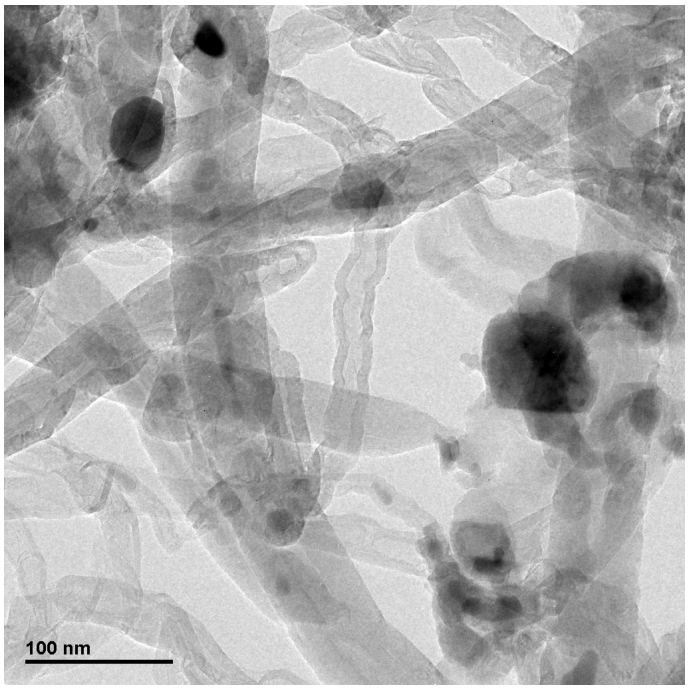

(c)

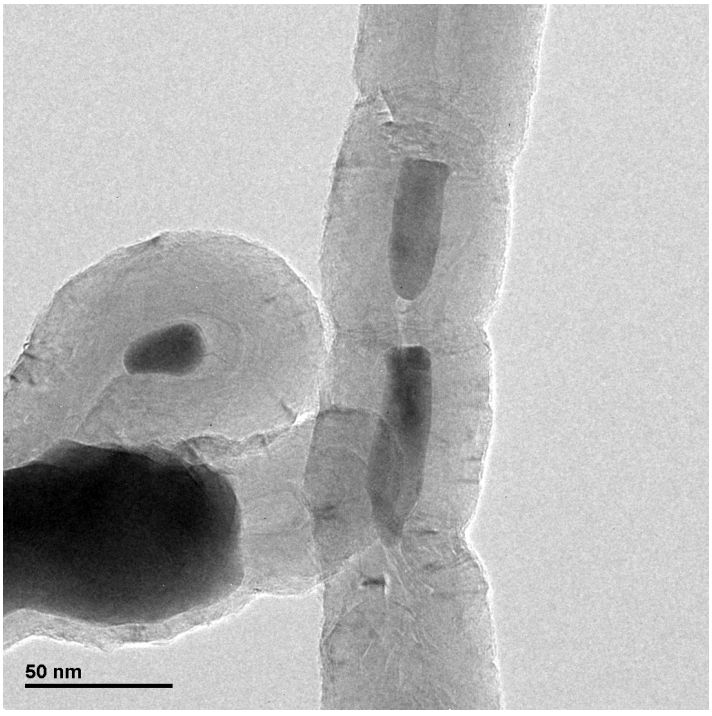

(d)

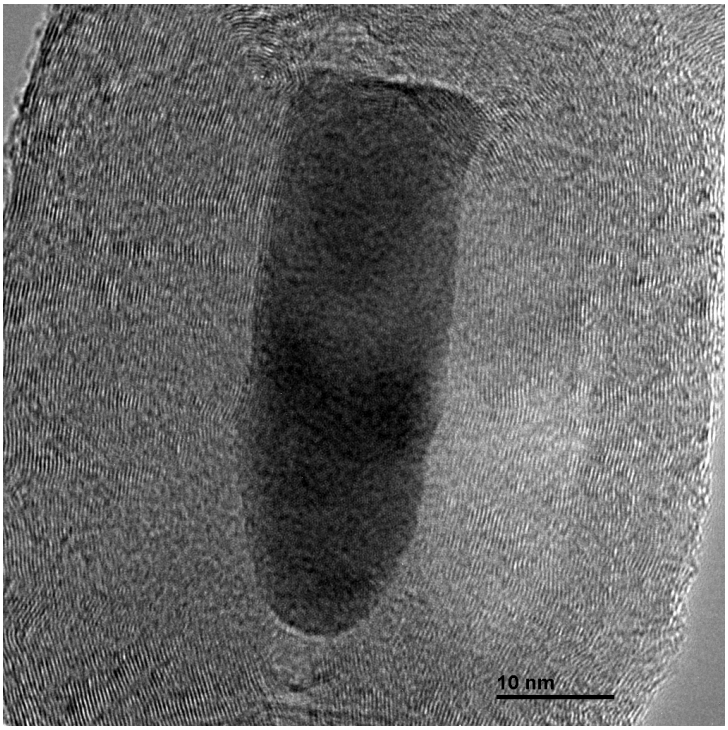

(e)

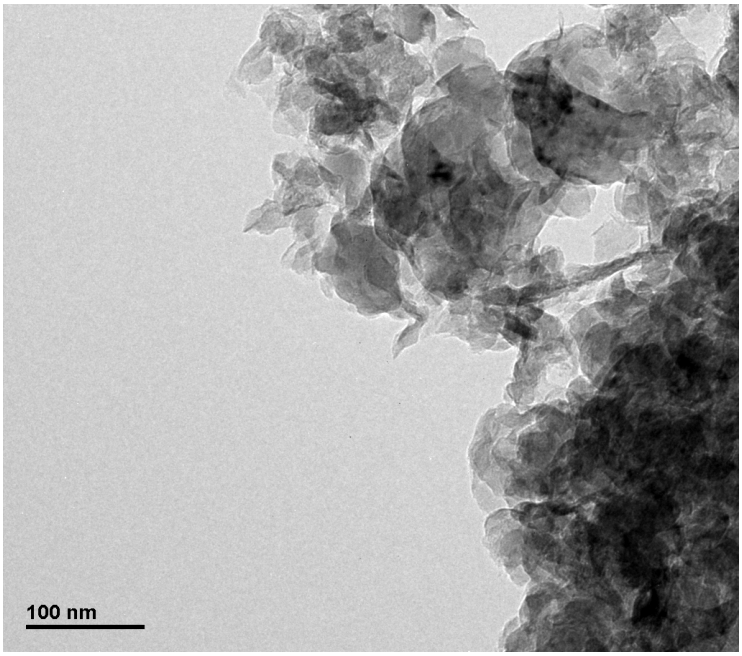

Figure 15.—SEM (a) and TEM (b) to (e) images of carbon products produced by catalytic decomposition of methane.

Summary of Accomplishments

Experimental verification of feedstock-flexible operation of the catalytic reactor was conducted. Hydrogen production via catalytic reforming of methane-containing gases mimicking landfill gas using bench-scale unit was conducted.

Catalytic reformation of CH_4-CO_2 mixtures was studied experimentally and analytically (using AspenPlus). The catalytic activity of a number of commercial and synthesized transition metal catalysts (Ni, Fe, Pt, Pd, Ir, Ru and Rh) were evaluated. Ni-based catalyst was down-selected for further evaluation and the operational conditions for its efficient and stable operation were determined. The thermodynamic analysis of methane pyrolysis in autothermal regime (in presence of relatively small amounts of oxygen) using AspenPlus chemical process simulator was conducted. Methane conversion, products yields, process enthalpy and Gibbs energy flows as a function of temperature, pressure and O_2/CH_4 ratio have been determined. The experimental data were in a fairly good agreement with the simulation results.

Efficient catalysts for methane pyrolysis based on high-surface area carbons and metal-doped carbons have been developed and tested. The technical feasibility of the production of high-value filamentous carbon products (multi-wall carbon nanotubes) from non-diluted methane and pipeline quality NG was demonstrated.

A hydrogen production demonstration unit with the capacity of 1 SCFM (5.6 kW_{th}) was designed and fabricated. The main components of the system (reformer, gas conditioning and separation systems) were tested under simulated operational conditions.

Carbon products of the catalyzed methane pyrolysis process were analyzed and characterized using several materials characterization techniques (SEM, TEM, FIB, XRD).

Publications Related to This Project

1. N. Muradov, A. Raissi, T. Robertson, “Hydrogen Production via Catalytic Reformation of Low-quality Methane Containing Feedstocks,” *Hydrogen Power Theor. Eng. Solutions Symp.*, Italy, 2003
2. N. Muradov, F. Smith, “Thermocatalytic Hydrogen Production from Natural Gas with Drastically Reduced CO_2 Emissions,” *Hydrogen Power Theor. Eng. Solutions Symp.,* Porte Conte, Italy, 2003
3. N. Muradov, C. Huang, A. Raissi, F. Smith, “Hydrogen Production from Natural Gas with Reduced CO_2 Emissions,” *Proc. XV World Hydrogen Energy Conf*., Yokohama, Japan, 2004
4. N. Muradov, A. Raissi, F. Smith, M. Elbaccouch, “Hydrogen Production via Catalytic Reformation of Landfill Gas and Biogas,” *Proc. XV World Hydrogen Energy Conf*., Yokohama, Japan, 2004
5. N. Muradov, F. Smith, A. Raissi, “Catalytic Properties of Carbons for Methane Decomposition Reaction,” *Carbon for Catalysis International Symposium,* Lausanne, Switzerland, 2004
6. N. Muradov, F. Smith, A. Raissi, “Catalytic Activity of Carbons for Methane Decomposition Reaction,” *Catalysis Today*, accepted for publication
7. *U.S. Patent No. 6,670,058 (2003),* “Thermocatalytic Process for CO_2-free Production of Hydrogen and Carbon from Hydrocarbons,” N. Muradov
8. *U.S. Patent Application No. 60/578212 (2004),* “A Method for Zero-emission Liquid Hydrogen Production from Methane and Landfill Gas,” C. Huang, A. Raissi, N. Muradov

Acknowledgments

This work was supported by the National Aeronautics and Space Administration (NASA) Glenn Research Center under the contract No. NAG3–2751. We thank Dr. Ali T-Raissi for helpful discussions.

References

9. Janis Keating: Cheaper energy by going to waste. Distributed Energy, 22, January/February 2004
10. Landfill Gas-to-Energy Project Opportunities. EPA 430-K-99-007, 1999.
11. Mariana Souza, Donato Aranda, Martin Schmal: Reforming of methane with carbon dioxide over $Pt/ZrO_2/Al_2O_3$ catalysts. J. Catalysis, 204, 498, 2001
12. Shaobin Wang, Max Lu: Catalytic activities and coking characteristics of oxides-supported Ni catalyst for CH_4 reforming with CO_2. Energy and Fuels, 12, 248, 1998.
13. Acrion’s CO_2 WashTM Process, http://www.acrion.com.CO2wash.htm
14. Michael Callahan: Catalytic pyrolysis of methane and other hydrocarbons. Proc. Conf. on Power Sources, 26, 18, 1974Nazim Muradov: Hydrogen via methane decomposition: an application to decarbonization of fossil fuels. Int. J. Hydrogen Energy 2001; 26:1165

16. Nazim Muradov: How to produce hydrogen from fossil fuels without CO_2 emission. Int. J. Hydrogen Energy 1993; 18: 211
17. Meyer Steinberg: Fossil fuel decarbonization technology for mitigating global warming. Int. J. Hydrogen Energy 1999; 24: 771,
18. L. Fulcheri, Y. Schwob: From methane to hydrogen, carbon black and water. Int. J. Hydrogen Energy, 1995; 20: 197.
19. Nazim Muradov: CO_2-free Production of hydrogen by catalytic pyrolysis of hydrocarbon fuel. Energy and Fuels 1998; 12:41
20. Nazim Muradov: Catalysis of methane decomposition over elemental carbon. Catalysis Commun. 2001; 2: 89
21. James Richardson: A gas-fired heat pipe reformer for small scale hydrogen production, Natural Gas Conversion IV, Studies in Surface Science and Catalysis, vol. 107, Eds. M.de Pontes et al., 1997, Elsevier, Oxford
22. Ullmann's Encyclopedia of Industrial Chemistry, Vol.A-13, VCH, 1985

Hydrogen Production from Used Lube Oil via Supercritical Water Reformation

PI: A. Raissi (Florida Solar Energy Center)
K. Ramasamy (Florida Solar Energy Center)
M. Elbaccouch (Florida Solar Energy Center)
N. Mohajeri (Florida Solar Energy Center)

Abstract

Used lubricating oils (lube oils) are generated throughout the year and collected in central locations in many communities. Used lube oil can be valuable as a re-refined lubricant or as an energy source. Supercritical water reformation creates the opportunity to produce hydrogen from heavy hydrocarbon like used lube oil. Lube oil is a complex mixture of aliphatic and polycyclic hydrocarbons formulated to withstand high service temperatures. Both synthetic and mineral based oils contain a high concentration of hydrogen (about 13 to 14 wt %). At the Florida Solar Energy Center, we are developing a thermocatalytic process that employs supercritical water as the reaction medium for converting lube oil to mostly high-pressure hydrogen and carbon dioxide. Supercritical steam reformation experiments were carried out using a range of commercially available catalysts at various reactor temperatures, pressures, and residence time. In particular, we have quantified the extent of coke formation and developed a method to minimize carbon lay down. The role of supercritical water in this process is also being investigated.

Introduction

In these modern days the importance of hydrogen has been raised greatly due to the recent environmental awareness. In general, the hydrogen production processes of interest are those that have near term applicability, utilize local resources/feedstock (available at or near hydrogen production site), cost-effective (cost of hydrogen production comparable to that from steam-methane reformation process), produce no emission of criteria pollutants like sulfur dioxide, nitrogen dioxide and with very minimal carbon dioxide emission and not be an off-the-shelf technology (i.e., steam-methane reformation, SMR). In this project we choose used lubricating oil as our local resource. The rationale for using lube oils was that it has potential to produce hydrogen for NASA at a much lower cost than that from the present processes for the steam reformation of natural gas and enough used lubricating oil is available in U.S. (every year, Floridians alone generate close to 45 million gallons of used lubricating oil) through out the year with out any seasonal fluctuations and it is available at very cheap cost, typically 10 cents/gal. Used lube oil can be valuable as a re-refined lubricant or as an energy source. There are number of methods to clean the used lubricating oil and reuse as valuable products. Even the most recent lubricant re-refine technology recovers only 65 percent of the used lube oil by using the energy intensive operations like vacuum flashes, solvent extractions, distillation, demetallization etc. these re-refine technology produce lots of sludge as a end product and causes a sludge disposal problem. This hydrogen production from lube oil via thermo catalytic supercritical water reformation process not only answers the economic related problems but also has ability to find ways to reduce the environmental problem that are related to used lubricating oil disposal.

Background

Used lubricating oil itself is a complex mixture of low and high (C_{15}-C_{50}) molecular weight aliphatic and aromatic hydrocarbons, lubrication additives, metals, and various organic and inorganic compounds (table 1). The chemical composition of used lubricating oil varies widely and depends on the original crude oil, the processes used during refining, the efficiency and type of engine the oil is lubricating, the gasoline combustion products, the additives added to the fuel and to the original oil, and the length of time that the oil remains in the engine.

TABLE 1.—COMPOSITION OF LUBRICATING OIL

Compound Class	Formula	Wt% in Oil
Alkyl-monoaromatics	C10H14-1, Butyl benzene	4.2
	C7H8, Toluene	4.2
Cycloalkanes	C6H12-1, Cyclohexane	12.0
	C6H12-2, Methylcyclopentane	12.0
	C8H16-14, n-Propylcyclopentane	12.0
	C10H20-1, n-Butylcyclohexane	12.0
Diaromatics	C12H10, Biphenyl	2.1
(except naphtalenes)	C12H8O, Dibenzofuran	2.1
	C13H10, Fluorene	2.2
Monoaromatics	C8H6S, Benzothiophene	10.8
Naphthalenes	C10H8, Naphthalene	3.2
	C11H10-1, 1-Methylnaphthalene	3.2
Polynuclear aromatics	C18H12, Chrysene	1.6
	C18H12-D1, Benzanthracene	1.6
	C14H10-2, Phenanthrene	7.4
Straight-chain and branched	C9H20-E4, 2,4-Dimethyl-3-ethylpentane	3.4
Additives	C7H6O3, Salicylic acid	3.0
	C4H4O3, Succinic anhydride	3.0

Used lubricating oil has a density (at 20 ◦C) of about 0.88 g ml^{-1} and dynamic viscosity of 0.50 m^2s^{-1}. Since lubricating oil is a very complex mixture and it is designed to with stand very high temperature in internal combustion engines it is almost impossible to break down to its constituent element hydrogen and carbon by using thermal energy alone. Therefore, a new thermo catalytic process is being developed that employs supercritical steam to transform lube oil into hydrogen and other components.

Elemental analysis of the used lubricating oil shows it contains 13.37 wt% (table 2) of hydrogen in it. The lubricating oil hydrogen content is two times higher than the other similar source biomass and around three-weight percentage higher than the vegetable oil. The high hydrogen content in the used lubricating oil makes it as a valuable and attractive resource for hydrogen production.

TABLE 2.—ELEMENTAL ANALYSIS OF LUBRICATING OIL

Elements	wt %
Hydrogen	13.37
Carbon	84.35
Oxygen	2.51
Sulfur	0.22
Nitrogen	<0.5

The use of supercritical water has several advantages over the regular atmospheric steam. Supercritical fluid can be defined as a substance heated above its critical temperature (T_c), and which is also compressed above its critical pressure (P_c). Water becomes a supercritical fluid at temperature above 374.2 ◦C and pressure over 22.1 MPa. A key advantage of chemistry in supercritical water is that it becomes possible to vary the properties (figs. 1 to 4) of the reaction medium such as density, viscosity, and diffusivity by manipulating the pressure and temperature and optimizing the reaction medium without changing solvent water.

In the supercritical region, densities are a fraction of that of normal liquid water, while solubility behavior is closer to that of high-pressure steam. The loss of bulk polarity by the water phase and low dielectric constant results in small polar and non-polar organic compounds, to become completely miscible with supercritical water and the viscosity of the supercritical fluid is far less than that of the liquid solvent with very high diffusivity, which enhances the mass transfer rate of the supercritical water process.

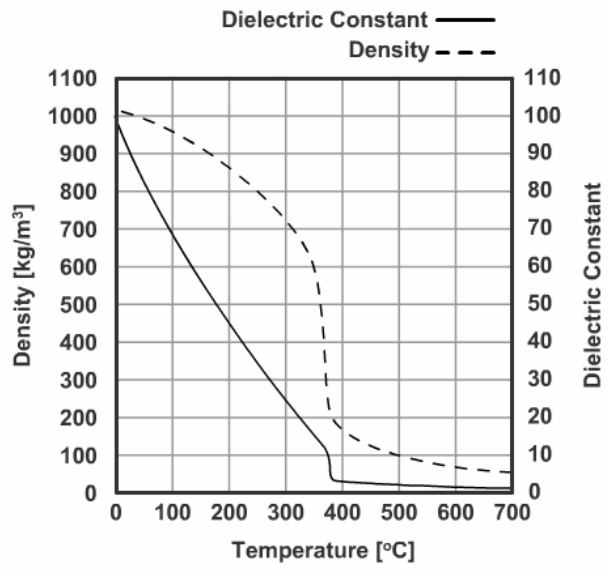

Figure 1.—Density and dielectric constant of water versus temperature at 25 MPa.

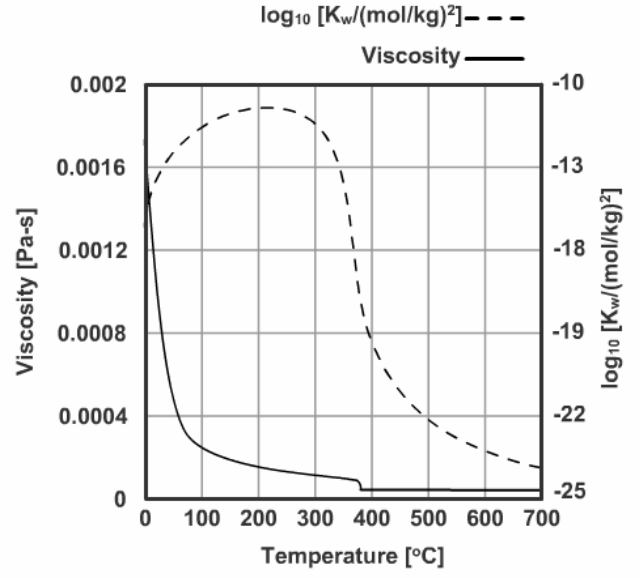

Figure 2.—Viscosity and ion product of water versus temperature at 25 MPa.

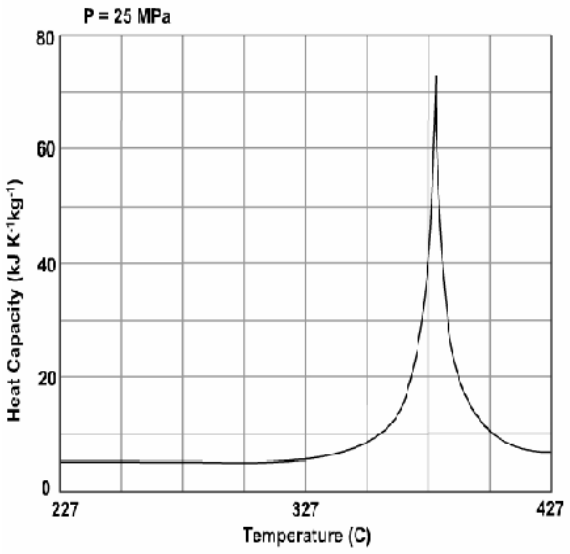

Figure 3.—Isobaric heat capacity of water versus temperature at a pressure of 25 MPa.

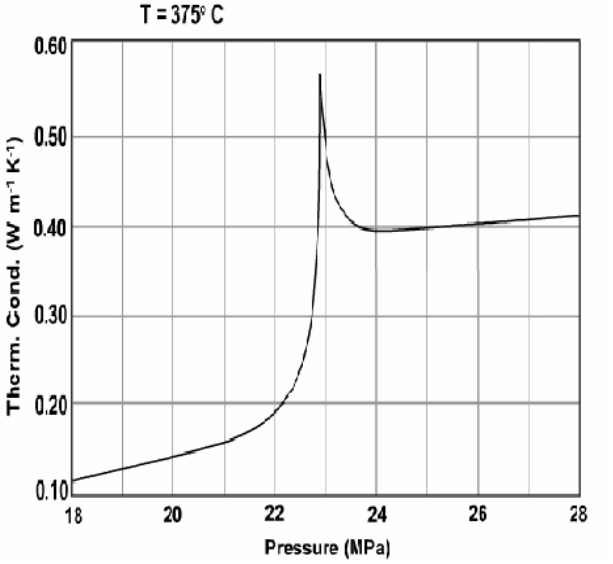

Figure 4.—Thermal conductivity of water versus pressure at a temperature of 375 °C.

Larger organic compounds and polymers hydrolyze to smaller molecules at typical supercritical conditions, and thus solubilize via chemical reaction. The ease of dispersion of the organic and oxidizing species within a single supercritical phase, in conjunction with the high diffusivity, low viscosity, and relatively high density of super critical water reaction medium results in very rapid reaction kinetics. In addition, high heat transfer rate is achieved due to the high thermal conductivity of supercritical water. In supercritical water conditions, the reactions occur in a homogeneous phase, so interface mass transfer limitations are avoided and very high reaction efficiencies can be achieved.

Another advantages of using supercritical water as a reaction medium for hydrogen production system is that thermal energy is used instead of mechanical power to pressurize (22.1 MPa) product gases - minimal energy is needed to feed incompressible liquid water and lube oil into the high pressure reactor where they react to generate high pressure hydrogen and carbon dioxide as the end products. This is important because almost 90 percent of the total energy expended for liquefying hydrogen is spent for compressing the gas.

Experimental

The flow diagram of the hydrogen production system from used lubricating oil via supercritical water reformation is shown in figure 5. The experimental setup consists of four zones. They are feed and preheat sections, reaction zone, product separation and purification section, and analytical section.

In the feed and preheat zone, oil and the water are pumped at 22.1 MPa pressure using high performance liquid chromatography pumps (HPLC pumps from the Lab Alliance can deliver liquid at the flow rate of 100 ml/min at 4000 psi continuously. The real time pressure and flow rate monitoring also available in this system. The stand-alone keypad unit enables gradient pumping). Water is preheated to steam at the desired temperature using a ceramic heater and mixed with oil before entering the reaction zone.

The reaction zone forms within a Parr Instrument Company instrumentation reactor made of high temperature Inconel alloy 600, 22 in. in length and 1 in. i.d. The reactor volume is about 1 liter. This reactor also designed with adjustable catalyst support system. The adjustable catalyst support system gives flexibility in varying the catalyst zone length, which allows varying reactant residence time in the reactor. This reactor is designed to reach the maximum pressure of 27.5 MPa at 570 ◦C) wherein the reactants are heated to the desired temperature over a special catalyst. Fluid pressures and temperatures are monitored, in real time, at the inlet as well as at the outlet of the reactor.

In the product separation zone, the product mixture passes through a series of two inline filters with increase in order of filter size to recover the char that is produced in the reaction zone and then the high pressure liquid gas mixture pass to backpressure regulator (the back pressure regulator with the pressure range between 0 to 42 MPa at 350 ◦C has been designed from Tescom, Inc.) that knocks down the pressure to near atmospheric. Then the low pressure, high temperature liquid-gas mixture enters a condenser where the liquid and gaseous components are separated. The gaseous portion is directed to the analytical section; the liquid portion is collected at the condenser bottom and sampled for analysis, separately.

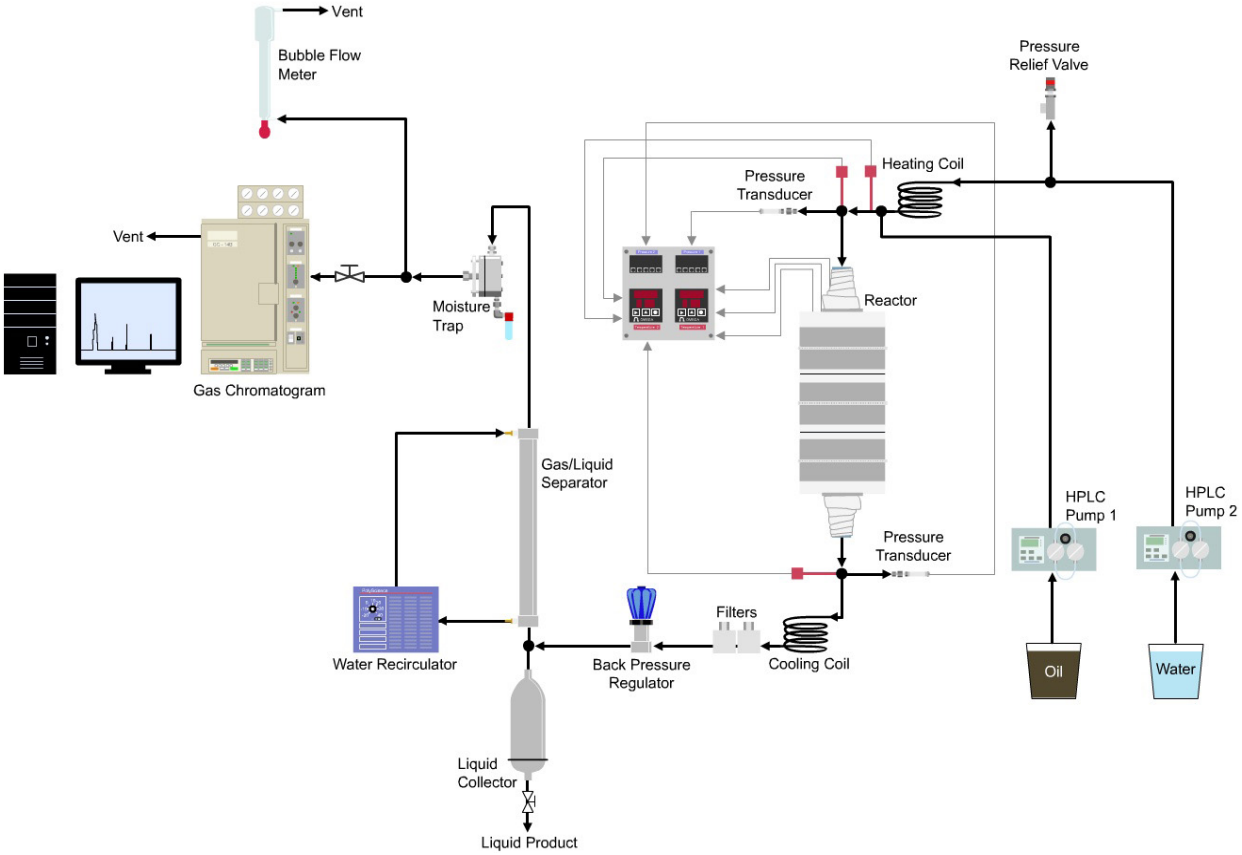

Figure 5.—Flow diagram depicting supercritical steam reformation of used lubricating oil.

In the analytical section, the product gas is diverted into two paths. One is sent to a volumetric bubble flow meter and to a vent. The other one is sent to a gas chromatogram, where the permanent gases such as hydrogen, carbon dioxide, carbon monoxide, and low molecular weight hydrocarbons such as methane, ethane and ethylene are analyzed using a Thermal Conductivity Detector (TCD) and the higher MW hydrocarbon such as hexane, pentane and benzene are analyzed using a Flame Ionization Detector (FID).

For safety, the reactor is enclosed with safety shields while in operation and all process parameters including the flow rates, temperatures and pressures are controlled further down the reactor. In addition, a pressure relief valve has been installed and Special corrosion resistant stainless steel 316 tubing and fittings are used throughout.

Experiments can be carried out with this setup with a maximum hydrogen production capacity of 100 SCCM and the maximum achievable temperature and pressure of 550 ◦C and 26 MPa. This maximum achievable temperature and pressure is 175 ◦C and 4 MPa higher than the supercritical water condition. This will give enough room to vary the temperature and pressure and find the optimum one.

Results and Discussion

A series of bench-scale, steam-reforming experiments were carried out using off-the-shelf samples of virgin synthetic lubricating oil (i.e., Mobil One) as well as to determine optimum process conditions for hydrogen production.

a) Experiments with nickel based catalyst at 380 ◦C
b) Experiments with nickel based catalyst at 480 ◦C
c) Experiments with Alkali salts (KOH) as a catalyst

a) Experiments with Nickel Based Catalyst at 380 °C

The first sets of experiments were carried out with the nickel-based catalyst to find out the performance of common commercially available steam reforming catalyst against the lube oil.

Figures 6 and 7 are the GC-TCD chromatograms that were recorded at the end of 1st and 5th hr through the experiment. These graphs were produced at a temperature 380 ◦C and a pressure at 23 MPa in the presence of a 25 to 35 percent alumina supported nickel catalyst with 1 to 4 oil to water feed ratio.

As depicted in figure 11, the volume of hydrogen produced at the end of 5^{th} hr through the experiment was reduced by 50 percent compared to that of hydrogen produced at the end of first hour. But the chromatogram shows, at all time during the experiment the selectivity towards the produced hydrogen and the other gas were same. When the system was opened coke formation was found in side the reactor and on the nickel alumina catalyst.

Even though supercritical water condition heavily favors the hydrocarbon solubility, some high molecular weight hydrocarbon, inorganic materials and additives hinder the performance and ends up with some unconverted oil and char production. The char formation may greatly deactivate the nickel-based catalyst and the sulfur present in oil also poisons the catalyst and reduces the performance very quickly.

The change in conversion with in 5 hr of the experiment reveals the deactivation of the nickel based catalyst and proves the nickel based catalyst are not suitable for the used lube oil reformation.

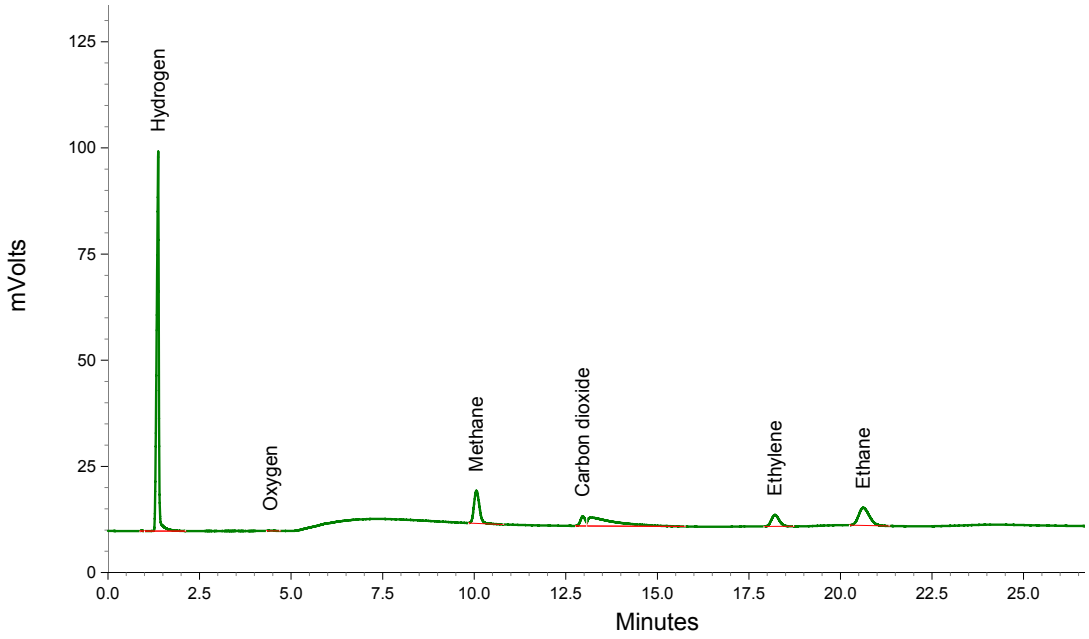

Figure 6.—GC chromatogram of effluent gas sampled after 1 hr through the run.

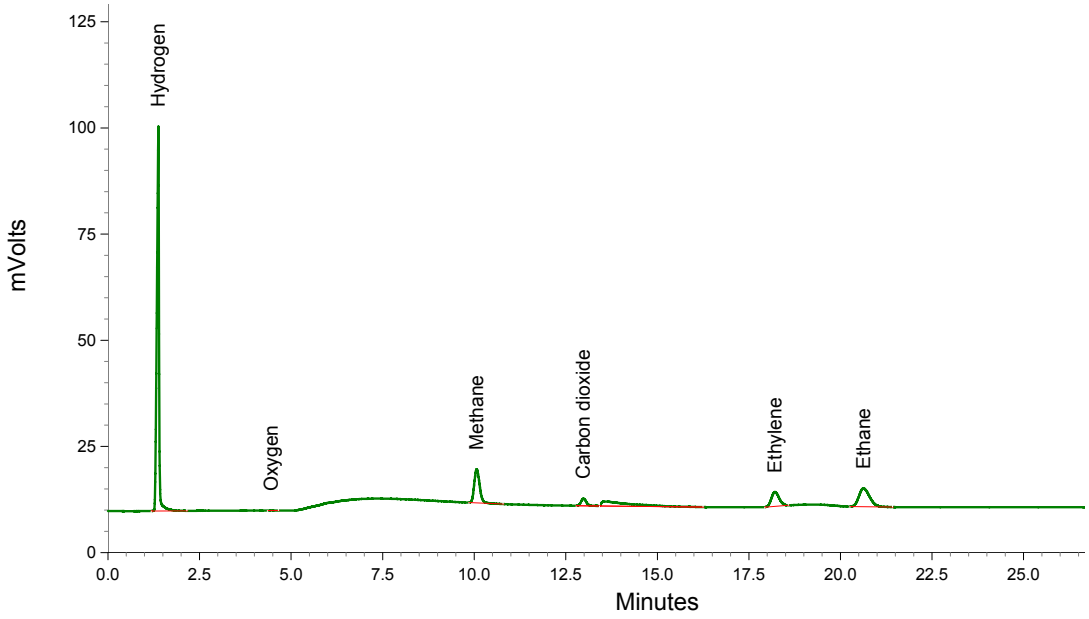

Figure 7.—GC results for the effluent gas sampled after 5 hr through the run.

b) Experiments with Nickel Based Catalyst at 480 °C

As mentioned in the background section, by varying the pressure and the temperature we can change the property of the supercritical water. This gives opportunity to change the property of the solvent without changing the solvent water. It is also interesting to see the change in chemistry between supercritical water and used lube oil at higher temperature. Experiments were conducted at the temperature 480 ◦C, which is 100 ◦C higher than the previous experiments and the pressure at 24 MPa in front of the Ni based catalyst. This run was forced to stop after 1hr of the experiment due (after 120 ml of the oil was pumped) to the clogging in the system. The blockage had occurred at the point were the supercritical water at 450 ◦C and the lube oil room temperature being mixed which is basically a ¼ in. Tee. When we opened the system the ¼ in. Tee it was completely blocked by the white colored material.

To find out the cause for the clogging and to find an approach to run the experiment at high temperature with out any clogging trouble, we ran several tests by changing different parameters. Since the block occurred only at the point where the steam and oil are mixing, we decided to change the flow pattern in the mixing zone and the volume of the mixing zone (size of the Tee). Figure 8(a) illustrate how steam and oil were mixed at initial stages. In this approach, the high flow rate of steam, which is flowing perpendicular to the oil flow and hits the surface of the Tee and causes turbulence, which increases the oil's residence at the Tee. To reduce the turbulence and oil residence time inside the Tee the direction of the flow of oil and steam were changed (see fig. 8(b)). Tests were conducted with the new setup and clogging problem occurred at the same place as in the previous configuration after the same amount of oil was pumped. In the next experiment, oil was introduced into the steam in the manner shown in figure 8(c). In this setup tubing that carries steam was inserted all the way in to the Tee. A test conducted with this configuration again resulted in Tee clogging after just 40 min through the test apparently due to the constriction created inside the mixing zone. Finally as depicted in figure 8(d), the size of the Tee was increased from ¼ in. to ½ in. and with this configuration it was possible to run the reactor for 6 continuous hours without clogging problem. However, a grayish greasy residue was found along inside walls of the Tee joint.

To find out the components those are present at the white blocking material FTIR test was conducted. The FTIR (see fig. 9) result tells that mostly the blocking material was made up of alkyl group components. We planned to do atomic absorption spectrometry test to find out if there is any metals present in the blockage material.

The figure 10 shows the chromatogram results of the 480 ◦C experiment. The chromatogram result shows that the high temperature experiment has better selectivity as well as conversion as compared to the experiments with the nickel catalyst at 380 ◦C and the conversion of gas is reduced by 50 percent like the low temperature experiment. This high temperature experiment produced large amount of carbon dioxide and lower level hydrocarbon compounds like methane, ethylene and ethane. The experiments is planned to run for the same pressure and temperature with carbon based catalyst and alkali catalyst to see how much of the lower hydrocarbon can be converted in to hydrogen and carbon dioxide.

Figure 11 depicts the comparison between the conversion at 380 and 480 ◦C experiments for 1st hr, 5th hr of the experiments with the nickel-based catalyst and the 1 to 5 hr experiments with out catalyst.

When we increase the temperature form 380 to 480 ◦C the conversion was increased between 15 to 20 percentages for the experiments with catalyst and for the experiment with out catalyst the conversion was increased by 45 to 50 percent. Even at this increased conversion, still the overall hydrogen yield was very low.

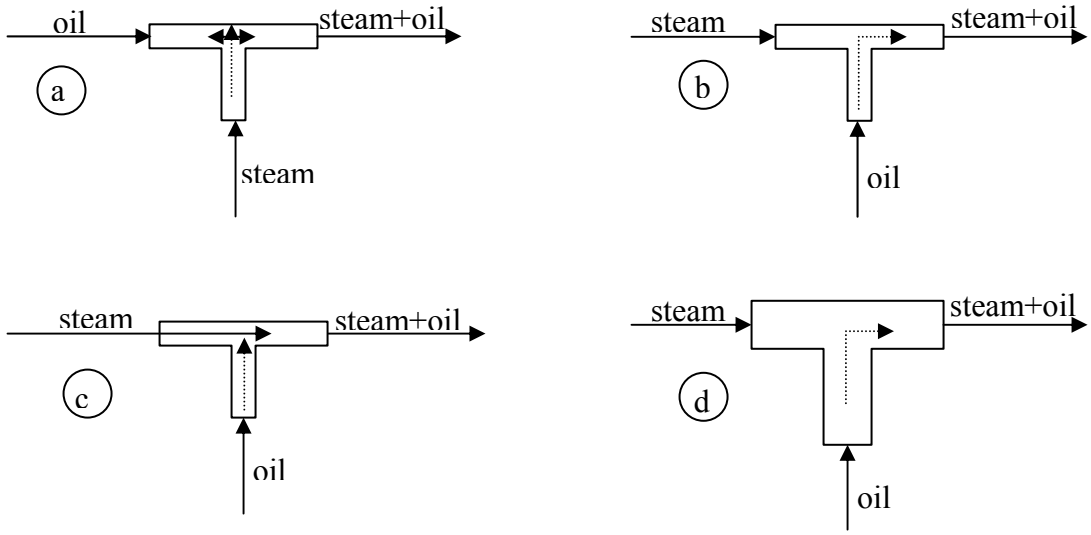

Figure 8.—(a) to (d)Flow and mixing pattern of oil and steam in the mixing zone.

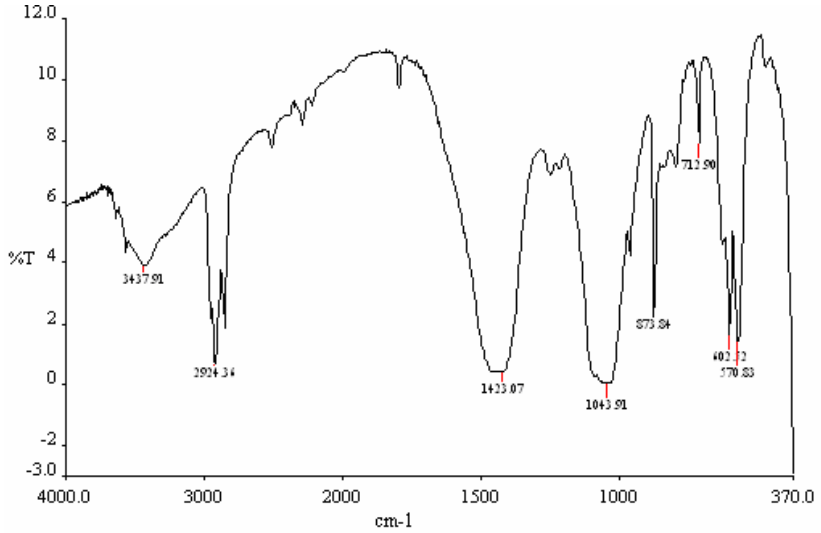

Figure 9.—FTIR spectrum of the material recovered from the mixing zone.

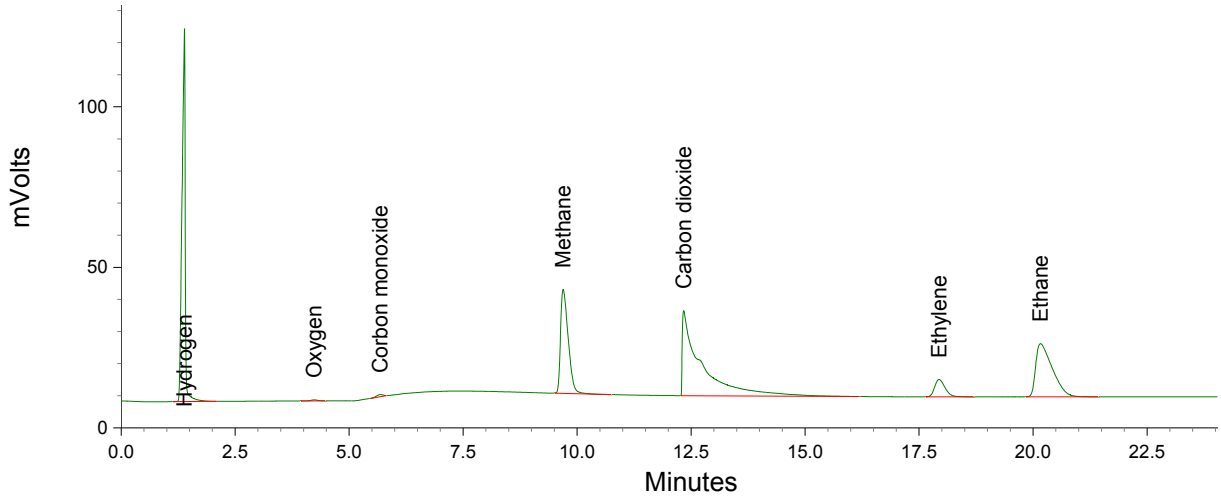

Figure 10.—GC chromatogram for tests at 480 °C.

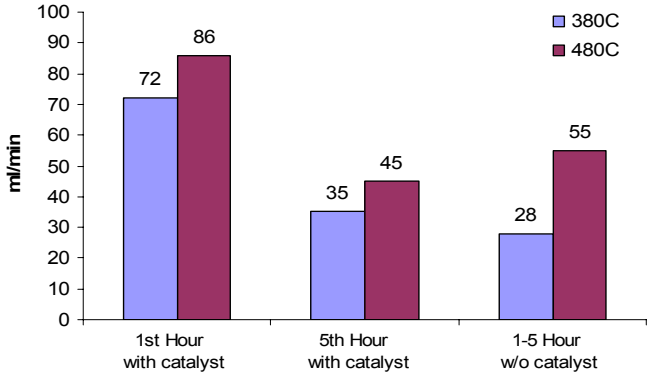

Figure 11.—Comparison between 380 and 480 °C experimental runs (with catalyst).

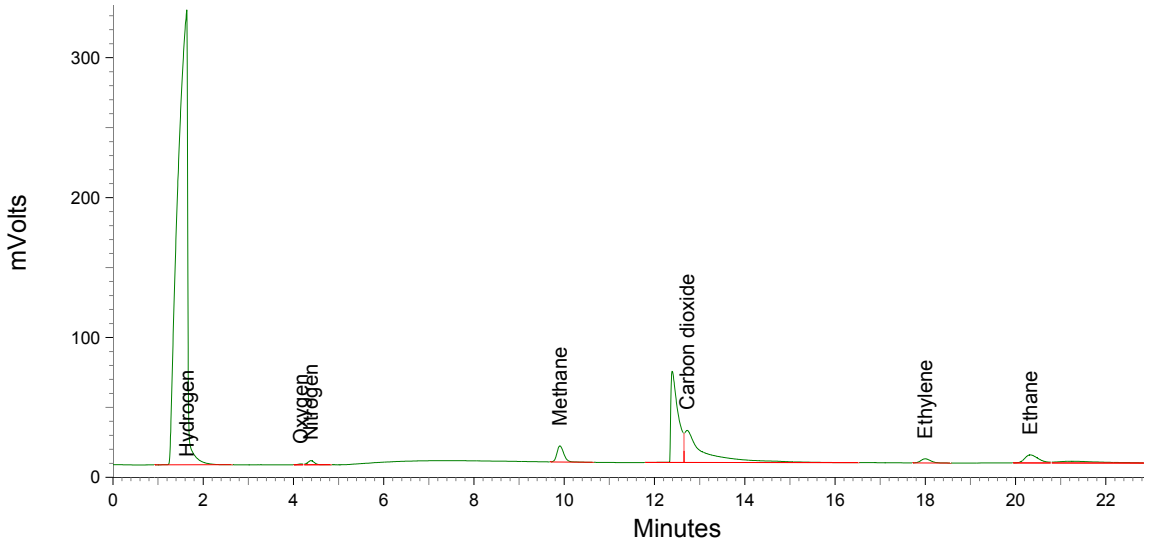

Figure 12.—GC results for SCW reformation of oil in the presence of 0.05 M KOH.

c) Experiments with Alkali Salts (KOH) as a Catalyst

Results from Kruse et al. tells that addition of alkali salts in the reformation increases the hydrogen and carbon dioxide formation and reduces the formation of carbon monoxide and char. Alkali metal hydroxides such as KOH and LiOH were usually dissolved in the water before use instead of packing into the reactor.

The addition of alkali metal hydroxides leads to the formation of formates, which subsequently degrades to hydrogen and carbon dioxide. Formic acid is supposed to be an intermediate product of the water-gas shift reaction.

$$H_2O + CO \rightarrow HCOOH \rightarrow H_2 + CO_2$$

Thus, the use alkali salts as a catalysts seems to be one of the key points for gasification in supercritical water, both towards the amount of residual chars and tars and towards the proportion of hydrogen in the synthesized gas. Our recent investigations on the gasification of used lube oil in supercritical water also show a positive impact of alkali metal additives.

The experiments were conducted with KOH for 0.05 M concentration at 380 ◦C temperature and 23 MPa pressure with 4 to 1 oil to water ratio. The chromatogram results were shown in figure 12. The selectivity towards hydrogen remains the same for the whole 5-hr of the experiment since KOH is dissolved in the water before it mixes with oil and avoid the possibility of the catalyst deactivation, the conversion of hydrogen and carbon dioxide bit higher compared to that of the experiments with the 25 to 35 percent nickel catalyst (alumina supported). These promising earlier results encourage carry out more research that is related to alkali metal catalyst in supercritical water steam reformation.

Future Work

Identify other more active catalysts that improve the yield of the hydrogen production by testing both commercially available hydrocarbon processing (steam-reforming) catalysts as well as a string of special carbon-based catalysts developed at FSEC and elsewhere; and alkali metal based compositions such as NaOH, K_2CO_3, LiOH etc.

Determine optimum reaction conditions (i.e., temperature, pressure, steam-oil ratio, residence time, etc.) the yields maximum hydrogen production. Of particular interest is to quantify the extent of conversion (or hydrogen yield), susceptibility to coke formation, catalyst activity and stability. Three approaches can be employed to decrease carbon deposition on the catalyst. The first one is based on enhancing steam adsorption on the catalyst with the objective of gasifying any carbon or carbon precursor formed on the catalyst surface. The second approach is to affect surface reactions in the presence of other metals. The third is to find the optimum dielectric constant of water for dissolving hydrocarbons completely by varying the pressure and temperature of the supercritical water.

Hydrogen Storage and Recovery in Ammonia Borane Complex

PI: A. T-Raissi (Florida Solar Energy Center)
N. Mohajeri (Florida Solar Energy Center)

Summary

Ammonia is a superior hydrogen carrier that is low-cost, readily available and produces no greenhouse gases when used as transportation fuel. Unfortunately, it is extremely toxic and a sub-ambient temperature fuel. One approach to mitigate this is to complex ammonia with a suitable hydride so that the resulting material is neither toxic nor requires sub-ambient handling. A class of compounds known as amine-boranes (ABs) meets this requirement. The simplest known stable AB compound is ammoniaborane, NH_3BH_3 that contains 19.6-wt % hydrogen. While molecular precursors such as NH_3BH_3 have very high hydrogen storage capacity, their regeneration is difficult. Others like borazine ($B_3N_3H_6$) are volatile liquids. Polymeric ABs may overcome some of the limitations of molecular ABs since they are non-volatile solids and more stable over time.

In this report, we review the viability of these selected amine-borane complexes as prospective hydrogen carriers on board vehicles and present our recent findings.

Introduction

Species with empirical formula BH_2NH_2 and $B_xN_xH_y$ are considered group IIIB chemical hydrides. These species have been the focus of investigation as a means of high capacity hydrogen storage material for a long time. Among these species, ammoniaborane, BH_3NH_3, has the highest hydrogen content at 19.6 wt% and has been considered for use in the disposable hydrogen storage systems for fuel cell applications and as a solid propellant for generating H_2/D_2 gas (ref. 1a to i). Its volumetric energy density (4.94 kWh/L) is superior to that of liquid H_2 (2.36 kWh/L). At ambient conditions, ammoniaborane is a white crystalline solid, which is stable in water and air. Although amine-boranes (ABs) have very high H_2 storage capacity, their regeneration is the main obstacle to their use as transportation fuel.

The release of hydrogen gas from ammoniaborane is accomplished via thermolysis. This process begins at temperatures well below 140 ◦C but a temperature of about 1200 ◦C is needed to release the last mole of H_2 and to form boron nitride (BN). The overall process is exothermic but heat must be supplied to activate the material (ref. 2a to f). Since high temperatures are required for complete dehydrogenation of BH_3NH_3 and chemical inertness of BN, it is better to stop dehydrogenation reaction at an intermediate stage. Then, poly-(aminoborane), borazine ($B_3N_3H_6$), and hydrogen are the main intermediate decomposition products.

Conversion between aminoborane and borazine would provide a theoretical storage capacity of 13 wt % hydrogen. Borazine ($B_3N_3H_6$) 1 is a planar boron-nitrogen heterocycle, which was first synthesized in 1926 by thermal decomposition of diammoniate of diborane. Alternatively, BH_3NH_3 can be heated at 140 to 160 ◦C in tetraglyme solution to form borazine with 67 percent yield (ref. 3a and b). Several other synthetic procedures have also been reported in the literature (ref. 4a to d). Borazine is isoelectronic with benzene and in the gas phase, stable up to 500 ◦C when pure and fully anhydrous. However, borazine undergoes extensive decomposition when stored as a liquid at room temperature (ref. 5). In addition, heating liquid borazine at 70 ◦C for 2 to 3 days yields polyborazylene. Borazine has the same colligative properties as benzene; however, the two are very different chemically. The π-electron density along the boron-nitrogen bond is not distributed evenly due to the difference in electronegativities between boron and nitrogen atoms. Therefore, the molecular orbitals of the π system are lumpy in appearance. This uneven distribution makes borazine prone to addition reactions and thus less stable than benzene.

Cyclotriborazane 2, ($B_3N_3H_{12}$), is the inorganic analog of cyclohexane (ref. 6a,b). It is a stable compound, either in the solid state or in solution, over an extended period of time and it does not lose

hydrogen unless heated to above 100 ◦C (ref. 7a and b). Conversion between 2 and 1 would provide a theoretical hydrogen storage capacity of about 7.4 wt % H_2.

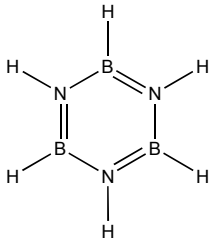

1

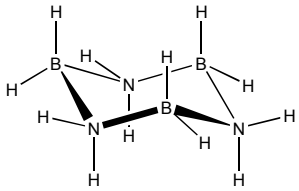

2

In this study we have focused on borazine/cyclotriborazane cycle.

Experimental

All precautions for working with moisture- and air-sensitive compounds were observed.

- Reagents. Cyclotriborazane was prepared according to a method described by Dahl and Schaeffer (ref. 7a). Borazine and polyborazylene were obtained from Boron Biologicals and was used as received. All other chemicals were from Aldrich or Acros.
- Analytical measurements. Thermogravimetric (TG) Analysis and Differential Temperature Analysis (DTA) were performed on a Diamond TG/DTA instrument (PerkinElmer, Inc.) using Pyris V6 (PerkinElmer, Inc.) software. Gas Chromatography/Mass Spectrometry and Direct Probe Inlet analysis of solids were performed on a GCMATE-II GC/MS-MS system (JEOL Ltd.) equipped with a 30 m, 0.32 mm i.d., and 0.25 μm film HP-5 capillary column and an ionization potential of 70 eV. IR Spectra were recorded on a Spectrum 2000 FTIR spectrometer (PerkinElmer, Inc.).

Results and Discussions

- **Borazine/Cyclotriborazane Cycle**. One object of this work was to prepare cyclotriborazane so that its characteristics for hydrogen release and conversion to borazine could be investigated. Cyclotriborazane was synthesized by adding hydrochloric acid to borazine, followed by reduction with sodium borohydride in diglyme. Previously, Dahl and Schaeffer (ref. 7a) had reported that by heating 2 to 205 °C for 150 min, three moles of H_2 can be produced per mole of sample taken, and borazine can be recovered with 75 percent yield.

The reported purification method for cyclotriborazane via sublimation, so far, has proven to be very slow and inefficient to reproduce in our laboratory. However, when the solution was exposed to the atmosphere, the excess $NaBH_4$ was precipitated as boric acid. After filtration and solvent evaporation under reduced pressure, the remaining white solid material was analyzed by IR, TG/DTA, GC/MS, and Direct Inlet Probe mass spectrometry.

The IR spectra of $B_3N_3H_6.3HCl$ and 2 in KBr pellets are shown in figure 1(a) and (b).

The N-H band for $B_3N_3H_6.3HCl$ at 3277 cm^{-1} was broad and for 2 was resolved into two peaks at 3308 and 3260 cm^{-1}. The B-H band for $B_3N_3H_6.3HCl$ and 2 appear at 2517 and 2371 cm^{-1}, respectively. It is worth mentioning that the IR spectrum of 2 indicates an almost completely pure sample.

In order to better understand the thermal characteristics of 2, TG/DTA was performed. The samples were analyzed in nitrogen atmosphere and a tared pan. The heating rate was set to increase at a rate of 40 ◦C/min from 26 to 400 ◦C. The TG/DTA data for cyclotriborazane decomposition shows one major exotherm with ΔH = –1019 J/g for the heat of the reaction. This step is associated with the loss of hydrogen that begins at 209 ◦C. The total weight loss for the sample was 59 percent of initial sample weight and remained almost constant above 240 ◦C. In other words, cyclotriborazane conversion to borazine, at our experimental conditions, was well below 100 percent. While, in Dahl and Schaeffer experiment, they removed three moles of H_2 from 2, with no residue remaining, by isothermal heating at 205 ◦C for 150 min.

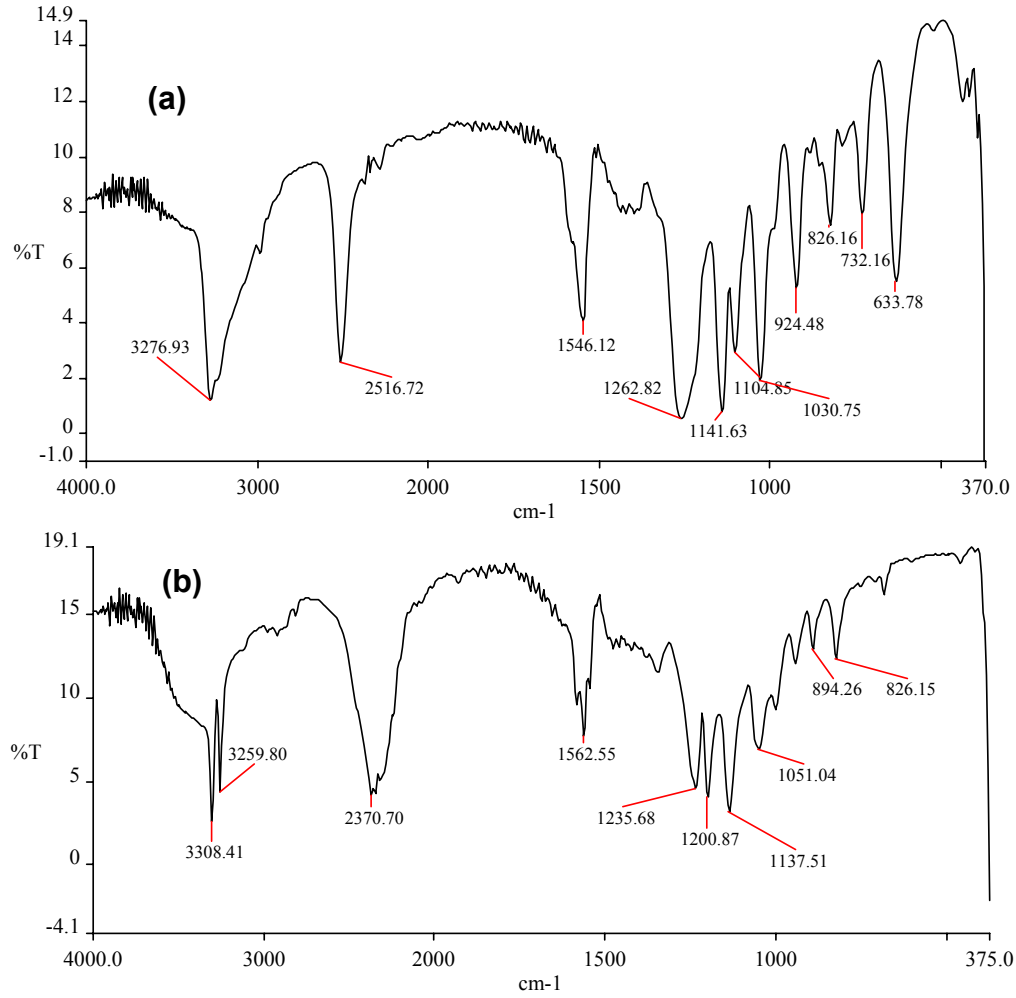

Figure 1.—IR spectra of (a) $B_3N_3H_6$. 3HCl, and (b) $B_3N_3H_{12}$.

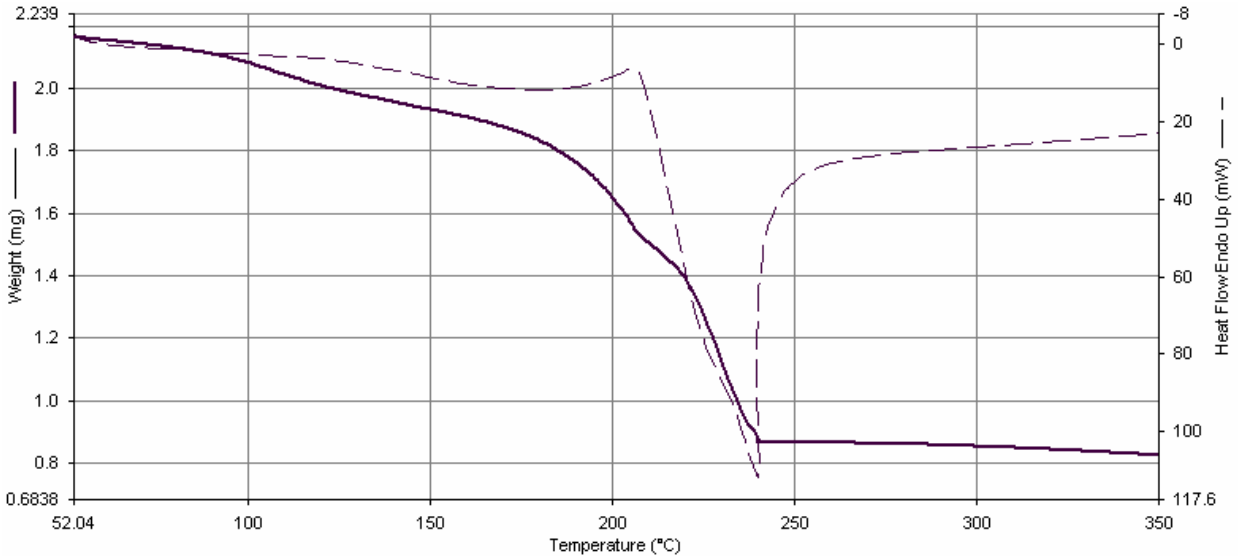

Figure 2.—TG/DTA analysis of cyclotriborazane.

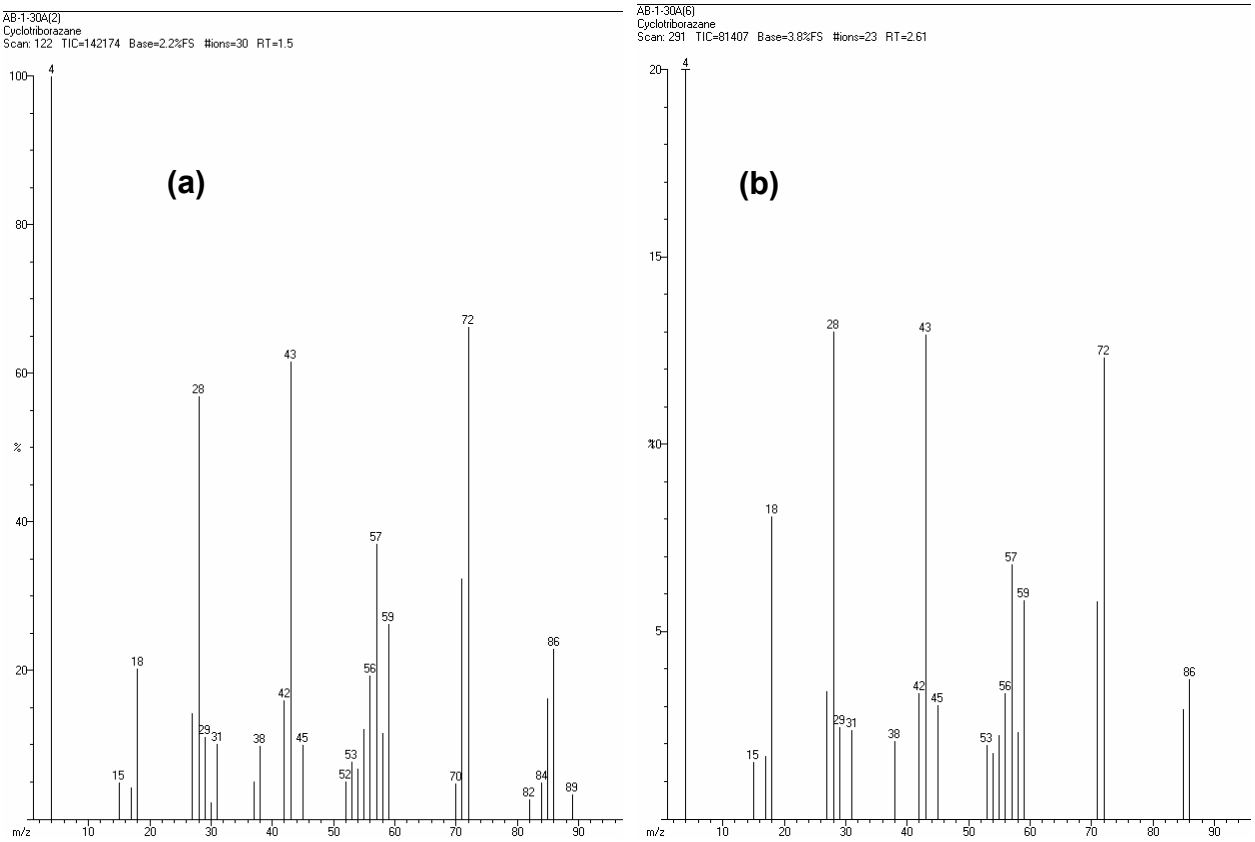

Figure 3.—Mass spectra of cyclotriborazane: (a) Direct inlet probe, (b) GC/MS.

We conducted GC/MS and Direct Inlet Probe analysis of cyclotriborazane. First, the sample was submitted for MS analysis via Direct Inlet Probe set to ramp from 30 to 300 ◦C at a rate of 32 ◦C/min. The compound started to vaporize at about 100 ◦C, which is also the sublimation temperature for cyclotriborazane (fig. 3(a)). Mass numbers at 89, 59, 58, 45, 31, and 29 correspond to residual diglyme in the solid. For GC/MS method, the sample was injected into 100 ◦C inlet port and column oven temperature programmed to 100 to 250 ◦C. From both methods, it became clear that fragmentation pattern for cyclotriborazane is different than that of borazine (ref. 8a to d). Compared to borazine, cyclotriborazane undergoes far less fragmentation. These observations may be due to the higher molecular stability of cyclotriborazane. Although, the mass number 87 for $^{11}B_3N_3H_{12}^+$ is absent but mass number 86, which corresponds to $^{11}B_3N_3H_{11}^+$ and $^{10}B_3N_3H_{12}^+$, is present.

Further investigation of cyclotriborazane synthesis, identification, and thermolysis is required to access the viability of borazine/cyclotriborazane as a viable hydrogen storage compound.

References

1. (a) Ayers, O.E., and Patrick, R.E., “Hydrogen Gas Generators for Use in Chemical Lasers,” *U.S. Pat. 3,948,699* (1976). (b) Chew, W.M., Ayers, O.E., Murfree, J.A., and Martignoni, P., “Method for Producing Hydrogen or Deuterium from Storable Solid Propellant Compositions Based on Complex Metal Boron Compounds,” *U.S. Pat. 4,064,225* (1977). (c) Chew, W. M., Ayers, O. E., Murfree, J. A., and Martignoni, P., ”Solid Propellants for Generating Hydrogen,” *U.S. Pat. 4,061,512* (1977). (d) Hu, M.G., Van Paasschen, J.M., and Geanangel, R.A., “New Synthetic Approaches to Ammonia-Borane and its Deuterated Derivatives,” *J. Inorg. Nucl. Chem.*, 39, 2147 (1977). (e) Artz, G.D., and Grant, L.R., “Solid Propellant Hydrogen Generator,” *U.S. Pat. 4,468,263* (1984). (f) Artz, G. D., and Grant, L.R., “Solid H_2/D_2 Gas Generators,” *U.S. Pat. 4,673,528* (1987). (g) Chen, X, Rusta-Sallehy, A, and

Frank, D., “Method and Apparatus for Generating Hydrogen Inside of a Fuel Cell,” *US2003/0091877 A1* (2003). (h) Jones, P.B., Browning, D.J., Mepsted, G.O, and Scattergood, D.P., “Portable Hydrogen Source,” *WO 02/18267 A1* (2002). (i) Rusta-Sallehy, A., and Frank, D., “Chemical Hydride Hydrogen Generation System and an Energy System Incorporating the same,” *US2003/0091879 A1* (2003).

2. 2) (a) Geanangel, R.A. and Wendlandt, W.W., “A TG-DSC Study of the Thermal Dissociation of $(NH_2BH_2)_x$,” *Thermochimica Acta*, 86, 375 (1985). (b) Sit, V., Geanangel, R.A. and Wendlandt, W.W., “The Thermal Dissociation of NH_3BH_3,” *Thermochimica Acta*, 113, 379 (1987). (c) Fabre, A., Goursat, P. and Lespade, P., “Etude de la Formation du Nitrure de Bore a par Pyrolyse du Borazane,” *Silicates Industriels*, 9-10, 167 (1991). (d) Fabre, A., Tetard, D., Goursat, P., Lecompte, A., Dauger, A. and Lespade, P., “Etude de la Decomposition Thermique du Borazane BH_3NH_3 en Hyperclave et de L'evolution Structural des Pyrolysats,” *Silicates Industriels*, 3-4, 45 (1993). (e) Wolf, G., Baumann, J., Baitalow, F. and Hoffmann, F. P., “Calorimetric Process Monitoring of Thermal Decomposition of B-N-H Compounds,” *Thermochimica Acta*, 343, 19 (2000). (f) Baitalow, F., Baumann, J., Wolf, G., Jaenicke-RoBler, K., and Leitner, G. Thermal decomposition of B-N-H compounds investigated by using combined thermoanalytical methods. *Thermochimica Acta,* 391, 159 (2002).
3. (a) Hough, W.V., Guibert, C.R., and Hefferan, G.T., “Method for the Synthesis of Borazine,” U.S. Pat. 4,150,097 (1979). (b) Wideman, T. and Sneddon, L.G., “Convenient Procedures for the Laboratory Preparation of Borazine,” Inorg. Chem., 34, 1002 (1995).
4. (a) Jaska, C.A., Temple, K., Lough, A.J., and Manners, I., “Rhodium-catalyzed formation of boron-nitrogen bonds: a mild route to cyclic aminoboranes and borazines,” Chem. Commun., 962 (2001). (b) Jaska, C.A., Temple, K., Lough, A.J., and Manners, I., “Transition Metal-Catalyzed Formation of Boron-Nitrogen Bonds: Catalytic Dehydrocoupling of Amine-Borane Adducts to Form Aminoboranes and Borazines,” J. Am. Chem. Soc., 125, 9424 (2003). (c) Dahl, G.H., and Schaeffer, R., “The convenient laboratory preparation of borazole,” J. Inorg. Nuclear Chem. 12, 380 (1960). (d) Sneddon, L.G., and Wideman, T., “Method for Synthesis of Borazine,” U.S. Pat. 5,612,013 (1997).
5. Mamantov, G., and Margrave, J.L., “Decomposition of liquid borazine,” J. Inorg. Nucl. Chem. 20, 348 (1961).
6. (a) Böddeker, K.W., Shore, S.G. and Bunting, R.K. “Boron-Nitrogen Chemistry. I. Syntheses and Properties of New Cycloborazanes, $(BH_2NH_2)_n$,” J. Am. Chem. Soc., 88, 4396 (1966). (b) Leavers, D.R., and Taylor, W.J., “Dipole Moment of Cyclotriborazane,” J. Phys. Chem., 81, 2257 (1977).
7. (a) Dahl, G.H. and Schaeffer, R., “Studies of Boron-Nitrogen Compounds. III. Preparation and Properties of Hexahydroborazole, $B_3N_3H_{12}$,” J. Am. Chem. Soc., 83, 3032 (1961). (b) Shore, S.G. and Hickam, C. W., “The Molecular Weight and Stability of Cyclotriborazane, $B_3H_6N_3H_6$, in Liquid Ammonia,” Inorg. Chem., 2, 638 (1963).
8. (a) Porter, R.F., and Solomon, J.J., “Chemical Ionization Mass Spectrometry of Borazine,” *J. Am. Chem. Soc.* 93, 56 (1971). (b) Melcher, L.A., Adcock, J.L., Anderson, G.A., and Lagowski, J.J., “Mass Spectra of Unsymmetrically B-Substituted Borazines,” *Inorg. Chem.*, 12, 601 (1973). (c) Miller, J.M., and Wilson, G.L., “Pitfalls in the Interpretation of the Mass Spectra of Polyisotopic Molecules,” *Inorg. Chem.*, 13, 498 (1974). (d) Wilson, R.G., “Ion mass spectrum of borazine ($B_3N_3H_6$),” *J. Appl. Phys.* 44, 5056 (1973).

System Analysis of Hydrogen Production and Utilization at KSC

PI: A. T-Raissi (Florida Solar Energy Center)
M. Elbaccouch (Florida Solar Energy Center)
K. Ramasamy (Florida Solar Energy Center)

Abstract

The objectives of this study were to design and optimize a hydrogen production plant for the National Aeronautics and Space Administration (NASA). The plant was modeled using Aspen Plus Chemical Process Simulator (CPS) and was based on the steam reformation of used automotive lubricating oil. The economics and financial viability of the plant were investigated using Icarus Process Evaluator (IPE) (Aspen Technology, Inc.). The model consists mainly of 1) a reforming unit simulated as a Gibbs reactor to fractionate the large oil molecules, 2) a carbon monoxide shift unit simulated as an equilibrium reactor to enhance the production of hydrogen, 3) a flash reactor to knock out excess water from the product stream, 4) a pressure swing adsorption (PSA) unit to recover pure hydrogen, and 5) a combustor to burn the off-gas stream. The temperature of the Gibbs reactor was pre-set to 650 to 950 ◦C. The flow rate of oil is varied in order to produce gaseous hydrogen enough for one, two, three, and four NASA shuttle launches. The performance of the reformer was investigated as a function of the steam-to-oil ratio. The economics of the Aspen plant for one, two, three, and four shuttle launches were investigated using IPE. The plant costs were evaluated as a function of the plant's direct field costs, indirect field cost, and non-field costs. The equivalent cost of gaseous hydrogen produced was calculated with respect to the number of shuttle launches.

Introduction

The objective of this work was to simulate an economically viable process for the production of hydrogen (H_2) by steam reforming automotive lubricating oil. The simulation was carried out using Aspen Plus Chemical Process Simulator (CPS). In addition, Aspen Technologies' Icarus Process Evaluator (IPE) was employed in conjunction with the Aspen Plus flowsheet to develop detailed plant costs and economics.

This project is a continuation of a research program aimed at simulating chemical plants for the production of H_2 via a variety of technologies and feed stocks (refs.1 to 3). Recently, there has been a growing interest in utilizing Aspen technology platforms in designing chemical models for H_2 processing and production (refs.4 to 6). There has been a demand by the NASA Kennedy Space Center (NASA KSC) to identify and characterize technologies for the efficient H_2 production from locally available resources. NASA KSC's criteria for the prospective H_2 production technology include (ref. 7): 1) near term applicability, 2) local feed stocks, 3) cost-effective comparable to that from steam-methane reformation (SMR) process (ref. 8), 4) environmentally benign, and 5) innovative process.

Liquid hydrogen for KSC shuttle launch and Delta programs is produced in and shipped from New Orleans, Louisiana, and McIntosh, Mississippi. Each launch requires about 50 semi-tractor trailers to drive 690 and 575 miles respectively for the hydrogen delivery. The cost of hydrogen is $7 million per year with $1.8 million for the trucking cost. Local H_2 production near KSC could save $1.8 million per year and eliminate the increased highway usage and enhance safety.

Background

Lubricating oil is an important local resource. One of the more valuable lubricating oil is the motor oil used in passenger cars, vans, and trucks. Every year, privately owned automobiles and light trucks in Florida, USA generates over 45 million gal of used crankcase oil. Used oil has value in reuse as a lubricant or as an energy source. Used oil is managed by the independent collectors, transporters, processors, and re-refiners. Transporters collect the oil from service stations, fleet garages, and other

locations, and transport it to processors or re-refiners. In Florida, major used oil centers are located at Tampa-St. Petersburg, Miami, Ft. Lauderdale, Pompano Beach, Ocoee, Jacksonville-Orange Park, Boynton Beach, Sanford, Ft. Pierce, and Plant City, with the combined annual capacities exceeding 35 million gal of used oil collected. In Florida, processors typically pay about ¢10 per gal of used oil delivered.

Used crankcase oil is a complex mixture of low and high (C_{15}-C_{50}) molecular weight aliphatic and aromatic hydrocarbons (HCs), lubrication additives, metals, and various organic and inorganic compounds. The chemical composition of used mineral-based crankcase oil varies widely and depends on the original crude oil, the processes used during refining, the efficiency and type of engine the oil is lubricating, the gasoline combustion products, the additives added to the fuel and to the original oil, and the length of time the oil remains in the engine. The oil is typically 73 to 80 wt % aliphatic HCs (primarily alkanes and cycloalkanes with l-6 rings), 11 to 15 percent monoaromatic HCs, 2 to 5 percent diaromatic hydrocarbons, and 4 to 8 percent polyaromatic HCs (ref. 9). A typical waste automobile lubricating oil is composed of about 58 wt % paraffins (typical $C_{25}H_{52}$) and 42 wt % naphthane ($C_{17}H_{14}$), and has a density of about 0.88 $g.ml^{-1}$ at 20 ◦C (ref. 9).

Calculations have shown that one gallon of waste automotive lubricating oil will produce approximately 1.38 kg of H_2 via steam reformation process. Thus, the cost of H_2 from used oil will be less than ¢10 per kg of H_2 equivalent. Currently, NASA pays more than $2 per lb of liquid H_2 (ref. 9). The average annual liquid H_2 requirement for the space shuttle is about 25 kg/hr for one launch per year (ref.10). Therefore, for one shuttle launch per year, approximately 260,000 gal per year of used oil (assuming 1 kg of liquid H_2 is produced from each gallon of used oil collected) is needed. In Florida, within a short distance from KSC, enough used oil is available (at less than about ¢10 per kg of H_2 equivalent) to fuel well over one hundred Shuttle launches per year.

Results and Discussions

Aspen Plus Process Simulation

Figure 1 illustrates the Aspen Plus flowsheet for the steam gasification of used oil to produce pure gaseous H_2. The simulation consists mainly of a Gibbs reactor at atmospheric pressure for the thermal cracking of used oil while reforming with steam, carbon monoxide shift reactor, a flash reactor to knock out excess water from the main product stream, a pressure swing adsorption (PSA) unit to recover pure H_2, and a combustor to convert the off-gas into heat. All of the feed streams were introduced into the Aspen model at ambient conditions. The composition of the used oil feed to the Aspen model is published elsewhere (ref. 7). All of the unit operations in the plant run adiabatically with the exception to the Gibbs reactor whose temperature was pre-set. Heat exchangers were used to cool and heat the processing units of the plant. The off-gas stream was directed into a combustor where it was burned with air to generate heat used to sustain the adiabatic requirement of the plant. The Gibbs reactor minimizes the total Gibbs free energy of the feed streams to the reactor assuming that all of the components defined in the simulation in the component specification sheet are viable products (ref. 1). The Gibbs reactor reforms the complex oil mixture by fractionating it down into simple hydrocarbon molecules, such as H_2, H_2O, CO, CO_2, CH_4, etc. An exothermic carbon monoxide shift reactor, modeled as an equilibrium reactor, increases the H_2 production and diminishes the carbon monoxide concentration in the product stream ($CO + H_2O \leftrightarrow CO_2 + H_2$). The shift reactor operates around 15 to 20 atm using compressors assumed to be isentropic with 86 percent efficiency.

At present, the PSA is the standard purification method for H_2 production, and is extremely efficient for high purity hydrogen greater than 99.999 percent (ref. 11). Since the shift rector is exothermic, the product stream was cooled down and water was knocked out using a flash reactor before it was directed into the PSA unit for purification and separation of H_2. A typical industrial PSA unit produces a high purity H_2 stream using a number of beds operating at different stages. For the purpose of this simulation, the entire unit was simulated as ‘black box’ due to the unsteady-stat nature of the PSA. 15 percent of the pure H_2 produced from the PSA was recycled in order to meet the 70 mol % H_2 requirements in the feed stream to the PSA (ref. 12).

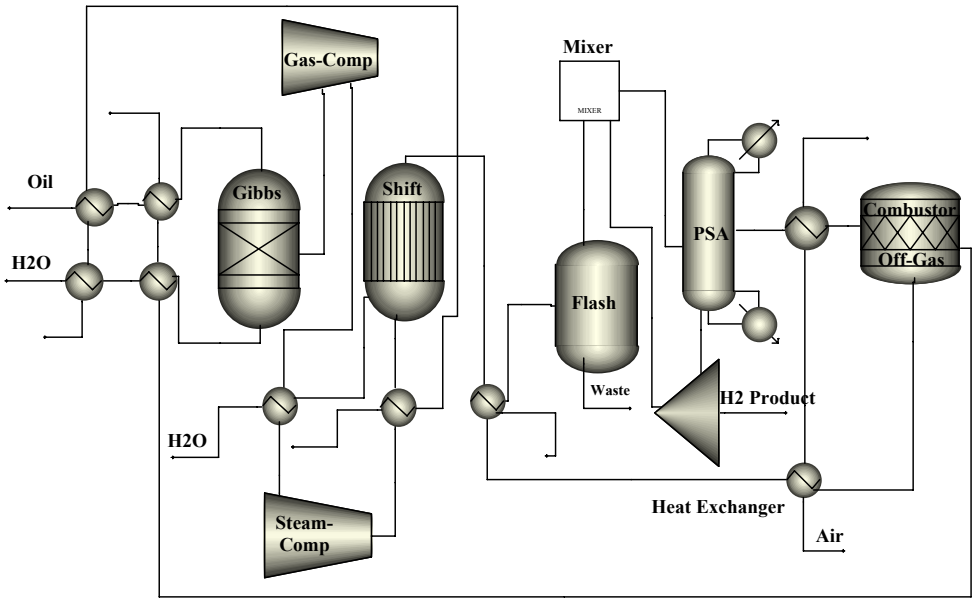

Figure 1.—Aspen Plus flowsheet for hydrogen production by steam reformation of used automotive lubricating oil.

Table 1 has optimized unit operation parameters for the Aspen flowsheet as a function of KSC launches for a Gibbs reactor at 650 ◦C. Since H_2 production rate at KSC is a function of the number of Shuttle launches per year, the economic analysis for the unit production costs is carried out as a function of H_2 production rate at KSC (25 kg H_2 per launch) (ref. 10). Figure 2 shows a plot of KSC shuttle launches as a function of the flow rate of pure H_2 produced from the PSA unit, and the flow rate of the used oil at a Gibbs reactor temperature of 650 ◦C. It is obvious that the flow rate of oil increases as the number of launches increases at a constant flow rate of water to Gibbs reactor (11.5 kmol.hr^{-1}). Most of the H_2 was produced in the Gibbs reactor, and the carbon monoxide equilibrium reactor enhanced the H_2 production. The off-gas stream was burned with air to generate heat for the adiabatic operation of the model.

TABLE 1.—OPTIMIZED UNIT OPERATION PARAMETERS AS A FUNCTION OF THE NUMBER OF LUNCHES FOR A GIBBS REACTOR AT 650 °C.

No. Launches	Unit	One	Two	Three	Four
Gibbs React Temp	◦C	650	650	650	650
Oil Gibbs React Feed	kmol.hr^{-1}	1	4.4	7.8	11.3
H_2O Gibbs React Feed	kmol.hr^{-1}	11.5	11.5	11.5	11.5
H_2 Gibbs React Prod	kmol.hr^{-1}	11.4	24.9	39.1	53.4
H_2 Shift React Prod	kmol.hr^{-1}	3.8	4.3	4.7	5.0
H_2 PSA React Prod	kmol.hr^{-1}	12.5	24.8	37.2	49.7
Off-Gas Stream	kmol.hr^{-1}	10.2	14.5	19.6	24.0
H_2O Shift React Feed	kmol.hr^{-1}	20.0	7.0	7.0	7.0
H_2 in Off-Gas Stream	kmol.hr^{-1}	2.7	4.4	6.6	8.8
H_2 in Combustor Prod	kmol.hr^{-1}	0.003	0.004	0.007	0.009
Shift React Prod	◦C	213	198	198	198
Combustor React Prod	◦C	1368	1660	1640	1909
Shift React Press	atm	20	15	15	15

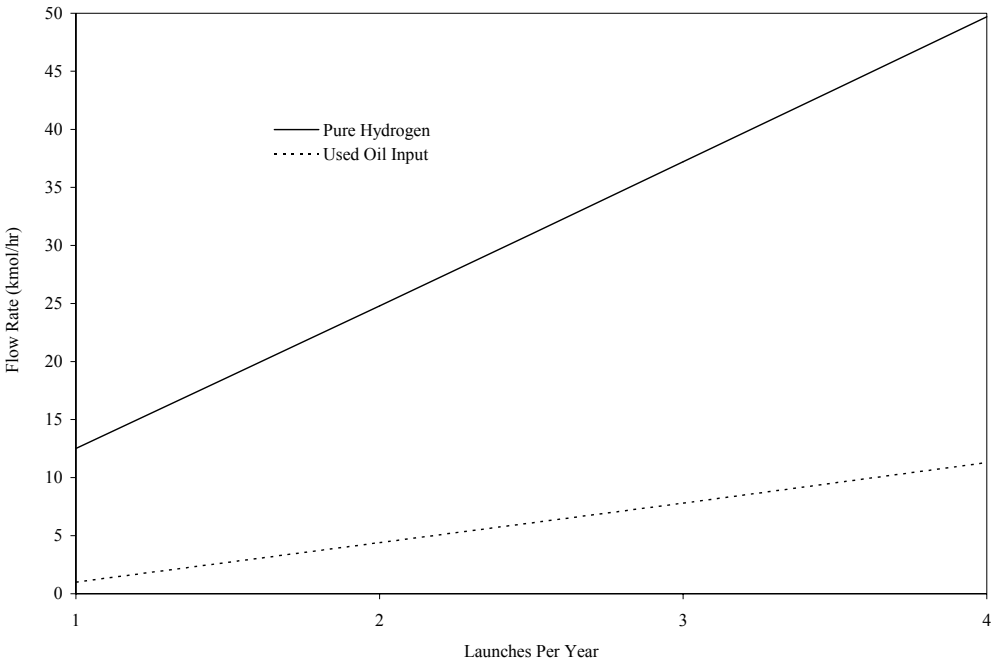

Figure 2.—KSC shuttle launches as a function of Aspen Plus flowrates of gaseous hydrogen and used oil at a Gibbs reactor temperature of 650 °C.

Table 2 shows the trend of H_2 production, approximately for one KSC launch, as a function of varying the Gibbs reactor temperature. The table shows that there is a slight increase in the H_2 flow rate as the temperature of the Gibbs reactor increases at a constant oil flow rate of one $kmol.hr^{-1}$. It seems that it is more efficient to meet the KSC launch requirement by increasing the flow rate of oil (table 1) than changing the temperature of the Gibbs reactor (table 2).

TABLE 2.—OPTIMIZED UNIT OPERATION PARAMETERS AS A FUNCTION OF GIBBS REACTOR TEMPERATURE WITH 1 $kmol.hr^{-1}$ USED OIL INPUT

Gibbs React Temp		650 ◦C	700 ◦C	750 ◦C	850 ◦C	950 ◦C
Oil Gibbs React Feed	$kmol.hr^{-1}$	1	1	1	1	1
H_2O Gibbs React Feed	$kmol.hr^{-1}$	11.5	10.0	8.5	7.5	7.5
H_2 Gibbs React Prod	$kmol.hr^{-1}$	11.4	12.1	12.2	12.5	12.9
H_2 Shift React Prod	$kmol.hr^{-1}$	3.8	5.1	6.1	7.0	7.2
H_2 PSA React Prod	$kmol.hr^{-1}$	12.5	14.7	15.5	16.5	17.1
Off-Gas Stream	$kmol.hr^{-1}$	10.2	10.1	10.3	10.5	10.6
H_2O Shift React Feed	$kmol.hr^{-1}$	20.0	25.0	27.4	30.0	31.0
H_2 in Off-Gas Stream	$kmol.hr^{-1}$	2.7	2.6	2.7	3.0	3.0
H_2 in Combustor Prod	$kmol.hr^{-1}$	0.003	0.003	0.003	0.003	0.003
Shift React Prod	◦C	212	212	215	215	215
Combustor React Prod	◦C	1368	1068	949	806	730
Compressor Pressure	atm	20	20	21	21	21

Gibbs Reactor Sensitivity Analysis

In this section, the focus is on the Gibbs reactor (reformer) of the Aspen model. That is because most of the H_2 was produced by the reformer, and that all the heat input to the plant was acquired by the reformer. The rest of the plant operated auto-neutrally meaning that its heat input was generated from combusting the off-gas stream, and heating and cooling the processing streams via heat exchangers. For

an efficient and optimized process design, the model requires that the plant does not generate carbon. At a given reformer temperature and pressure, there is a definite steam-to-oil molar ratio (X_W) above which no carbon forms in the Gibbs reactor. The desired theoretical state for the reformer operation is that for which the concentration of carbon, carbon dioxide, and water species are equal to zero.

Figure 3 represents the equilibrium concentration of the major products from the reformer, at 1 atm, 650 ◦C, and 1 kmol.hr^{-1} of used oil, as a function of the normalized molar concentration of the input steam. Note that above 0.9 the concentration of carbon is zero, and concentration of carbon dioxide, carbon monoxide, and water diminish significantly.

Figure 4 shows qualitative trends of the energetic and yield of liquid H_2 via steam reformation of lube oil as a function of the temperature of the reformer at 1 atm and 1 kmol.hr^{-1}. There is only a slight increase in the heat input to the reformer as its temperature was increased from 650 to 950 ◦C. This is in agreement with the results of table 2 where the flow rate of H_2 increases only from 11.4 to 12.9 kmol.hr^{-1} as the reformer temperature is increased from 650 to 950 ◦C.

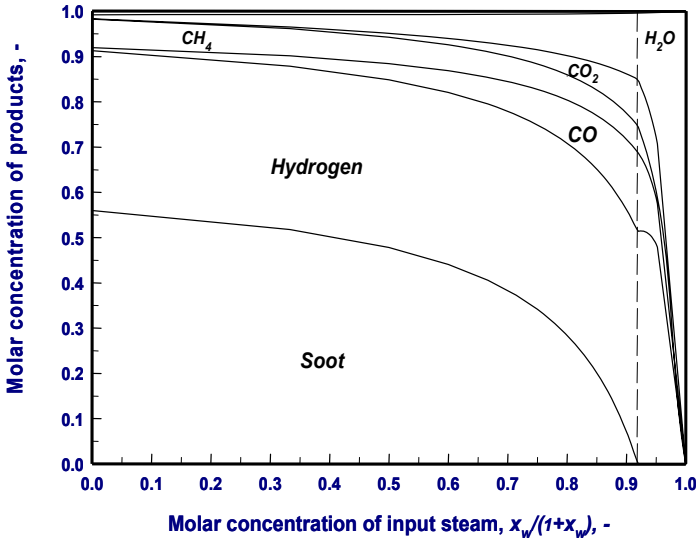

Figure 3.—Equilibrium concentration of reformer's products as a function of the normalized input steam to the reformer at 1 atm, 650 °C, and 1 kmol.hr^{-1} used oil.

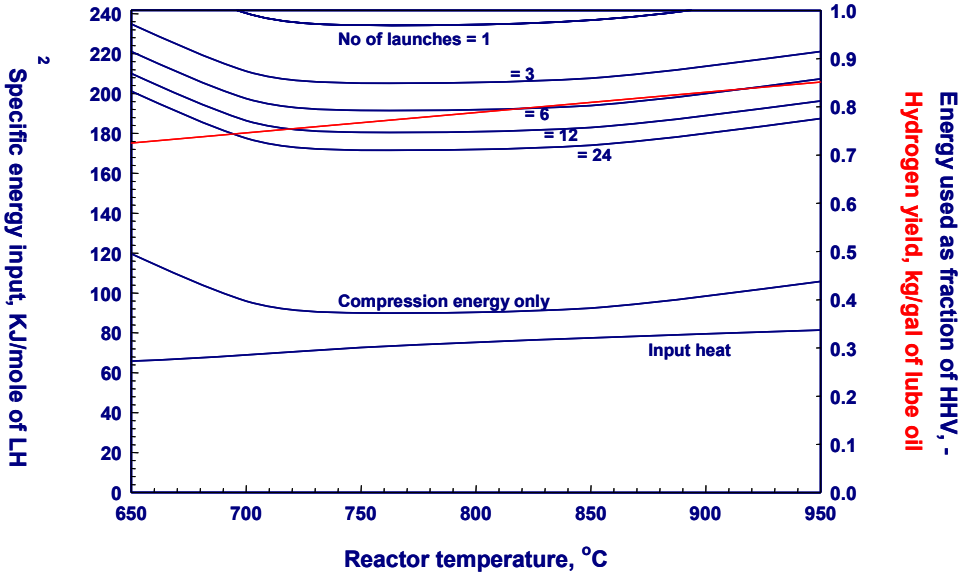

Figure 4.—Energetic and yield of liquid hydrogen production via steam reformation of lube oil.

Figure 4 also depicts the compression energy needed to convert gaseous H_2 into liquid H_2 (ref. 13). Results indicate a parabolic compression energy performance as a function of the reformer's temperature. The extent of compression energy required decrease from 650 to 720 ◦C, then levels off until 850 ◦C, followed by an increase from there on. Figure 4 results are in agreement with the data of table 1 where hydrogen yield per gallon of lube oil decreases as the number of KSC launches increases at a given reformer temperature. In addition, the specific energy input per mole on liquid H_2 decreases as the number of lunches increases.

Aspen Icarus Economic Analysis

IPE was used to link and map the Aspen flow units to different types of processing equipment to provide detailed cost data. IPE has cost libraries and built-in expert sizing programs allowing detailed costs consideration of equipment handling and setting, capital, operating, maintenance, raw materials, taxes, piping civil, structural, steel instrumentation, utilities, inculcations, paint materials, and many other specifications. Hydrogen requirement for multiple KSC launches is assumed to be a linear function of the H_2 needed for a single launch (25 kg H_2). The cost of used oil is assumed to be ¢10 per kg of H_2 produced with an escalation rate of 3.5 per period.

Table 3 lists the major assumptions and design criteria used in the IPE calculations based on the Aspen model given in table 1. The design criteria was used in figures 5 to 8 to calculate the direct field costs, indirect field costs, non-field costs, and average wage rates for one, two, three, and four shuttle launches respectively. The sum of the direct field costs, indirect field costs, and non-filed costs in figures 5 to 8 gives the total capital costs of the plant. That is $8,182,916, $6,710,290, $5,834,608, and $6,774,656 for one, two, three, and four KSC launches respectively. Also, the IPE operating costs for one, two, three, and four launches are $2,077,340, $2,103,403, $2,112,215, $2,174,919 per year respectively.

TABLE 3.—DESIGN CRITERIA USED IN COST CALCULATIONS OF THE ASPEN ICARUS PLANT

Design Parameter	Unit	Item	Design Parameter	Unit	Item
Period description		Year	Escalation parameters		
Number of weeks per period	Weeks/period	52	Project capital escalation	%/Period	5
Number of periods for analysis		20	Products escalation	%/Period	5
Tax rate	%/Period	40	Raw material escalation	%/Period	3.5
Interest rate/desired rate of return	%/Period	20	O&M labor escalation	%/Period	3
Economic life of period	Period	10	Utilities escalation	%/Period	3
Salvage value (% of initial capital cost)	%	20	Project capital		
Depreciation method		Straight line	Working capital %	%/Period	5
Residence time of reactions	min	5	Operating costs		
Facility operation			Operating charges	%/Period	25
Operating mode		24 h/day	Plant overhead	%/Period	50
Length of start-up period	Weeks	20	Other expenses	%/Period	8
Operating hr per period	Hr/period	8,000			
Labor costs					
Operator	Cost/operator/h	20			
Supervisor	Cost/supervisor/h	35			
Utility costs					
Electricity	Cost/kWh	0.0354			
Fuel	Cost/MMBTU	2.56			

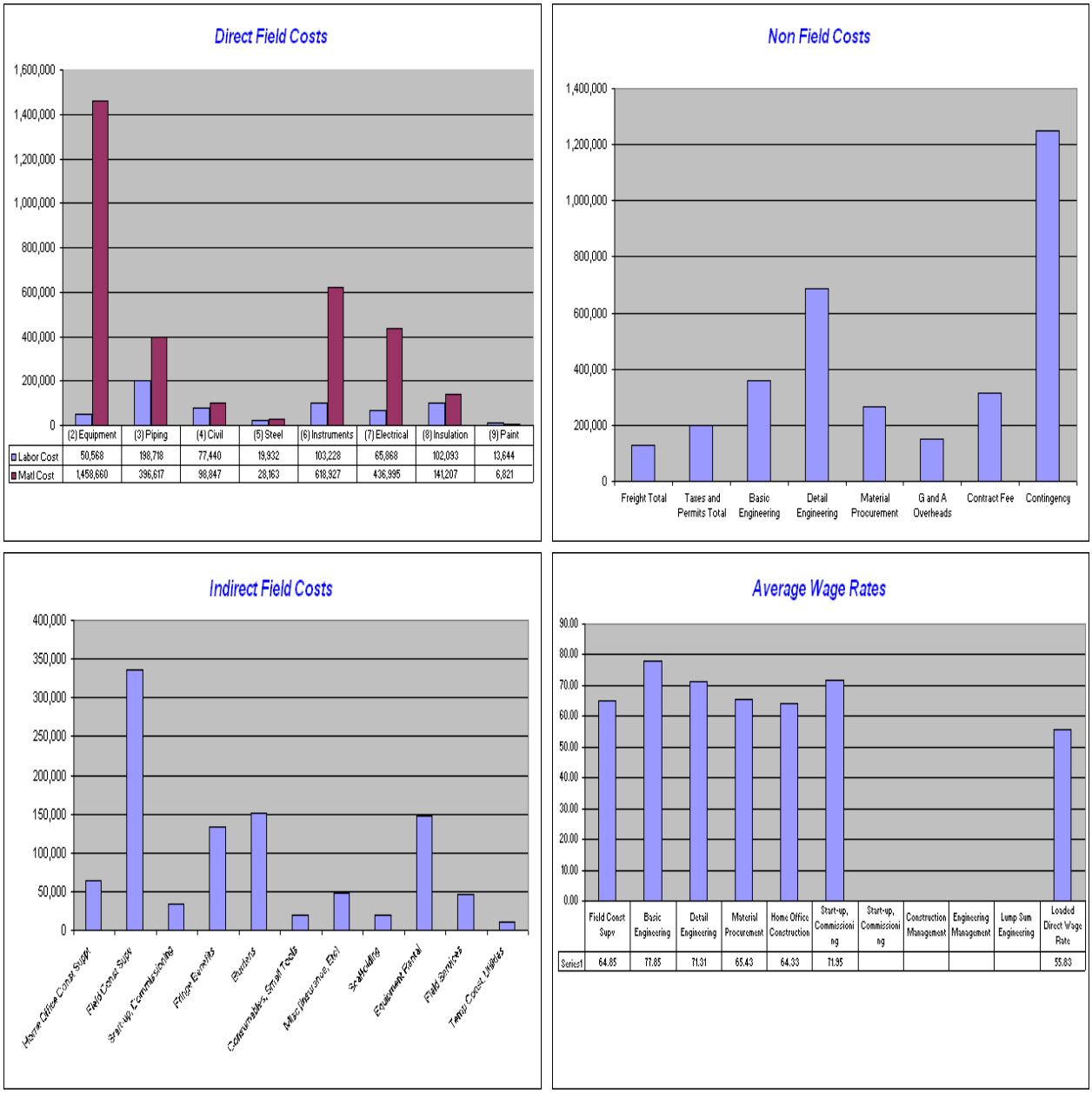

Figure 5.—Aspen Icarus cost analysis for one shuttle launch.

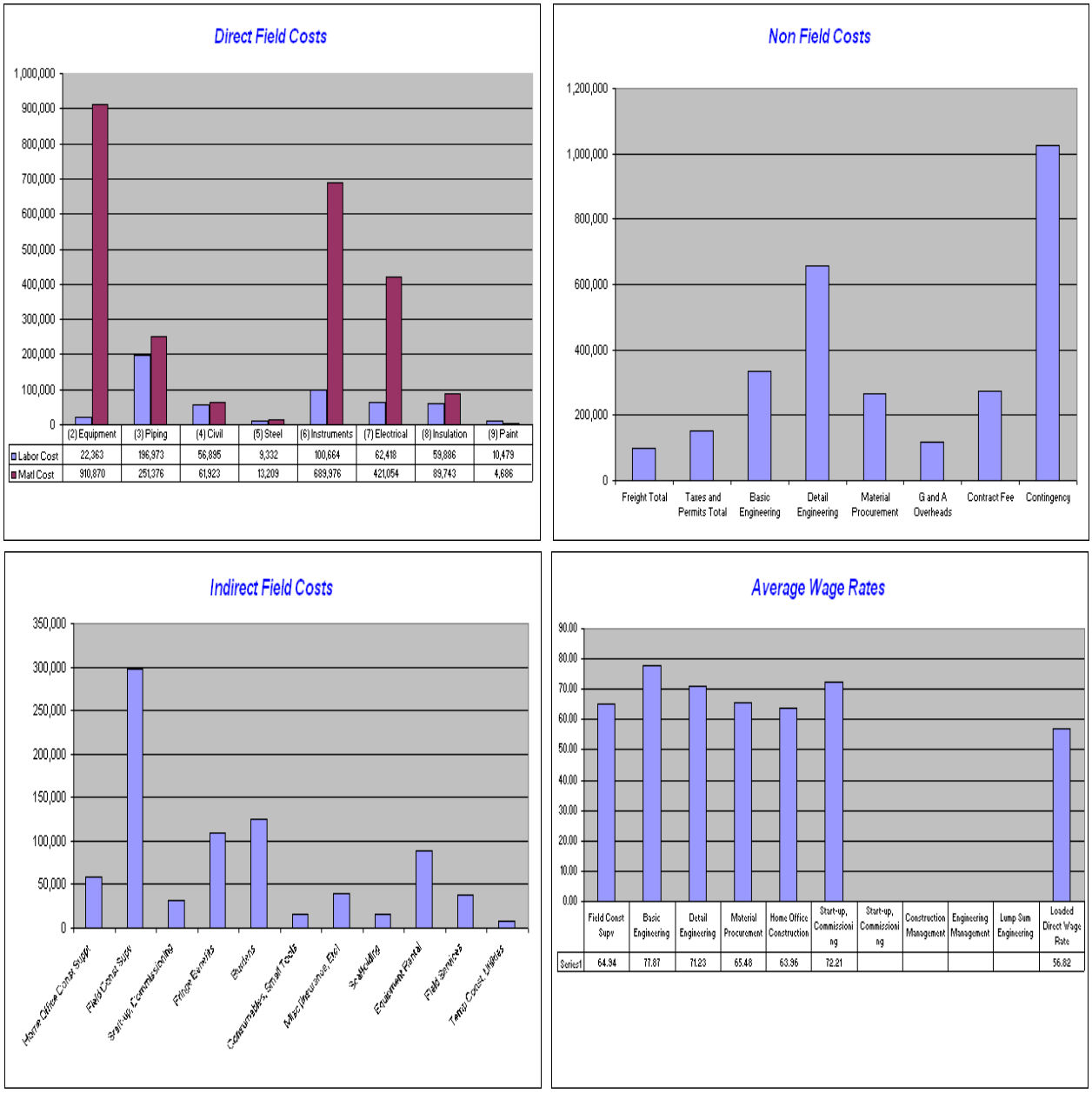

Figure 6.—Aspen Icarus cost analysis for two shuttle launches.

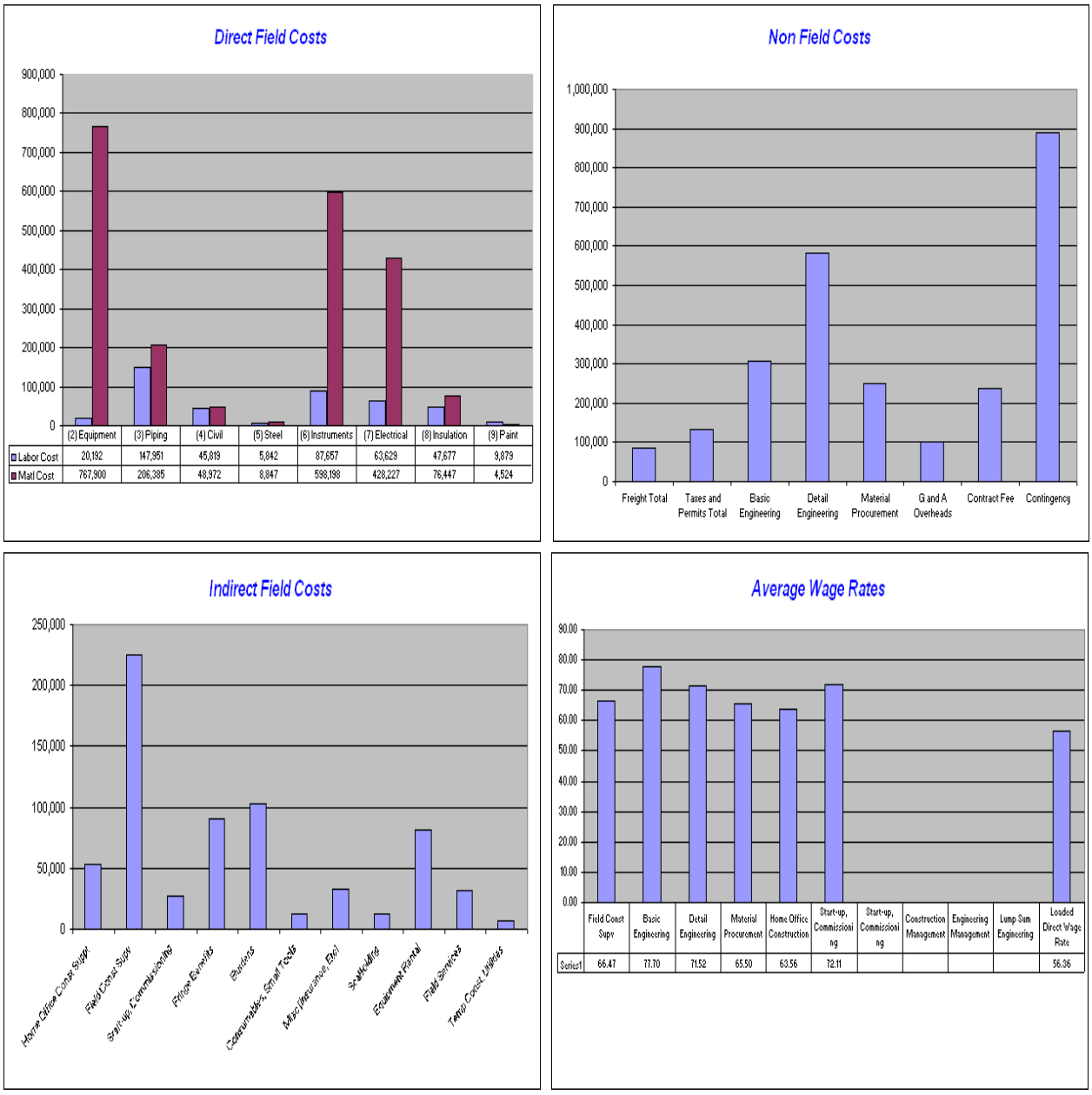

Figure 7.—Aspen Icarus cost analysis for three shuttle launches.

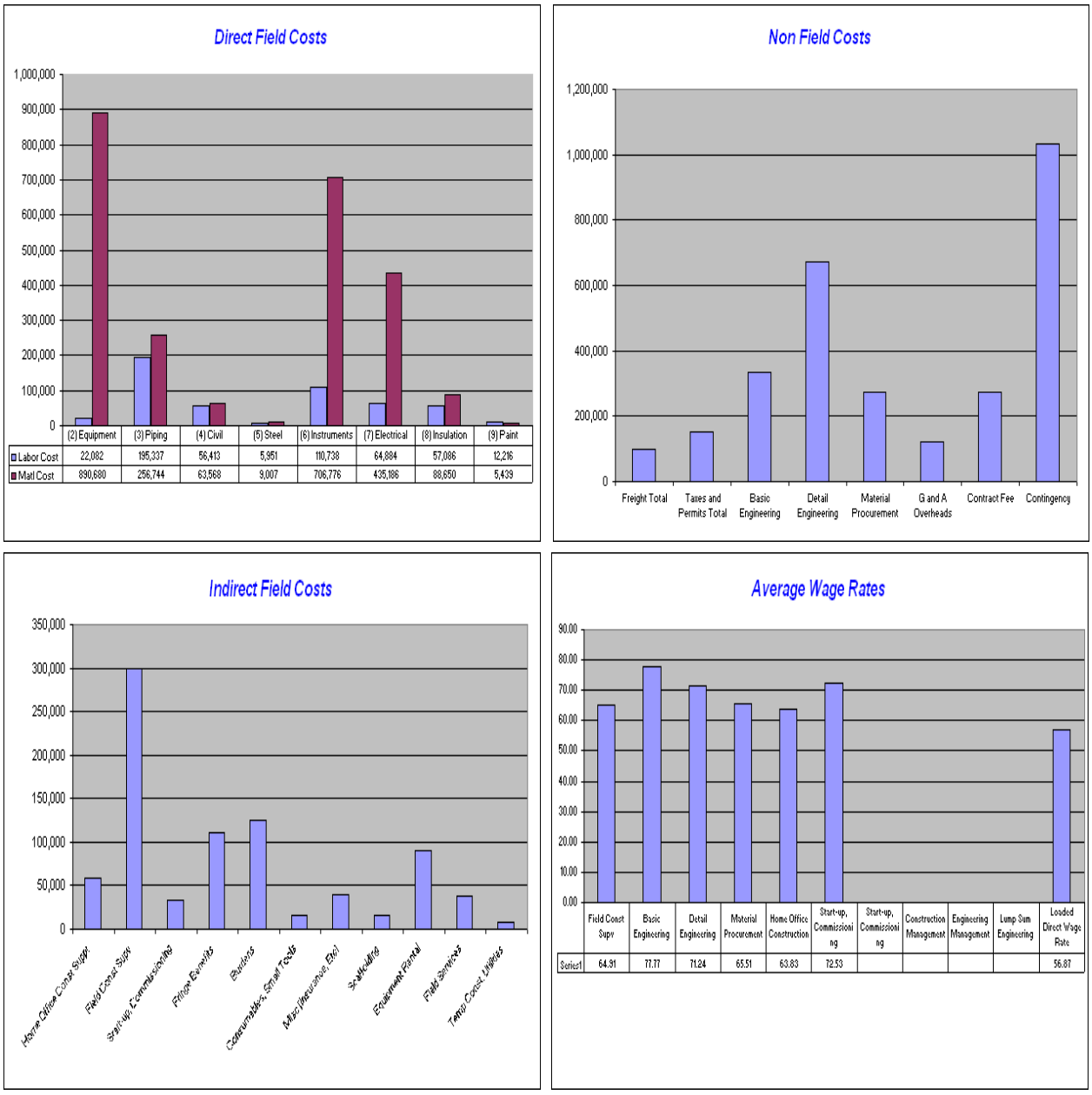

Figure 8.—Aspen Icarus cost analysis for three shuttle launches.

Total costs for each KSC launch is normalized with respect to the cost of gaseous H_2 and plotted in figure 9. Obviously, the cost of H_2 production decreases as the number of launches increases.

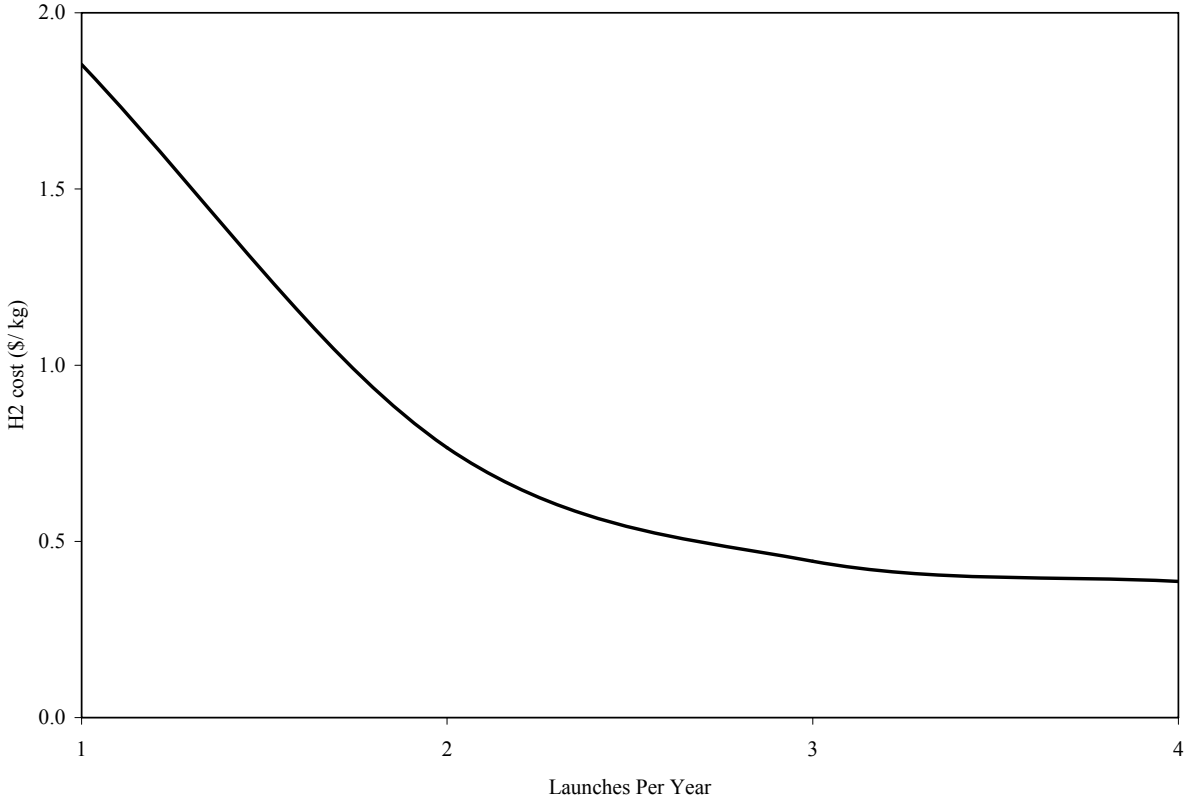

Figure 9.—Cost of gaseous hydrogen production from used oil for multiple launches.

Conclusions

This study simulates Aspen Plus and Icarus to design and cost a plant for the production of gaseous hydrogen by the steam reformation of used lube oil. The used oil inlet to the reformer was varied at a constant reformer temperature and steam input of 650 ◦C and 11.5 kmol.hr^{-1} respectively to produce pure H_2 sufficient for one, two, three, and four KSC shuttle launches. Varying the temperature of the reformer (650 to 900 ◦C) while keeping the used oil input constant at one kmol.hr^{-1} did not have a big impact on H_2 production. Most of the H_2 was produced within the reformer, and the carbon monoxide shift unit enhanced the H_2 production. The plant generated its energy auto- neutrally via burning the off-gas stream with air, and passing the processing streams through heat exchangers. The reformer was the only unit operation that required positive heat input.

The sensitivity analysis of the reformer at 650 ◦C, 1 atm, and 1 kmol.hr^{-1} of used oil showed that operating the plant above 0.9 ratio of steam-to-oil was the optimum ratio because the reformer did not produce carbon, and had the minimum output of CO, CO_2, and H_2O. Also, the analysis showed that the positive heat input to the reformer remained almost steady although the temperature of the reformer was varied from 650 to 950 ◦C. Also, the compression energy needed to convert gaseous H_2 to liquid H_2 is calculated qualitatively as a function of the temperature of the reformer.

Cost consideration for the four launch scenarios was performed using IPA. Calculations of the direct costs, indirect costs, and non-filed costs of the plant yield lots of detailed capital data. The cost of the plant was normalized with respect to gaseous H_2 production to give the cost of H_2 per kg for one to four KSC launches. The Aspen IPA simulation concludes that a plant model for four launches was the most economical scenario.

It should be noted that further Aspen IPA analysis will be taken place in the near future to 1) develop a desulfurization unit to remove sulfur prior to the reformer, 2) simulate a liquefaction plant and link it to the H_2 produced from the PSA, 3) link the model with Aspen-Adsim suite to better represent the PSA unit with adsorption-desorption capabilities, and 4) utilize IPE to develop sizing data for the types and specifications of the processing vessels.

References

1. Elbaccouch, M. and T-Raissi A. Aspen Plus process model for the production of gaseous hydrogen via bagasse gasification. In the Proceedings of the *15th World Hydrogen Energy Conference*, Yokohama, Japan, 2004.
2. Huang, C. and T-Raissi A. Analysis of Sulfur-Iodine Thermochemical Cycle for Solar Hydrogen Production. Part I: Decomposition of Sulfuric Acid. *J. of Solar Energy*.
3. Muradov N.Z., T-Raissi, A. and Robertson, T. Hydrogen Production via Catalytic Reformation of Low-Quality Methane Containing Feedstocks. Presentation at the *Hydrogen Power Theoretical and Engineering Solutions International Symposium (HYPOTHESIS)*, Porte Conte, Italy, 2003.
4. Skolnik, E. and Putsche V. Analysis Tools: Documentation for the 27 component models developed for the Integrated Systems Task. A publication on the International Energy Agency, 1999.
5. Kinoshita, C.M. and Turn, S.Q. Production of Hydrogen from Bio-Oil Using CaO as a CO_2 Sorbent. *Int. J. Hydrogen Energy* 2003; 28(10):1965-2003.
6. Mansary KG, Al-Taweel AM, Ghaly AE, Hamdullahpur F and Ugursal VI. Mathematical Modeling of a Fluidized Bed Rice Husk Gasifier: Part I – Model Development. *Energy Sources* 2000; 22(1):83-98.
7. T-Raissi, A., Elbaccouch, M., Mohajeri, N., Ramasamy, K., Solanki, A., Muradov, N.Z., and Block, D.L. NASA-Hydrogen Research at Florida Universities, Mid-Year Review Meeting, Task IV-A, System Analysis of Hydrogen Production & Utilization at KSC, http://www.hydrogenresearch.org/home.htm, Tallahassee, FL, March 30, 2004.
8. Tindall, B.M., and King, D.L. Designing steam reformers for hydrogen production. *Hydrocarbon Processing* 1994; 73(7):69-70.
9. Used Mineral-Based Crankcase Oil, Chemical and Physical Information. http://www.atsdr.cdc.gov/toxprofiles/tp102-c3.pdf.
10. Bain, A. NASA Kennedy Space Center Base Center Hydrogen Operations. Florida Solar Energy Center – University of Central Florida, Submitted to NASA-KSC, FSEC-CR-1359-02, October 2002.
11. Kratz, W.C., Rarig, D.L. and Pietrantonio, J.M. Hydrogen and Carbon Dioxide Coproduction from SMR OFF Gas by Pressure Swing Adsorption. *AICHE Symposium Series* 1988, 84(264):36-43.
12. Ruthven, D.M. Principles of Adsorption and Adsorption Processes. John Wiley & Sons, Inc., 1984.
13. T-Raissi, A., Barile, R.G., Dutta, S. and Block, D.L. Hydrogen for Power Applications, Task 2.0, Storage of Hydrogen in Solids, Liquid, and Gaseous Forms, Submitted to Solar Energy Research Institute, July 1988.

Development of Optical Systems for Mass and Two Phase Flow Gauging

PI: S. Van Sciver (Florida State University)
J. Justak (Advanced Technologies Group)

Description

The purpose of this project is to develop optical techniques that can detect solid hydrogen mass in liquid helium or two phase flow and to demonstrate these techniques in laboratory scale experiments. This project is a joint effort between the Cryogenics group at Florida State University and Advanced Technology Group (formerly Florida Laser Systems Inc.). The first task was to develop an optical mass gauging system for solid hydrogen in liquid helium. Subsequently, we will utilize similar technology to measure and monitor two-phase flow in liquid nitrogen and hydrogen. Much of the work is supported by a numerical modeling effort to simulate fluid dynamic behavior.

Objectives

The first objective of this work was to develop a prototype Solid Hydrogen Optical Mass Gauging System (SHOMGS) for determining concentrations of solid H_2 particles in LHe and hydrogen slush. The SHOMGS consists of a tunable light source and a spectrometer interfaced with a computer. The device uses the wavelength dependent absorption characteristics of different cryogenic fuels in conjunction to measure the fuel mass in a tank. The bench-top experiment consists of a spherical volume with optical access that can be immersed in a liquid helium bath. To demonstrate the technology, the spherical volume can be loaded with different quantities of solid hydrogen and the received optical signal compared to the mass injected. The second objective is to apply optical gauging techniques to study two-phase flow systems. In this case, the different optical absorption characteristics of liquid and vapor will be used to measure void fraction and mass flow rate. The two-phase flow experiments will be conducted in the Cryogenics laboratory at FSU. These new experiments will allow optical access for flow regime monitoring and optical gauging. Results from these experiments will be compared with numerical simulations.

Benefits to NASA

Future space flight hardware will require systems that can measure of the mass of the on board fuels under microgravity conditions. Advanced propulsion systems for future spaceflights will require densified fuels such as hydrogen slush or possibly solid hydrogen containing atomic species such as carbon or boron. Measurement of the fuel mass is a unique problem when the fuel is in the solid state since common methods such as heat capacity or PVT may not work. The SHOMGS, which directly measures the fuel mass, has the potential to be an accurate, light-weight and non-invasive technique for mass gauging.

Understanding two phase flow phenomena in cryogenic fluid systems is also of critical interest to NASA for developing fluid management systems for both earth and microgravity conditions. Of significant interest in two-phase flow systems if the ability to independently measure and monitor the flow regime as it depends on the mass flow rate and vapor fraction. As with mass gauging, optical flow monitoring methods offer significant advantage to conventional fluid monitoring techniques particularly for micro-gravity conditions. Preliminary work will scope the technologies and where possible test performance in bench top two-phase flow experiments.

Results

The Advanced Technology Group (ATG) has developed the prototype SHOMGS, which has been tested at FSU using a small hydrogen particle generator. The details of this preliminary work were

reported at the 2003 Space Cryogenics Workshop, to be published in Cryogenics, Vol. 44 (2004). We have since operated this SHOMGS several times with the new sH_2 particle generator to quantify the performance of the device. This work forms the basis for the masters degree of one graduate student (Thomas Adams) nearing completion of his work.

We have also carried out considerable numerical analysis of the various processes involved in the operation of the SHOMGS and subsequent two phase flow studies. In particular, we have numerically simulated the freezing of a liquid hydrogen drop in a liquid helium bath. We have also simulated the flow dynamics of solid hydrogen particles in a liquid helium flow field to investigate their dynamic behavior. Both these works were published in Cryogenics vol. 44 (2004).

The main activity for the remainder of this program will consist of further improvements in the SHOMGS and calibration of the instrument against known quantities of densified hydrogen. As a first step, we plan further runs with the existing equipment to improve operational experience. Subsequently, ATG, Inc. plans to improve the hardware by adding a second (reference) spectrometer to eliminate some of the instabilities in the first prototype. Further testing is planned. In parallel, we plan to begin an effort to use optical techniques to measure mass flow in forced single and two phase flow systems. A suitable two-phase flow apparatus with optical access is available to support these experiments. A numerical simulation effort will be carried out in parallel with the experiments.

Findings from these experiments will be published in the literature, reported at conferences and on the FSU Hydrogen webpage.

Experimental and Numerical Investigations of Cryogenic Multiphase Flow

PI: S. Van Sciver (Florida State University)
Y. Hussaini (Florida State University)

Description

This task is focused on experimental and numerical simulation of multiphase flow for future propulsion cryogenic systems. Three projects make up the effort. The first is an experimental program to study multi-phase flows of propulsion cryogens using a cryogenic flow visualization apparatus developed at FSU. Experiments will utilize LN_2 and LHe as substitutes for LO_2 and LH_2. In addition, experiments are planned to generate slurry flows of solid hydrogen particles in liquid helium and visualize their transport. The second subtask involves a numerical simulation of flow states in multi-phase cryogenic flows including liquid/vapor and solid particle/liquid flows. The goal of the numerical work is to develop algorithms that can be compared to the experimental results and guide future experiments. The final subtask, conducted in collaboration with Advanced Technology Group (ATG), involves the development of fluid optical quality sensor. A bench top test of a sensor developed by ATG will be conducted using the multiphase flow experimental apparatus at FSU.

Objectives

This activity involves a collaboration between the Cryogenics group at FSU-NHMFL, the School of Computational Sciences (SCS) at FSU and Advanced Technology Group (ATG), a small business located in Stewart, Florida. The main focus is toward basic understanding of the flow conditions that are expected to occur in advanced fuel handling systems needed to supply cryogenic fuels for rocketry. The leading effort is an experimental study of multiphase cryogenic flow using facilities available at FSU. Measurements include pressure drop and heat transfer in cryogenic flows to Reynolds number ~ 10^5 with flow regime visualization. Modern flow visualization techniques will be used to quantitatively probe the flow states. This work will be supported by numerical simulation of multiphase flows performed by SCS. Also, the FSU cryogenic flow visualization facility will be employed in testing a fluid optical quality sensor developed by ATG.

Benefits to NASA

Advanced propulsion systems for future spaceflights may require a variety of hydrogen fluid systems including two phase flow, densified or hydrogen slush or possibly solid hydrogen in liquid helium. Understanding two phase flow phenomena in cryogenic fluid systems is of critical interest to NASA for developing fluid management systems for both earth and microgravity conditions. Of significant interest in two-phase flow systems if the ability to independently measure and monitor the flow regime as it depends on the mass flow rate and vapor fraction. Optical flow monitoring methods offer significant advantage to conventional fluid monitoring techniques particularly for micro-gravity conditions.

Results

During the first quarter, the experimental work has focused on completing the two phase flow test loop. This has involved hardware fabrication and instrumentation development and calibration. In the analysis area, most of the effort has gone into completing the computational algorithm for H_2 particle solidification in a liquid helium bath. This is a coupled problem of conduction/solidification and convection heat transfer. Finally, the optical flow sensor work has only just gotten underway with first quarter activities involving specification of requirements for the application and selection of hardware components.

Over the remainder of the project, we will focus our effort on experimental measurements of two phase flow and flow quality sensor testing. This work will begin with two phase liquid nitrogen followed by solid hydrogen/liquid helium flow studies. Measurements will include temperature, pressure and flow rate for various conditions. We will also perform numerical analyses of the multiphase flow systems to compare with experimental findings.

Findings from these experiments will be published in the literature, reported at conferences and on the FSU Hydrogen webpage.

Measurement of Transport Properties of Densified $LH_2$and LO_2

PI: S. Van Sciver (Florida State University)
D. Celik (Florida State University)
D. Hilton (Florida State University)

Description

This experimental program is designed to produce high-resolution transport property measurements for cryogenic propulsion fluids (mainly LO_2 and LH_2) in regions where data are either incomplete or unavailable. The data acquired through this program are to be compared to existing correlations such as in property codes (GASPAK (Cryodata Inc.), REFPROP (NIST)). Although there was a significant effort at NBS (now NIST) in the 1960s and 1970s, we are not aware of any on-going precision transport property measurement programs for propulsion cryogens. Reestablishing this capability will benefit the long-term development goals of NASA as well as having significant scientific impact through fundamental investigations of the transport properties of simple and complex cryogenic liquids.

Objectives

This program is designed to produce measured values for the transport properties (and density)of subcooled LO_2 and LH_2. The region of primary interest is subcooled liquid below the normal boiling point (56 to 93 K for LO_2 and 14 to 20 K for LH_2 for pressures up to 0.7 MPa), where available data is either scarce or non-existent. A measurement precision of better than ± 1 percent is the required goal, which requires considerable effort to refine measurement technique. Longer term, the equipment developed through this program will be used to investigate transport in other cryogenic fluids of interest to the broader engineering community.

Benefits to NASA

Access to accurate property data is an essential component to engineering design. Many of the new propulsion systems under development for future space exploration will utilize densified fuels such as hydrogen slush (two phase liquid + solid) and subcooled LH_2 or LO_2. However, there are very few experimental data available on the properties of these fluids and until recently there has been almost no effort to remedy this situation. Our program will provide this basic engineering data for a variety of future NASA projects.

Results to Date

After a review of the literature on transport properties of LH_2 and LO_2, two experimental test cells were designed to carry out precision measurements: one for the measurement of thermal conductivity and density and the second for the measurement of viscosity. The thermal conductivity and density measurement apparatus is of similar design to that used by Diller, et al at National Bureau of Standards-Boulder in the 1960s, although our experimental cells are refrigerated using a Gifford-McMahon cryocooler allowing a wider operating temperature range (15 to 90 K). The viscosity measuring device is an original design although similar to devices used at NIST for precision measurements on conventional (non-cryogenic) fluids.

The thermal conductivity and density measurements on subcooled LO_2 are nearly complete. After considerable effort at improving our instrumentation to achieve the 1 percent precision goal, we are now producing high quality data. The density measurements versus temperature and pressure are complete and a brief report on those findings is in preparation. The thermal conductivity measurements are in progress and a considerable amount of data have been collected, but due to long thermal time constants, this effort will not be complete until the end of August.

The viscosity measurement cell that we developed uses the laminar capillary flow technique, which has never before been done for cryogenic fluids. The main part of the experiment is a large copper block containing three small fluid reservoirs. Two of the reservoirs are connected by a narrow stainless steel capillary. The third reservoir is used to supply a level difference to one of the two measurement reservoirs. The level in these two reservoirs is measured continuously using co-axial capacitive level gauges connected to precision measuring bridges. With an initial level difference between the two reservoirs, h_0, the levels will equilibrate exponentially with a time constant, τ, related to the flow velocity and thus the fluid viscosity. Two additional requirements are that the flow must be laminar setting a limit on the Reynolds number (< 1200) and the Dean number (< 7), which minimizes the effect of the helicity of the capillary. In the process of design, we have made the apparatus so that these corrections although potentially important have minimal effect on the results. The fluid will be subcooled by the same method utilized in the thermal conductivity measurements; that is by applying pressure from an external supply of helium gas.

The viscosity measuring apparatus is complete and the first measurements are in progress. As an initial test, we are conducting measurements on liquid nitrogen since more reliable data exist for this fluid to compare to our measurements. To date, we have been able to produce data that is within the required 1 percent precision, but varies in magnitude from REFPROP values by about 5 percent. We are currently have several potential explanations for this deviation and need to work more on the data to confirm their origin. Following that, our next step will be to carry out measurements on LO_2.

Both the thermal conductivity and viscosity apparatus will soon be used for measurements on subcooled LH_2. To provide a source of para-hydrogen for these measurements, we have decided to build a dedicated ortho-para converter that can be used with either apparatus. This converter consists of a copper cylinder filled with catalyst that can be immersed in a reservoir of LHe. The conversion occurs at 20 K and should produce 99^+ percent para-hydrogen. The converted gas can then be transferred to either experiment. The design of the o-p converter is complete and assembly will begin soon. The equipment should be available in time for the subcooled hydrogen measurements scheduled for later this year.

Follow-on Activities

For the remainder of Year 2, we intend to focus on completing all transport properties of subcooled LO_2 and building the ortho-para converter. The thermal conductivity and density measuring apparatus will be the first to be modified to conduct measurements with subcooled LH_2. These modifications will consist of attaching the cell to the lower stage of the two-stage cryocooler to achieve temperatures between 15 and 30 K. The o-p converter will be used to supply para- hydrogen to the cell. It may be also necessary to replace the thermometry as the currently in use platinum thermometers should not have the sensitivity to make measurements below 20 K.

Once the viscosity measurements on subcooled LO_2 are complete, we will begin preparations for similar measurements with subcooled para-hydrogen. Since we have only one two- stage cryocooler, these measurements may be necessary to wait until the thermal conductivity measurements are complete. Given the similarity of the above two tasks, much of the instrumentation developed for the thermal conductivity measurements will be shared with the viscosity experiments.

Results on both sets of measurements will be compared to available property databases and where necessary models will be developed for anomalous behavior. Findings from these experiments will be published in the literature, reported at conferences and on the FSU Hydrogen webpage.

Reverse Turbo Brayton Cycle Cryocooler Development for Liquid Hydrogen Systems

PI: L. Chow (University of Central Florida)
J. Kapat (University of Central Florida)
Q. Chen (University of Central Florida)
L. An (University of Central Florida)
C. Ham (University of Central Florida)
K. Sundaram (University of Central Florida)
T. Wu (University of Central Florida)
N. Dhere (Florida Solar Energy Center)
N. Arakere (University of Florida)
D. Rini (Rini Technologies, Inc.)
J. Vaidya (Electrodynamics Associates, Inc.)
B. Notardonato (NASA KSC)
G. Haddad (NASA KSC)

Description

Spaceport operations of the near future are one of the prominent applications for usage of large quantities of cryogenic propellants. Efficient storage and transfer of these fluids is necessary for reducing the launch costs. Also, for future manned and unmanned deep space missions and other missions to Mars, NASA is planning for extended cryogenic propellant storage durations of the order of several months as opposed to a few days or weeks. The goal of this task is to develop a reverse turbo Brayton cycle cryocooler for zero boil-off (ZBO) of cryogenic propellants. This cryocooler will be capable of extracting a few tens of watts (20 to 30 W) of heat at liquid hydrogen temperature (~18 K).

Objective

To develop reliable, compact, lightweight, highly efficient in its class and affordable cryocoolers for distributed cooling of liquid hydrogen systems for spaceport applications.

Benefit to NASA

All the previous attempts of cryocoolers by NASA for zero boil-off (ZBO) of cryogenic propellants in space have cooling powers of less than 2 W at liquid hydrogen temperature. These versions of flight-like cryocoolers would be more appropriate for cooling of sensors and super conducting materials in a spacecraft. The present cryocooler under development with a few tens of watts of cooling power at liquid hydrogen temperature would be ideal for ZBO of cryogenic propellants in NASA's future robotic missions to Mars and for other human space missions.

Task 4. Miniature Centrifugal Compressor Design Verification by Numerical Simulation and Testing (With Appropriate Scaling)

Numerical study of the miniature centrifugal compressor provided the results with air at the design condition and was presented in previous reports. However, the compressor was designed to compress helium, and air is used only for experimental convenience (details are mentioned under Task 5). The performance of the compressor using helium as working fluid was predicted by dimensional analysis and numerical studies were conducted to evaluate the predictions.

The similarity principle (dimensional analysis) can be expressed as:

$$\underbrace{pr_{tt}, \eta_{tt}, \frac{\hat{P}}{\rho_{00} N^3 D^5}}_{\text{Performance Variables}} = f\left\{\underbrace{\frac{\dot{m}\sqrt{RT_{00}}}{p_{01} D^2 \sqrt{\gamma}}, \frac{ND}{\sqrt{\gamma RT_{00}}}, \frac{ND^2}{\nu}}_{\text{Similarity Variables}}, \gamma\right\}$$

This equation predicts the performance of a new compressor if it comes from scaling of an existing compressor. It also predicts the performance of a compressor if we change its inlet conditions or working fluid. In order to better understand the theory of similitude, neon, which has the same γ (specific heat ratio) as helium but molecular weight close to air, is also considered. Through dimensional analysis, the compressor speeds at design point are found to be 313,000 and 141,000 rpm, when the working gases are helium and neon respectively. Table 1 shows the design and test speeds (~ 10 percent off-design speeds) for different working fluids obtained using the above principle.

TABLE 1.—DESIGN AND TEST SPEEDS FOR DIFFERENT GASES

Working Fluid	Neon	Helium	Air
Design speed (rpm)	141,000	313,000	108,000
Test speed (rpm)	-	350,000	120,000

Performance of the compressor is plotted in figure 1. The performance curves of air, neon, and helium at design condition are in a very close region. Helium and neon results have almost the same values of efficiency at a same pressure ratio. CFD results thus verify the dimensional analysis.

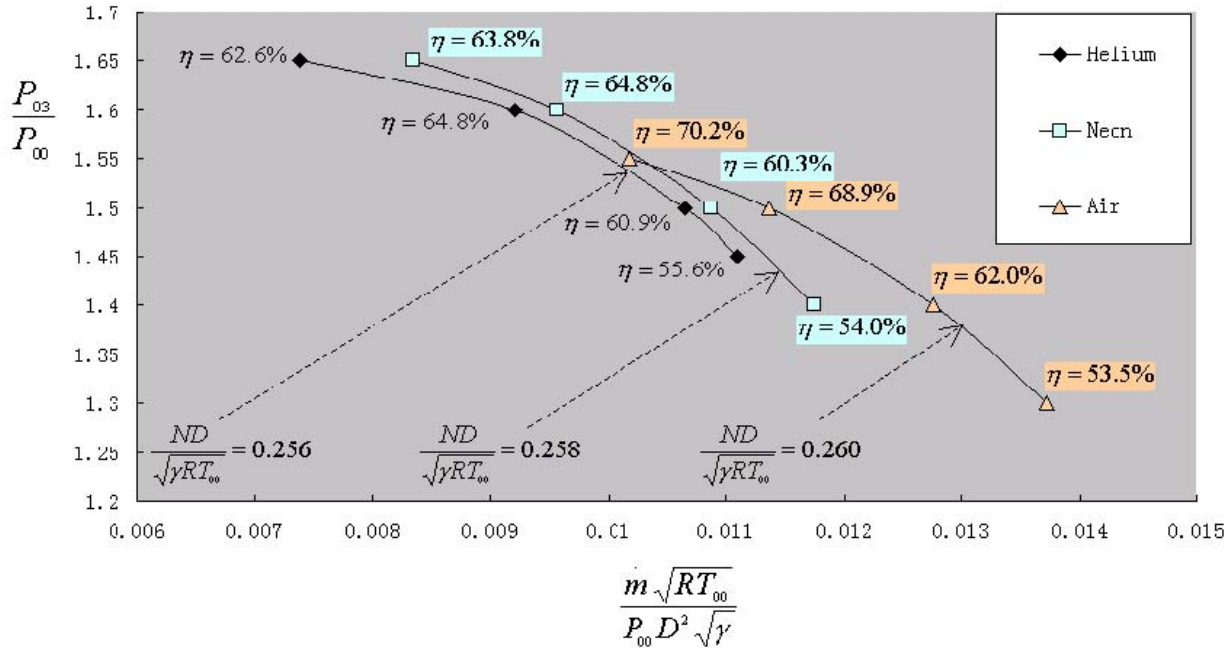

Figure 1.—Performance of the compressor at design speed (with air, neon, and helium).

Task 5. Integration and Preliminary Testing of the Motor/Compressor Assembly

A new integrated motor/compressor assembly is designed and being built to do the performance test of the 120,000 rpm single-stage air compressor. The motor is designed to run at 200,000 rpm with 2 kW input power.

The test rig is designed and built mainly for accomplishing the following tasks:

1. To test the single-stage of the final two-stage 350,000 rpm (exact design speed being 313,000 rpm) helium compressor for the one-step RTBC cryocooler operating between 18 and 300 K. The single-stage compressor is designed for compressing air (for experimental convenience and based on geometric scaling as mentioned in Task 4) and it can provide a pressure ratio of 1.55 at 120,000 rpm (exact design speed being 108,000 rpm).
2. To test the performance of the 2 kW motor at full load. The 2 kW PMSM has been tested with no load at 200,000 rpm and the results were mentioned in previous reports.
3. To verify various issues of the compressor/motor assembly like aerodynamics design, suitable bearings, effective motor cooling system, structural stability of the assembly, and rotordynamics.

Figure 2 shows the solid model of the motor/compressor test rig. The test rig is designed and is being sent out for fabrication.

The main features of this motor/compressor assembly test rig include:

1. Single shaft design – eliminates the difficult-to-do high-speed (flexible) coupler and improves the rotating stability.
2. Water-cooled bearing and motor casing – provides optimum motor operating conditions and reduces the related losses.
3. Spring-preloaded bearing system – a carefully design structure will improve the ceramic ball bearing performance at high speeds.
4. Closed-frame structure – provides a closed gas passage, which means that this compressor can be tested with almost any gas at arbitrary inlet conditions.
5. Precision impeller tip clearance control – a thread-scale structure is designed to measure and control the impeller tip clearance with the accuracy of up to 10 microns.
6. Multi-component shaft integration – the single shaft design required that the different components: impeller, magnet, shaft and plug, which were made with different materials, to be combined together. Electric beam welding and adhesive bonding were used effectively for this purpose. Properly integrated shaft will have better rotordynamic characteristics.

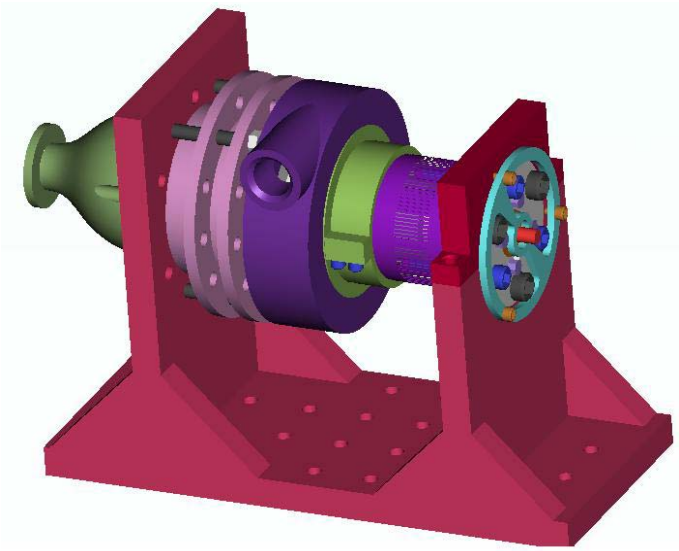

Figure 2.—Solid model of the motor/compressor test rig.

Figure 3 shows the rotor-bearing structure. The motor shaft is made with Titanium, which also holds the permanent magnet. The impeller is made with Aluminum. The holding between them is by adhesive bonding. The Titanium plug is welded to the shaft with electric beam welding.

Figure 4 shows the solid model of the base structure. This structure provides position reference for all the other components. It can hold the compressor side bearing and provide water-cooling for it.

Figure 5 shows the design of the water-cooled motor casing. The casing is made with Stainless Steel and has a maximum potential of 70 W heat load at full load. A thermal analysis is given later to show the cooling effect with heat transfer simulation.

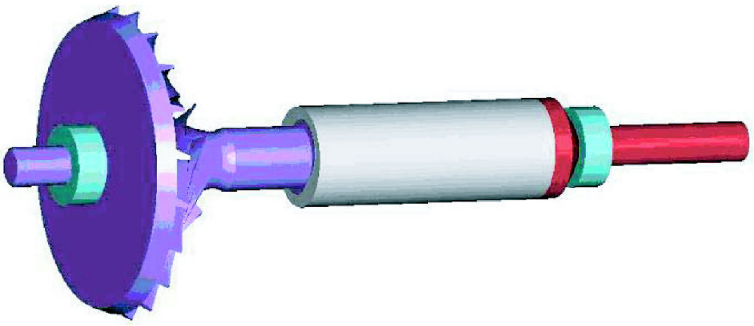

Figure 3.—Rotor-bearing system.

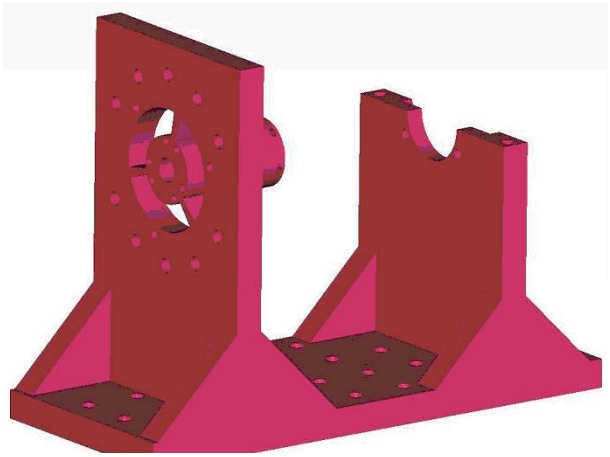

Figure 4.—Base structure.

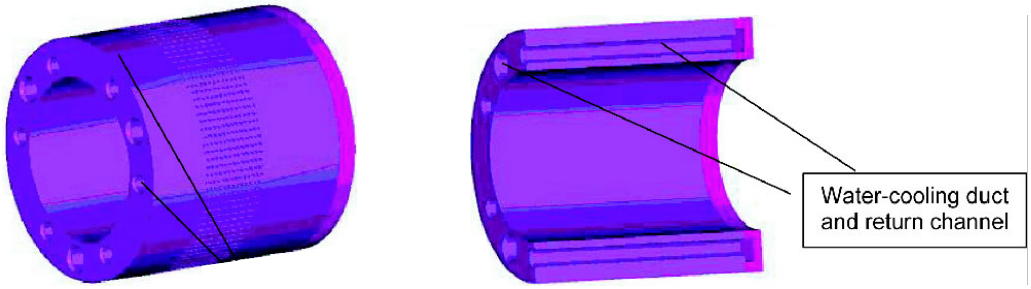

Figure 5.—Motor casing with cooling structure.

Figure 6 shows the tip-clearance measure-control structure and its working mechanism. The gas inlet passage components: guide-vane, end-board and the inlet holder, will be threaded together and supported by the motor case. Between the gas inlet assembly and the motor case these is a precision thread (1 mm pitch distance), with the scale (100 tic marks) on the motor case outside with which the tip gap can be precisely measured and controlled.

Figures 7(a) and (b) show the bearing spring preload structure. The preloaded bearing will have better stability and less loss when the shaft system spins at high speed.

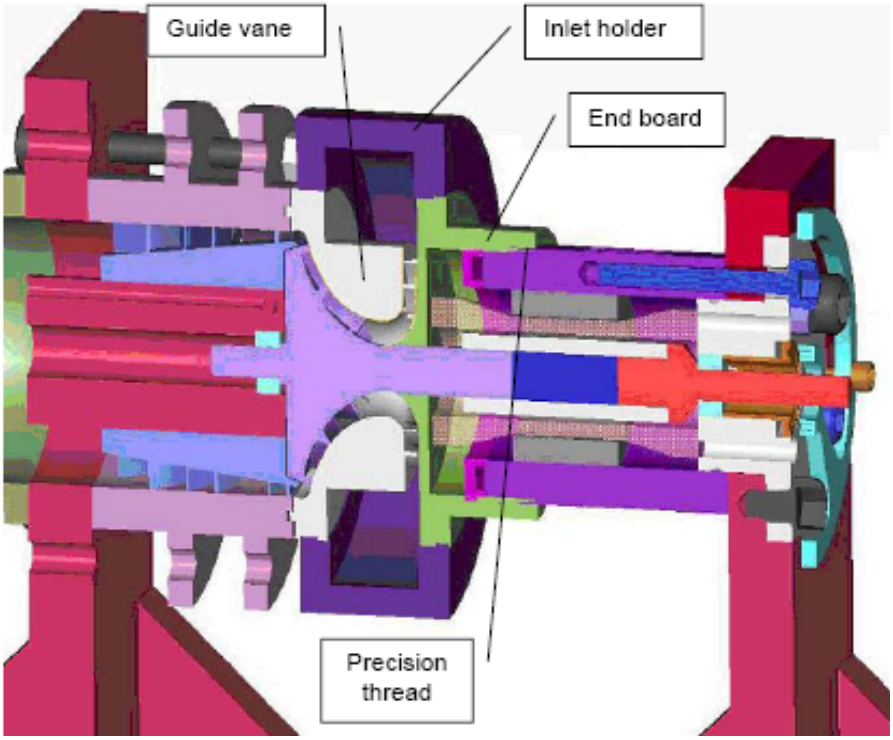

Figure 6.—Impeller tip clearance measure/control structure.

Figure 7.—(a) Ball bearing spring preload structure—side view.

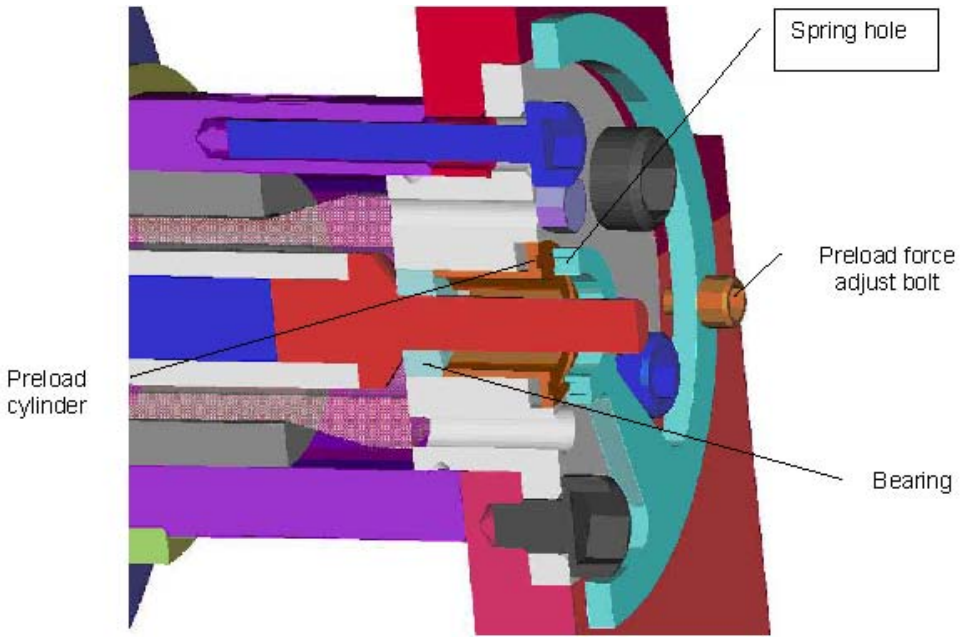

Figure 7.—(b) Ball bearing spring preload structure—elevation.

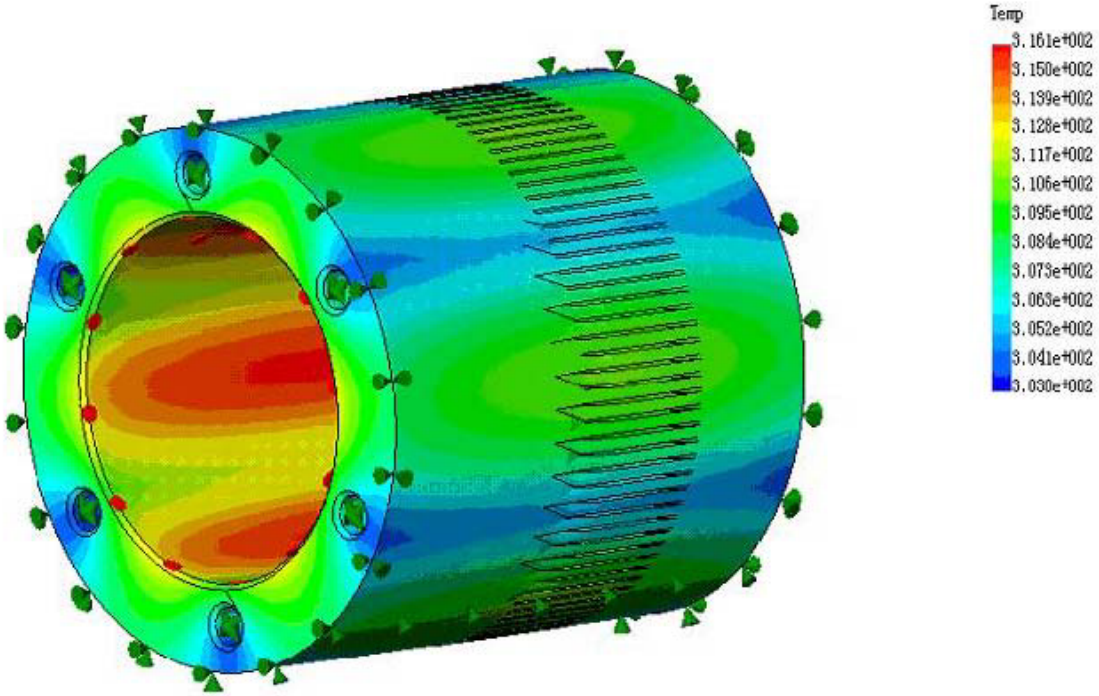

Figure 8.—Thermal simulation of water-cooling of the motor case.

Figure 8 shows the thermal simulation of motor casing at full heat load (70 W). This simulation is based on the simplified structural model of the motor casing. The simulation results show that the case temperature can be controlled below 50 ◦C with proper cooling duct design and water supply.

(Parameters used in simulation: duct size – 3.8 mm, cooling water temp. – 20 ◦C, water speed – 1 m/s, heat load – 70 W, casing material – Stainless Steel)

Metal Hydrides for Hydrogen for Hydrogen Separation, Recovery and Purification

PI: M. Hampton (University of Central Florida)
D. Slattery (Florida Solar Energy Center)

Introduction

The typical space shuttle launch from Kennedy Space Center requires the use of 483,000 gal of hydrogen, of which 98,000 gal are lost to boil-off. Additionally, over 75 million standard cubic feet per year of helium are lost from processes used for purging lines and systems that will or have contained liquid hydrogen. These huge quantities of hydrogen and helium represent a substantial financial investment that could be preserved with the use of the appropriate technologies.

With the increasing momentum towards a hydrogen economy sites of local production are growing in number. The hydrogen obtained from these local production facilities, whether it be from biomass, landfill gas or electrolysis, will not meet the stringent requirements for purity. Before use, this gas would require purification.

Goals

The goals of this project have been to determine technologies that are capable of selectively removing hydrogen from a helium stream in order to recover pure hydrogen, and pure helium. A secondary consideration has been to identify a system capable of absorbing hydrogen from boil-off. It is our goal to recommend technologies that we believe are appropriate for use by NASA and that will be transparent to the mission of the Center. It is believed that these goals are compatible with the needs of a future hydrogen economy, as well.

Benefit to NASA and Beyond

The systems resulting from this study will allow NASA to save many dollars by recapturing hydrogen boil-off and recovering the helium purge gas. Preventing the escape of hydrogen boil-off will also greatly enhance the safety of liquid hydrogen transfer and storage operations. The spin-off of this technology to the private sector will help to maintain the recognition of NASA as a world leader in the utilization of hydrogen.

Results and Discussion

There are a number of commercially used methods for separating gas mixtures. Early in this project, we decided upon the use of metals that form hydrides for the following reasons. Hydride formers can selectively absorb hydrogen, letting other gases pass through the system without reacting. The characteristics of hydrides can vary over a wide range and the absorption rate of the hydrogen can be tailored to meet the specific need. Because they can absorb hydrogen very rapidly, they can be used to recover the hydrogen that is lost to boil-off. Additionally, hydrides can be used to pressurize the hydrogen if it is to be fed to a liquefaction facility. Especially important is that because they selectively absorb the hydrogen, they allow for the recovery of helium purge gas that is pure enough for reuse.

A complete review of the literature had been conducted and a list of viable candidate compounds had been assembled. Initial studies were conducted, $LaNi_5$ and Mg_2Ni had been identified as those most appropriate for further study. We had determined that these materials could be activated by ball milling, then we had confirmed that $LaNi_5$ has the ability to absorb hydrogen at a rate compatible with NASA's needs. Because of questions from the NASA review panel as to whether the hydrogen absorption rate was truly adequate, we investigated methods for increasing kinetics, had found that the addition of small amounts of aluminum greatly increased kinetics.

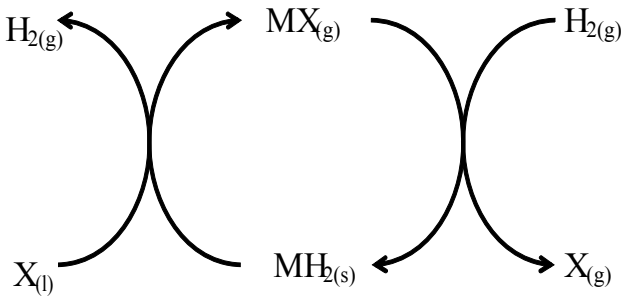

Figure 1.—Gas phase reaction cycle.

During this second contract year, we also looked at methods to purify the helium to the less than 1 percent hydrogen in helium required by NASA. A gas phase reaction was identified that was capable of removing trace amounts of hydrogen from the helium. The chemistry involved in this reaction was investigated and found to be extremely complex. Understanding of the mechanism is vital to making the reaction reversible. The goal is to have a cycle as shown in figure 1. The helium containing low levels of hydrogen flow through a chamber that contains the compound MX in the gas phase. A very rapid reaction occurs and the compound MH_2 precipitates out. The gaseous X is easily condensed from the helium. An additional advantage of this cycle is that if we can also show that the reverse reaction, in which compound X reacts with compound MH_2 occurs to release H_2 and regenerate MX, this would also have value in areas outside of NASA's needs.

This gas phase reaction appears to allow rapid and efficient removal of the residual hydrogen from a hydrogen/helium mixture, figure 2. The left hand plot in figure 2 is a gas chromatogram that was generated by passing a 20 percent hydrogen/80 percent helium mixture through a tube containing compound MX in the solid phase. While the gas was flowing, the tube was heated causing MX to vaporize and interact with the gas stream. At approximately 2 min intervals, exit gas samples were injected into the gas chromatograph. The initial injection produced two peaks, the first corresponding to helium and the second to hydrogen. Subsequent injections exhibited progressively smaller hydrogen peaks, with the hydrogen peaks completely disappearing by the fourth injection and then reappearing after all of compound MX had reacted. The right hand plot in figure 2 shows volume percent of hydrogen as a function of time. It can be seen that the concentration of hydrogen was efficiently reduced from 20 percent to less than 1 percent, well below the purity level specified by NASA for reuse of helium.

Further study of the gas phase reaction revealed some unexpected and heretofore unreported chemistry. It was found that the destination of hydrogen could be directed to the organic or to the inorganic part of a compound. Determination of the mechanism of this chemistry will have major ramifications in the realms of hydrogen storage and sensing. Proposals are currently being prepared for submission to support this work. Furthermore, this area of research will be continued in the 2005 contract year and is expected to lead to the filing of a patent application.

An additional study this year involved the effect of increasing the concentration of aluminum in the hydride former. We previously determined that the addition of several mol % aluminum to the $LaNi_5$ resulted in more rapid kinetics. We have done additional studies and determined that the addition of aluminum, up to 50 mol % causes no decrease in the amount of hydrogen that can be absorbed, as shown in figure 3. This will become very significant later in our research when a cost analysis is performed.

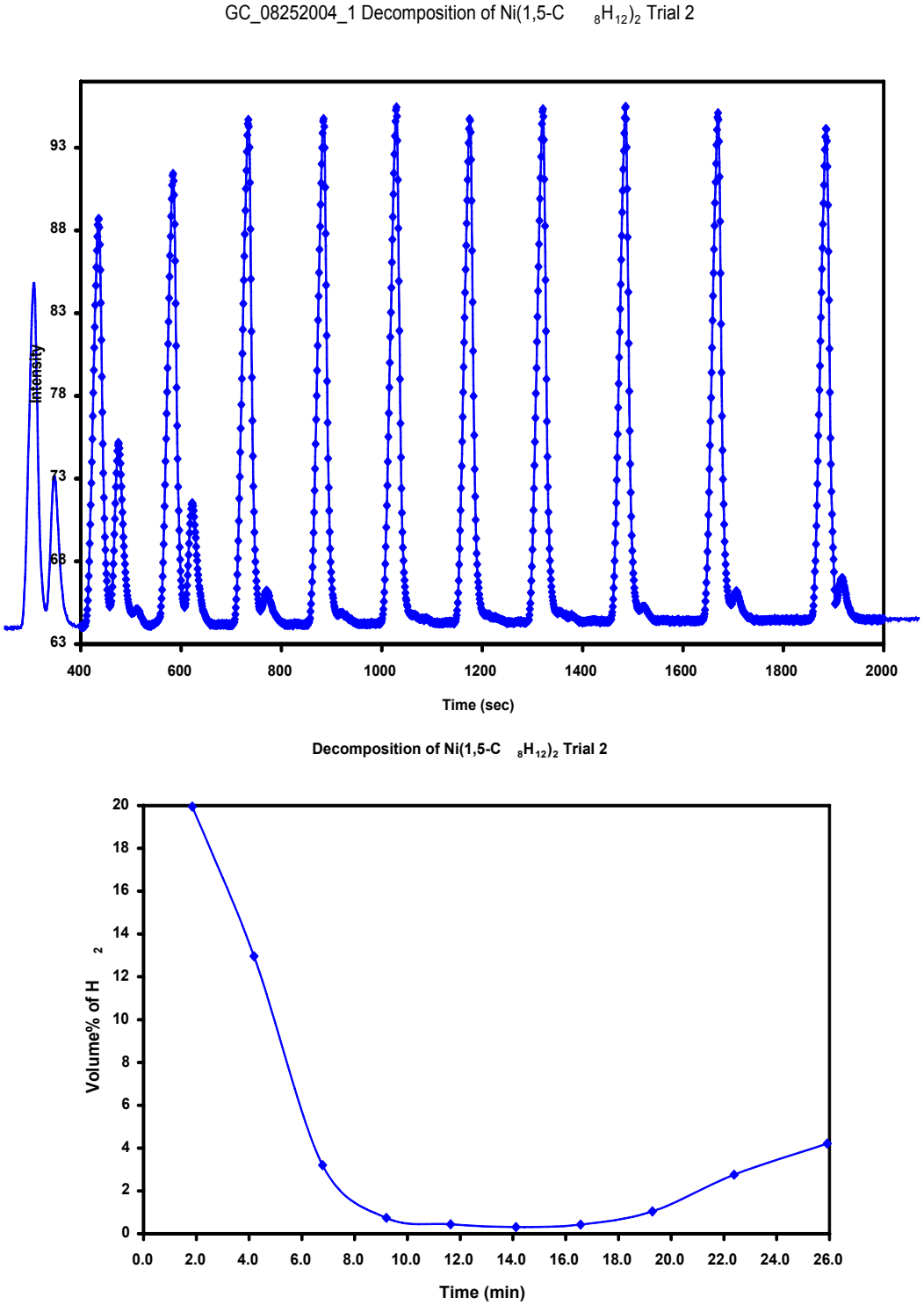

Figure 2.—Left hand plot: GC trace generated by repeated injection of exiting gas stream from gas reaction tube; Right hand plot: Gas composition plot derived from GC trace.

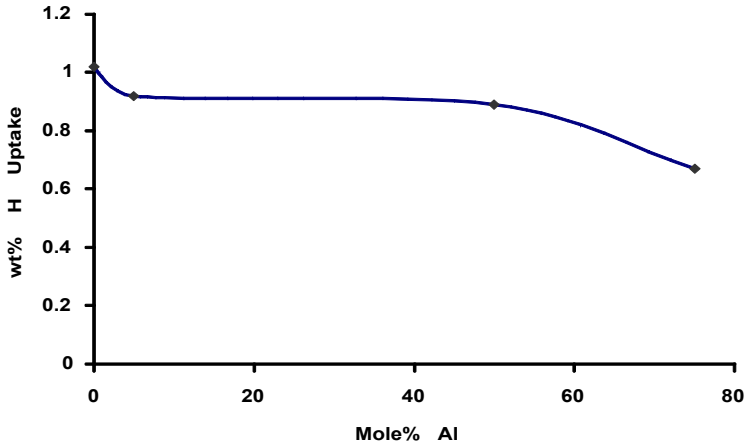

Figure 3.—Hydrogen uptake with addition of Al.

Summary

During this second year of funding, the effects of the addition of aluminum to lanthanum nickel were studied. The kinetics of hydriding in lanthanum nickel were found to be improved by the addition of several mol % of elemental aluminum. Furthermore,. it was shown that the addition of up to 50 mol % aluminum resulted in only a slight decrease in the hydrogen capacity of the hydride former. These results will have a significant impact on the cost of a hydrogen-helium separation/recovery system.

A gas phase reaction was identified that has the ability to remove residual amounts of hydrogen from a helium stream, allowing the helium to meet purity requirements for reuse. Preliminary details of the chemistry of this reaction were ascertained and some unexpected and heretofore unreported chemistry was revealed. This discovery will lead to additional funding, patent applications and publications.

Two journal articles, “Effects of various catalysts on hydrogen release and uptake characteristics of $LiAlH_4$” and “Effect of Ti_xAl_y catalysts on hydrogen storage properties of $LiAlH_4$ and $NaAlH_4$” were accepted for publication in the *International Journal of Hydrogen Energy*. An additional article “Hydrogen uptake characteristics of mechanically alloyed Ti–V–Ni” has been submitted to the *Journal of Alloys and Compounds.*

High Selective Nano-MEMS Low Temperature Sensor

PI: S. Seal (University of Central Florida)
S. Shukla (University of Central Florida)
W. Fei (University of Central Florida)
S. Deshpande (University of Central Florida)
I. Mukherjee (University of Central Florida)
D. Bera (Univrsity of Central Florida)
J. Cho (University of Central Florida)
S. Kuiry (University of Central Florida)
L. Ludwig (NASA-KSC)

Objectives

- Continue to synthesize non-agglomerated and monodispersed doped SnO2 nanoparticles, nanorods, Pd nanorods through a cost-effective chemical synthesis.
- Install and use of UV excitation for enhance sensitivity
- Use of FTIR to screen sensor materials and to understand gas-sold interaction on surface of nanoparticles – A novel approach
- Continue development and upgrade of the prototype sensor and sensor test bed.

Dr. Shukla: Continued development on the doped tinoxide, additional in collaboration with Dr. Cho (Professor), we have integrated nano doped tin-oxide on a MEMS device. The results are highlighted below.

Problems and Solutions

Room temperature sensitivity of H is a problem, we are developing nanoparticle based MEMS sensor to sense H in room temperature. The current research are in well agreement with NASA objective: Some key results are highlighted below.

Research to Date

(A) Development of Microelectromechanical System (MEMS) Device For Room Temperature Hydrogen Sensing

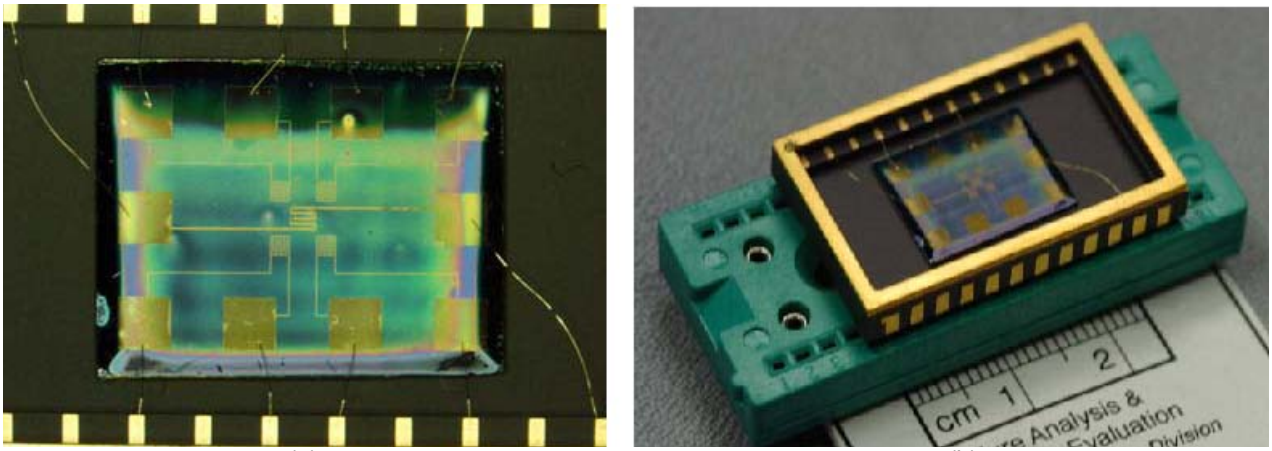

(a) (b)

Figure 1.—(a) Typical photograph of wire bonded MEMS device sol-gel dip-coated with nanocrystalline indium oxide (In2O3)-doped tin oxide (SnO2) thin film hydrogen (H_2) sensor.Four interdigitated electrodes and one temperature sensor are visible in the center of the MEMS device. Each electrode configuration is connected to Au pads, which are wire bonded to an integrated circuit (IC) chip. In (b), the IC-chip is installed in a 32-pin socket.

(B) Particle Size Measurement (AFM Analysis)

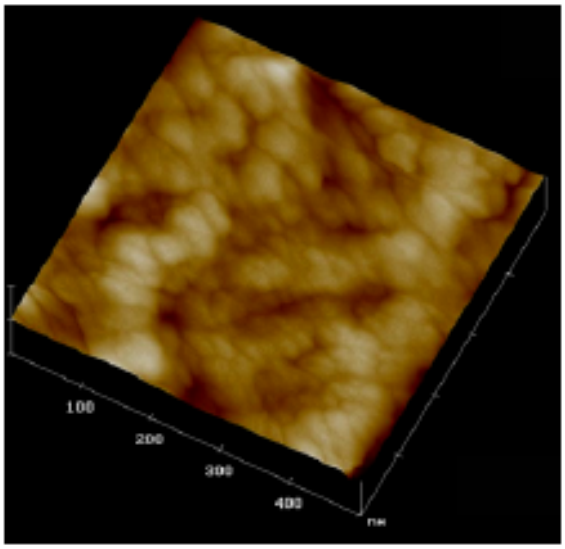

Figure 2.—Typical AFM analysis of In2O3-Doped SnO2 thin film sensor sol-gel dip-coated over the MEMS device. Average nanoparticle size = 50 nm.

(C) Room Temperature Hydrogen Sensing

- Hydrogen Sensitivity Tests at low H concentration

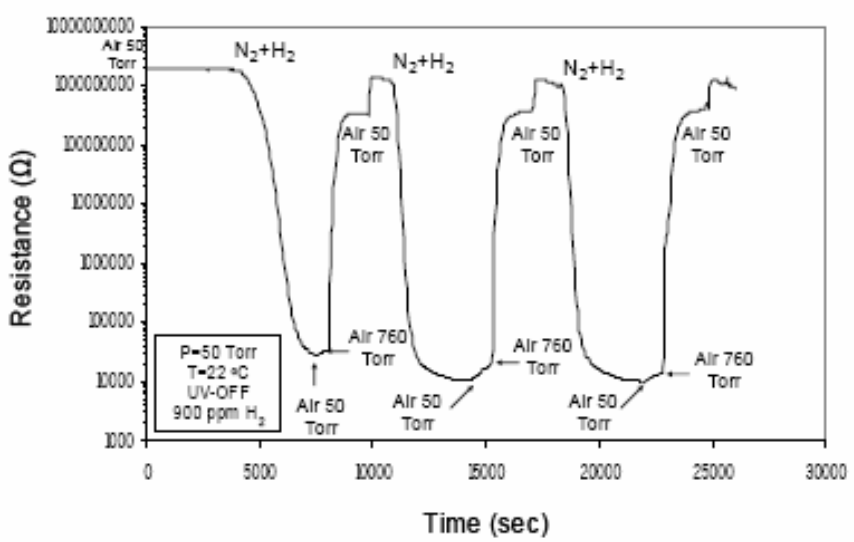

Figure 3.—Typical cyclic hydrogen-sensing test results conducted under dynamic condition. very high sensitivity (S = Rair/Rhydrogen, where rhydrogen and rair are sensor resistance values in air with and without the hydrogen) value as high as 110000 is recorded at room temperature for 900 ppm hydrogen, which is the largest ever reported in the literature. The recovery time at room temperature is as low as few minutes. Unconventional recovery is demonstrated here for the first time.

In the materials development, D. Bera (Ph.D. Student) and Dr. S. C. Kuiry are working on other nanomaterials, ceria and nano tin oxide whiskers and rods for high sensitive sensor development. The results will be reported in the next report.

Sensor Deployment

An extra component to the research task.

Objectives

1. To find an efficient way to model hydrogen sensor performance in networks, simulating post deployment conditions through computer simulation.
2. Using this model/ simulation to study as well as tweak sensor related parameters in order to get optimal post deployment performance – targeted performance attributes being: maximization of sensor lifetime & reduction of false-positives while keeping sensor response time in control.

Basic Methodologies

A Windows-based software simulation has been prepared to model the working of the sensor network after deployment. The model takes into account all the sensor related parameters like sensor response and recovery times, geographic parameters like distances between sensors and orientation of deployment, and deployment specific parameters like ratio of active to passive sensors when deployed.

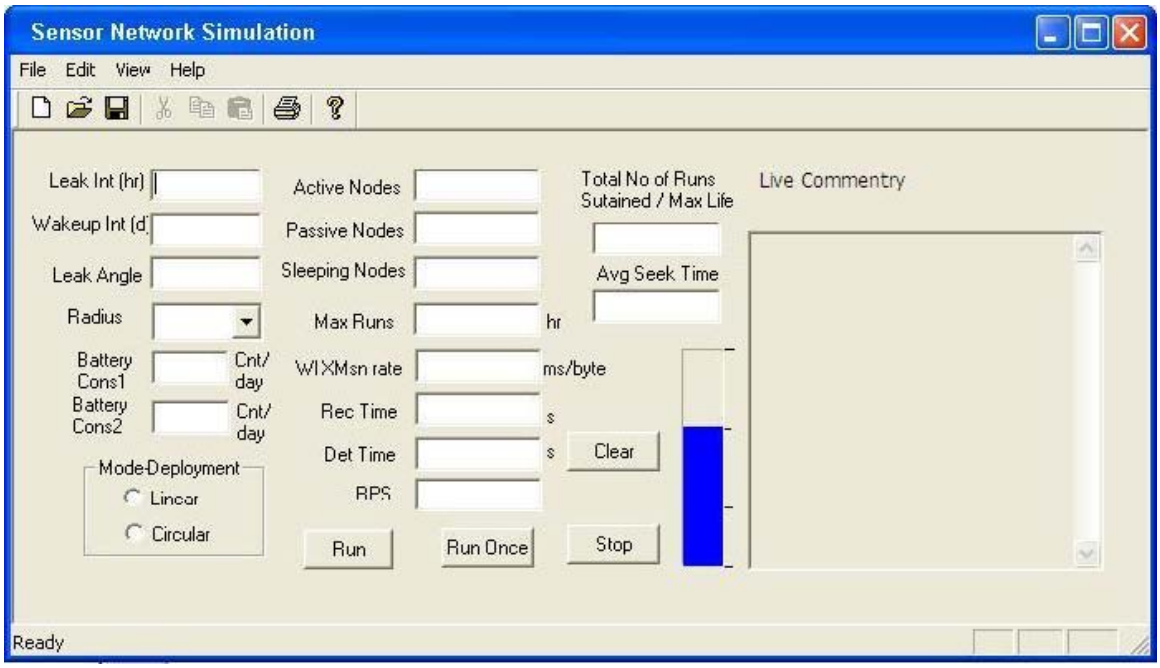

3. Sensor lifetime can be suitably defined, like for example the time when network dies or does not have enough sensors to give a response within threshold time.
4. Given the battery decay rates, we can trigger and simulate the leaks mathematically, and then follow the sequence of steps according to the logic of the sensor behavior and network communication behavior.
5. Continuous leaks can be simulated at prespecified intervals till the network burns out – this process can be repeated after modifying sensor parameters to do the necessary optimization
6. Individual leak-triggered events can give useful information and network uptimes, false positives (false-alarms) and cost of the network.

Problems

In normal deployment, network lifetime is too less, necessitating frequent overhauling and replacing of numerous sensors to keep the network performing. More importantly, performance is not predictable, and typically the need for replacement is only realized when the network fails once to sound the alarm on time - with potentially disastrous consequences. Also, due to these very reasons, the network performance attributes also have to be factored in sensor evaluation – a suitable method has to be found for this.

Using the methodologies described above, these performance optimizations have been achieved.

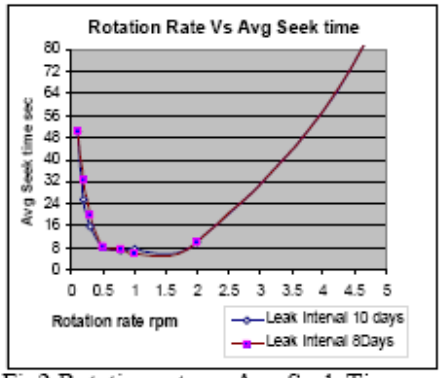

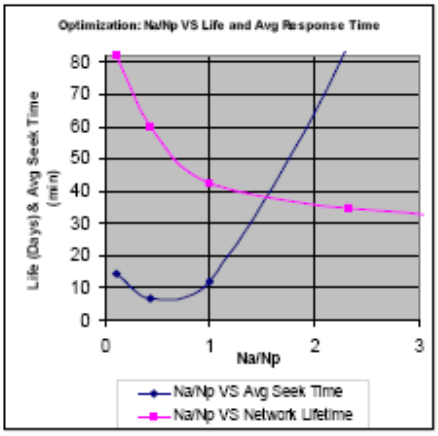

Fig2 Rotation rate vs Avg Seek Time

Fig3 Optimization Curve →

r vs avg. Seek time

&

r vs network lifetime

where r= no of Active Sensors to Passive sensors

Hence, using this system:

7. The performance of the network can be optimized. Deployment can be tweaked to maximize the desired parameters. Specifically, depending on our response time threshold, a lifetime of 45 to 60 days was achieved in our test conditions, for 1:2 ratio of active to passive sensors.
8. The network performance is predictable through computer simulation – no surprises.
9. False alarms can be removed almost 100 percent.

Objective

Acquisition and Use of Fourier Transform Infrared Spectrometer (FTIR) to characterize the surface chemistry of tin oxide for gas sensing.

Research to Date

The Fourier Transform Infrared Spectrometer (FTIR) had been installed calibrated thoroughly under different conditions and is ready for use. This FTIR offers adequate accuracy (0.1 cm-1) for characterization of surface chemistry and structural information on tin oxide nanopowders. Detailed experimentation will follow soon.

The newly acquired custom-built FTIR accessory, Diffuse Reflectance Unit offer powerful analytical means on screening of nano doped tin oxide based sensor materials and prediction of its performance.

Problems and Solutions

The problems happened during the installation and calibration of the instrument had been solved through intensive tests and interactions with the manufacturer.

How FTIR relates to the project objective: This FTIR instrument with in-situ diffuse reflectance attachment contains a temperature, atmosphere and pressure tunable chamber, where nano doped tin oxide powers is to be analyzed. It allows the in situ study of the chemical interactions and reactions taking place at tin oxide nanoparticle surfaces when gases are adsorbed. This will led us to a better understanding of the fundamental H_2 sensing mechanisms, which explain the enhanced sensitivity and selectivity of our tin oxide sensors. The intended outcome includes:

- In-situ surface chemistry of tin oxide nanoparticles
- Surface composition change due to surrounding atmosphere, handling, storage conditions, thermal history.
- Moister effect on H_2 gas sensing behavior

Furthermore, the variations of the background absorption over the total infrared range can be related to the variations of the free carriers density, that is to the variations of the electrical conductivity. Therefore, this technique makes it possible to correlate the surface reactions with the changes of the electrical conductivity.

Relationship of FTIR with the NASA Objectives

This FTIR study on nano doped tin oxide sensor will give us better understanding of the gas sensing mechanism and optimized materials. The finally developed low temperature H_2 sensor with high sensitivity and selectivity will fill the existing technological void in hydrogen sensing in the space delivery system. Besides, these nanomaterials-based sensors can be used for detecting other gases, thus making an impact on one of the long-term goals of socioeconomic developments.

Publications

1. S. Shukla and S. Seal, “Nanocrystalline Tin Oxide: A Hydrogen Sensor,” In: “Encyclopedia of Sensors,” Edited by C. Grimes, American Scientific Publishers (in preparation)
2. S. Shukla, S. Seal, and L. Ludwig, “Effect of Ultraviolet Radiation on Room Temperature Hydrogen Sensitivity of Nanocrystalline Sol-Gel-Doped Tin Oxide MEMS Sensor,” (in preparation)
3. S. Shukla, R. Agrawal, H. Cho, L. Ludwig, and S. Seal, “Giant Room Temperature Hydrogen Sensitivity of Nanocrystalline Sol-Gel-Doped Tin Oxide MEMS Sensor,” Adv. Mater. (in review)

4. S. Shukla and S. Seal, “Theoretical model for film-thickness dependent gas-sensitivity variation in nanocrystalline tin oxide sensor,” Phil. Mag. Letts. (in review)
5. S. Shukla and S. Seal, “Constitutive Equation for Gas Sensitivity of Nanocrystalline Tin Oxide Sensor,” Sens. Letts. (in press)
6. S. Shukla and S. Seal, “Sol-Gel Derived Nanocrystalline Semiconductor Oxide Thin Film Gas Sensors,” In: “Encyclopedia of Nanoscience and Nanotechnology,” Edited by H. S. Nalwa, American Scientific Publishers (in press)
7. S. Shukla, S. Seal, L. Ludwig, and C. Parrish, “Inverse-catalyst-effect observed for nanocrystalline doped-tin oxide sensor at lower operating temperatures,” Sens. Actuators B (in press)
8. S. Shukla and S. Seal, “Theoretical Model for Nanocrystallite Size Dependent Gas Sensitivity Enhancement in Nanocrystalline Tin Oxide Sensor,” Sens. Letts., 2 (1), 73-77 (2004)
9. S. Shukla, S. Patil, S. Seal, L. Ludwig and C. Parrish, “Room Temperature Hydrogen Gas Sensor Based on Nanocrystalline 6.5 mol % Indium Oxide Doped-Tin Oxide Thin Film,” Sens. Actuators B 97 (2-3), 256-265 (2004)
10. S. Shukla and S. Seal, “Room Temperature Gas Sensitivity of Nanocrystalline Pure Tin Oxide,” J. Nanosci. Nanotech., 4 (1/2), 141-145, (2004)
11. S. Shukla, S. Seal, Pho Nguyen, Hou Ng, and Meyya Meyyappan, “Transmission Electron Microscopy Sample Preparation of Nanocrystalline Tin Oxide Fibers Sensor Using Focused Ion-Beam Microscopy,” Sens. Letts. 1 (1), 75-78 (2003)
12. S. Shukla, S. Patil, S. Kuiry, S. Seal, L. Ludwig and C. Parrish, “Synthesis and Characterization of Sol-Gel Derived Nanocrystalline Tin Oxide Thin Film as a Hydrogen Gas Sensor,” Sens. Actuators B 76, 343-353 (2003)
13. S. Seal and S. Shukla, “Nanocrystalline SnO Gas Sensor in View of Surface Reactions and Modifications,” JOM 54 (9), 35-38, 60 (2002)

Conferences

1. S. Shukla, L. Ludwig, R. Agrawal, J. Duarte, H. Cho, and S. Seal, “Room Temperature Hydrogen Sensitivity of Nanocrystalline Doped-Tin Oxide Sensor under UV-Light,” TMS 134th Annual Meeting and Exhibition, San Francisco, California (2005)
2. S. Shukla and S. Seal, “Novel Single Crystal Model for Semiconducting Oxides Thin Film Gas Sensors,” TMS 134th Annual Meeting and Exhibition, San Francisco, California (2005)
3. S. Shukla, L. Ludwig, R. Agrawal, J. Duarte, H. Cho, and S. Seal, “Photo-Deactivated Room Temperature Hydrogen Gas Sensitivity of Nanocrystalline Doped-Tin Oxide Sensor,” Oral Presentation, 29th Annual Cocoa Beach Conference and Exposition on Advanced Ceramics and Composites, Cocoa Beach, Florida (2005)
4. S. Shukla and S. Seal, “Constitutive Equation for Semiconducting Oxides Thin Film Gas Sensors,” Oral Presentation, 29th Annual Cocoa Beach Conference and Exposition on Advanced Ceramics and Composites, Cocoa Beach, Florida (2005)
5. S. Shukla, L. Ludwig, R. Agrawal, H. Cho, and S. Seal, “Effect of UV-Radiation on Room Temperature Hydrogen Gas Sensitivity of Nanocrystalline Doped-Tin Oxide Sensor Incorporated into MEMS Device,” Oral Presentation, MRS Fall Meeting, Boston, Massachusetts (2004)
6. S. Shukla, L. Ludwig, and S. Seal, “A Novel Theoretical Model for Semiconducting Oxides Gas Sensors,” MRS Fall Meeting, Boston, Massachusetts (2004)
7. S. Shukla, J. Duarte, S. Seal and C. Perrish, “Nanostructured Functional Hydrogen Separation Membranes for Space Applications,” Florida Space Grant Consortium (FSGC) STD Awardees Meeting, Kennedy Space Center (KSC-NASA), Florida (2004)
8. S. Shukla, S. Seal, L. Ludwig and C. Parish, “Development of Low Temperature Hydrogen Sensor Based on Nanocrystalline Doped Tin Oxide,” Oral Presentation, Florida Chapter of the American Vacuum Society and Florida Society for Microscopy-Annual Symposium, Orlando, Florida (2004)
9. S. Shukla, S. Seal, L. Ludwig and C. Parish, “Low Temperature Hydrogen Sensing Behavior of Nanocrystalline Doped Tin Oxide Sensor,” Oral Presentation, 28th Annual Cocoa Beach Conference and Exposition on Advanced Ceramics and Composites, Cocoa Beach, Florida (2004)
10. S. Shukla, S. Seal, L. Ludwig and C. Parish, “Modeling and Sensing Hydrogen at Lower Operating Temperatures using Nanocrystalline Tin Oxide Thin Films,” Oral Presentation, 204th Meeting of The

Electrochemical Society, Co-sponsored in Part by the Electronics Division of The American Ceramic Society, Orlando Florida (2003)
11. S. Shukla, S. Patil, S. Kuiry, S. Seal, Ludwig and C. Parish, “Sol-Gel Derived Nanocrystalline Tin Oxide Based Hydrogen Gas Sensor,” Oral Presentation, TMS 132nd Annual Meeting and Exhibition, San Diego, California (2003)
12. S. Shukla, S. Patil, S. Kuiry, S. Seal, Ludwig and C. Parish, “Room Temperature Hydrogen Gas Sensor Based on Nanocrystalline Tin Oxide Thin Film,” Oral Presentation, 27th Annual Cocoa Beach Conference and Exposition on Advanced Ceramics and Composites, Cocoa Beach, Florida (2003)
13. S. Shukla, S. Patil, S. Kuiry, S. Seal, Ludwig and C. Parish, “Development of Nanocrystalline Hydrogen Gas Sensors,” Oral Presentation, NASA Hydrogen Research at Florida Universities-Midterm Review Meeting, Tampa, Florida (2003)
14. S. Shukla, S. Patil, S. Kuiry, S. Seal, Ludwig and C. Parish, “Room Temperature Hydrogen Gas Sensor Based on Doped Metal Oxide Semiconductor Thin Film,” Poster Presentation, Florida Chapter of the American Vacuum Society and Florida Society for Microscopy-Annual Symposium, Orlando, Florida (2003)
15. S. Patil, S. Shukla, S. Kuiry, L. Ludwig, C. Parish and S. Seal, “Nanocrystalline Oxide Thin Films For Oxygen Sensor,” Poster Presentation, (Honorable Mention) Florida Chapter of the American Vacuum Society and Florida Society for Microscopy-Annual Symposium, Orlando, Florida (2003)

Novel Technique for the Detection and Location of Hydrogen Leaks

Principal Investigator: G. Sellar (University of Central Florida)
A. Balasubramaniam (University of Central Florida)

Introduction

Description and Objectives

The objective of this project was to experimentally prove a new concept for detection and location of leaks from hydrogen systems. This new technique, conceived by Dr. Robert Youngquist at KSC is based on measurement of the Doppler broadening of a Rayleigh scattered laser beam from a mixture of air with helium or hydrogen. In the Maxwell-Boltzmann distribution of molecular velocities in a gas, the low molecular mass of the hydrogen molecules relative to nitrogen and oxygen molecules leads to substantially higher velocities for the hydrogen molecules. These high velocities lead to increased Doppler broadening in the Rayleigh scattered spectrum. A laser source, spectrum analyzing receiver, and scanning system will ultimately allow production of an image of the helium or hydrogen concentration.

Benefits to NASA

The goal is to ultimately reduce the time and cost of locating leaks in hydrogen systems by at least an order of magnitude.

Traditional Techniques

Safe operation of hydrogen systems requires the use of a non-hazardous gas to test for and locate leaks. Hydrocarbon 'tracer' gases, while relatively easy to detect, are composed of large molecules that often will not escape though leaks that will allow hydrogen to escape, therefore helium is used for this purpose. Helium, however, is difficult to detect and exceedingly difficult to image by remote sensing techniques.

Both absorption and emission spectroscopy are not applicable to helium or hydrogen due to lack of absorption and emission lines at moderate temperatures at any wavelengths that will propagate through air. While Raman spectroscopy has been successfully used to remotely sense hydrogen, the sensitivity is limited by the extremely low Raman interaction cross-section, and this approach is not applicable to helium, since helium is not Raman-active. The Raman approach therefore requires that hazardous quantities of hydrogen (which is flammable) be allowed to continue to leak while technicians engage in a search for the source of the leak.

The remaining traditional techniques for remote sensing of gases are based on detection of variations in *density*. These approaches are limited by background *clutter* due to natural variations in the density of air resulting from natural variations in temperature, and therefore do not have the potential to detect low concentrations of helium or hydrogen.

Rayleigh Doppler Technique

Dr. Robert Youngquist of KSC has invented a novel technique based on measurement of the *Doppler broadening* of a *Rayleigh-scattered* laser beam. The molecules of a gas scatter electromagnetic radiation in what is known as *Rayleigh scattering*. The distribution of velocities of the molecules varies with the composition of the gas, so when light of a single frequency is scattered from a gas, the frequency spectrum of the scattered light is *broadened* in an effect known as *Doppler broadening.* Thus it is possible to determine the composition of a gas by measuring the Doppler broadening of Rayleigh-scattered light.

We have developed a model that predicts the spectrum of the Doppler broadened light, and the signal-to-noise ratio for this technique as a function of the key hardware design parameters. This model includes both direct detection and heterodyne detection approaches. An example predicted spectrum is shown in figure 1.

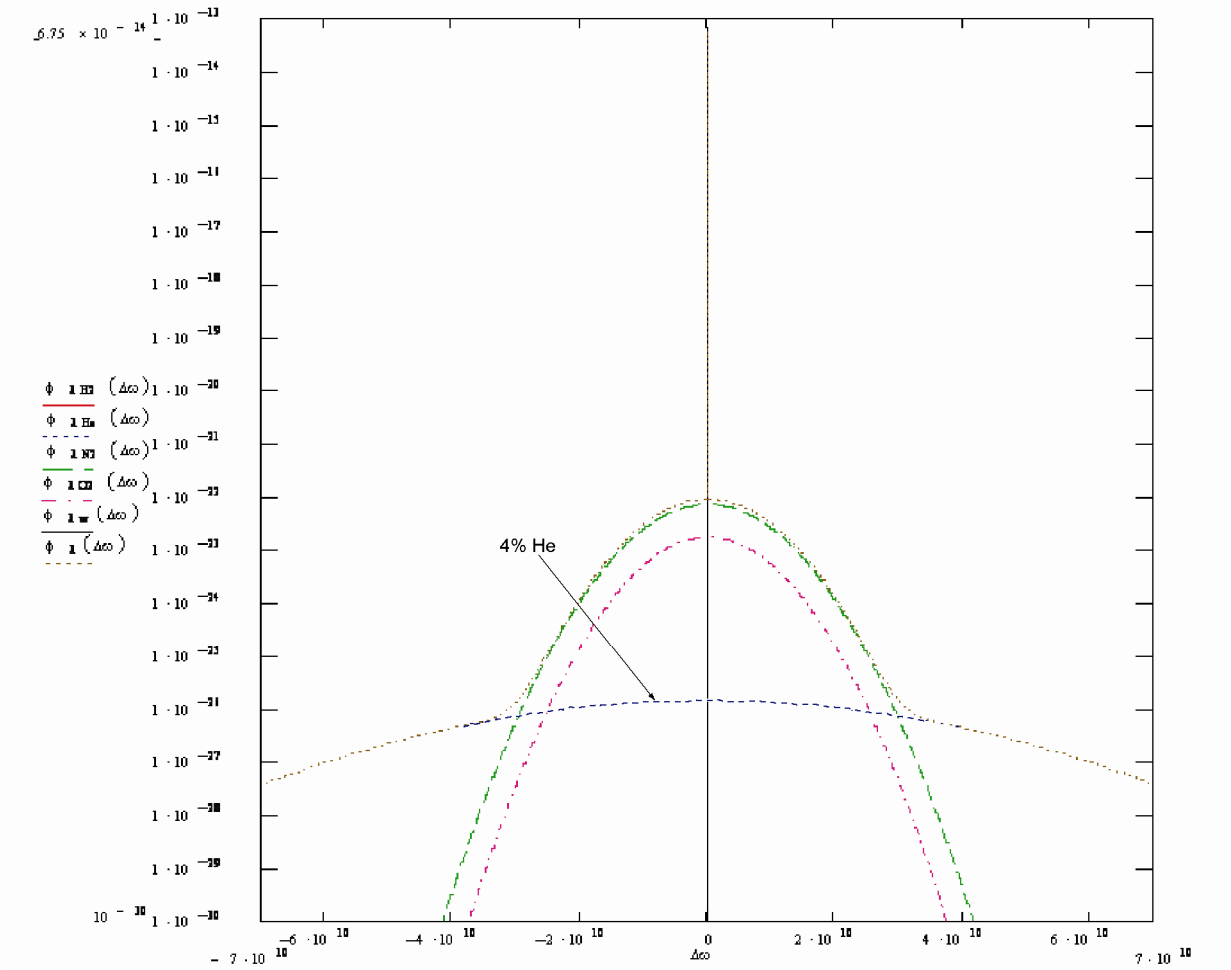

Figure 1.—Predicted spectrum scattered from a mixture of 4 percent He in air. Individual contributions from O_2, N_2, and He gas constituents are traced in color, the central spike is scatter from solid surfaces, and the sum is traced in black.

Results

Systems Design, Integration, and Subsystem Testing

A theoretical model and a design trade study led to the selection of two detection techniques that have the potential to provide an acceptable signal-to-noise ratio: direct detection employing a vapor absorption filter to suppress the surface scatter, and homodyne detection with a high-frequency detector.

Systems integration and subsystem-level testing were completed. Figure 2 shows the transmit and receive optics for the homodyne-detection approach and figure 3 shows testing of the iodine vapor absorption cell with the doubled-YAG laser from Crystal Laser. This laser proved unable to tune to the strong absorption line in the iodine spectrum and was returned to the vendor and replaced by a laser supplied by Lightwave Electronics which is more powerful and tunable over a wider spectral range.

Testing of the initial design of the Fabry-Perot interferometer comprised of off-the-shelf components is shown in figure 4.

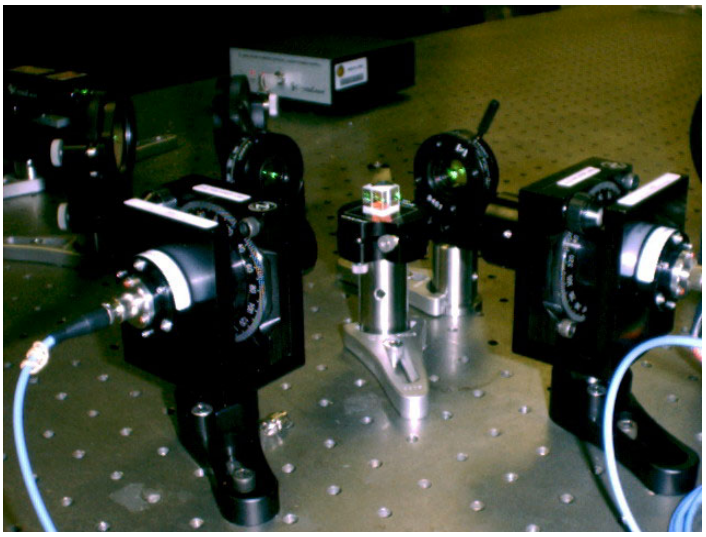

Figure 2.—Transmit and receive optics for the homodyne-detection approach.

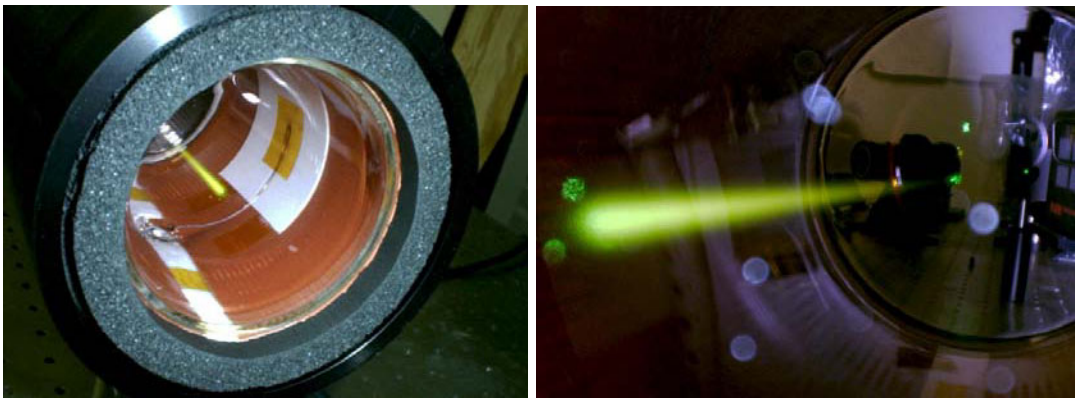

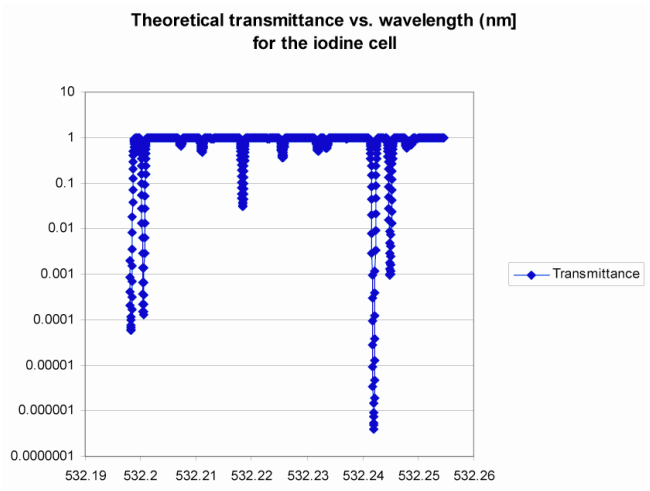

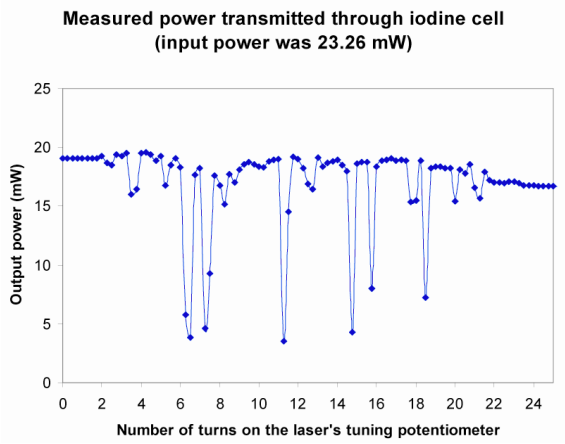

Figure 3.—Testing of the iodine vapor absorption cell (upper left and upper right); Iodine absorption spectrum on a logarithmic scale (lower left); Measured absorption spectrum on a linear scale over the range of the doubled-YAG laser from crystal laser (lower right).

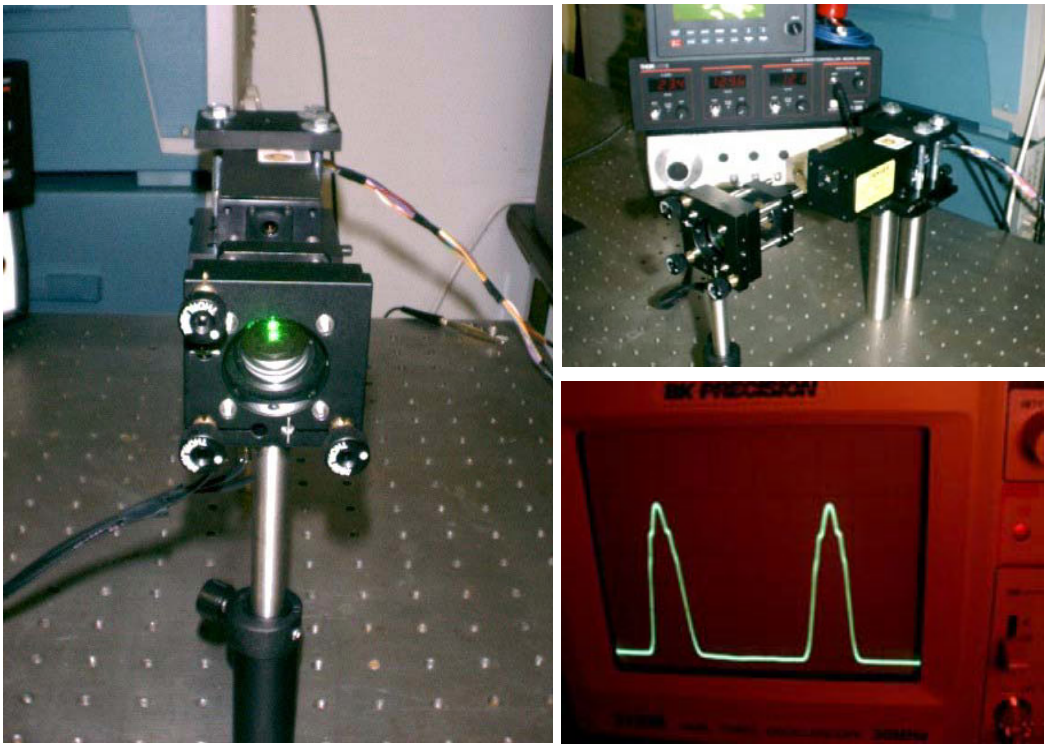

Figure 4.—Testing of the initial design of the Fabry-Perot interferometer including the instrumental response function (lower right)

System-Level Testing

A detectable signal was not obtained with the homodyne approach. It was observed that the insertion efficiency of the fiber-optic couplers is an order of magnitude lower than expected. This is believed to be due to the use of alignment mechanisms designed for communications fibers - which operate at 1530 nm and have a much larger core diameter – with fibers designed for 532 nm. It was also discovered that the –150 dBm noise floor advertised for the electronic spectrum analyzer was achievable only under the impractical conditions of zero bandwidth and infinite integration time. Use of custom electronic filter circuitry rather than a general-purpose spectrum analyzer may be a better approach.

For the direct-detection approach, the results shown in figure 5 were obtained with a Fabry-Perot system employing 25 mm diameter mirrors polished to a flatness of λ/10 with the spacing scanned by an open-loop piezoelectric system.

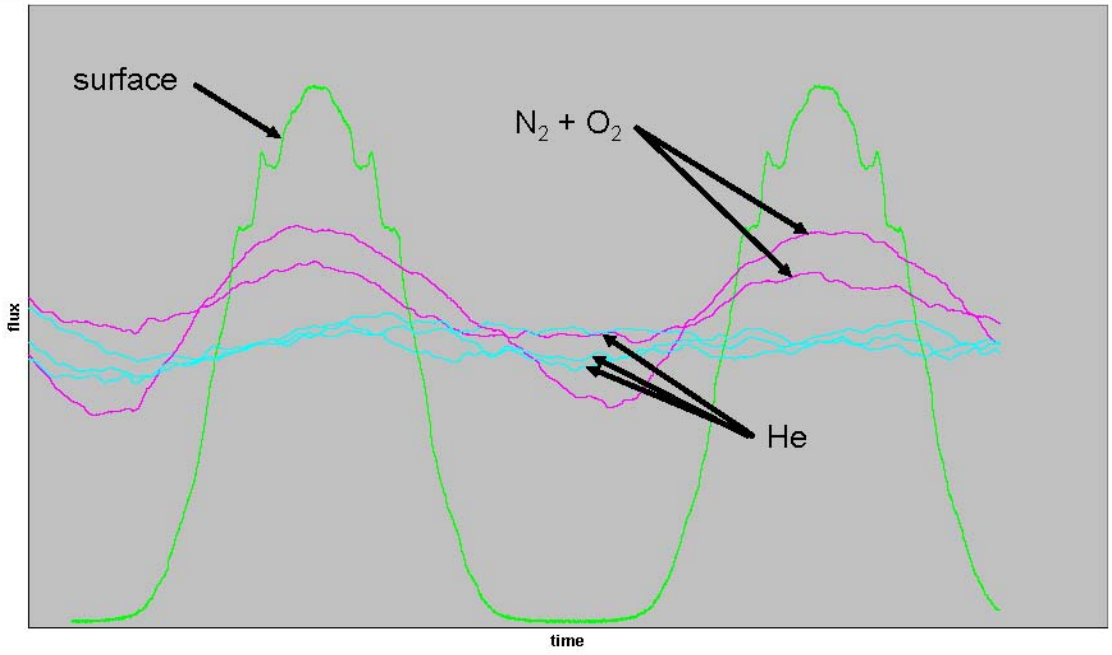

Figure 5.—Doppler spectra obtained with the direct detection technique, exhibiting an increase in flux at the frequencies with the highest Doppler shift from the laser (peak) frequency when the helium leak was active, indicating detection of these low-mass, high-velocity He Atoms. Spectra from several experiments are shown superimposed.

Discussion

Many lessons were learned and design improvements implemented as a result of subsystem-level and system-level testing:

Homodyne Detection Approach

- Improvements to the homodyne approach include addition of a beam trap to reduce flux from surface reflections and use of the unscattered beam as an efficient source for the local oscillator for the homodyne-detection approach, as illustrated in figure 6.
- Fiber coupling optics should be specially re-designed for the smaller cores of fibers designed for 532 nm wavelength.
- The local-oscillator power is limited by available laser power and the efficiency of the coupling optics rather than by detector saturation.
- In practice, the noise-floor of the electronic spectrum analyzer was much higher than expected.

Direct Detection Approach

- A wavemeter was sourced, procured (used), refurbished, recalibrated, and tested. Testing with the wavemeter confirmed that the first laser did not satisfy the requirements as it failed to meet both the power and the tunable range specifications.
- A 100 mW, single-longitudinal-mode, doubled Nd:YAG laser that met these requirements was ultimately successfully procured from an alternate vendor.
- Modeling/optimization of vapor cell pressure (illustrated in)indicated that a new cell with higher vapor pressure would enable blocking of a significant portion of the flux scattered from O_2 and N_2 in addition to blocking the flux scattered from surfaces. This development was ultimately not pursued due to budget limitations.
- Walk-off (flatness and alignment) losses in the first Fabry-Perot system were significant;

- The open-loop piezo-electric transducers used to align and move the Fabry-Perot mirrors in the first system exhibited significant low frequency drift. Either a closed-loop system with capacitive sensors or a pressure-modulated system is required to overcome this limitation. The pressure-modulation approach has the lower cost.
- The optimum reflectance for the Fabry-Perot mirrors for this application is 98 percent, which requires a custom coating design and fabrication.
- An improved Fabry-Perot system was designed and fabricated. The prototype system, which had mirrors of 25 mm diameter, fabricated flat to λ/10, and employed open-loop piezoelectric modulation, was replaced with a custom-designed Fabry-Perot with mirrors 100 mm in diameter, fabricated flat to λ/100, and employing pressure modulation.
- Due to the long lead-time required for the 100 mm, pressure-modulated system, a pair of 25 mm, λ/100 mirrors were fabricated as an intermediate step. Testing with these mirrors in piezoelectrically-modulated system showed that performance was limited by the alignment instability of the piezoelectric transducers, such that performance was not significantly improved by upgrading the mirrors alone.
- Other improvements to the direct-detection approach included addition of a collection lens to increase the efficiency, use of a photomultiplier tube to improve sensitivity, and additional of a 300 mm focal length lens to match the central fringe of the Fabry-Perot interference pattern to the sensitive area of the photomultiplier tube as shown in figure 8.

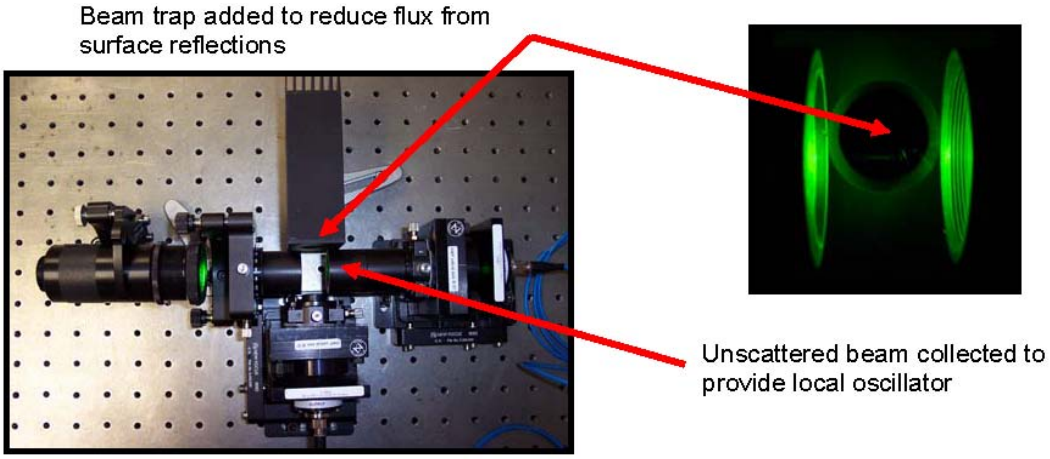

Figure 6.—Two improvements to the homodyne-detection experiment.

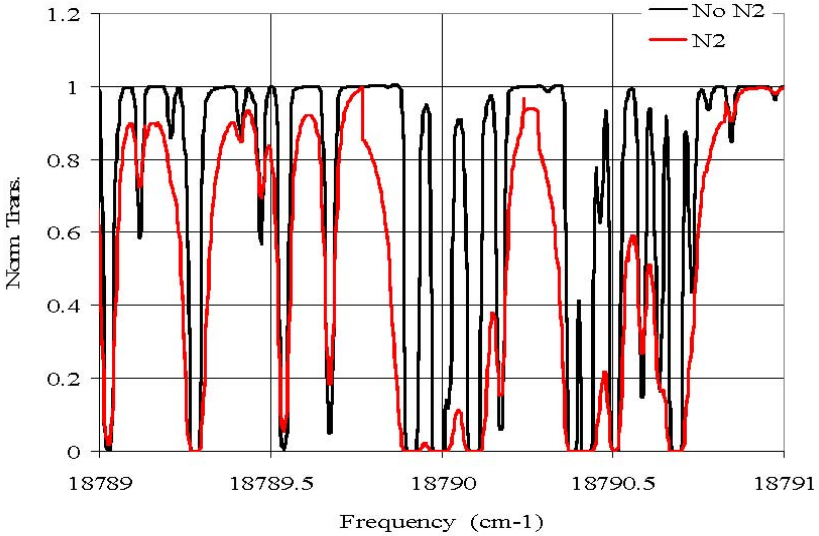

Figure 7.—Modeled effect of adding N2 to pressure-broaden the absorption lines in the iodine vapor absorption cell.

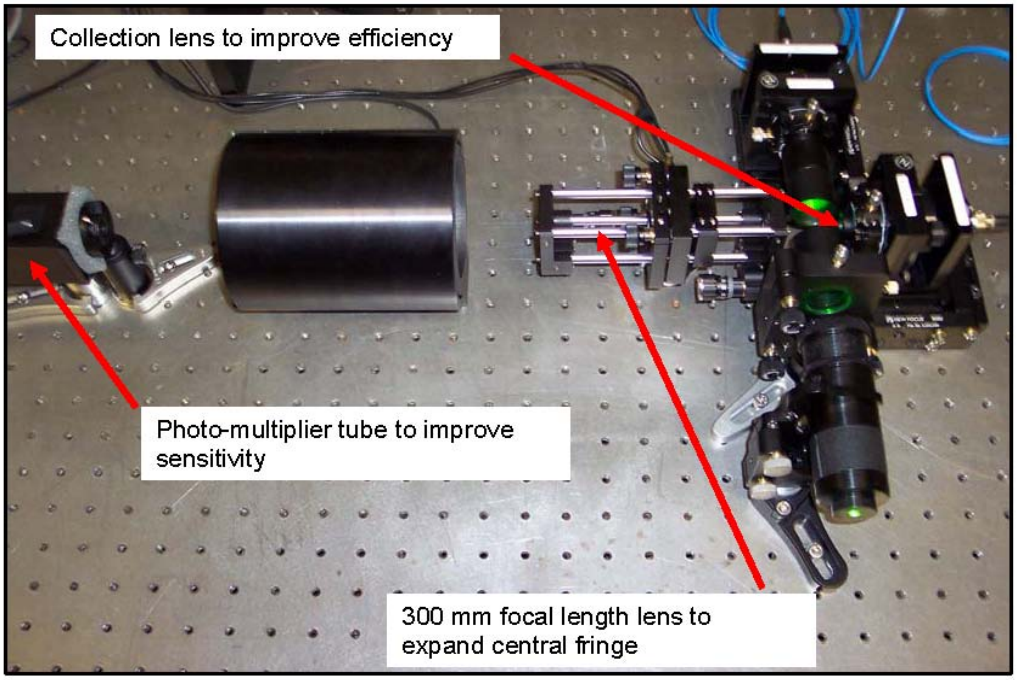

Figure 8.—Three improvements to the direct-detection experiment.

Conclusions

Considerable progress was made on the development of a system for detection of hydrogen in air by measuring the Doppler broadening of Raleigh-scattered light. As detailed in the Discussion section, eleven significant lessons were learned and eleven improvements were formulated in response, of which six proved possible to implement within the schedule and budget constraints.

Development of Cryogenic Shape-Memory Actuator Materials for Switches, Seals and Valves

PI: R. Vaidyanathan (University of Central Florida)

Project Summary

Shape-memory alloy actuators are widely recognized as having the following advantages for space-related applications: (i) high power/weight and stroke length/weight ratios (ii) integration of sensor and actuator in a single element (iii) clean, debris -less, spark-free operation and (iv) ability to function in zero-gravity environments with small, controlled accelerations. The goal of this project is to lower the operating temperature range of shape-memory alloys in order for them to be used in hydrogen related technologies. The immediate benefit to NASA KSC is the development of a shape-memory thermal conduction switch for application in cryogenic liquefaction, densification and zero boil-off systems. This is being extended to include the potential use of shape-memory alloy actuator elements for cryogenic seals, valves, fluid-line repair, self-healing gaskets, and even to ambient debris-less separation and latch/release mechanisms.

In Year 1 of this project, NiTiFe powders were arc-melted. The NiTiFe buttons were subsequently thermomechanically processed in order to successfully demonstrate shape-memory and actuator properties. A range of compositions were fabricated and tested. In Year 2, the alloys developed were incorporated in a prototype cryogenic thermal conduction switch and successfully tested. In order to investigate deformation in these materials *in situ,* during loading at cryogenic temperatures, for the first time a facility for cryogenic loading during neutron diffraction was developed at Los Alamos National Laboratory. The goals in Year 3 are to (i) improve on the aforementioned prototype as outlined in this proposal (ii) to test the fabricated alloys at Los Alamos National Laboratory at cryogenic temperatures (iii) to continue using dilatometry, indentation and calorimetry at UCF to optimize these alloys, while additionally measuring stresses and strains during actuation and (iv) to scale-up alloy production quantities by recourse to hot isostatic processing (HIP).

Project Description

Objectives and Approach

Shape-memory alloys when deformed can produce strains as high as 8 percent. Heating results in a phase transformation and associated recovery of all the accumulated strain, a phenomenon known as shape-memory. This strain recovery can occur against large forces, resulting in their use as actuators. The goal of this project is to lower the operating temperature range of shape-memory alloys in order for them to be used in cryogenic switches, seals, valves, fluid-line repair and self-healing gaskets for hydrogen related technologies. This is primarily accomplished by:

16. **Alloy development**: The Ni-Ti-Fe alloy system, previously used in Grumman F-14 aircrafts and activated at 120 K, is further developed through arc-melting a range of compositions and subsequent thermomechanical processing.
17. **Materials testing and evaluation**: A combination of indentation, diffraction, calorimetry and dilatometry techniques are employed to optimize the fabricated alloys. Particularly, a unique *in situ* cryogenic loading capability during neutron diffraction, developed in partnership with Sierra Lobo at NASA KSC, is used to investigate these alloys at Los Alamos National Laboratory.
18. **Cryogenic actuator design and prototype construction**: Designs of cryogenic actuators are analyzed and implemented. Initial emphasis is placed on developing a cryogenic thermal conduction switch for NASA KSC and this is followed by focusing on seals and valves.

Previous Work During Year 1 and Year 2

The first step of this project involved commissioning of an arc-melting facility at UCF for fabricating cryogenic NiTiFe shape-memory alloys. Following the successful commissioning of this facility, selected compositions of NiTiFe alloys were arc-melted (fig. 1(a)). The resulting buttons (fig. 1(b)) were

subsequently thermomechanically processed to produce strips (fig. 1(c)) that exhibited shape-memory and actuator properties (fig. 2(a) and (b)). The strips were incorporated in a cryogenic thermal conduction switch for NASA KSC in figure 2(c) and preliminary tests have been successful.

The fabricated alloys were characterized using indentation, diffraction and calorimetry techniques. A differential scanning calorimeter capable of measurements as low as 120 K was commissioned at UCF. A liquid helium dilatometer has been acquired and is currently being commissioned. Instrumented indentation was used to mechanically characterize the arc-melted buttons. In partnership with Sierra Lobo at NASA KSC and Los Alamos National Laboratory, a unique low temperature loading capability for *in situ* neutron diffraction measurements was implemented on the Spectrometer for Materials Research at Temperature and Stress (SMARTS) at Los Alamos National Laboratory. The *in situ* diffraction measurements, during loading at 216 K, observed twinning in NiTiFe prior to a reversible phase transformation at higher stresses. Constrained recovery measurements, wherein the alloys were allowed to warm up during loading, were also recorded. The testing represented a situation that was identical to a shape-memory alloy working in a cryogenic actuator application. The testing procedures provided valuable insight into optimizing cryogenic NiTiFe shape-memory alloys and a range of publications and presentations have resulted.

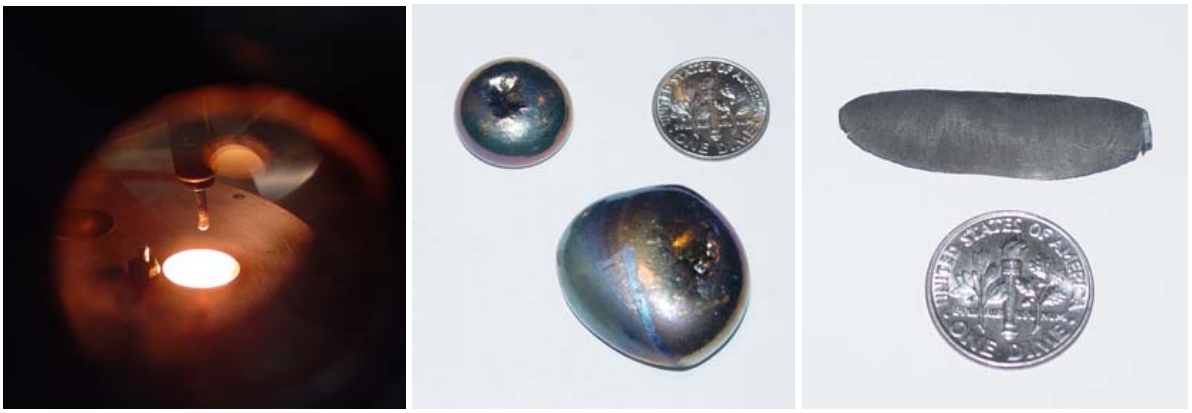

(a) (b) (c)

Figure 1.—Processing of nitife alloys. Nitife powders in (a) Were arc-melted to form buttons in (b), Which were subsequently thermomechanically processed to give elements in (c). Such a strip element is tested in figure 2(a) and b.

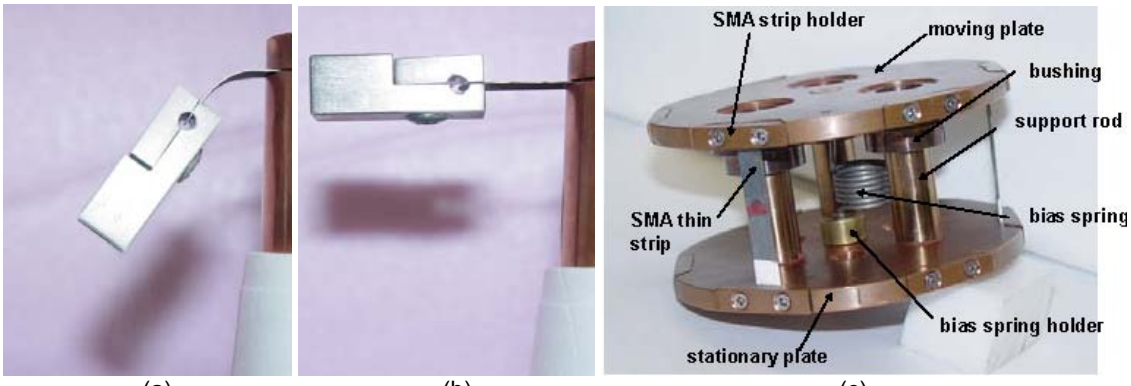

(a) (b) (c)

Figure 2.—Demonstration of a cryogenic nitife shape memory actuator. The strip in figure 1 was dipped in liquid nitrogen in (a) and actuates as it warms up in (b). Such a strip has been incorporated in a cryogenic thermal conduction switch for NASA KSC in (c) and preliminary tests have been successful.

Future Work

Leveraging the aforementioned successes, the following are future activities:

19. **Cryogenic conduction switch prototype enhancement and optimization**: Preliminary testing has been successful and displacement has been observed associated with a low hysteresis (2°) reversible rhombohedral phase transformation in NiTiFe. The displacement is important to obtain adequate contact force as well as to make-and-break conductive heat transfer though indium foils. It will be maximized through further thermomechanical processing of the NiTiFe elements and possible reduction in bending stiffness of the elements my geometrical alterations. A design modification may also be necessary to eliminate thermal gradients between the two ends of the shape-memory elements. The necessary changes will be incorporated and backed up with subsequent testing.
20. **Cryogenic testing of NiTiFe alloys at Los Alamos National Laboratory**: Testing at temperatures as low as 216 K was achieved last year at Los Alamos National Laboratory during mechanical loading and neutron diffraction. Lower temperatures were not attainable due to heat leak from the actuator pump. A modified design of the compression platens will be implemented and testing at lower temperatures performed.
21. **Indentation, calorimetry and dilatometry testing, and alloy optimization**: The liquid helium dilatometer acquired will be commissioned for testing alloy compositions with sub-77 K transformation temperatures. Instrumented indentation and calorimetry will be continued to be used to characterize the fabricated alloys. In conjunction with other related projects, a thermomechanical analyzer will be procured from PerkinElmer, Connecticut, for quantifying stresses and strains during actuation. The indentation, diffraction, dilatometry and calorimetry testing will provide input to tailor thermomechanical processing of the NiTiFe alloys.
22. **Alloy production scale-up by hot isostatic processing (HIP)**: A commercial furnace will be used for HIP of optimized compositions. A problem has been the incomplete mixing of starting powders. A mixer and a hand press will be procured for this purpose. The objective is to have the alloys available in bulkier forms for actuator designs that can incorporate larger shape-memory alloys elements in various applications.

Collaborations and Partnerships

The proposed work leverages support for shape-memory alloy research to Dr. Raj Vaidyanathan at UCF from NASA KSC, a National Science Foundation (NSF) CAREER award, UCF-UF SRI and Los Alamos National Laboratory, a U.S. Department of Energy facility.

Benefits to NASA

The immediate benefit to NASA KSC is the development of a shape-memory thermal conduction switch for application in cryogenic liquefaction, densification and zero boil-off systems. This will be extended to include the potential use of shape-memory alloy actuator elements for cryogenic seals, valves, fluid-line repair, self-healing gaskets, and even to ambient debris-less separation and latch/release mechanisms. Broader impacts include the continuation of an active and diverse partnership between a state-university (UCF), a major U.S. national laboratory (Los Alamos National Laboratory) and NASA, and realization of the vast commercialization potential of cryogenic shape-memory alloys. The UCF-Los Alamos National Laboratory-NASA KSC partnership has already led to testing welded space shuttle flow liners

Selected Publications (Related)

1. V.B. Krishnan, J.D. Singh, T.R. Woodruff, W.U. Notardonato and R. Vaidyanathan, “A Shape Memory Alloy Based Cryogenic Thermal Conduction Switch,” Advances in Cryogenic Engineering, American Institute of Physics, (2004) 50A 26-33.

2. C.R. Rathod, S. Rajagopalan and R. Vaidyanathan, “Mechanical Characterization of Shape-Memory Alloys using Diffraction and Instrumented Indentation,” Shape-Memory and Superelastic Technologies, International Organization on Shape-Memory and Superelastic Technology, (2004) 331-339.
3. R. Vaidyanathan, “Shape-Memory Alloys,” Kirk-Othmer Encyclopedia of Chemical Technology, Wiley InterScience, John Wiley & Sons Inc., NY, 2002 edition.
4. V. Krishnan, W.U. Notardonato and R. Vaidyanathan, “Design, Fabrication and Testing of a Shape Memory Alloy based Cryogenic Thermal Conduction Switch,” Smart Mater. Struct. (2004 submitted)
5. S. Rajagopalan, A.L. Little, M.A.M. Bourke and R. Vaidyanathan, “Elastic Modulus of B19’ Shape-Memory NiTi from in situ Neutron Diffraction during Loading, Instrumented Nanoindentation and Extensometry,” Appl. Phys. Lett. (2004 submitted)
6. V.B. Krishnan, J.D. Singh, T.R. Woodruff, W.U. Notardonato and R. Vaidyanathan, “A Shape Memory Alloy Based Cryogenic Thermal Conduction Switch,” Advances in Cryogenic Engineering, American Institute of Physics, (2004) 50A 26-33.
7. V. Livescu, T.R. Woodruff, B. Clausen, T. Sisneros, M.A.M. Bourke, W.U. Notardonato and R. Vaidyanathan, “Design and Rationale for an in situ Cryogenic Deformation Capability at a Neutron Source,” Advances in Cryogenic Engineering, American Institute of Physics, (2004) 50A 83-89.
8. C.R. Rathod, S. Rajagopalan and R. Vaidyanathan, “Mechanical Characterization of Shape-Memory Alloys using Diffraction and Instrumented Indentation,” Shape-Memory and Superelastic Technologies, International Organization on Shape-Memory and Superelastic Technology, (2004) 331-339.

Prototype and Simulation Model for a MEMS Magneto-Caloric Refrigerator

PI: S. Bhansali (University of South Florida)
V. Bethanabotla (University of South Florida)
M. Rahman (University of South Florida)
S. Sambandam (University of South Florida)
S. Shevade (University of South Florida)

Problem

Demonstrate the feasibility of GdSiGe based magnetocaloric refrigeration for liquefaction of hydrogen.

Objective

Establish the feasibility of reduced magnetic field based active magnetic refrigeration (AMR) cycle as a liquefaction technology for hydrogen.

Approach

Evaluate properties of GdSiGe material, develop cooling elements and magnetocaloric cooler and develop simulation models of the magnetocaloric cooler.

Background

Micro cryo-cooling has been a subject of intense research and development in the recent past. Low temperature coolers have been used for decades to reduce cooling temperatures down to the cryogenic range for a variety of applications. Thus, realizing micro cryo-coolers that can operate at low temperature with high cooling capacity, and in a small size has been a challenge. This research focuses on development of micro-cooling technology based on the magnetocaloric effect. Magnetocaloric refrigeration is being explored as an efficient pathway for cooling hydrogen for storage.

The objective of this research is to establish the feasibility of reduced magnetic field based active magnetic refrigeration (AMR) cycle as a liquefaction technology for hydrogen. The research aims to design, fabricate and validate a magnetocaloric microcooler capable of operating in the temperature range from 77 to 20 K.

This process is environmentally friendly and requires that magnetocaloric materials be exposed to an alternating magnetic field. Analysis and experimentation in the last two years have positioned the investigators to both (a) demonstrate the feasibility of magnetocaloric refrigeration and (b) Experimentally validate the critical parameters required for design of scalable cooling systems. Simulation of cooling hydrogen from 77 to 20 K suggests a multi-stage GdSiGe based magnetocaloric refrigeration system.

The specific accomplishments in the past year are as follows:

- Thermodynamic analysis of a magnetic refrigeration system for near room temperature application using Gd as the magnetic material.
- Conceptual design and analysis of a magnetic refrigeration system near hydrogen liquefaction temperature.
- Design of two prototypes with circular and trapezoidal microchannels.
- Computational studies of a large size magnetic cooler.
- Analysis of heat transfer in a Gd microcooler with circular tubes for fluid flow.
- Analysis of heat transfer in a composite Si-Gd microcooler with trapezoidal channels.
- Development of microfabrication processes and fabrication of trapezoidal flow channels in silicon.

- Development of processes to synthesize magnetocaloric material (GdSiGe) in different forms with optimal properties.
- Understanding the multiple phase formations, phase stability and interface stability in thin film GdSiGe synthesis.
- Developed suitable diffusion barrier layer (SiN) between magnetocaloric material and silicon at high process temperatures.
- Development of in-situ temperature sensors through deep impurity diffusion for accurate temperature measurements.

Significant progress has been made, over the past two years, in design of a prototype, understanding material issues, developing numerical models and thermodynamic models to simulate the microcooling system and fabricate prototype systems.

Analysis of fluid flow and heat transfer in microchannels with rectangular and square cross section was carried out. When subjected to the magnetic field, heat transfer processes during the heat up and cool down phases of a magnetic material were studied. The application of the magnetic field was simulated by using the concept of volumetric heat source distributed uniformly over the entire solid material. The strength of the source was calculated from energy balance during magnetization of the material. Equations governing the conservation of mass, momentum, and energy were solved in the fluid region. In the solid region, heat conduction equation with heat generation was solved. From the simulation results, plots of Nusselt number and heat transfer coefficient were obtained over the length of the channel. A thorough investigation for velocity and temperature distributions was performed by varying channel aspect ratio, Reynolds number, and heat generation rate in the substrate. It was found that the peripheral average heat transfer coefficient and Nusselt number is larger near the entrance and decreases downstream because of the development of the thermal boundary layer. With the increase in Reynolds number, the outlet temperature decreased and the average Nusselt number increased.

An analysis of a magnetic refrigeration cycle was carried out. The system consists of heat exchangers and beds of magnetic materials operating near room temperature. The beds are periodically magnetized and demagnetized and the working fluid flows are arranged to meet the cycle requirements. Sensitivity analysis has been performed. Cooling power, magnetic field, and temperature span trends are simulated. The cooling and heating effects were estimated based on the magnetocaloric effect of gadolinium. Findings indicate that the higher the magnetic field is the higher the cooling power with the same temperature span. It was also observed that the cooling power decreases with the increase in the temperature span for various magnetic fields. *COP* versus temperature span was also considered. The trend indicates that $COP_{actual}/ COP_{Carnot}$ decreases with an increase in the temperature span. These trends agreed with those shown by experimental data.

Results and Discussion

Task 1: Deposit and Characterize MCE Thin Films

In continuation of the work done previously, attempts have been made to synthesize and stabilize $Gd_5Si_2Ge_2$ phase in thin film form. Previous work established the formation of required precursor phases for forming the $Gd_5Si_2Ge_2$ phase by annealing. A high temperature annealing has also led to the formation of G $Gd_5Si_2Ge_2$ phase, however in small volume fraction. To improve the content of this phase and stabilize it, further work has been progressed by depositing GdSiGe thin films and annealing in vacuum. Our earlier work used Pt as barrier layer between GdSiGe and Si. Results showed Pt acts as barrier at low temperatures (700 ◦C), however, at higher temperatures (1150 ◦C) leads to the formation of silicide phases in the film. Alternatively SiO_2, and Si_3N_4 were considered attractive materials for diffusion barrier layers for this fabrication. Both of the materials are compatible with Si processing and routinely used as diffusion barriers in Si at temperatures greater 1000 ◦C. As past studies had found the GdSiGe alloy to be highly reactive with oxygen, Si_3N_4 was selected as the diffusion barrier material based on past work from literature that suggests silicon nitride is thermally stable at high temperatures till 1600 ◦C.

Experimental Details

Films of 300 nm Si_3N_4/ Si were deposited using PECVD at 300 ◦C. 100 nm thick GdSiGe was deposited on these films by sputtering. The films were vacuum annealed at temperatures upto 1150 ◦C. The films were then studied to determine the phase and surface morphology using XRD, and SEM. The stability of Si_3N_4 as a barrier layer was studied using SIMS. PECVD silicon nitride was deposited on the wafer by flow of precursors in gases SiH_4 :NH_3 : He: N_2 in the ratio 10: 4: 800: 200, at a pressure of 120 Pa, and R.F. power 50 W. Next GdSiGe films were deposited on the substrate using a custom dc/RF-magnetron sputtering system (designed in-house). For sputtering, the vacuum chamber was pumped down to a base pressure of $1.5x10^{-4}$ Pa using a cryopump. For sputtering, the argon was flown in at 30 sccm to purge the chamber and a throttle valve was used to maintain the pressure. For the deposition process, the chamber pressure was maintained at 5 Pa by throttling the valve. Sputtering was done at RF power of 150 W. The targets were cleaned by pre-sputtering to remove any surface oxides that may have formed on the target. Pre-sputtering was carried out for 10 min. The substrate was rotated during deposition to obtain uniform thickness over the wafer. The 100 nm thickness of the deposited GdSiGe thin films was confirmed by the surface profilometer. Next the films were vacuum annealed at $1x10^{-4}$ Pa in the temperature range 700 to 1150 ◦C. The structure and morphology of the films were analyzed by x-ray diffraction (Philips model X'pert Pro) and SEM (Hitachi model S800). The compositional gradient of the film and the interface was studied by secondary ion mass spectrometry.

Results

A critical element in establishing an effective diffusion barrier is to have a high quality Si_3N_4 film that is not porous. Figure 1 (a) schematically illustrate the process used to evaluate the porosity of the nitride. As shown in the figure, the Si_3N_4 coated substrate was immersed in KOH solution for 30 min to evaluate the quality of the film. The solution was maintained at 70 ◦C. KOH attacks Si about 300 times faster than PECVD Si_3N_4. Any pinhole in the nitride leads the etchant to the Si surface, resulting in significant pitting of the underlying substrate.

Next, the substrate nitride was stripped using phosphoric acid and the surface of silicon was examined using optical microscope. Figure 1(b) shows an optical micrograph of the silicon surface. It can be seen the surface of the wafer is intact and without pitting. This confirms that silicon nitride films are not porous and free from pinholes. Figure 1(c) shows a pitted etched surface of silicon for comparison.

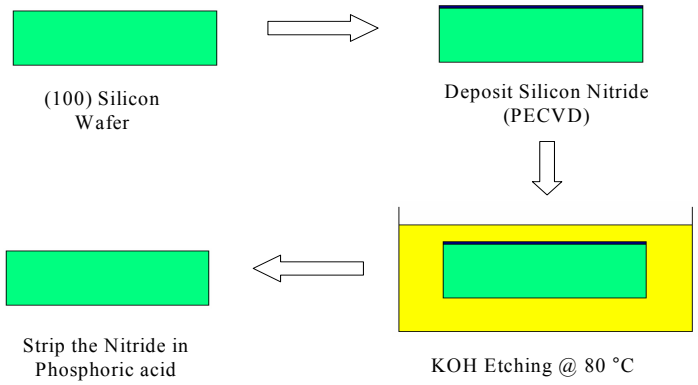

Figure 1.—(a)Process for testing the porosity of silicon nitride thin film.

Figure 1.—(b) Smooth surface of silicon nitride.

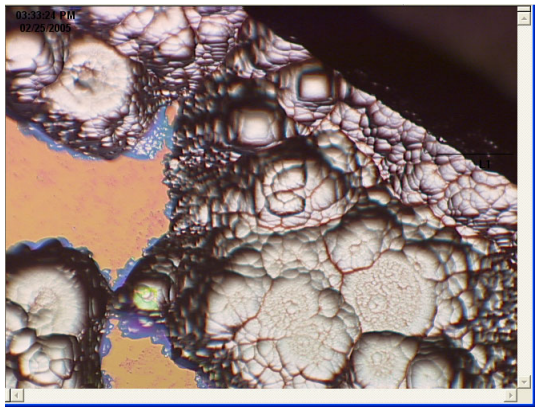

Figure 1.—(c) Etched pitted surface.

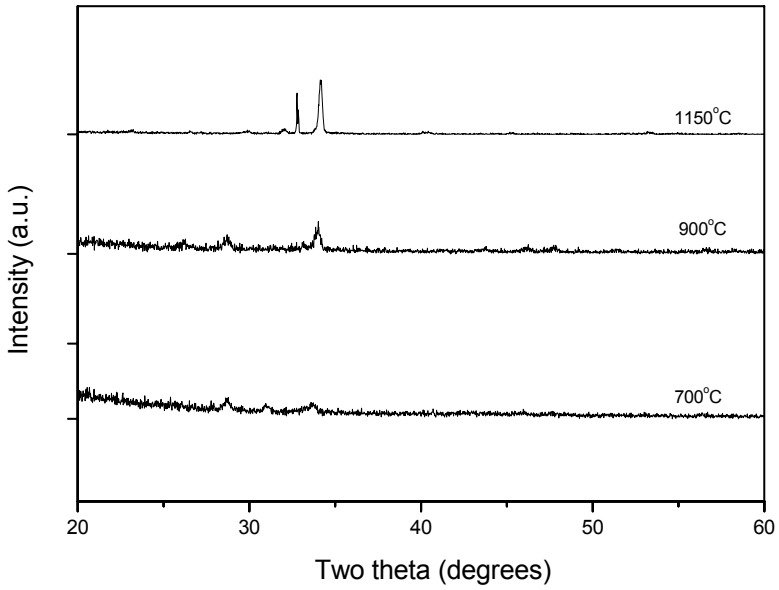

Figure 2.—XRD profiles of films annealed at different temperatures.

GdSiGe films were deposited on to silicon nitride films and vacuum annealed with an aim of developing the magnetocaloric $Gd_5Si_2Ge_2$ phase in thin film form. Due to the strong affinity of the material with oxygen, generally it is has been difficult to keep the bulk material oxygen free during annealing The traditional approach in annealing this material is to wrap it in Ta foil and put in an evacuated quartz ampoule. These samples were instead directly placed in a vacuum furnace without any passivation. Figure 2 shows the XRD patterns of (100 nm GdSiGe/300 nm Si_3N_4/Si) films annealed at different temperatures for 1 hr.

Annealing at 700 ◦C resulted in the formation of $GdSi_2$ phase. Increasing annealing temperature enhanced the formation of $GdSi_2$ phase at 900 ◦C. At 1150 ◦C, the $Gd_5Si_2Ge_2$ phase started forming along with even higher level of crystallization of $GdSi_2$. The crystallization studies suggest that optimizing the time of annealing at 1150 ◦C could result in the stoichiometric film.

Figure 3 shows the morphological changes in the structure of the film with the change in annealing temperature. Figure 3 is the SEM of the sputtered film. Figure 3(a), (b), and (c) show the surface morphology of the films after annealing at 700, 900 and 1150 ◦C respectively. At lower temperatures (700 ◦C) surface of the films are smooth with no noticeable texturing, reflecting very little presence of the crystalline phase as evidenced in the XRD. Increasing to 900 ◦C, results in a film that is textured. The increased texture of the film can be attributed to the formation of the crystalline phase in the film. Increasing the annealing temperature to 1150 ◦C has resulted in significant texturing in the film, the texturing is the reflection of increased crystallinity in the film that was evidenced by XRD.

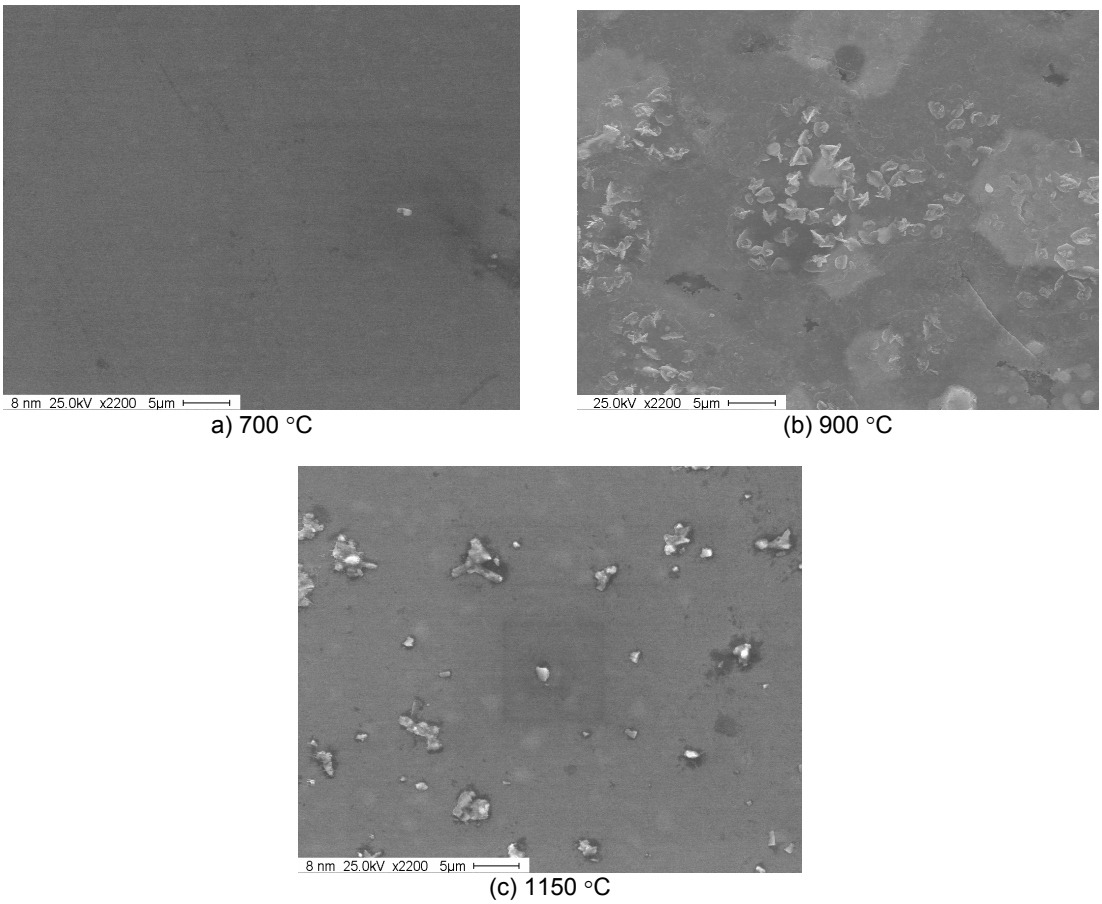

a) 700 °C (b) 900 °C

(c) 1150 °C

Figure 3.—Scanning electron micrographs of thin films annealed at different temperatures. It can be seen in the XRDs that at low temperatures the alloy forms a Si rich phase and no Ge- based phase can be seen. When annealed at 1150 °C though the desired GdSiGe phase appears, the crystalline phases are Si rich and Ge deficient.

To understand the distribution of the materials and to ensure the stability of the interface, ,the elemental composition of the as deposited and annealed film was studied by SIMS depth profiling figure 4(a) shows the distribution of different elements along the depth of the film for an as-grown sample. For the first six hundred sec (equivalent to 100 nm of the film) stable high counts of Gd, Si and Ge (102 to 103 counts per sec) can be seen, confirming that the deposited film has the three elements consistently distributed across the film thickness. At 600 Sec the Gd and Ge signals drop while the Si, SiN and N signals rise, confirming the presence of Si_3N_4. The interface between the alloy and Si_3N_4 is sharp. The signals for the SiN are stable till about 2100 sec indicating the uniformity of the Si_3N_4 barrier after which the beam looks at bulk Si. The profiles show peaks at the interfaces due to multiple charge exchanges. Silicon nitride layer is also stable and homogenous with sharp interface with Si substrate.

Figure 4(b) shows the SIMS profile of this sample after annealing at 1150 ◦C the temperature at which the desired phase is formed. It can be seen that the elemental profile is totally redistributed. Based on figure 4(a), the thickness of the GdSiGe layer in the annealed sample (fig. 4(b)) corresponds toapproximately 600 sec of sputter time. The SIMS profile shows that the diffusion barrier has totally broken down and is absent. It shows an enrichment of Gd with a signal strength of 104 counts per sec compared to 103 counts per sec in as-grown sample. Si is also observed to be enriched and Ge is significantly depleted compared to figure 4(a). The nitrogen in the sample and the consequent nitride

profile is also diffused. The nitrogen seems to be moving to the surface faster than the bulk. Gd appears to be diffused through silicon nitride layer into Si substrate along with Ge. The significant enrichment of the surface in Gd and Si explains the formation of $GdSi_2$ phase in the sample. The Ge fixation (possibly near the original interface) shows the small crystalline peak.

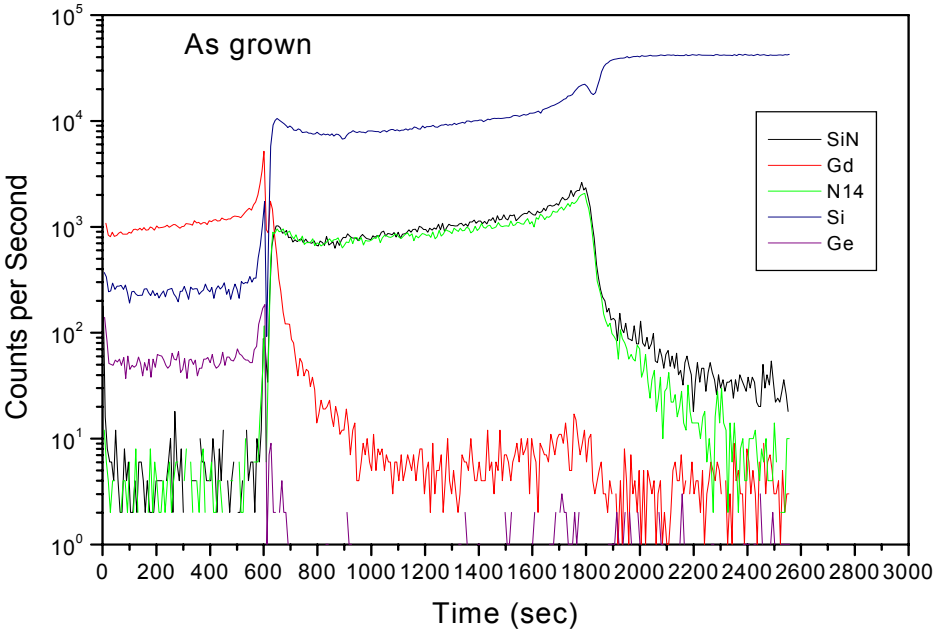

Figure 4.—(a) SIMS depth profiling of as-deposited film on SiN/Si.

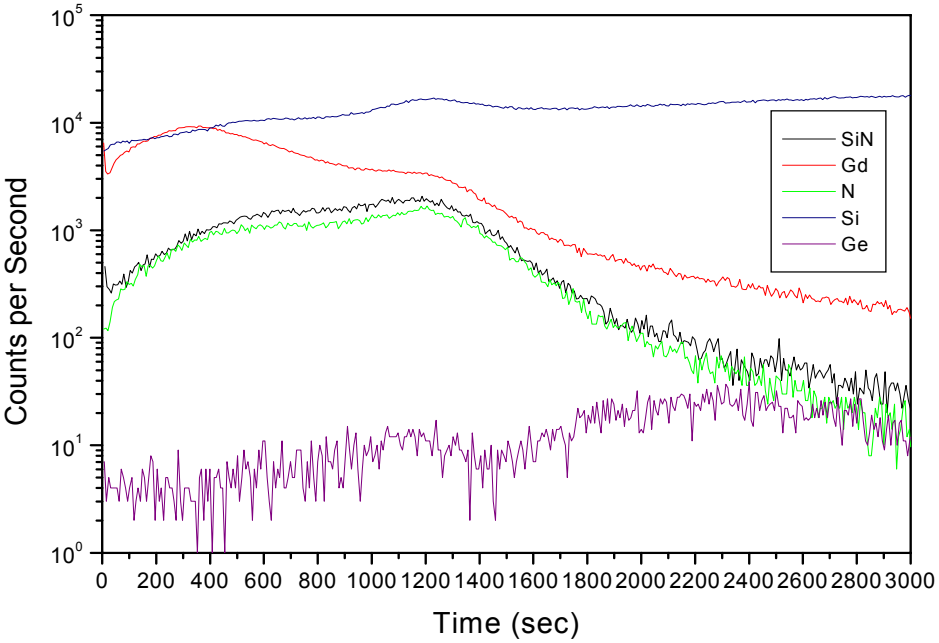

Figure 4.—(b) SIMS depth profiling of thin films annealed at 1150 °C.

Although silicon nitride is expected to be stable till 1600 ◦C, the results confirm that PECVD deposited Si_3N_4 is unstable as a diffusion barrier in GdSiGe alloy system. A potential contributor to the decomposition of this layer could be hydrogen in the nitride film. It is well known that hydrogen gets chemically fixed in silicon nitride films during growth and can have upto 10 percent hydrogen. Hydrogen in the nitride films exhibit deleterious effects and are prone to being unstable when subjected to high temperature treatment. The presence of hydrogen in the film results in dangling Si and N bonds in the film. Generally these bonds can be terminated by annealing of the film that causes its densification too. In our experiments, the nitride films were not annealed. We hypothesize that the annealing of the GdSiGe/SiN/Si stack resulted in the dangling bonds interacting with the elements in the thin film (primarily Ge) and thus compromised the diffusion barrier. Tests are underway to confirm the role of hydrogen in the failure of the diffusion barrier. Alternatively other possible diffusion barriers such as TiN, TaN are being studied.

Task 2: Fabrication of a Micro Cooling Channel Prototype

We have fabricated the microcooler with trapezoidal microchannels. Eight microchannels, each 300 μm wide, 150 μm deep and around 1 in. long have been fabricated in a 1 x 1 in. area on 2 in. silicon wafer. The structure of the trapezoidal channel is shown in figure 5. The fabrication procedure of the microchannels is schematically illustrated in figure 6.

A 250 μm thick silicon wafer was used for the fabrication. A 3000 Å thick oxide was thermally grown on the wafer. The inlet and outlet ports were then patterned on the wafer using lithographic techniques. This was followed by wet etching in TMAH for 100 μm. The channels were then patterned and wet etching for 150 μm was performed. The combined etching of 250 μm formed the inlet and outlet ports (holes). The wafer was then cleaned and gold was deposited on specific areas of the wafer. Diffusion was carried out at 950 ◦C which formed the temperature sensors.

A 5 mm thick GdSiGe disc has been bonded to the open end of the channels using crystalbonds and microconnectors have been attached to the inlets and outlets. The schematic of the microcooler system is shown in figure 7(a) and the fabricated prototype in figure 7(b).

To measure the temperature of the heat transfer fluid at the inlet at outlet, in-situ temperature sensors with deep impurities have been developed, so that the simulation results can be validated. Figure 8 shows output of a typical characteristic of the test temperature sensor that has been fabricated.

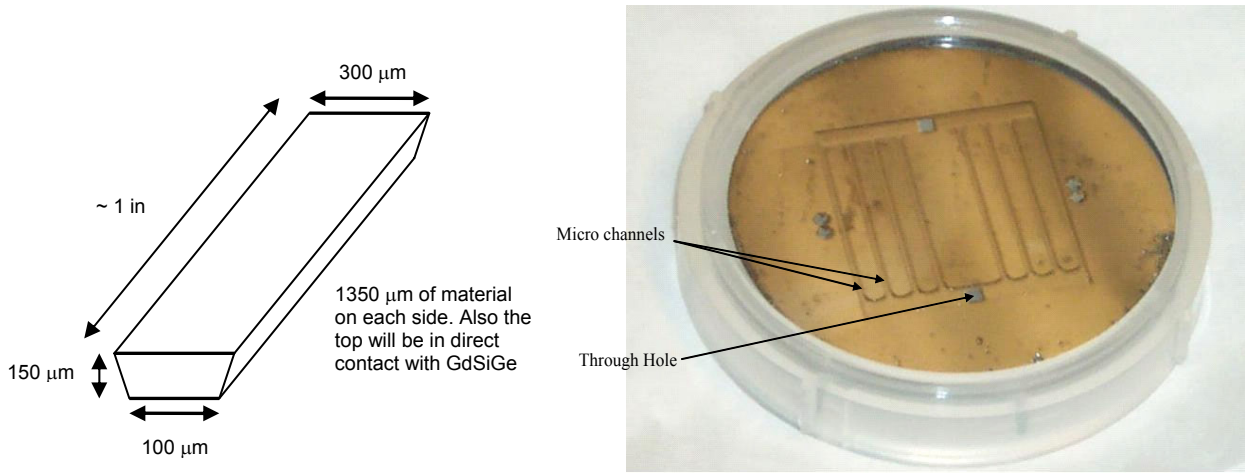

Figure 5.—Trapezoidal channel.

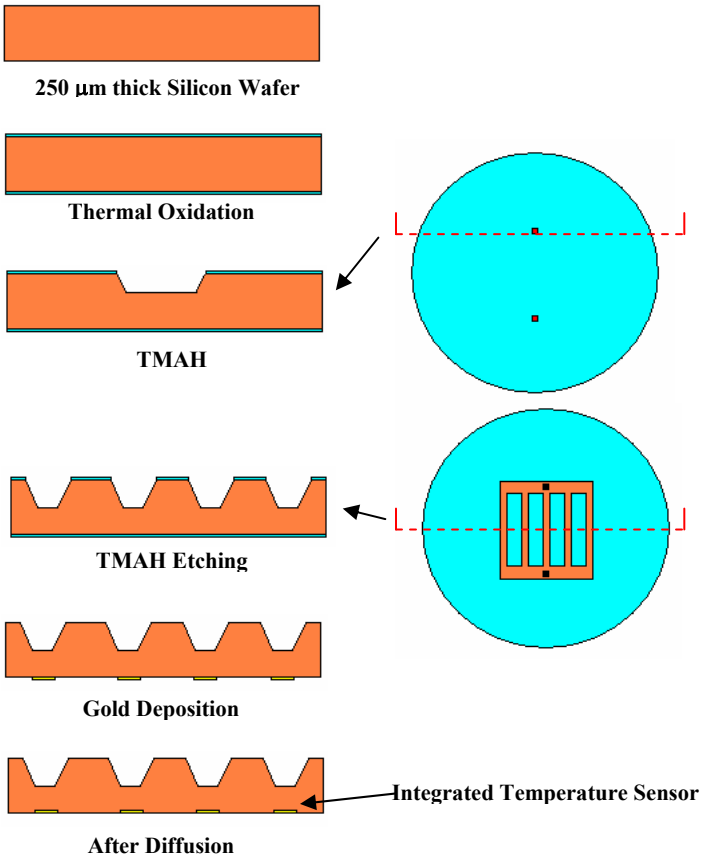

Figure 6.—Process flow of the fabrication of the microchannels with integrated temperature sensors.

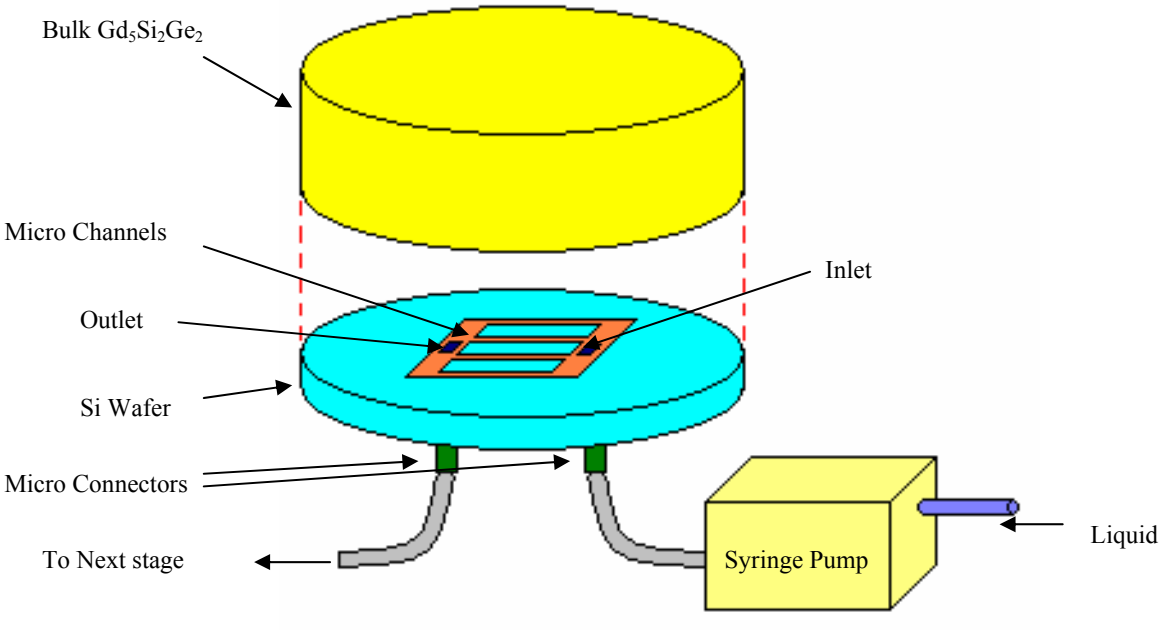

Figure 7.—(a) Schematic of the microcooler system.

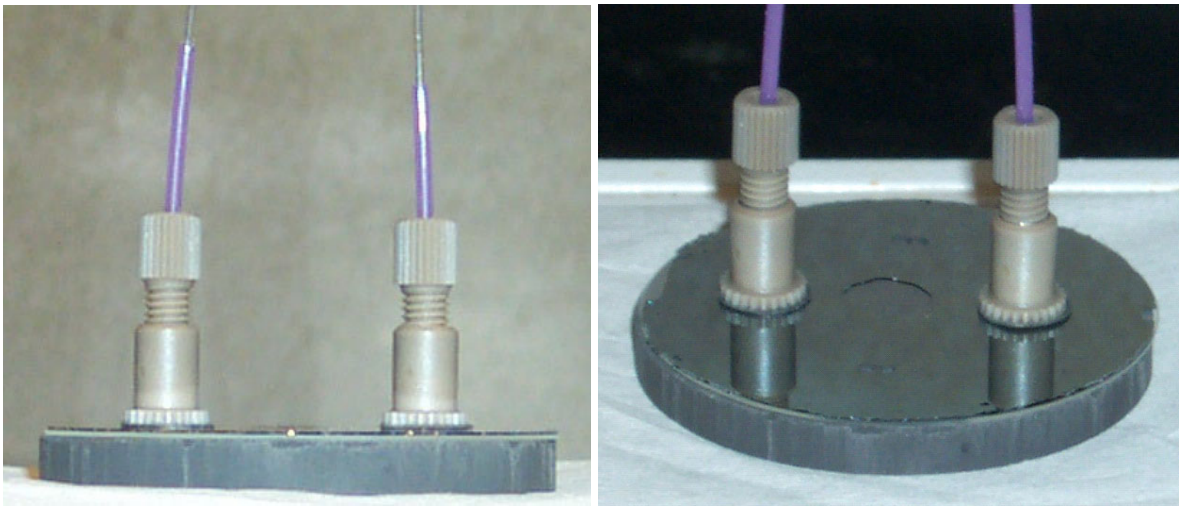

Figure 7.—(b) Photograph of microfabricated prototype.

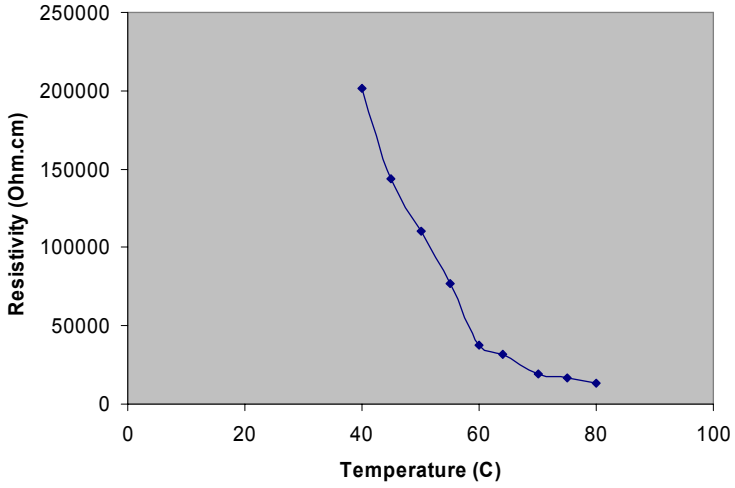

Figure 8.—Output characteristics of temperature.

$Gd_5Si_2Ge_2$ bulk material has been synthesized by high temperature alloying process and the powdered. To make the cooling disk, the powder has been compacted by cold press and sintered at 800 ◦C. The magnetic and magnetocaloric properties of the disk has been studied and is shown in the figure 9.

Figure 9 shows the dependence of magnetization on temperature. Figure 10 shows a transition from paramagnetic to ferromagnetic at 276 K. The change in magnetic entropy has been studied and plotted in the following figure 10. The characteristics in the figure 10 indicates sharp transitions at 260 and 276 K.

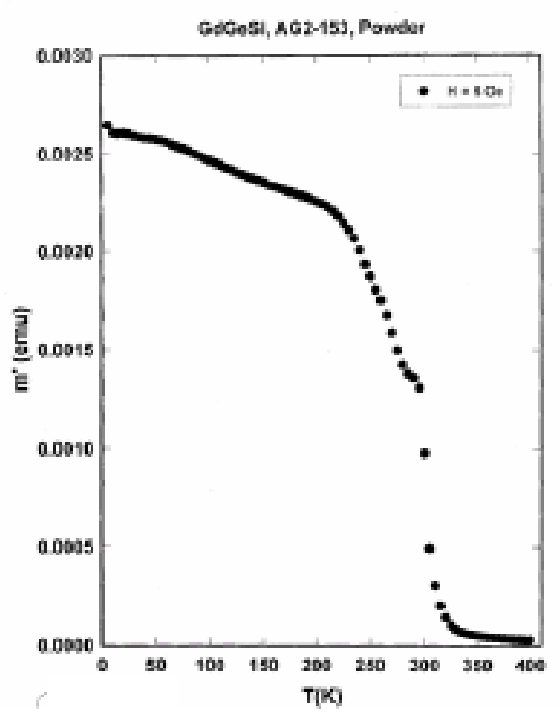

Figure 9.—Dependence of magnetization on temperature.

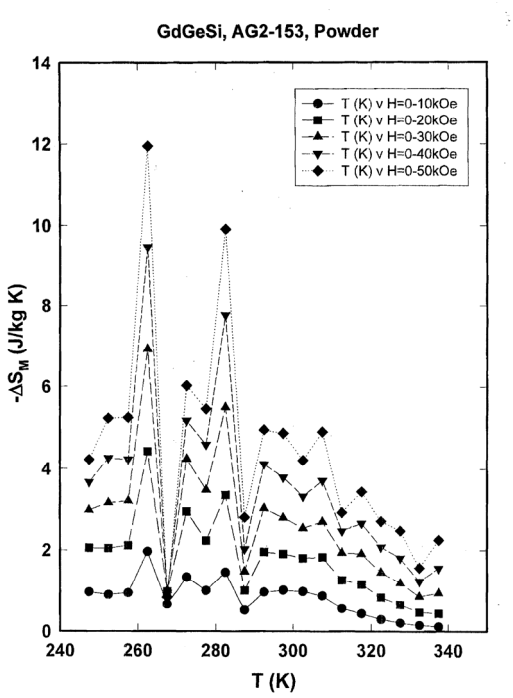

Figure 10.—Dependence of magnetization entropy with temperature.

Task 3: Modeling of Magnetic Cooler Heat Exchanger for Periodic Heating and Cooling (Magnetization and Demagnetization)

The transient heating and cooling process, when the heat exchanger is exposed to the fluctuating magnetic field was studied. The volumetric heat source was turned on and off for certain period of time, and the variations of temperature and Nusselt number were studied. The results computed were for Gadolinium substrate and water as the working fluid. The parameters were calculated at different sections along the length of the channel for different time intervals.

Figure 11 shows the variation of volumetric heat generation rate with time. When a magnetic field of 5T is applied to the microchannel heat exchanger, 6.4E8 W/m^3 of heat is generated and the magnetic material heats up. When the magnetic field is removed, the material cools down. The negative heat generation rate of –6.4E8 W/m^3 shows the condition when the magnetic field of 5T is removed.

Figure 12 shows the variation of maximum temperature in the substrate with time for heating and cooling cycles. Reynolds number is 1600. The maximum temperature in the microchannel is found in the solid region at the outlet edge of the channel. A sinusoidal behavior of the temperature is seen for the heating and cooling cycles. After a small time period the maximum temperature maintains fluctuations between 330 and 100 ◦C.

Figure 13 shows the variation of peripheral average interface temperature with time at different locations along the length of the channel for Re = 1600. During the heating phase as the fluid passes along the length of the channel it gains heat. The solid-fluid interface temperature increases as the fluid moves downstream due to the development of thermal boundary layer starting with the entrance section as the leading edge. During the cooling phase the solid-fluid interface temperature decreases. Fluid cools down as the heat is taken out from the fluid. The highest values of interface temperature are seen near the outlet of the channel.

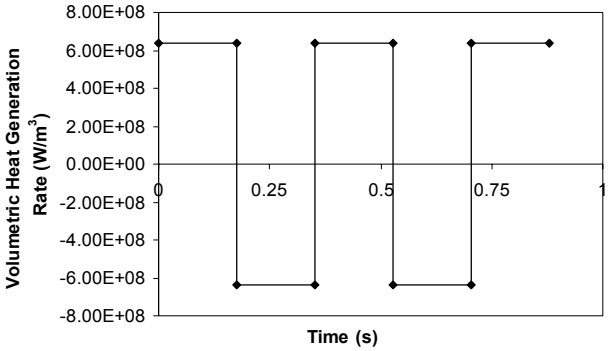

Figure 11.—Variation of volumetric heat generation rate with time.

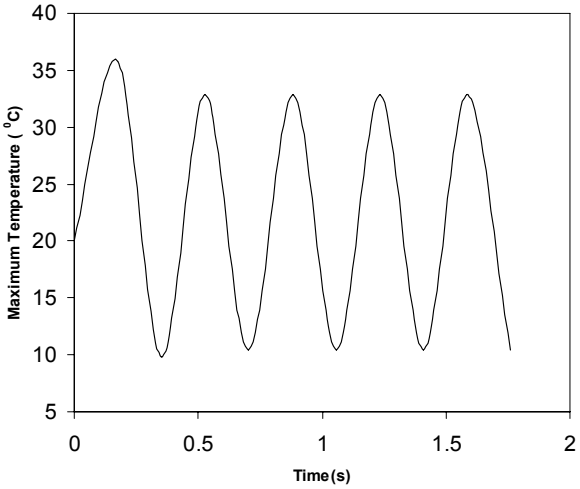

Figure 12.—Variation of maximum temperature in the substrate (Re = 1600, Bc = 0.05 cm, Hc = 0.1 cm, g0 = 6.4E8 W/m^3).

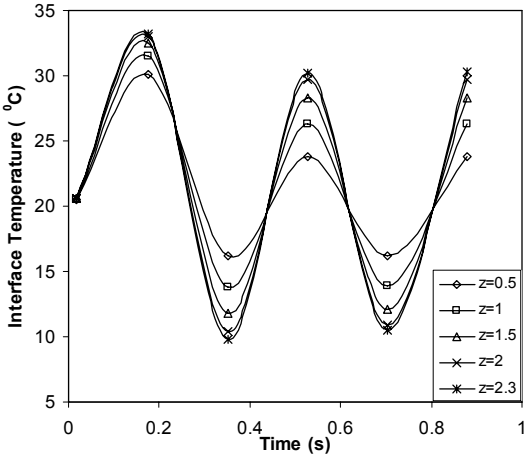

Figure 13.—Variation of interface temperature with time at different sections in the rectangular channel (Re = 1600, Bc = 0.05 cm, Hc = 0.1 cm, g0 = 6.4E8 W/m^3).

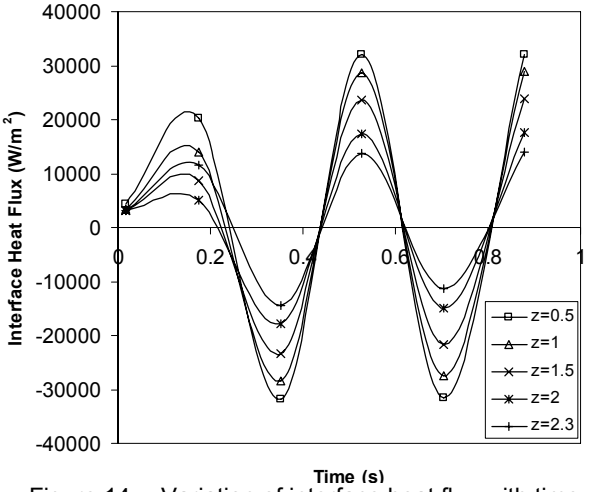

Figure 14.—Variation of interface heat flux with time at different sections in the rectangular channel (Re = 1600, Bc = 0.05 cm, Hc = 0.1 cm, g0 = 6.4E8 W/m^3).

Figure 14 shows the variation of interfacial heat flux in the channel with time at different sections of the channel for Re = 1600 and dimensions of 0.05*0.1cm. Interface heat flux also shows a sinusoidal behavior and it shows higher values near the entrance of the channel. During the cool down phase, the heat flux near the entrance also becomes lower. This is because of larger transport rate at the leading edge of the thermal boundary layer that develops starting at the entrance section.

Figure 15 shows the variation of heat transfer coefficient with time at different locations along the length of the channel for Re = 1600 and dimensions of 0.05*0.1cm. After 0.2 sec heat transfer coefficient remains almost constant for further heating and cooling cycles. Heat transfer coefficient decreases along the channel length. Fluid gets heated as it passes through the channel. The temperature difference between fluid and solid decreases as one moves along the length of the channel. Thermal boundary layer grows until fully developed flow is established. Therefore, the heat transfer coefficient is higher at the entrance and decreases downstream. The variation is larger at the entrance because of the rapid development of thermal boundary layer near the leading edge.

Figure 16 shows variation of Nusselt number with Fourier number at different locations along the length of the channel for Re = 1600 and dimensions of 0.05*0.1 cm. The trends are analogous to that seen for the variation of heat transfer coefficient presented in figure 15.

Figure 17 shows the interface temperature variation for heating and cooling cycles. The heat generation rate is 12.8E8 W/m3 and the channel dimensions are 0.05*0.1 cm. As compared to figure 13, it is seen that the interface temperature variation increases as the heat generation rate is doubled. The increase is seen in all locations within the channel. Figure 18 shows the Nusselt number variation for g0 = 12.8E8 W/m3 and channel dimensions of 0.05*0.1 cm. It may be noted that at all locations, the Nusselt number is highest at the beginning of the transient, decreases rapidly with time and undershoots before settling to a constant value for that location. The undershoot is caused by rapid distribution of heat between solid and fluid as they both store and release thermal energy at different rate until settling for a periodic equilibrium condition.

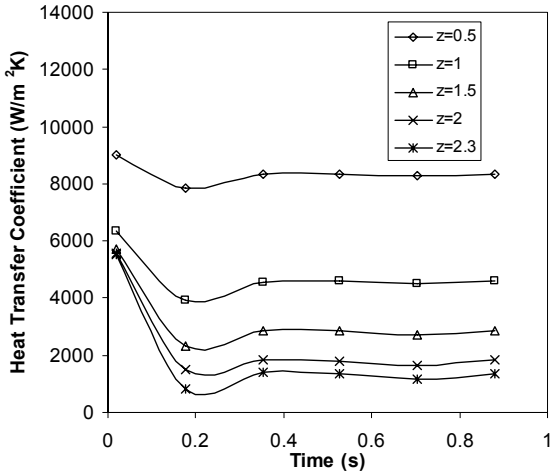

Figure 15.—Variation of heat transfer coefficient with time at different sections in the rectangular channel (Re = 1600, Bc = 0.05 cm, Hc = 0.1 cm, g0 = 6.4E8 W/m^3).

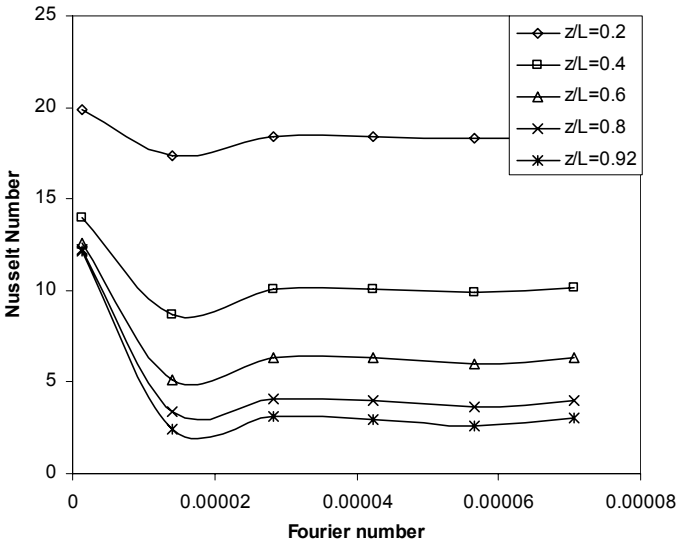

Figure 16.—Variation of Nusselt number with time at different sections in the rectangular channel (Re = 1600, Bc = 0.05 cm, Hc = 0.1 cm, g0 = 6.4E8 W/m^3).

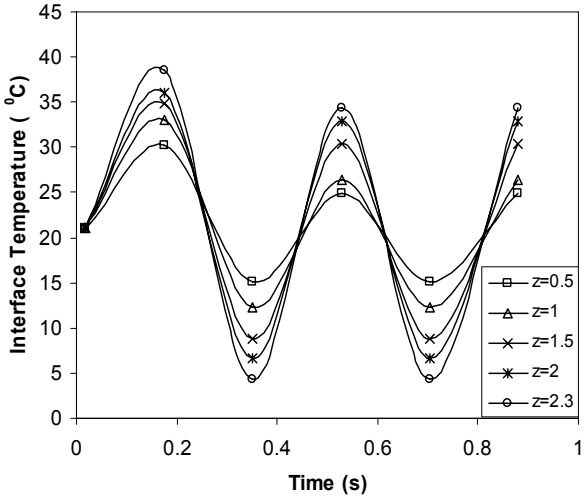

Figure 17.—Variation of interface temperature with time at different sections in the rectangular channel with double heat generation rate (g0 = 12.8E8 W/m^3, Re = 1600, Bc = 0.05 cm, Hc = 0.1 cm).

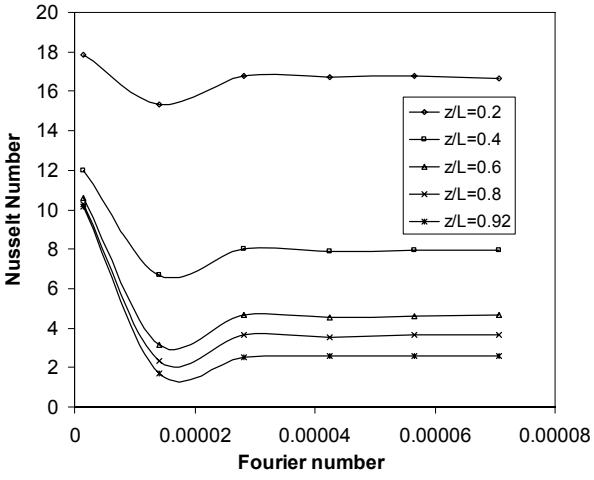

Figure 18.—Variation of Nusselt number with time at different sections in the rectangular channel with double heat generation rate (g0 = 12.8E8 W/m^3, Re = 1600, Bc = 0.05 cm, Hc = 0.1 cm).

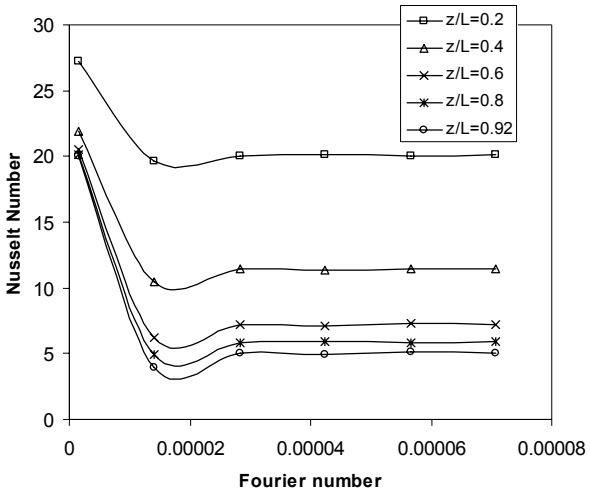

Figure 19.—Variation of Nusselt number with time at different sections in a square channel (Re = 1600, Bc = 0.1 cm, Hc = 0.1 cm, g0 = 6.4E8 W/m^3).

Figure 19 shows the variation of Nusselt number with Fourier number at different locations along the length of the channel. Reynolds number of the fluid is 1600 and channel dimensions are 0.1 x 0.1 cm. As compared to a rectangular channel with dimensions of 0.05*0.1 cm, more amount of fluid is passing through this square channel. Therefore, the values of interface temperature are lower than that of the rectangular channel and consequently the Nusselt number is higher.

Task 4: Thermodynamic Analysis of the Magnetic Refrigeration Cycle for Hydrogen Liquefaction.

The above model allows a quantitative analysis of the thermodynamic cycle for a magnetic refrigerator. Sensitivity analysis has been performed using gadolinium metal as the magnetic material and water as the working fluid. Cooling power, temperature span, and coefficient of performance are analyzed by simulations. Calculations have been carried out for the proposed model operating at near room temperature in a magnetic field between 1 and 5 T and using 3 kg of Gd spheres packed in two identical magnetocaloric beds. The other parameters are the lowest working fluid temperature of 273 K limited by the freezing temperature and the temperature at the hot heat exchanger limited by the ambient temperature. The temperature span was varied over small range. The primary objective of these calculations was to observe the effect of the variation of the temperature span on the system performance.

Figure 20 shows the cooling power as a function of the magnetic field. The cooling power was evaluated from the magnetization data. A temperature spans of 10, 15, and 20 K were considered in this case. As can be seen for an increase in the magnetic field, there is an increase in the cooling capacity. When the applied field is increased, the cooling load increases because the increased adiabatic temperature change from the higher field produces more cooling. Figure 21 presents cooling power as a function of temperature span for various magnetic fields. In this case it can be observed that the cooling power decreases with an increase in the temperature span. This result is expected because the system is working on a higher temperature range causing a decrease in the cooling capacity. It may be also noticed that the sensitivity of the temperature span is higher at larger values of the magnetic field.

Figure 22 shows the coefficient of performance (COP) dependence on temperature span for various magnetic fields. The COP ranges from about two to eleven, which compares favorably with commercial vapor cycle refrigerators. The Carnot cycle, which is completely reversible, is a perfect model for a refrigeration cycle operating between two fixed temperatures. The Carnot limit to the COP of a refrigerator is the maximum coefficient of performance that may be attained by a refrigerating machine. Figure 23 presents the ratio of COPactual/ COPCarnot versus temperature span for 3T, 5T, and 7.5T magnetic

fields. COPactual is the coefficient of performance predicted by present model under the same working conditions. No refrigerating cycle may have a coefficient of performance higher than that for a reversible cycle operating between the same temperature limits. The ratio of COPactual/ COPCarnot is presented as a percentage of the Carnot cycle performing in a similar temperature range. The percentage of Carnot COP is less than 35 percent as is generally true for most real refrigerators. As expected the ratio of COPactual/ COPCarnot drops with increasing temperature span. When the magnetic field is increased the tendency of the ratio decreases. These trends agreed with those shown by experimental data. Figure 24 presents predicted and experimental ratios of COPactual/ COPCarnot versus Temperature span for 5T magnetic field. The experimental data used is that presented by Zimm et al. (ref. 7). As can be seen there is a reasonably good agreement between predictions by the proposed model and those from the experimental data. Figure 25 shows the behavior of the ratio of COPactual/ COPCarnot with the temperature span for various working fluids under a 5T magnetic field. As can be seen R134a and Ammonia exhibit better efficiency than that showed by water as the working fluid. R134a shows ratio higher than 35 percent over the entire temperature span. Figures 26 and 27 present cooling power and COP dependence on temperature span for R-134a. Vineyard (ref. 11) presented a complete study about alternative refrigerants for a household refrigerator. He tested various viable refrigerants including pure and mixture refrigerants. Table 2 compares results for coefficient of performance between present model and commercial refrigerators as presented by Vineyard (ref. 11). It can be seen that magnetic refrigerator provides significantly higher coefficient of performance compared to vapor compression refrigerator of the same capacity. Therefore, magnetic refrigeration has a great potential to reduce operating cost and maintenance cost when compared to the conventional method of compressor based refrigeration.

TABLE 2.—COP COMPARISON BETWEEN THIS MODEL AND COMMERCIAL REFRIGERATORS

COP (Typical 18 ft^3 refrigerator)		
Magnetic refrigerator	Commercial vapor cycle refrigerators (ref. 11)	
N/A	Refrigerant R134a	Refrigerant R22
11	2.26	2.29

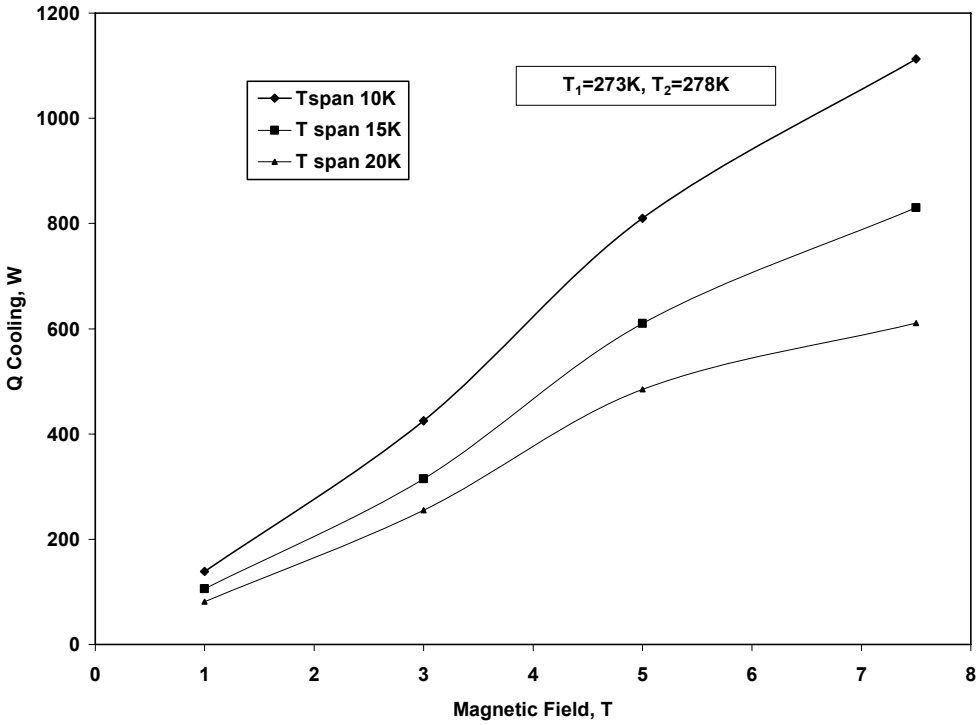

Figure 20.—Cooling power versus magnetic field for various temperature spans.

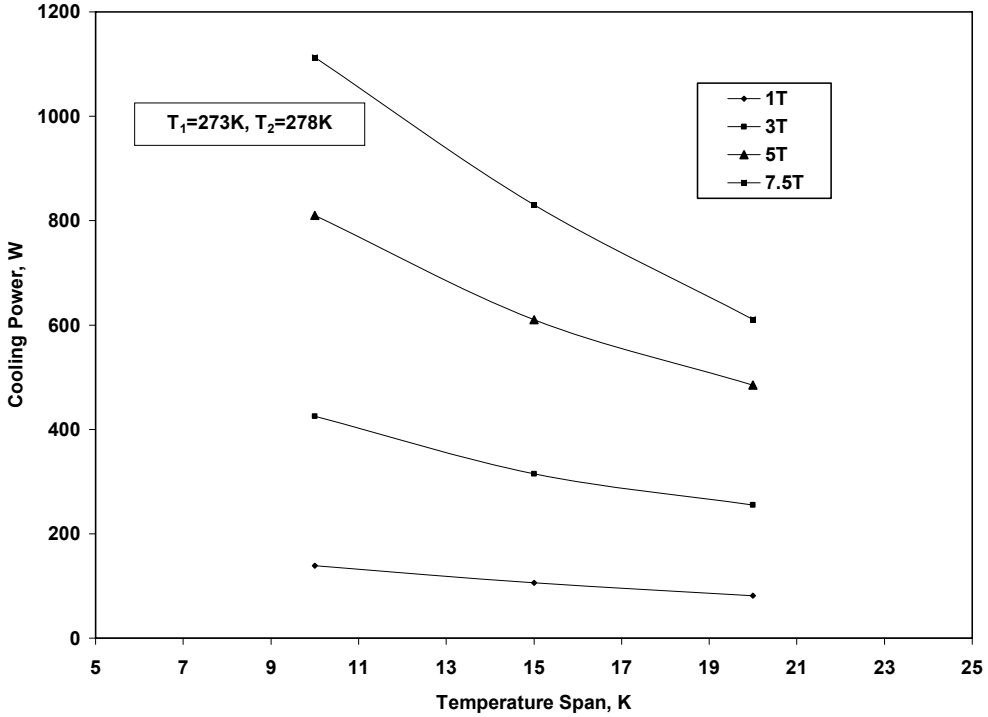

Figure 21.—Cooling power versus temperature span for various magnetic fields.

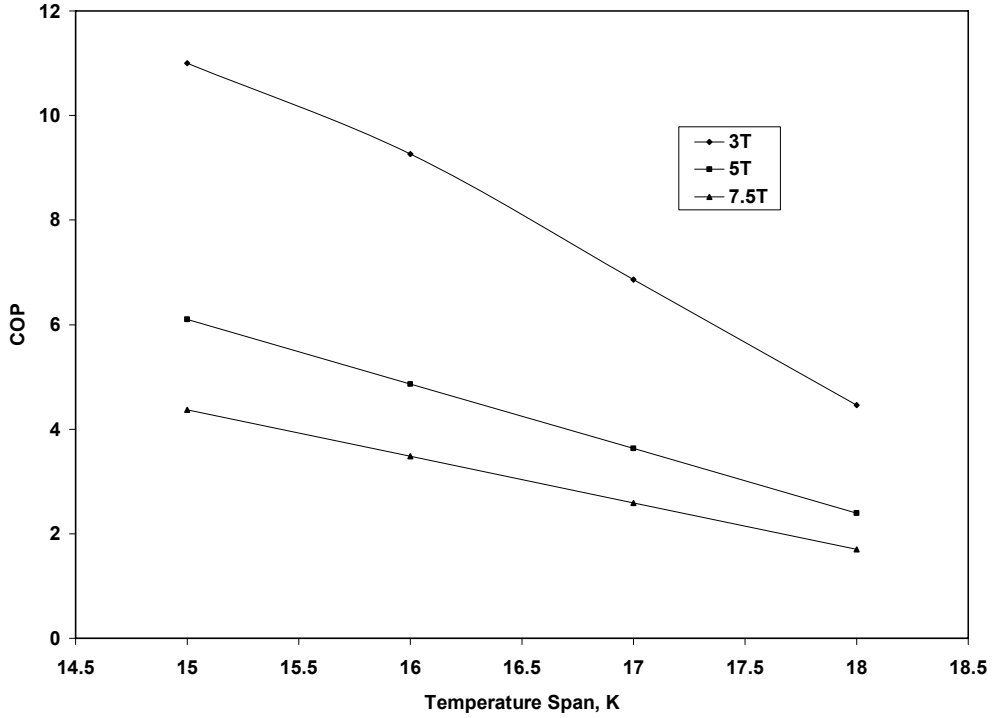

Figure 22.—COP versus temperature span for different magnetic fields.

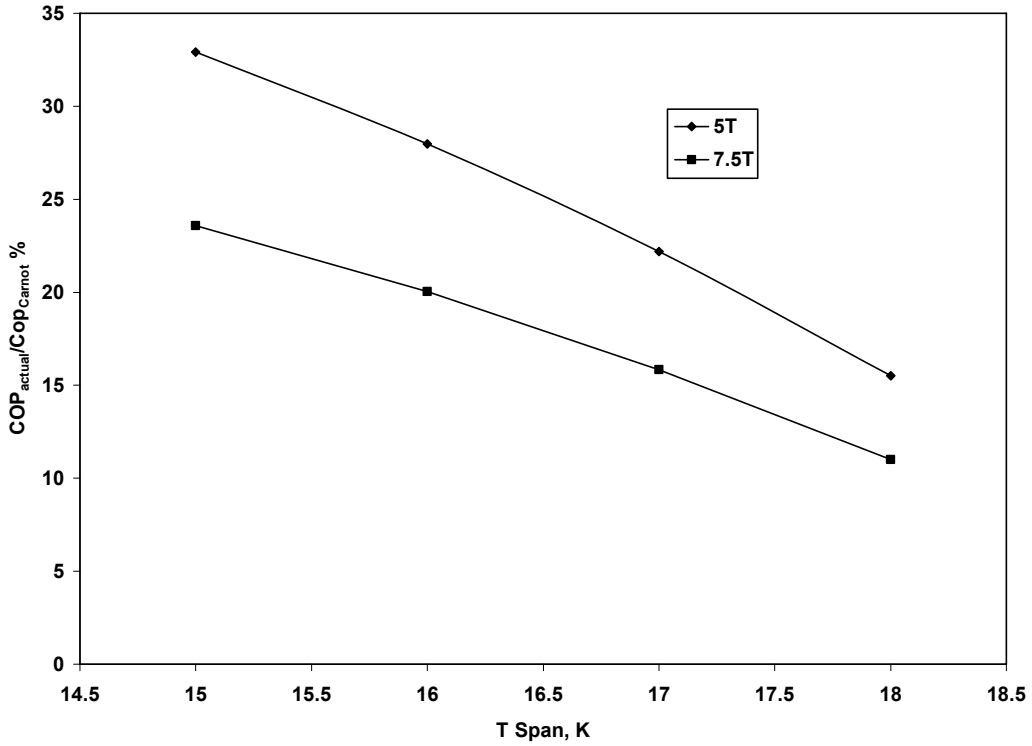

Figure 23.—COPActual/COPCarnot versus temperature span for various magnetic fields.

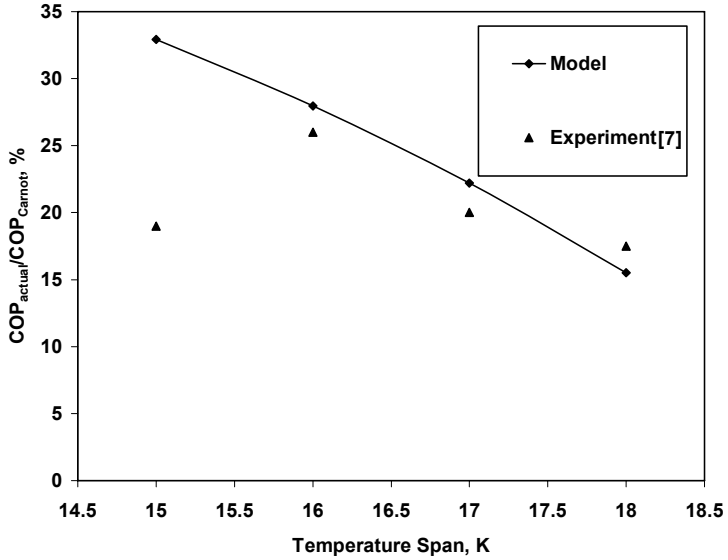

Figure 24.—Predicted and experimental COPactual/COPCarnot versus temperature span for 5T magnetic field.

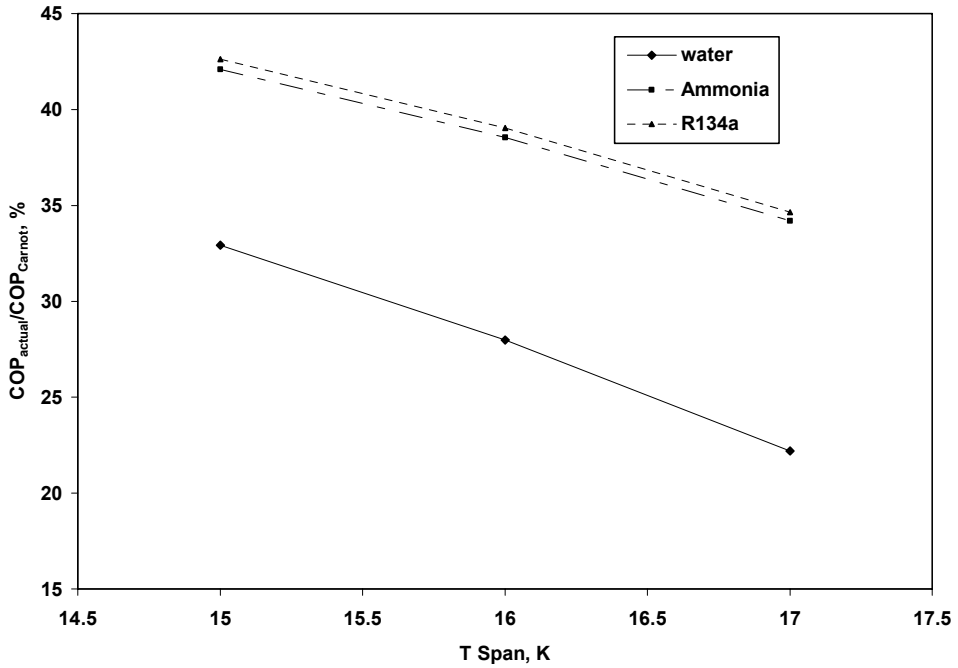

Figure 25.—COPactual/COPCarnot versus temperature span for various fluids with a 5T magnetic field.

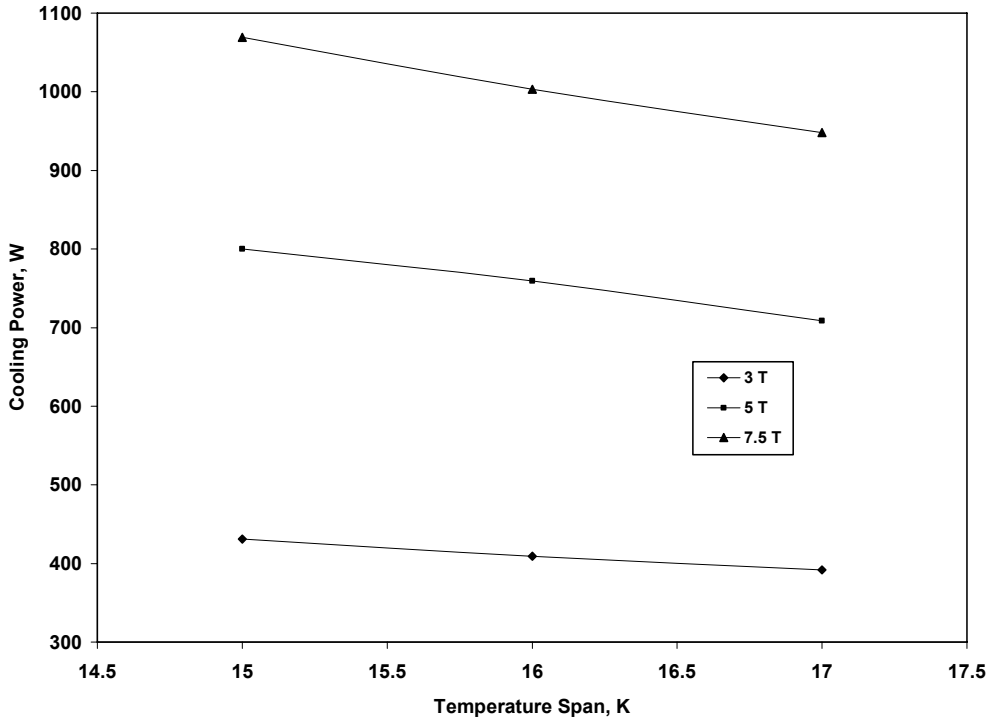

Figure 26.—COP versus temperature span for different magnetic fields with R-134a.

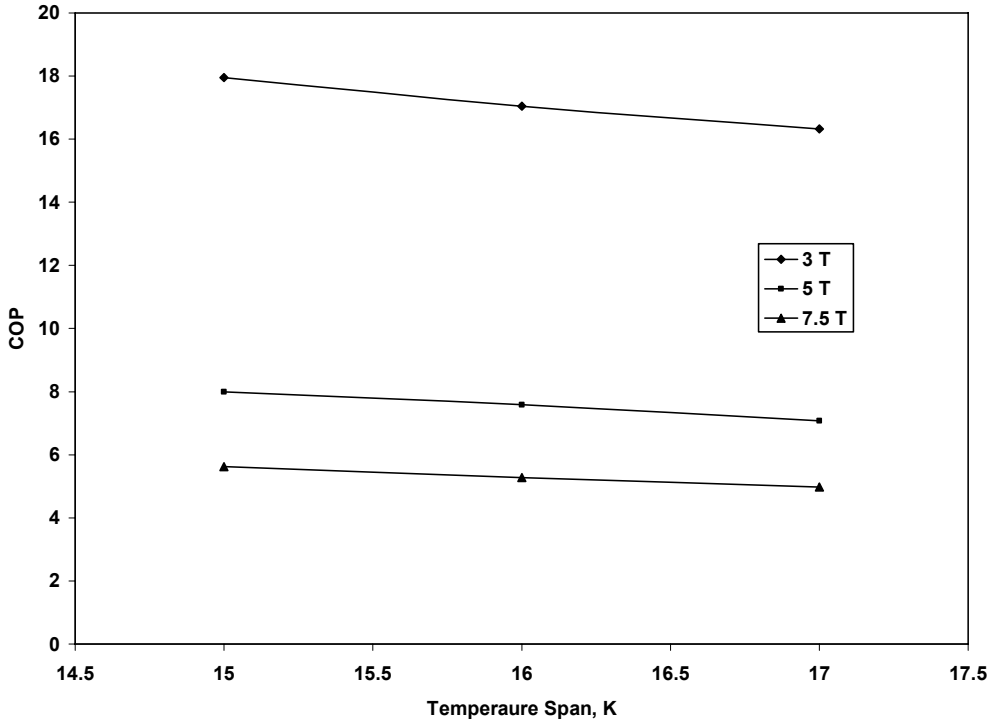

Figure 27.—COP versus temperature span for different magnetic fields and R-134a.

Conclusions

The stability of Si_3N_4 as a diffusion barrier in deposition of GdSiGe thin films on Si has been studied. Thin films of GdSiGe were deposited on PECVD nitride coated Si substrate. The films were annealed in vacuum to crystallize the GdSiGe desired phase. SIMS analysis of the interface of GdSiGe/Si_3N_4/Si films indicates a breakdown of the SiN diffusion barrier with depletion of GdSiGe films into silicon nitride and Si upon annealing at 1150 ◦C. It is hypothesized that the dangling hydrogen bonds in Si3N4 contribute to the breakdown.

The trapezoidal microchannels were designed with circular and trapezoidal microchannels. The eight microchannels with 150 μm deep in 2 in. wafer were fabricated using MEMS technology. The combined etching of 250 μm formed the inlet and outlet ports to flow refrigerant. The in-situ temperature sensors through deep impurity diffusion were installed into the wafer and tested by changing the temperature. GiSiGe block was assembled with the microchannel and its prototype of microcooler was shown in the presentation.

For the transient analysis with time dependent heat source, periodic behavior of temperature in the solid as well as in the fluid was seen as the magnetic field was introduced and released. Interface heat flux also showed a periodic behavior and it showed higher values near the entrance of the channel. It is seen that after a certain period of time, local heat transfer coefficient and Nusselt number distribution reach an equilibrium condition and does not change any more with time.

The thermodynamic characteristics of the magnetic refrigerator have been studied. A method has been presented for evaluating each process in the cycle and the corresponding working fluid temperatures, and the net cooling power. Sensitivity analysis was performed to study the behavior of the cycle. For this cycle, two important performance parameters were evaluated: the coefficient of performance and the refrigeration capacity. It was shown that the ratio of COPactual/ COPCarnot decreases as consequence of an increase in the temperature span. The cooling load increases with increase in the magnetic field. The model showed good agreement with experimental data. Various working fluids were studied finding that R-134a exhibits better performance. Magnetic refrigeration

exhibits a great potential by showing a very high coefficient of performance when compared to commercial vapor cycle refrigerators.

Publications and Patents

Publications

1. S.C. Kim, B. Bethala, S. Ghirlanda, S. Sambandam, S. Bhansali, “Design and Fabrication of a Magnetocaloric Microcooler,” ASME International Mechanical Engineering Congress and Exposition, Nov 2005, (Abstract accepted)
2. S.C. Kim, B. Bethala, S. Ghirlanda, P. Khanna and S. Bhansali, “Characterization of Diffusion Barriers for Gd-Si-Ge Films on Silicon Substrate,” 4th International Surface Engineering Congress & Exposition, Aug 2005 (Abstract submitted)
3. P.S.C. Rao and M.M. Rahman, “Transient Conjugate Heat Transfer in a Circular Microtube Inside a Rectangular Substrate,” AIAA Journal of Thermophysics and Heat Transfer, (Submitted for Review).
4. P.S.C. Rao, M.M. Rahman, and H.M. Soliman, “Numerical Simulation of Steady State Conjugate Heat Transfer in a Circular Microtube Inside a Rectangular Substrate,” Numerical Heat Transfer, (Submitted for Review).
5. S.N. Sambandam, B. Bethala, S.B. Hansali, D.K. Sood, “Search for a Suitable Diffusion Barrier Layer for Annealing Films of Gd-Si-Ge Sputter Deposited on Silicon, International Conference on Metallurgical Coatings and Thin Films, Sandi ego, May 2005, (Paper accepted).
6. M.M. Rahman and L. Rosario, “Thermodynamic Analysis of Magnetic Refrigerators,” Proc. 2004 ASME International Mechanical Engineering Congress and Exposition, Vol. 3, Anaheim, California, November 2004.
7. P.S.C. Rao and M.M. Rahman, “Analysis of Steady State Conjugate Heat Transfer in a Circular Microtube Inside a Substrate,” Proc. 2004 ASME International Mechanical Engineering Congress and Exposition, Vol. 1, Anaheim, California, November 2004.
8. S.N. Sambandam, S. Bhansali, V.R. Bhethanabotla, “Study on magnetocaloric GdSiGe thin films for microcooling applications,” TMS Annual Meeting, Charlotte, NC, March 14-18, 2004.
9. S.S. Shevade and M.M. Rahman, “Transient Analysis of Microchannel Heat Transfer with Volumetric Heat Generation in the Substrate,” Proc. TMS Annual Symposium, Charlotte, North Carolina, March 2004.
10. M.M. Rahman and S.S. Shevade, “Development of Microchannel Heat Exchanger for Magnetic Refrigeration Applications,” Proc. International Conference on Mechanical Engineering (ICME-2003), Dhaka, Bangladesh, December 2003 (keynote paper).
11. M.M. Rahman, S.S. Shevade, and V. Bethanabotla, “Analysis of Transient Heat Transfer in a Microchannel Heat Exchanger During Magnetic Heating of the Substrate Material,” Proc. 2003 ASME International Mechanical Engineering Congress and Exposition, Vol. 1, Washington, D.C., November 2003.
12. M.M. Rahman and S.S. Shevade, “Microchannel Thermal Management During Volumetric Heating or Cooling,” Proc. First International Energy Conversion Engineering Conference, Portsmouth, Virginia, August 2003.

Hydrogen Gas Sensors by Surface Acoustic Waves

PI: V. Bhethanabotla (University of South Florida)
B. Joseph (University of South Florida)

Problem

Sensor technology development using SAW devices and nanomaterial sensing layers.

Objective

To develop sensitive, selective and fast-responding SAW hydrogen sensors that operate at room temperature. To utilize these advances in the development of SAW and other acoustic wave sensors for other gases.

Approach

Synthesis of nanomaterials and their utilization as SAW sensor materials, guided by theoretical calculations at multiple scales.

Background

Design, construction and testing of inexpensive, solid-state sensors that respond sensitively, selectively, and rapidly to hydrogen and other gases is the motivation for this research. Specifically, such sensors for hydrogen detection are of interest to NASA, and to the hydrogen-based economy that holds current promise for automotive transportation and other terrestrial uses.

To achieve the specific objective of such a hydrogen sensor, our research took an approach that combines the somewhat developed surface acoustic wave (SAW) transducer technology (Ballantine et al., 1997) with nanomaterial sensing layers. Solid-state SAW devices are mass produced in current cell phone, TV and other radio frequency uses, and a suitably designed hydrogen sensor can be similarly produced inexpensively. They also lend themselves to wireless interrogation, and a passive, non-power consuming SAW sensor that can be wirelessly interrogated for gas concentration is a distinct possibility in the near future.

Nanomaterials hold the promise of producing sensing materials for SAW devices that can lead to enhanced selectivity, sensitivity and speed of response. While there is substantial recent literature lending support to these assertions, we only point to the relevant ones for hydrogen sensing. Thus, Penner and co-workers have demonstrated Pd nanowire hydrogen sensors that showed milli-second to second response times (Walter et al., 2002, Favier et al., 2001), and Dai and co-workers have demonstrated similarly effective hydrogen sensors with Pd-coated single walled carbon nanotubes (SWNTs) (Kong et al., 2001). Lowering the limits of detection, development of more robust fabrication processes than are possible in these nano-sized devices, improving and achieving selectivity, and transferability of the techniques to sensors for other gases were our motivations to utilize these nanomaterials in our SAW-based sensors, starting from the groundwork laid by these recent researchers.

Most hydrogen sensors utilize the enormous capacity of Pd to absorb hydrogen, however, several issues of reaction kinetics, mechanical stability, and reversibility are present with Pd-based hydrogen sensors. Metal oxides have been utilized as successful alternatives, which have required high (400+ ◦C) temperatures for effective operation, which in turn requires higher power to operate.

Our approach was to leverage the mass, electroacoustic and elastic response mechanisms of SAW devices (Ballantine et al., 1997), with the advantages afforded by the nanomaterials of Pd-alloys as sensing layers. We aimed to construct field devices in using suitably designed high frequency SAW devices. We also aimed to understand the mechanisms by which the nanomaterials worked, utilizing electronic structure and molecular dynamics simulations, and macroscopic sensor response modeling utilizing electrical equivalent circuits, mechanical perturbations methods, and finite element techniques. The final result is expected to be superior sensors hydrogen and other gases and vapors.

Results and Discussion

This section gives some highlights of the results achieved as well as discusses them. It is organized according to the tasks and deliverables presented at the beginning of this report.

Device Fabrication

200 MHz SAW devices on Y-Z lithium niobate were designed, and successfully fabricated by optical lithography, using standard etching process. The 200 MHz SAW sensors are dual-delay line devices with 50 finger pairs. Figure 1 shows optical micrographs of the inter-digital transducers (IDTs) on the 200 MHz SAW sensor. Electron beam lithography was utilized in fabricating the 900 MHz device shown in figure 1. The sub-micron (about 350 nm) line-widths required for this device necessitated electron-beam lithography, which is suitable for a university environment that avoids expensive sub-micron mask fabrications.

To expand the research to other gas and organic vapor detection, high frequency (about 100 MHz) thickness shear mode resonators were fabricated by etching the central portion of quartz blank by chemical methods. The concept and devices are shown in figure 2.

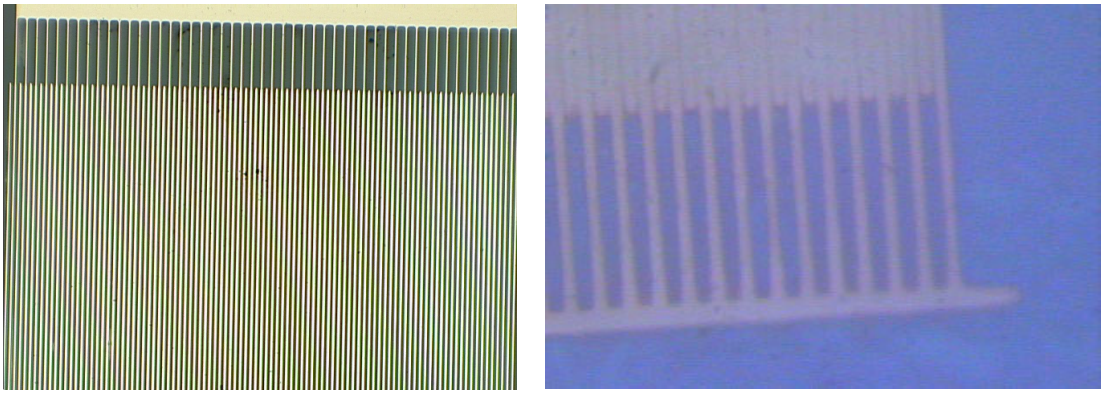

Figure 1.—Optical micrograph of fabricated 200 MHz (left) and 900 MHz (right) IDTs.

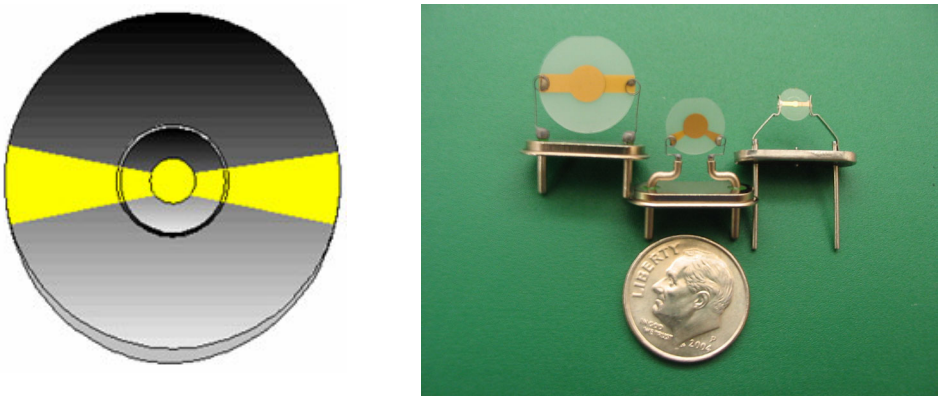

Figure 2.—Milled TSM device schematic, showing the thinned-down central quartz blank, and comparison of 10, 20, and 100 Mhz devices.

Radio Frequency Test-Bed with Gas and Organic Vapor Dilution Systems

A fully instrumented and automated radio-frequency test bed (fig. 3) has been designed and fabricated at the Sensor Research Laboratory (SRL) to test SAW sensors. Two dilution systems consisting of arrays of mass-flow controllers (MKS 1479A series) to (i) achieve gas concentrations of a few volume percent to ppm range, and (ii) multiple organic vapors concentrations of low volume to high ppm ranges using vapor bubblers have also been constructed. The target analytes (e.g., hydrogen gas or hydrocarbon vapor) are mixed with an inert or other gas mixture (nitrogen or contaminated nitrogen, for example) to get the desired concentration.

Solenoid valves are used to select specific gas flow lines. The gases go through the mixing chamber to the temperature controlled test cell, where the SAW device is placed. The two-port radio-frequency measurements are done by an S-parameter Vector Network Analyzer. An RF switch is used to switch between the two delay-lines. We have interfaced an Agilent 4294A (Agilent Technologies) impedance analyzer for impedance spectroscopy studies to characterize these micro- and nano-structured materials *in-situ*, and a Keithley 2010 digital multi-meter (Keithley Instruments Inc.) primarily for 4-point resistivity measurements. A Dell PC (Dell Inc.) uses PCI bus data acquisition and GPIB to communicate with the instrumentation via a Labview interface. The set-up permits us to analyze high-speed and long-term response characteristics at sub/supra ambient temperatures, and pressures, with and without contaminants.

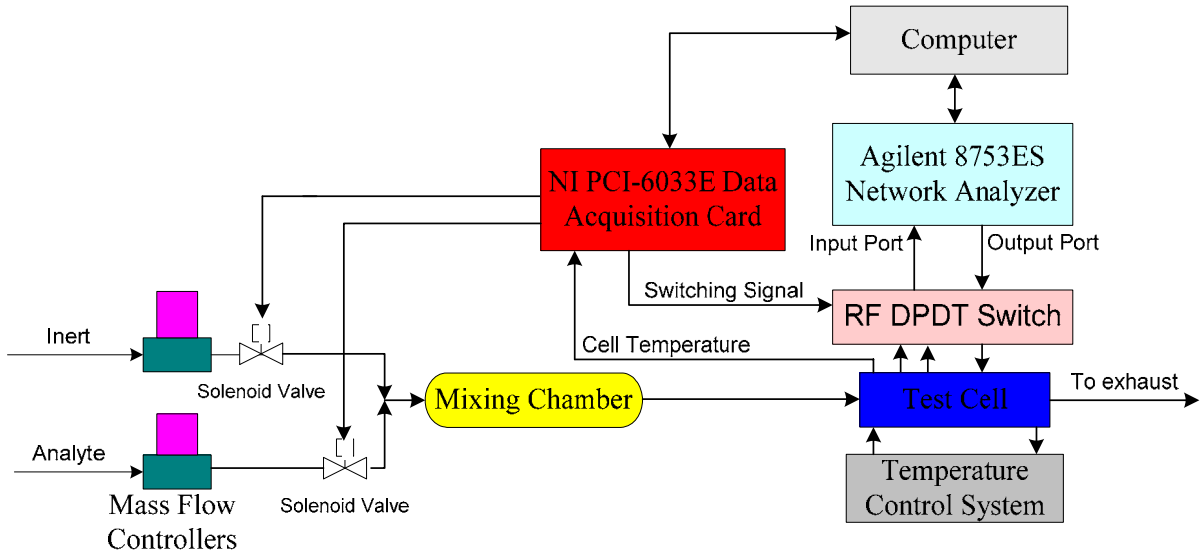

Figure 3.—Schematic of gas dilution test-bed.

Test Results for Hydrogen and Hydrocarbon Sensors

Figure 4 shows the reproducible room temperature response of the 200 MHz SAW device after a sensing bi-layer of 115 nm hydrogen-phthalocyanine (by e-beam evaporation) and 200 nm nanocrystalline Pd (by sputtering, grain size of 32 nm determined by XRD and AFM) were deposited. The nanocrystalline Pd reduced the response time to order of a few seconds, a significant improvement over existing Pd based hydrogen sensors, where the response times are in order of hundreds of seconds. Figure 4 includes the transport delay of about 20 sec, and therefore, the sensing film actually begins to respond in the sub-second range. Furthermore, an anomalous behavior is seen. The center lobe peak frequency increases with hydrogen concentration, contrary to what has been previously reported by others with micro-crystalline Pd (Jakubik et al., 2003), and needs to be understood.

Superiority of the 100 MHz TSM device in hydrocarbon sensing in terms of higher sensitivity and lower limits of detection are shown in figure 5. Results for a polymer-coated TSM device exposed to benzene of various concentrations show the much larger response of the 100 MHz device.

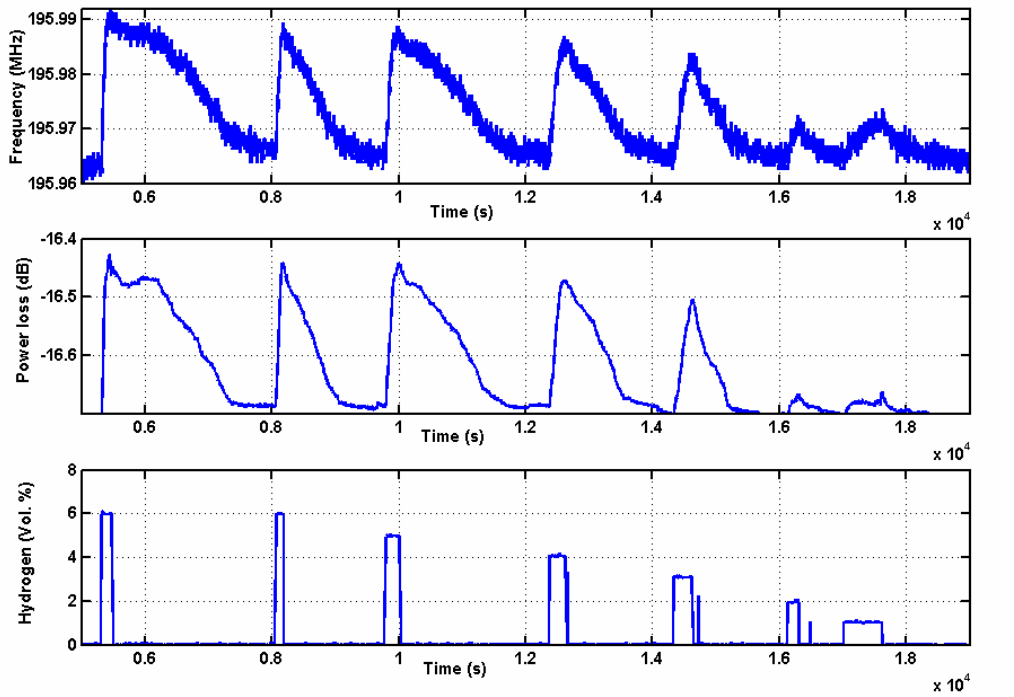

Figure 4.—Response of 200 MHz hydrogen SAW sensor at 24 C.

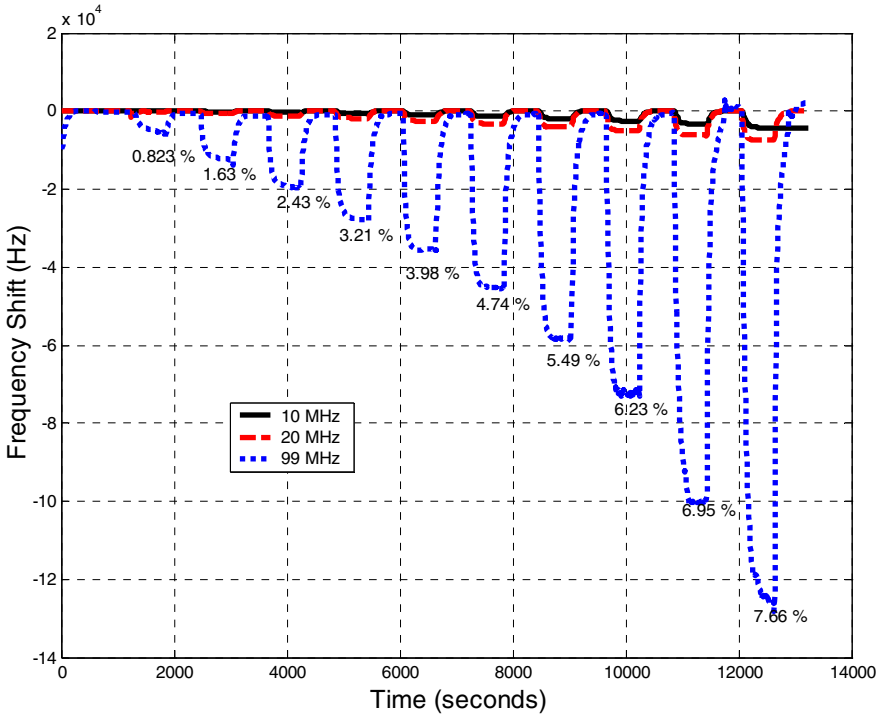

Figure 5.—Responses of 10, 20 and 100 MHz TSM devices to benzene exposures.

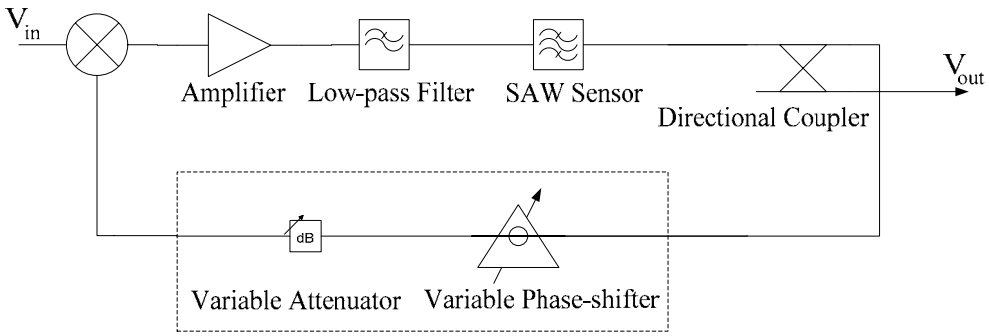

Figure 6.—Schematic diagram of oscillator circuit.

Oscillator Circuit Design and Testing for 200 MHz SAW Sensors

We fabricated a conventional feedback radio-frequency oscillator circuit (fig. 6) consisting of (a) an amplifier (MAN-1LN), (b) a low-pass filter (PLP-200), (c) a directional coupler (TDC-10-1), (d) the device under test, i.e., the SAW sensor, (e) a (variable) phase shifter, and (f) an (variable) attenuator. Two oscillator circuit layouts were laid next to each other on a printed circuit board, for the dual-delay line SAW sensors. The dual-delay line configuration is addressed later in this section.

Using reflectance measurements on the Agilent 8753ES vector network analyzer, the fabricated SAW sensor was seen to have a loss of around 20 dB at center frequency of 198 MHz, with a (wrapped) phase lag of 180°. The amplifier had a frequency-independent gain of about 28 dB. The assembled circuit had a phase shortfall of 15°. No attenuator was found needed. The final design uses a voltage-controlled variable phase shifter (Mini-Circuits JSPHS-150). Figure 7 shows the power spectrum of the oscillator circuit output. A home-built phase shifter was used for this test. As can be seen from the figure, the oscillator circuit is able to lock on to the center frequency of the SAW sensor, and the output from the directional coupler is at a power level of –10 dBm.

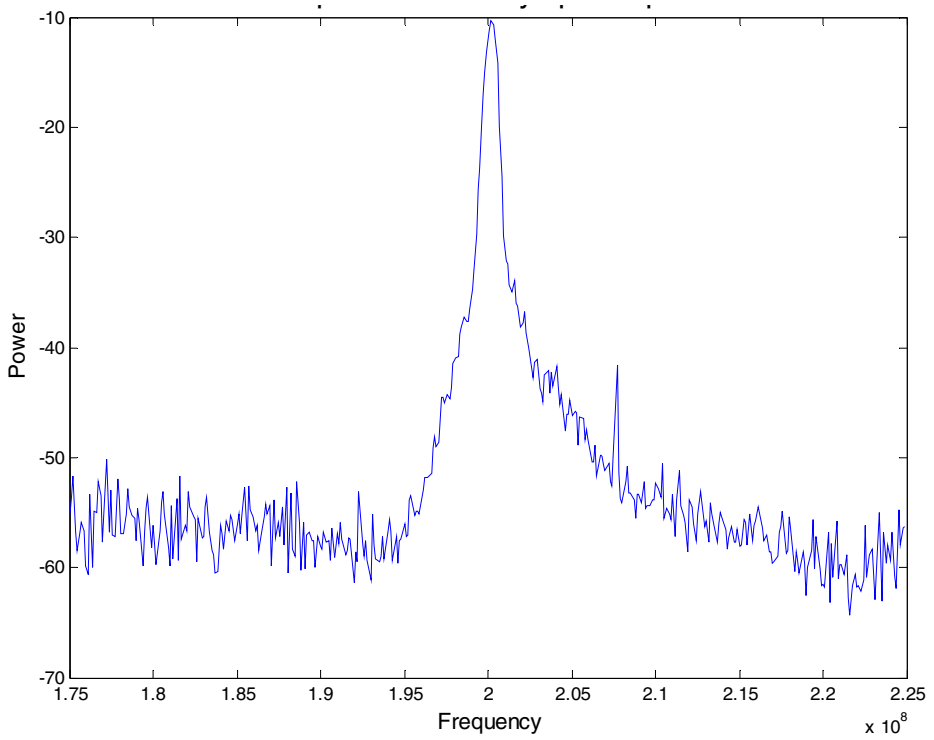

Figure 7.—Power spectrum plot of phase-shifted oscillator.

Square-Law Frequency Mixers for Dual Delay Lines

In a dual delay line scheme, one SAW delay line is deposited with a sensing layer and acts as the measurement device. The other serves as an environmental reference, primarily, ambient temperature compensation. Both delay lines are identical in design (except for the sensing layer), and their respective center frequencies are tracked by individually oscillator circuits. To achieve ambient temperature adjustment, we need to track the difference between the individual center frequencies. This is achieved by a combination of a square-law radio frequency mixer, and a low pass filter. The frequency mixer we used (Mini-Circuits ZX05-1) consisted of two inputs – a local oscillator (LO) input, and a low-power radio frequency (RF) input. We use an amplifier (ZJL-3G Mini-Circuits) to amplify one of the coupler outputs (~–10 dBm) to meet the input power requirements of the LO input (7 to 10 dBm). The output of the other coupler was fed directly to the RF input. We used SLP-5 from Mini-circuits for the low pass filter stage. This filtered output will be then fed to a frequency counter (Agilent 5334B) to record the variations in differential frequency with time. The frequency counter has been interfaced to a Dell PC together with the rest of the test-bed instrumentation to continuously log data.

Nanomaterial Synthesis

Nanomaterial Pd was synthesized in several ways. Initially, we sought to reproduce the technique used by Penner and co-workers, that of step-edged deposition. This was successful, and yielded nanoparticles and nanowires.

Due to difficulties in scale-up in synthesis with this technique, we chose to utilize synthesis in alumina templates. These templates were successfully fabricated by anodization of aluminum in our group. A template made with 37 nm pores is shown in figure 9. Current efforts are towards the deposition of Pd nanowires in these templates. Later efforts will be towards the deposition of Pd alloys in these templates.

To proceed ahead with the hydrogen sensor development, we utilized nanocrystalline Pd deposited in our own optimized sputter process. A 32 nm grain size was achieved as shown in the AFM image in figure 10. This structure, and grain size were also established in X-ray measurements.

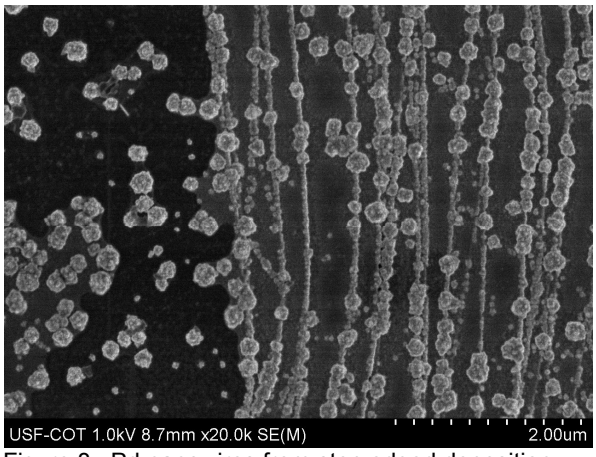

Figure 8.–Pd nanowires from step edged deposition on graphite.

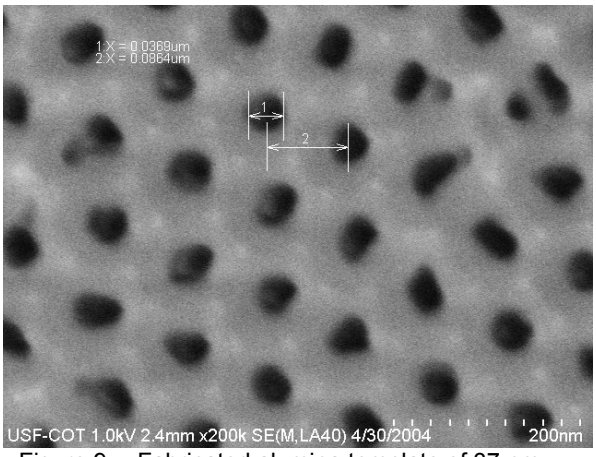

Figure 9.—Fabricated alumina template of 37 nm pores.

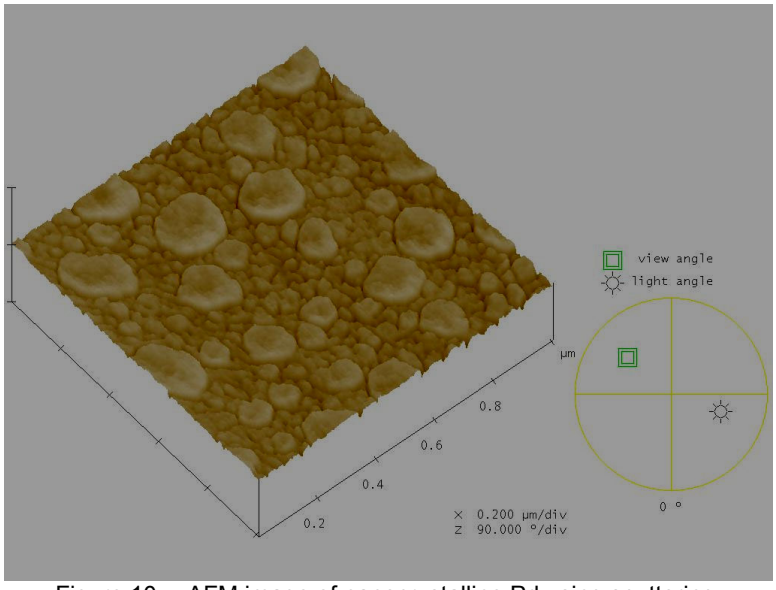

Figure 10.—AFM image of nanocrystalline Pd using sputtering.

Theoretical Studies

Molecular dynamics simulations of nanowires and nanoclusters of Pd and Pd alloys were carried out to understand the structural, melting and surface segregation properties of these nanomaterials as a prelude to simulations of their interactions with hydrogen in sensing applications. These studies helped us in the processing of the materials, in choosing the alloying metal, and in understanding the role of nano-size on sensing. Numerous results are being presented in several publications and are not elaborated here.

As an example, the dependence of melting points of Pt-Pd clusters of two sizes as a function of composition is shown in figure 11. Please email PI for preprints and reprints. For typical results, see Sankaranarayanan et al. (2005).

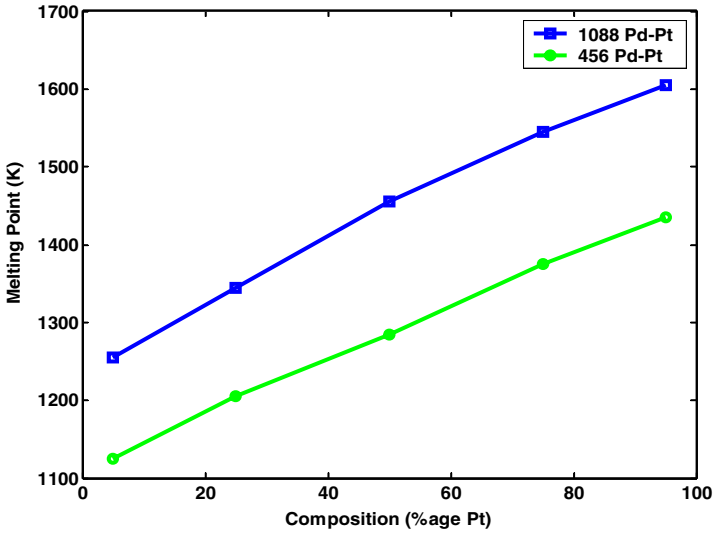

Figure 11.—Melting point variations with composition for $(Pd_x\text{-}Pt_{(1-x)})_{456}$ (circles) and $(Pd_x\text{-}Pt_{(1-x)})_{1088}$ (squares).

Problems Encountered in the Research

On the device fabrication front, we are encountering difficulties with the electron beam lithography, where the stage drifts not allowing us to connect the IDT structures to the bonding pads. As a consequence we are unable to test our hypothesis on the advantages to be gained by utilizing higher frequency devices.

On the sensing layer fabrication front, we are facing problems of electrodeposition of nanowire materials into alumina templates. This is an electrochemistry issue which will be worked out eventually, and lead to the first reported fabrication of Pd nanowires in templated synthesis. We are facing the problem of electron beam and thermal evaporators getting contaminated with the phthalocyanine materials, necessitating the fabrication of a separate evaporator. Alternative techniques of Langmuir-Blodgett films were tried and resulting hydrogen sensors were successful, however, the phthalocyanine films contained fatty acids (a necessity in LB techniques). This reduced the signal strength of the resulting sensors, with similar characteristics as from evaporated films.

We faced the problem of oscillator circuit skipping slowing down progress towards a field hydrogen sensor. This is a result of the delay-line design on the SAW device. This is being addressed with newer designs and with the frequency measurement being replaced by a phase measurement. We are currently developing circuits for such measurements.

Conclusions

This past year, we aimed to fabricate moderate (200 MHz) and higher (900 MHz) SAW devices in $LiNiO_3$ and rather high frequency (100 MHz) TSM devices in quartz. We succeeded in two of these three objectives. While we could draw the structures and process them in the desired substrate for the GHz devices, we found stage drifts in the converted SEM ebeam lithography tool prevented us from fabricating functioning structures. The 200 MHz SAW devices combined with synthesized nanomaterials were demonstrated in successful tests as hydrogen sensors with a few seconds of response time. Improvements in response times, recovery times, limits of detection and sensitivity are envisioned with further development of devices and sensing materials. The 100 MHz TSM device was utilized to construct a very successful hydrocarbon sensor, exhibiting superior sensitivity and limit of detection. Both results for the SAW hydrogen sensor and for the TSM hydrocarbon sensor were disclosed separately, and a patent is already filed for the SAW sensor. Oscillator circuits were designed and constructed for the 200 MHz SAW sensor to achieve a field device. It is found that better stability (a few tens of Hz) is achievable with

these circuits over wide temperature ranges for the dual delay-line configuration, enabling inexpensive field devices. However, the current design of the SAW tended to make the circuit skip, and phase measurements are planned as possibly superior, with circuits under design currently.

Nanomaterial synthesis, especially of transition metal nanowires has been advanced as a result of this research. Fabrication of nanoporous alumina, nanoparticles and nanowires of Pd are specific achievements.

Theoretical work utilizing molecular dynamics simulation has led to significant understanding of the surface melting, surface segregation and structural behavior of the nanomaterials we utilize in constructing superior hydrogen sensors with SAW devices. Pd-coated nanorods, carbon nanotubes and tobacco mosaic viruses, are planned for experimentation as possibly better sensing materials for hydrogen detection. Similar metal and oxide coated carbon nanotubes are planned for tests in sensing of other gases.

Publications and Patents

1. Subramanian, K.R.S. Sankaranarayanan, Bhethanabotla, V.R., and Joseph, B., "A Molecular Dynamics Study on Melting of Pd-Pt Nanoclusters," *to appear in Phys. Rev. B,* April, 2005.
2. Miao, L., Bhethanabotla, V.R., and Joseph, B., "Molecular Dynamics Simulations for Melting of Palladium Nanoclusters and Nanowires," revised manuscript submitted to *Phys Rev. B*, March, 2005.

The fifteen national-level conference presentations made and listed below were each written up as articles and published as peer-reviewed Conference Proceedings papers, in addition to the presentations made at the meetings. Many of these are currently being written up as journal articles.

Patent Applications and Disclosures

3. Bhethanabotla, V. R. and Bhansali, S., "Surface Acoustic Wave Hydrogen Sensor," non-provisional patent application filed in July, 2004.
4. Bhethanabotla, V.R., and Williams, R.D., "High Frequency Thickness Shear Mode Acoustic Wave Sensors for Gas and Organic Vapor Detection," invention disclosure filed November, 2004.

Conference Presentations: National Conferences

5. Srinivasagupta, D., Ortiz, O., Bhansali, S., Bhethanabotla, V.R., and Joseph, B., "Palladium Nanowire Synthesis on Graphite Electrode Step-Edges via Electrodeposition: Molecular Modeling and Experimentation," *204th Meeting of The Electrochemical Society,* Orlando, Florida, October 12-17, 2003.
6. Ortiz, O., Bhansali, S., and Bhethanabotla, V.R., "Enhancing Sensitivity of SAW Sensors using Nanostructured Materials," *204th Meeting of The Electrochemical Society,* Orlando, Florida, October 12-17, 2003.
7. Chaudhari, A., Srinivasagupta, D., Chennapragada, P., Bhethanabotla, V.R., and Joseph, B., "Development of Surface Acoustic Wave Sensors Using Nanostructured Sensing Materials for Gas Detection," *AICHE 2003 Annual Meeting,* San Francisco, CA, November, 2003.
8. Srinivasagupta, D., Bhethanabotla, V.R., Joseph, B., "Brownian Dynamics Simulation of Palladium Nanowire Synthesis on Graphite Step-Edges by Electrodeposition," *AICHE 2003 Annual Meeting,* San Francisco, CA., November, 2003.
9. Sambandam, S.N., Vedawyas, M., Bhansali, S., and Bhethanabotla, V.R., Simulation of Sputter Deposition Process in Multicomponent Metallic Glasses," AIChE 2003 Annual Meeting, San Francisco, CA., November, 2003.
10. Rahman M. M., Shevade S. S., and Bhethanabotla V. R., "Flow in a Microchannel with Time Varying Heat Source," *2003 ASME International Mechanical Engineering Congress and Exposition,* Washington D.C., November 16-21, 2003.
11. Sambandam, S.N., Bhansali, S., and Bhethanabotla, V.R., "Synthesis and Characterization of Amorphous Metallic Alloy Thin Films for MEMS Applications," *MRS Fall Meeting,* Boston, MA, December, 2003.

12. Sambandam S.N., Bhansali S., Bhethanabotla V.R., “Study on Magnetocaloric GdSiGe Thin Films for Microcooling Applications,” *TMS*, Charlotte, NC, March 14-18, 2004.
13. Sankaranarayanan K.R.S.S., Bhethanabotla, V.R., and Joseph, B., “Molecular Dynamics Simulation of Graphite Supported Bimetallic Transition Metal Nanoclusters,” *AIChE Annual Meeting,* Austin, TX, 2004.
14. Sankaranarayanan K.R.S.S., Bhethanabotla, V.R., and Joseph, B., “Computer Simulation of the Melting Behavior of Bimetallic Nanoclusters,” *AIChE Annual Meeting,* Austin, TX, 2004.
15. Miao, L., Bhethanabotla, V.R., and Joseph, B., “Molecular Dynamics Simulations for Melting of Palladium Nanoclusters and Nanowires,” *AIChE Annual Meeting,* Austin, TX, 2004.
16. Miao, L., Bhethanabotla, V.R., and Joseph, B., “Melting and Structure Evolution of Palladium and Graphite-supported Palladium Nanoclusters: A Molecular Dynamic Simulation Study,” *AIChE Annual Meeting,* Austin, TX, 2004.
17. Williams, R., Upadhyayulu, A., Bhethanabotla, V.R., “Organic Vapor Sensing with Enhanced Sensitivity using Polymer-coated Thickness Shear Mode Devices,” *AIChE Annual Meeting,* Austin, TX, 2004.
18. Chaudhari, A., Srinivasagupta, D., Cular, S., Bhethanabotla, V.R., and Joseph, B., “Surface Acoustic Wave Sensors Using Nanocrystalline Palladium for Hydrogen Gas Detection,” *AIChE Annual Meeting,* Austin, TX, 2004.
19. Cular, S., Showalter, S., and Bhethanabotla, V.R., “Acoustic Wave Sensor Application to Biological Sensing in Liquid Environments,” *AIChE Annual Meeting,* Austin, TX, 2004.

Conference Presentations: Regional Conferences

20. Chaudhari, A., Ortiz, O., Bhansali, S., and Bhethanabotla, V.R., “Sensitive, Selective & Fast Responding Surface Acoustic Wave Sensor For Hydrogen,” *Florida Chapter of the American Vacuum Society and Florida Society for Microscopy - 2003 Annual Symposium, March 17-20, 2003,* University of Central Florida, Orlando, Florida.
21. Ling Miao, Venkat Bhethanabotla, Babu, Joseph, “Molecular Dynamics Simulation of the Melting and Freezing of Palladium Nanoclusters and Nanowires,” *AVS Symposium,* Orlando, FL, March 2004.
22. Chennapragada, P. and Bhethanabotla, V.R., “Nano-porous Alumina Templated Synthesis of Pd Nanowires,” *AVS Symposium,* Orlando, FL, March 2004.
23. Waters, P., Volinsky, A., Sambandam, S., Bhethanabotla, V.R., and Bhansali, S. “Annealing Effects on Mechanical Properties of Metallic Glass Films,” *AVS Symposium,* Orlando, FL, March 2004.
24. Williams, R.D., and Bhethanabotla, V.R., “Polymer Sorption using a Thickness Shear Mode Resonator,” *AVS Symposium,* Orlando, FL, March, 2005.
25. Cular, S., Showalter, S.K, Bhethanabotla, V.R., and Cernosek, R.W., “Acoustic Wave Sensors: Applications to Biological Sensing in Liquid Environments,” *AVS Symposium,* Orlando, FL, March, 2005.
26. Srinivasan, K., and Bhethanabotla, V.R., “Tobacco Mosaic Virus (TMV) as a New Surface Acoustic Wave (SAW) Chemical Sensor Material,” *AVS Symposium,* Orlando, FL, March, 2005.
27. Shepard, J., Bhethanabotla, V.R., and Toomey, R., “Heavy Metal Ion Detection using Peptide-Modified Hydrogel Layers on a Quartz Crystal Microbalance,” *AVS Symposium,* Orlando, FL, March, 2005.
28. Sankaranarayanan, K.R.S.S. “Molecular Dynamics Simulation of Melting of Supported and Un-supported Pd-Pt Bimetallic Nanoclusters,” *AVS Symposium,* Orlando, FL, March, 2005.
29. Williams, R.D., and Bhethanabotla, V.R., Detection of Lower Explosion Limit Hydrocarbons using Polymer-coated High Frequency Thickness Shear Mode Devices,” *AVS Symposium,* Orlando, FL, March, 2005.
30. Cular, S., Bhethanabotla, V.R., and Branch, D.W., “Novel Shear Horizontal Surface Acoustic Wave Device for the Extraction of Multiple Film Properties,” *AVS Symposium,* Orlando, FL, March, 2005.
31. Srinivasan, K., and Bhethanabotla, V.R., Carbon Nanotubes as Enhanced Surface Acoustic Wave (SAW) Chemical Sensor Materials,” *AVS Symposium,* Orlando, FL, March, 2005.
32. Miao, L., Bhethanabotla, V.R., and Joseph, B., “Molecular Dynamics Simulation of Melting and Structural Evolution of Graphite-supported Palladium Nanoclusters,” *AVS Symposium,* Orlando, FL, March, 2005.

References

1. Ballantine, D. S. (1997). Acoustic wave sensors: theory, design, and physico-chemical applications. San Diego, Academic Press.
2. Favier, F., E. C. Walter, et al. (2001). "Hydrogen sensors and switches from electrodeposited palladium mesowire arrays." Science **293** (5538): 2227-2231.
3. Jakubik, W. P., M. W. Urbańczyk, et al. (2003). " Palladium and phthalocyanine bilayer films for hydrogen detection in a surface acoustic wave sensor system." Sensors and Actuators B **96(1-2)**: 321-328.
4. Kong, J., M. G. Chapline, et al. (2001). " Functionalized carbon nanotubes for molecular hydrogen sensors." Adv. Mater. 2001 **13(18)**: 1384-86.
5. Sankaranarayanan, K. R. S. S., Bhethanabotla, V.R., and Joseph, B. (2005). "A molecular dynamics study on melting of Pd-Pt nanoclusters." Physical Reviews B.
6. Walter, E. C., F. Favier, et al. (2002). "Palladium mesowire arrays for fast hydrogen sensors and hydrogen-actuated switches." Anal. Chem. **74(7)**: 1546-1553.

Development of Rectenna Solar Energy Conversion for Local Hydrogen Production

PI: K. Buckle (University of South Florida)
S. Bhansali (University of South Florida)
Y. Goswami (University of Florida)
E. Stefanakos (University of South Florida)
T. Weller (University of South Florida)
S. Krishnan (University of South Florida)
M. Sarehraz (University of South Florida)

Problem

To develop an antenna/rectifier system to harvest solar energy utilizing the wave nature of solar radiation.

Objective

To collect inexpensive energy from the sun to locally produce hydrogen.

Approach

To collect solar energy as a source of electricity for local hydrogen production. The rectenna concept consists of an array of antennas with MIM diodes used to convert solar energy to dc electrical power then collect the dc power to use as a power source. The research approach to the rectenna is to push the development of MIM diode technology and simultaneously develop the antenna array and interface technology.

Background

The concept of collecting solar energy by antennas was first proposed by R. Bailey in 1972 as an alternative to solar photovoltaic cells (ref. 1). According to Bailey, it must be possible to collect solar energy by means of and antenna, using the wave nature of light, and to convert that energy into dc-power by employing a very fast rectifier. The concept of using a rectifying antenna (rectenna) to function as a solar collector was based on scaling of microwave antenna theory. However, the proof-of-concept was never demonstrated because of a lack of the kind of nano-patterning technology required to scale the antenna problem to the wavelength of visible light. In the past few years the advent of nano-technology has made the theoretical possibility of solar energy harvesting by means of a rectenna more viable. As solar collectors, rectennas have a promising future: their conversion efficiencies are much higher than those of their photovoltaic cell counterparts, making them more favorable as the solar collectors of the future. The rectenna has been thoroughly studied for the past fifty years, mainly for power transmission purposes with efficiencies exceeding 80 percent at a single microwave frequency of 2.5 GHz (ref. 2). It is not clear that such high efficiencies are achievable in practice for a rectenna operating in the solar radiation spectrum. Solar radiation is quite different in nature compared to monochromatic microwave radiation. The rectenna project at the USF Clean Energy Research Center sought to define the problems associated with rectennas in the solar spectrum and to make a contribution to solving those problems using the technologies available in 2004 and projecting those technologies into the future.

Results and Discussion

The Rectenna Project, at the USF Clean Energy Research Center, during this year concentrated on three tasks: a 74 GHz slot antenna, MIM diode development, and Antenna Design Improvements. The results of this effort will be discussed in detail for each of the three tasks.

Task I.—74 GHz Antenna

The 74 GHz slot antenna was a task carried over from the first year and successfully completed in May of 2004. The work effort during the reporting time consisted of the following sub tasks, which were all completed:

- Development of micro bolometers for testing antennas at 74 GHz.
- Design of a 3λ/4 slot antenna at 74 GHz.
- Simulation of the 3λ/4 slot antenna design to determine predicted radiation pattern, gain, input impedance, and bandwidth.
- Fabrication of the 74 GHz 3λ/4 slot antenna and Bismuth bolometer for characterization tests.
- Tested the antenna to determine the experimental input impedance and radiation pattern.
- Three 74 GHz antennas were fabricated by December 2003 and were tested. The layout drawing for the antenna is shown in figure 1 and the antenna in its test configuration is shown in figure 2.

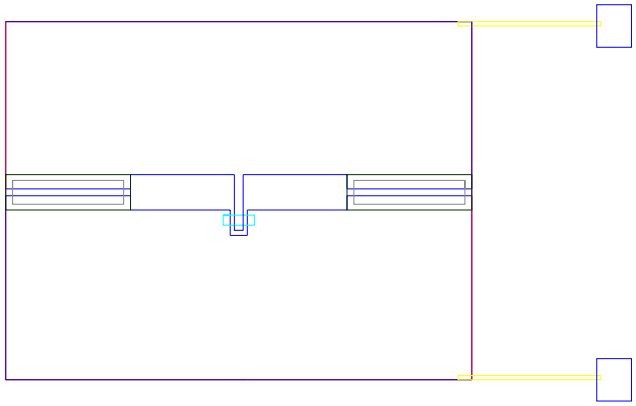

Figure 1.—Slot antenna layout drawing.

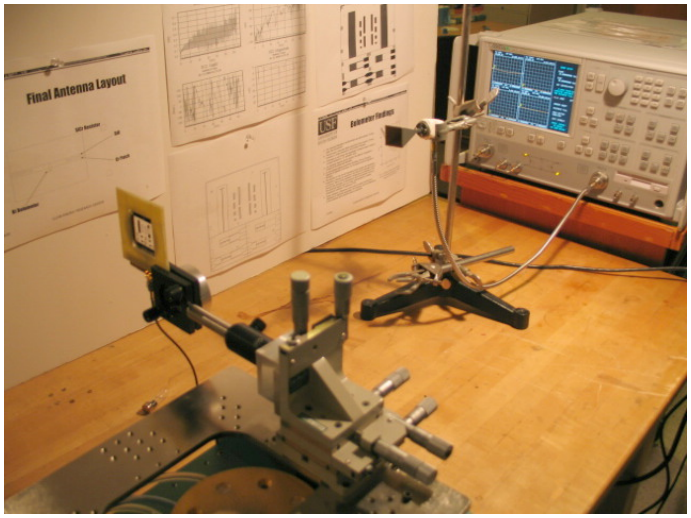

Figure 2.—(a) Slot antenna test configuration.

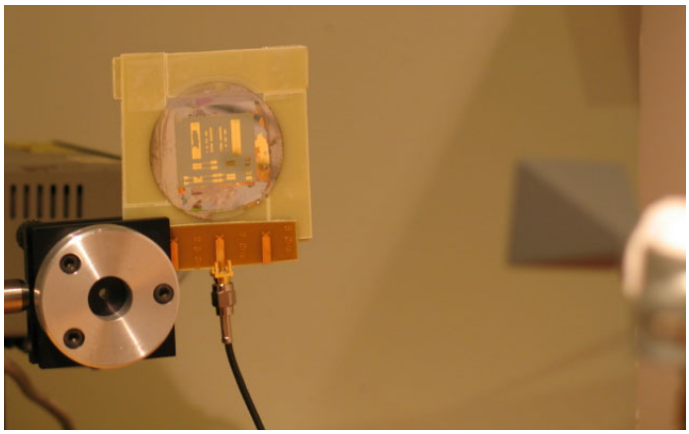

Figure 2.—(b) Antenna and instrumentation test fixture.

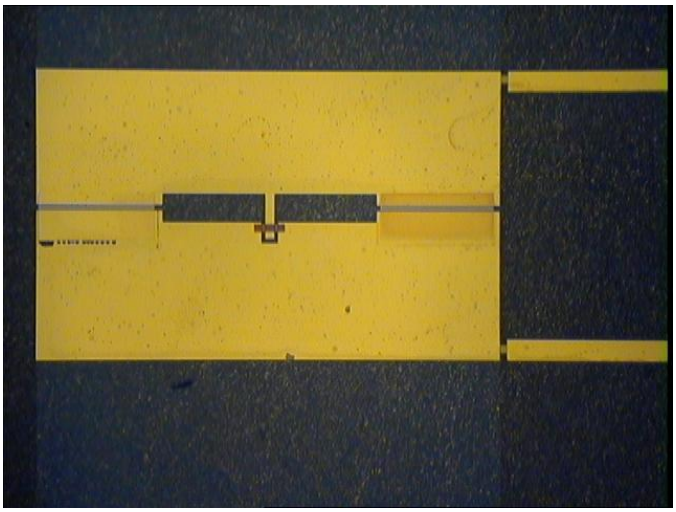

Figure 2.—(c) Detail of antenna under test.

"S" parameter tests were run on the 74 GHz antenna during February 2004. The problem of biasing the antenna for pattern measurements and the development of an improved fixture for the antenna pattern measurement consumed most of February. Antenna pattern measurements were made in March 2004. Analysis of the results indicated some calibration and measurement problems. The set was recalibrated and new pattern measurements were made in April 2004. The 74 GHz antenna measurements were finished in May 2004.

Task II.—Development of Thin-film MIM Diode

Development, fabrication and characterization of MIM diodes using a lift off process for the metal layers and sputter deposition for the insulating layer were the areas of interest for MIM research during the past year. The following sub tasks were completed and the results reported here.

- Designed MIM diode for fabrication using a lift off process.
- Analyzed various metal combinations for asymmetric operation in a MIM configuration.
- Fabricated several test MIM's to develop the fabrication process.
- Settled on Al-Al_2O_3-Cr-Au material combination.
- Fabricated test diodes using the process developed.
- Characterized the fabricated diodes.

- Redesigned the MIM diodes to operate at higher frequencies by using an e-beam lithography process.

After numerous preliminary efforts the process using sputtered aluminum with sputtered Al_2O_3 as the insulator and Cr with Au on top as the other electrode was selected for detailed development and evaluation.

The metals were chosen based on their work function difference and also their low resistivity. The work functions of aluminum and gold are 4.28 and 5.1 respectively. The area of the active region, or the MIM contact area, was selected as 50 x 50 μm. The reason for making the contact area this size is to ensure a high probability of tunneling from metal one to metal two through the metal oxide layer. The design of an individual MIM structure is shown in the figure 3.

The patterned mask designs were shot using optical lithography at the USF clean room facility. The metal deposition processes were carried out using sputter deposition and e-beam evaporation of the top layers. During the fabrication of previous MIM diodes, it became apparent that it was necessary to have an in-situ oxide deposition in order to have a clean metal oxide layer.

In the design, Aluminum is used as the bottom electrode with aluminum oxide as the dielectric layer and Chrome topped by Gold as the top electrode. Aluminum is deposited in a sputtering chamber to a thickness of 70nm. During the process Aluminum gets oxidized very quickly when exposed to atmospheric conditions, i.e., by breaking the vacuum. Hence the process of Aluminum and aluminum oxide deposition has to be carried out sequentially inside the deposition chamber without exposing the sample by not breaking the vacuum.

In order to get an approximate value of the thickness of the insulator region, some dummy wafers were introduced in the sputtering chamber and aluminum oxide was deposited on the wafers changing the power source for a particular time under constant pressure. By carrying out this experiment we were able to observe the characteristic changes and identify the best parameter suited for the thin-film deposition.

The device was patterned for deposition of the top layer. A thin Chrome layer of 5 to 10 nm was covered by a Gold metal layer using E-beam evaporation with a thickness of 80 nm forming the MIM structure. The I-V characteristic of this device was measured using a Pico ammeter.

An analysis of the measured data from MIM diodes fabricated at USF was performed to verify the existence of the tunneling phenomenon and to determine the non-linearity of the diodes fabricated. Using previously recorded I-V data the resistance and sensitivity of a diode are plotted by taking the derivatives of the I-V data. The first derivative of I-V measurements results in the resistance of the diode and the second derivative yields the sensitivity of the diode. Figure 4(a) shows the I-V curve under forward bias mode. Figure 4(b) shows the resistance of the diode. From figure 4(b) we can notice that as the bias voltage goes up the resistance begins to drop. Figure 4(c) shows the sensitivity of the diode, from which the rectified part of the antenna current can be obtained.

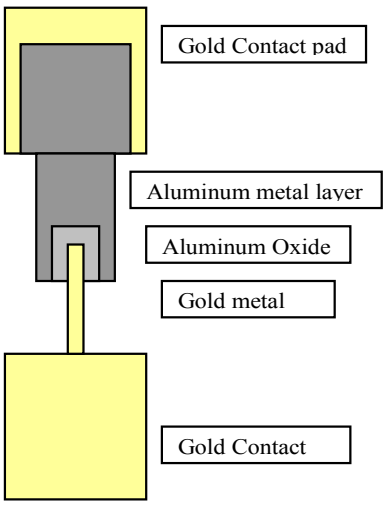

Figure 3.—MIM structure.

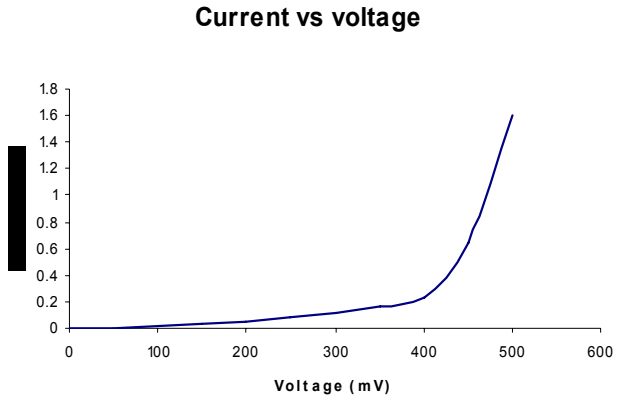

Figure 4.— (a) I-V plot.

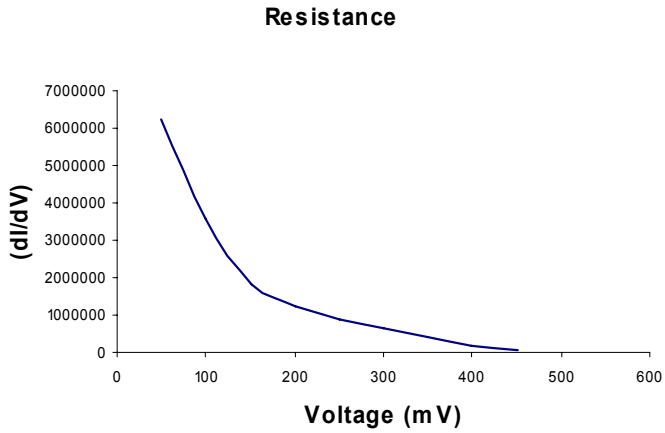

Figure 4.—(b) Resistance versus voltage.

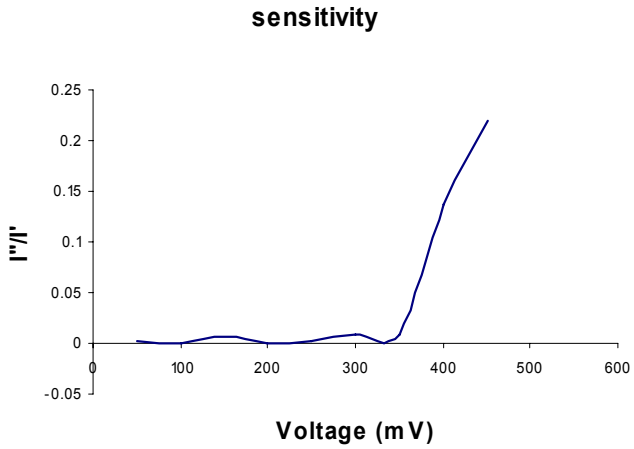

Figure 4.—(c) Current versus voltage.

According to Gundlach and Hölzl (ref. 3), the logarithmic derivative of the tunneling current with respect to the applied voltage exhibits a distinctive tunneling characteristic. This behavior is due to the voltage dependence of the tunneling length of the MIM junction. Since the shape of d ln I/dV versus V curve is typical for the tunneling current in MIM junctions, the observation of such a curve in diodes fabricated at USF indicates that the measured current is, at least predominantly, due to electron tunneling. The plot of log derivative of current versus bias voltage is given in figure 5. From the plot it can be concluded that the peaks occurring are the tunneling phenomenon.

The MIM's were characterized and tested using a Keithley 2400 Source Meter Unit (SMU) (Keithley Instruments Inc.). A Keithley 2400-SMU in series with a micromanipulator probe station, was used for studying the behavior of the fabricated devices. For preliminary characterization selected devices on the wafer were tested by sweeping the voltage. Data from each sample was recorded manually and plotted in a spreadsheet as part of a device performance database.

Figures 6 and 7 show measured I-V characteristics of an Al- Al_2O_3-Cr diode for both directions of bias voltage taken in the shielded probe station. In figure 6, aluminum is supplied a positive voltage. In figure 7, Chromium is supplied with a positive bias and aluminum is supplied with negative bias. The current when the Al layer was positively biased is larger than when the Cr layer is positively biased. The yield on the device was more than 70 percent. The yield was estimated from the I-V curves that resulted from testing all the diodes on the wafer.

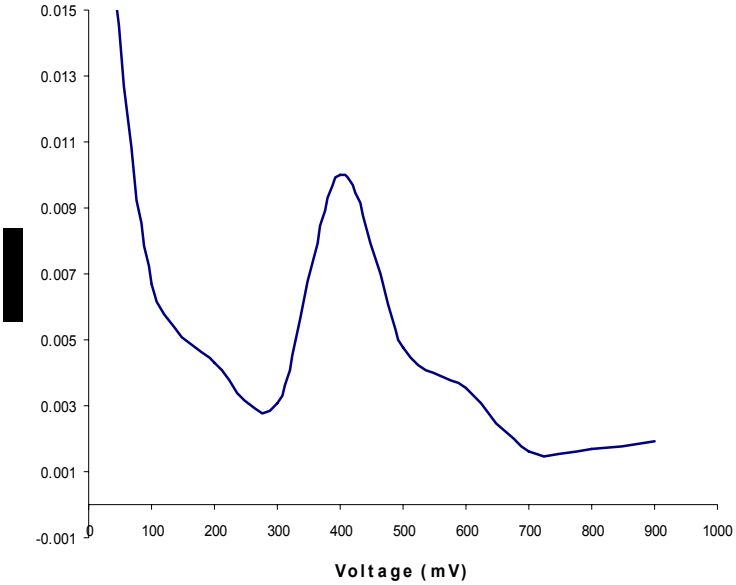

Figure 5.—*d* ln *I*/*d*V versus V characteristics of Al/Al_2O_3/Au junction.

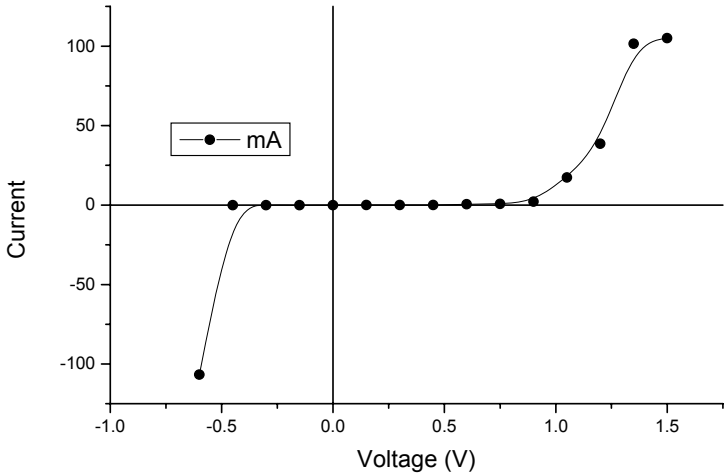

Figure 6.—Al-positive bias and Cr- negative bias.

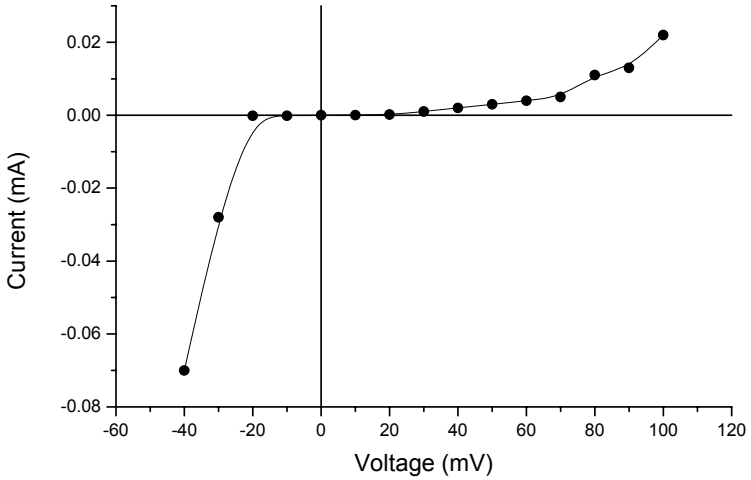

Figure 7.—Al-negative bias and Cr- positive bias.

Task III.—Antenna Design Improvements

The antenna treated as an energy receiving system, its characteristics, and improvement were the goals of this task during the past year. In order to make progress on this task the following sub tasks were completed:

- Defined the antenna system problem at THz frequencies.
- Quantified the power spectrum and bandwidth of solar radiation.
- Defined and examined the elements of antenna loss mechanisms.
- Examined half wave rectification versus full wave rectification and invented a feed mechanism to allow for full wave rectification using two diodes.
- Studied the polarization effects of solar radiation and determined the most efficient feed must allow for two orthogonal polarizations.
- Examined the efficiency issues of ultra high frequency diodes particularly the relationship of efficiency to power level.
- Concluded that the solar spectrum does not have a high enough power density to allow a configuration with a diode for each antenna element.
- Studied high gain antennas and array combination prior to rectification.
- Concluded that arrays of high gain antennas over a reflecting ground plane with the combination of energy prior to rectification has the highest probability of success.

Three major accomplishments from the past years efforts will be emphasized in the final report. The invention of a feed structure that allows full wave rectification with two diodes, the development of an electromagnetic feed structure to permit the collection of two orthogonal polarizations, and the understanding of the relationship between power level and efficiency for high frequency rectifiers and the importance of this relationship for solar energy collection.

Generally speaking, rectification is the conversion of an alternating current (ac) to a direct current (dc) by means of a diode. There are two types of rectification schemes: half-wave and full-wave rectification. The former can be achieved by using a single diode and the latter by using two or four diodes. Obviously, full-wave rectification is 100 percent more efficient than half-wave rectification. Full-wave rectification by four diodes is achieved in a bridge configuration, while full-wave rectification with two diodes is accomplished by using a center tapped transformer with two out-puts, which are 180◦ out of phase with the respect to each other.

For the rectenna project the big challenge was to find a way to make an inexpensive and much lower loss transformer. This was accomplished by using two transmission lines, one of which was a half-wave length longer than the other. (A half-wave length is equal to 180◦). However, this requires two feeds for excitation of the antenna, which was realized by the electromagnetic coupling (EMC) feed technique. This made full-wave rectification possible using two diodes, since port one and port two were designed to be 180◦ out of phase, see figure 8.

To validate the results obtained by simulation, see figure 9, two prototype antennae were fabricated at 2.7 GHz. It was more practical to build the prototypes at a lower frequency (between 2 and 3 GHz) rather than higher frequency for validation of the full-wave rectification concept. This is because lower frequency prototyping has the advantage of eliminating higher frequency parasitic losses and involves much less complicated procedures for fabrication and measurement. As can be seen, from the measured results in figure 10, the results correlate well with the simulation results. In order to compare the phase of the received signals at ports one and two (P1 and P2), the phase at port one was first measured and subsequently normalized, see figure 11. The phase at port two was then measured, see figure 12. As we can see, the two ports are 150◦ out of phase, which can be further improved by tuning the length of the transmission lines with respect to each other to obtain the desired 180◦.

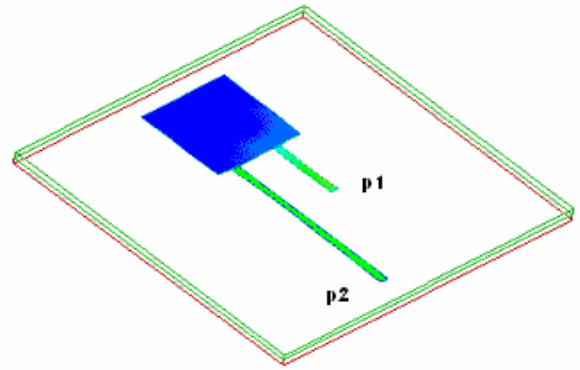

Figure 8.—Patch antenna fed by two EMC transmission lines.

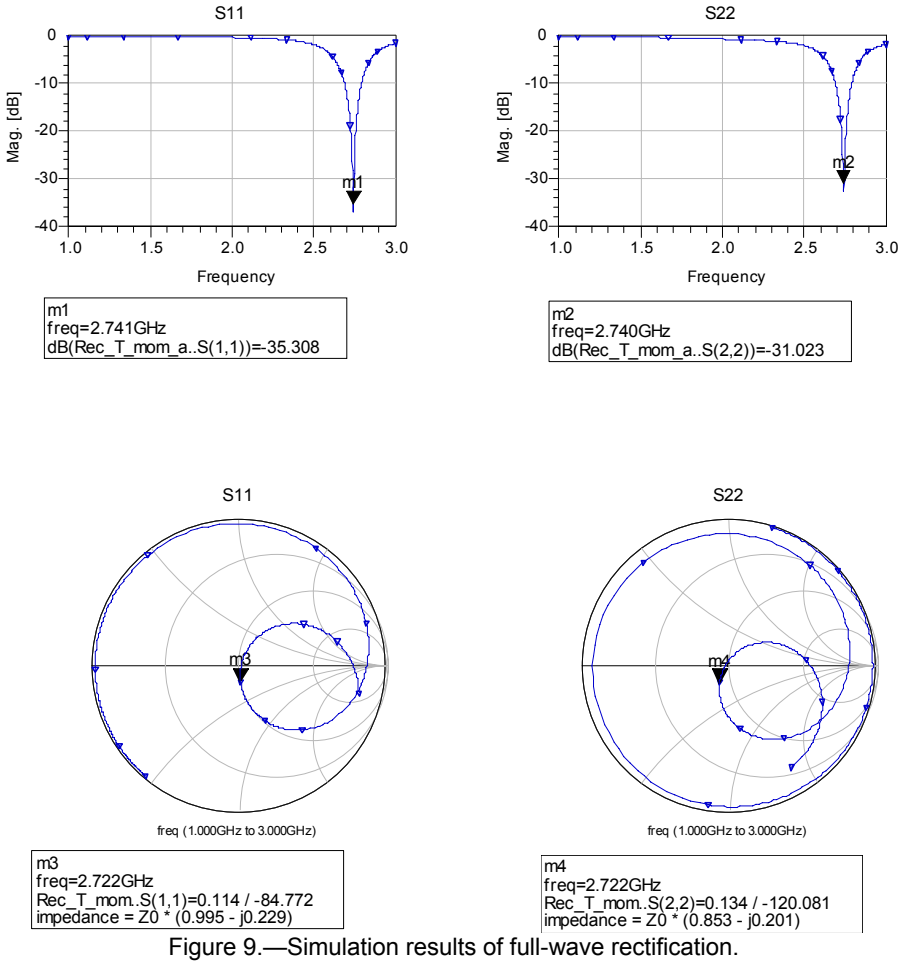

Figure 9.—Simulation results of full-wave rectification.

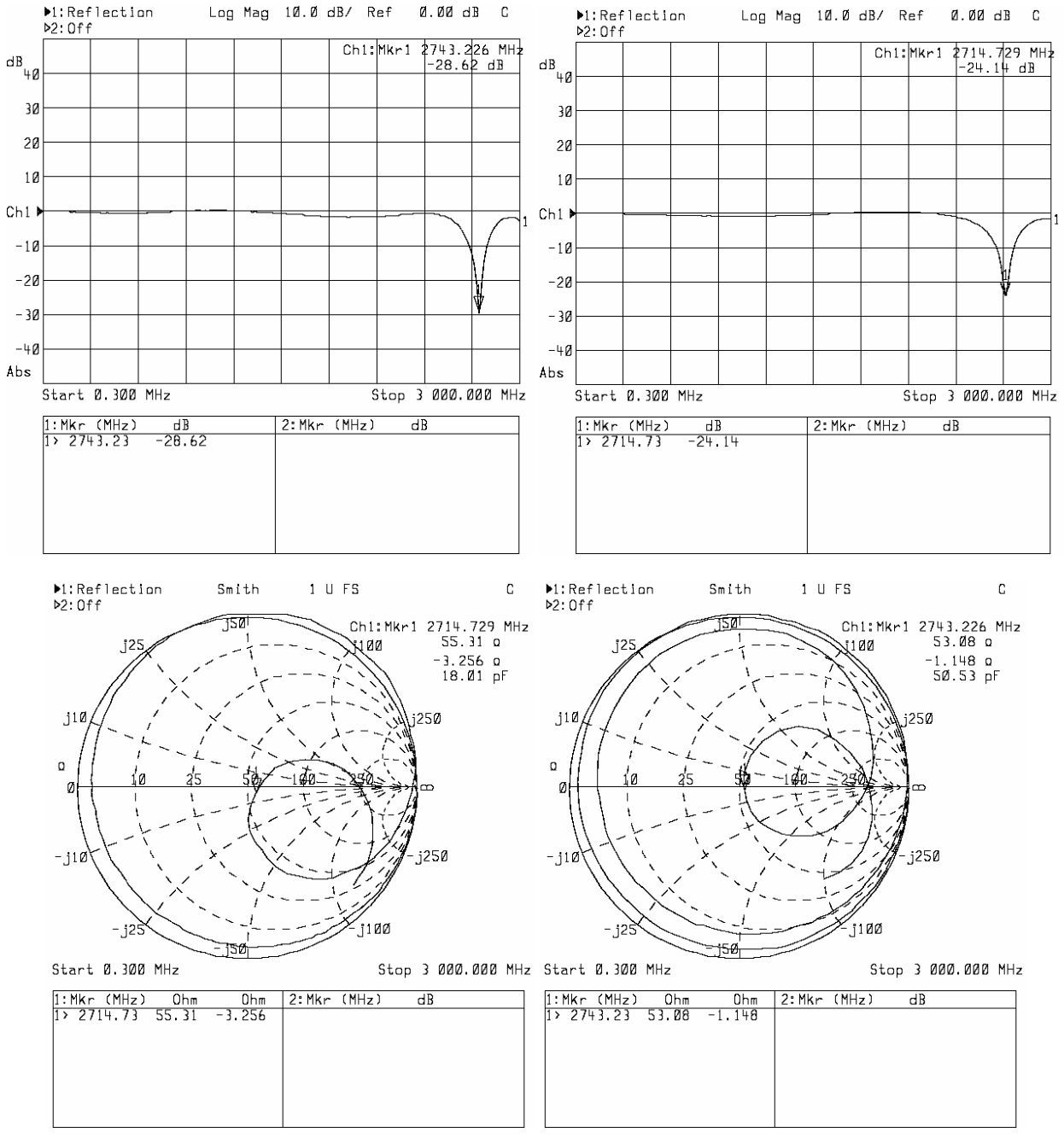

Figure 10.—Measured results of full-wave rectification test.

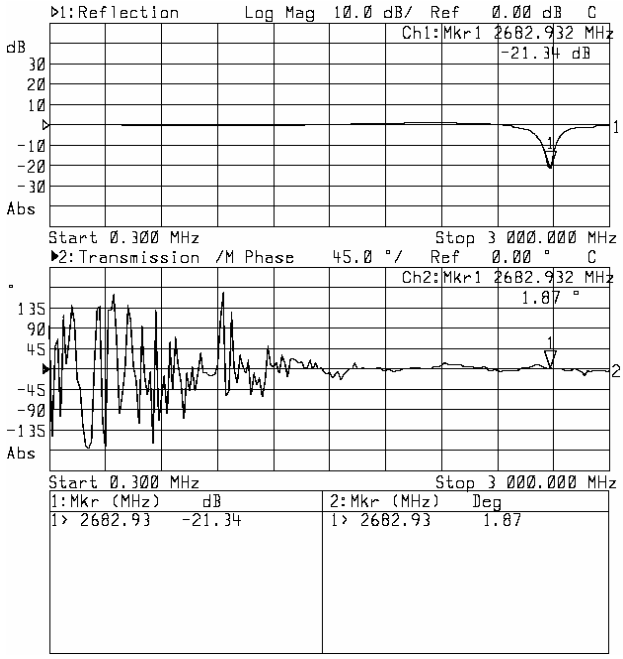

Figure 11.—Measured phase at port one.

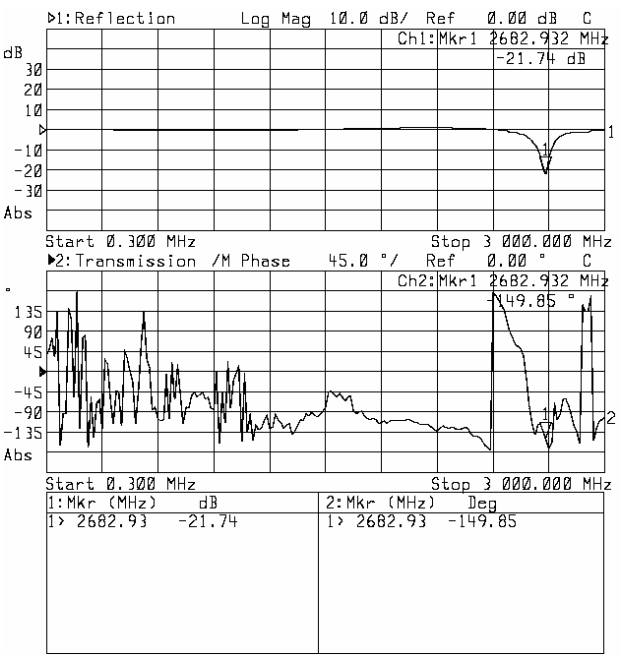

Figure 12.—Measured phase at port two.

The capture of two orthogonal polarizations is very important for the collection of solar energy as the radiation from the sun is randomly polarized and a linearly polarized antenna, such as a half wave dipole, will collect half as much energy as an antenna with two orthogonal linear polarizations. During this years investigations an electromagnetic feed was developed to solve the polarization problem. Traditionally, planar antennas are fed by microstrip lines on the same surface as the patches. The feed line is directly connected to the patch at its edge; however, it does not have to contact the patch directly. The line can be brought into close proximity with the patch, in such a away that a small gap is left between the patch and the line. The capacitance of the gap provides the coupling mechanism from the feed line to the patch. However, since the coupling is very weak, this technique does not offer any advantage over the direct feed technique. If the feed is on a different layer (a lower layer than the patch) it can be brought underneath the patch, which results in a very strong coupling see figure 13. The patch is considered to be electromagnetically coupled to the feed line, also known as an EMC patch. The patch is etched on the top substrate (superstrate) without any ground plane, while the feed line is etched on the bottom substrate with the ground plane at its back. The two substrates may be of different thickness and relative dielectric constant, which gives more freedom in designing the antenna. The feed line is extended underneath the patch (also called overlap), and is left open-circuited. The fringing fields from the open-circuited end supply the main coupling to the patch. This coupling technique is primarily capacitive. An approximate equivalent circuit is shown in figure 14. The parallel RLC resonant circuit represents the patch itself, and the capacitor is the coupling from the feed line to the patch. The coupling can be controlled by two factors the inset feed (overlap) and the patch width. The coupling increases as the inset increases and reaches its maximum at the center of the patch length. On the other hand, as the patch's width increases the coupling decreases.

Two electromagnetically coupled patch antennas were designed and fabricated at 7-GHz. The first antenna is a single feed, linearly polarized EMC patch, and functions as a transmitter, see figure 13. The second antenna is a double feed, dual polarized EMC patch, and functions as a receiver, see figure 15. Both antennas are designed and built on glass substrates with the following parameters:

Relative dielectric constant……($\varepsilon_r = 4.6$)

Substrate thickness……(h = 0.5 mm)

Patch width and length……...(W = L = 9 mm)

Feed-line width and length……..(W = 0.8 mm, L = 10 mm)

The double feed antenna was designed for verification of dual polarization, and was measured as follows. The single feed antenna was used as a single linearly polarized transmitter. The double feed antenna (with one of the ports P_2 terminated in a 50 Ω load) functions as a dual linearly polarized antenna. Subsequently, the receiving antenna was rotated by 90◦ around its center, and the 50 Ω termination changed to the port P_1.

The electromagnetically coupled patch antenna along with the dual polarization antenna, have been investigated. The advantages of the EMC feed technique are as follows:

7. The technique places the feed network closer to the ground plane (reduction of radiation from transmission line).
8. The patch-ground plane spacing can be increased (increase in bandwidth).
9. Matching possibility by changing the overlap between patch and feed.
10. The absence of a physical connection between patch and feed (facilitates the fabrication of the antenna).

The dual polarized antenna is capable of capturing two linearly orthogonal polarized waves simultaneously, while a single linear polarized antenna is only capable of capturing a single linearly polarized wave. Since solar radiation is randomly polarized, the dual polarized antennas are approximately 100 percent more efficient than linearly polarized antennas for harvesting solar power.

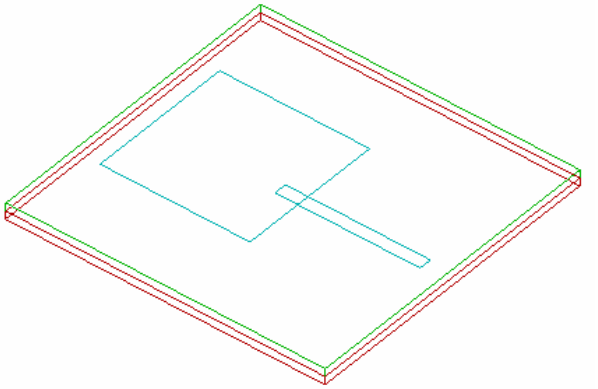

Figure 13.—Electromagnetically coupled patch antenna.

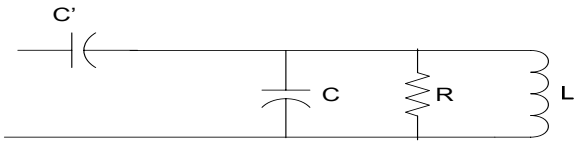

Figure 14.—Electromagnetically coupled patch equivalent circuit.

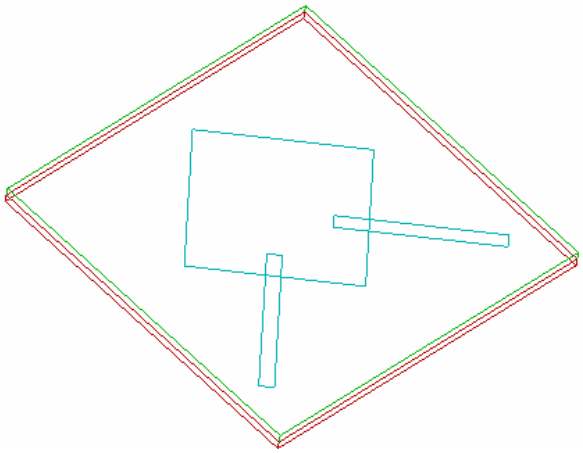

Figure 15.—Electromagnetically coupled patch antenna with dual polarization.

The exceptionally low efficiencies of rectennas at THz frequencies, measured by other researchers, could not be completely explained by poor impedance matching and bad polarization match. The efficiency of the high frequency rectifiers was suspected as the primary source of poor performance. A concerted effort was undertaken to determine the properties of the high frequency diodes and to understand why the performance was so bad.

Rectification is the conversion of an alternating current (ac) to a direct current (dc) by means of a diode. The overall efficiency of a rectifier is defined as:

$$\eta_o = \frac{dc\_ouput\_power}{rf\_incident\_power}$$

A typical circuit representation of a rectifier is shown in figure 16. The R_s represents the source resistance. The matching section consists of an inductor, which is also responsible for preventing the higher harmonics from being reflected back to the source. The dc filter at the output suppresses the higher harmonics.

The conversion efficiency of a diode is related to the loss across the diode. If the diode is driven as a half-wave rectifier, its maximum conversion efficiency is limited by the losses in it.

$$\eta_{max} = \frac{1}{1+\frac{V_D}{2Vo}}$$

In this expression, V_o is the output dc voltage and V_D is the drop across the conducting diode. Since nearly all of the dissipation of the rectenna element takes place within the diode, the efficiency of the rectenna element can be approximated by the following expression.

$$\eta_o = \frac{dc\_ouput\_power}{(dc\_ouput\_power)+(dissipated\_diode\_power)}$$

However, there will be some additional loss (reflection loss) due to mismatch between the source and rectifier. The following expression is more appropriate, since it also takes into account the loss due to mismatch.

$$\eta_o = \frac{dc\_ouput\_power}{rf\_incident\_power}$$

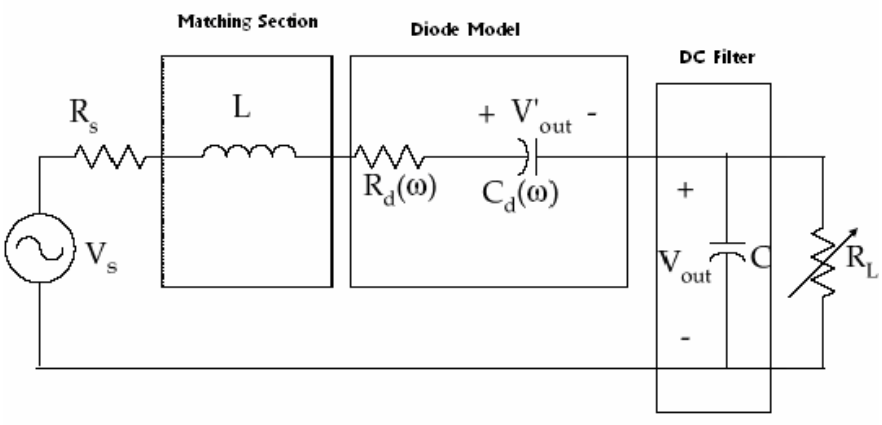

Figure 16.—High frequency rectifier equivalent circuit.

To calculate the efficiency of a rectifier, one first needs to have a model of the rectifier circuit. The diode used in this model is a zero-bias Schottky diode, which can be modified for an MIM diode as well. In general, a diode can be modeled as a combination of resistance and capacitance, see figure 17.

R is the nonlinear resistance of the barrier at the rectifying contact and it is a function of the current. This barrier resistance is very large in the reverse direction and small in the forward direction. It becomes increasingly smaller as the current is increased over the exponential part of the dc characteristics. The resistance *r* is the parasitic series resistance, also known as spreading resistance. It is due to the constriction of current-flow lines in the semiconductor near the contact. In the case of a circular contact, the spreading resistance may be calculated by the following formula from the potential theory.

$$r = \frac{1}{2.\sigma.d}$$

Where σ is the conductivity of the semiconductor, and *d* is the diameter of the circular contact area. The nonlinear barrier capacitance C is due to storage of charge in the boundary layer. The magnitude of capacitance can be calculated according to the parallel plate capacitance formula.

$$C = \varepsilon_r \varepsilon_0 \frac{A}{D}$$

Where A is the contact area, and D is the barrier thickness. As one can see, this capacitance changes as the barrier thickness D changes, which in turn, is a function of the applied voltage, see figure 18.

There are two distinct regions in a Schottky diode's output dc voltage versus input RF power. These are known as the square law and linear regions and in the square law region

$$V_o \propto V_i^2 \propto P_i$$

In the linear region the output voltage is proportional to the input voltage V_i, thus V_o is proportional to the square root of the input power.

$$V_o \propto V_i \propto \sqrt{P_i}$$

This behavior can be ascribed to the nonlinear behavior of the barrier to the applied voltage. The square law region starts at an input power smaller than –20 dBm, while the linear region starts at an input power higher than –10 dBm. The interval in between is known as the transitional region. The input values given above for each interval are approximate values and can differ slightly from diode to diode. In the square law region, the barrier resistance is much larger than the spreading resistance (*r* << R), which results in more internal loss. In the linear region on the other hand, the barrier resistance is much smaller than the spreading resistance (*r* >> R), which results in less loss inside the diode.

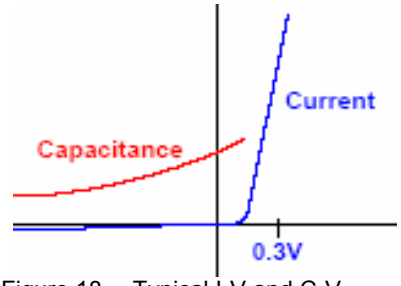

Figure 18.—Typical I-V and C-V characteristic of Schottky diode.

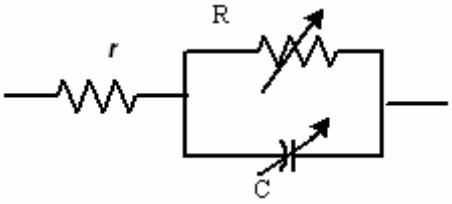

Figure 17.—Diode equivalent model.

The rectification efficiency of a diode is related to the loss across the diode. Since nearly all of the dissipation of the rectenna element takes place within the diode, the efficiency of the rectenna element can be approximated by the following expression (under condition of zero loss due to reflection).

$$\eta_o = \frac{dc\_ouput\_power}{(dc\_ouput\_power) + (dissipated\_diode\_power)}$$

In order to achieve high rectification efficiency, the diode must be operated in the higher end of the linear region, where the loss is only due to spreading resistance. Note: the effect of the barrier capacitance so far has been ignored, which is a major source of loss at higher frequencies by shunting the barrier resistance.

In order to determine the operating region of a diode connected to a single element antenna (e.g., λ/2 dipole with λ = 460 nm), we needed to calculate the available RF power at the terminal of the antenna. Since a λ/2 dipole has an average bandwidth of 15 percent, the available power density from the sun in this bandwidth (S = 99.43 W/m^2) is needed to start the available RF power calculation. The power density is related to the electric field and the intrinsic impedance of free space, where the intrinsic impedance of free space η = 377 Ω.

$$S = \frac{E^2}{\eta}$$

The open voltage at the terminal (V_T) of an antenna is equal to the electric field times the effective height of the antenna (effective height of λ/2 dipole h = 0.32λ).

$$V_T = E.h$$

The power at the terminal, in the presence of a reflecting ground plain, can be calculated, using the following equation, where R_T is equal to the radiation resistance of λ/2 dipole 75 Ω.

$$P_T = \frac{|V_T|^2}{2R_T}$$

The available RF power at the terminal of a λ/2 dipole is 5.5 pW, which is approximately –82 dBm. This is obviously far from the diode's linear region for high rectification efficiency. Usually, microwave rectifiers reach their maximum efficiency (80 percent) around 50 mW of RF input power (17 dBm), which means fifty six thousand λ/2 dipoles are needed to drive the diode in its maximum efficiency region. The 50 mW of solar power can be collected in an area of 15 X 15 mm, when the dipoles are spaced λ/2 on center from each other.

In order to reduce the number of array elements, we can sacrifice some efficiency (e.g., efficiency of 65 percent can be achieved around RF input power of 5 mW), which will reduce the number of antennas to approximately five thousand six hundred. Further, replacing the λ/2 dipole with a traveling wave antenna, which is usually built in multiple wavelengths (e.g., a poly rod antenna can be designed to be 50λ long; see figure 19. The retina in our eye is a good example of a rod antenna array. The elements of the array are 100λ long and there are about 125 million of them working together responsible for detecting visible light in our eye.

Replacing the λ/2 dipole with a surface wave antenna, such as a dielectric rod antenna, can improve the antenna's gain considerably. The gain of a λ/2 dipole is 2.15 dB; in contrast, a poly-rod antenna has a typical gain of 20 dB.

As shown in figure 20 a typical dielectric rod antenna consists of a feed, launcher and radiator. The feed consisting of a monopole inside a waveguide excites the waveguide (TE_{10} mode in rectangular and TE_{11} mode in circular wave guide), which is coupled at the launcher into a surface wave in the dielectric. The surface wave in the dielectric is a hybrid mode (HE_{11} mode known as dipole mode, see figure 21. A hybrid mode has both electric and magnetic components in the direction of the wave's propagation. The

EM wave is partially confined inside the dielectric rod and travels sinusoidally down the rod (surface-wave), and some of the wave travels exponentially outside the dielectric (evanescent-wave). The terminal of the radiator is tapered in order to match the impedance of the rod to free space for efficient radiation of the surface wave into free space.

Dielectric rod antennas are end-fire, high gain antennas. Figure 22 shows the relation between the beam width and gain to the relative length of the antenna. The gain of the dielectric rod antenna was approximated by Hansen and Woodyard.

$$G \cong \frac{7l}{\lambda}$$

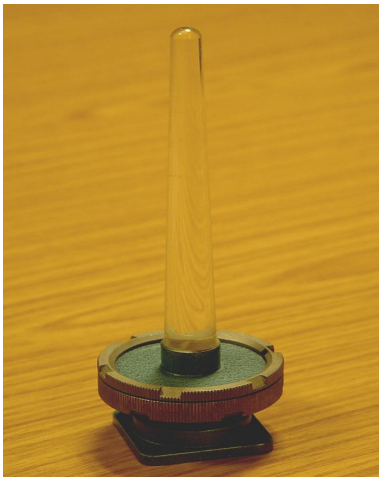

Figure 19.—Polyrod antenna.

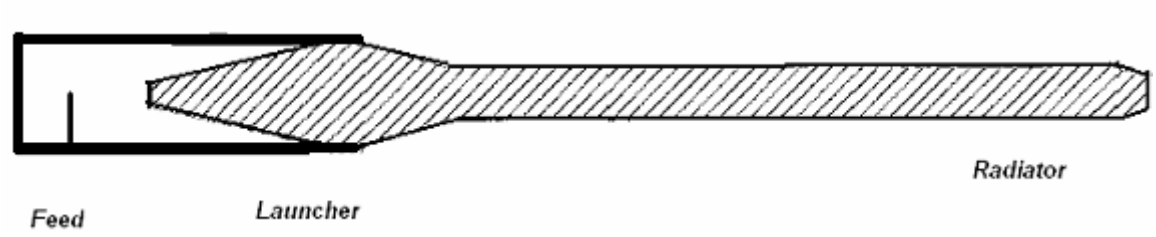

Figure 20.—Dielectric rod antenna.

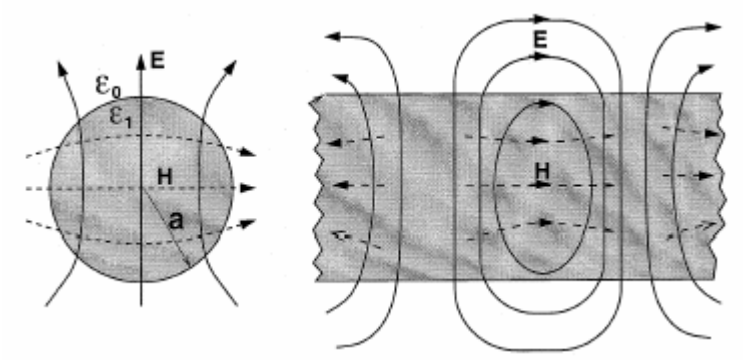

Figure 21.—The dielectric-rod with dipole mode (a) cross section; (b) side view

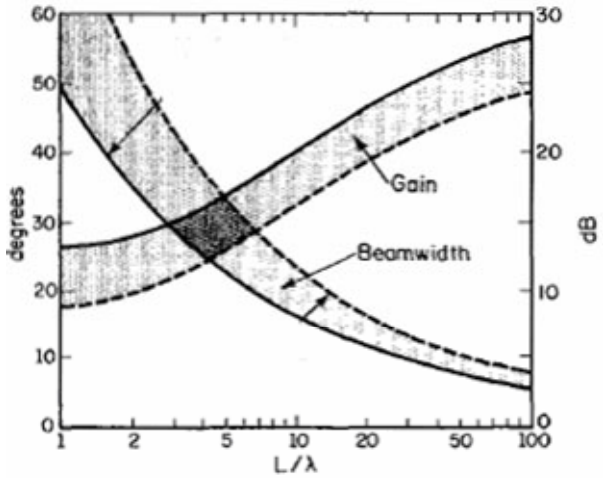

Figure 22.—Gain and beam-width of surface-wave antenna as a function of relative antenna length.

The following expression gives the approximate half-power beam-width of the maximum gain design of a poly-rod antenna.

$$BW = 55\sqrt{\frac{\lambda}{l}} \quad degrees$$

The Friis transmission equation relates the received power to transmitted power, between two antennas separated by a distance R >> $2D^2/\lambda$ (D being the largest dimension of the antennas).

$$P_r = \left(\frac{\lambda}{4\pi R}\right)^2 G_t.G_r.P_t$$

Where the term $(\lambda/4\pi R)^2$ is called the free-space loss factor, G_t and G_r are the gain of transmitting and receiving antennas, respectively. By dividing the received power of the λ/2 dipole by its gain (5.5 pW/1.64 = 3.35 pW), we can calculate the received solar power of an isotropic antenna. In order to calculate the received power of a poly-rod antenna, we can simply multiply the received power of the isotropic antenna by the poly-rod's gain (3.35 pW*100 = .335 nW). This improvement in the received power, compared to the single λ/2 dipole, was achieved by increasing the array dimension vertically rather than horizontally. It should be noted, that the achievable gain is determined by the overall aperture and, consequently, is not much higher than the λ/2 dipole array of the same aperture size. The difference is the poly-rod elements can be spaced much farther apart than dipole elements so that the number of array elements can be considerably reduced.

The conclusion of this study of rectification efficiency indicates that the individual elements in an antenna array designed to collect solar energy need to have considerable gain in order for a reasonable number of elements to be connected in an array to feed a single rectifying element. Otherwise the rectifiers are operating in a very inefficient region and the entire.

Conclusions

The rectenna project has made four significant contributions to the state-of-the-art in solar energy harvesting through the application of rectennas to collect light energy using the wave nature of optical radiation in the 2004 fiscal year.

The understanding of rectification efficiency at ultra high frequencies led to the conclusion that a viable rectenna in the optical spectrum must utilize high gain dielectric antennas connected in an array utilizing a dielectric waveguide to deliver sufficient power to a single rectifier to allow efficient rectification to dc power. Simulations and experiments at lower frequencies indicate that the array should have approximately 1000 elements if each antenna element has a gain of 15 Db_i.

The invention, experimental verification, and patent application for a method of full wave rectification at microwave and higher frequencies utilizing two rectifiers and an electromagnetic, non-conducting, dual feed with phase shifting.

The invention, experimental verification, and patent application for a method to capture two orthogonal polarizations with a single antenna and electromagnetic coupling to double the energy capture potential of the rectenna.

The invention, experimental verification, and patent application for a multi layer system consisting of MIM diodes, microstrip electromagnetic coupled feed structure, a non-radiating dielectric waveguide, and an array of dielectric rod antennas.

Publications and Patents

Publications

1. Rectenna Developments for Solar Energy Collection, Kenneth Buckle, Elias Stefanakos, Thomas Weller, Shekhar Bhansali, Yogi Goswami, Mohammad Sarehraz, Subramanian Krishnan, IEEE 31st Photovoltaic Specialists Conference, Orlando, FL, Jan. 4, 2005.
2. Rectenna Developments for Solar Energy Collection, Mohammad Sarehraz, Kenneth Buckle, Thomas Weller, Elias Stefanakos, Shekhar Bhansali, Subramamin Krishnan, and Yogi Goswami, invited paper, USAF Space Power Workshop, Manhattan Beach, California, April 18 - April 21, 2005.
3. Fabrication and Characterization of Thin-Film MIM Diodes for a Rectenna, S. Krishnan, S. N. Sambandam, S. Bhansali, K. A. Buckle, T. Weller, E.K. Stefanakos, IEEE Device Research Conference, University of California, Santa Barbara, June 20- 22, 2005.
4. Thin Film Micro-bolometers for Microwave Power Detection, Masters Thesis of Eid Alsabbagh March 29, 2004, Major Professor: Tom Weller, Ph.D.
5. Design and Fabrication of Thin Film M-I-M Diode, Master Thesis of Subramanian Krishnam, May 26, 2004,Major Professor: Dr. Elias Stefanakos.
6. Novel Rectenna for Collection of Infrared and Visible Radiation, Ph.D. Dissertation of Mohammad Sarehraz, March 23, 2005, Major Professor: Dr. Kenneth Buckle.

Patents

7. An Aperture Rectenna for Converting High Frequency Wave Radiation into DC Power, Shekhar Bhansali, Kenneth Buckle, Yogi Goswami, Elias Stefanakos, Thomas Weller, Invention Disclosure 3-17-2003.
8. A Method to Obtain Full Wave Rectification of Radiation Received From an Antenna, Mohamed Sarehraz, Kenneth Buckle, Elias Stefanakos, Thomas Weller, Yogi Goswami, Invention Disclosure 2-3-2004.
9. The Dual Polarized Solar Antenna, Mohammad Sarehraz, Kenneth Buckle, Elias Stefanakos, Thomas Weller, Yogi Goswami, Invention Disclosure 3-25-2005.
10. The Solar Antenna and Array, Mohammad Sarehraz, Kenneth Buckle, Elias Stefanakos, Thomas Weller, Yogi Goswami, Invention Disclosure 3-25-2005.

References

11. R.L. Baily, "Journal of Engineering Power," 1972.
12. W.C. Brown, “The History of Power Transmission by Radio Waves,” *IEEE Trans. Microwave Theory and Techn*.32, pp.1230-1242, Sep 1984.
13. K.H. Gundlach and J. Hölzl, “Logarithmic conductivity of Al-Al_2O_3-Al tunneling junctions produced by plasma- and by thermal oxidation,” Surf. Sci.,Vol. 27, p. 125 (1971).

Development of a Numerical Simulation Model for Thermo-Fluid Analysis and Design Optimization of Cryogenic Storage Systems With Zero Boiloff

PI: M. Rahman (University of South Florida)
S. Ho (University of South Florida)
S. Hong (University of South Florida)
S. Mukka (University of South Florida)

Objective

The development of a finite-element numerical simulation model for the analyses of fluid flow and heat transfer in zero boil-off (ZBO) cryogenic storage systems was the objective of the present investigation. The model was used to explore the effects of each design parameter.

Approach

The numerical simulation was carried out by solving equations for the conservation of mass, momentum, and energy. The physical model equations were discretized using finite-elements and incorporated in the solver of the commercial code FIDAP.

Background

Liquid storage of hydrogen has very significant advantage over gaseous or chemical storage because of much lower storage volume and ease of regeneration of the fuel with its demand. Traditional cryogenic storage tanks suffer loss of hydrogen due to boil-off of the cryogen induced by heat leak to the tank from the surrounding environment. In order to control the tank pressure within its structural limits, the stored fluid needs to be bled off periodically. The Zero Boil Off (ZBO) concept has evolved as an innovative means of storage tank pressure control by a synergistic application of passive insulation, active heat removal, and forced mixing within the tank. A cryocooler (with a power supply, radiator, and controls) is integrated into a traditional cryogenic storage subsystem to reject the storage system heat leak. Therefore, the fuel can be stored for a very long time without any loss.

In recent years, a number of efforts have been done toward the guidelines of building cryogenic storage systems, especially with the ZBO concept. Hasting et al. (ref. 1) introduced an overview of the efforts in the development of the ZBO storage systems at NASA, showing that the ZBO system has mass advantage over passive storage. Kittel (ref. 2) suggested an alternative approach for the long term storage of cryogenic propellants using a re-liquefier, which uses the propellant vapor as the working fluid. Salerno et al. (ref. 3) presented a proposed Mars reference mission and the concomitant cryogenic fluid management technology with a combination of both active and passive technologies to satisfy a wide range of requirements. Hofmann (ref. 4) presented a theory to boil-off gas-cooled shields for cryogenic storage vessels using analytical method to determine the effectiveness of intermediate refrigeration. Haberbusch et al. (ref. 5) developed a design tool for thermally zero boil-off densified cryogen storage system model for space. The model predicts that a ZBO densified liquid hydrogen storage system minimizes the overall storage system mass and volume for nearly the same input power for cooling. Kamiya et al. (refs. 6 and 7) consecutively presented the development of a large experimental apparatus to measure the thermal conductance of various insulations and used that for the testing of insulation structures. The apparatus could test specimens with dimensions up to 1.2 m diameter and 0.3 m thickness. Different insulation structures, a vacuum multilayer insulation with glass fiber reinforced plastic (GFRP) and a vacuum solid insulation, were tested.

Most of the efforts have been done by using analytical approach or simplified calculations, which can be limited to simple geometric design. Numerical simulation using computational fluid dynamics (CFD) has the advantage of modeling complex geometry and loading situations. This report presents a detailed

analysis and numerical simulation using finite element method for fluid flow and conjugate heat transfer in a ZBO cryogenic storage system.

Introduction

The study considered a cylindrical tank with elliptical top and bottom as shown in figure 1. The tank wall is made of aluminum and a multi-layered blanket of cryogenic insulation (MLI) has been attached on the top of the aluminum. The tank is connected to a cryocooler via a heat pipe to dissipate the heat leak through the insulation and tank wall into the fluid within the tank. The condenser section of the heat pipe dissipates heat to the cryocooler while the evaporator section picks up heat from the fluid within the tank. The hot fluid is directed to the heat pipe using a fluid circulation system within the tank. This system consists of a pump, a spray head for discharge of fluid and a collector tube network feeding to the pump. Different heat pipe sizes, different locations of hot fluid collection and discharge, and different discharge velocities were investigated to put together an optimum design for the ZBO hydrogen storage system. Equations governing the conservation of mass, momentum, and energy were solved in the fluid region. The steady-state velocity and temperature distributions were computed. The numerical simulation results presented in the paper will be very useful to analyze the effects of each design parameter and to optimize the design of ZBO systems for specific applications.

The 3-D structure of the tank with an array of pump-nozzle units is presented in figure 2. The symmetry of the problem suggests the use of an axisymmetric model instead of the 3-D model. Modeling and solving the problem in three dimensions is possible, but it will cost a lot more computing resources while the additional information that it will provide may not be necessary. An axisymmetric model, on the other hand, consumes less computing resources but can still give valuable information. Therefore, this investigation has employed an axisymmetric model for the computation presented in this paper. 3-D modeling and simulations are being considered for future work.

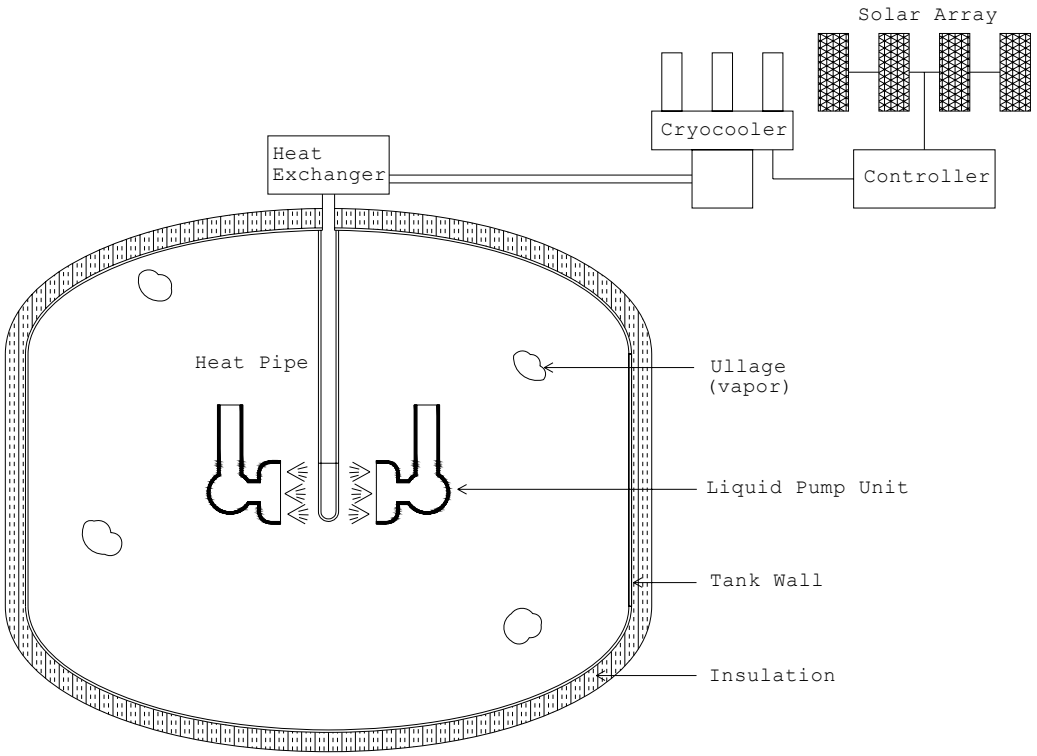

Figure 1.—Schematic of the cryogenic storage system for hydrogen.

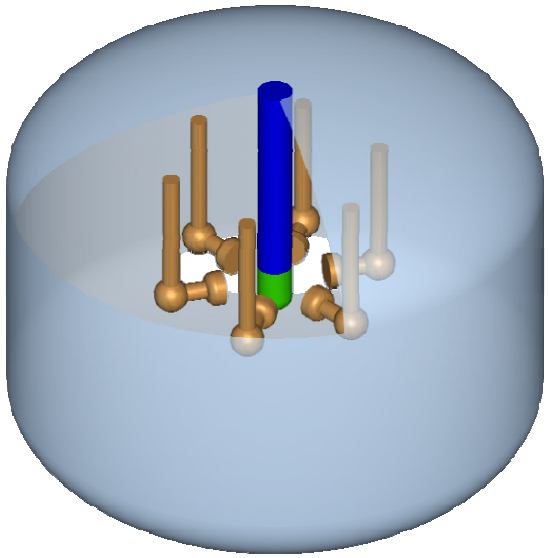

Figure 2.—Liquid hydrogen storage tank with heat pipe and fluid circulation system.

Nomenclature

A-C	Length parameters, m
C_p	Specific heat of fluid, J/(kg.K)
E-H	Length parameters, m
k	Thermal conductivity of fluid, W/(m.K)
l_m	Mixing length, m
l_n	Distance from the nearest wall, m
l_c	Characteristic length scale of the flow, m
L-P	Length parameters, m
p	Pressure, Pa
R	Length parameter, m
r	Radial coordinate, m
T	Temperature, K
u	Velocity, m/s
V	Normal flow speed discharged from nozzle surface, m/s
z	Axial coordinate, m
κ	von Karman constant
μ	Viscosity of fluid, kg/(m.s)
ρ	Density of fluid, kg/m^3
σ	Fluid stress, Pa

Subscripts

0	Laminar (viscosity)
t	Eddy (viscosity)
r	Radial direction
z	Axial direction
rr	Normal (stress) in radial direction
rz	Shear (stress) in *r*-*z* plane
zz	Normal (stress) in axial direction
$\theta\theta$	Normal (stress) in tangential direction

Mathematical Model

To describe the fluid flow and heat transfer of liquid hydrogen in the tank, it is necessary to determine the distributions of velocity and temperature in the entire domain by solving the coupled equations of the conservation of mass, momentum, and energy. To reduce the computational work, the real 3-D model shown in figure 2 can be replaced by an axisymmetric model as shown in figure 3. All the governing equations are then written in the axisymmetric form. For a steady incompressible flow, the equations for the conservation of mass and momentum can be written as

$$\frac{1}{r}\frac{\partial}{\partial r}(ru_r)+\frac{\partial u_z}{\partial z}=0 \tag{1}$$

$$\rho\left(u_r\frac{\partial u_r}{\partial r}+u_z\frac{\partial u_r}{\partial z}\right)=\frac{1}{r}\frac{\partial}{\partial r}(r\sigma_{rr})-\frac{\sigma_{\theta\theta}}{r}+\frac{\partial\sigma_{rz}}{\partial z} \tag{2}$$

$$\rho\left(u_r\frac{\partial u_z}{\partial r}+u_z\frac{\partial u_z}{\partial z}\right)=\frac{1}{r}\frac{\partial}{\partial r}(r\sigma_{rz})+\frac{\partial\sigma_{zz}}{\partial z} \tag{3}$$

where

$$\sigma_{rr}=-p+2\mu\frac{\partial u_r}{\partial r} \tag{4}$$

$$\sigma_{\theta\theta}=-p+2\mu\frac{u_r}{r} \tag{5}$$

$$\sigma_{rz}=\mu\left(\frac{\partial u_r}{\partial z}+\frac{\partial u_z}{\partial r}\right) \tag{6}$$

$$\sigma_{zz}=-p+2\mu\frac{\partial u_z}{\partial z} \tag{7}$$

For modeling the turbulent flow, the total viscosity is defined as the sum of the laminar and eddy viscosities and written as

$$\mu=\mu_0+\mu_t \tag{8}$$

The mixing length model is a simple yet effective model, in which the eddy viscosity is computed using the equation

$$\mu_t=\rho l_m^2\sqrt{\left(\frac{\partial u_r}{\partial z}+\frac{\partial u_z}{\partial r}\right)\frac{\partial u_r}{\partial z}} \tag{9}$$

where

$$l_m=\min\{\kappa l_n,0.09l_c\} \tag{10}$$

$$\kappa\approx 0.41 \tag{11}$$

Assuming that there is no heat generation and viscous dissipation and pressure work are negligible, the equation for the conservation of energy can be written as

$$\rho C_p\left(u_r\frac{\partial T}{\partial r}+u_z\frac{\partial T}{\partial z}\right)=\frac{1}{r}\frac{\partial}{\partial r}\left(kr\frac{\partial T}{\partial r}\right)+\frac{\partial}{\partial z}\left(k\frac{\partial T}{\partial z}\right) \tag{12}$$

To completely define the problem, appropriate boundary conditions are required on every boundary segment of the computational domain. For the continuity equation (1) and the momentum equations (2) and (3), the relevant boundary conditions are applied as follows: prescribed velocity on nozzle face, zero

radial velocity on the centerline of the tank, and zero velocity for solid surfaces. For the energy equation (12), constant heat flux is applied on the heated surfaces of the wall, insulated (no heat flux) on the centerline, and constant temperature on the evaporator section of the heat pipe. The solution obtained by solving the equations (1) to (3) and (12) associated with their boundary conditions gives four primary parameters: two velocity components, pressure, and temperature.

Numerical Solution Procedure

An axisymmetric model of the storage tank is presented in figure 3. The axis of the tank is shown as the centerline coincident with the z-axis. The cylindrical wall and the ellipsoidal top and bottom are shown as a straight line and two elliptic arcs. The heat pipe is located along the centerline and has two sections: the tip (evaporator) whose surface is kept at constant low temperature, and the handle (adiabatic section), considered insulated. The condenser section of the heat pipe is located outside the tank in the heat exchanger unit as shown in figure 1. Heat transmitted from the evaporator to the condenser section of the heat pipe is eventually dissipated to the ambient using a cryocooler/radiator assembly also shown in figure 1. The pump-nozzle unit includes a spray nozzle, which faces the tip of the heat pipe, the pump, and the inlet tube.

The essential dimensions are denoted in general form as the capital letters A-C, E-H, and L-R. Their numerical values employed for the simulations in this paper are given in table 1. The lengths G, H, and P can have several different values corresponding to various simulation cases.

TABLE 1.—NUMERICAL VALUES OF LENGTHS IN FIGURE 3

Length,	A	B	C	E	F	G	H
(m)	1.50	0.65	1.30	0.30	0.05	(*)	(*)
Length,	L	M	N	O	P	Q	R
(m)	0.25	0.10	0.10	0.10	(*)	0.15	0.10

(*) See table 2 for numerical values corresponding to each simulation case

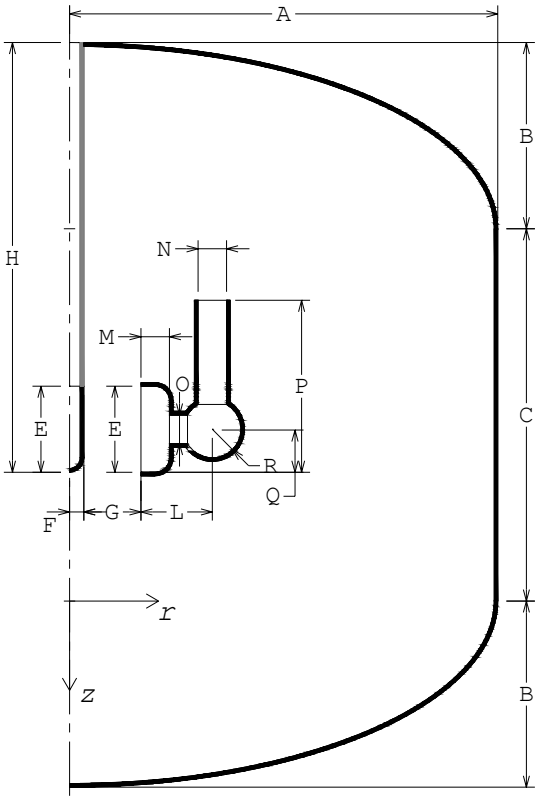

Figure 3.—Axisymmetric model of liquid hydrogen storage tank.

Nine simulations were carried out to investigate the effects of the discharging fluid speed at the nozzle and the gap between the nozzle and the heat pipe. Four more simulations were done for considering the effects of the length of the heat pipe and the inlet tube. The simulation cases with related dimensions and discharging speeds are given in table 2.

TABLE 2.—SIMULATION CASES AND RELATED PARAMETERS

Simulation no.	V, m/s	G, m	H, m	P, m
1	0.01	0.1	1.5	0.9
2 (basic case)		0.2		
3		0.3		
4	0.03	0.1		
5		0.2		
6		0.3		
7	0.05	0.1		
8		0.2		
9		0.3		
10	0.01	0.2	1.0	
11			2.0	
12			1.5	0.6
13				1.2

The boundary conditions in details are given in table 3. The constant fluid properties, given in SI units, were taken at reference temperature, T_{ref} = 20 K, as follows: ρ = 71.10 [kg/m^3], μ = 13.59E-6 [kg/(m.s)], C_p = 9530 [J/(kg.K)], k = 0.09844 [W/(m.K)].

TABLE 3.—BOUNDARY CONDITIONS

No.	Entity	Velocity, m/s	Temperature, K	Heat flux, W/m^2
1	Wall	0	-	1.0
2	Centerline	u_r = 0	-	0
3	Heat pipe handle	0	-	0
4	Heat pipe tip	0	18	-
5	Pump wall	0	-	-
6	Nozzle	u_z = 0, u_r = -V (*)	-	-

(*) See table 2 for values of V related to each simulation case

The governing equations (1) to (3) and (12) along with the boundary conditions were solved using the finite element method. In each element, velocity components, pressure, and temperature were approximated by using the Galerkin procedure (ref. 8), which led to a set of algebraic equations that defined the discretized continuum. Four-node quadrilateral elements were used. Layers of regular elements of higher density were assigned along the solid surfaces where high rates of momentum and heat transfer exist. A mesh with approximately 23000 elements was used. The fully coupled successive substitution algorithm was used to solve the nonlinear system of equations. Two convergence criteria were used: the relative errors of the solutions and the residual of the nonlinear equations. The relative error criterion is reached when the relative error at an iteration is less than a tolerance. The residual criterion checks whether the ratio of the residual vector at an iteration to a reference residual vector is less than another tolerance. The iterative procedure is considered converged when both criteria are satisfied. The tolerances for the present simulations are 0.0001 and 0.01 for relative error and residual, respectively.

Results and Discussion

Figure 4 shows the velocity vector field for the basic case (simulation 2). The color of the velocity vector represents the magnitude of velocity or speed. The pump creates a pressure difference that drives the hot fluid in the tank toward the inlet. The flow enters the inlet tube of the pump and increases its

speed. At the neck of the pump outlet connected to the nozzle, the flow reaches maximum speed. The flow then expands to fill the hollow space inside the nozzle and reduces speed.

After being discharged from the nozzle, the flow spread into two streams spraying on the cool tip of the heat pipe. One stream goes up along the tip of the heat pipe, then the heat pipe handle, until it reaches the top, sweeps along a short portion on the top before being collected at the pump inlet, making the first family of circulations. The other stream moves down along the tip of the heat pipe, then the centerline, until it reaches the bottom, sweeps along the wall of the tank over a longer distance before going to the pump inlet again, making the second family of circulations. On the heat pipe and the centerline, the speeds of the streams become maximum.

The circulations can be also observed on a streamline plot as shown in figure 5. The second family of circulations covers the entire bottom and sidewall of the tank, while the first one covers only a small region between the heat pipe and the pump unit.

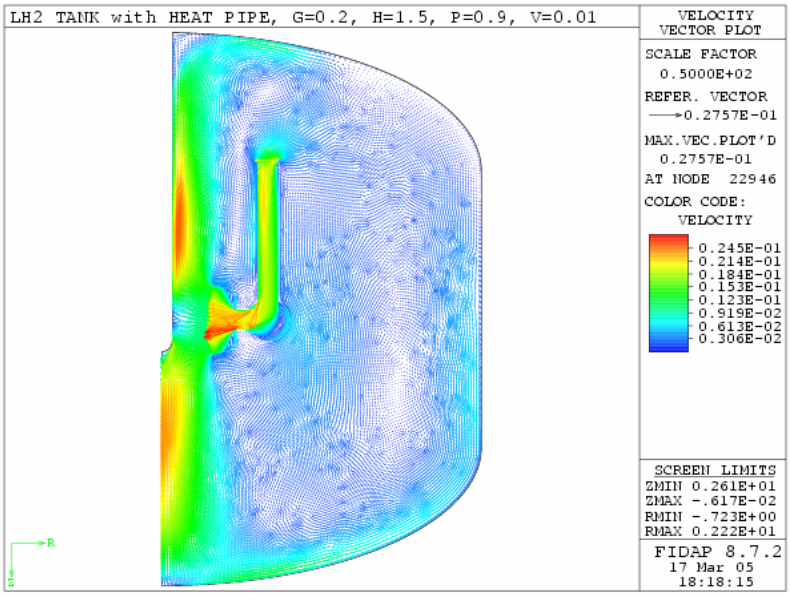

Figure 4.—Velocity vector field, simulation 2, m/s.

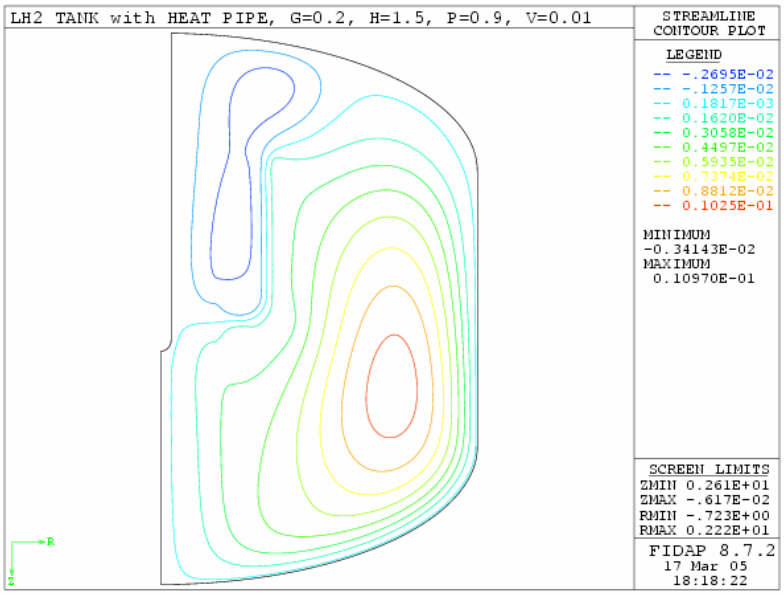

Figure 5.—Streamlines, simulation 2.

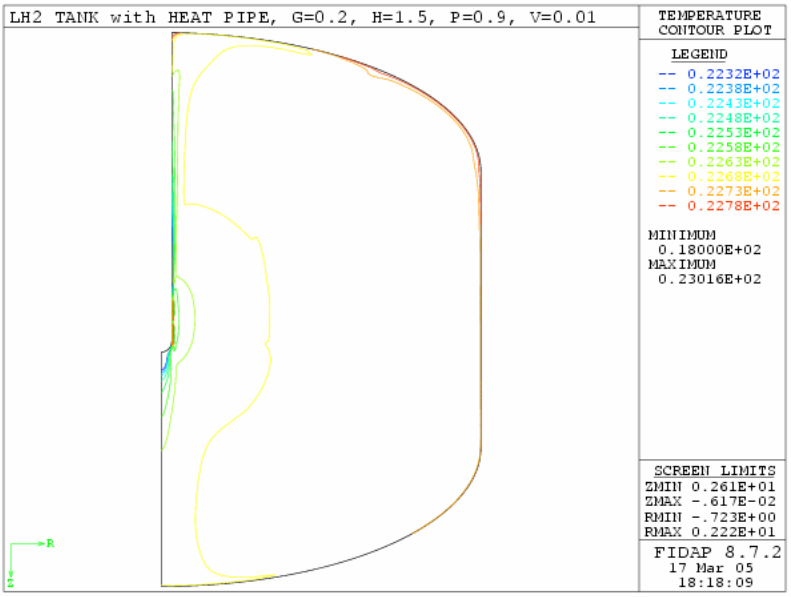

Figure 6.—Temperature, simulation 2, K.

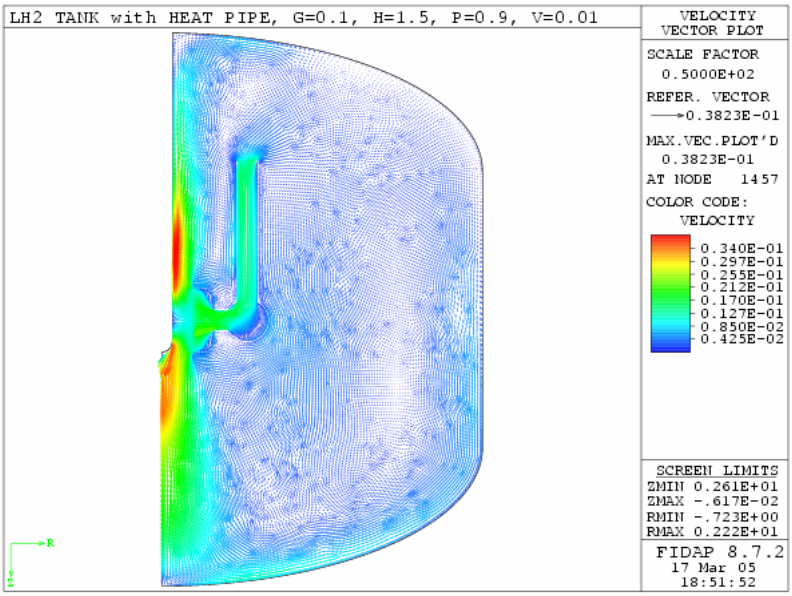

Figure 7.—Velocity vector field, simulation 1, m/s.

The temperature distribution in figure 6 shows that only a small region right next to the cool tip of the heat pipe has lower temperature while almost the entire region is at relatively higher temperature.

Figure 7 shows the velocity vector field for simulation 1. In this case, it can be seen that the closer gap between the nozzle and the heat pipe has a strong effect on the speed distribution. The speed inside the inlet tube is more uniform on its entire length, while the maximum speed along the heat pipe and the centerline are higher and more concentrated.

The streamline plot for simulation 1 shown in figure 8 indicates that the first family of circulations is pressed toward the heat pipe, as the result of a stronger jet velocity impacting on the heat pipe. The distribution of temperature for simulation 1 shown in figure 9, analogous to the basic case, predicts high temperature almost everywhere except the small region near the heat pipe.

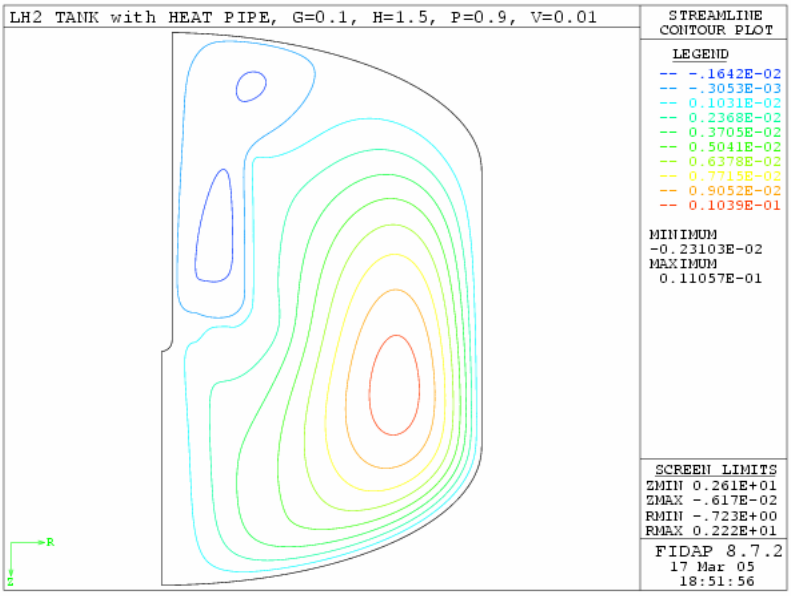

Figure 8.—Streamlines, simulation 1.

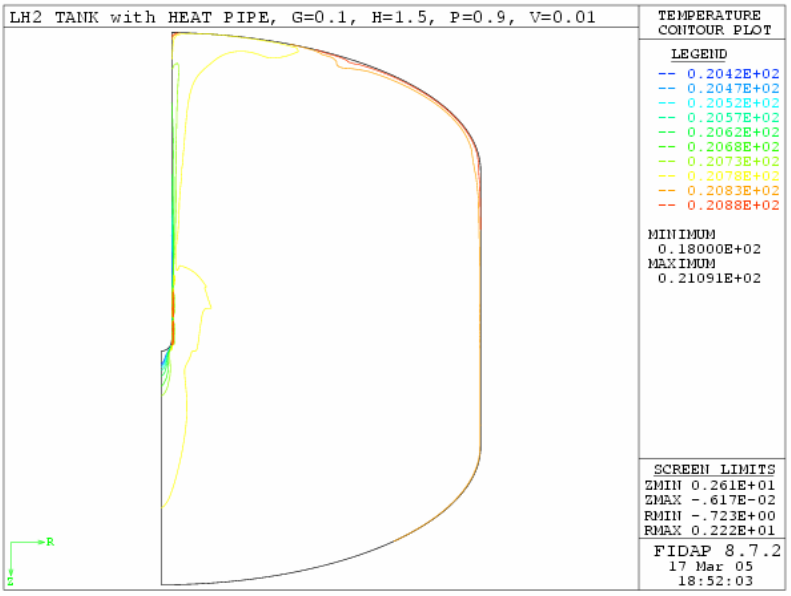

Figure 9.—Temperature, simulation 1, K.

For simulation 3, the gap between the nozzle and the heat pipe is larger than that of the other two cases. Figures 10 to 12 show the velocity vector field, streamlines, and temperature, respectively. The fluid speed in the inlet tube is higher than that of the basic case while the speeds of the flows sweeping along the heat pipe and the centerline are lower. In this case, the circulations are not being pressed toward the heat pipe.

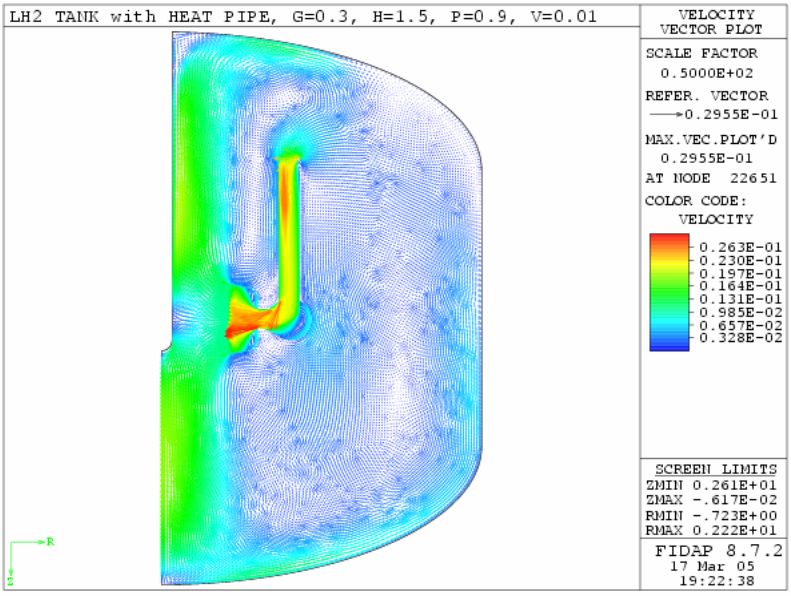

Figure 10.—Velocity vector field, simulation 3, m/s.

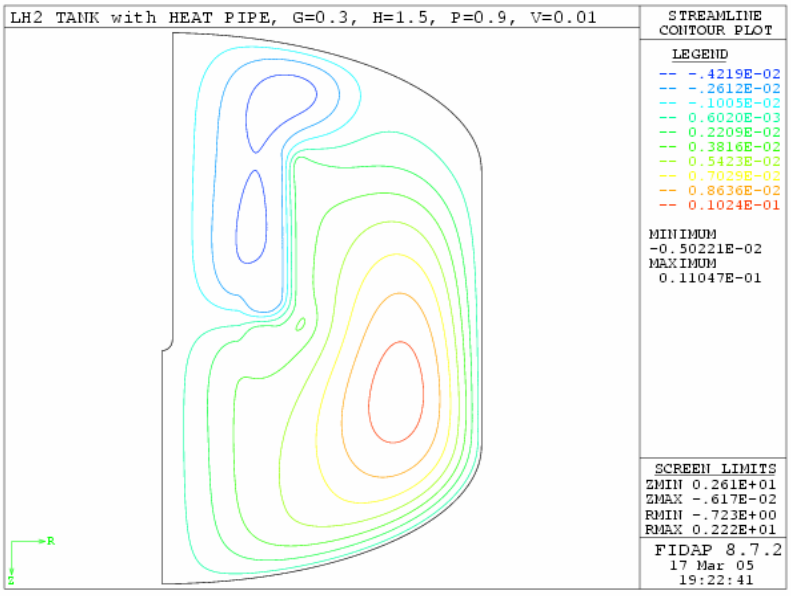

Figure 11.—Streamlines, simulation 3.

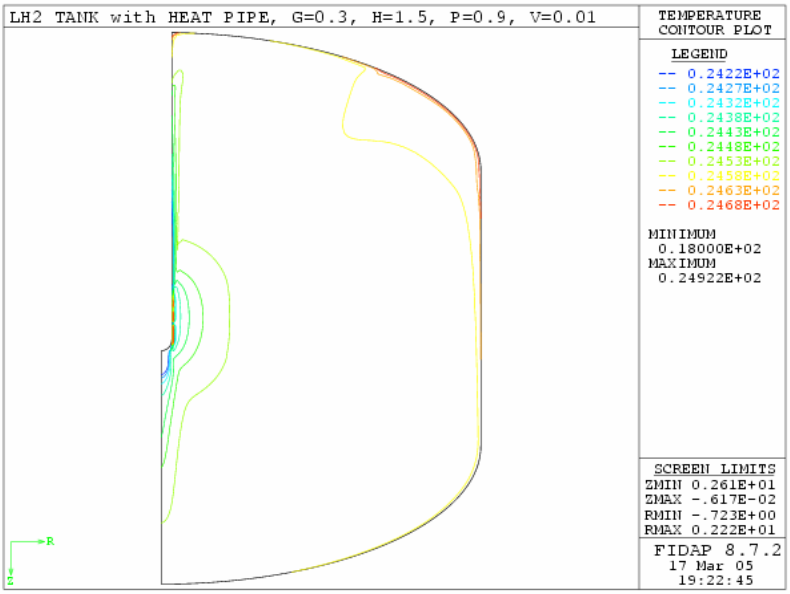

Figure 12.—Temperature, simulation 3, K.

The average speed can be used as a parameter for assessing the mixing effectiveness, which plays the role of leveling the temperature difference in the system, while the average temperature can be used for assessing the cooling effectiveness, which represents the capability of removing heat in the system. For a zero boil-off system, the maximum temperature is also an important parameter since it shows if the evaporation can happen.

Figures 13 to 15 present the combination results from the simulations 1-9 on mixing and cooling effectiveness of the system. Figure 13 shows the effect of the spraying gap G and the nozzle speed V on the average speed taken over the entire computation domain. As the gap increases, the average speed also increases linearly. The higher the discharge speed, the higher the average speed is. Therefore, increasing the gap can help improve the mixing effectiveness. However, the cooling effectiveness varies differently.

Figure 14 presents the effect of spraying gap and discharge speed on the average temperature. The average temperature is also taken over the entire region. Figure 14 shows that as the gap increases, the temperature also increases. This behavior can be explained based on the velocity pattern. For the smaller gap case, the flow from the nozzle tends to press toward the heat pipe and forces it to have better contact with the cool tip, inducing the heat transfer process more effectively. Figure 14 also shows that as the discharge speed increases, the average temperature decreases. Therefore, to keep the fluid cooler, smaller gap and higher spraying speed are recommended, in which the former contradict with the mixing effectiveness. In zero boil-off systems, the cooling effectiveness has higher priority over the mixing effectiveness.

Figure 15 shows the effect of spraying gap and discharge speed on maximum temperature. The trend is the same as that for average temperature. The results from the solutions show that for each simulation, the maximum temperature is higher than the average temperature by a fraction of a degree (0.2 to 0.3 K).

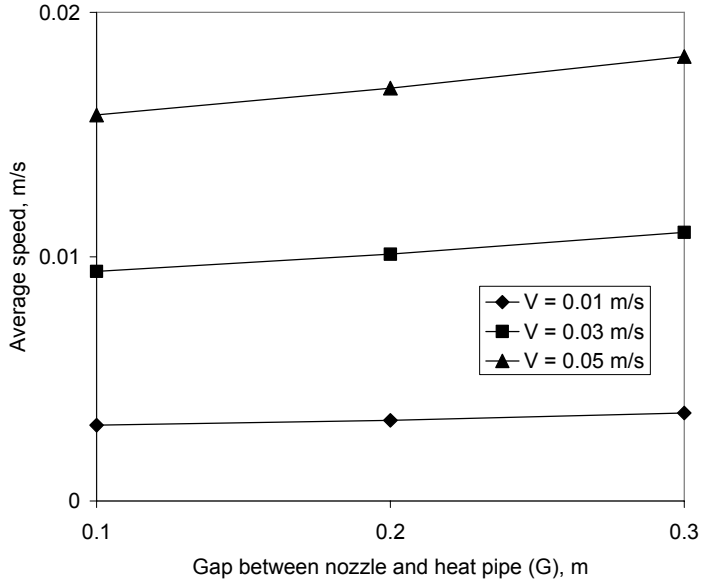

Figure 13.—Effect of spraying gap and discharge speed on mixing.

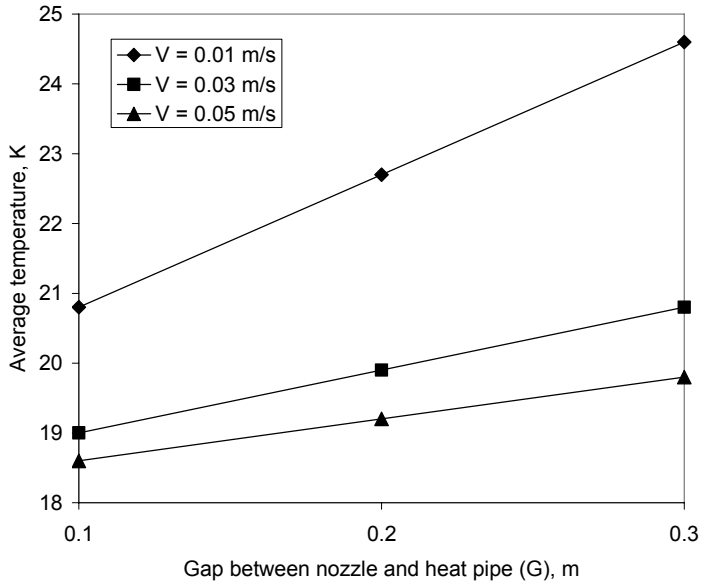

Figure 14.—Effect of spraying gap and discharge speed on cooling.

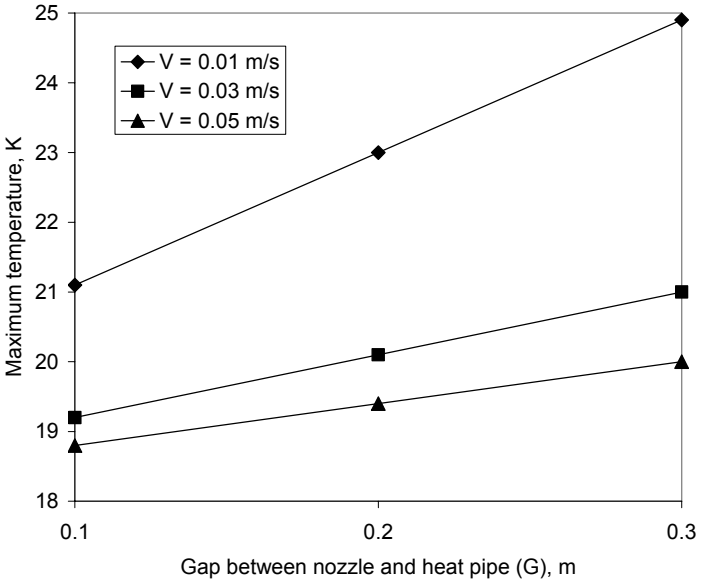

Figure 15.—Effect of spraying gap and discharge speed on boil-off.

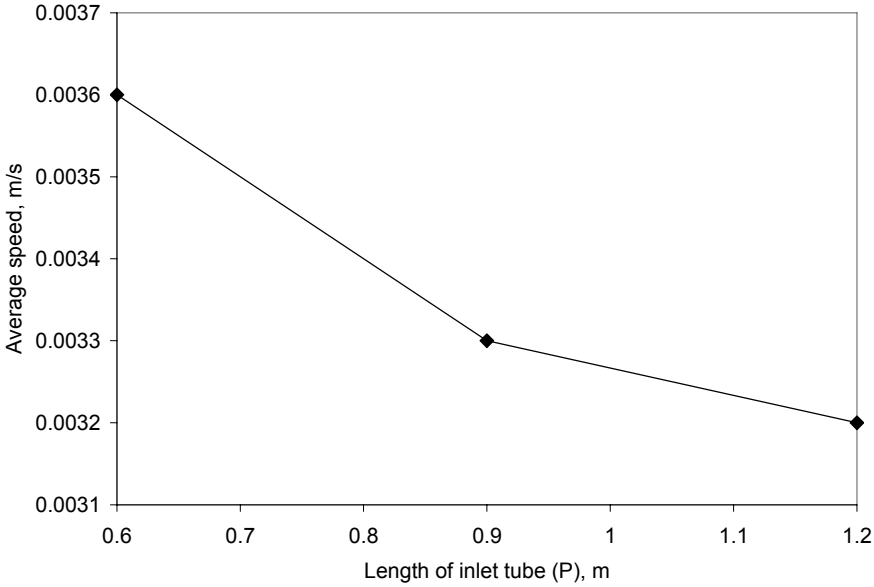

Figure 16.—Effect of inlet length (P) on mixing.

From simulations 2 and 12-13 (where the length of the inlet tube, P, changes but the length of the heat pipe, H, is the same for all three simulations), the results show that the average temperature and the maximum temperature do not change significantly (just on the order of a fraction of a degree, if any). Thus the length of the inlet tube of the pump has very little effect on the cooling effectiveness and boil-off of the system. But it does have effect on the mixing effectiveness as shown in figure 16. As the length of the inlet tube increases, the average speed decreases. The change can be up to 10 percent as the length is short, but when the length becomes longer, the change would not be that much. For mixing effectiveness, a shorter inlet tube is better. This can be explained by examining the streamlines of simulation 12, the case with shortest inlet tube, as shown in figure 17. A shorter inlet tube gives more space for the inlet to collect fluid from many directions and allow the first family of circulation to expand and be comparable in size as the second one, resulting in much stronger overall circulation, thus better mixing.

The results from simulations 2 and 10-11 (where the length of the heat pipe, H, changes but the length of the inlet tube of the pump, P, is the same) does not show any strong difference at first glance: the average speed as well as the average and maximum temperatures remain about the same. As discussed in the previous paragraph, the length of the inlet tube, P, seems to have no effect either. However, when comparing the results from simulations 2, 10-11 and 12-13, it is found that the change related to (H-P), i.e., the distance from the inlet to the top of the tank can be significant. Figure 18 shows how the average and maximum temperatures changes due to different distance from inlet to the top of the tank. As the distance increases, both the average temperature and the maximum temperature decrease up to some limit (0.5 to 0.6 m). Farther than that limit, the distance has no significant effect on any of these temperatures, which is well expected.

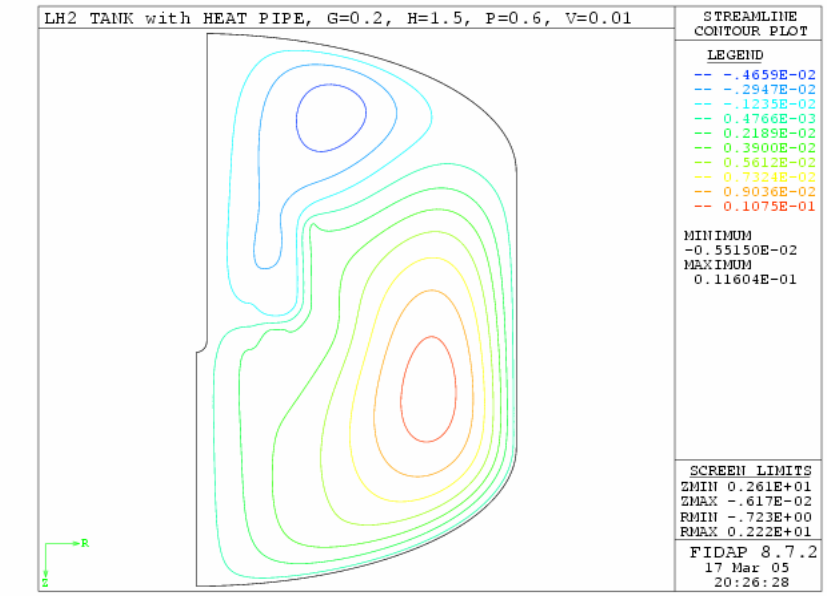

Figure 17.—Streamlines, simulation 12.

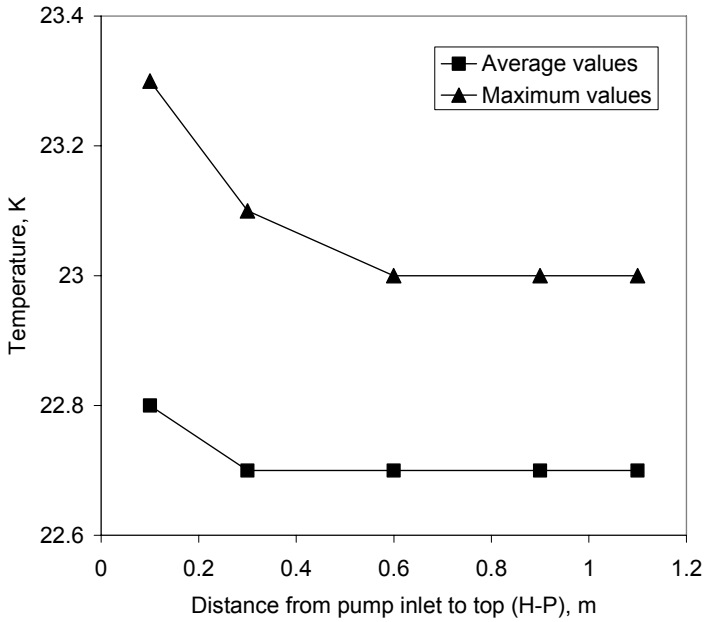

Figure 18.—Effect of distance from inlet to top on cooling and boil-off.

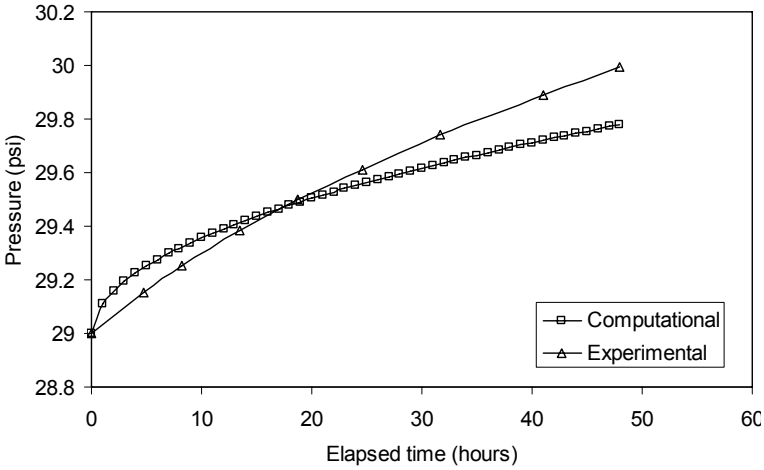

Figure 19.—Comparison of simulation results with experimental data for transient heat transfer.

Conclusions

The numerical simulations give better understanding of the fluid flow and heat transfer phenomena needed for the design of a cryogenic storage tank for liquid hydrogen. For this design with heat pipe and array of pump-nozzle units, it is found that the gap between the nozzle and the heat pipe plays an important role in controlling mixing and cooling effectiveness of the system. The other parameters such as the length of the inlet tube, or the distance from the inlet section to the top of the tank may have some significance on the mixing or cooling performance of the system. These guidelines are very useful in designing cryogenic storage systems. This suggests that numerical modeling and simulation can be satisfactorily used in design to obtain good predictions for various operating conditions.

References

14. L.J. Hastings, D.W. Plachta, L. Salerno, P. Kittel, “An overview of NASA efforts on zero boiloff storage of cryogenics propellants,” Cryogenics 41 (2002), pp.833-839.
15. P. Kittel, “Propellant preservation using re-liquefiers,” Cryogenics 41 (2002), pp. 841-844.
16. L.J. Salerno, P. Kittel, “Cryogenics and the human exploration of Mars,” Cryogenics 39 (1999), pp. 381-388.
17. A. Hofmann, “Theory of boil-off gas cooled shields for cryogenic storage vessels,” Cryogenics 44 (2004), pp. 159-165.
18. M.S. Haberbusch, R.J. Stochl, A.J. Culler, “Thermally optimized zero boil-off densified cryogen storage system for space,” Cryogenics 44 (2004), pp. 485-491.
19. S. Kamiya, K. Onishi, E. Kawagoe, K. Nishigaki, “A large experimental apparatus for measuring thermal conductance of LH_2 storage tank insulations,” Cryogenics 40 (2000), 35-44.
20. S. Kamiya, K. Onishi, E. Kawagoe, K. Nishigaki, “Thermal test of the insulation structure for LH_2 tank by using the large experimental apparatus,” Cryogenics 41 (2001), 737-748.
21. C.A.J. Fletcher, *Computational Galerkin Methods*, Springer-Verlag, New York, 1984.

Publications

22. M. M. Rahman and S. Ho, “Zero Boil-Off Cryogenic Storage of Hydrogen,” *Proc. NHA 16th Annual Hydrogen Conference*, Washington, D.C., March-April, 2005.
23. S. K. Mukka and M. M. Rahman, “Computation of Fluid Circulation in a Cryogenic Storage Vessel,” *Proc. AIAA Second International Energy Conversion Engineering Conference*, Providence, Rhode Island, August 2004.
24. S. K. Mukka and M. M. Rahman, “Analysis of Fluid Flow and Heat Transfer in a Liquid Hydrogen Storage Vessel for Space Applications,” *Proc. Space Technology and Applications International Forum (STAIF-2004)*, Albuquerque, New Mexico, February 2004.

By-Product Hydrogen Production

PI: E. Stefanakos (University of South Florida)
B. Krakow (University of South Florida)
G. Moore (University of South Florida)
J. Wolan (University of South Florida)
M. Smith (University of South Florida)

Problem

Hydrogen production is dependent on natural gas whose supply is dwindling and whose price is increasing. In a single product production facility, coal is not competitive with natural gas for hydrogen production at current prices. Hydrogen production by direct electrochemical dissociation of water requires a voltage that is higher than the band gap of common solar cells.

Objective

Introduce conversion of the energy supply for hydrogen production from natural gas to clean technologies for using the more plentiful coal supplies or to using waste streams. This can be done in Florida if the hydrogen can be a lucrative byproduct of IGCC electric power generation or of fertilizer manufacture.

Approach

Develop techniques for manufacturing hydrogen in Florida as a lucrative byproduct of IGCC electric power generation and of fertilizer manufacture. The work involves laboratory experiments conducted on small systems to advance the technology and design and analysis of full size commercial plants to establish economic viability.

Background

Sulfuric acid is the leading chemical commodity by far in terms of quantity produced. 39.62 million metric tons were produced in the U.S. in 2000. 75 percent of this acid is produced and used in Florida. A lot of hydrogen could be produced with byproduct sulfuric acid without approaching saturation of the Florida market for sulfuric acid.

Sulfuric acid is made by oxidizing sulfur and sulfur compounds in steps. It is done with oxygen from air. If the oxygen were derived from water, byproduct hydrogen would be produced.

In oxidizing the sulfur electrolytically from the +4 to +6 valence state (which is its valence state in sulfuric acid), 0.8 million metric tons of hydrogen could be produced annually, 0.6 metric tons of it in Florida..

In the oxidation from the 0 to +4 state, 1.6 million metric tons of hydrogen could be produced annually, 1.2 million metric tons of it in Florida.

In the past, almost all the sulfur used for sulfuric acid production was mined. Now a majority of it is obtained from refineries who produce it as a means of disposing of waste hydrogen sulfide. They convert the hydrogen sulfide to sulfur and water by partial oxidation, using oxygen from air in the Claus process. If the sulfur were produced by electrolytic decomposition, 0.8 million metric tons of byproduct hydrogen could be produced. There are no refineries in Florida so as long as the hydrogen sulfide decomposition is largely confined to refineries, that production is not in Florida. As IGCC power plants proliferate, they will become a Florida source of hydrogen sulfide for more hydrogen production.

Nevertheless, potential Florida production of byproduct hydrogen in sulfuric acid manufacture exceeds the total current U.S. hydrogen production of 1.2 metric tons a year. Florida could go from zero to dominant as a source of hydrogen.

Benefits to NASA

Commercial hydrogen is made predominantly from natural gas, near natural gas deposits.

It is not made in Florida which does not have natural gas deposits.

The lack of hydrogen production in Florida is a problem for NASA who has to move hydrogen long distances to satisfy its needs at Cape Canaveral. Also, the erratic prices of natural gas and hydrogen create budgeting problems.

The overall goal of this research program is:

To develop procedures by which hydrogen production in Florida would be economically competitive with hydrogen derived from natural gas in the midwest

Immediate goals were to:

Produce hydrogen by clean technologies using plentiful U.S. coal supplies or using process/waste streams - we are particularly interested in waste streams of SO_2 and H_2S.

Focus is on techniques that can be economically viable in Florida. This drives us to Byproduct Production since hydrogen produced as a single product from coal is bound to follow the pattern of production from natural gas so that the hydrogen would be produced near the mine mouth. NASA would again have to move it long distances to satisfy its needs at Cape Canaveral.

Two techniques to which we are giving considerable attention are:

- H_2SO_4 production with byproduct H_2 and
- Extraction of H_2 from syngas at IGCC power plants

TABLE 1.—TOP 5 CHEMICALS PRODUCED IN THE U.S. COMPILED FROM CHEMICAL AND ENGINEERING NEWS, JUNE 25, 2001

2000 rank (by mass)	Chemical	2000 Production (in 10^4 kg)
1	Sulfuric acid	39.62
2	Ethylene	25.15
3	Lime	20.12
4	Phosphoric acid	16.16
5	Ammonia	15.03

Sulfuric acid is the leading chemical commodity by far in terms of quantity produced (see table 1). It is manufactured by oxidizing sulfur and sulfur compounds with oxygen from air. If the oxygen were derived from water by an electrochemical or photoelectrochemical route, one to four million tons of hydrogen would be produced as a valuable byproduct with the 39 billion kg of sulfuric acid.. Three quarters of this acid is produced in Florida. This is done by fertilizer manufacturers who need the sulfuric acid for their manufacturing process. It is also done for sulfur clean up in coal fired electric power production. Coproduction of hydrogen with the sulfuric acid could provide a lucrative additional product for them and a bountiful supply of hydrogen for Cape Canaveral and other hydrogen users in Florida.

IGCC Power Plant

In an IGCC power plant, (fig. 1) a coal/water slurry and oxygen are fed into the gasifier which produces a dirty gas that is cleaned up producing slag, acid gas and clean gas which is largely a mixture of CO and hydrogen. The slag is a salable product. The clean gas powers the generators. The acid gas is largely hydrogen sulfide, an intensely poisonous gas that has no ready market or easy disposal route. It is processed to produce sulfuric acid at the TECO IGCC power plant. Two hundred tons of sulfuric acid are produced daily and sold for $30/ton, yielding $6,000/day.

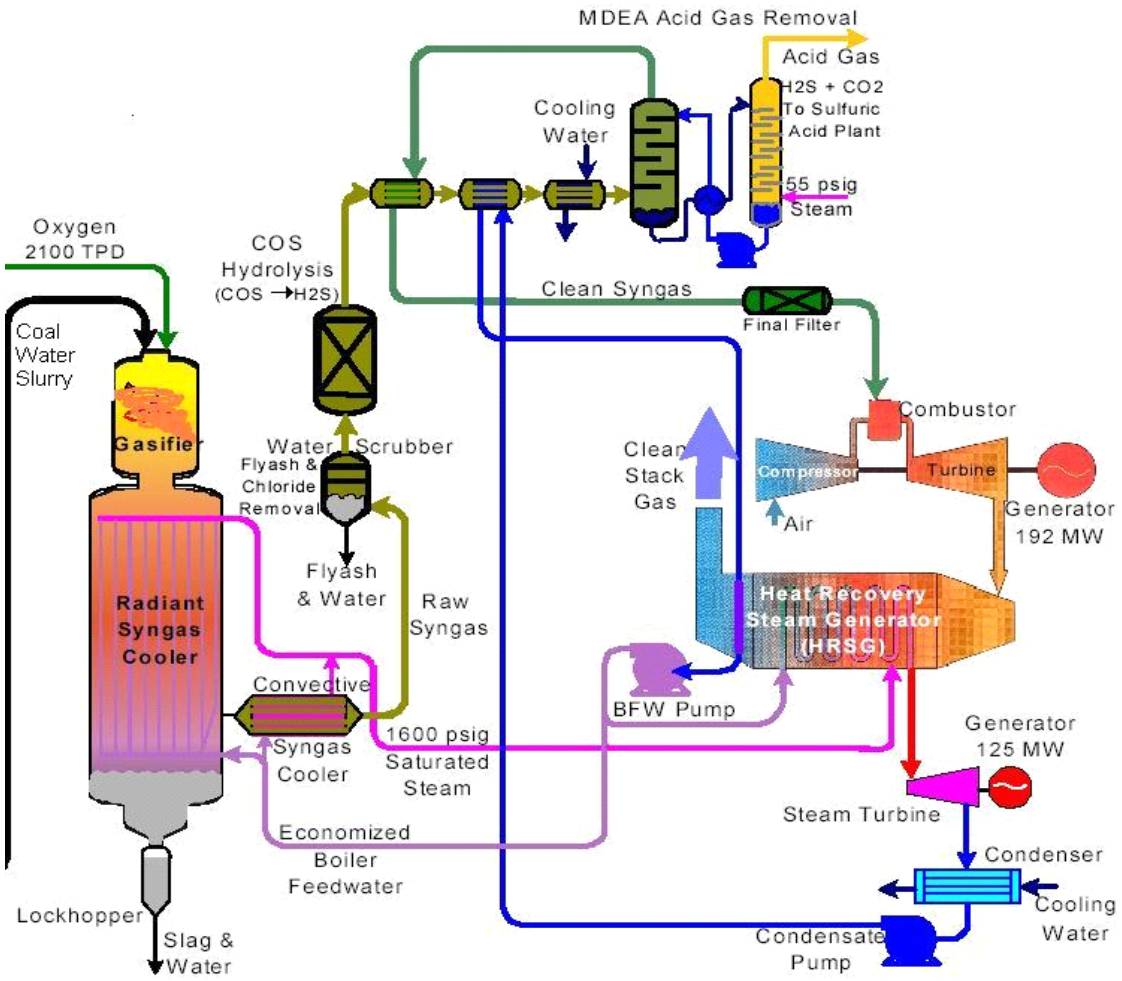

Overall Flow Diagram

Figure 1.—IGCC power plant.

The sulfuric acid production process involves burning the hydrogen sulfide to produce sulfur dioxide that is oxidized to sulfur trioxide in a catalytic conversion system and hydrated to produce the saleable sulfuric acid.

In this research project, we are showing how the catalytic converter can be replaced profitably by an electrolytic conversion that would produce the sulfuric acid and byproduct hydrogen. Four to sixteen tons of hydrogen could be coproduced with the 200 tons of sulfuric acid daily.

Electrochemical Cell Reactions

The overall electrochemical reaction is shown in equation (2). Equations (3) and (4) show the two electrode reactions. As previously stated, the voltage necessary to transfer the electrons for this reaction under standard conditions is only .17 V. This is well below the 1.1 eV band gap of crystalline silicon.

$$SO_2 + H_2O \rightarrow H_2SO_4 + 2H^+ + 2e \quad (3)$$

$$2H^+ + 2e \rightarrow H_2 \quad (4)$$

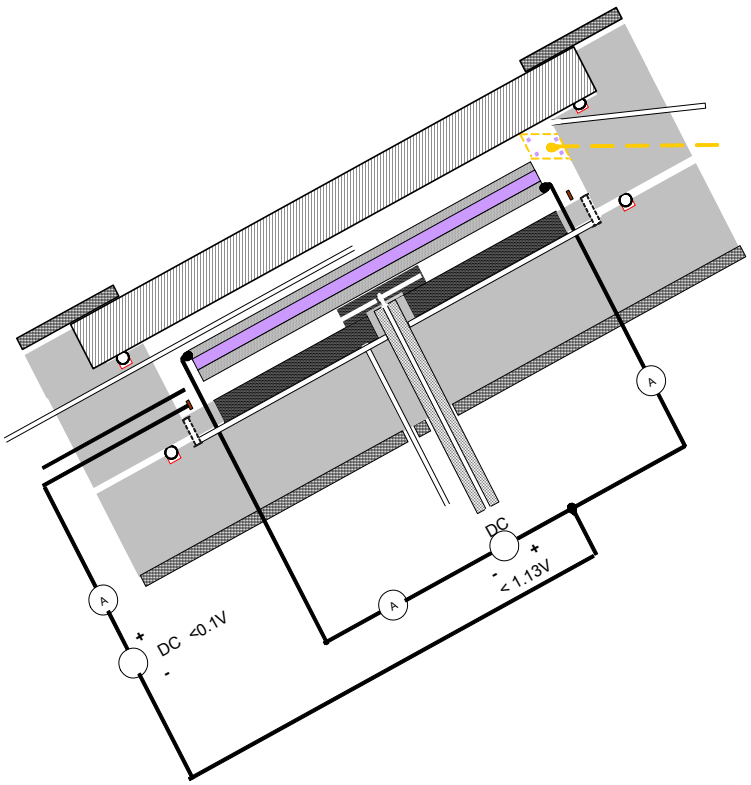

Figure 2.—Electrochemical configuration.

Laboratory System

Figure 2 shows a very versatile electrolytic cell that we have built for experimenting with this technique. It is round when we look down at the end of it and this figure shows a sagittal cross-section through the middle. Sulfur dioxide and water are pumped in through a tube at the bottom of the cell and flow radially over the lower surface of the positive electrode (below the insulating layer shown in purple). The sulfuric acid produced flows through grooves near the periphery and in the base of the cell to an exit tube through which it is withdrawn. The flow rate is controlled by metering pumps that insert the sulfur dioxide and water. The cell pressure is controlled by a back pressure regulator on the sulfuric acid exit tube. A small insertion tube in the negative compartment allows addition of small quantities of water or sulfuric acid to adjust the acid concentration in that compartment.

The hydrogen ions produced at the positive electrode flow to the negative (upper) compartment across the electrolyte bridge around the periphery of the electrodes. There they are converted to hydrogen gas that rises to the top where it can be removed through a withdrawal tube.

Sulfuric acid is produced from sulfur dioxide and there is no need to handle sulfur trioxide.

A large glass window at the top provides a clear view of the negative compartment and can provide light access for photoelectrochemical experiments. The low voltage cited in equation (1) facilitates the photoelectrochemical process. The electrodes, leads and insulator will be replaced by a simple semiconductor device.. This device is a simple wafer of p type semiconductor with a Schottky barrier or n junction on the top surface. When light comes in the glass window at the top of the cell and strikes the semiconductor device, it produces the current and voltage for the electrolytic process. The Schottky barrier or n junction is all that is required. Unlike photovoltaic cells, there is no need to apply any electrode or current collector to it because the electrolyte serves that purpose. Moreover, the electrolyte provides complete coverage without the shadowing and lateral surface resistance losses that occur with the grid collectors commonly used on photovoltaic cells. As shown here, we will operate the cell at a due south tilt of 28◦, the latitude in central Florida. This is a good angle for efficient collection of solar energy

in central Florida. There is no need for the elaborate (expensive) semiconductor systems that are being pursued to overcome the higher voltage requirements of equation (1) - the requirement does not exist here.

Figure 4 shows current-voltage data acquired with the laboratory cell. The blue curve represents measurements made with a sulfuric acid electrolyte and no sulfur dioxide. Measurements were started with a low voltage (1 volt) at which water could not be electrolyzed so amperage was negligible. Voltage was increased in steps until current was substantial.

After the voltage was cut back to a point near the beginning of the current rise, SO_2 was introduced. With SO_2 in the cell, current rose and we could see the increased bubbling of hydrogen from the negative electrode by looking through the window. Reduction of the voltage reduced the amperage and hydrogen production but they continued to exist to voltages well below the voltage required to electrolyze water.

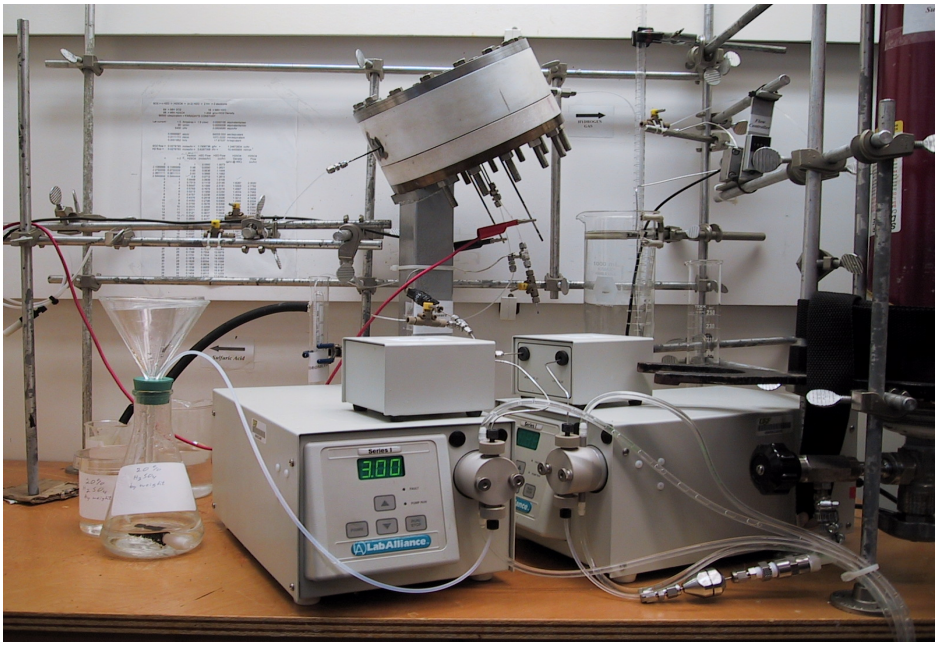

Figure 3.—Laboratory cell and flow control system.

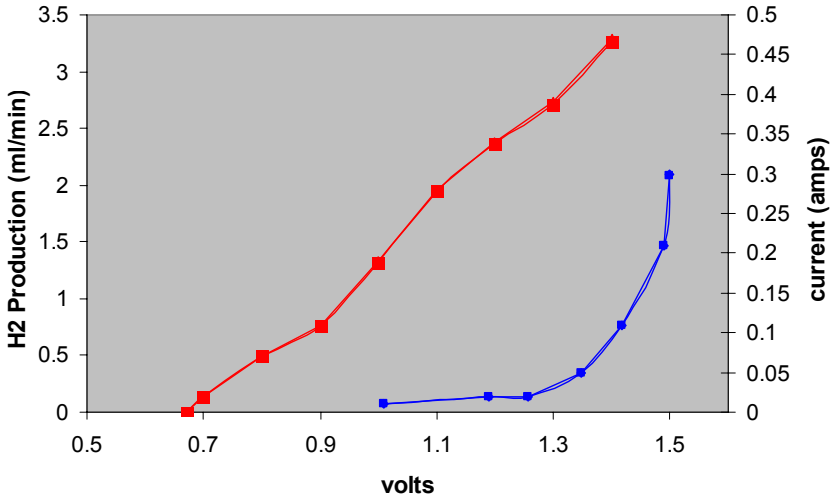

Figure 4.—Voltage-current data.

Hydrogen Production Potential at ICGG Power Plants

The sulfuric acid production process at the TECO IGCC power plant is outlined in figure 5. Hydrogen sulfide in the acid gas is burned in the decomposition furnace to produce sulfur trioxide which is oxidized in three catalytic reactors to produce sulfur trioxide. This is hydrolyzed to produce sulfuric acid.

Electrolysis of the sulfur dioxide would produce byproduct hydrogen and eliminate the need for the catalytic reactors.

Hydrogen sulfide is a reducing gas in its own right and provides the possibility of scavenging our anode with H_2S directly instead of with SO_2 derived from it. That would produce 4 times as much hydrogen as we get by scavenging with sulfur dioxide and replace the need for the entire system shown in figure 5.

Another potential source of hydrogen is the clean syngas. As the fuel for the generator, it is the most valuable product of the gasifier. However, it might be used more effectively in the context of byproduct hydrogen production. It is a mixture of hydrogen and carbon monoxide that is all being burned. Much of the hydrogen could be extracted from it by pressure swing absorption or membrane separation. If one of these well established techniques were implemented, a large amount of hydrogen could be derived and most of the burned gas would be CO.

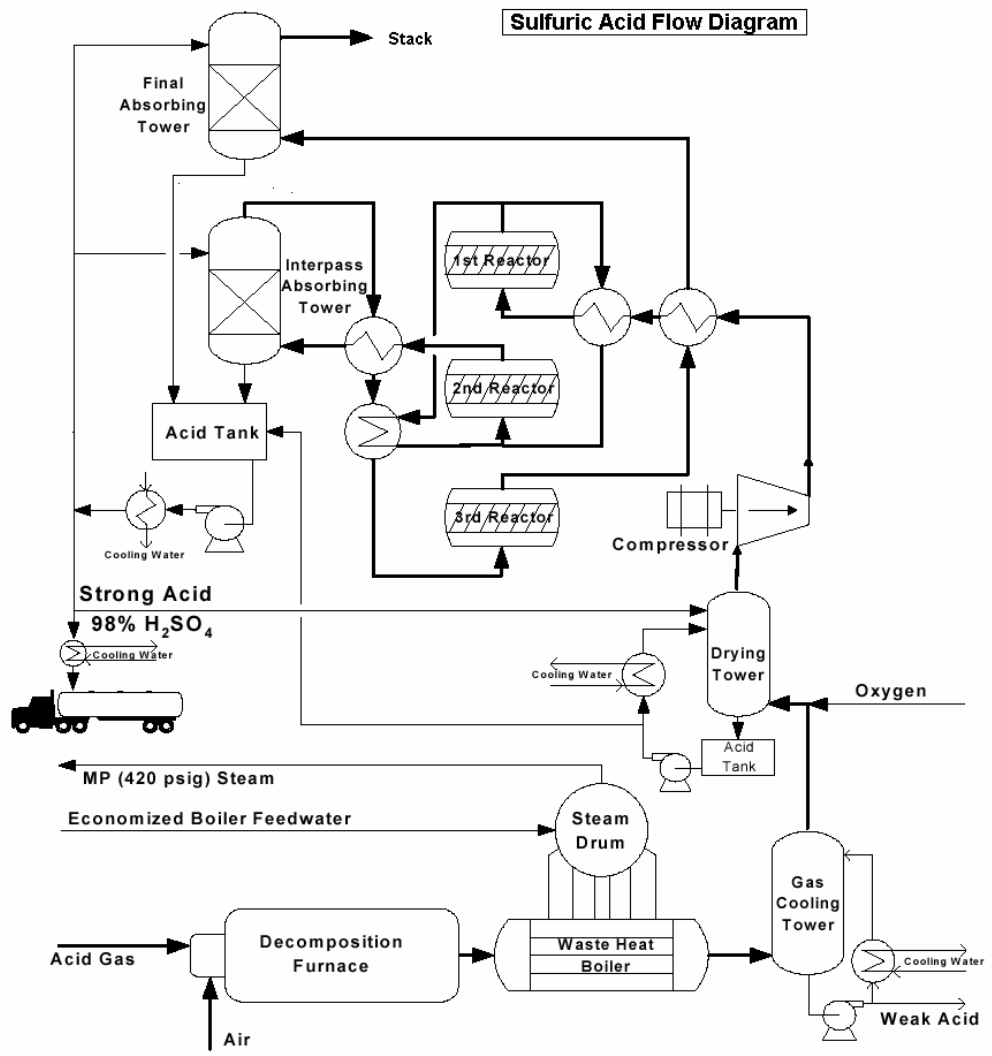

Figure 5.—Sulfuric acid production at TECO IGCC power plant.

Industrial Contacts

While doing the laboratory research, we are also pursuing requirements for commercial implementation of the technique.

We have had favorable feedback from the fertilizer industry who are interested in byproduct production of hydrogen from sulfur dioxide oxidation. The Florida Institute of Phosphate Research and CF Industries have agreed to help us solicit DOE funds to develop this capability.

TECO has expressed interest in the electrolytic oxidation of both sulfur dioxide and hydrogen sulfide but objects to the concept of extracting hydrogen from the syngas. Lloyd Webb had 2 objections to extracting hydrogen from the syngas. First, that would require the burning a relatively larger amount of carbon monoxide and they are under pressure to go in the opposite direction – to sequester the carbon and burn only hydrogen. Secondly, the plant has no surplus gasification capacity. They need the energy in the hydrogen. Diversion of any of the hydrogen to another purpose would force derating of the power plant at times of peak fuel demand. That is something they do not ever want to do.

An alternative that Webb suggested was that they could burn a higher sulfur coal and coproduce hydrogen with the additional sulfuric acid. They do not now have the capacity to handle more sulfur but if our electrolytic slip stream would handle the additional sulfur it could produce the additional sulfuric acid with byproduct hydrogen. They now burn 3 percent sulfur coal and produce 200 tons/day of sulfuric acid containing 65 tons of sulfur. Sale of the sulfuric acid yields revenue of $6,000/day. If they burned 6 percent sulfur coal they would get an additional 65 tons of sulfur. A supplementary system that would oxidize the additional 65 tons of sulfur by electrolysis, would provide an additional 200 tons/day of sulfuric acid (worth an additional $6,000) with coproduction of 4 tons of hydrogen if SO_2 is electrolyzed or 16 tons of hydrogen if H_2S is electrolyzed. Also, the higher sulfur coal would be cheaper.

If NASA builds its own IGCC plant they could arrange for both surplus gasification capacity and capability of oxidizing high sulfur coal. Hydrogen derived from the synthesis gas might be used for rocket fuel while the electrolytic hydrogen from sulfur electrolysis is used for fuel cells.

Economic Analyses

Information is being acquired and organized to evaluate the economic competitiveness of the approach. We propose to compare production costs for the kind of electrochemical plant we are proposing with the production costs at existing sulfuric acid plants.

Some figures from a very preliminary cut at such analysis are given in tables 2 and 3. They suggest that the process can be economical in the near term with hydrogen prices of $0.50/lb.

TABLE 2.—ESTIMATED MANUFACTURING COST OF HYDROGEN UTILIZING THE SULFUR WATER CYCLE ELECTROYLSIS AT AN IGCC PLANT

Estimated plant capital cost (a)	$1,500,000
Plant life	5 years
Capital recovery rate	20%
Operating capacity factor	80%
Hydrogen rate	333 lb/hr
Sulfuric acid rate	16667 lb/hr
Electric load	2430 kW
Annual plant capital costs	$303,176
Annual O&M – Electrical	$723,768
Annual O&M – Other	$150,000
Hydrogen cost	$0.50/lb

Electric Power Research Institute Report EM-789 June 1978 with capital cost inflated by the Electrical machinery and equipment Index and adjusted for size.

TABLE 3.—COMPARISON OF HYDROGEN PRODUCTION COSTS $/lb

Method	2002	2010	2030
SMR (a)	$0.43	$0.57	$1.47
E. sulfur cycle	$0.50	$0.54	$0.88
E. PV/antenna(a)	$3.47	$2.27	$0.88
E. solar thermal(a)	$2.49	$1.39	$1.05

Hydrogen Production via Methane Nonoxidative Aromation

PI: J. Wolan (University of South Florida)
A. Kababji (University of South Florida)

Problem

Portable, low thermal budget, on-site H_2 production will be required for fuel cells in a consumer market.

Objective

Optimize the production of hydrogen from methane using zeolite based catalyst.

Approach

Two setup reactors have been built, the catalytic reactor (CR) to investigate the production of benzene along other hydrocarbons and the catalytic membrane reactor (CMR) with 100 percent selectivity to hydrogen production.

Background

The nonoxidative aromatization of methane to benzene and other high C/H ratio hydrocarbons reaction is considered a novel technology. Most of the literature concentrates on the manufacturing of benzene besides the other hydrocarbons rather than hydrogen using the ZSM zeolite based forms of catalysts.

Modifications to produce ultra high purity hydrogen along with benzene and other hydrocarbons are considered, these modifications include the technology, the design of the setup and the reactor itself.

The reaction shown below is highly endothermic, optimum reaction temperature found in literature ranges between 700 to 850 °C, and the thermodynamic equilibrium conversion of methane is 18 percent at 750 °C.

$$6CH_4 \xrightarrow{Mo/HZSM-5} C_6H_6 + 9H_2 \left(\Delta H = 523\, kJ/mol\right)$$

Methane aromatization is evaluated under two sets of conditions: 1) Without hydrogen permeation in a fixed bed conventional catalytic reactor (CR); and 2) With hydrogen permeation in a catalytic membrane reactor (CMR).

Results and Discussion

Four types of catalysts were prepared by incipient wetness co-impregnation of the ammonium form of the Zeolite. Calcined in air at 500 °C, reduced and activated using a special recipe.

Reaction temperature 600 to 750 °C, down from a range of 650 to 850 °C, depending on optimum flow rate of reactant (methane) described as space velocity.

TABLE 1.—CATALYST FORMULAS PREPARED
AND THE REASON OF THEIR INVESTIGATION.

Catalyst formula	Reason prepared
Mo/ZSM-5	Original and reference
Mo/H-ZSM-5	Active sites study
Ru-Mo/H-ZSM-5	Improving conversion and stability
Pd-Mo/H-ZSM-5	Never been studied

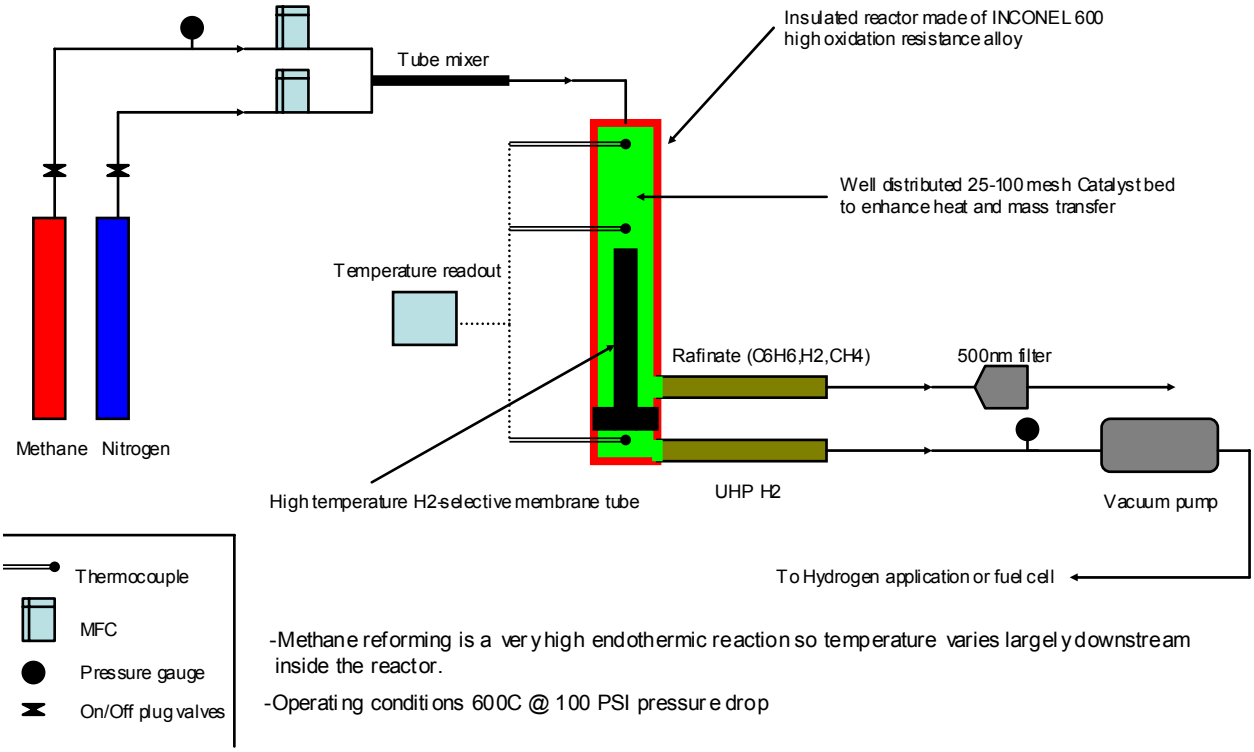

Figure 1.—Schematic of the catalytic membrane reactor (CMR).

Figure 2.—Catalytic membrane reactor (CMR) setup.

Figure 3.—Catalytic reactor (CR) setup used for screening catalyst samples.

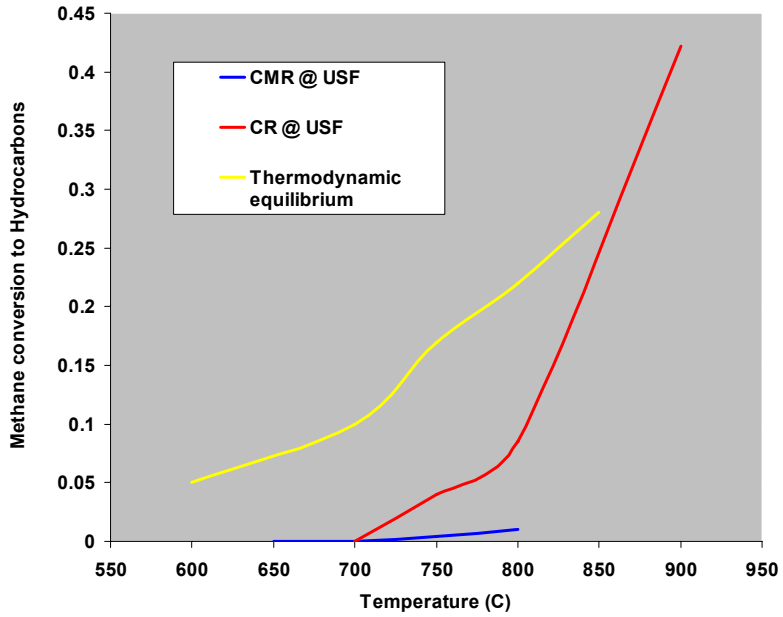

Figure 4.—Methane conversion to hydrocarbons only, the CR achieved 30 percent methane conversion at 850 °C.

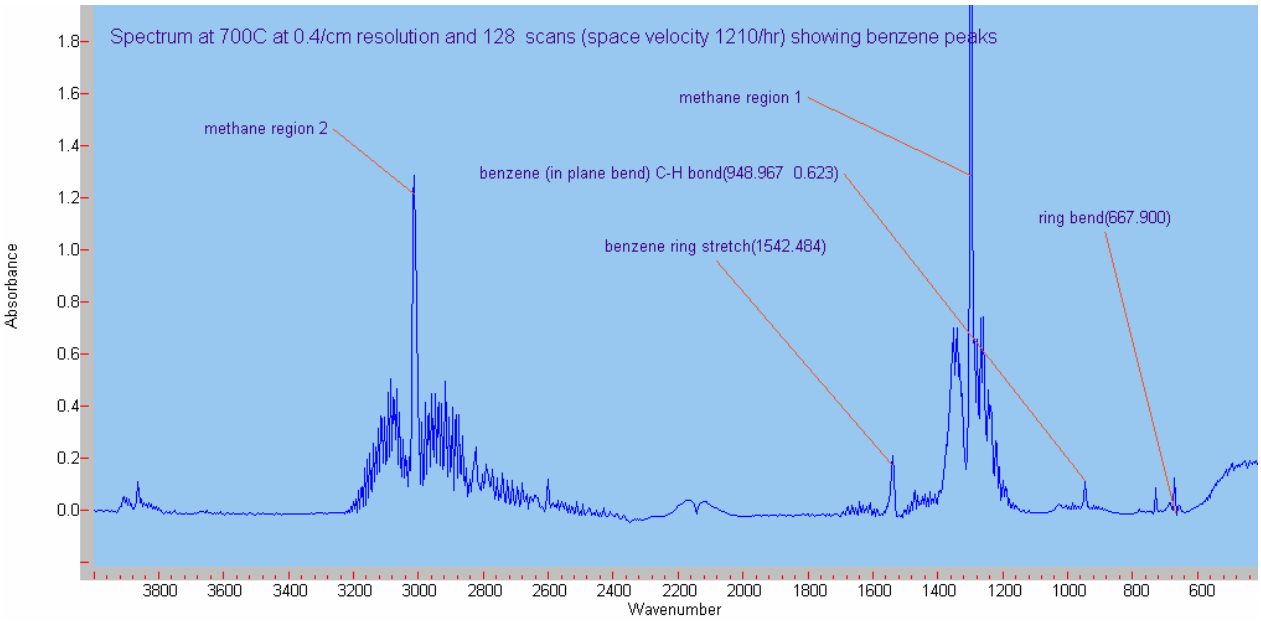

Figure 4.—FTIR spectrum showing major benzene and other hydrocarbons peaks along unconverted methane at 700 °C.

Conclusions

The catalytic and catalytic membrane reactors have been built and tested. These reactors have been operated in parallel to screen different catalyst samples for inherent catalytic activity (using the catalytic reactor) and test promising catalytic materials for the production of hydrogen (using the catalytic membrane reactor). Several promoted catalysts were prepared with a Zeolite support based on improved catalyst recipes found in the literature review. Preliminary characterization of several of these catalysts has been performed using the catalytic reactor. Initial experiments examining the use of the catalytic membrane reactor have also been performed.

Software Agents and Knowledge Discovery and Data Mining for Enhanced Safety and Control of Hydrogen Operations

PI: L. Bunch (University of West Florida)

Introduction

Safety remains one of NASA's primary concerns in all aspects of hydrogen production, storage, delivery, and use. The Institute for Human and Machine Cognition (IHMC) conducted research and development for automated safety and health monitoring of industrial chemical processes as well as the NASA space shuttle fueling and launch process. One element of the program addresses improved plant safety and control through enhanced anomaly detection, diagnostic, and notification methods. The IHMC has been funded to investigate the potential utility of recent advances in Computer Science for this purpose. In particular, Software Agents (SA) have been studied for alarm root cause diagnosis and multimodal notification of plant personnel of off-nominal operating conditions. Recent advances in Knowledge Discovery and Data Mining (KDD) have been investigated as the basis for automated design of the software and hardware required for effective diagnostic systems. The first year of this effort focused on industrial chemical process control system applications such as those required for on-site liquid hydrogen (LH_2) production at NASA KSC. We developed the initial prototypes for three applications in the chemical process domain including abnormal condition monitoring, alarm root cause diagnostics, and machine learning based diagnostics. These results are detailed in section 2 of this report. For the second year, funding was substantially reduced and we therefore focused all of the remaining resources on adapting the monitoring application to the NASA KSC shuttle tanking and launch system and enhancing the monitoring capabilities. The resulting KAoS Reactive Monitoring and Event Notification (KARMEN) software agent system enables users to perform automated live monitoring of complex process conditions that were typically only detected manually or during post-analysis of recorded process data. The year 2 results are presented in section 3.

State-of-the-Art Achievements

Through this research, IHMC has advanced the state-of-the-art for automated safety and health monitoring of chemical/industrial processes as well as the space shuttle fueling and launch process. We have also advanced the complementary area of remote user notification. Current process monitoring technology supports manual monitoring of real-time process data, pre-defined limits and exceedance alarms, and post-analysis of saved process data. Our agent-based software provides the following advances in this area:

- Automated real-time monitoring of complex process conditions that were previously only detected during post-analysis,
- Dynamic user-defined limits and alarm conditions that were previously only predefined in the control system and shared by all users.
- Current remote user notification technology supports statically mapping process alarms/events to a single mode of notification, selecting a recipient based on pre-defined user work schedules. Our software provides the following advances in this area:
- Notification concerning dynamically-defined process conditions rather than exclusively the pre-defined alarms and events,
- Adapting the notification mode based on the user's online presence in addition to their physical presence or schedule,
- Applying individual user preferences and corporate policies concerning the notification mode and recipients based on the event context.

This research has sparked keen interest in the industrial sector, from both commercial process control and on-line monitoring equipment providers. They clearly agree that these are useful new capabilities that advance the state-of-the-art.

Research

Our alignment with NASA's safety objectives and control technologies has been key. PCGOAL is used by several centers to monitor shuttle launches and there has been increasing NASA interest in PCGOAL based monitoring and notification for remote users. Also, our integration with standard industry control systems is increasingly important as more NASA systems employ commercial control solutions. NASA colleagues from KSC and GRC identified some additional application domains for us to explore. The GRC propulsion systems research involving novel control and sensor technologies includes requirements for propulsion systems health and safety monitoring using 'Smart Efficient Components' that autonomously detect abnormal conditions. The KSC Advanced Technology Development Center cryogenic technology research program at SLC-20 can benefit from our work through automated monitoring for equipment that is transient or 'roll-on' including high-speed LO_2 pump testing equipment that is currently visual-only.

Chemical Process Safety Automation Research

We created a virtual chemical plant for our research using two commercially licensed products. The physical plant is simulated using Aspen Technology's Hysys Dynamics high-fidelity process simulation tools (ref. 1). This simulated process is controlled using the Emerson DeltaV Distributed Control System (DCS) software (ref. 2). We also acquired a Benzene-Toluene separation model from Emerson which sufficiently demonstrated characteristics common to Hydrogen processing environments such as a continuous chemical process with sufficient complexity and a representative sample of final elements (e.g., valves, pumps, tanks, heat exchangers, sensors) for our initial development.

Software Agents for Chemical Process Monitoring

Software Agents are computer programs that may be launched on a network by individual users to perform specified tasks. This capability is highly relevant to condition monitoring of modern, complex systems involving a multiplicity of sensors and processors interconnected by hard-wired or wireless interconnections (refs. 4 to 6) often implementing standard interfaces such as Ole for Process Control (OPC) (ref. 3). In the current work the utility of Software Agents for the following interrelated purposes is investigated: (1) model individual process components and interactions as a Multi-Agent system to perform root cause analysis; (2) monitor specific combinations of process conditions of interest to individual plant operators, supervisors, and other personnel and notify them through modes the individuals select and in accordance with corporate policy and personal preferences.

A schematic of the system simulation for Software Agent studies is shown in figure 1. KAoS is an extensible set of agent services including policy administration, deconfliction, propagation, and enforcement. The KAoS policy services rely on DAML/OWL, a declarative, description-logic based markup language, and an integrated theorem prover (JTP) to provide representation and reasoning about notification policies and procedures (refs. 7 to 10). To date most work on complex plant condition monitoring has focused on improving methods of identifying faults (refs. 6 and 12), with little attention given to the equally important issue of notification of the relevant personnel when off-nominal plant operation occurs. Software Agents offer the capability to monitor specific combinations of process conditions and send appropriate notifications as the conditions change. The notification can occur based on user-specified aggregates and in accordance with the users preferred mode of notification. This contrasts with current process control and monitoring systems are generally confined to exceedance alarms, control operator displays, and perhaps other more sophisticated information from post-analysis of data collected.

The following schematic shows the Agent system configuration for such aggregate condition monitoring and multimodal notification.

In this simulation each Agent represents a process component in the control system and provides real-time access to all operational data about that component. For example, one plant user or supervisor might wish to be notified when the flow rate through a particular valve exceeded a certain level for a specified duration (flow > 4.2 kpph for 60 sec). Each condition monitoring agent is configured and deployed by the user to evaluate logical expressions of conditions across multiple components, such as

an assigned severity (Critical, Warning, Advisory), and combinations of conditions of interest to the user steam valve flow < 4.2 kpph AND feed valve position > 35 percent for 30 sec. Notifications are generated as the monitored conditions are satisfied/unsatisfied, governed by Policies representing organizational requirements and personal preferences. Notification modes may include E-mail, Instant Message, Pager, and Operator Displays. Notification policies typically cover such factors as event type, severity, the recipient's organizational role and location, and the plant area in which the event occurred. For example, a policy might be to page an onsite Field Operator immediately when a critical H_2 Plant monitored condition is satisfied and the Process Engineer is unavailable.

Figure 3 shows the user interface for Agent configuration and deployment. The lower-left of figure 3 depicts how the user browses the hierarchical tree of components and associated parameters available in the DCS. For each selected component parameter in the hierarchy, the user assigns a comparison operator (greater than, less than, equal, etc.), provides a scalar value to which the parameter value will be compared, and optionally provides a duration in seconds which the condition must remain true before it is considered satisfied. Each such atomic condition is added to a logical expression using the and/or radio buttons. The evaluation of this expression is the aggregate condition that the Agent is monitoring; notification is generated when the entire expression evaluates to true. As shown on the right in figure 3, the condition monitoring Agent is assigned basic notification information including severity (Critical, Warning, Advisory, Log) and an initial target user or role to notify when the conditions are satisfied.

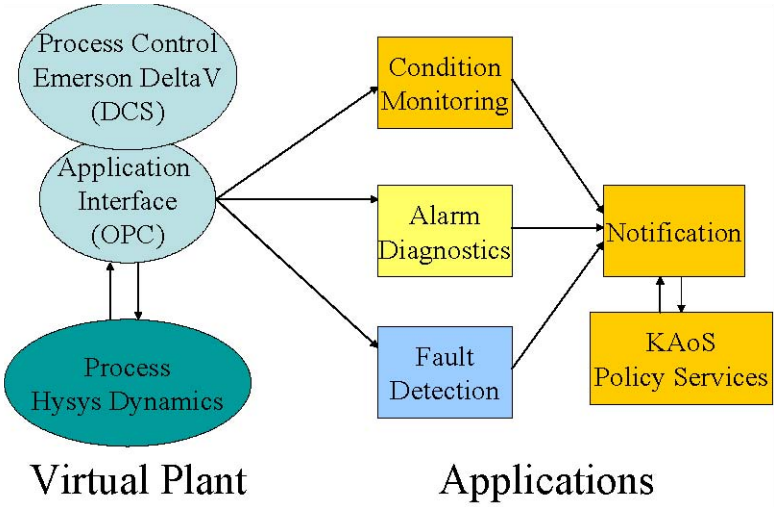

Figure 1.—Schematic of the simulation environment and applications for software agents.

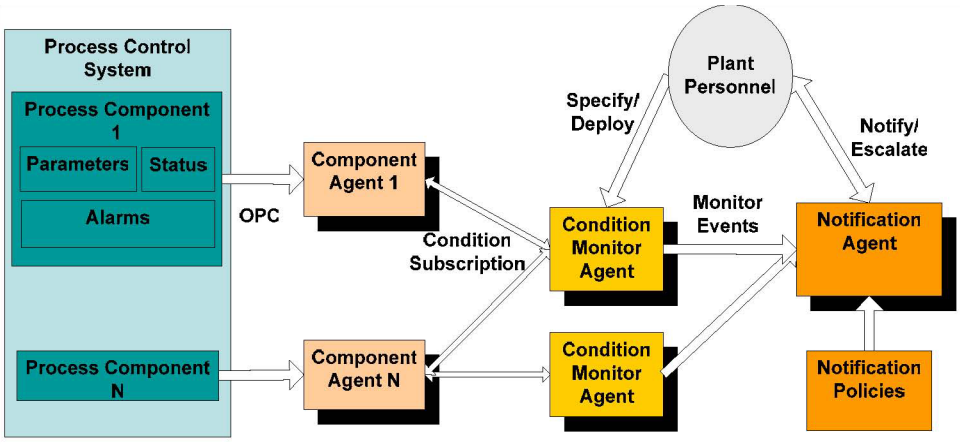

Figure 2.—System configuration for the multi-agent process condition monitoring and notification software.

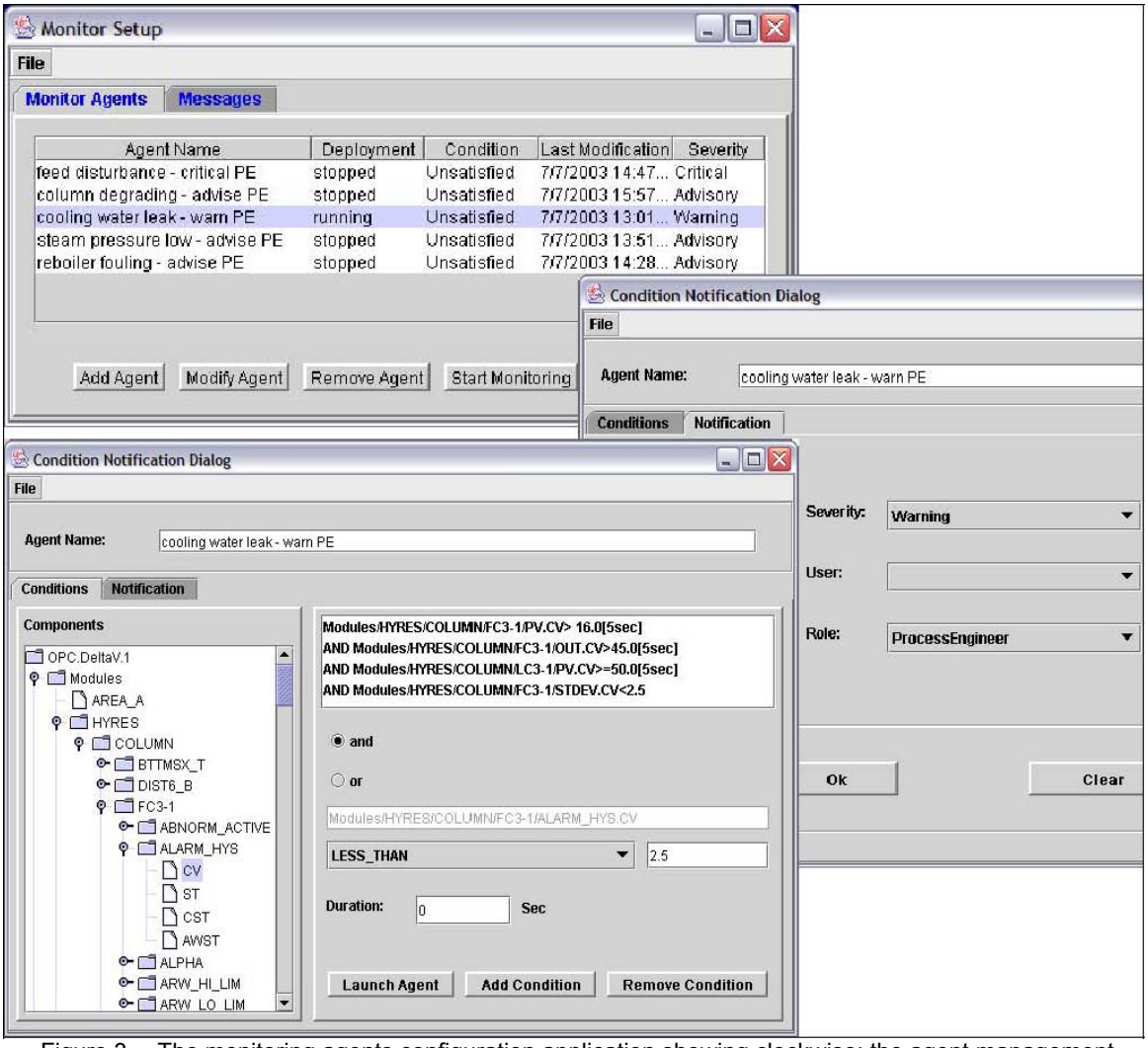

Figure 3.—The monitoring agents configuration application showing clockwise: the agent management and deployment screen, the notification configuration screen, and the monitoring configuration screen.

Notifications are generated as the monitored conditions obtain and abate. The default behavior of the notification agent is to display messages in the Monitor application shown in figure 3. All other notification actions are governed by Policies representing organizational requirements and personal preferences. For example, a policy might be to page an onsite Field Operator immediately when a critical H_2 Plant monitored condition is satisfied and the Process Engineer is unavailable. Each policy obliges the notification agent to take certain actions based on the qualities of the monitored event and the current disposition of the plant personnel. The current event characteristics that can trigger a policy include the event type (satisfied/unsatisfied condition, activated/deactivated alarm: see MonitorStatus in fig. 4), the assigned event severity (critical, warning, advisory, log), and the plant area in which the event occurred based on the component hierarchy defined in the DCS. The user characteristics that can trigger a policy include the user's organizational role (operator, process engineer, area manager, etc.) and the user's current physical and computational presence (nearby/remote, online/offline: see Existing in fig 4). The qualities of the notification action that policies can oblige include the mode, latency, and focus of attention (ref. 11). Notification modes currently include e-mail, instant message, pager, operator displays, and the IHMC Monitor application. The latency controls how quickly the user is notified (Immediate, Deferred, Archive). The focus of attention controls how forcefully the user's attention is obtained and depends on the features available in the notification mode (e.g., instant message chat session that interrupts the user versus a queued message in the background).

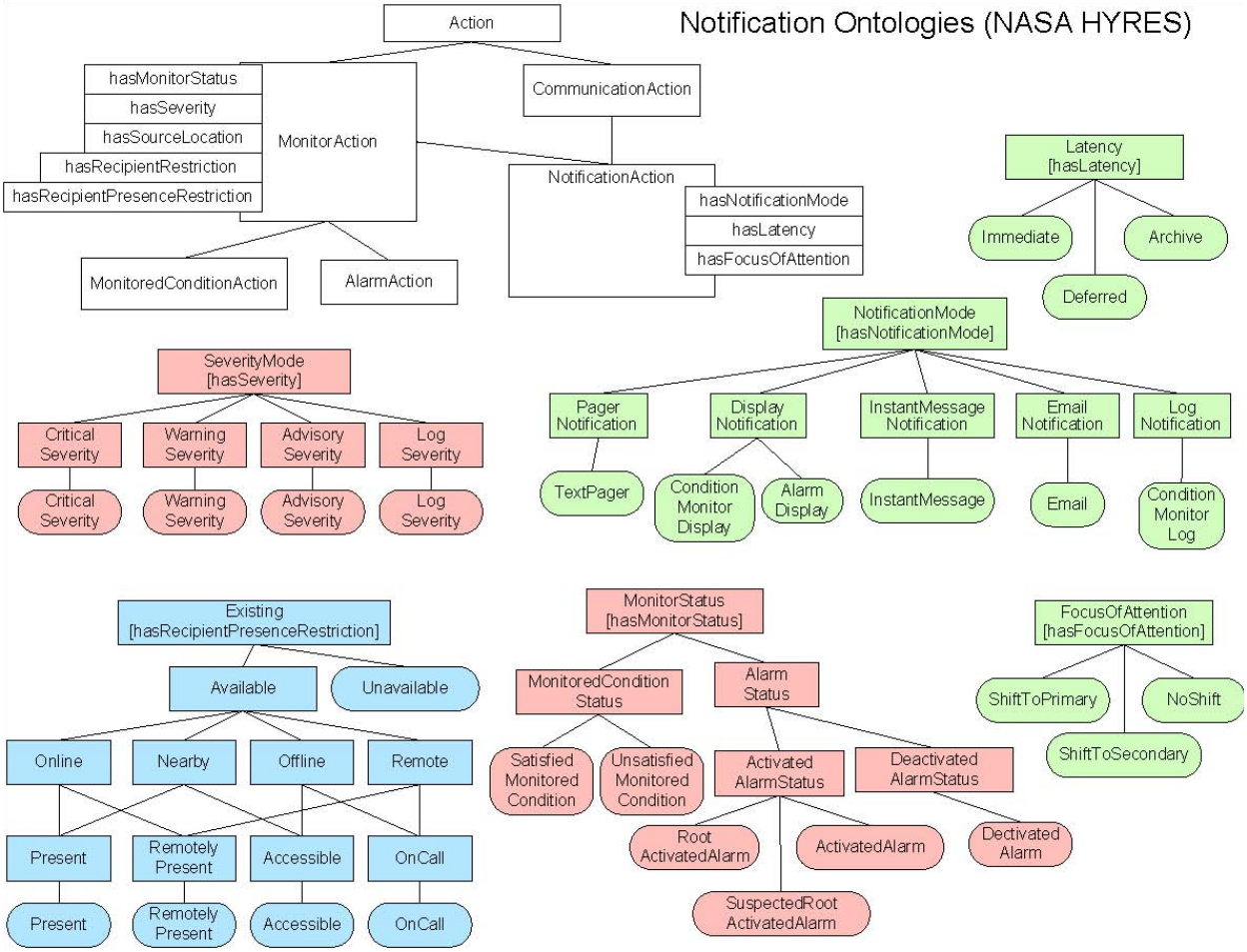

Figure 4.—Graphical representation of the DAML-based notification ontologies for monitored event characteristics (red), user presence (blue), and notification directives (green).

The notification obligation policies are created using the KAoS Policy Administration Tool (KPAT) shown in figure 5. The attributes of the policy are from the ontological concepts shown in figure 4. Multiple policies can apply to a single event such as using the pager mode for critical events, using the instant message mode for critical events when the user is online, and using the primary focus of attention for critical events. Each policy is assigned a priority with organizational policies having higher priority than personal preferences. KAoS will use the priority to resolve policy conflicts thereby enforcing organizational policies over personal ones.

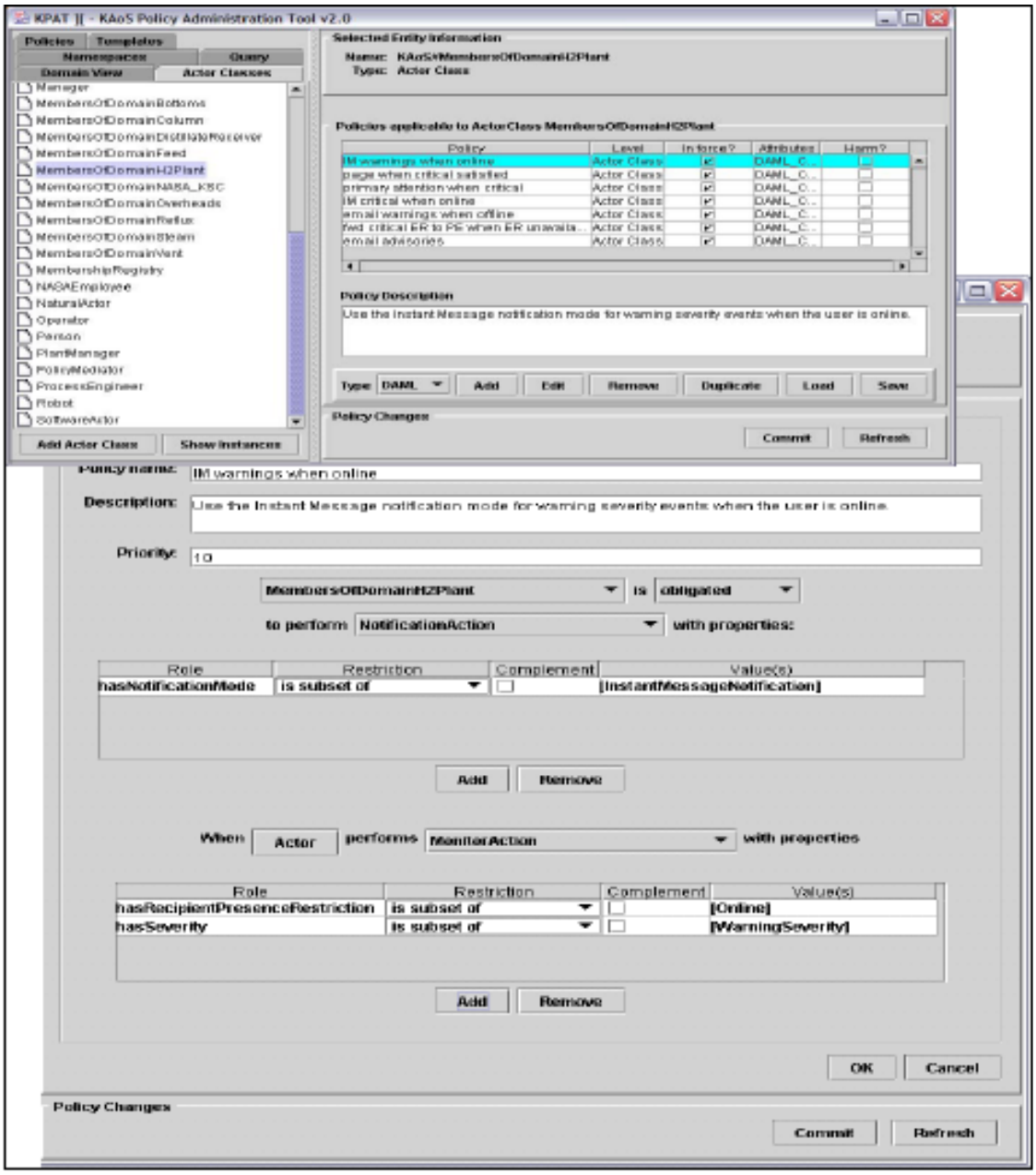

Figure 5.—The KAoS Policy Administration Tool (KPAT) shown with a set of notification policies (top) and the configuration of one notification policy (bottom).

Software Agents for Alarm Root Cause Diagnosis

In many practical circumstances a malfunction of one or more process components affects other related components that may enter alarm states. Several alarms appear on the control operator's display in a short time making it difficult for the operator to diagnose the root cause quickly (ref. 12, p. 166). Within this part of the project we describe an infrastructure for processing all incoming alarms, identifying the root cause alarms versus alarms arising in consequence of the roots, and presenting the diagnostic results to the operator visually.

This infrastructure is shown schematically in figure 6. Within this system, a Software Agent models each process component. The agent relationships model the topology of the process component

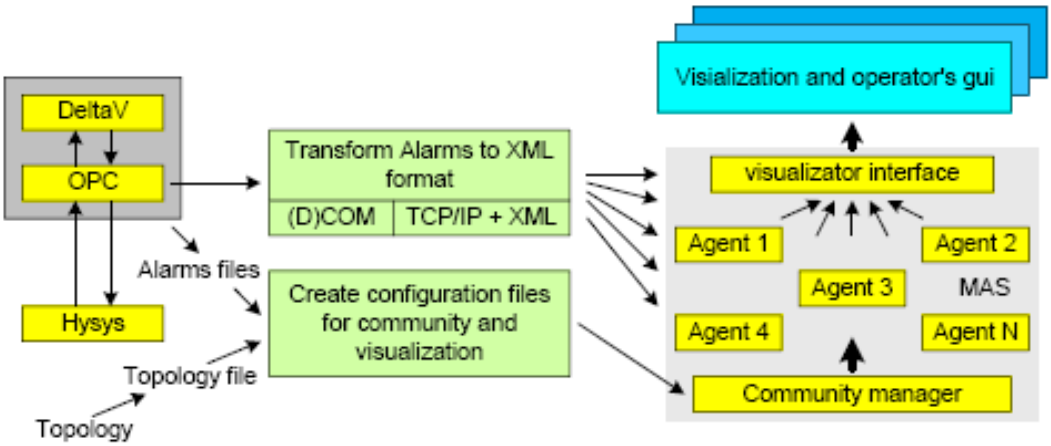

Figure 6.—System configuration for the multi-agent alarm root cause diagnosis system.

input/output relationships. Each Agent receives alarms activated by the component it represents and alarming agents collaborate with related Agents in order to identify potential root causes.

The root cause detection algorithms utilize component topology, component types, and alarm types, with the goal of effectively diagnosing root causes without encoding expert knowledge specific to the particular process. Expert-system based solutions would require a separate knowledge base describing the relations between the components for each process control case. In contrast, the proposed Agent based solution is general enough and is expected to work for an arbitrary manufacturing case, provided that there are Agents that represent all of the components available. The Agent-based algorithms developed within the project include rule-based and topology-based search methods, which appear to have promise for this purpose.

The alarm root cause determination process itself is carried out by the multi-agent system. The input to this diagnostic process is alarm records from the DeltaV OPC server via the OPC-XML interface. Using a multi-agent system provides some advantages in comparison with using an expert system:

- Prediction – the system can predict the problems (determine root causes) in the process by applying general rules and process topology, thus discovering problems that never appeared before and would not be covered by the expert system rules.
- Generality – the system can be easily fit on different process (unlike an expert system that is tied to the concrete process).
- Modularity – the process can be simply extended with a new type of component; adding some new rules based on the physical characteristics of this component we can predict the behavior of the process (even when we have no knowledge about the entire process). When using an expert system, one is forced to add a concrete rules based on the observation of the process's behavior.
- The root cause detection system processes all incoming alarms and according to the results of the inference process can assign alarm type to each of the function blocks. Alarm types and their meanings may differ according to the inference method used (topology-based versus rule-based search).
- Root Alarm
  - Topology-based search: given the topology of the process, this is the first function block with alarm among the set of blocks with alarm, i.e., it has no predecessor with alarm (a possible origin of troubles).
  - Rule-based search: based on an appropriate rule, this block was identified as the main source of problems. Unlike topology-based search, the function block does not have to generate alarms to be marked as root.
- Normal Alarm
  - Topology-based search: a block with alarm which was not evaluated to be a possible root (i.e., according to the topology it is a successor of at least one other block with alarm).
  - Rule-based search: this alarm type is usually set to the sensor that originally signals the alarm (depends on the rule – can be also set to any other function block type).

- Suspected Non-Alarming Component
  - Topology-based search: a block without alarm that is a predecessor of at least two other blocks with alarm (a possible origin of troubles).
  - Rule-based search: block is suspected to be the possible original of troubles.
- Suspected Non-Alarmable Component
  - Topology-based search: a block which can not signal alarm but is situated between blocks signaling alarm (possible malfunction).
  - Rule-based search: set according to the rule to signal possible malfunction of the function block.
- Not Specified – none of the previous alarm types was assigned to this function block. Function block probably isn't in any error state.

The Multi-Agent system supports two inference modes: topology-based search and rule-based search. Topology-based search is based only on the topology of the process components while rule-based search exploits some background knowledge about the individual process components. This knowledge is stored in form of rules in the rules database. The topology captures only the lowest-level information of the monitored process. This makes the root cause detection algorithm process-independent. On the other hand, the topology itself cannot provide sufficient basis for correct root cause detection. Rules which take into account knowledge of the process components are necessary to make the root cause detection more reliable. The rule-based search utilizes agents that are specialized to model specific component types (e.g., pump, valve, tank, heat exchanger). The Agents apply first principle rules based upon the type of alarming component, the alarm type, and the component topology. For example, in the case of high pressure/level alarms from a tank a search is performed for other alarming components contributing to high mass/energy input and low mass/energy output. The formal structure of the rules is split into 4 parts. The first two – Input state and Block state - represent the condition part of the rule. Update state and Action state describe actions and agent state changes that will take place when the rule is invoked.

- Input state – contains conditions that the input message must meet. The input message that agent receives describes state of its neighborhood and raised alarm – e.g., alarm type, source, etc.
- Block state – conditions in this part of the rule have to fit the agent's (function block) inner state. The agent compares its state (e.g., its type, whether the agent generates alarm, etc.) with all conditions stated in the rule.
- Update state – when all conditions from the previous two states are met, the agent will update its alarm type according the type stated in this part.
- Action state – this part specifies the agent's further behavior - whether the message with the search (determination) request will be sent to the following agent or the determination process will stop and the result-collecting process will start.

Each Agent is assigned the type of component it represents (sensor, pump, valve, etc.). Only agents that represent sensors can signal alarms. Each sensor has assigned a variable it monitors (pressure, temperature, etc.). When a new alarm arises, rule-based search is invoked first. This means that the corresponding agent searches its rule database for any rule whose condition can be satisfied. If the agent finds such a rule, it carries out actions specified in the action part of the rule. If no rule can be applied at the given moment, the topology-based root cause detection algorithm is initiated. Thus the topology-based search is considered to be a complementary option to the rule-based one. It is invoked only when the rule-based search cannot be satisfied.

Knowledge Discovery and Data Mining for Diagnostic System Design

Knowledge Discovery and Data Mining (KDD) refers to machine learning methods that create predictive models from data sets, large or small. Depending upon the specific methodology employed these models may give insight into the associative relationships or the causal relationships among the variables represented by the data. Modern plants are instrumented with a large number and variety of sensors, which generate large data sets, and the distribution of these sensors is initially specified at the design stage. KDD is particularly useful for (1) using simulated data from the design stage to develop deployable fault detection and diagnosis algorithms and (2) providing design guidance in the deployment of sensors to permit faults to be identified accurately, specifically, and quickly.

The steps associated with the design of a plant are shown schematically in figure 7. Plant design begins with the simulation of a notional configuration. For purposes of the portions of the systems performing the diagnostic function on the plant, these simulations are performed for both normal operating ranges and for simulated malfunctions. An initial algorithm for diagnosis of anomalies is exercised and recorded for comparison with other techniques. These results will suggest improvements in plant design, such as sensor type and/or placement, which will be incorporated into the next iteration of the design. In the present work we have concentrated on the elements of this iterative procedure noted in blue in the above figure.

As previously noted the plant used in the simulations is a Benzene-Toluene distillation plant. The PFD Window, the workspace where the individual components of the chemical plant in question are pieced together and the final layout displayed, is shown in figure 8. The operational parameters of any component can be viewed and changed by clicking on its symbol and making the necessary changes on the panel that pops up.

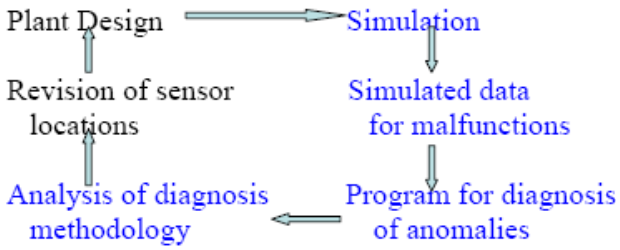

Figure 7.—Schematic of design process for fault detection system for a complex plant.

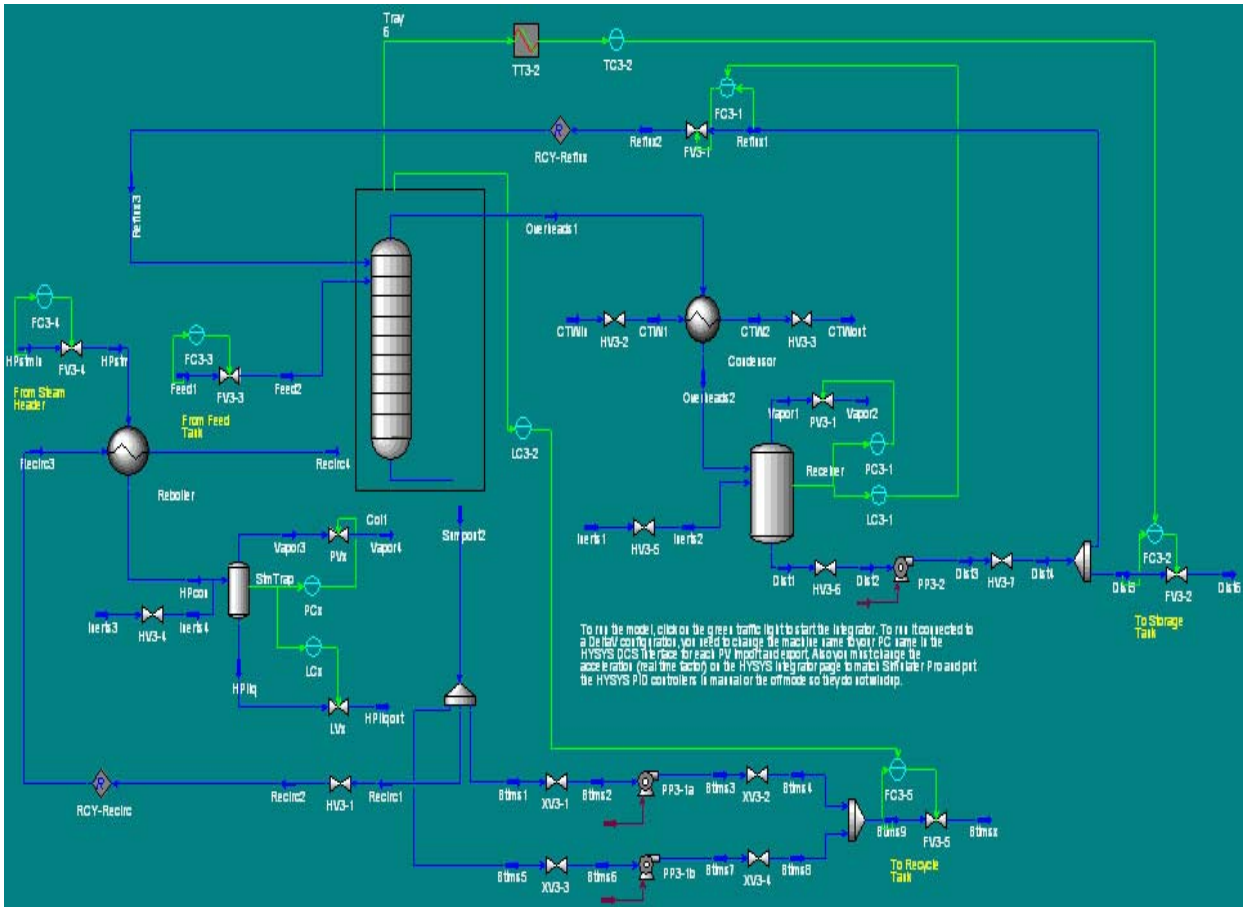

Figure 8.—PFD window for Benzene-Toluene distillation.

In this configuration the finished Benzene product comes out at the far right of the diagram, and the finished Toluene product comes out at the lower right side of the diagram. The original mixture is fed into the process through a valve just to the left of the large column bounded by the black box. This particular model came from a library of predefined configurations, and it is the process considered to test the effectiveness of the KDD method used in this first phase of the work (described below).

There are three major operational variables that affect production volume, purity levels of each finished product, and plant stability during normal operation. These are, the rate at which the raw material is fed into the system, the temperature at which the distillation column operates, and the amount of steam, and hence heat, that is transferred to the fraction of material that has fallen down the distillation column and is then reintroduced to the same column for increased purity. While these parameters determine the external forces imposed on the system, other parameters are vital as simple monitors of efficiency and yield, as well as the overall health of the system. The plant operates by means of physical controllers, depicted as green circles, that are manipulated by either human intervention or other controllers that monitor particular processes. Many pertinent physical quantities, such as temperature and pressure at either end of the distillation column, or the level of liquid Benzene stored in a receiving tank prior to further refinement, can be recorded in large buffers for immediate graphical analysis, or saved to a text file for more accurate, computational scrutiny.

Several KDD procedures appear possible for fault detection and diagnosis in complex systems. The first is the description of the system as a flow graph and backtracking from identified sensor/gauge anomalies to locate probable sources of failure. This is a good, old idea whose principal disadvantage is the combinatorial complexity resulting from the occurrence of multiple independent faults. The second is the description of the system as a Bayes net and computation of conditional probabilities of nodes representing system components from values of sensors and/or gauges (refs. 16 and 17). This is a recently developed approach limited chiefly by statistical difficulties. The third is the development of descriptive decision rules that represent the normal and abnormal behavior of the system, which is the most reliable technique for deterministic systems. A fourth approach is the use of non-monotonic reasoning systems. These are similar to the decision rules but are compressed into a small set of rules to derive the smaller set of needed rules. A final option is the use of neural network classifiers, which are which are implicit stochastic or deterministic rule system implemented in a network structure and learned by a training network. All of these methods require considerable data to develop reliable diagnostic algorithms.

In this initial phase of the work we selected the third of these alternatives. A simple, computationally efficient version of this methodology has been developed at IHMC called Second-Order Relation Compression for Extraction of Rules (SORCER) (refs. 18, 19, and 20). SORCER attempts to produce the shortest decision table consistent with the “training” data, since shorter tables are easier to understand and can be managed and applied more efficiently. The advantages of generating tables with a (near) minimal number of rows become more apparent when dealing with extremely large sets of examples. The size of a model can be taken as a simple measure of comprehensibility, and we believe the classifiers produced by SORCER have advantages of familiarity and simplicity, which are key supports of human comprehensibility.

Our work focused on the simplest possible procedure for generating an anomaly detection program from a system simulation:

25. Run the system in normal and malfunctioning modes.
26. Sample the state values of the simulated system under normal mode and, separately, for each malfunctioning mode.
27. From the data for each such mode, form a table or list of characteristic state or sensor/gauge values.
28. Order the tables hierarchically, normal mode at the root, hence first checked.
29. To assess anomalies in the actual physical system, record sensor/gauge values and find which table agrees best with them.
30. Report the condition of the actual physical system in real time.

While the development of a rule based system is very tedious if done by hand (as in our experiments), it can be automated once developed. The deployed procedure is in principle very fast, since it only uses look-up tables. Using the design, we can (and did) investigate some of the problems that are likely to arise using other machine learning formats, e.g., neural nets. We experimented on

deriving samples from a simulated system, segmenting variables, forming look-up tables or lists, and using the tables or lists to identify failures in new data from simulated malfunctioning systems.

SORCER looks at a range of values for several variables of interest and then, for each parameter, creates a predefined number of discrete states that span these ranges. All the values for a single parameter occupy one column of this table while each row contains the values of all the system variables during a single snapshot of time. In essence, each row would represent a particular state of the system. So if we run a simulation of our distillery with predefined values for our three forcing parameters and no faults, and then let our system visibly settle into a steady state for some assuring length of time, we can then pause the simulation to retrieve the current parameter values from the buffer and enter them as a row in a table representing the steady states of a healthy chemical plant. Similarly, to determine the combinations of parameter values that would indicate a failure of some sort, we would introduce the fault into our model and proceed to vary the forcing parameters over as much of the previous range as possible.

This is exactly the procedure used to collect the data characteristic to the model of interest. Two of the three forcing variables were held constant while the third was varied over a range of stable values. Once exhausted, one of the other two parameters is varied slightly, and our remaining parameter travels the spectrum again. All simulations were monitored to be sure they did in fact result in a stable, non-wavering set of system values. A normal looks like the following, where the fifth column represents 21 additional columns.

Feed rate	Temperature	Steam	Toluene purity	Parameters	Fault
8,000	88	4,000	98%	…	None
8,100	88	4,000	97%	…	None
8,200	88	4,000	96.4%	…	None
….	….	….	…	…	None
11,000	91	4,300	98%	…	None

Abnormal data tables have the same structure, but generally with different numbers in fourth and fifth columns, and the fault column contains a specification of the particular failure or failure modes under which the data are produced.

Once this data collection is done for the standard operation case and those system failures one is concerned with, it is anticipated that our program could detect any combination of forcing parameters and degree of failure within the ranges already simulated. After choosing an appropriate scenario, the simulation is started and data is collected for analysis. A buffer containing values of the important parameters discretized based on the ranges contained in the table representing normal operation, and similarly for the failure tables. Then, each row of our new table is labeled, under the paradigm of standard operation, as a state the system has occupied within the window of time our buffer length represents. Many of these states are the same within the discretization, so SORCER is used to compress the table down to those which are unique. The standard or normal operation table is then referenced to see if it contains any entries equal to those derived from the current simulation buffer. If the current model contains a fault, one would expect to find these states not in the standard table, but in the failure table that correlates most closely to the failure in question. Also, the standard table and each of the failure tables should, so far as possible, be mutually exclusive of one another. That is, none should share common entries with any other.

Thus, SORCER might produce from the normal data table a simple rule of the form:

If 8000 < Feedrate < 11,000 & 88 < Temp < 91 & 4,000 < Steam < 4,300 & [normal parameter ranges] then NORMAL

A fault detection rule has the same form but with different values, and, of course, the consequent of the conditional specifies the particular fault or faults.

In practice because of discretization and because ranges of values produced by various normal or abnormal conditions are not continuous, SORCER produces a set of rules for the normal case, and a set of rules for each abnormal case. If particular parameters are irrelevant to a normal or abnormal functioning, they do not occur in the corresponding rule set. The rule sets constitute the tables for monitoring the health of the system and diagnosing faults.

While collecting data for the standard operation table, the first forcing parameter, the raw material feed rate, was incremented from 8,000 through 11,000 lb/hr in steps of 100. The temperature of the distillation column, as measured at the middle tray of the column, ranged from 88 through 91 ◦C in single degree increments. Finally, the amount of steam flowing to the Reboiler, which reheats the fallen product that is reintroduced into the distillation column, was varied from 4,000 through 4,300 lb/hr in increments of 100. Instead of having produced 496 entries, the total is 355. This is due to the fact that a large minority of the simulations did not result in steady state conditions.

In one of the faults on which this study focused the Reboiler experienced some type of clogging due to contaminants or a general inefficiency in thermal coupling, simply not transferring heat to the material. The coupling parameter for standard operation is $8x10^4$Btu/F*hr while the value chosen for the fault is $2.67x10^4$Btu/F*hr. Due to time constraints, two of the forcing variables were kept constant while only the feed rate was changed. The feed rate went from 8,000 to 11,000, as before, but the column temperature was held at 90 ◦C, and the flow of steam was fixed at 4,100 lb/hr. An enlarged view of the portion of the system with the Reboiler is shown in the following figure.

The second fault was loss of condenser water. This was implemented by closing valve HV3-3 that slows the amount of cold water flowing through the Condenser. Instead of one level of failure, the severity of this fault was varied. The valve, which is normally open half way, was opened to 45, 40, and 35 percent. For each setting of the valve, the feed rate was varied from 8,000 to 8,500 lb/hr to produce eighteen entries in this second fault table. An enlarged view of the portion of the system containing the Condenser is shown in figure 10.

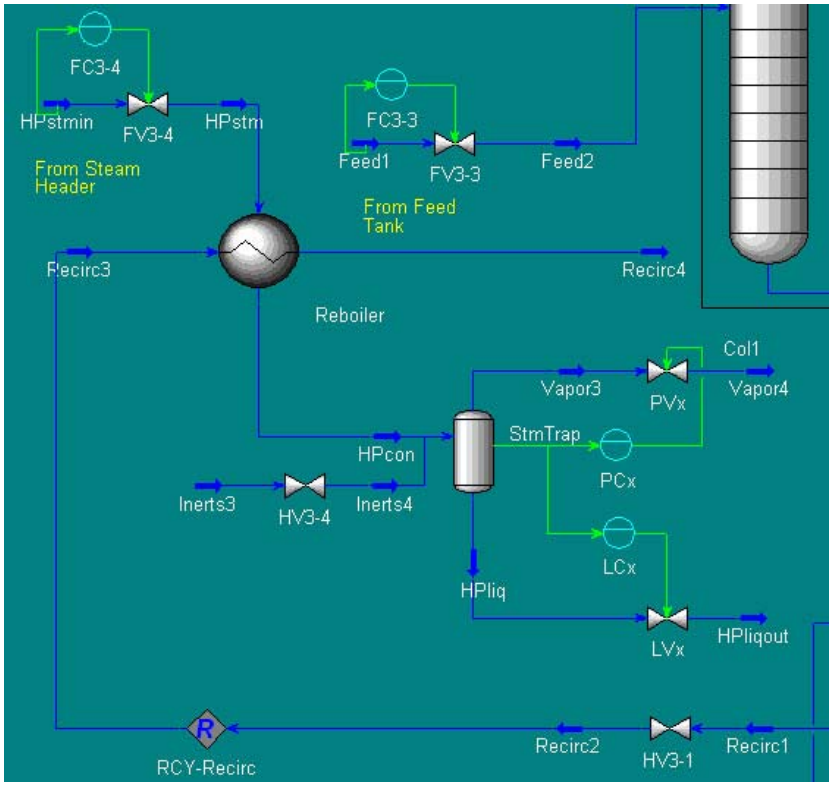

Figure 9.—Simulated system in the vicinity of the reboiler.

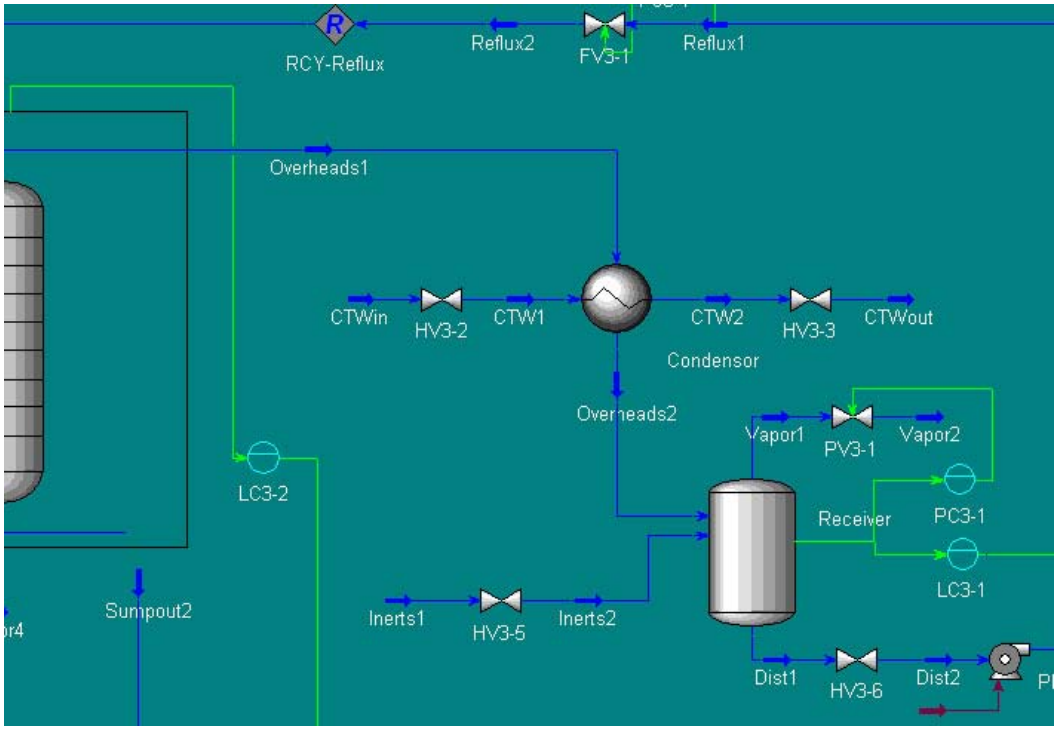

Figure 10.—Simulated system in the vicinity of the value closed to simulate loss of condenser water.

The variables needed to monitor the health of the system comprise a set of twenty-five quantities, including the variables which describe the forcing parameters, most of which were utilized by a particular chemical engineer in his own research. These variables included the levels of both Toluene and Benzene in each of the final products, for purity, the amount of each product produced in a given unit of time, and the level of engagement of each controller responsible for these quantities. Also of importance were the temperatures and pressures at the top and bottom of the distillation column, as well as the activity level of the controller responsible for the temperature at the center of the distillation column. It was necessary to consider the amount of product flowing through various components of the chemical plant, such as the flow from the top or bottom that reenters the column.

Another point of interest is the number of discrete states allowed for each variable. This is determined by how SORCER discretizes the standard table, and the user can set it. In particular, discrete levels of three through six states for each variable were looked at closely. Since one is trying to approximate the behavior of complex, non-linear functions with piecewise rules, the discretizations chosen are critical for accuracy. In general, one would expect to need much finer discretizations than those used in our experiments.

It is important to emphasize that the rule sets for a normal or abnormal condition need not all use the same discretization—different discretizations of variables and parameters may be useful for the discrimination of circumstances producing a fault.

Twelve sample simulations were run to test the three rule tables, four for each table. One of the more successful levels of discretization was five, which means five possible values for each variable. Although it did not have the largest number of successes, six, it did lead to no overlap in any of the three rule tables. The other three levels all lead to a single, shared entry between the standard operation and Condenser fault tables. The next best level would be four, with eight successes. A level of three produced seven successes, and there were six successes at the sixth level.

The first standard operation sample was chosen such that the values of the three forcing parameters would lie well within the ranges represented in the respective rule table, as with the rest of the samples. In particular, the triple in question is (89.5, 4150, 8950). It lie's between two exact entries in the rule table. The upper bound is (90, 4200, 9000) while the lower bound is (89, 4100, 8900). This sample was not detected at any level of discretization. The next sample has a triple with values that are closer to an entry in the table. The sample is (88.85, 4175, 9120) and it is closest to the table entry (89, 4200, 9100). This

was not detected in any situation either. The third triple, with values (89.1, 4180, 9120), was closer than the last sample to its neighbor in the table, and it was not detected as well. The final triple (89, 4200, 9100) was picked to be an exact entry in the table, and it was successfully detected at every level of discretization.

The samples corresponding to a decrease in Reboiler efficiency were the most highly detected of all the test samples. The standard thermal coupling of the Reboiler is $8x10^4$, but it was set to $2.67x10^4$in the first sample, the same as that in the fault table. The triple (90, 4100, 8362) was used in each of the four cases. The first two parameters are the same as in the rule table because their values were not varied in the table itself, but the third value was varied and the sample value lies within the range expressed. The first sample was detected at all discretization levels. The second sample, with a coupling of $3x10^4$, was not detected at a level of five, but it was detected at three, four, and six. The third sample had a coupling of $2.70x10^4$, which is significantly closer to the fault in the table. It was detected at all levels, as was the fourth sample with a coupling of $2.80x10^4$.

The Condenser normally operates with a cold-water valve open at 50 percent. The forcing parameters in this fault table were varied over the same range as in the last. That is, the first two values were held at 90, and 4100, while the third value lies between 8,000 to 8,500. The first sample has a triple of (90, 4100, 8372) with the valve open at 38 percent. This sample was only detected at a level of four. The second sample had the same triple, but the valve was open 40 percent, one of the exact values of failure in the table. This sample was detected at every level of discretization. Next was a triple of (90, 4100, 8300), one of the exact triples found in the table, but it carries a failure value of 42 percent. It was not detected by any level of discretization. The fourth and final triple (90, 4100, 8146) had a 40 percent value of failure. This was detected in every level of discretization except six.

Remembering that rules for the normal or for a fault condition need not all have the same discretization of variables, we can summarize the results in a simple table:

Condition	Normal	Reboiler fault	Condenser fault
% of cases detected	25	100	75

The performance is poor, but not surprising, for the Normal case. What it shows is that a much finer discretization is needed to provide a rule set that captures the standard operating cases. That in turn indicates the need to fully automate loops in which simulated data is generated, rules are derived, new normal and abnormal simulated data are generated and used to test the rules , and new data generated, etc. The procedure and problem naturally lends itself to boosting techniques, in which the data used for training in any loop are exactly or nearly those cases on which the rule sets failed in earlier loops., What is surprising, to us anyway, is how well the simple discretizations used in these experiments capture the faults.

Shuttle Tanking and Launch Safety Monitoring Research

For the second year of research, we adapted our chemical process monitoring software agents to also operate with the shuttle tanking and launch system. Our KSC contacts for this project provided the PC Ground Operations and Logistics (PCGOAL) trace-based simulation tools which enabled us to play back and monitor actual operations data recorded from over 20,000 sensors during the fueling and launch of STS-113 from T-7 hr through T+1 hr. Significant enhancements were also made to the monitoring software for the shuttle application involving describing monitoring conditions to agents, more powerful monitoring condition evaluation capabilities, and the ability to manage and control the resulting dynamic population of agents. We have taken a human-centered approach to monitoring automation that complements the user's ability to identify relevant monitoring contexts with the software agent's ability to rapidly and vigilantly assess the process state. This frees our agents from needing complete and accurate models of the systems being monitored and also distinguishes our work from related multi-agent approaches to chemical and manufacturing systems diagnostics.

A brief description of KARMEN is followed by more detailed coverage of recent results involving how users describe process conditions to agents, how the resulting ad-hoc population of agents are deployed and managed by the framework, and the role of ontologies and policies in creating and controlling these agents. From the users' perspective, KARMEN is a desktop application for creating and deploying

software agents to continuously monitor a process and notify the user as the conditions obtain and abate. Agent creation begins with condition specification. The user browses the space of sensors, valves, and other control elements comprising the process and selecting among the data streams each component provides. We apply semantic web techniques to provide rich and flexible descriptions and classifications of sensors through both enumeration and common properties such as type, limits, capabilities, location, and status. The user next selects the control elements to monitor, then uses a graph-based interface to assemble the process variables into a logical expression. For example, liquid hydrogen (LH_2) leak sensors are placed at intervals along a shuttle fueling line in pairs of primary and secondary (SEC) detectors. In this case there are over 50 sensors to monitor that are individually very sensitive and therefore prone to false positives. The graph in figure 11 expresses the condition that the high or low limit has been exceeded for a pair of primary and secondary LH_2 leak sensors concurrently. The same expression is also depicted in formula 1. The user launches the agent into the KARMEN system where the agent survives indefinitely monitoring the process conditions and notifying the user. Perhaps through the KARMEN application if it is running, otherwise through email, text pager, or other modes.

$$(P1 \geq Phi \;\&\; S1 \geq Shi) \mid (P1 \leq Plow \;\&\; S1 \leq Slow) \mid (P2 \geq Phi \;\&\; S2 \geq Shi) \mid \ldots \qquad (1)$$

From a systems perspective, KARMEN is a set of host environments configured to run these agents as well as a collection of services for managing them and the resources they consume. When a new agent is requested a central coordinator service determines where the agent is deployed based on the components referenced, the monitored condition expression and its sub-expressions, as well as available host resources and overlap with existing agents. The coordinator service establishes data feeds among agents and can move agents from host to host to balance processing and network load as well as keeping the agents running. Policies play an important role in restricting user access to sets of components, setting constraints on the resources agents are allowed to consume, and defining preferences concerning how the notification service will deliver messages.

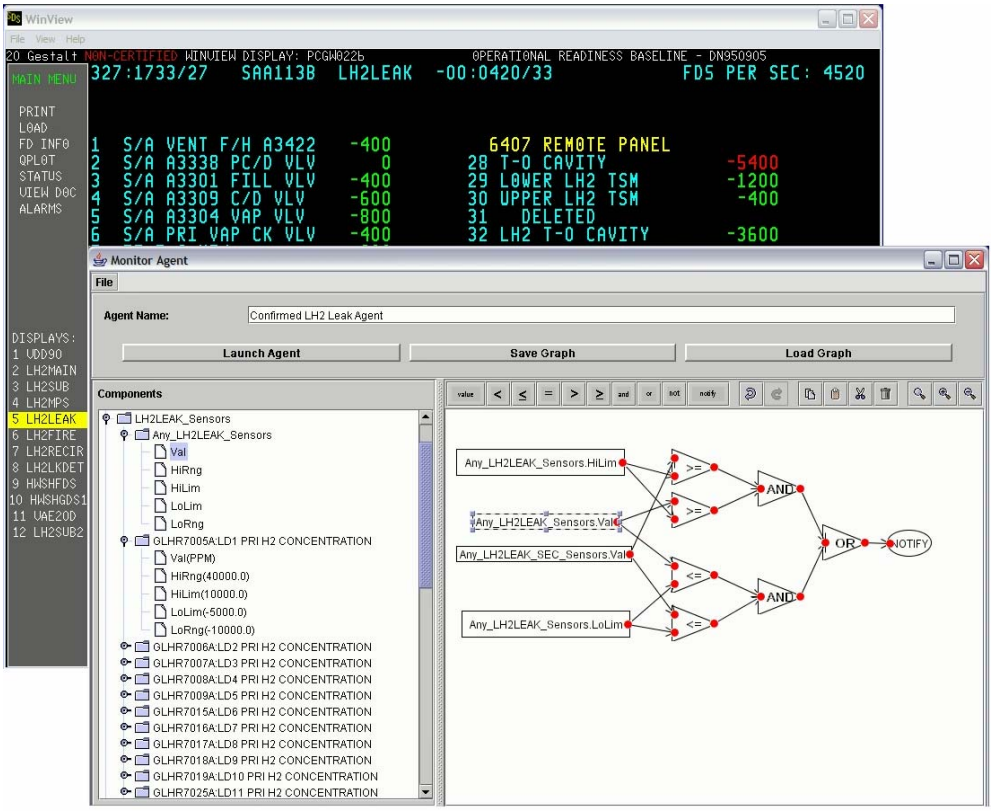

Figure 11.—Users construct graphical expressions to describe process conditions to monitoring agents, in this case involving the set of values from the operator screen shown in the background.

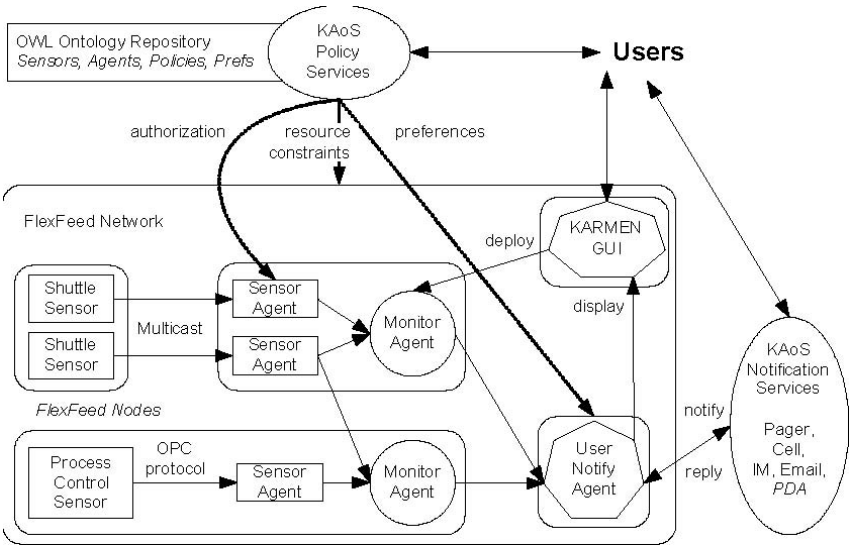

Figure 12.—A high-level depiction of the relationships among KARMEN system components

Architecture

KARMEN relies upon multi-agent frameworks developed at IHMC to manage and control its Java agent population as shown in figure 12. The FlexFeed agile computing framework provides mobile agent hosting, networking, and coordination. The KAoS policy framework provides tools and services for defining polices that constrain agent actions and resource usage as well as oblige agent actions including user notification. KARMEN and KAoS both rely upon semantic web ontologies developed using the W3C standard Web Ontology Language (OWL). KAoS also provides an extensible base ontology with services to query the ontology.

FlexFeed Agent Networking Framework

Flexible Data Feeds

Flexible Data Feeds (FlexFeed) is a Java agent framework that facilitates communication between agents and manages the computing and network resources within a distributed multi-agent system (refs. 21 and 22). KARMEN agents rely on the FlexFeed API for mobile deployment and access to information feeds among heterogeneous sensor, intermediate, and user nodes. FlexFeed supports policies that restrict communication among agents and limit agent resource usage. The transport mechanism, message distribution, and filtering are each handled at the framework level, hiding these implementation details from the data producers and consumers. This architecture allows the framework to transparently customize the routing and transformation data streams while abstracting from the agent the tasks associated with the protocol selection, policies, and load balancing. Multiple communication protocols and lookup services can coexist in the network and FlexFeed will determine what protocols to use in order to distribute messages between any two nodes. This API provides two main components: the FlexFeed Manager, that handles agent lookup and delivery of data, and the FlexFeed Coordinator which is the intelligent component that is responsible for establishing and maintaining data streams in the framework. The Coordinator distributes processing load and bandwidth consumption across the framework preserving the resources on the nodes. Upon multiple requests on the same sensor, the Coordinator has the ability to discover and use intermediate processing nodes to minimize the network bandwidth and improve load balancing.

KAoS Policy Services

KAoS is a collection of policy services compatible with several software agent and robotic frameworks, as well as traditional distributed services platforms (e.g., CORBA, Web Services, Grid Computing) (refs. 7 to 10). In the context of KARMEN, KAoS is used to define, manage, deconflict, and enforce policies restricting agent access to sensor data, bounding agent resources, and governing the mode of notification to users. The KAoS Policy Ontologies (KPO; http://ontology.ihmc.us/) are represented in the W3C standard Web Ontology Language (OWL) (ref. 23). KAoS relies on an integrated theorem prover along with KAoS-specific extensions to support representation and reasoning about policies. The current version of KPO defines basic ontologies for actions, actors, groups, places, various entities related to actions (e.g., computing resources), and policies. As the application runs, classes and individuals corresponding to new policies and instances of application entities are also transparently added and deleted as needed. Through various property restrictions, a given policy can be appropriately scoped to various domains, for example, either to individual agents, to agents of a given class, to agents belonging to a particular group, or to agents running in a given physical place or computational environment. Additional aspects of the action context can be precisely described by restricting values of its properties. Groups of people, agents, and resources are also structured into ontologies to facilitate policy administration.

OWL Ontology Representation and Reasoning

Our system employs OWL to organize and classify process components, monitoring states, notification modes and salience, as well as users and organizational roles. OWL is a powerful description logic-based language developed for the semantic web. It provides vocabulary for describing properties and classes including relations between classes (e.g., disjointness), cardinality (e.g., “exactly one”), equality, rich typing of properties, characteristics of properties (e.g., symmetry), and enumerated classes. Combined with the reasoning capability of Stanford’s Java Theorem Prover (JTP; http://www.ksl.stanford.edu/software/jtp/), these ontologies enable users to effectively describe sophisticated monitoring conditions in a way that is accessible to agents. To make the use of OWL simple to non-specialist users, a number of graphical user interfaces have been defined. We employ ontological classifications of process control components and events for expressing potentially large and complex aggregate monitoring conditions. to dynamically define custom limits and alarm conditions that were previously only predefined in the control system.

Process Monitoring

Some key challenges in monitoring automation include enabling users to easily describe conditions of interest to the monitoring software, allowing users to dynamically change the conditions being monitored without affecting the process control, automatically changing the monitored conditions in response to changes in the process state, efficiently evaluating the system state for the given conditions, and effectively communicating the process state back to the user Describing Process Conditions.

Describing Monitor Conditions

KARMEN users define process conditions for agents using a graph-based tool to build expressions concerning process state as shown in figure 11. Users browse for individual sensors or classes of sensors and add these inputs to the graph. Nodes are then selected to compare, combine, and transform these sensor inputs into a logical expression. When the user launches the agent, each sub-expression can be assigned to an existing agent in the FlexFeed network for evaluation or new agents be created as needed. One particularly valuable aspect of the research involves enabling users to monitor complex and aggregate process conditions that could not previously be monitored at runtime. Defining ontologies of process variables in OWL enables users to organize and classify sensors by relevant properties to easily express complex monitoring conditions for groups of related sensors (e.g., monitor for any sensor value from shuttle main engine one that exceeds 90 percent of its associated high alarm limit). Using ontological classes in monitoring expressions allows users to define complex aggregate conditions concisely. For example, the class of “all sensors on main engine one with a high limit value” can be constructed in the ontology based on the common properties of individual sensors such as location and

limits. Such an ontology class can then be incorporated into a monitoring expression such as “sensor current value greater than 90 percent of sensor’s high limit.” This allows users to define conditions at a variety of scopes from the very narrow and specific to system-wide.

Monitoring Capabilities

The most basic capabilities of the process monitoring agents for this system include comparing process variables to scalar values and other process variables (e.g., monitor for a valve’s actuator position greater than its predefined high alarm limit). We effectively extend the alarm functionality commercial control systems provide with the added value of making this capability available for ad-hoc and remote use. The ability to inject new conditions non-intrusively into an operational environment is critical. We further incorporate monitoring statistical summaries of sensor behavior including standard deviation, variance, mean, and rate of change over a given time period or number of samples. Users can also employ mathematical expressions to derive new aggregate conditions (e.g., monitor the product of pressure and temperature sensor readings), annotate process variables such as defining progressive high and low limits, and access system annotations such as maximum, minimum, and average observed values from historical data. These feature support live, flexible monitoring using new combinations of parameters not inherent in the control system. Adding remote monitoring capabilities carries the responsibility to control access to sensitive data. The KAoS policy services leverage the ontologies defined for classifying sensors to also define and enforce authorization policies that restrict access to process data such as “IHMC personnel can only access sensors in the shuttle main engine class” which will deny authorization to access feeds from these sensors to all agents created by IHMC personnel. Such policies could also describe reductions of sampling rate or precision which the agents would enforce.

User Notification

Notifications are generated as the monitored conditions obtain and abate. The mode, salience, and recipients of each notification are governed by KAoS policies representing organizational requirements and users’ personal preferences. Notification modes may include E-mail, Instant Message, Pager, and Operator Displays. Notification policies typically cover such factors as event type, severity, the recipient’s organizational role and presence, and the plant area in which the event occurred. For example, a policy might be to “page an onsite Field Operator immediately when a critical H_2 Plant monitored condition is satisfied and the Process Engineer is unavailable.” The selection of mode, recipients, and salience is made at runtime based on information gathered about the user’s presence and the modes available (e.g., the user’s instant message client indicates user is available and the user’s schedule indicates she is onsite).

The default behavior of the Notification agent is to display messages in the KARMEN application interface. All other notification actions are governed by KAoS policies representing organizational requirements and personal preferences. Each policy obliges the notification agent to take certain actions based on the qualities of the monitored event and the current disposition of the concerned personnel. We have developed a set of initial ontologies depicted in figure 13 for notification that draws heavily on the work of Schrekenghost and colleagues (ref. 11).

The current event characteristics that can trigger a policy include the event type (satisfied/unsatisfied condition, activated/deactivated alarm: see ConditionStatus in fig. 13), the assigned event severity (critical, warning, advisory, log), and the plant area in which the event occurred based on the component hierarchy defined in the ontology. The user characteristics that can trigger a policy include the user’s organizational role (operator, process engineer, area manager, etc.) and the user’s current physical and computational presence (nearby/remote, online/offline: see fig. 13). The qualities of the notification action that policies can oblige include the mode, latency, and focus of attention. Notification modes currently include e-mail, instant message, pager, operator displays, and the IHMC Monitor application. The latency quality controls how quickly the user is notified (immediate, deferred, archive). The focus of attention quality controls how forcefully the user’s attention is obtained and depends on the features available in each notification mode (e.g., instant message chat session that interrupts the user versus a queued message in the background).

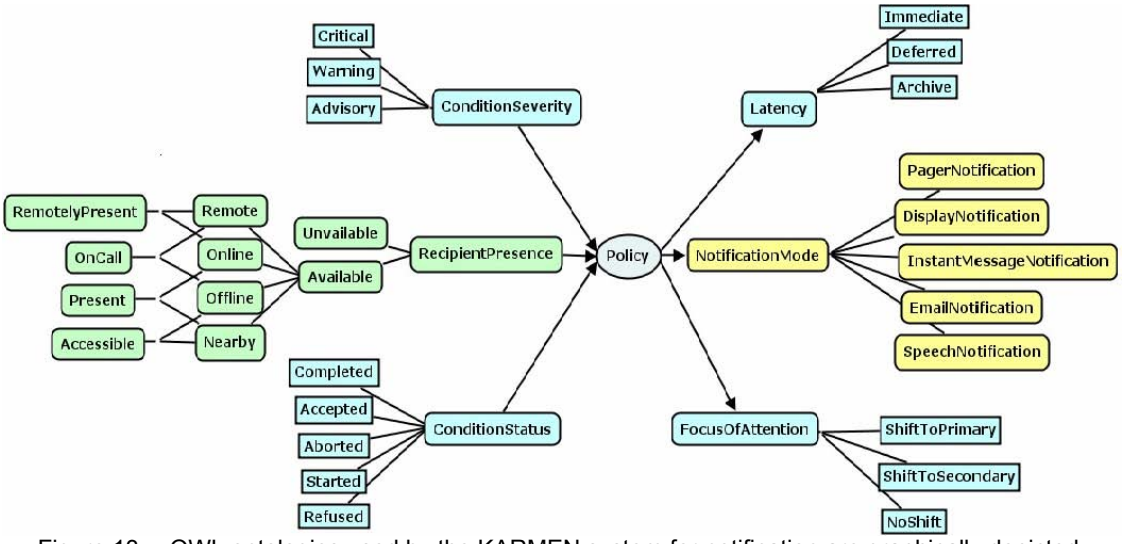

Figure 13.—OWL ontologies used by the KARMEN system for notification are graphically depicted.

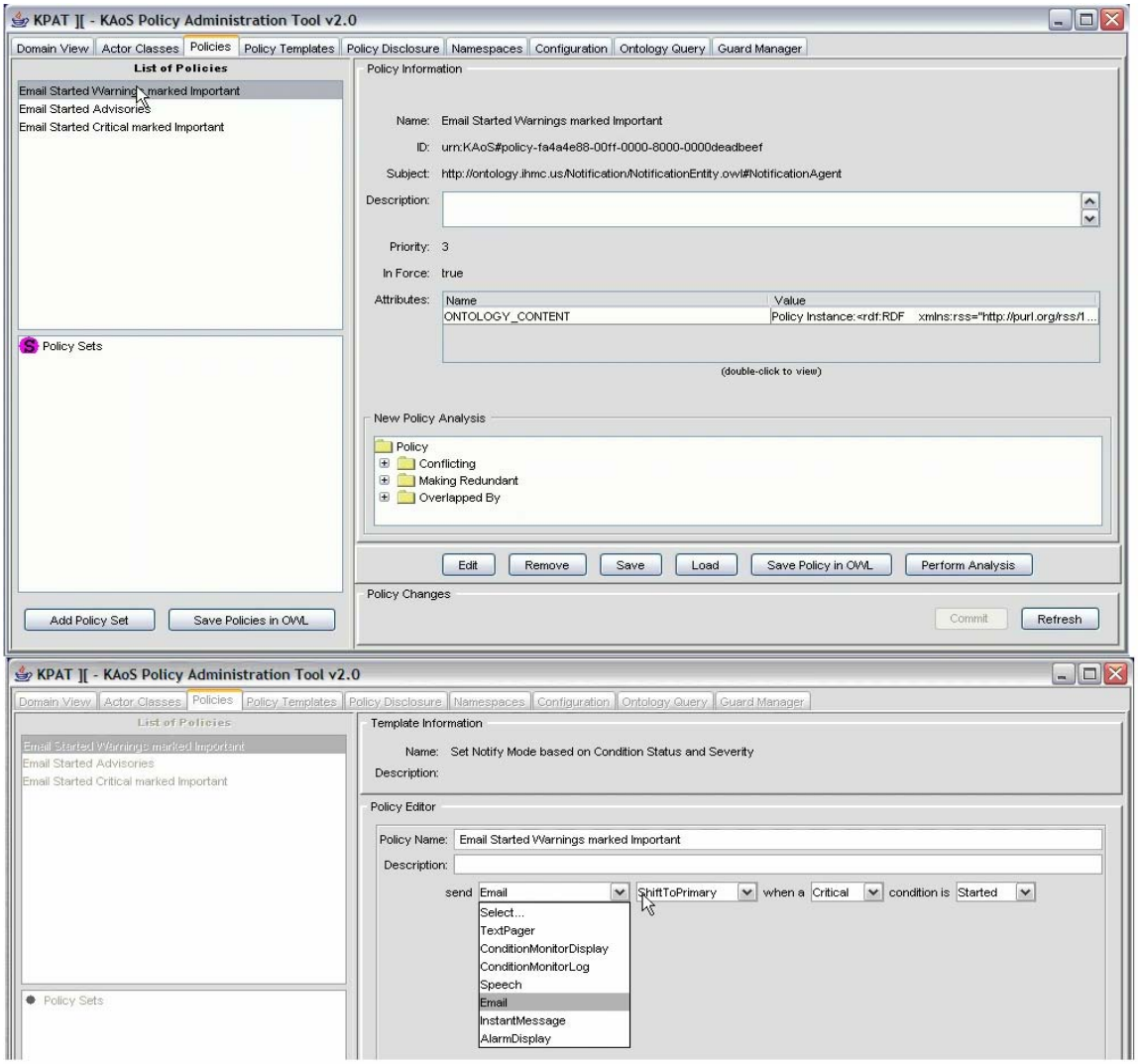

Figure 14.—The KAoS Policy Administration Tool (KPAT) screen displaying a sample set of policies that govern notification modes in the KARMEN system.

The notification obligation policies are created using the KAoS Policy Administration Tool (KPAT) shown in figure 14. The attributes of the policy are from the ontological concepts shown in figure 13. Multiple policies can apply to a single event such as using the pager mode for critical events, using the instant message mode for critical events when the user is online, and using the primary focus of attention for critical events. Each policy is assigned a priority. KAoS uses the priority to resolve policy conflicts thereby enforcing organizational policies over personal preferences. The user notification agents can require and obtain acknowledgement of notifications and escalate the notification mode and recipients when acknowledgement is not received in a specified timeframe. In the near future, agents will select notification mode and salience based on the recipient's responsiveness to previous notification attempts by learning the most effective mode of contacting each user according to the time, user presence, and condition severity. Monitoring agents can begin recording a set of sensor values when the specified conditions obtain, stop recording when the conditions abate (or after a certain duration), then include a graph of the recorded data as an attachment to electronic notifications. Summaries could be extended to several formats including movies, spreadsheets, and PDF files.

Conclusions

The work reported herein represents several unique accomplishments. By bringing to bear modern developments in Computer Science we have (1) implemented the first procedure that can enable designers to make optimal design decisions for plant diagnostics in the simulation environment (e.g., sensor type and placement); (2) developed the first methodology that permits user-specified, multimodal communication of off-nominal plant behavior. These new capabilities are important in their own right, and they also suggest future work that will further augment the capability to monitor and diagnose the health of the most complex plants of all types.

The KDD work makes clear the desirability of automating data generation and evaluation in the simulation environment. Because of the interdependence of component behavior, plus noise, for example, sampling density—or discretization level—will have to be identified empirically through several cycles of data generation, sampling and testing. Equally, an automated system of software generation must determine empirically when it is looking at transient simulated data and when it is looking at steady state data—and the same criteria must be embedded in deployed software. Engineering knowledge can help with these judgments, but our experiments show that accuracy can be quite sensitive to how sample data are obtained and discretized. These conclusions apply no matter whether one is using rule-based machine learning algorithms, Bayes net estimators, neural nets, or other procedures to generate the anomaly detection and failure diagnosis software.

Within the Software Agent context the potential utility for root cause analysis needs to be further investigated, as does the automation of such tasks as loop turning, alarm prediction and prevention, lock-out/tag-out maintenance procedures, and component reliability assessments.

Finally, the potential synergism of KDD and Software Agents warrants investigation. It may be, for example, that the former offers advantages for root cause analysis that could be integrated with Software Agent capabilities for user notification.

References

31. Aspen Technologies Hysys Dynamics (http://www.aspentech.com).
32. Emerson Process Management DeltaV Distributed Control System (http://www.easydeltav.com).
33. OLE for Process Control. (http://www.opcfoundation.org).
34. F.M.T Brazier, B. Dunin-Keplicz, N.R. Jennings, J. Treur. Modelling Distributed Industrial Processes in a Multi-Agent Framework. In: G. O'Hare, S. Kirns (eds.), Towards the Intelligent Organisation: a Coordination Perspective, Springer Verlag (1996).
35. N.R. Jennings, S. Bussmann: Agent-Based Control Systems. IEEE Control Systems Magazine 23(3). (June 2003).
36. B. Köppen-Seliger, S.X. Ding, P.M. Frank: EU IST Programme: Proposal Submission and Two Successful IAR Initiatives "MAGIC" and "IFATIS." Plenary lecture IAR annual meeting, Strasbourg, 2001.

37. J.M. Bradshaw, P. Beautement, L. Bunch, S.V. Drakunov, P. Feltovich, R.R. Hoffman, R. Jeffers, M. Johnson, S. Kulkarni, A.K. Raj, N. Suri, A. Uszok: Making Agents Acceptable to People. In N. Zhong and J. Liu (Eds.), Intelligent Technologies for Information Analysis: Advances in Agents, Data Mining, and Statistical Learning, Berlin: Springer Verlag, in press, (2003).
38. M. Johnson, P. Chang, R. Jeffers, J. Bradshaw, V-W. Soo, M. Breedy, L. Bunch, S. Kulkarni, J. Lott, N. Suri, A. Uszok: KAoS Semantic Policy and Domain Services: An Application of DAML to Web-Services-based Grid Architectures. Proceedings of the AAMAS 03 Workshop on Web Services and Agent-Based Engineering, Melbourne, Australia, (July, 2003).
39. A. Uszok, J. Bradshaw, R. Jeffers, N. Suri, P. Hayes, M. Breedy, L. Bunch, M. Johnson, S. Kulkarni, J. Lott: KAoS policy and Domain Services: Toward a Description-logic Approach to Policy Representation, Deconfliction, and Enforcement. In Proceedings of IEEE Fourth International Workshop on Policy (Policy 2003). Lake Como, Italy, 4-6 June, Los Alamitos, CA: IEEE Computer Society, pp. 93-98, (2003).
40. J.M. Bradshaw, A. Uszok, R. Jeffers, N. Suri, M. Burstein: Representation and Reasoning for DAML-based Policy and Domain Services in KAoS and Nomads. Proceedings of the Autonomous Agents and Multi-Agent Systems Conference (AAMAS 2003). Melbourne, Australia, New York, NY: ACM Press, pp. 835-842, (2003).
41. D. Schreckenghost, C. Martin, C. Thronesbery: Specifying Organizational Policies and Individual Preferences for Human-Software Interaction. In: Etiquette for Human-Computer Work, Papers from the AAAI Fall Symposium. Technical Report FS-02-02, AAAI Press (2002).
42. T.L. Blevins, G. K. McMillan, W. K. Wijsznis, M. W. Brown: Advanced Control Unleashed Plant Performance Management for Optimum Benefit. The Instrumentation, Systems, and Automation Society (2003).
43. J.D Moffett, J.A. McDermid: Policies for Safety-Critical Systems: the Challenge of Formalisation. Fifth IFIP/IEEE International Workshop on Distributed Systems: Operations and Management, Toulouse, France, (Oct. 1994).
44. JADE. http://jade.cselt.it, Java Agent DEvelopment Framework
45. FIPA. http://www.fipa.org, Foundation for Intelligent Physical Agents
46. Uri N. Lerner, Hybrid Bayesian Networks for Reasoning about Complex Systems, Ph.D. Thesis, Stanford University, (October 2002).
47. Uri Lerner, Brooks Moses, Maricia Scott, Sheila McIlraith, Daphne Koller Monitoring a Complex Physical System using a Hybrid Dynamic Bayes Net, Proceedings of the 18th Annual Conference on Uncertainty in Artificial Intelligence (UAI-02) Edmonton, Canada, (August 2002).
48. R. Hewett and J. Leuchner, Second-order Relations and Decision Tables, Technical Report 97-27, CSE Department, Florida Atlantic University, Boca Raton, FL, (1997).
49. R. Hewett and J. Leuchner, A Local Joinability Condition and a Computational Technique for Second Order Relations and Decision Tables, Technical Report 97-54, CSE Department, Florida Atlantic University, Boca Raton, FL, (1997).
50. J. Leuchner, and R. Hewett, A Formal Framework for Large Decision Tables. In Proceedings of International Conference of Knowledge Retrieval, Use, and Storage for Efficiency Symposium (KRUSE' 97), 165-179, (1997).
51. M. Carvalho and M. Breedy, "Supporting Flexible Data Feeds in Dynamic Sensor Grids Through Mobile Agents." In Proceedings of the 6th International Conference in Mobile Agents, Barcelona, Spain, October 2002.
52. N. Suri, J.M. Bradshaw, M. Breedy, P. Groth, G. Hill, R. Jeffers, and T. Mitrovich, "An Overview of the NOMADS Mobile Agent System," Sixth ECOOP Workshop on Mobile Object System. Available: http://cui.unige.ch/~ecoopws/ws00.
53. J. Hendler, T. Berners-Lee and E. Miller, "Integrating Applications on the Semantic Web," Journal of the Institute of Electrical Engineers of Japan, vol. 122(10), October, 2002, pp. 676-680.
54. L. Bunch, M. Breedy, J.M. Bradshaw, M. Carvalho, N. Suri, A Uszok, R.J. Hansen, M. Pechoucek, and V. Marik. Software Agents for Process Monitoring and Notification. In Proceedings of the 2004 ACM Symposium for Applied Computing. March 2004.
55. L. Bunch, M. Breedy, J.M. Bradshaw, M. Carvalho, D. Danks, N. Suri. Flexible Automated Monitoring and Notification for Complex Processes. Proceedings of the IEEE International Conference on Networking, Sensing, and Control. March 2005.

Appendix A

Linan An
Professor
University of Central Florida
4000 Central Florida Boulevard
Orlando, FL 32816
407-823-1009
lan@pegasus.cc.ucf.edu

Nagaraj Arakere
University of Florida
104 MAEC
Gainesville, FL 32611-6300

Upendra Avachat
Researcher
Florida Solar Energy Center
1679 Clearlake Road
Cocoa, FL 32922-5703
321-638-1229
uavachat@fsec.ucf.edu

Colin Bateman
Professor
Brevard Community College
1519 Clearlake Road
Cocoa, FL 32922
321-433-7618
bateman@brevardcc.edu

Shekhar Bhansali
Assistant Professor
University of South Florida
4202 E. Fowler Avenue
Tampa, FL 33620
813-974-2897

Venkat Bhethanabotla
Associate Professor
University of South Florida
4202 E. Fowler Avenue
Tampa, FL 33620
813-974-2897

Gary Bokerman
Asst in Hydrogen
Florida Solar Energy Center
1679 Clearlake Road
Cocoa, FL 32922-5703
321-638-1428
gbokerman@fsec.ucf.edu

Ken Buckle
Professor
University of South Florida
4202 E. Fowler Avenue
Tampa, FL 33620
813-974-2897

D. Celik
Assistant Instructor
Florida State University
300-Magnet Lab, Mail Code 2740, 1800 E. Paul
Dirac Drive
Tallahassee, FL 32310-3706
850-644-0867
dcelik@magnet.fsu.edu

Quanfang Chen
Assistant Professor
Unviersity of Central Florida
4000 Central Florida Boulevard
Orlando, FL 32816
407-823-2152
qchen@mail.ucf.edu

Hyoung-Jin Cho
Assistant Professor
University of Central Florida
4000 Central Florida Boulevard
Orlando, FL 32816
407-207-7245
joecho@mail.ucf.edu

Louis Chow
Professor
University of Central Florida
ENG2, P. O. Box 162450 - ENGR I 219,
Mechanical, Materials and Aerospace Engineering
Orlando, FL 32816-2450
407-823-3666
lchow@mail.ucf.edu

Neelkanth Dhere
Program Director
PV Division
Florida Solar Energy Center
1679 Clearlake Road
Cocoa, FL 32922-5703
321-638-1442
ndhere@fsec.ucf.edu

Yogi Goswami
Director, Florida Energy Research Institute
University of South Florida
ENB 260A, Department of Chemical Engineering,
4202 E. Fowler Avenue
Tampa, FL 33620
813-974-0956
goswami@eng.usf.edu

Vinaykumar Hadagali
Researcher
Florida Solar Energy Center
1679 Clearlake Road
Cocoa, FL 32922-5703
321-638-1229
vhadagali@fsec.ucf.edu

Chan Ham
Assistant Research Scholar
University of Central Florida
4000 Central Florida Boulevard
Orlando, FL 32826
407-658-5598
cham@mail.ucf.edu

Michael Hampton
Associate Professor
University of Central Florida
4000 Central Florida Boulevard
Orlando, FL 32816
407-823-2136
mhampton@mail.ucf.edu

D. Hilton
Postdoctoral Associate
Florida State University
300-Magnet Lab, Mail Code 2740
1800 E. Paul Dirac Drive
Tallahassee, FL 32310-3706
850-644-1703
dhilton@magnet.fsu.edu

Mohamed Hussaini
Professor
Florida State University
218 Love Building
Tallahassee, FL 32310
850-644-0601
myh@csit.fsu.edu

Anant Jahagirdar
Researcher
Florida Solar Energy Center
1679 Clearlake Road
Cocoa, FL 32922-5703
321-638-1229
ajahagirdar@fsec.ucf.edu

J. Justak
Advanced Technologies Group
377 E. Butterfield Road
Suite 900
Lombard, IL 60148
630-964-9700

Jay Kapat
Professor
University of Central Florida
4000 Central Florida Boulevard
Orlando, FL 32816
407-823-2179
jkapat@mail.ucf.edu

Burt Krakow
Senior Research Associate
University of South Florida
Electrical Engineering Department, 4202 E. Fowler
Avenue, ENB 118
Tampa, FL 33620-5350
813-974-4784
krakow@eng.usf.edu

Clovis Linkous
Senior Research Scientist
Florida Solar Energy Center
1679 Clearlake Road
Cocoa, FL 32922-5703
321-638-1447
calink@fsec.ucf.edu

George Moore
Senior Research Associate
University of South Florida
4202 E. Fowler Avenue
Tampa, FL 33620
813-974-2897

Anil Pai
Researcher
Florida Solar Energy Center
1679 Clearlake Road
Cocoa, FL 32922-5703
321-638-1442

Geoige Philippidis
Senior Program Manager
Florida International University
HCET-CEAS, 2105 University Park, 10555 West
Flagler Street, EC 2100
Miami, FL 33174
305-348-6628
georgep@hcet.fiu.edu

Muhammad Rahman
Associate Professor
University of South Florida
4202 E. Fowler Avenue
Tampa, FL 33620
813-974-2897

Karthikeyan Ramasamy
Research Associate
Florida Solar Energy Center
1679 Clearlake Road
Cocoa, FL 32922-5703
321-638-1518
karthikeyan@fsec.ucf.edu

Daniel Rini
President-Owner
Rini Technologies, Inc.
3267 Progress Drive
Orlando, FL 32826
407-384-7840

Sudipta Seal
Associate Professor
University of Central Florida
4000 Central Florida Boulevard
Orlando, FL 32816
407-823-5277
sseal@pegasus.cc.ucf.edu

Glenn Sellar
Research Scientist
Jet Propulsion Laboratory
4800 Oak Grove Drive
Pasadena, CA 91109-8099
818-354-4229
gsellar@mail.jpl.nasa.gov

Matt Smith
Engineer
University of South Florida
4202 E. Fowler Avenue
Tampa, FL 33620
813-974-2897

Rajiv Srivastava
Chemical Engineering Program Manager
Florida International University
HCET, EC 2100, 10555 West Flagler Street
Miami, FL 33174
305-348-6621
Rajiv.Srivastava@fiu.edu

Elias Stefanakos
Director, CERC
University of South Florida
4202 E. Fowler Avenue
Tampa, FL 33620
813-974-2897

Kalpathy Sundaram
Professor
University of Central Florida
4000 Central Florida Boulevard
Orlando, FL 32816
407-823-5326
sundaram@mail.ucf.edu

Jay Vaidya
Electrodynamics, Inc.
409 Eastbridge Drive
Oviedo, FL 32765
407-977-1825
info@electrodynamics.net

Raj Vaidyanathan
Associate Professor
University of Central Florida
4000 Central Florida Boulevard
Orlando, FL 32816
407-882-1180
raj@mail.ucf.edu

Steven Van Sciver
Professor
Florida State University
300-Magnet Lab, Mail Code 2740, 1800 E. Paul Dirac Drive
Tallahassee, FL 32310-3706
850-644-0998
vnsciver@magnet.fsu.edu

John Wolan
Assistant Professor
University of South Florida
4202 E. Fowler Avenue
Tampa, FL 33620
813-974-2897

Thomas Wu
Associate Professor
University of Central Florida
4000 Central Florida Boulevard
Orlando, FL 32816
407-823-5357
tomwu@mail.ucf.edu

REPORT DOCUMENTATION PAGE

Form Approved
OMB No. 0704-0188

1. AGENCY USE ONLY (*Leave blank*)	2. REPORT DATE	3. REPORT TYPE AND DATES COVERED
	August 2006	Final Contractor Report

4. TITLE AND SUBTITLE

NASA Hydrogen Research at Florida Universities
Program Year 2003

5. FUNDING NUMBERS

WBS 561581.02.01.03.12
NAG3–2751

6. AUTHOR(S)

David L. Block and Ali Raissi

7. PERFORMING ORGANIZATION NAME(S) AND ADDRESS(ES)

Florida Solar Energy Center
1679 Clearlake Road
Cocoa, Florida 32922–5703

8. PERFORMING ORGANIZATION REPORT NUMBER

E–15559

9. SPONSORING/MONITORING AGENCY NAME(S) AND ADDRESS(ES)

National Aeronautics and Space Administration
Washington, DC 20546–0001

10. SPONSORING/MONITORING AGENCY REPORT NUMBER

NASA CR—2006-214326

11. SUPPLEMENTARY NOTES

Project manager, Timothy D. Smith, Aeronautics Division, NASA Glenn Research Center, organization code PRV, 216–977–7546.

12a. DISTRIBUTION/AVAILABILITY STATEMENT

Unclassified - Unlimited
Subject Categories: 28, 33, and 34

Available electronically at http://gltrs.grc.nasa.gov

This publication is available from the NASA Center for AeroSpace Information, 301–621–0390.

12b. DISTRIBUTION CODE

13. ABSTRACT ***(Maximum 200 words)***

This document presents the final report for the NASA Hydrogen Research at Florida Universities project for program year 2003. This multiyear hydrogen research program has positioned Florida to become a major player in future NASA space and space launch projects. The program is funded by grants from NASA Glenn Research Center with the objective of supporting NASA's hydrogen-related space, space launch and aeronautical research activities. The program conducts over 40 individual projects covering the areas of cryogenics, storage, production, sensors, fuel cells, power and education. At the agency side, this program is managed by NASA Glenn Research Center and at the university side, co-managed by FSEC and the University of Florida with research being conducted by FSEC and seven Florida universities: Florida International University, Florida State University, Florida A&M University, University of Central Florida, University of South Florida, University of West Florida and University of Florida. For detailed information, see the documents section of www.hydrogenresearch.org. This program has teamed these universities with the nation's premier space research center, NASA Glenn, and the nation's premier space launch facility, NASA Kennedy Space Center. It should be noted that the NASA Hydrogen Research at Florida Universities program has provided a shining example and a conduit for seven Florida universities within the SUS to work collaboratively to address a major problem of national interest, hydrogen energy and the future of energy supply in the U.S.

14. SUBJECT TERMS

Hydrogen; Cryogenic fluids; Cryogenic storage; Thermodynamics; Sensors; Hydrogen production

15. NUMBER OF PAGES

302

16. PRICE CODE

17. SECURITY CLASSIFICATION OF REPORT	18. SECURITY CLASSIFICATION OF THIS PAGE	19. SECURITY CLASSIFICATION OF ABSTRACT	20. LIMITATION OF ABSTRACT
Unclassified	Unclassified	Unclassified	